

School of Ocean & Earth Science & Technology
1000 Pope Road
Honolulu, HI 96822

soest

University of Hawaii

AD-A286 580



August 31, 1994

Mrs. Carlena Leufroy
Administrative Contracting Officer
Office of Naval Research
565 S Wilson Avenue
Pasadena, CA 91106-3212

SUBJ: Contract N00014-87-K-0181

DTIC
NOV 23 1994

Dear Mrs. Leufroy:

Attached please find Final Technical Reports, Performance Reports, or transmittal documents for subject grant under the direction of C. Barry Raleigh, Dean, School of Ocean and Earth Science and Technology. Also attached are publications resulting from the research made possible through subject ONR grant.

We are presenting the reports and publications, provided by the PI's, in the proposal/contract format. We will continue to seek the information requested from those who have left the University of Hawaii.

The School of Ocean and Earth Science and Technology, University of Hawaii is grateful for the continued support of the Office of Naval Research for our marine geophysical, oceanographic and atmospheric studies.

Respectfully submitted,

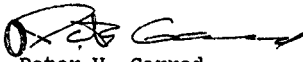

Richard L. Longfield
Director of Administration

94-36124



422 902

94 11 25 07


Peter V. Garrod
Interim Director of Research

RLL:cy

DTIC QUALITY ASSURED 2

Department of Geology and Geophysics • Department of Meteorology • Department of Ocean Engineering
Department of Oceanography • Hawaii Institute of Geophysics • Hawaii Institute of Marine Biology
Hawaii Natural Energy Institute • Hawaii Undersea Research Laboratory • Sea Grant College Program
Joint Institute for Marine and Atmospheric Research • Waikiki Aquarium



AN EQUAL
OPPORTUNITY
EMPLOYER

**Best
Available
Copy**

Contract N00014-87-K-0181
Page Two

Final Reports for ONR Omnibus Proposals

September 1, 1994

Accession For	
NTIS CRA&I	<input checked="" type="checkbox"/>
DTIC TAB	<input type="checkbox"/>
Unannounced	<input type="checkbox"/>
Justification	<i>per. Dts</i>
By _____	
Distribution/	
Availability Codes	
Dist	Avail
<i>A-1</i>	

94-31854



TABLE OF CONTENT

- A. Administration
- B. Dynamics of Small-scale Ocean Motions (P. Muller)
- C. Seismic Anisotropy (G. Fryer)
- D. Low Frequency Modulus Measurements on Marine Sediments and Sedimentary Rocks (M. Manghnani)
- E. Diagnostic and Sedimentological Studies (J. Schoonmacher)
- F. Geoacoustic Studies (M. Manghnani)
- G. Marching the Elastodynamic Wave Equation (N. Frazer)
- H. Theoretical & Computational Studies in Marine Seismology (N. Frazer)
- I. Correction and Quantitative Analysis of SeaMARC II Sonar (T. Reed)
- J. Development of an In-situ Dissolved Hydrogen Sensor for Marine Applications (F. Sansone)
- K. Long-Term ULF/VLF Ambient Ocean Noise Measurements from the Wake Island Hydrophone Array (McCreery)
- L. Calibration of the Acoustic Characteristics of the SeaMARC II System (H. Matsumoto)
- M. Application of Advanced Multichannel Laser Raman... in Marine Chemistry (S. Sharma)
- N. Sensory Perception by Zooplankton: ... a Carnivorous Marine Copepod (J. Yen)

Contract N00014-87-K-0181

Administration

The overall coordination, direction and administration of the projects in the Contract N00014-87-K-0181 was the responsibility of C. Barry Raleigh, Dean of the University of Hawaii School of Ocean and Earth Science and Technology (SOEST). In 1989, the Board of Regents of the University approved the creation of SOEST with the Hawaii Institute of Geophysics (HIG) as a unit of the School.

Dr. Roy Wilkens, HIG-P staff scientist, is the appointed central point for coordination of subtask operational requirements and site review coordination. Any inquiries regarding the individual subtask reports should be directed to Dr. Wilkens or the subtask investigator as appropriate.

All funds received under this grant for the Administration of the contract have been obligated as defined in the contract award.

We are grateful for the continued support of the Office of Naval Research for marine, oceanographic, geophysical and meteorological research at SOEST.

C. Barry Raleigh
C. Barry Raleigh

Contract: N00014-87-K-0181
Physical Oceanography

Dynamics of Small-Scale Oceanic Motions

Peter Muller

1993 *reypo*

Posted: Wed, Feb. 9, 1994 2:11 PM EST

Msg: GGJE-6083-2841

From: P.MULLER

To: ONR.OAP.DIV. (rec)

CC: P.MULLER/OMNET

Subj: ** ONR P.I. Report (PO) ***

<<<<

Peter Muller
University of Hawaii
1000 Pope Road, MSB 307
Honolulu, HI 96822

(808) 956-8081

SCIENCEnet Mailbox: P.MULLER/OMNET

Dynamics of Small-Scale Oceanic Motions

Research Goals:

Description and modeling of the kinematical structure and dynamical processes of oceanic motions that have horizontal scales from a few meters to a few kilometers. Understanding the role that these small-scale motions play in the redistribution and mixing of momentum, potential vorticity, heat, and salt.

Objectives:

Identify the processes that affect the kinematical and dynamical evolution of near-inertial internal gravity waves, especially those processes that can transfer energy out of near-inertial internal waves into the internal wave continuum.

Approach:

Theory and numerical modeling.

Tasks Completed:

Theoretical analysis of model equations that filter out high frequency internal waves, low frequency (geostrophic) currents and barotropic motions and that describe efficiently the kinematical and dynamical evolution of near-inertial internal gravity waves. Determination of the Green's function for a linearly stratified ocean. Analytical representation of the horizontal and vertical dispersion of near-inertial wave packets for a linearly stratified ocean.

Scientific Results:

Fluctuations in the atmospheric windstress excite inertial oscillations in the surface mixed layer and a fraction of the

energy from these oscillations penetrates the ocean interior as near-inertial internal waves. The further kinematic and dynamic evolution of these near-inertial internal waves is not well understood. These waves do not propagate well. (Their horizontal and vertical group velocity approaches zero as their frequencies approach the Coriolis frequency). These waves also do not interact well. (Resonant interactions among near-inertial internal waves are impossible). To investigate the effects that determine the evolution of near-inertial internal waves, model equations have been derived that filter out the effect of high frequency internal waves, low frequency (geostrophic) currents and barotropic motions, but retain the effects of windstress forcing, nonlinear self-interaction, lateral variations of ocean depth, buoyancy frequency and Coriolis frequency, the meridional component of the earth's rotation, and the interaction with a prescribed mean flow. These equations are well suited for theoretical investigations and numerical simulations. The dispersion of near-inertial wave packets for a linearly stratified ocean can be represented analytically.

Accomplishments:

Theoretical analysis of filtered model equations for near-inertial internal waves that allow focused theoretical investigations and efficient numerical simulations.

ONR-Sponsored Publications

- P Lien, R. C. and P. Muller, 1992: Normal mode decomposition of small-scale oceanic motions. *J. Phys. Oceanogr.*, 22, 1583-1595.
- P Muller, P., 1993: Diapycnal mixing in the ocean: a review. In: *Large Eddy Simulation of Complex Engineering and Geophysical Flows*. Cambridge University Press, 455-487.
- PS Schneider, N. and P. Muller, 1993: On the sensitivity of the surface equatorial ocean to the parameterization of vertical mixing. *J. Phys. Oceanogr.* (accepted)
- PS Muller, P., 1993: Ertel's potential vorticity theorem in physical oceanography.
- PI Garwood, R. W., Jr., P. Muller and A. Guest, 1993: Modeling the equatorial entrainment zone: Response to diurnal surface forcing.
- PI Lien, R. C., E. Firing and P. Muller, 1993: Observation of strong inertial oscillations after typhoon Ofa.

PI Kloosterziel, R. C. and P. Muller, 1994: Evolution of near-inertial wave packets, Part I: Projection onto normal modes.

PI Kloosterziel, R. C. and P. Muller, 1994: Evolution of near-inertial wave packets, Part II: Complete solution.

Statistics

- 1 Papers published, refereed journals
- 2 Papers submitted, refereed journals
- 1 Books or chapters published, refereed publication
- 0 Books or chapters submitted, refereed publication
- 0 Invited presentations
- 0 Contributed presentations
- 0 Technical reports and papers, non-refereed journals
- 0 Undergraduate students supported
- 2 Graduate students supported
- 0 Post-docs supported
- 1 Other professional personnel supported

EEO/Minority Support

- 0 Female grad students
- 0 Minority grad students
- 1 Asian grad students
- 0 Female post-docs
- 0 Minority post-docs
- 0 Asian post-docs

Patents and awards

Influences:

D'Asaro, E. A., 1989: The decay of wind-forced mixed layer inertial oscillations due to the Beta effect. J. Geophys. Res., 94, 2045-2056.

Hasselmann, K., 1970: Wave-driven inertial oscillations. Geophys. Fluid Dyn., 1, 436-502.

Kunze, E., 1985: Near inertial wave propagation in geostrophic shear. J. Phys. Oceanogr., 15, 544-565.

Watson, K. M., 1990: The coupling of surface and internal gravity waves. J. Phys. Oceanogr., 20, 1233-1248.

<<<<

Posted: Thu, Nov 5, 1992 4:58 PM EST Msg: LGJC-5440-3880
From: P.MULLER
To: ONR.OAP.DIV (rec)
CC: P.MULLER/OMNET
Subj: ** ONR P.I. Report (PO) ***

<<<<
Peter Muller
University of Hawaii
1000 Pope Road, MSB 307
Honolulu, HI 96822

(808)956-8081

SCIENCEnet Mailbox: P.MULLER/OMNET

Dynamics of Small-Scale Oceanic Motions

Research Goals:

Description and modeling of the kinematical structure and dynamical processes of oceanic motions that have horizontal scales from a few meters to a few kilometers. Understanding the role that these small-scale motions play in the redistribution and mixing of momentum, potential vorticity, heat, and salt. Contribute to the construction of a global numerical model that will predict this redistribution and mixing.

Objectives:

Identify the processes that affect the kinematical and dynamical evolution of near-inertial internal gravity waves, especially those processes that can transfer energy out of near-inertial internal waves into the internal wave continuum. Simulate these processes in a numerical model. Assess the feasibility of monitoring the upper ocean internal wave field from routinely taken measurements with ship mounted Acoustic Doppler Current Profilers. Assess the feasibility of using such observations for verification and calibration of numerical models.

Approach:

Blend of data analysis, theory and numerical modeling.

Tasks Completed:

Derivation of model equations that filter out high frequency

internal waves, low frequency (geostrophic) currents and barotropic motions and describe efficiently the kinematical and dynamical evolution of near-inertial internal gravity waves. Initial theoretical analysis and numerical implementation of these equations. Preparation of current measurements taken by a ship mounted Acoustic Doppler Current Profiler in the wake of hurricane Ofa for model-data comparison.

Scientific Results:

Fluctuations in the atmospheric windstress excite inertial oscillations in the surface mixed layer and a fraction of the energy from these oscillations penetrates the ocean interior as near-inertial internal waves. The further kinematic and dynamic evolution of these near-inertial internal waves is not well understood. These waves do not propagate well. (Their horizontal and vertical group velocity approaches zero as their frequencies approach the Coriolis frequency). These waves also do not interact well. (Resonant interactions among near-inertial internal waves are impossible). To investigate the effects that determine the evolution of near-inertial internal waves, model equations can be derived that filter out the effect of high frequency internal waves, low frequency (geostrophic) currents and barotropic motions, but retain the effects of windstress forcing, nonlinear self-interaction, lateral variations of ocean depth, buoyancy frequency and Coriolis frequency, the meridional component of the earth's rotation, and the interaction with a prescribed mean flow. These equations are well suited for theoretical investigations and numerical simulation.

Accomplishments:

Derivation of filtered model equations for near-inertial internal waves that allow focused theoretical investigations and efficient numerical simulation.

ONR-Sponsored Publications

- P- Lien, R.-C., and P. Muller, 1992: Consistency relations of gravity and vortical modes in the ocean. *Deep Sea Res.*, 39, 1595-1612.
- PS- Schneider, N., and P. Muller, 1992: On the sensitivity of the surface equatorial ocean to the parameterization of vertical mixing. *J. Phys. Oceanogr.*
- PS- Muller, P., 1992: Diapycnal Mixing in the Ocean: a review. In: "Large Eddy Simulation of Complex Engineering and Geophysical Flows, Cambridge

University Press." (in press)

- PS- Lien, R.-C., and P. Muller, 1991: Normal mode decomposition of small-scale oceanic motions. J. Phys. Oceanogr. (in press)
- PI- Kunze, E., and P. Muller, 1991: Internal wave-driven Ekman flow in the ocean interior.
- PI- Garwood, R.W., Jr., P.C. Chu, P. Muller and N. Schneider, 1991: Modeling the equatorial entrainment zone: Response to diurnal surface forcing.
- PI- Lien, R.-C., E. Firing and P. Muller, 1992: Observations of strong inertial oscillations after the passage of typhoon Ofa.
- PI- Muller, P., 1991: Ertel's potential vorticity theorem revisited.
- R- Lien, R.-C., and P. Muller, 1991: Estimates of small-scale horizontal divergence and relative vorticity in the ocean. In: "Dynamics of Oceanic Internal Gravity Waves. Proceedings, 'Aha Huliko'a Hawaiian Winter Workshop, School of Ocean and Earth Science and Technology, Special Publication." 143-156.

Statistics

- 1 Papers published, refereed journals
- 3 Papers submitted, refereed journals
- 0 Books or chapters published, refereed publication
- 0 Books or chapters submitted, refereed publication
- 0 Invited presentations
- 0 Contributed presentations
- 1 Technical reports and papers, non-refereed journals
- 0 Undergraduate students supported
- 2 Graduate students supported
- 0 Post-docs supported
- 1 Other professional personnel supported

FFO Minority Support

- 0 Female grad students
- 0 Minority grad students
- 0 Asian grad students
- 0 Female post-docs
- 0 Minority post-docs
- 0 Asian post-docs

Patents and awards

Influences:

D'Asaro E.A., 1989: The decay of wind-forced mixed layer inertial oscillations due to the Beta effect. J. Geophys. Res., 94, 2045-2056.

Hasselmann, K., 1970: Wave-driven inertial oscillations. Geophys. Fluid Dyn., 1, 463-502.

Kunze, E., 1985: Near inertial wave propagation in geostrophic shear. J. Phys. Oceanogr., 15, 544-565.

Watson, K.M., 1990: The coupling of surface and internal gravity waves. J. Phys. Oceanogr., 20, 1233-1248.

<<<<

TELEMAIL - P.MULLER

November 8, 1991

0 Minority grad students
0 Asian grad students
0 Female post-docs
0 Minority post-docs
0 Asian post-docs

Patents and awards

Influences:

Brink, K.H. 1989: Evidence for wind-driven current fluctuations in the Western North Atlantic. J. Geophys. Res., 94, 2029-2044.

Luther, D., Chave, A.D., Villoux, J., and P. Spain, 1990: Evidence for local and nonlocal barotropic responses to atmospheric forcing during bempex. Geophysical Research Letters, 17, 949-952.

<<<<

Posted: Fri, Nov 8, 1991 7:28 PM EST

Msg: BGJB-4990-4028

From: P.MULLER

To: ONR.OAP.DIV (rec)

CC: P.MULLER/OMNET

Subj: ** ONR P.I./Report (PO) ***

<<<<

Peter Muller

University of Hawaii, Department of Oceanography

1000 Pope Road, MSB 301

Honolulu, Hawaii 96822

(808) 956-8081

SCIENCEnet Mailbox: P.MULLER/OMNET

The Dynamics of Oceanic Internal Gravity Waves

Research Goals:

Understanding the dynamics of oceanic internal gravity waves and their role in redistributing and mixing momentum, potential vorticity, heat, and salt.

Objectives:

Review our current knowledge and understanding of the dynamics of oceanic internal gravity waves. Assess the feasibility of constructing a global model to predict the internal wave field and (diapycnal) mixing.

Approach:

Conducting workshop with leading experts in the field.

November 8, 1991

Tasks Completed:

A four-day workshop on "The Dynamics of Oceanic Internal Gravity Waves" was convened from January 15 to 18 in Honolulu, Hawaii. The workshop brought together ocean theorists, modelers and observers and a few meteorologists.

The lectures of the participants are published in the proceedings volume:

Muller, P. and D. Henderson, 1991: Dynamics of Oceanic Internal Gravity Waves. Proceedings, "Aha Huliko'a Hawaiian Winter Workshop", School of Ocean and Earth Science and Technology, Special Publication.

and in the summary article:

Muller, P., E. D'Asaro and G. Holloway, 1991: Internal Gravity Waves and Mixing. EOS, Transactions, American Geophysical Union.

Scientific Results:

Internal waves and their effect on larger scales remain a basic and important issue. Recent progress suggests that we have the tools and conceptual framework to predict the internal wave field and diapycnal diffusivities globally in the not too distant future. Such optimism is not warranted for the prediction of internal wave induced momentum fluxes and isopycnal dispersion. Present understanding is focussed on the upper ocean and thermocline. We are less clear about internal wave behavior in shallow seas, the abyss and near boundaries.

Accomplishments:

Identification of the issues that need to be addressed in order to understand the physics necessary for the construction of a global internal wave model.

ONR-Sponsored Publications

- PS- Muller, P., E. A'Asaro and G. Holloway, 1991: Internal Gravity Waves and Mixing. EOS, Transactions, American Geophysical Union.
- R- Muller, P., and D. Henderson, 1991: Dynamics of Oceanic Internal Gravity Waves. Proceedings, "Aha Huliko'a Hawaiian Winter Workshop, School of Ocean and Earth Science and Technology, Special Publication."

Statistics

- 0 Papers published, refereed journals
- 0 Papers submitted, refereed journals

TELEMAIL - P.MULLER

November 8, 1991

- 0 Books or chapters published, refereed publication
- 0 Books or chapters submitted, refereed publication
- 0 Invited presentations
- 0 Contributed presentations
- 2 Technical reports and papers, non-refereed journals
- 0 Undergraduate students supported
- 0 Graduate students supported
- 0 Post-docs supported
- 0 Other professional personnel supported

EEO/Minority Support

- 0 Female grad students
- 0 Minority grad students
- 0 Asian grad students
- 0 Female post-docs
- 0 Minority post-docs
- 0 Asian post-docs

Patents and awards

Influences:

WAMDI Group (Hasselmann, S., Hasselmann K., Bauer, E., Janssen, P.A.E.M., Koman, G.J., Bertotti, L., Lionello, P., Guillaume, A., Cardone, V.C., Greenwood, J.A., Reistad, M., Zambresku, L., and J.A. Ewing, 1988: The WAM Model-A Third Generation Ocean Wave Prediction Model. J. Phys. Oceano. 18, 1775-1810.

<<<<

TELEMAIL - P.MULLER

November 5, 1990

Posted: Mon, Nov 5, 1990 8:07 PM EST
From: P.MULLER
To: ONR.OAP.DIV (rec)
CC: P.MULLER/OMNET
Subj: ** ONR P.I. Report (PO) ***

Msg: FGJA-4470-4134

<<<<
Peter Muller
University of Hawaii, Department of Oceanography
1000 Pope Road, MSB 307
Honolulu, HI 96822

808/956-8081

SCIENCEnet Mailbox: P.MULLER/OMNET

Dynamics of small-scale oceanic motions

Research Goals:

Description and modeling of the kinematical structure and dynamical processes of oceanic motions that have horizontal scales from a few meters to a few kilometers. Understanding the role that these small-scale motions play in the redistribution and mixing of momentum, potential vorticity, heat, and salt.

Objectives:

Arriving at a complete kinematical description of small-scale motions in terms of gravity and vortical (i.e., potential vorticity carrying) motions.

Assessing the feasibility of monitoring internal wave parameters from routinely taken measurements with ship mounted Acoustic Doppler Current Profilers.

Determining and parameterizing the effect of internal gravity waves absorbed in critical layers.

Approach:

Theoretical and data analyses.

Tasks Completed:

Estimation of frequency spectra of relative vorticity and horizontal divergence from three-point measurements in the IWEX (Muller et al., 1976) array. Comparison with the predictions of Garrett and Munk spectral models.

Development of software to calculate spectra and to extract inertial and tidal amplitudes from Acoustic Doppler Current Profiler data taken under a variety of circumstances.

November 5, 1990

Theoretical estimation of the amount of momentum and energy lost in critical layers by an internal gravity wave field of Garrett and Munk spectral intensity propagating downward into an ambient geostrophic shear.

Scientific Results:

Estimates of relative vorticity and horizontal divergence from three-point measurements suffer from aliasing and mutual contamination. Both effects can be expressed by array response or filter functions. Estimated frequency spectra of horizontal divergence agree well with the prediction of the Garrett and Munk model at all resolved horizontal scales. Estimated spectra of relative vorticity are not reproduced by the Garrett and Munk model at small horizontal scales. The number of horizontal levels in the IWEX array is not sufficient to determine whether this discrepancy is due to the existence of small-scale vortical motions or to the Garrett and Munk spectral model not correctly representing small-scale internal gravity waves.

Internal waves absorbed in vertical critical layers of an ambient geostrophic shear are found to generate transverse Ekman flows of $O(0.01 \text{ cm s}^{-1})$, which is insignificant, and to lose energy at a rate of up to 5 nanowatts per kilogram, which is comparable to the energy loss rate suggested for internal wave breaking due to chance superposition.

Accomplishments:

Estimate of relative vorticity and horizontal divergence for horizontal scales from about 1 km to 5 m and in the frequency range between the local Coriolis and Brunt Vaisala frequencies.

Theoretical estimate of the momentum and energy lost by internal waves in vertical critical layers of an ambient geostrophic shear.

REFERENCES

Muller, P., D. J. Olbers and J. Willebrand, 1978: The IWEX spectrum. J. Geophys. Res., 83, 479-500.

ONR-Sponsored Publications

P Chu, P. C., R. Garwood, Jr., and P. Muller, 1990:
Unstable and damped modes in coupled ocean mixed layer and cloud models. J. Marine Systems, 1, 1-11.

November 5, 1990

- PS Garwood, R. W., Jr., P. C. Chu, P. Muller and N. Schneider, 1990: Modeling the equatorial entrainment zone: Response to diurnal surface forcing. J. Geophys. Res.
- PI Kunze, E. and P. Muller: Internal wave-driven Ekman flow in the ocean interior.
- PI Lien, R. C. and P. Muller: Consistency relations of gravity and vortical modes.
- PI Muller, P. Diapycnal mixing in the ocean. Proceedings of LES Workshop, Lecture Notes in Engineering, Springer-Verlag.
- R Garwood, R. W., P. C. Chu, P. Muller and N. Schneider, 1989: Equatorial entrainment zone: The diurnal cycle. In: Proceedings of the Western Pacific International Meeting and Workshop on TOGA/COARE, 435-443.
- C Lien, R. C. and P. Muller: Normal mode decomposition of small-scale oceanic motions. AGU/ASLO Ocean Sciences Meeting, New Orleans, February 1990.
- C Karcher, M., A. Lippert, and P. Muller: The influence of spatially varying eddy-diffusivity on the deep circulation. European Geophysical Society XV General Assembly, Copenhagen, Denmark, April 1990.
- C Schneider, N., P. Muller, and R. W. Garwood, Jr.: Richardson number adjustment of the Yoshida jet. International TOGA Scientific Conference, Honolulu, July 1990.
- IC Muller, P.: Diapycnal mixing in the ocean: a review. AGU/ASLO Ocean Sciences Meeting, New Orleans, February 1990.

Statistics

- 1 Papers published, refereed journals
- 1 Papers submitted, refereed journals
- 0 Books or chapters published, refereed publication
- 0 Books or chapters submitted, refereed publication
- 1 Invited presentations
- 3 Contributed presentations
- 1 Technical reports and papers, non-refereed journals
- 0 Undergraduate students supported
- 1 Graduate students supported
- 1 Post-docs supported
- 0 Other professional personnel supported

TELEMAIL - P.MULLER

November 5, 1990

EEO/Minority Support
0 Female grad students
0 Minority grad students
0 Asian grad students
0 Female post-docs
0 Minority post-docs
1 Asian post-docs

Patents and awards
<<<<

TELEMAIL - P.MULLER

November 30, 1989

Posted: Thu, Nov 30, 1989 3:53 PM EST

Msg: KGIJ-4104-7699

From: P.MULLER

To: D.Bretschneider

CC: P.MULLER/OMNET

Subj: ** OAR P.I. Report (PO) ***

<<<<

Peter Muller

University of Hawaii, Department of Oceanography

1000 Pope Road, MSB 307

Honolulu, HI 96822

(808) 948-8081

SCIENCEnet Mailbox: P.MULLER/OMNET

Dynamics of small-scale oceanic motions

Research Goals:

Description and modeling of the kinematical structure and dynamical processes of oceanic motions that have horizontal scales from a few meters to a few kilometers. Understanding the role that these small-scale motions play in the redistribution and mixing of momentum, potential vorticity, heat, and salt.

Objectives:

Arriving at a complete kinematical description of small-scale motions in terms of gravity and vortical (i.e., potential vorticity carrying) motions. Developing and applying consistency relations for the vortical mode. Developing and applying methods to separate gravity and vortical motions.

Approach:

Theoretical and data analyses.

Tasks Completed:

Derivation of the algebraic formulae that underlie a normal mode decomposition into gravity and vortical modes. Normal mode decomposition of the IWEX data set (Muller, et al., 1978). Development of consistency relations for vortical motions and application to a few miscellaneous data sets.

Scientific Results:

Small-scale motions can be viewed as a superposition of gravity and vortical motions. Vortical motions carry the potential vorticity of the flow and are "stagnant." Gravity motions do not carry potential vorticity and "propagate." A separation can be obtained by a normal mode decomposition based on the eigenvectors of the linearized problem. Normal mode decomposition of the IWEX data set is complicated by aliasing and Doppler shifting but indicates that current finestructure is vortical motion.

November 30, 1989

Accomplishments:

Normal mode decomposition of the IWEX data set into gravity and vortical modes. Development of new consistency relations for gravity and vortical motions.

REFERENCES:

Muller, P., D. J. Olbers and J. Willebrand, 1978: The IWEX spectrum. J. Geophys. Res., 83, 479-500.

ONR-Sponsored Publications

- PS Chu, P. C., R. Garwood and P. Muller: Unstable and damped modes in coupled ocean mixed layer and cloud models, J. Mar. Systems.
- PI Kunze, E. and P. Muller: Internal wave-driven Ekman flows in the ocean interior.
- PI Lien, R. C. and P. Muller: Consistency relations for gravity and vortical motions: Theory and application.
- PI Lien, R. C. and P. Muller: Normal mode decomposition of small-scale motions in the ocean.
- R Kunze, E. and P. Muller, 1989: The effect of internal waves on geostrophic shear. In: "Parameterization of small-scale processes, Proceedings, 'Aha Huliko'a Hawaiian Winter Workshop, Hawaii Institute of Geophysics, Special Publication," 271-285.
- C Chu, P. C., R. W. Garwood, Jr., and P. Muller: Thermodynamic feedback between clouds and the oceanic surface mixed layer, International Liege Colloquium on Ocean Hydrodynamics, Liege, May 1989.
- C Lien, R. C. and P. Muller: Consistency test of one-dimensional measurements: Gravity or vortical motion? AGU Fall Meeting and ASLO Winter Meeting, San Francisco, December 1988.
- IC Muller, P.: Separation of vortical and gravity motion, American Meteorological Society Conference on Waves and Stability in the Ocean and Atmosphere, San Francisco, April 1989.

Statistics

- 0 Papers published, refereed journals
- 1 Papers submitted, refereed journals
- 0 Books or chapters published, refereed publication
- 0 Books or chapters submitted, refereed publication
- 1 Invited presentations

TELEMAIL - P.MULLER

November 30, 1989

- 2 Contributed presentations
- 1 Technical reports and papers, non-refereed journals
- 0 Undergraduate students supported
- 2 Graduate students supported
- 0 Post-docs supported
- 1 Other professional personnel supported

EEO/Minority Support

- 0 Female grad students
- 0 Minority grad students
- 1 Asian grad students
- 0 Female post-docs
- 0 Minority post-docs
- 0 Asian post-docs

Patents and awards

<<<<

TELEMAIL - P.MULLER

December 21, 1988

Posted: Wed Dec 21, 1988 4:00 PM EST
From: P.MULLER
To: D.EVANS.ONR
CC: P.MULLER/OMNET
Subj: ** ONR P.I. Report (P0) **
<<<<

Msg: GGII-3836-3625

Principal Investigator - Peter Muller

Title of Research Project - Dynamics of small-scale oceanic motions

Abstract

RESEARCH GOALS: Understanding (i) of the fundamental processes that govern the dynamics of small-scale oceanic motions, with emphasis on internal gravity waves, vortical motion, turbulence and mixing, and (ii) of the effect of these motions on larger-scale flows.

OBJECTIVE: Complete and consistent kinematical description of small-scale motions, viewed as a superposition of gravity and vortical motions. Estimate of Ertel's potential vorticity and linear perturbation potential vorticity. Development and application of consistency relations that test kinematical hypotheses.

APPROACH: Theoretical investigations and analysis of existing data sets.

TASKS COMPLETED: Estimate of linear perturbation potential vorticity from the Internal Wave Experiment (IWEX) data set. Derivation of consistency relation for the vortical mode.

SCIENTIFIC RESULTS: Small-scale motions can be decomposed into a gravity and a vortical mode. The vortical mode carries the potential vorticity of the flow.

The amplitude and space and time scales of (linear perturbation) potential vorticity at small scales are estimated from the IWEX data set (Muller et al., 1978). The IWEX array resolves horizontal and vertical scales from a few meters to about one kilometer. The (linear perturbation) potential vorticity has a variance of about $1.0E-6$ $1/s^2$, implying a Rossby number and vertical strain of order 10. The associated total energy is $2.0E-4$ m^2m/s^2 and the associated inverse Richardson number is 0.7. The horizontal wavenumber spectrum has a $+2/3$ power law. The vortical mode might hence be the major contributor to the observed shear in the ocean.

December 21, 1988

Consistency relations were derived for vortical motions (i.e., linear relations among one-dimensional cross-spectra of horizontal velocity and vertical displacement). Contrary to internal gravity wave consistency relations (Fofonoff, 1969), which only exist in frequency space, vortical mode consistency relations also exist in horizontal and vertical wavenumber space. These consistency relations provide a powerful tool for the analysis of low resolution data sets.

ACCOMPLISHMENTS: Estimate of (i) (linear perturbation) potential vorticity at small scales, and (ii) contribution of the vortical (i.e., potential vorticity carrying) mode to the energy and shear of small-scale motions.

REFERENCES: Fofonoff, N. P., 1969. Spectral characteristics of internal waves in the ocean. Deep Sea Res., 16*, Suppl., 59-71.

Muller, P., et al., 1978. The IWEX spectrum. J. Geophys. Res., 83*, 479-500.

PI'S Institution and Address

University of Hawaii, Department of Oceanography
1000 Pope Road, MSB 429
Honolulu, HI 96822

(808) 948-8081

SCIENCEnet Mailbox: P.MULLER/OMNET

Papers published in refereed journals

- | | |
|------|--|
| PI | Lien, R. C. and P. Muller, Ertel's potential vorticity at small scales |
| PI | Lien, R. C. and P. Muller, Consistency relations for gravity and vortical motions: Theory and application |
| 88-P | Muller, P., R. C. Lien and R. Williams, Estimates of potential vorticity, JPO 18* (1988) 401 |
| 88-P | Muller, P., Small-scale turbulence and mixing in the ocean, Elsevier Oceanography Series 46* (1988) 285 |
| 87-P | Muller, P. and H. Ross, On the meridional structure of the equatorial mixed layer, Oceanologica Acta 6* (1987) 7 |

TELEMAIL - P. MULLER

December 21, 1988

- 87-P Garwood, R. W., Jr., P. C. Gallacher and P. Muller, Reply to "Comments on 'Wind direction and equilibrium mixed layer depth: General theory'" by H. J. S. Fernando, JPO 17* (1987) 171

Papers accepted or in press, refereed journals

Books or chapters published, refereed non-serial publications

Books or chapters accepted or in press, refereed non-serial

Invited presentations at scientific conferences

- 87-IC Muller, P., Small-scale vortical motions, International Liege Colloquium on Ocean Hydrodynamics, Liege, May 1987

Contributed presentations at scientific conferences

- 87-C Muller, P. and R. Williams, The vortical mode in IWEX. AGU Fall Meeting and ASLO Winter Meeting. San Francisco, December 1986.

Technical reports and papers in non-refereed journals

- 87-R Muller, P. and D. Henderson, Editors, Dynamics of the oceanic surface mixed layer. Proceedings, 'Aha Huliko'a Hawaiian Winter Workshop, Hawaii Institute of Geophysics, Special Publication (1987) 310 pp.

Patents filed or granted

Number of undergraduate students supported (at least part time) - 0

Number of graduate students supported (at least part time) - 1

Number of post-docs supported (at least part time) - 0

Number of other professional personnel supported (at least part time) - 1

TELEMAIL - P. MULLER

December 21, 1988

Awards, Honors and Prizes (please list)

Names of Graduate Students (GS) and Post-Docs (PD)

Ren-Chieh Lien
<<<<

Contract: N00014-87-K-0181
Seismology & Acoustics

Seismic Anisotropy

Gerard Fryer



University of Hawaii at Manoa

Hawaii Institute of Geophysics
2525 Correa Road • Honolulu, Hawaii 96822
Cable Address: UNIHAW
April 4, 1990

Dr. Randall S. Jacobson
Office of Naval Research, Code 1125GG
800 N. Quincy St.
Arlington VA 22217-5000

Dear Dr. Jacobson,

Enclosed is the Final Technical Report for ONR Grant N00014-89-J-1483, *Seismic Anisotropy and Large-Scale Anisotropy in the Ocean Floor*.

Thank you for your support of this work.

Sincerely,

Gerard J. Fryer
Principal Investigator

Dist.: Administrative Grants Officer
ONR Resident Representative N47092
Administrative Contracting Officer
California Inst. of Technology
565 South Wilson Ave.
Pasadena, CA 91106-3212

Director, Naval Research Laboratory
Attn: Code 2627
Washington, DC 20375

Defense Technical Information Center
Building 5, Cameron Station
Alexandria, VA 22314

cc: Paul K. Kakugawa
Assistant Director
Office of Research Administration
University of Hawaii at Manoa

FINAL TECHNICAL REPORT

ONR Grant N00014-89-J-1483

**SEISMIC ANISOTROPY AND LARGE-SCALE POROSITY
IN THE OCEAN FLOOR**

Grant Duration: 1 January 1985 - 31 December 1989.

Principal Investigator: Gerard J. Fryer
Internet: gfryer@soest.hawaii.edu
Telephone: (808) 948-7875

Institution: Hawaii Institute of Geophysics
University of Hawaii at Manoa
2525 Correa Road
Honolulu, HI 96822

FINAL TECHNICAL REPORT

Seismic Anisotropy and Large-Scale Porosity in the Ocean Floor

N00014-89-J-1483

1 January 1989 - 31 December 1989

Gerard J. Fryer, P.I.

Hawaii Institute of Geophysics

University of Hawaii at Manoa

2525 Correa Road

Honolulu, HI 96822

Rationale for the Study

Fracturing, flow layering, brecciation, and vesiculation in the lavas forming the uppermost igneous crust result in high porosity and induce an elastic anisotropy. Anisotropy resulting from horizontal fracturing or interbedded horizontal lava flows displays no azimuthal dependence, making it hidden to traditional seismology and inviting misinterpretation of seismic data. Porosity too seems poorly constrained by seismic data, largely because of inadequacies in existing theoretical velocity-porosity relationships. Fracture-induced anisotropy and large-scale porosity, however, must be strongly affected by ocean-floor processes such as hydrothermal deposition and crustal ageing. This project was one in a continuing series of ONR-funded projects to assess the seismic effects of this anisotropy and porosity, to see if these properties can be deduced from field seismic measurements, and to explore how they might be used to investigate bottom processes.

Project Objectives

This project had two specific goals. Under previous ONR support (Contract N00014-87-K-0181) we had claimed that measurement of anisotropy can be accomplished seismically if both source and receiver are on the bottom, provided that both *SH* and *SV* information is obtained. We wished to verify this claim using data from a high-resolution shallow water experiment run by Rondout Associates and Woods Hole Oceanographic Institute using on-bottom sources and three-component receivers (only if we could demonstrate our abilities on shallow-water sediments could measurement on deep-water crust be contemplated). During 1988 we had managed to model the horizontal geophone data from one line by invoking transverse isotropy in the bottom, but without also explaining the vertical data our claim for anisotropy was unconvincing. We wished to refine our models so that all seismic energy was adequately explained.

The second objective was to refine our understanding of velocity-porosity relationships in volcanic ocean floor. In 1988 we presented an explanation of how hydrothermal sealing of cracks and fractures can explain the rapid increase in seismic velocities with age in young igneous crust by modifying the mean void aspect ratio, but that explanation was purely qualitative. We wished to tighten the theory, predict some hard numbers from it, and see if our explanation could withstand comparison with ocean drilling results.

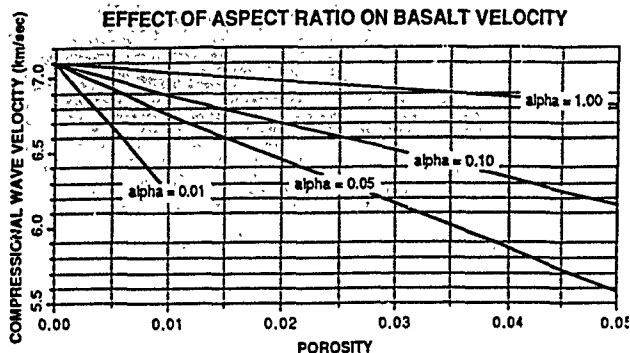


Figure 1: P -velocity versus porosity for different aspect ratios α .

Accomplishments

Our analysis of the Rondout/WHOI shallow water data is now complete. Through iterative match of synthetic seismograms to data we have been able to match all three components on two crossing lines using the same transversely isotropic structure, demonstrating that ocean bottom anisotropy can be measured without resorting to downhole seismometers. The anisotropy demanded by the data is large (P -wave speed variation of 12%), but is entirely consistent with the bottom being made up of interbedded sand and silty clays. A paper describing this work has been submitted to *Geophysical Journal International*, where it is currently in review. A preprint of this paper is included as the Appendix to this report.

Our theory of crustal ageing is advancing and is necessarily expanding into an assessment of depth-dependent variation as well. Our basic idea is this: in volcanic crust, which has void space varying from thin fractures to the much more quiddimensional interstices between pillows, hydrothermal mineralization seals the thin voids first so that the mean aspect ratio increases with time (i.e., void space becomes more circular). Porosity resulting from narrow voids has a very strong effect on velocity (Figure 1). When there is a distribution of aspect ratios, sealing the narrowest voids will reduce porosity only slightly but will dramatically increase the velocity. Such change of mean aspect ratio, both with depth and with age, is strongly supported by sonic and neutron porosity logs from the drilling program. At site 504B (6 Ma), we find that the velocity varies less and less rapidly with porosity as depth increases (Figure 2), suggesting a downhole increase in the mean aspect ratio. At the much older Site 418A (110 Ma), within the 400 m of basement logged, all depths display the same velocity-porosity relationship as is found at about 400 m into basement at 504B (although porosities themselves still systematically decrease downhole). If the crust at 418A ever evolved through a 504B-like stage, then there

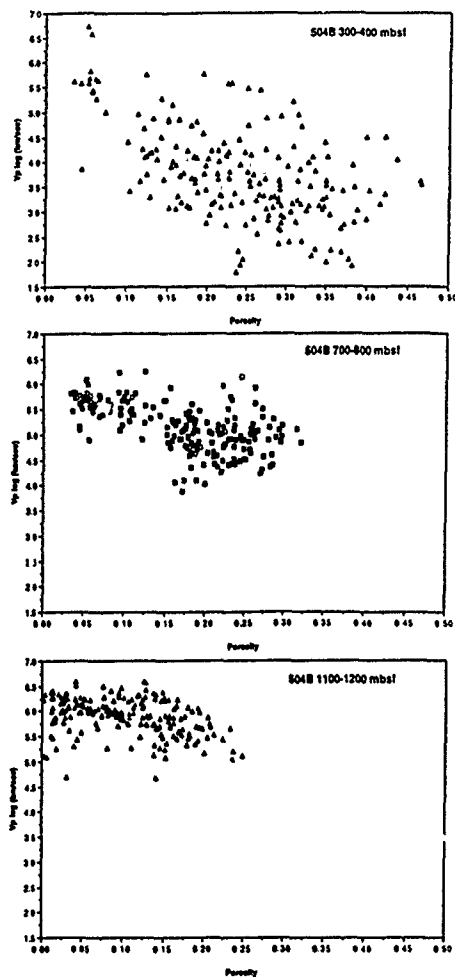


Figure 2: Velocity-Porosity distributions at Hole 504B from downhole logs. The decrease in slope downhole indicates an increase in the mean aspect ratio (see Figure 1). Basement begins at 300 m below seafloor (mbsf).

must have been subsequent crack filling and reduction in the mean aspect ratio within the upper few hundred meters, precisely what we would have predicted if alteration products seal narrow voids first. A paper describing this work will be submitted in summer 1990.

Through appeal to rock physics, seismic wave propagation, downhole logging, and hydrothermal geochemistry, we are now expanding the porosity study into a multidisciplinary investigation (funded by ONR) of how geological processes affect seismic structure of the shallow crust.

Publications Supported by This Project

- Berge, P. A., and G. J. Fryer, 1989. *In situ* measurement of anisotropy in marine sediments [Abstract], *Seismological Research Letters*, 60, 16.
- Berge, P. A., and G. J. Fryer, 1989. *In situ* measurement of anisotropy in marine sediments using multicomponent data [Abstract], *SEG Research Workshop on Recording and Processing Vector Wavefields, Snowbird, Utah, August 13-17, 1989, Technical Abstracts*, 71.
- Berge, P. A., S. Mallick, G. J. Fryer, N. Barstow, J. A. Carter, G. H. Sutton, and J. Ewing, *In situ* measurement of transverse isotropy in shallow-water marine sediments, submitted to *Geophys. J. Int.* [Reproduced here as Appendix.]
- Fryer, G. J., and R. H. Wilkens, 1989. Making sense of seismic velocities in shallow oceanic crust [Abstract], *Seismological Research Letters*, 60, 16.

PUBLICATIONS FUNDED BY ONR, N00014-87-K-0181

Subtask: Seismic Anisotropy

P.I. Gerard J. Fryer

The following papers and thesis were supported or partially supported by N00014-87-K-0181. ONR has already recieved copies of all these papers.

Frazer, L.N., and G.J. Fryer, 1989, Useful properties of the system matrix for a homogeneous anisotropic visco-elastic solid, *Geophys. J. RAS DGG EGS*, **97**, 173-177.

Fryer, G.J., and L.N. Frazer, 1987. Seismic waves in stratified anisotropic media — II. Elastodynamic eigensolutions for some anisotropic systems, *Geophys. J. R. Astron. Soc.*, **91**, 73-101.

Fryer, G.J., D.J. Miller, and P.A. Berge, 1989. Seismic anisotropy and age-dependent structure of the upper oceanic crust, in Sinton, J.M. (ed.), *Evolution of Mid Oceanic Ridges*, pp. 1-8, Geophysical Monograph 57, American Geophysical Union, Washington, D.C.

Miller, D.J., Transverse isotropy: some consequences for travel time inversion and models of the oceanic crust, M.S. Thesis, University of Hawaii, 52pp.

Phinney, R.A., R.I. Odom, and G.J. Fryer, 1987 Rapid generation of synthetic seismograms in layered media by vectorization of the algorithm, *Bull. Seismol. Soc. Am.*, **77**, 2218-2226.

Contract: N00014-87-K-0181
Seismology & Acoustics

**Low Frequency Modulus Measurements on Marine Sediments
and Sedimentary Rocks**

M. Manghnani

Low Frequency Attenuation and Modulus Measurements on Marine Sediments & Sedimentary Rocks

Measurements on Synthetic Materials

Our efforts during the current contract period (March 1987 - February 1988) have focused on (a) improving the repeatability and precision of our low-frequency measurements, particularly at very low frequencies (< 0.1 Hz), on well-characterized samples, (b) establishing the useful frequency range of our apparatus, and (c) begin measurements on well characterized sedimentary rocks.

Figure 2 shows our measurements of the Young's modulus and Q^{-1} of a sample of Lucite, a synthetic polymer. Also shown on this plot are the Lucite data of Spencer (1981) and the straight line fit of Lagakos et al. (1986) to their data for Lucite in the frequency range 200 Hz - 1 MHz. Between 1 Hz and 100 Hz our data is in good agreement with the extrapolated line of Lagakos et al. (1986) and also with the modulus data of Spencer (1981). Apparently, a resonant peak exists in our data at a frequency of about 300 Hz, which distorts our results above about 100 Hz. We have observed this distortion in all our data to date and consequently now only collect data up to 100 Hz. However, note that we have extended our frequency range down to 0.01 Hz which gives us a span of four decades. While we are encouraged by our results to date, we feel that the long-term repeatability should continue to receive attention and support.

Again, turning to Figure 2, note the well-defined relaxation peak at about 0.1 Hz. Spencer (1981) fitted his Lucite data with a relaxation peak at 5 Hz, which was the lowest frequency that he measured. Our data clearly demonstrate the large error in estimating the center of a peak from data which only spans one side of it.

Figure 3 shows Young's Modulus and Q^{-1} for a well-characterized synthetic sample of recemented glass beads, supplied to us by Schlumberger. Note the well defined linear variation of modulus with log frequency. The offset at 0.1 Hz is a point where data collection was stopped and restarted several hours later. We interpret this offset as being due to temperature variation as the offset did not appear in a continuous run from 0.05 to 0.5 Hz. Temperature variations are undoubtedly also causing noise, particularly in the phase (Q^{-1}) measurements at very low (< 1 Hz) frequencies. For this material, Q^{-1} is almost independent of frequency i.e. it is very close to being linearly viscoelastic. For small (< 0.1) values of Q^{-1} which are frequency independent, linear viscoelastic theory (e.g. Kolsky, 1964) predicts the

BEREA SANDSTONE (room-dry)

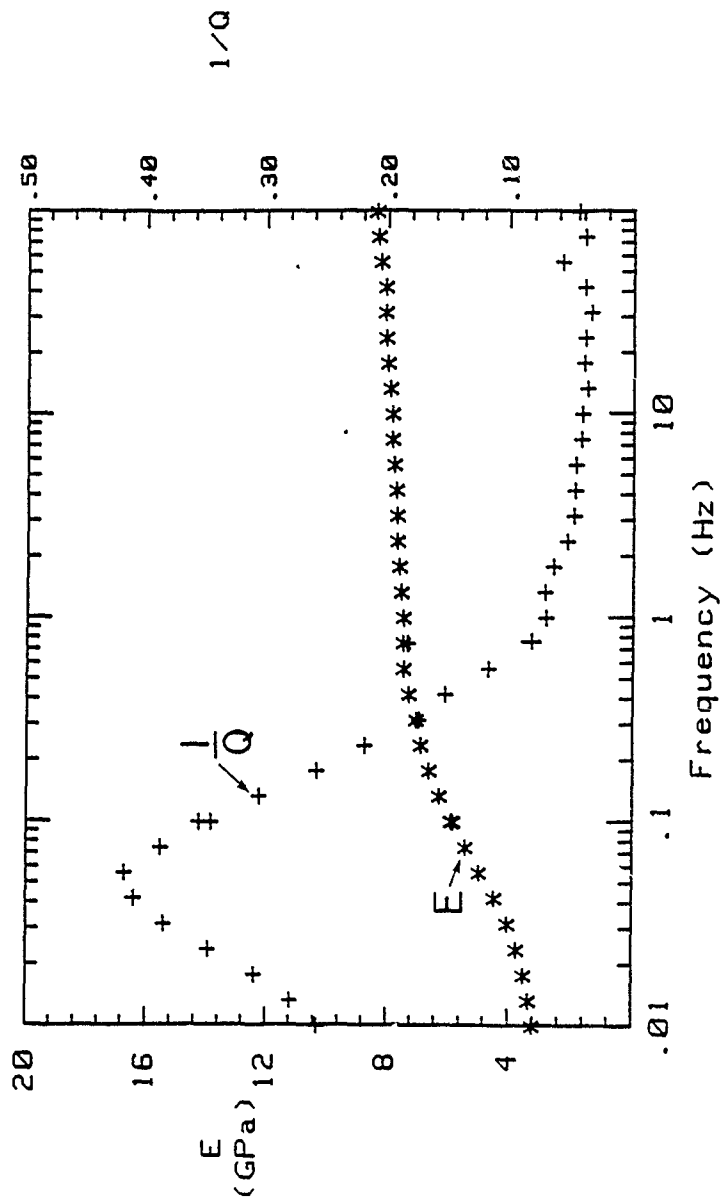


Figure 4. Measurements on Berea Sandstone in the room-dry condition. Note the well defined peak in Q^{-1} at 0.06 Hz.

BEREA SANDSTONE (vacuum-dry)

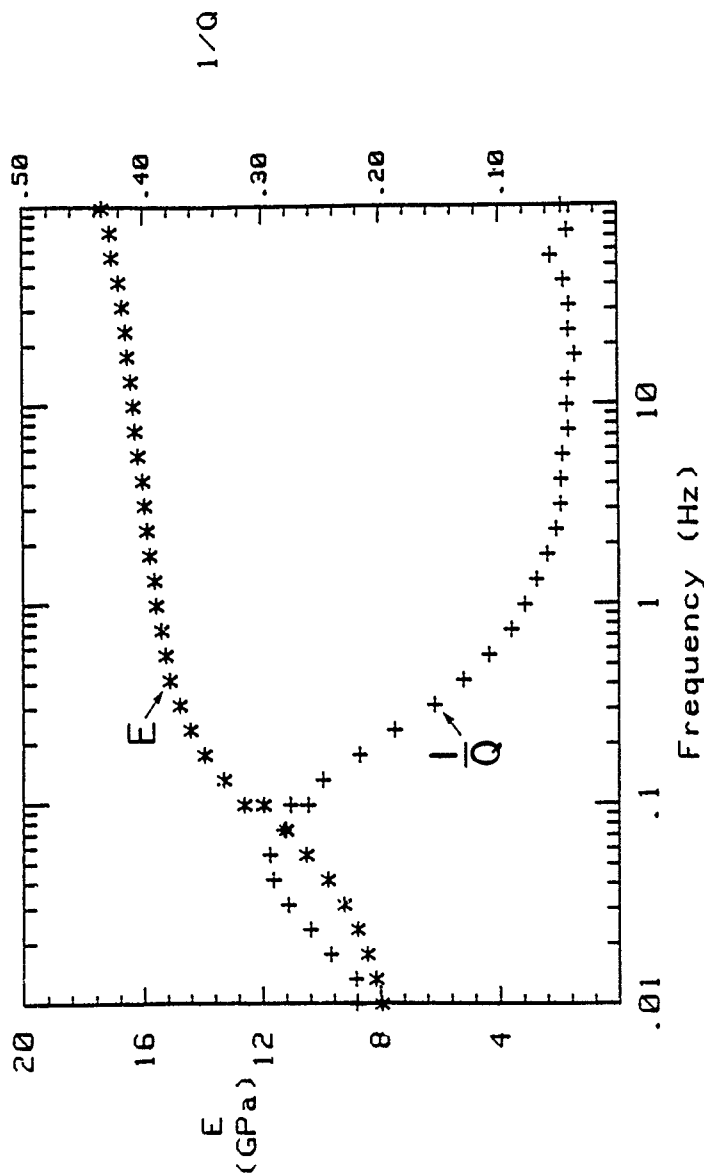


Figure 5: Measurements on the same sample as Figure 4, but with the sample in the vacuum-dry condition. Note the dramatic increase in the modulus values as well as the lowering of the attenuation peak at 0.06 Hz.

relationship

$$E = E_0 \left[1 + \frac{2Q^{-1}}{\pi} \log_e \frac{f}{f_0} \right]$$

where E is the magnitude of the complex Young's Modulus, Q^{-1} is its attenuation, f is the frequency and E_0 is the value of E at a reference frequency, f_0 . This equation can be rearranged to give

$$E = E_0 + 1.466 E_0 Q^{-1} \log_{10} \frac{f}{f_0}$$

Using this relationship, we obtain a predicted value of 0.057 for Q^{-1} from the slope of E versus $\log_{10} f$ in Figure 3, which is in fairly good agreement with the measured values of Q^{-1} of about 0.07.

3. Measurements on Sandstone

Figures 4 and 5 show the modulus and Q^{-1} data we obtained for a 4.95 cm diameter sample of Berea Sandstone in the room-dry and vacuum-dried states, respectively. Note the large change in modulus, which increases from 8 to 17 GPa. Also note the large peak in the attenuation at 0.06 Hz which decreases in amplitude for the dried sample. We are presently working on modelling this peak with a Cole-Cole distribution of relaxation times, similar to theory described by Spencer (1981). Note also the linear variation of modulus with log of frequency. The slope of this variation is again consistent with the values of Q^{-1} of about 0.04, above 1 Hz.

4. Measurements on Other Sedimentary Rocks

We are presently making similar modulus and attenuation measurements on other types of sedimentary rocks such as claystone, siltstone and limestone. We also plan to analyze the porosity and fabric of all the rocks so far investigated.

D. PROPOSED RESEARCH AND PLAN

We propose to continue measuring attenuation and Young's modulus in consolidated sediments in the frequency range 0.01 - 100 Hz. The emphasis will be on collecting as much data as possible on a wide variety of sediments including shales, mudstones and limestones. Measurements will be made on these in both the vacuum-dry and water-saturated conditions. We will also perform the measurements in a temperature controlled enclosure to reduce the noise at low frequencies as well as improving the overall repeatability of the results. In addition, with the addition of a temperature-controlled enclosure, we will be able to make the measurements at multiple temperatures (approximately in the range of 0-30°C). The data of Lagakos et al. (1986) show clearly that modulus values, at least for polymers, are strongly temperature-dependent. Estimation of the temperature coefficients of the modulus is therefore of great importance in extrapolating laboratory data to the marine environment.

Lucite

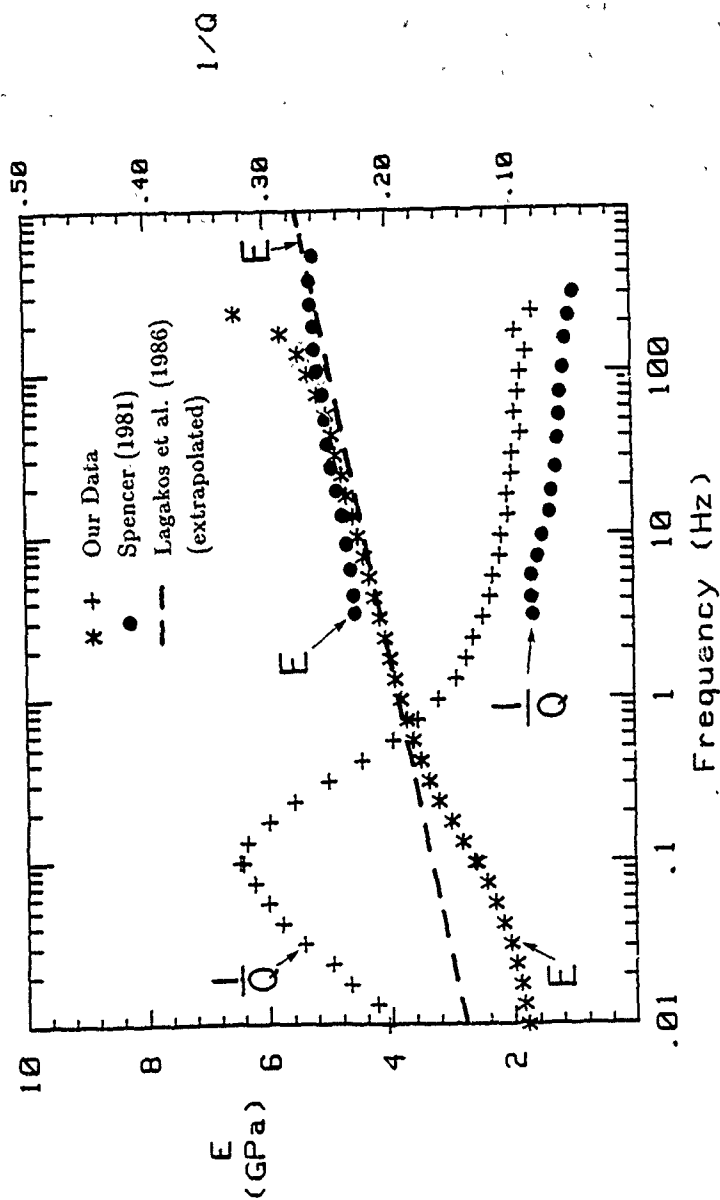


Figure 2: Measurements on a sample of synthetic polymer (Lucite) by ourselves, Spencer (1981) and the extrapolated straight-line fit of data obtained by Lagakos et al. in the frequency range 200 Hz to 1 MHz. Note how a peak in the attenuation (Q^{-1}) which was placed at 10 Hz by Spencer (1981) actually occurs at 0.1 Hz according to our own data, which extends down to 0.01 Hz.

RECEMENTED GLASS BEADS

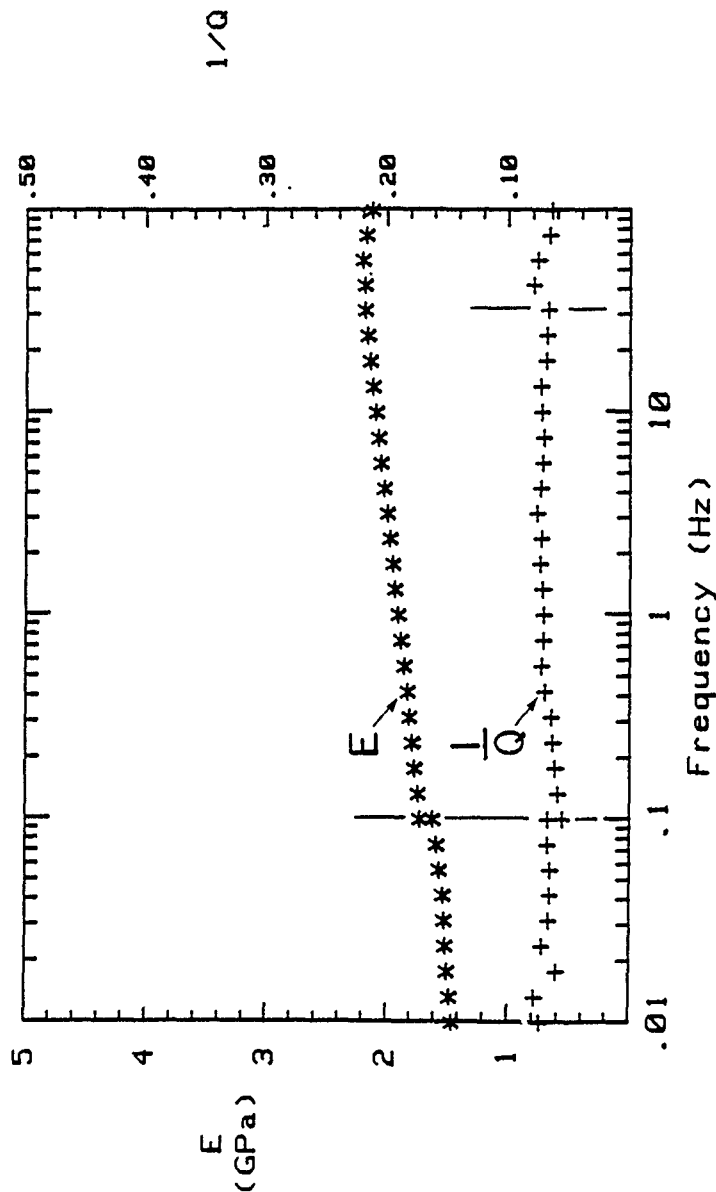


Figure 3: Measurements on a synthetic sample of recemented glass beads. Note the independence of Q^{-1} on frequency as well as the expected linear variation of modulus with log of frequency.

Low Frequency Attenuation and Modulus Measurements on Marine Sediments and Sedimentary Rocks

STATEMENT OF THE PROBLEM

Geoacoustic models of the seafloor are of fundamental importance in underwater acoustics, and in various types of marine geological and geophysical studies of the ocean floor and the underlying crust. Hamilton (1980) defines a geoacoustic model as "a model of the real seafloor with emphasis on measured, extrapolated, and predicted values of these properties important in underwater acoustics and those aspects of geophysics involving sound transmission." The ability to make accurate predictions of low-frequency sound propagation in the ocean basins, however, depends on having an adequate knowledge of the low-frequency elastic properties of the environment (Stoll, 1980, 1985, Dunn, 1986 among others).

Dispersion of velocity and attenuation in sedimentary rocks is a pervasive, yet poorly understood aspect of seismic exploration. As stated in last year's proposal, our goals are to study the dispersion in velocity and attenuation by carrying out experiments in three non-overlapping frequency bands (seismic: 1-100 Hz; resonance sonic: 1-10 kHz; ultrasonic: 0.5-2 MHz). To further these goals, we are currently conducting such experiments on sandstones having different porosities and pore fabrics. We plan to emphasize this aspect of our work in the remaining contract period and during the next year.

PROGRESS (1 January - 31 December 1988)

1. Equipment and Software Development

A problem which occurred several times with the mechanical part of the equipment was that operators would tighten down the fixed end of the sample without lowering the displacement probe, causing damage to the probe. We have now added an audible alarm circuit which triggers when the displacement becomes less than about 100 microns.

A dial gage is now kept clamped to the equipment to measure the absolute position of the displacement probe, as well as providing a means of recalibrating it. It was found that the amount of prestress exerted on the sample assembly by the shaker, which can be increased by lowering the sample assembly onto the shaker, had a significant effect on the modulus and phase values. Although Spencer (1981) did not give the amount of prestress that he used, it is possible that the larger shaker in his system was capable of more prestress than ours, which is only capable of several Newtons. We are now able to at least keep this prestress reasonably constant by always positioning the bottom end piece in the same position relative to the shaker. A more satisfactory solution will be to add a pressure plate capable of applying a variable prestress to the sample assembly, similar to that used by Liu and Peselnick (1983). The optimum prestress could then be determined empirically by increasing it until the modulus values stabilize. We are presently working on this problem and hope to install such a pressure plate in the next few months.

Another problem occurred at very low frequencies with the shaker coil over-

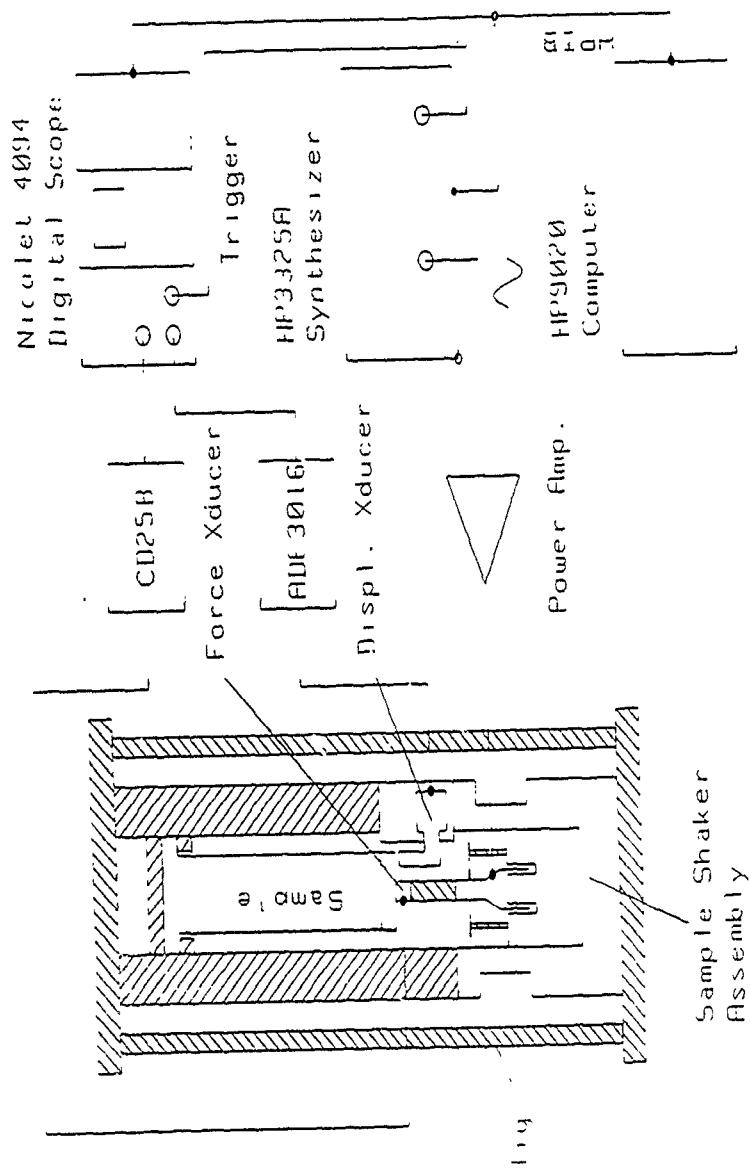


Figure 6. Diagram of the experimental equipment used to measure Young's Modulus and attenuation of cylindrical samples.

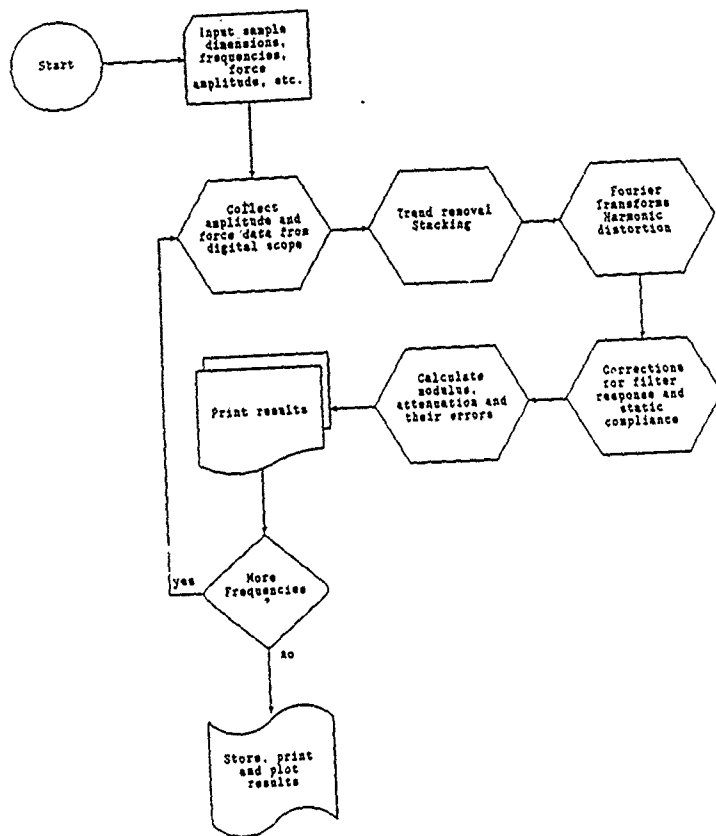


Figure 7 Flowchart of the data-processing algorithm, written in HP BASIC

We shall attempt to establish straight line fits to the modulus data where appropriate, and where possible, see if these fits are consistent with higher frequency data obtained using resonant and ultrasonic techniques. Where relaxation peaks occur, we will attempt to model them using a Cole-Cole distribution of relaxation times (Spencer, 1981).

We will use Dunn's (1987) technique of sealing the edges of the sample with an aluminum sleeve before saturation to reduce the "open-pore" effect. Although this technique does not completely eliminate the "open-pore" effect, it should reduce it to a negligible amount below 30 Hz (Figure 1). One useful side benefit of sealing the samples may be a method of measuring unconsolidated sediments. The main problem is friction between the lower sample end-piece and the sealing sleeve. If this friction can be accurately estimated, or shown to be negligible, we should be able to measure completely unconsolidated material. A useful calibration experiment will be to measure a sealed cylinder containing water alone, since the attenuation of water is known to be almost negligible, and its modulus is also well-determined. Any friction between the sealing cylinder and the end pieces should therefore be readily observable for water.

The result of our work will be the ability to quantitatively predict the variation of modulus and attenuation over at least four decades of frequency for a wide variety of consolidated, and possibly unconsolidated sediments.

F. EXPERIMENTAL METHODS

The instrumentation to be used for the proposed measurements is shown in Figure 6. The apparatus can measure the complex Young's modulus of rock samples at selectable frequencies between 0.01 to 100 Hz and at strain amplitudes near 10^{-8} . A sinusoidally varying strain is applied to the sample using an electromechanical shaker (Gearing and Watson 20-B) which is driven by a 100 W d.c.-coupled power amplifier attached to an HP-3325A frequency synthesizer. Cylindrical samples of consolidated sediments 3.8 to 5 cm in diameter, and up to 15 cm in length with steel end pieces similar to those used by Spencer, are used for the measurements. The strain is measured using a capacitive displacement transducer (Ade 2101/2001 K) and the force by an in-line piezoelectric force transducer (PCB 208A). Both transducer outputs are digitized using a Nicolet 4094 digital oscilloscope having 12 bit resolution and sampling rates of between 200 and 10⁶ seconds. A Hewlett-Packard 9020 computer controls the synthesizer and digital oscilloscope enabling rapid calculation of Young's modulus and attenuation to be made and plotted at any frequency between 0.01 and 100 Hz. A flowchart of the data-processing algorithm, written in HP BASIC, is shown in Figure 7.

For interpreting the low-frequency attenuation and modulus data we will also use our AccuSorb 2100E Gas Adsorption Analyzer. This instrument will be used to measure adsorption and desorption isotherms for calculating surface area and pore volume distribution in a sample. The AccuSorb can determine surface areas above 0.001 m²/g and pore size distribution from 0.06 m diameter to the upper limit of the physical absorption technique.

Low Frequency Modulus Measurements on Marine Sediments & Sedimentary Rocks

M. Manghnani B. Lienert

B. PROGRESS (January 1 - September 1, 1989)

This year, we have concentrated our efforts on measuring Q_K^{-1} for a suite of unconsolidated marine sediments. We have also devoted considerable effort toward developing techniques for removing bubbles of gas from the samples. These bubbles, which we now conclude are present in virtually all fluids at atmospheric pressure, were removed fairly easily when the cylinder contained water alone, simply by bleeding the cylinder after standing it upright for several days. Figure 1 shows typical data collected for pure water after such bleeding. Repeated measurements have indicated that the value of Q_K^{-1} is constant over the frequency range 0.1-100 Hz and has a value of 0.01 ± 0.002 . Note also that it can be reliably estimated from the slope of K versus $\log f$ using constant- Q theory (Lienert and Manghnani, 1989) as shown in Figure 1 by the dashed line. All of the subsequent data for Q_K^{-1} that we shall describe here will therefore have this value of 0.01 subtracted.

Bleeding the cylinder proved unsatisfactory when a sample of sediment was measured, as indicated by the results in Figure 2, which are for a piston-core sample of pelagic ooze collected 100 km north of Hawaii (water depth = 2 km). In spite of repeated bleeding, the modulus values for this sample remained less than 2.2 GPa, the bulk modulus of pure water. Although no published values of K exist for rocks, it is possible to estimate K/G from V_P/V_S ratios using the equation

$$\frac{K}{G} = \left(\frac{V_P}{V_S} \right)^2 - \frac{4}{3} \quad [5]$$

obtained from the ratio of equations [1] and [2]. Since V_P/V_S for consolidated rocks range from 1.6-1.8, equation [5] implies that $\frac{K}{G}$ ranges from 0.3-0.5, i.e., one third to one half the shear modulus. Published values for shear modulus for consolidated rocks range from 20-30 GPa (Jackson et al., 1987), implying that K is about 7-15 GPa, more than three times the bulk modulus of water. The introduction of solid material into water would therefore increase, rather than decrease K , since the two compressions act in parallel. We concluded that bubbles of air, or some other gas, was reducing K below 2.2.

We first tested the possibility of pressurizing the contents of the cylinder to 10-20 atmospheres. Such an approach was appealing, as it was also an essential first step in fulfilling one of our future objectives, namely to measure Q_K^{-1} under higher pressures. In order to pressurize the cylinder, it was necessary to install a stronger seal between the piston and cylinder walls, as the present seal, a layer of silicone rubber sealant 0.1 mm thick, is incapable of withstanding pressures much greater

PEL. OOZE

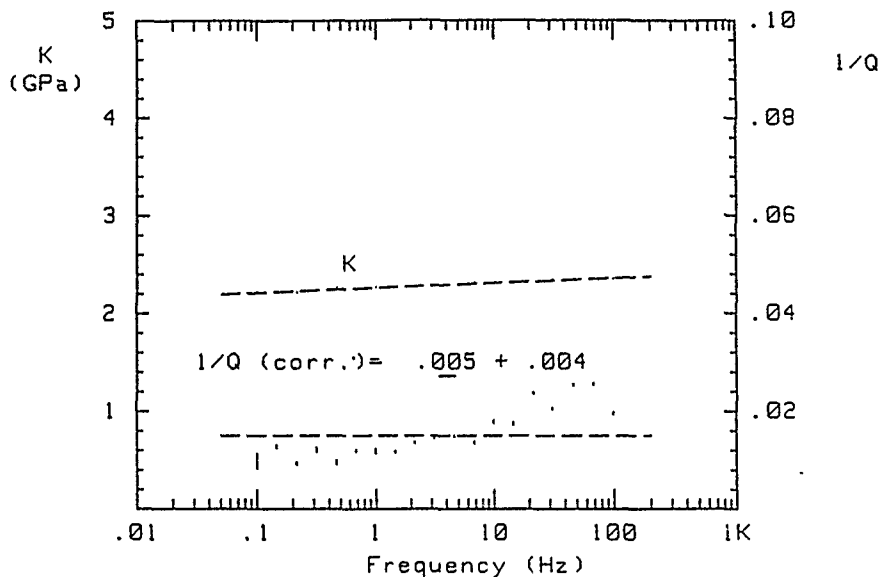


Figure 3: Measurements for the same sample as Figure 2, but after eight hours of evacuation to remove bubbles. The dashed line fit through the Q_K^{-1} values is obtained from a least squares linear fit to the K values using constant- Q theory and has the background result of 0.01 for water subtracted.

than one atmosphere. We first machined a larger piston having a smaller clearance (0.03 versus 0.1 mm) with the cylinder walls.

We measured the effective modulus of this 0.03 mm seal with the cylinder empty and found it to be about a factor of ten larger than that of the 0.1 mm seal, i.e. about 1 GPa, or one-half the modulus of water. When the cylinder was filled with water and measured, the value of Q^{-1} increased from 0.01 to about 0.05. We interpret this result as follows: In a mechanical vibration involving two separate materials, rubber and water say, having energies W_{rubber} and W_{water} and fractional energy losses per cycle Q_{rubber}^{-1} and Q_{water}^{-1} , the total energy loss per cycle is given by

$$(W_{\text{rubber}} + W_{\text{water}})Q^{-1} = W_{\text{rubber}}Q_{\text{rubber}}^{-1} + W_{\text{water}}Q_{\text{water}}^{-1} \quad [6]$$

where Q^{-1} is the effective (i.e. measured) internal friction.

It is clear from equation [6] that the measured Q^{-1} depends not only upon Q_{rubber}^{-1} , but also on the strength of the rubber relative to the strength of the material being measured. For example, with the 0.1 mm seal, the strength (and therefore the energy) in the rubber is a factor of twenty lower than the strength of the water. Since our measured value of Q_{rubber}^{-1} is about 0.1, equation [6] then predicts that the contribution of the rubber to the measured Q^{-1} will be $0.1 \times 0.05 = 0.005$, slightly less than our measured value of 0.01. Similarly, equation [6] predicts that when the strength of the rubber seal is one half the strength of the water, the contribution of the rubber to the measured Q^{-1} will then be 0.05, in good agreement with our measured value. This result also implies that the value of Q^{-1} that we measure for water is entirely due to the rubber seal, i.e., Q_{water}^{-1} is zero at seismic frequencies within our limits of error.

We then tried machining two semicircular grooves in a piston having a 0.03 mm clearance and fitted these with two O-rings. We found that the effective modulus of this arrangement was even higher - about 2 GPa. Because Q^{-1} for rubber varies with frequency and may also change with time, it is better to minimize its contribution. We are therefore still using the 0.1 mm silicone rubber seal. However, we are experimenting with the O-ring piston and hope to reduce its effective modulus to a lower value by increasing its clearance with the cylinder walls. There is clearly a trade-off between the maximum pressure that the O-rings will withstand and their effective modulus.

To remove the bubbles, we instead placed the entire cylinder in a vacuum chamber with the bleed valve open, and held the pressure at close to the vapor pressure of water. This technique proved very effective as indicated by Figure 3, which shows the results for the same pelagic ooze as Figure 2 after eight hours of this treatment. The modulus values have now increased to above 2.2, while the values of Q^{-1} are close to 0.01, the value for pure water. This is an extremely important result, as it indicates for the first time that compressional energy losses in unconsolidated materials such as this ooze are essentially negligible.

In the process of measuring this sample we have also discovered a time dependence of the results for both K and Q^{-1} which is shown in Figures 4 and 5.

Pelagic Ooze

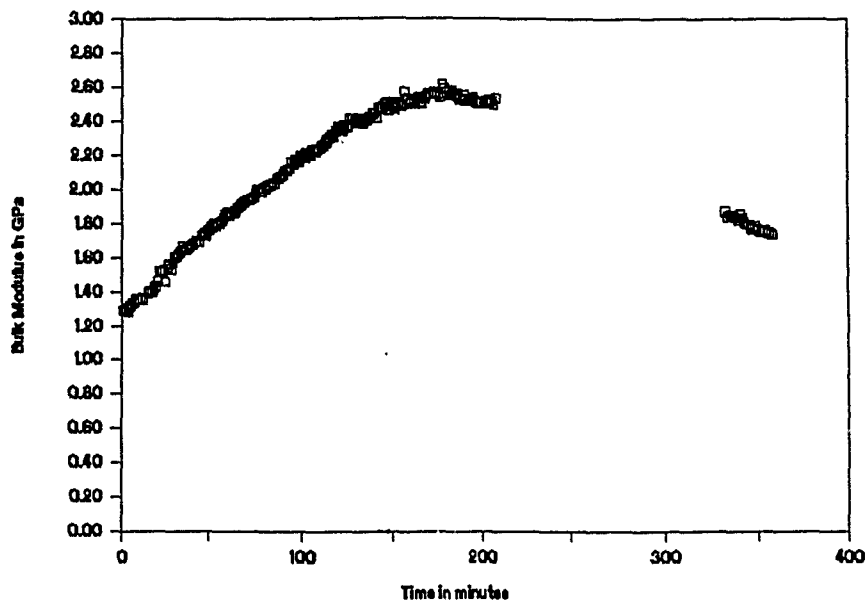


Figure 4. Variation of modulus values with time after the first measurement. The gap in the data occurred when the displacement output drifted off-scale

Pelagic Ooze

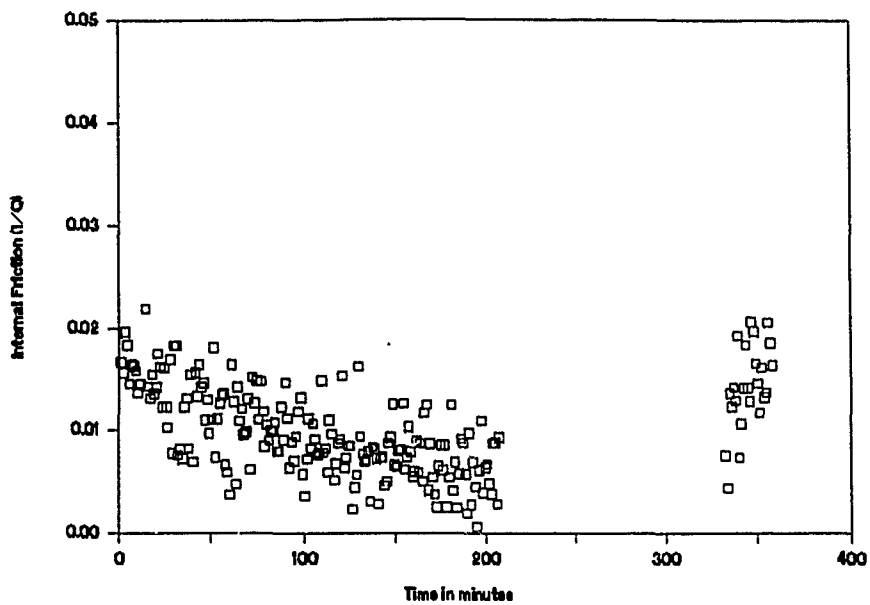


Figure 5: Variation in Q_K^{-1} with time.

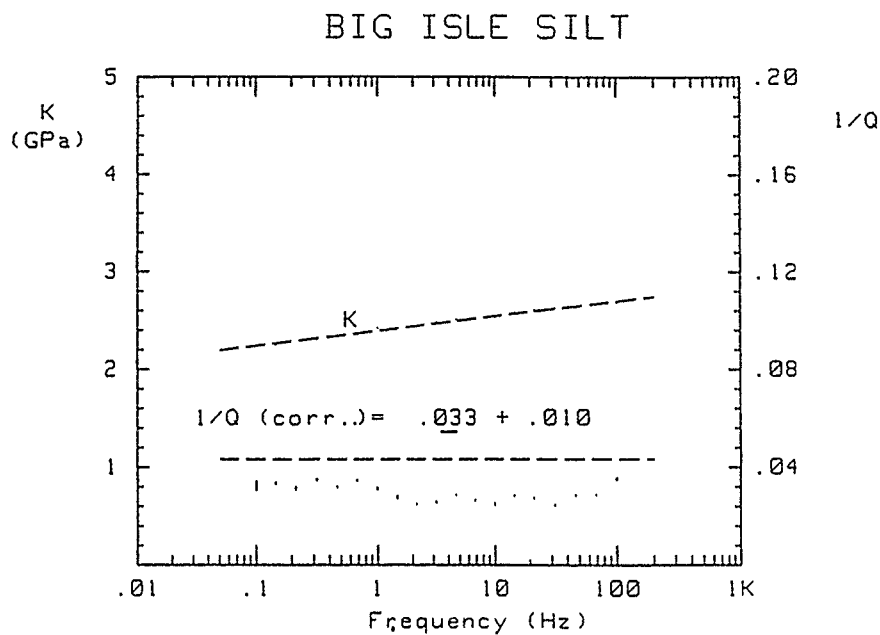


Figure 6: Results of K and Q_K^{-1} measurements on a sample of silt dredged 2 km off Keahole Point on the island of Hawaii.

respectively. We previously observed a time dependence for water in the form of an initial increase in K and decrease in Q_K^{-1} , which we attributed to stress-hardening of the silicone rubber seal. Since the values stabilized after about an hour, this caused little concern. However, the pelagic ooze, as well as showing the same initial increase in K , then showed a decrease (Figure 4). Figure 5 shows the corresponding time dependence of Q_K^{-1} (very little averaging was performed on each measurement, resulting in substantially increased noise). The time dependence of Q_K^{-1} is considerably less than for K , suggesting that reliable results can be obtained simply by taking the measurement about 1 hour after inserting the sample. An initial increase in shear modulus similar to that which we observed has been reported for soils by Anderson and Stokoe (1978).

We interpret the time dependent decrease in K to the release of gas from either the sample, or from reactions of the sample with the aluminum cylinder. We are presently machining a similar cylinder from stainless steel in order to minimize such reactions. If the gas release is still evident with this new cylinder, it is clearly coming from the sediment itself. This is clearly a subject for additional study, as such a gas release could be occurring even when the sediment is *in situ* on the sea floor and thus be affecting its seismic properties.

Figure 6 shows results for a silt dredged off Keahole Point on the island of Hawaii. This sample was evacuated before measurement to remove gas bubbles. Note that K is also now greater than 2.2 GPa. However, the Q^{-1} values are significantly larger - about 0.03 at 1 Hz and increasing to 0.05 at 100 Hz. Our initial conclusion is that grain size and possibly the quantity of clay have an important effect on Q_K^{-1} . We should have more data by the time of the site visit, allowing us to make more definitive conclusions.

The dramatic dependence of K upon dissolved gas that we have observed has important implications for the measurement of velocity in water-saturated materials in general. It can be seen from equation [1] that any reduction in bulk modulus, K , such as we have observed due to the presence of gas, will show up as a reduction in V_P . The amount of the reduction will depend on the relative contribution of the shear modulus, μ , to V_P . For a fluid, $\mu = 0$, which results in a V_P of only 0.43 km/s when $K = 0.2$ GPa, the value we obtained for the ooze when it contained gas.

Measured values of V_P for unconsolidated water-saturated sediments at ultrasonic frequencies are typically 1.4-1.6 km/s, implying that μ is about 2 GPa, assuming that these samples contain gas bubbles, i.e. $K \approx 0.2$ GPa. Substituting our gas-free value of K (2.2) in equation [1] then gives $V_P = \sqrt{\frac{K+4\mu/3}{\rho}} = 2.0$ to 2.2 km/s. There seems little doubt that at water depths exceeding 2 km, there are few, if any, gas bubbles in the *in situ* sediments, implying that laboratory-measured V_P values have been seriously underestimated.

Another important implication of this result is that it allows us to estimate both μ and K from ultrasonic velocity measurements alone, simply by measuring V_P before and after evacuation of the sample and assuming that $K = 0$ for the unevacuated sample measurement. We are presently working on ultrasonic velocity

measurements on the same sample for which Q_K has been measured and should have the results in time for the site visit.

We are presently installing a circulating fluid line around the equipment in order to control temperature. To facilitate comparison of our results by others in what is essentially "new territory", we have also measured glycerol, a fairly low- Q fluid, and compared the results with those obtained in our own laboratory at ultrasonic frequencies.

Another of our goals this year, as stated in the current year (1989) proposal, is to compare our results for E and Q_E^{-1} with results obtained from the resonant column technique, in cooperation with Dr. Bennell. With the limited resources on hand, we are moving cautiously, but steadily in this direction. To this effect, we have initially sent him samples of the two consolidated sandstones for which we have obtained values of E and Q_E^{-1} . We expect to send him samples of the unconsolidated materials on which we are presently working before the end of 1989.

Dr. Bennell is able to determine μ , Q_S^{-1} , E and Q_E^{-1} over a wide range of strains (10^{-3} to 10^{-7}) and pressures of up to 0.7 MPa (7 atm.), equivalent to about 60 m water depth (Bennell et al, in press). He has sent us six samples of sediments for which he is presently measuring the above four parameters, using the resonant column method:

Sample A	alluvial silt
B	continental shelf mud
C	uniform sand
D	silty sand
E	soft deep-sea clay
F	stiff glacial clay

Dr. Bennell's resonant column setup also enables him to perform ultrasonic measurements of V_P , Q_P^{-1} , V_S and Q_S^{-1} simultaneously with the μ and Q_S^{-1} determinations at seismic frequencies. While Dr. Bennell is studying these six samples in his laboratory, Janice Marsters (graduate student) is now preparing the same samples for measurement of K and Q_K^{-1} at low frequencies as well as ultrasonic V_P and V_S values. Using these data we will then be able to compare our results with Dr. Bennell's.

Resulting Talks and Papers

Lienert, B.R. and M.H. Manghnani, Internal friction (Q_E^{-1}) in solid materials in the frequency range 0.1-100 Hz, submitted to *J. Appl. Phys.*, 1989.

Lienert, B.R., Measurement of Q_P in fluids and unconsolidated sediments in the seismic frequency range (0.1-100 Hz). Paper presented at session S13: Scattering and attenuation of seismic waves, IUGG/IASPEI meeting, Istanbul, Turkey (August, 1989).

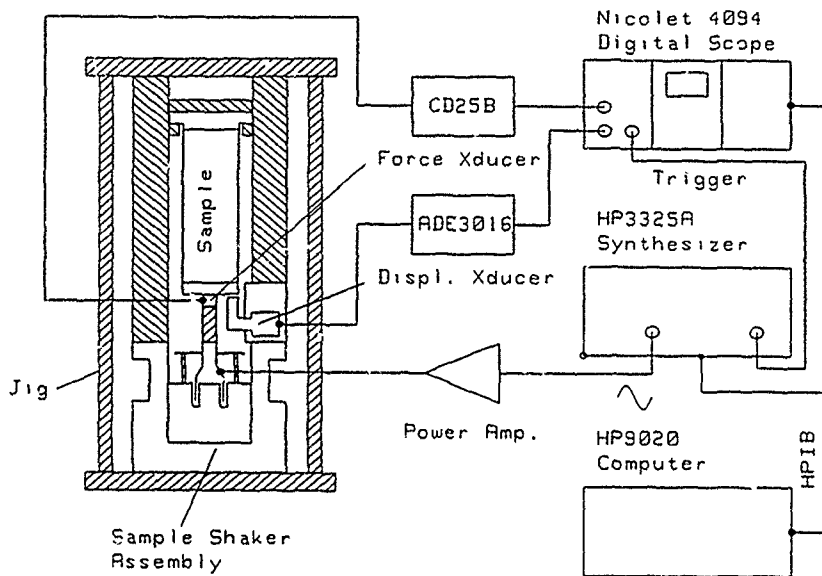


Figure 7: Block diagram of the low-frequency attenuation and modulus equipment

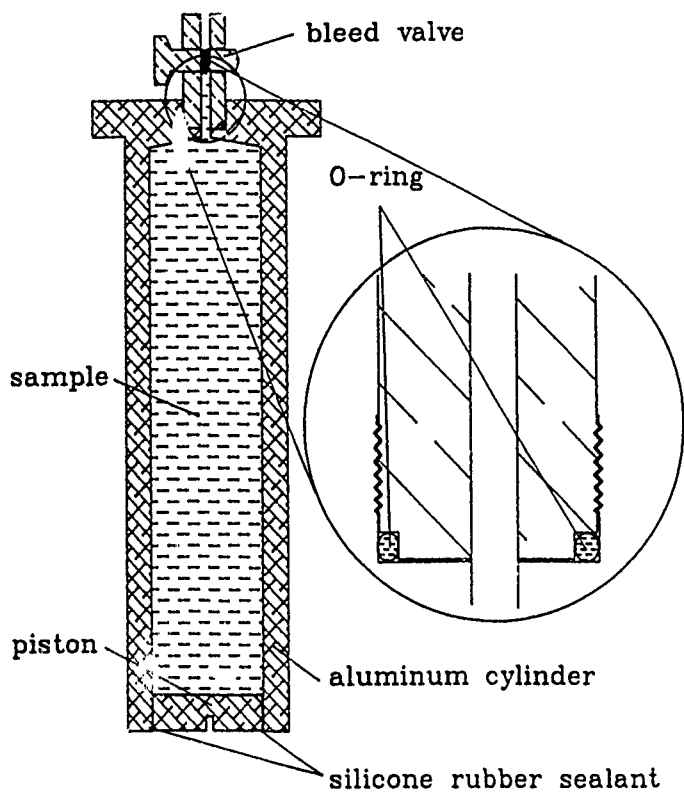


Figure 8: Sketch of the hydraulic piston insert used to measure K and Q^{-1} for unconsolidated sediments and fluids

Contract: N00014-87-K-0181
Seismology & Acoustics

Diagnetic & Sedimentological Studies

Jane Schoonmacher

GEOACOUSTIC MODELING OF MARINE SEDIMENTS

Murli H. Manghnani, Jane S. Tribble, Fred T. Mackenzie, Barry Lienert
Hawaii Institute of Geophysics
University of Hawaii
Honolulu, Hawaii 96822

Long-term Scientific Objectives

To understand the variations in physical, acoustic, and electrical properties of marine sediments in terms of various controlling factors including composition, diagenetic stage, sedimentology and microfabric. Observations will be incorporated into geoaoustic models with predictive capabilities.

Project Objectives

1. Analysis of regional, basin-wide systematics of acoustic and physical properties variations as related to stratigraphy and depth.
2. Investigation of correlations between velocity anisotropy and preferred orientation of mineral grains in marine sediments.
3. Systematic investigation of physical, acoustic and electrical properties of marine sediments as a function of composition, lithology, diagenetic characteristics, and microfabric.
4. Correlation of changes in microfabric and physical properties of clay-rich sediments during compaction and lithification.

Current Status and Progress

1. Data on sediment type, physical properties, and acoustic velocity from DSDP and ODP sites along an east-west transect across the western North Atlantic have been compiled. A regional stratigraphy has been constructed to be used as a framework for correlating variations in velocity with depth and lithology. Porosity-velocity systematics for siliceous sediments from the central basin and the New Jersey shelf are shown in Figure 1. Relatively high porosity-low velocity samples fall near the curve described by the Wood's equation. Compaction and diagenesis result in departure from the Wood's curve and approach to the curve described by the Wyllie equation. The increase in velocity with porosity loss is steeper at the basin sites than on the shelf; this may reflect differences in sedimentology, composition and microfabric.
2. Vp anisotropy in calcareous and clay-rich sediments has been investigated using X-ray pole figure goniometry measurements. Measurements on samples from several DSDP sites having anisotropies between 4.5 and 19.0% showed random distribution of the 1014 planes of calcite grains (Fig. 2). Anisotropy in these samples is therefore not caused by calcite texture. The correlation between Ap and calcite content was found to be positive for calcareous claystones and clay-bearing limestones from DSDP Leg 93 and ODP Leg 110, and negative for pelagic chalks of ODP Leg 122 (Figure 3). These differences are probably due to microfabric and distribution of flat-lying pores.
3. TEM and SEM microfabric studies of siliceous oozes, porcellanites, and cherts from ODP Legs 108 and 113 and DSDP Legs 85 and 86 are underway. Data from these studies will be used in interpretation of Vp and Vs measurements that are completed for these samples.
4. Our previous studies have shown the influence of smectite content on porosity retention during compaction of clay-rich sediments (Tribble, in press). TEM microfabric studies of shallowly-buried, smectite-rich sediments from the Barbados accretionary prism are currently underway to investigate this phenomenon.

5. Compressional and shear velocities, compressional attenuation, electrical resistivity, bulk and grain densities, and porosity have been measured on samples from ODP Leg 122. Differences with the shipboard measurements have been explained in terms of analytical problems with the shipboard techniques, and corrections have been determined.

References

O'Brien, D., Manghnani, M., Tribble, J., 1989. Irregular trends of physical properties in homogeneous clay-rich sediments of DSDP Leg 87 Hole 584, midslope terrace in the Japan trench. *Marine Geology*, **87**, 183-194.

Tribble, J. S., 1990. Clay diagenesis in the Barbados accretionary complex: Potential impact on hydrology and subduction dynamics. ODP 110, Pt. B, in press.

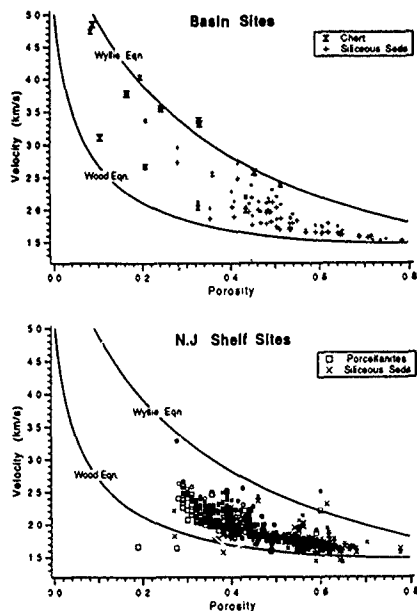
Tribble, J., Mackenzie, F., Urmos, J., 1990. Physical property changes accompanying the mud to shale conversion, Barbados convergent margin. In: *The Microstructure of Fine-grained Terrestrial Marine Sediments-From Muds to Shale*, Springer-Verlag, in press.

Tribble, J. S., Mackenzie, F. T., Urmos, J., Manghnani, M., and O'Brien, D., 1990. Effects of biogenic silica on acoustic and physical properties of clay-rich marine sediments. To be submitted to *Bull. Amer. Assoc. Petr. Geol.*

O'Brien, D. K., Manghnani, M. H., and Tribble, J. S., 1990. Preferred orientation and velocity anisotropy in marine clay-bearing calcareous sediments. In prep.

O'Brien, D. K., and Manghnani, M. H., 1990. Shore-based physical properties of Site 762 and comparison with shipboard data. In prep.

Figure 1. Velocity versus porosity for siliceous sediments from the western North Atlantic.



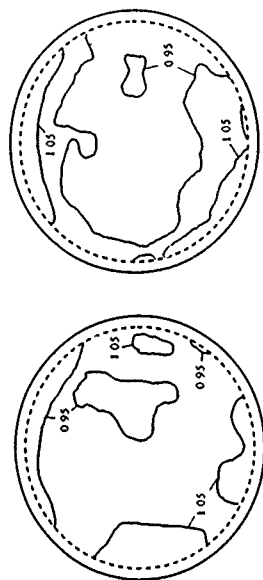


Figure 2. Examples of reflection scans of calcite 1014 planes in DSDP limestones. Contour intervals in terms of MRD (multiples of a random distribution) are indicated. N^2D values of about 1.0 indicate random orientation of planes.

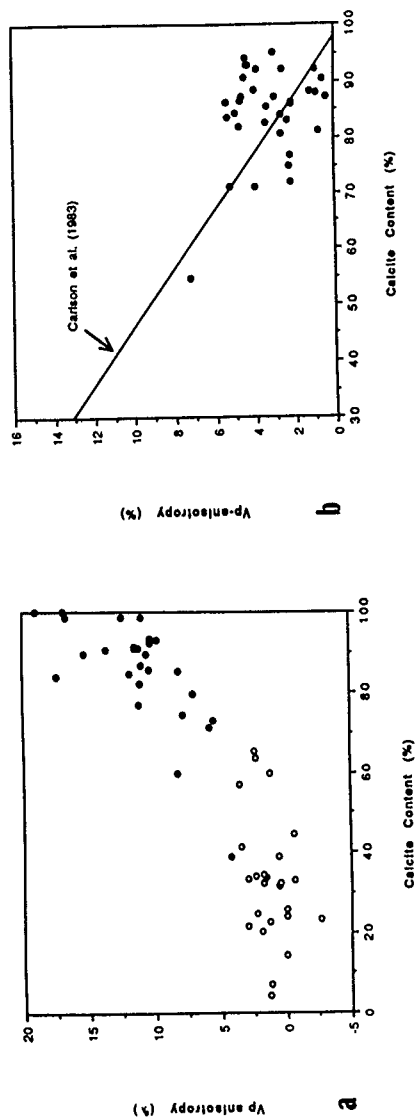


Figure 3. Calcite content versus velocity anisotropy for samples from a) calcareous claystones and carbonate-bearing claystones and b) pelagic chalk samples.

Publications resulting from "Diagenetic and Sedimentological Studies" subtask of ONR Omnibus Grant N00014-87-K-0181.

- 1994 Tribble, J.S., R.S. Arvidson, M. Lane, III, and F. T. Mackenzie. Crystal chemistry, and thermodynamic and kinetic properties of calcite, dolomite, apatite, and biogenic silica: Applications to petrologic problems. *Sedimentary Geology*, in press.
- 1993 O'Brien, D.K., M.H. Manghnani, J.S. Tribble, and H.-R. Wenk. Preferred orientation and velocity anisotropy in marine clay-bearing calcareous sediments. In: Rezak, R. and D.L. Lavoie, (eds.), *Carbonate Microfabrics*, Springer-Verlag, 149-161.
- 1992 Tribble, J. S., Mackenzie, F. T., Urmos, J., O'Brien, D. K., and Manghnani, M. H. Effects of biogenic silica on acoustic and physical properties of clay-rich marine sediments. *Bull. Amer. Assoc. Petrol. Geol.*, 76, 792-804.
- 1991 Tribble, J., Mackenzie, F., Urmos, J. Physical property changes accompanying the mud to shale conversion, Barbados convergent margin. In: R.H. Bennett, W.R. Bryant, and M.H. Hulbert (eds.), *The Microstructure of Fine-grained Terrigenous Marine Sediments-From Muds to Shale*, Springer-Verlag, p. 93-99.
- 1990 Tribble, J. S. Clay diagenesis in the Barbados accretionary complex: Potential impact on hydrology and subduction dynamics. In: Moore, J. C., A. Mascle, et al., *Proc. ODP, Sci. Results*, 110: College Station, TX (Ocean Drilling Program), 97-110.
- 1989 O'Brien, D., Manghnani, M., Tribble, J. Irregular trends of physical properties in homogeneous clay-rich sediments of DSDP Leg 87 Hole 584, mid-slope terrace in the Japan trench. *Marine Geology*, 87, 183-194.

Contract: N00014-87-K-0181
Seismology & Acoustics

Geoacoustic Modeling: Geoacoustic Studies

M. Manghnani/B. Lienert

B. PROGRESS REPORT 1988-1989

1. Geoacoustic Studies.

Sediments from Site 584 of DSDP Leg 87 in the Japan Trench have been the focus of both geoacoustic and sedimentological investigations in the past year. One interesting outcome of our work is the correlation of a zone of anomalous physical and acoustic properties with variations in biogenic silica content with depth. Measurements of porosity, bulk density and grain density as well as other physical and acoustic properties were made in our geoacoustic laboratory, and the very same samples were analyzed for mineralogy and amorphous silica content in our sedimentological laboratory. Physical and acoustic properties of this sediment sequence as a function of depth are portrayed in Figures 1-6. Some important aspects of these vertical profiles of physical, acoustic and electrical properties (measured by D. O'Brien as part of his ongoing Ph.D. dissertation work) are:

(a) Plots of the various physical properties with depth, especially compressional wave velocity data (Figure 4), suggest that the sediment column can be divided into 4 units:

Unit 1 (4-170 m): This unit consists of unconsolidated sediment. The properties of this unit do not vary appreciably.

Unit 2 (170-500 m): This unit (and all succeeding units) consists of consolidated sediment. Physical properties within this unit show a "normal" progression with depth, in which velocity and bulk density increase with depth, and porosity decreases with depth (Figures 1, 3, and 4).

Unit 3 (500-800 m): This is a region of anomalous physical properties (either greatly elevated or depressed).

Unit 4 (800-941 m): The properties of this unit show a resumption of the "normal" progression with depth.

(b) Both V_p and Q_p were measured in the horizontal and vertical directions (Figures 4 and 5). It was observed that $V_{ph} > V_{pv}$ (positive velocity anisotropy) and $Q_{pv} > Q_{ph}$ (negative Q anisotropy) from the top of the hole down to about 650 m. Below this depth, the trend was reversed such that $V_{pv} > V_{ph}$ (negative velocity anisotropy), and $Q_{ph} > Q_{pv}$ (positive Q anisotropy). This finding was not anticipated, especially because the sediment column is quite homogenous. It was discovered that this trend was caused by a change in the bedding inclination.

(c) Q_p decreases (attenuation increases) with depth (Figure 5) until about 650 m, where it starts to increase with depth. This observation is at first surprising, because it

DSDP Leg 87 Site 584

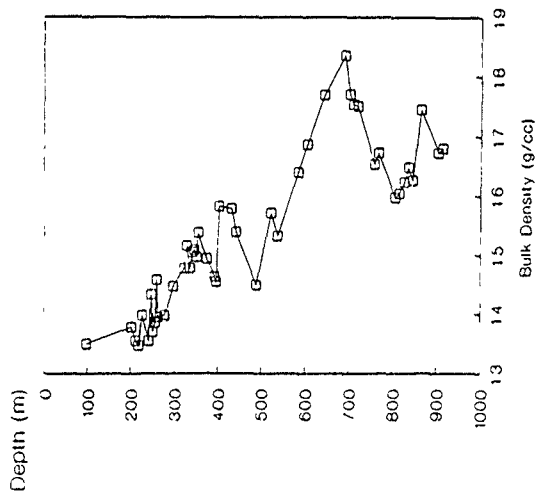


Figure 1. Trend of bulk density with depth for sediments of DSDP Leg 87, Site 584.

DSDP Leg 87 Site 584

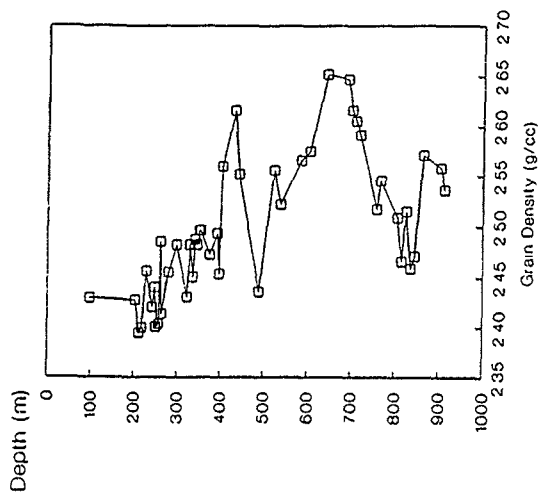


Figure 2. Variation of grain density for sediments of DSDP Leg 87, Site 584.

DSDP Leg 87 Site 584

Depth (m)

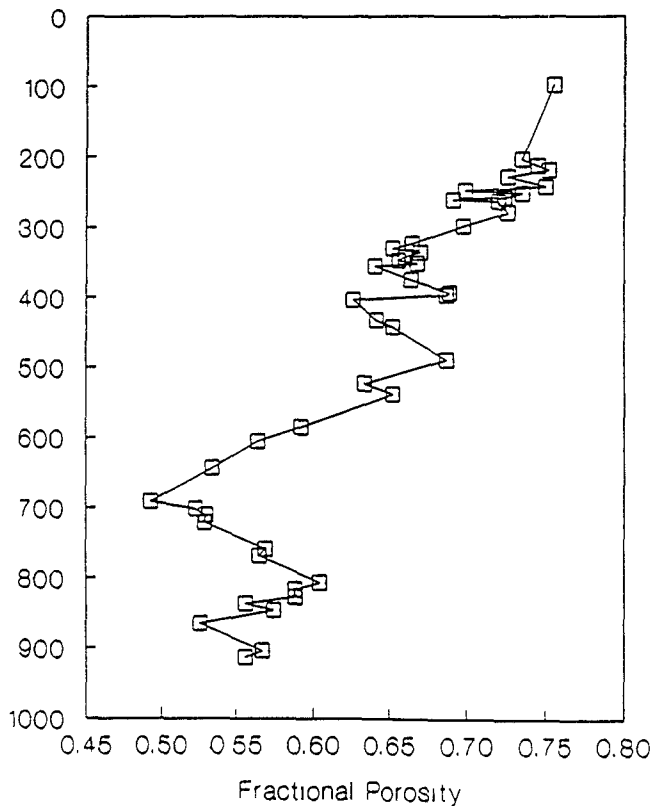
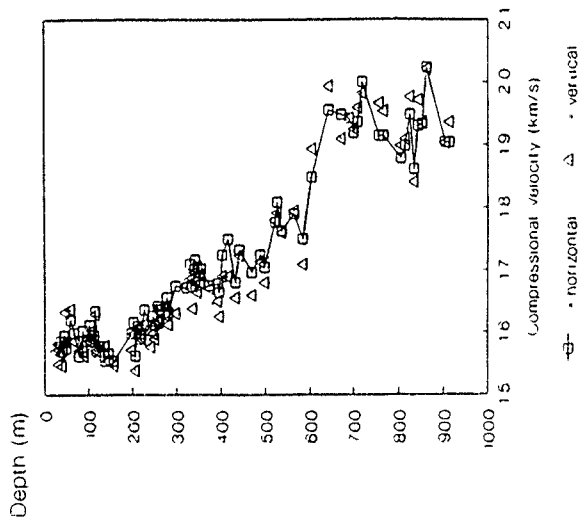


Figure 3. Porosity variation with depth at DSDP Leg 87, Site 584.

DSDP Leg 87 Site 584



DSDP Leg 87 Site 584

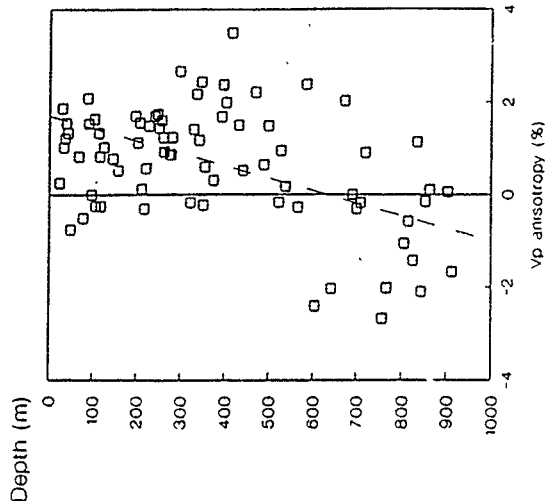
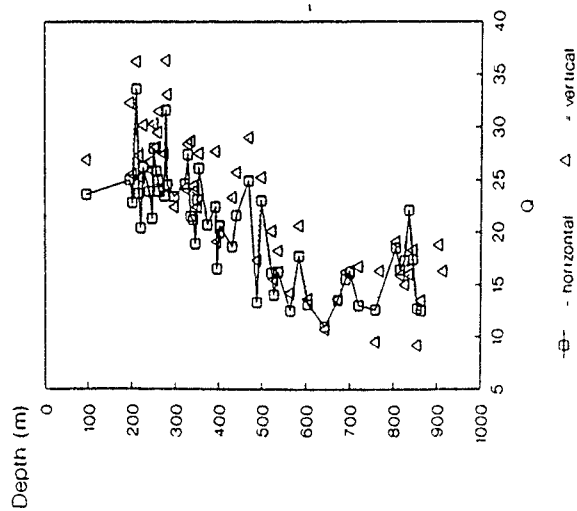


Figure 4. Plots of compressional velocity and velocity anisotropy vs depth for sediments of DSDP Leg 87, Site 584.

DSDP Leg 87 Site 584



DSDP Leg 87 Site 584

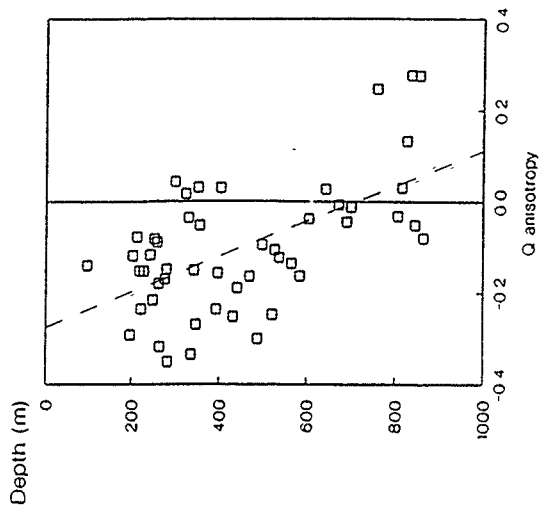


Figure 5. Variations with depth of Q_p and Q_v anisotropy for sediments of DSDP Leg 87, Site 584.

DSDP Leg 87 Site 584

Depth (m)

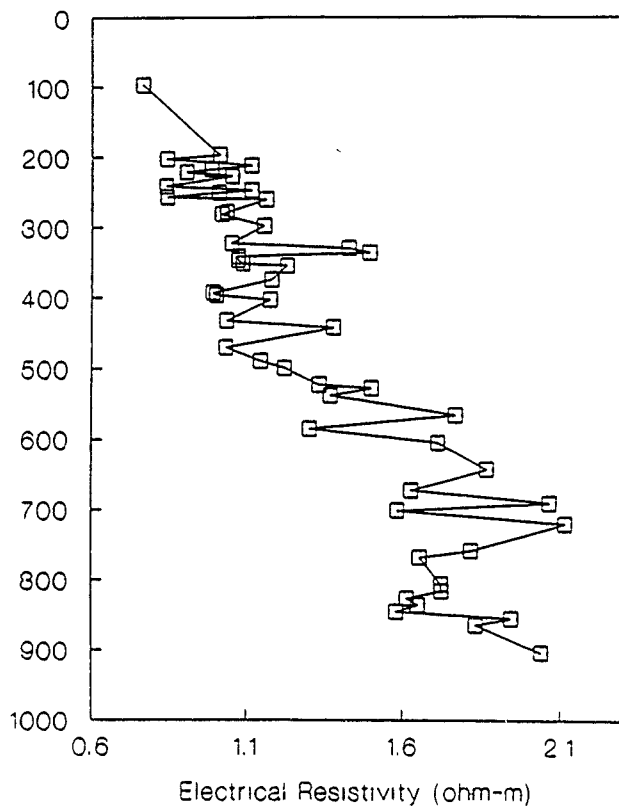


Figure 6. Plot of electrical resistivity vs depth for DSDP Leg 87, Site 584

is known that Q increases with depth in sands and within the earth's mantle. However, Goldberg et al. [1985] and Cheng et al. [1986] found Q_p to decrease with depth in soft sediments, and Cheng et al. reported Q_p values of the same magnitude as the present data (between 10 and 35). The trend of an initial decrease of Q_p followed by an increase with depth in clays was predicted by Hamilton [1976, 1980]. The present data are the first to document this trend. Sands have low porosities (about 25%) and undergo only a small amount of porosity reduction with compaction, because the grains are generally in contact with each other, and the framework is therefore quite rigid. Clays, however, initially have large porosities (about 70%) owing to a "house of cards" grain structure. A large porosity decrease with depth occurs as the grain structure collapses. The progressive grain structure collapse does not add rigidity to the sediment. As porosity decreases, there is less water (which has a very high Q_p) in the pores per unit volume of sediment (which has a very low Q_p). In addition, it can be expected that frictional dissipation will increase energy loss as more uncemented grains come into contact [Hamilton 1976, 1980]. This porosity decrease results in a net decrease in Q_p . It is not until the grain structure totally collapses (or diagenesis occurs) that the pressure on the grain framework increases the sediment rigidity, and causes the Q_p to increase with depth. This total framework collapse probably occurs at about 650 m in this hole.

(d) It was stated above that $Q_{pv} > Q_{ph}$ (horizontal attenuation is greater than vertical attenuation) at the top of the hole, and then reversed below 650 m. Because V_p is fastest in the horizontal direction at the top of the hole, it is surprising that the P-wave amplitude decays fastest in this direction as well. The present data are the first attenuation data for sediments collected in both horizontal and vertical directions, so no comparison with data from the literature is possible. The causes of these observations will be the subject of future research.

(e) Unit 3 is a region of anomalous properties as reflected in velocity, attenuation, electrical resistivity, bulk density, porosity and grain density (Figures 1-6). The anomaly is most obvious in porosity and grain density. Changes in these variables affect all the other properties. The grain density of Unit 3 has a maximum of 2.65 g/cc. The sediment is composed mostly of clay minerals, quartz, calcite, and feldspars with densities of 2.5 - 2.9 g/cc, and opal-A with a density of about 1.9 g/cc. The grain density of the sediment should greatly increase if there were a large decrease in the concentration of opal-A. An increase in one of the high density minerals would not greatly affect grain density, because the minerals have approximately the same density.

2. Applications of Biot Theory.

The Biot (1956a,b) theory of wave propagation in poroelastic materials has been used extensively in modeling phase velocity and attenuation in porous rocks and sediments. Recently the theory has been successfully employed for characterizing the variation of

V_p with depth z (Ogushwitz, 1985; Taylor-Smith, 1985) and for quantitatively describing dispersion phenomena (Winkler, 1985). Other authors (Murphy, 1982; White, 1986) have concentrated upon the variation of Q_p^{-1} with frequency, whilst Stoll (1974, 1985) has examined the compressional wave attenuation coefficient. The consensus of opinion from these studies is that the Biot (1956a,b) poroelastic model is adequate for describing the variation of V_p with depth, but is insufficient for characterizing attenuation/dispersion phenomena.

We have investigated the viability of the Biot (1956a,b) model for predicting V_p and Q_p^{-1} using laboratory data for deep-sea carbonate sediments from Kim et al. (1985) and Milholland et al. (1980). Our results are shown in Figure 6a. The variation of V_p with depth for DSDP sites 288 and 289 has been studied, with emphasis placed on the uncertainty in the modeled velocities that is due to experimental errors and to uncertainties in assumed parameters. The frame Poisson's ratio was then made the free parameter of the model and, by matching predicted and experimental velocities, the assumption of constant σ_1 throughout the carbonate sediment sequences has also been tested. Finally, the applicability of the Biot (1956a) theory in modeling Q_p^{-1} is examined for 14 chalk-limestone samples from DSDP sites 288, 289 and 316. For two samples, predicted values for Q_p^{-1} are found to be effectively zero if critical values of σ_1 are selected for modeling. These cases correspond to the "compatibility condition" as identified by Biot (1956a).

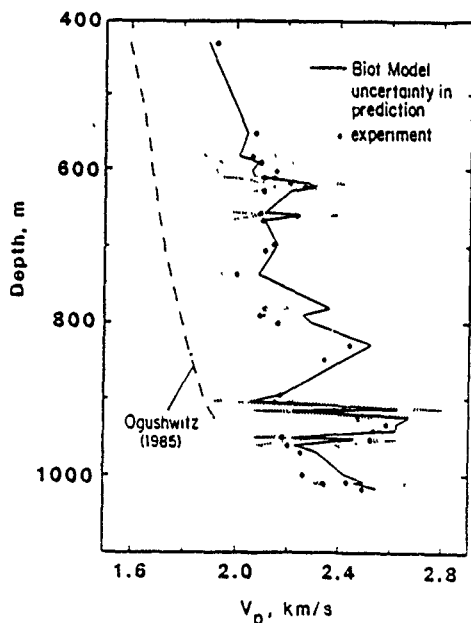


Fig 6a
Compressional wave velocity, V_p , versus depth for chalk-limestone sequence, DSDP site 289, deduced from the Biot theory [Hurley and Manghnani, 1987, submitted] Experimental measurements after Milholland et al. 1980]

3. Opal-A Work.

Significant progress has been made in the past year to document further the influence of the biogenic silica content of a sediment on the measured physical and acoustic properties. There are two primary reasons for this emphasis on biogenic silica:

(a) Opaline silica (opal-A) is the only common mineral component in marine sediments that has a density significantly different from other major components. The clay minerals, quartz, calcite, and feldspars all have densities in the range of 2.5-2.9 g/cm³, whereas opal-A has a density of about 1.9 g/cm³. Variations in the biogenic silica content of sediments, therefore, should be reflected by changes in grain density, and presumably by changes in other properties such as bulk density, acoustic velocity, etc. Hamilton [1978] reports empirically-derived relationships for the acoustic and physical properties of siliceous sediments that differ from analogous curves for sediments of different compositions. A number of investigators have also reported variations of velocity with sediment composition for sequences in which biogenic silica content varies [e.g., Wilkens and Handyside, 1985]. We have found essentially no data in the literature, however, with which the relationships with silica content can be quantified. Quantitative measurements of actual opaline silica content with depth have not been made on sediments (except in this study) for which physical and acoustic properties are known.

(b) Biogenic silica undergoes a series of diagenetic reactions with burial that alter its mineralogy, water content, density, and morphology. The properties of a marine sediment will be influenced, therefore, not only by its original biogenic silica content, but also by the pathway of silica diagenesis. Chert horizons, prevalent in Eocene-age sediments for example, are a familiar end product of this diagenetic pathway that have a clear physical and seismic signature (e.g., Tucholke, 1981). We have focused, however, on the lesser understood aspects of silica diagenesis, including the influence of the early stages of the diagenetic transformation of opal-A to opal-CT on sediment properties such as fabric. One very important result of our opal-A work is that it illustrates, as documented below, the necessity for doing rigorous mineralogical microfabric, and diagenetic studies in order to understand the behavior of the physical, acoustic, and electrical properties of a sediment sequence.

As mentioned above, one of our goals this year has been to quantify the biogenic silica content of several deep-sea sediment sequences. The method we chose is a chemical dissolution technique in which weight loss is measured after leaching of the opal-A from the sample [Follett et al., 1965; Eggiman et al., 1980]. This method was considered preferable to other techniques employing infrared spectroscopy and x-ray diffraction after conversion of the opal-A to opal-CT by heating [Chester and Elderfield, 1968; Goldberg, 1958], because of interference of quartz in the latter two methods. We needed a method that would be applicable to hemipelagic as well as pelagic sediments. The chemical dissolution technique is commonly used for soils, and to some degree for ocean surface sediments, but has not previously been used to our knowledge on a depth sequence of sediments. Because of the changes in solubility associated with early diagenesis of the silica, the technique had

to be calibrated for the type of sediments we were treating. Our method is outlined in Figure 7.

To date, we have analyzed two sediment sequences for amorphous silica content. Site 584 of DSDP Leg 87 in the Japan Trench was chosen to test the hypothesis that variations in opal-A content influence physical and acoustic properties. Shipboard smear-slide data indicated a variation in diatom content with depth, and our mineralogical studies showed no evidence of transformation of opal-A to opal-CT. Physical properties of this sediment sequence as a function depth (Figures 1-6) were discussed in the previous section.

Some relationships between the physical properties and opal-A content, as determined in our geoaoustics and sedimentological laboratories [Schoonmaker et al., 1987; O'Brien et al., 1987], are shown in Figures 8-10. Figure 8 shows the relationship between opal-A content and grain density for the sediments of Site 584. As expected, the two properties are inversely correlated. As shown in Figure 9, opal-A content is also correlated with porosity, probably reflecting pore space associated with the chambers of diatom tests. The influence of opal-A content on porosity will depend in part on the degree of fragmentation of the tests; whole tests should have the greatest effect on porosity. Finally, as predicted, opal-A content is negatively correlated with compressional wave velocity (V_p), as shown in Figure 10. Note that the opal-A contents, which vary between 7 and 13%, are relatively low, and their effect on acoustic velocity owing to mineral density differences alone would be rather small. We believe that the associated porosity differences are also an important factor in producing variations in acoustic velocity related to opal-A content.

Sediments from the second sequence analyzed, Site 467 of DSDP Leg 63, have undergone significant silica diagenesis and have been the focus of our diagenetic and fabric studies. The conversion of opal-A to opal-CT, and eventually to quartz, with increasing burial depth at this site follows a diagenetic pathway that can be traced on a plot of opal-A content vs. V_p (Fig. 11). The shallow part of the sequence contains relatively low percentages of opal-A, and acoustic velocities are independent of the opal-A content. These samples plot in zone A on the diagram. Moderate change in V_p with depth in this zone reflects primarily compaction of the clay-rich sequence. Samples containing more opal-A have higher velocities (zone B on Figure 11), defining a trend opposite to that shown by the sediments from Site 584 (see Figure 10). This apparent discrepancy is a result of silica diagenesis. The samples in zone B have all undergone partial diagenetic conversion of opal-A to opal-CT. This diagenetic reaction involves an increase in grain density and changes in the amount and nature of the porosity (see discussion of fabric changes below). The net result of the conversion to opal-CT is an increase in acoustic velocity. From our initial x-ray diffraction and SEM studies (as reported in last year's proposal), we suspected that the conversion was complete. We have shown, however, through the chemical leaching experiments and our TEM studies (see below) in the past year, that significant amounts of

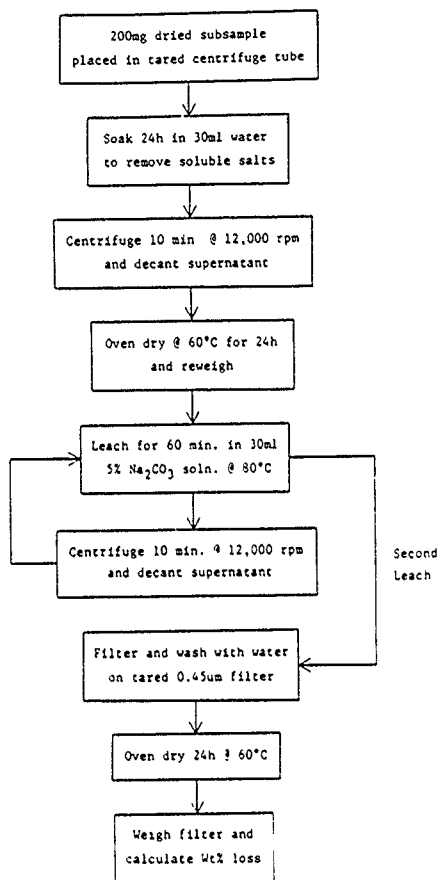
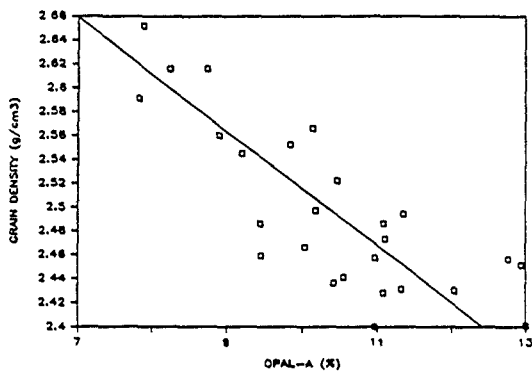


Figure 7. Opaline silica dissolution method

87-584



87-584

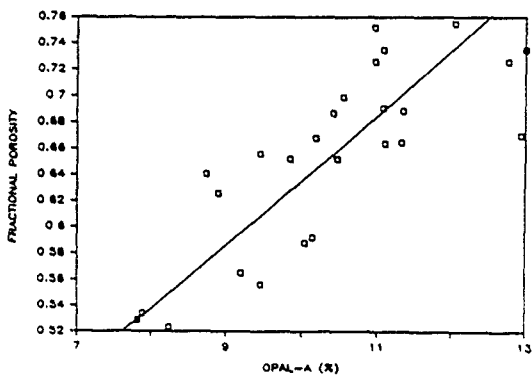
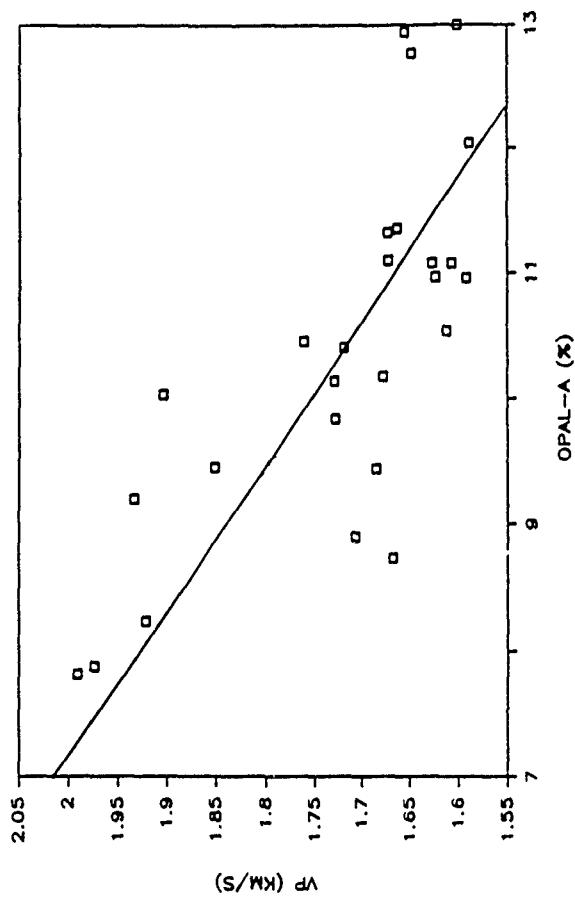


Figure 3. (Upper diagram) Variation of grain density with opaline silica content for the sediments of DSDP Leg 37, Site 584. Correlation coefficient = 0.64

Figure 9 (Lower diagram) Variation of porosity with opaline silica content for the sediments of DSDP Leg 37, Site 584. Correlation coefficient = 0.74

87-584



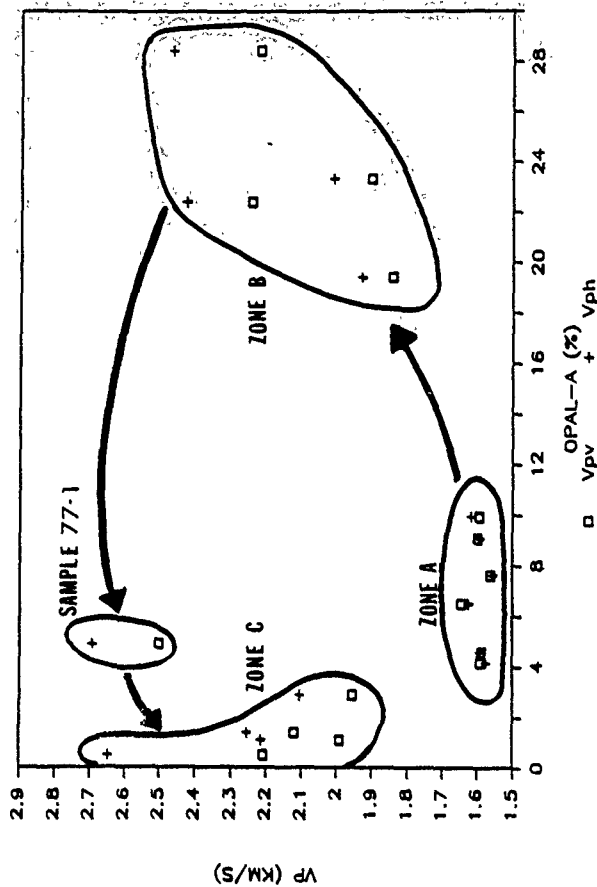


Figure 11. Plot of compressional wave velocity measured in both the vertical and horizontal directions vs opaline silica content for Leg 63, Site 467. The pathway of silica diagenesis observed at this site is indicated on the diagram. Zone A sediments contain biogenic silica present as opal-A. The opal-A has been partially converted to opal-CT in Zone B. Zone C sediments are characterized by microcrystalline quartz, a product of the recrystallization of the opal-CT.

opal-A remain, especially in the upper part of the opal-CT zone. The lowermost sample in the opal-CT zone, sample 77-1, has undergone nearly complete conversion, and therefore plots in the low opal-A, high velocity corner of the diagram. Samples from the lowest part of the sequence contain no opal-A or opal-CT, but are enriched in quartz. Although some of the quartz is detrital in origin, a portion of it is thought to originate authigenically from the conversion of opal-CT to quartz (see discussion of TEM work, below). These samples fall at the far lefthand side of Figure 11 (zone C), and their V_p values are essentially independent of opal-A content. The dependence of V_p on combined opal-CT + quartz content is shown in Figure 12.

4. Fabric Studies

Last year we began investigation of the microfabric of marine sediment using scanning electron microscopy (SEM). We obtained results that related diagenetic changes to fabric alteration, and the effects on acoustic and physical properties [Schoonmaker et al., 1987]. We focused on sediments from Leg 63, Site 467 in which the transformation of silica from opal-A to opal-CT was apparent. In continuing that work this past year we found that we could not examine the shallow half of the hole using SEM. Sample preparation required critical point drying which caused the disaggregation of the slightly-lithified shallow samples, destroying the fabric.

We decided to try a different technique, transmission electron microscopy (TEM), for the fabric studies. Sample preparation for TEM examination of fabric is a time-consuming, difficult task involving embedding blocks of the sample with resin, then examining thin sections of the material. The method we used is a liquid dehydration and spurr resin embedding technique modified from Bailey and Blackson [1984] and Jim [1985]. This method minimizes disruptions of the original microfabric of the sediment samples, especially of the poorly lithified samples from the upper part of the section. The details of this method are shown in Figure 13.

Nine samples were embedded. Sediments from the opal-A to opal-CT transition were sampled in detail and representative samples were collected from sediments above and below the opal transition. At the time of this writing, six samples covering the entire depth range have been surveyed by TEM. These samples are identified on Figure 14 which shows the V_p distribution with depth. To date, our study has been a qualitative one. The focus of our observations has been to document the following characteristics, which have an effect on acoustic and physical properties of the sediments as a function of burial depth:

1. clay platelet interrelations and orientations
2. porosity-nature (inter- vs. intra-granular), general size and shape

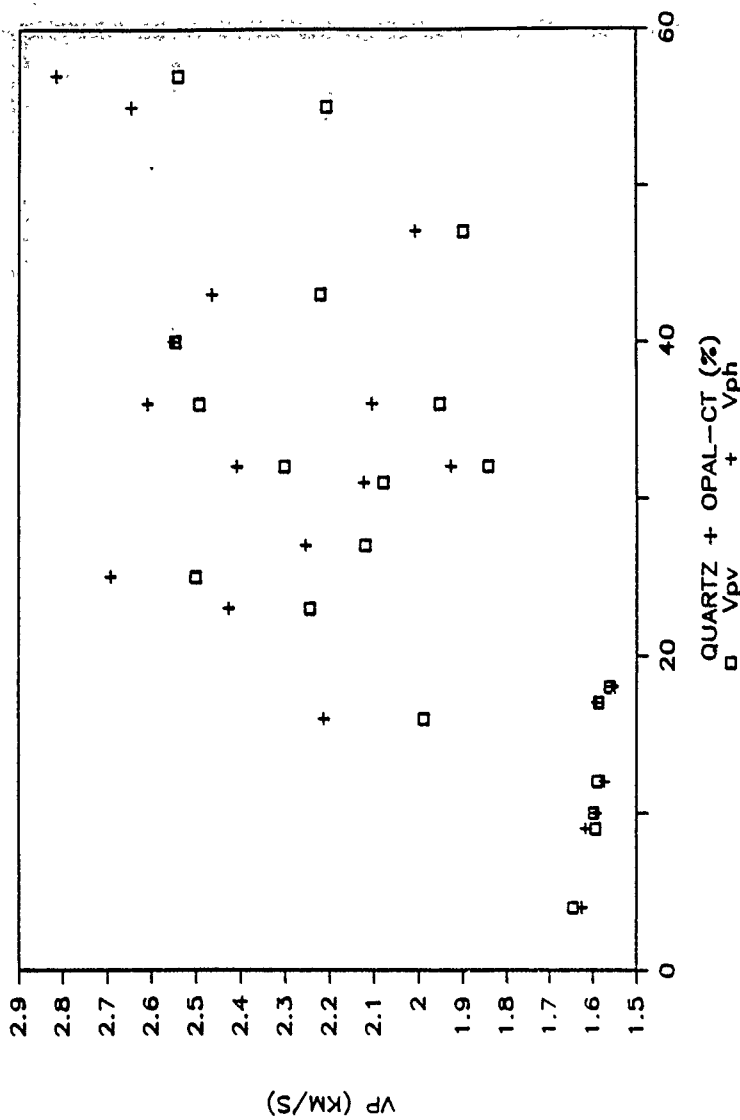


Figure 12 Variation of compressional wave velocity with the sum of quartz and opal-CT contents for sediments from HSDP leg 63, Site 467.

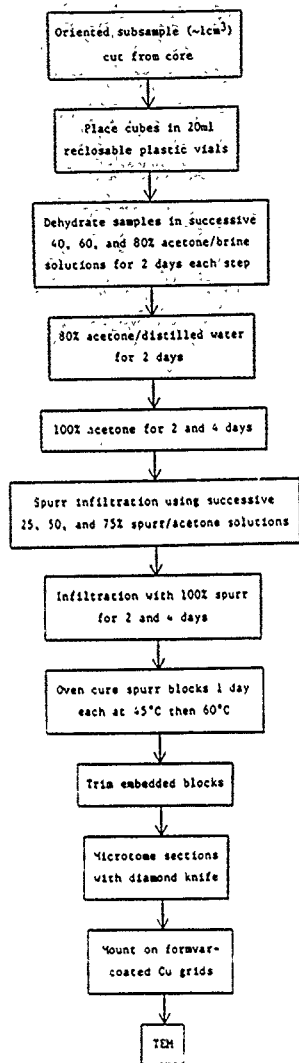


Figure 13. Spurr resin embedding and TEM preparation techniques

DSDP LEG 83
SITE 467

V_{ph} □
 V_{pv} △

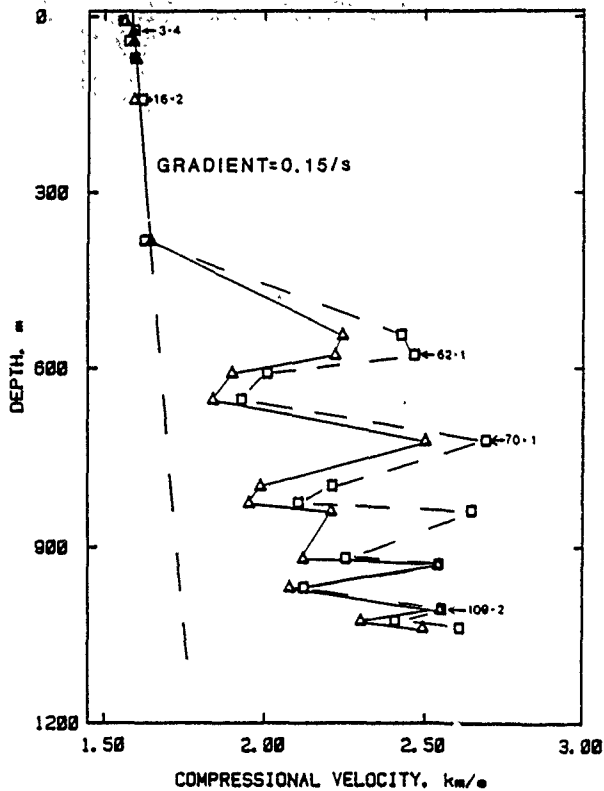


Figure 14 Compressional velocity vs depth for DSDP Leg 83, Site 467. Samples examined by TEM are indicated

3. authigenesis-formation of opal-CT, quartz, zeolites, pyrite, etc., and the effects on fabric

4. sense of overall sediment fabric and changes with depth.

Our observations are summarized below:

a. Clay platelet relationships

As has been observed by other investigators [e.g., Bratt, 1977], clay particles in shallowly-buried sediments show random orientations with respect to vertical. Plate 1 shows a representative photomicrograph of the sample from 24 m depth. The sediment grains are dominantly biogenic silica fragments and clay particles, and the clay platelets are randomly oriented and share edge-to-edge and edge-to-face contacts characteristic of the "house of cards" structure. With increasing depth, small domains of clay particles sharing face-to-face contacts form and begin to show some parallel orientation (Plate 2, 295 m). In sample 62-1 (576 m depth), a true orientation of clay domains has been established, and the rock has developed incipient fissility (Plate 3). The vertical compressional velocity increased from 1.59 km/s to 2.22 km/s over this depth range.

b. Nature of porosity

In the upper 500 m of section, intergranular porosity is high (see Plate 1). Intragranular porosity depends primarily on the biogenic silica content, although some samples also contain calcareous microfossils (forams) that contribute significantly to porosity. Plate 4 shows a radiolarian test with a large spherical interior chamber. Much of the brittle skeletal wall was plucked out during sectioning of the sediment, and therefore does not represent porosity, but the interior chamber is filled with resin indicating it was fluid filled when the sample was prepared. In contrast, the opal-CT zone (between about 500 and 725 m) is characterized by channel-like pores of irregular shape (Plate 3), with their long axes aligned parallel to the overall fabric. Smaller pores have been bridged and are being occluded by growth of opal-CT bladed cements and lepispheres. The sediments underlying the opal-CT zone have undergone the diagenetic conversion of opal-CT to microcrystalline quartz, and the sediment microfabric has been significantly altered. Plate 5 (1025 m depth) shows the dominance of intergranular microporosity in this quartz-rich sample. The pores are small, irregularly shaped, and are commonly bridged and partially filled with an authigenic clay.

c. Authigenesis

Diagenetic reactions leading to dissolution of some phases and precipitation of others can radically alter sediment fabric, and thus acoustic response. The major diagenetic reaction noted in site 467 sediments is the conversion of opal-1 to opal-CT to quartz. Plate

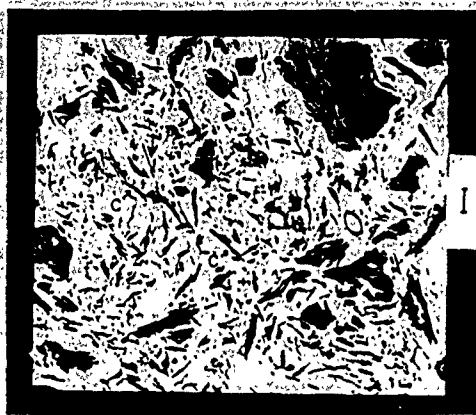


PLATE 1. Open clay fabric from shallowest sediments (Core 3-4, 24m) showing randomly oriented clay particles (C) and high porosity. Clay particles have mainly edge-to-face and edge-to-edge contacts. Larger particles are fragments of biogenic silica and other detrital sediments. Scale bar for all figures is one micron. (TEM).

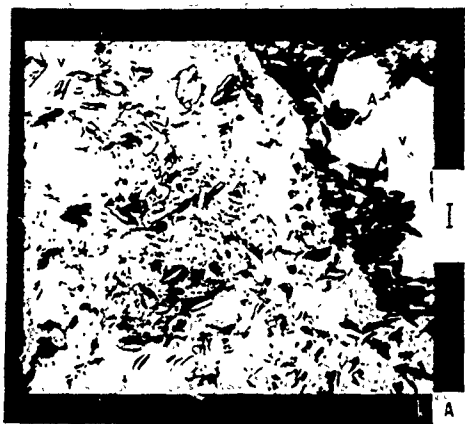


PLATE 2. A.) Incipient orientation of clay fabric. Clay particles show increased face-to-face associations and clay domains show slight preferred orientation. At top right an area of biogenic opal-A (A) shows characteristic conchoidal fracturing and plucked void (V) caused by sectioning. B.) Detail of clay particle associations. (Core 32-3, 295m; TEM).



PLATE 3. A.) Highly oriented clay domains within a matrix of opal-CT cement. Unaltered opal-A (A) is seen on the left margin. B.) Detail of opal-CT blades and lepispheres (CT) occluding pore space (P) and preferred orientation of clays. Scalloped holes and voids (V) are artifacts of sectioning. (Core 62-1, 576m; TEM).



PLATE 4. A.) Large circular pore (P) associated with biogenic silica. Much of the brittle opal-A of the test was plucked out (V) during sectioning. B.) Detail of test showing pitting and development of macroporosity along the outer margins of the test. (Core 16-2, 141.5m; TEM).

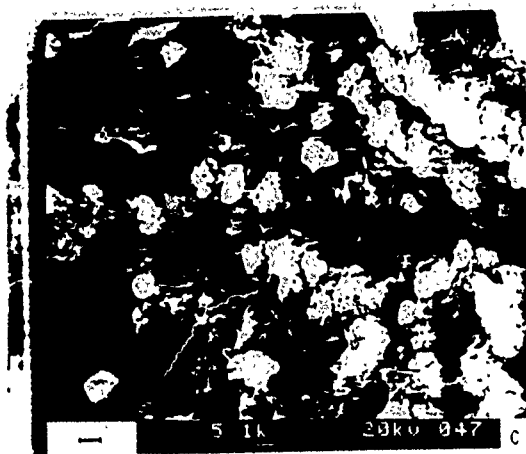


PLATE 3. A, B, and C. TEM photomicrographs of reaction zone below the spinel zone showing that the reaction is primarily intergranular. Dark, irregularly shaped features are reaction products. Scale bars are 1000 Å.

4 shows the relatively fresh opal-A of a radiolarian test in the upper part of the sequence. Note the increased micro-porosity of the opal-A along the edges of the test, apparently a sign of the early stages of dissolution. At depth the opal-A dissolves and is reprecipitated as opal-CT in the form of lepispheres and bladed cements (Plates 3 and 6b). It is apparent that the silica is locally redistributed by this process and that the nature of porosity is largely modified. Note in Plate 3a the relict opal-A at the left side of the photomicrograph. As noted above, Plate 5 shows small grains of microcrystalline quartz produced by the opal-CT to quartz conversion. Other diagenetically-produced phases noted in various samples include palygorskite, clinoptilolite, pyrite, and clay (illite?). The occurrence of pyrite, surrounded by opal-CT lepispheres, is illustrated in Plate 6.

d. Overall fabric

In this survey, we have tried to obtain a sense of changes in overall fabric that the sediment undergoes during burial. Starting with high porosity and random particle orientation (Plate 1), the sediment gradually develops a fabric characterized by elongated zones of oriented clay domains separated by zones of massive opal-CT (Plate 7). Finally, at the base of the hole, the fabric is dominated by small quartz grains and small, irregularly shaped pores bridged by clay. A faint parallel alignment of pore spaces and clay domains, however, is still apparent (Plate 5).

In Section 2 above, the role of these fabric studies in controlling sediment acoustic response is discussed.

4. Lithification Studies

The Barbados accretionary prism is made up of hemipelagic and pelagic sediments that have been scraped off the subducting Atlantic plate and incorporated into a thick wedge of sediments along the subduction zone. Two drilling legs (DSDP 78A and ODP 110; Dr. Schoonmaker participated in Leg 110) have sampled the sediments near the toe of the prism, whereas wells drilled on the island of Barbados have penetrated 3 km into the prism along its crest. During ODP 110, a transect of holes perpendicular to the front of the prism was drilled: one reference site on the Atlantic seafloor and 5 sites on the prism (Figure 15). At the reference site and 3 of the prism sites a specific unit of Miocene claystone/mudstone was sampled repeatedly at increasing depths from east to west along the transect. The increase in burial depth is a result of tectonic thickening of the section by thrust faulting and folding associated with the offscraping of the sediments.

The presence of a unit of claystone of identical age and nearly uniform composition at a variety of burial depths allows us to examine the changes in physical and acoustic properties as a simple function of compaction and early lithification. The variables of

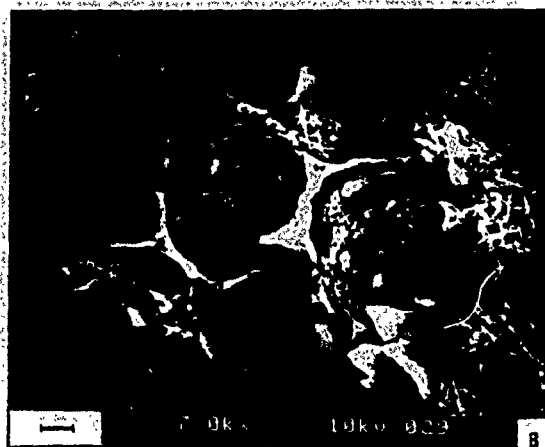
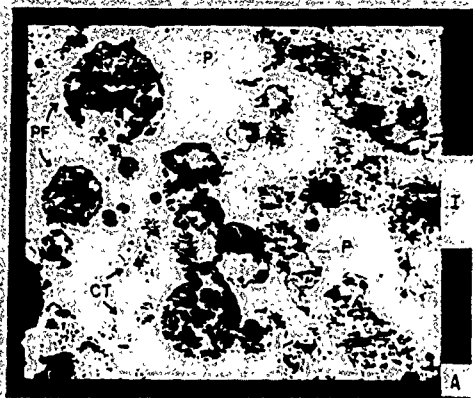


PLATE 6. A.) TEM photomicrograph of a large cavity (P) partially filled by pyrite framboids (PF) and incipient opal-CT lepispheres (CT). B.) SEM image showing void-filling pyrite framboids (PF) in a matrix of bladed lepispheres (CT). (Core 70-1, 652m).

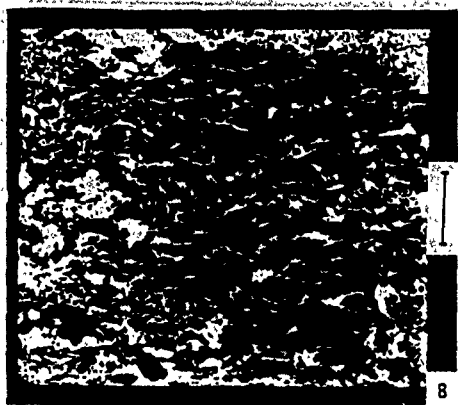
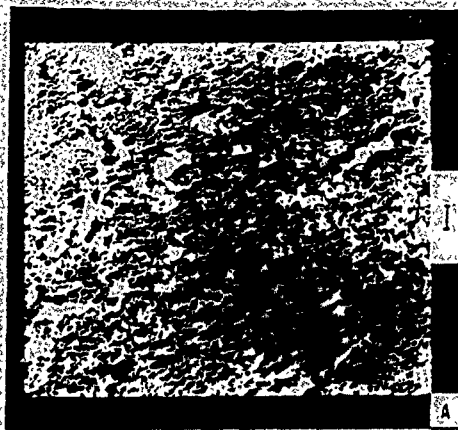


PLATE 7. A.) Sediment section dominated by massive opal-CT cement. B.) Detail showing preferred orientation of clay domains within the opal-CT matrix. (Core 70-1, 652m; TEM).

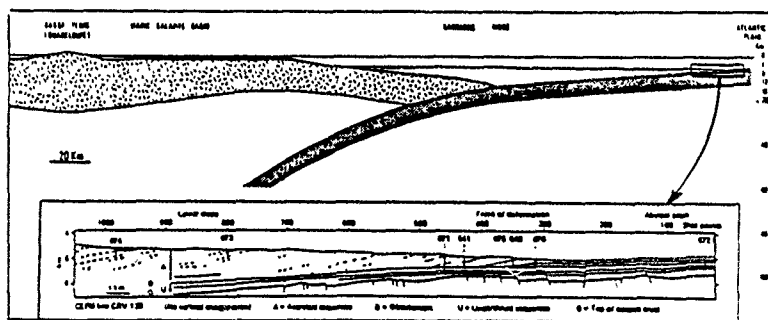
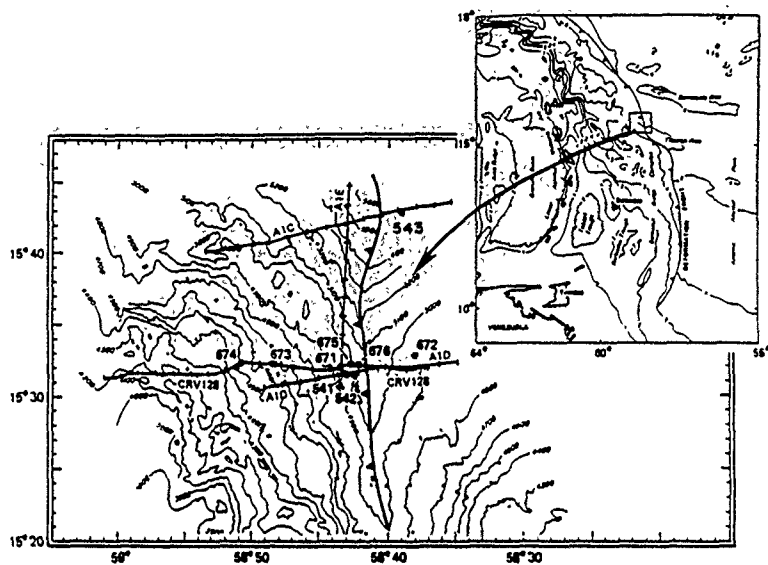


Figure 15. Location of drilling sites during ODP Leg 110 in the Barbados accretionary prism

age and original composition normally encountered in vertical sequences are eliminated. Structural deformation may be responsible for some of the observed "noise" in the data, but we believe the major trends observed reflect the effects of compaction and lithification owing to burial. This study is an extension of the one we conducted on samples of pelagic clay from DSDP Leg 86 in the Pacific [Schoonmaker et al., 1985]. The Leg 86 samples reached a maximum burial depth of 260 m and permitted us to evaluate the effects of compaction on essentially unlithified sediments. The Leg 110 samples have been buried to slightly more than 500 m and are at least partially lithified. In addition, the study of lithification of the Leg 110 claystones can be extended to 3 km burial depth by inclusion of mudstones of similar composition from wells on Barbados Island. The physical properties data for the Leg 110 samples are shipboard measurements; the data for the Barbados well samples are from our laboratory.

When plotted versus depth, the porosities of the Miocene claystone from the 4 different Leg 110 sites show a trend decreasing from roughly 65-75% for the shallow samples to 50-60% at depth (Figure 16). For each of the sites there is a superimposed zig-zag trend in the data that can be related in most cases to the location of faults in the respective sections, but these variations do not obscure the general trend. Bulk density shows a near mirror image trend of increase with depth. This is to be expected because the sediments are essentially uniform in composition, and thus in grain density. The plot of grain density vs. depth, however, does reveal a slight increase with depth, with much scatter, especially in the samples from Site 672A (Figure 17). As shown in Figure 18, the increase in grain density is also moderately correlated with a decrease in porosity. Two possible explanations for these trends are: 1. Variation in grain density reflects variable opaline silica contents, with high biogenic silica concentrations causing increased porosity. The depth trend might be a result of an original east-west variability in silica deposition and/or preservation from site to site. 2. Alternatively, progressive diagenetic alteration of the sediments with depth and occlusion of porosity by the growth of a relatively high density authigenic phase (e.g. pyrite or Mn-rich phases) could account for the observed trends. Further work is necessary to resolve this question.

The depth trends of V_p are shown in Figures 19 and 20. There are relatively few measurements of V_{pv} , and there is much scatter in the V_{ph} data, but general trends are still evident. For V_{pv} , the points for samples from deeper than about 250 m define a linear gradient of about 0.66 km/s/km. Above 250 m, the points deviate from this trend. This deviation is easily understood for samples from site 676A, because they are part of a repeated sequence emplaced at shallower depths by thrust faulting. It is not clear why samples from Site 672A deviate from the linear velocity gradient. The measurements of V_{ph} show more scatter, but a linear trend (gradient = 0.48 km/s/km) is still apparent. Points from depths less than about 200 m deviate from the trend as was the case for V_{pv} . These velocity gradients are somewhat higher than those measured at a number of other

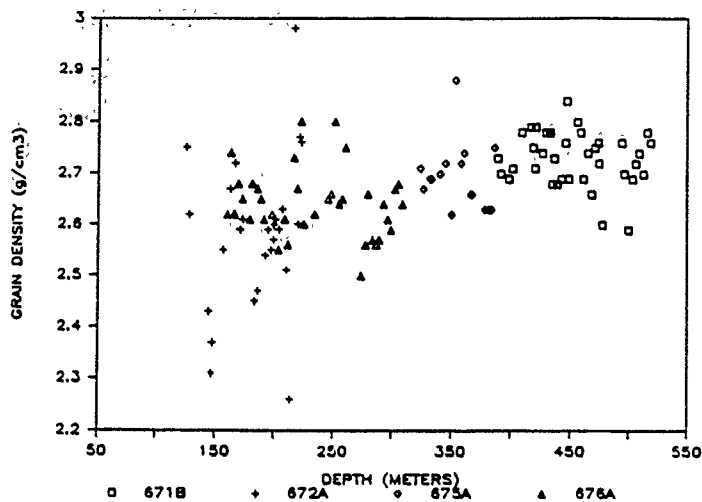


Figure 17. Variation of grain density with depth for Miocene claystone from four sites of ODP Leg 110.

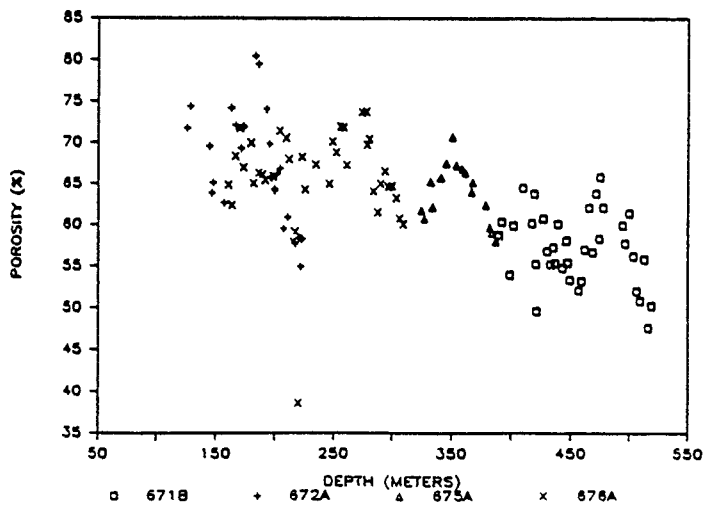


Figure 16. Variation of porosity with burial depth for Miocene claystone sampled at four drilling sites of ODP Leg 110.

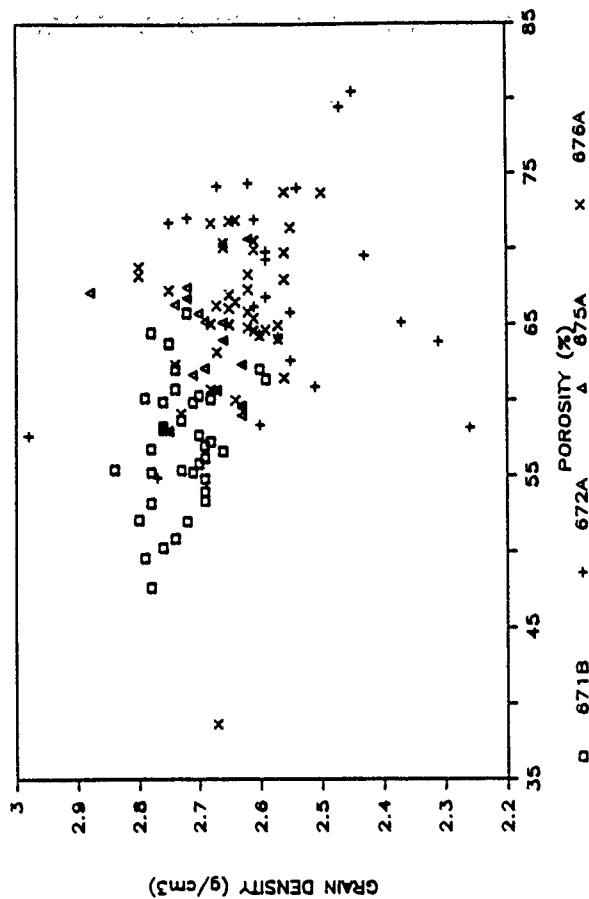


Figure 18. Correlation of grain density with porosity for Miocene claystones from four sites of ODP Leg 110.

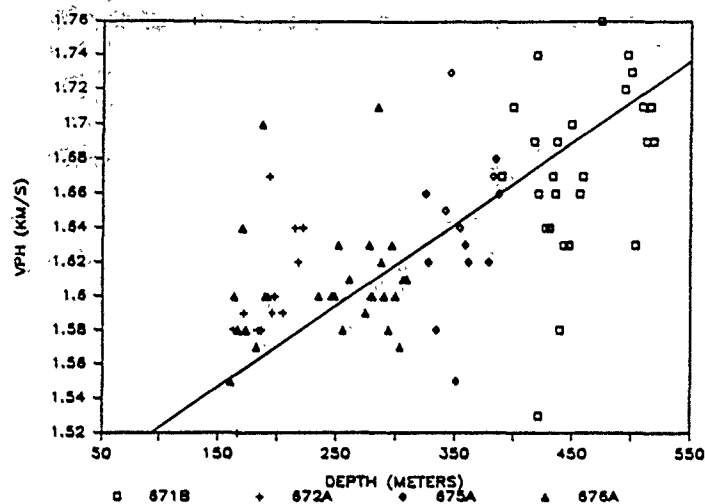


Figure 20. Trend with depth of compressional velocity measured in the horizontal direction for Miocene claystone from four different sites of ODP Leg 110.

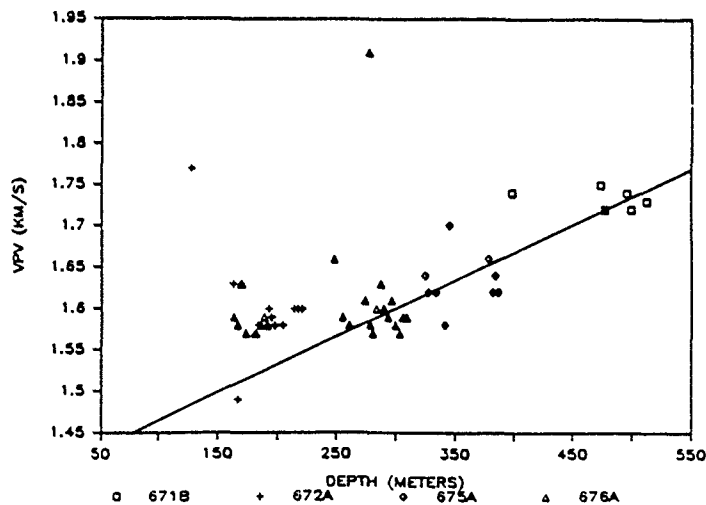


Figure 19. Trend with depth of compressional velocity measured in the vertical direction for Miocene claystone from four sites of ODP Leg 110.

sites [Schoonmaker et al., 1987]. Tectonic factors may play a role in accelerating lithification processes, or the natural range of velocity gradients for clay-rich sediments may be greater than indicated initially by our relatively small data set (9 sites).

It is informative to extend the depth range of the velocity trends by including samples from wells on Barbados Island in the data set. The well samples are Eocene, not Miocene, in age, but their compositions are similar to those of the Miocene claystones of Leg 110. Figure 21 shows the trends of velocity to over 3 km burial depth. The measurements of V_{pv} appear to follow the vertical V_{pv} gradient established in the upper 500 m of section by the Leg 110 samples. The V_{ph} data, however, follow a steeper gradient reflecting the development of anisotropy.

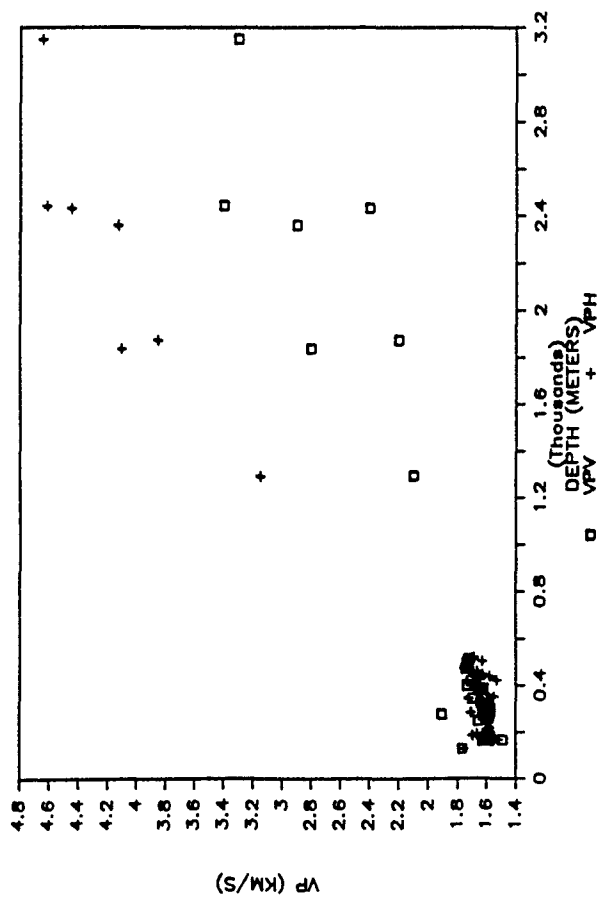
These preliminary results are intriguing, and we plan continued research into trends of physical, acoustic and diagenetic properties associated with lithification (see proposed research section).

5. Leg 93, Site 603

During DSDP Leg 93, a deep continental rise site (603) was drilled. Last year we obtained samples from this site, and preliminary acoustic and physical properties measurements were made on the upper 830 m of the site. In the past year, the bulk mineralogy of these samples was determined and quantified for the major components: total clay, quartz, feldspar, calcite, dolomite, and zeolites. The upper 400 m of section are calcareous with variable carbonate contents ranging up to 40% (Figure 22). Below 400 m, carbonate is present only in a few isolated layers, and the mineralogy is dominated by clay minerals (Figure 23). This change in lithology results in a slight trend of increasing V_p with decreasing carbonate and increasing clay content, but it is felt that this trend is an artifact of the depth distribution of the minerals, and does not reflect a lithologic control on velocity.

The depth trend of V_p , especially below 400 m, based on our acoustic measurements, is characterized by sharp fluctuations between high and low values of V_p (Figure 24). These alternations in V_p do not appear to be related to changes in abundance of any of the major mineral components. There is a crude correlation of % quartz with V_p (Figure 25), but it is not felt that the relationship is strong enough to account for the V_p fluctuations. Haggerty et al. [1987] reported the presence of a few isolated silt layers, thought to represent the turbidite deposition, below 700 m at this site. Above 700 m, small quantities of sand and silt are dispersed throughout the section, but no discrete silt layers were detected. These sediments are thought to have been fed to the site as muddy turbidites from the continental slope and then redistributed by bottom currents [Haggerty et al., 1987]. Perhaps grain-size variations (% silt and % sand) or variable cementation play important roles in determining the velocities of these sediments. While the samples were

Figure 21. Depth trends of vertical and horizontal compressional velocity for claystones from ODP Leg 110 and from a well drilled on Barbados Island.



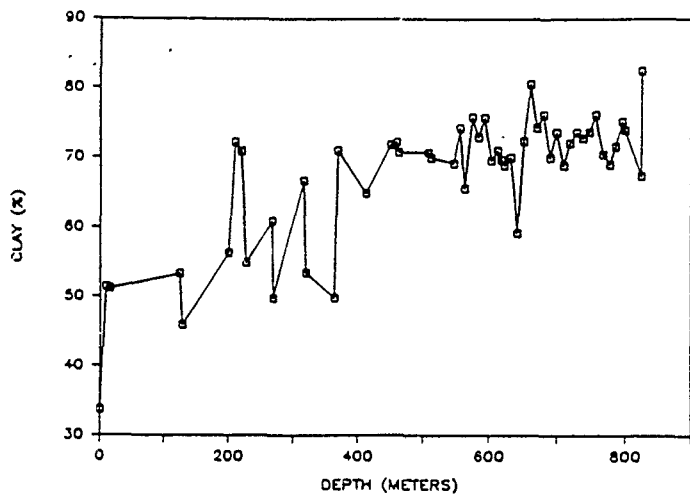


Figure 23. Clay mineral content vs depth for sediments from DSDP Leg 93, Site 603.

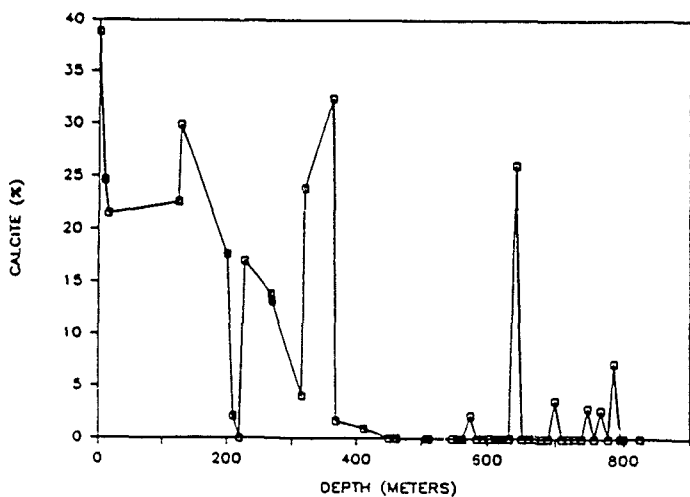
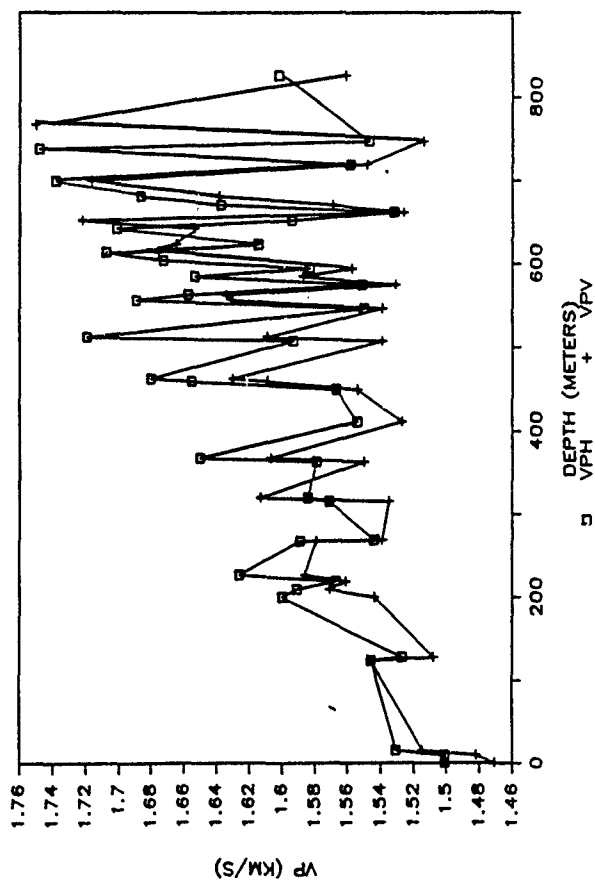


Figure 22. Variations in with depth of the calcite content of sediments from DSDP Leg 93, Site 603

Figure 24. Compressional velocity vs depth for sediments from DSDP Leg 93, Site 603.



93-603

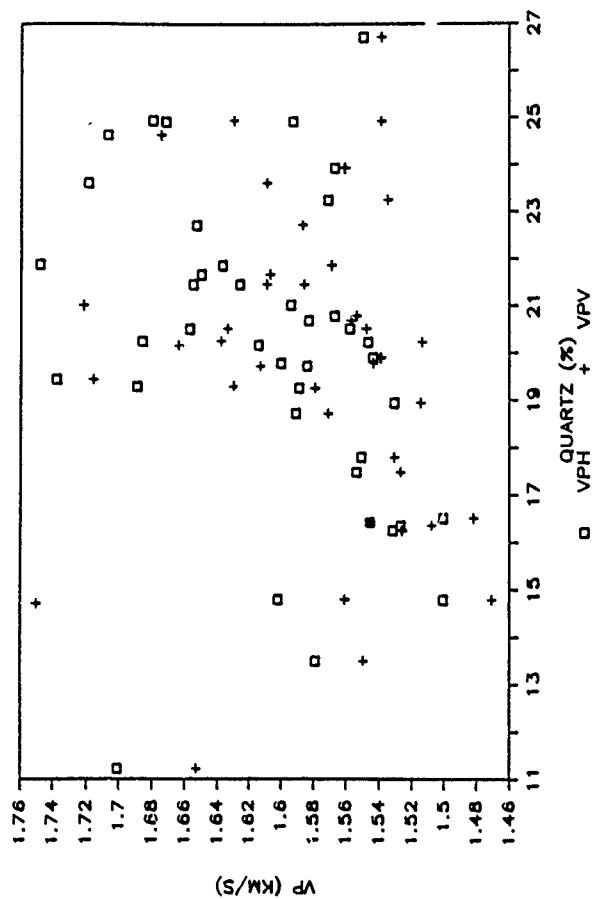


Figure 25 Correlation of compressional velocity with quartz content for DSDP Leg 93, Site 603.

being prepared for X-ray diffraction, qualitative notes were kept on the ease of cutting and grinding the samples from the bottom 100 m of the hole. The samples cut with difficulty correspond to velocity highs. More work is obviously necessary to identify the cause of the V_p fluctuations.

6. The following manuscripts reporting the results of our research are in press or preparation:

Hurley, M. and M.H. Manghnani,, Modeling of compressional wave velocities and attenuation in carbonate sediments, 1987, submitted to J. Acoust. Soc. Am.

O'Brien, D., M. Manghnani, and J. Schoonmaker, Physical and mineralogical properties of DSDP Leg 87, Hole 584, 1987. to be submitted.

Manghnani, M.H., D.C. Kim, D. O'Brien, R.H. Wenk and F.T. Mackenzie, Physical and acoustic properties of marine sediments: Roles of pore geometry and preferred orientation in anisotropic behavior, in preparation.

Schoonmaker, J., F.T. Mackenzie, M. Manghnani, and J. Urmos. Compressional velocity-depth profiles: The influence of compaction and diagenesis, submitted to Geology.

Schoonmaker, J. and F.T. Mackenzie, Progressive trends in diagenetic, acoustic, and physical properties during lithification of claystones in an accretionary prism setting, in preparation.

Contract: N00014-87-K-0181
Seismology & Acoustics

Marching the Elastodynamic Wave Equation

L. Neil Frazer

Dynamic Elasticity of Microbedded and Fractured Rocks

L. NEIL FRAZER

Hawaii Institute of Geophysics, University of Hawaii at Manoa, Honolulu

Microbedded rocks have an anisotropic frequency-dependent sound speed which depends on the intrinsic sound speeds of the individual microbeds and on the O'Doherty-Anstey effect. Fractured rocks have an anisotropic frequency-dependent sound speed which depends on the intrinsic sound speed of the unfractured rock, the frequency-dependent phase shift that occurs during reflection or transmission across a fracture, and the interface O'Doherty-Anstey effect. These effects are neglected by the quasistatic methods presently used to generate elastic constants. Here I introduce a new method for generating elastic constants that contain all the above effects. First, a statistical description of the rock is used to generate a sample of the rock. Then an exact two-way method is used to propagate just a few plane waves, of frequency f , a distance of several wavelengths from the source. If an equivalent homogeneous medium exists at frequency f , then the computed motions must also satisfy a one-way elastic wave equation for that equivalent medium. This one-way wave equation is used to invert for the elastic coefficients. When no equivalent medium exists, perhaps because f is too large, this is indicated by the inversion. Possible applications of the method are prediction of seismic sound speeds from measurements of bed thicknesses in cores; analysis of laboratory data for fracture constitutive relations; and inversion of multioffset vertical seismic profiling data for elastic coefficients comparable with those predicted from cores.

1. INTRODUCTION

Comparison of seismic data with well cores shows that seismic waves are not strongly scattered by heterogeneities that are much smaller than a wavelength. Rather, the net effect of such heterogeneities is to cause the medium to behave like a homogeneous medium with altered seismic sound speeds and decreased Q . If the heterogeneities or their pattern of distribution are not isotropic, then the resulting apparent medium is anisotropic. This paper is about heterogeneities, either fractures or microbeds, which are planar and parallel. Spherical inclusions and other low aspect ratio heterogeneities are not treated.

There are many different crack theories (see Figure 1), but for seismology applications, such theories can be classified in two ways. The first classification is crack versus fracture. Crack theories [e.g., Hudson, 1980, 1981; Nishizawa, 1982] consider distributions of small, on the scale of a seismic wavelength, unconnected, possibly subparallel cracks, whereas fracture theories [e.g., Schoenberg, 1983; Schoenberg and Douma, 1988] treat systems of infinite plane-parallel cracks. The second classification is static versus dynamic. Static theories [e.g., Budiansky and O'Connell, 1976; Hoening, 1979; Schoenberg and Douma, 1988] generate equivalent elastic constants by use of a static stress-strain relation, whereas dynamic theories [e.g., Hudson, 1980, 1981] generate elastic constants by inversion of an integral equation for the passage of finite frequency waves through the medium. Dynamic theories give estimates of Q , whereas static theories do not. At present, there is no dynamic theory for fracture systems, though Schoenberg [1980] has derived the dynamic response of a single fracture using his displacement discontinuity fracture model, and Pyrak-Nolte *et al.* [1987] have shown that his model gives a good fit to measurements of reflected and transmitted P waves normally incident on the fracture.

Microbedding theories could also be classified as static versus dynamic. Static theories [e.g., Backus, 1962] use a static stress-strain relation to generate elastic constants for a rock consisting of infinite plane-parallel microbeds. The static microbed theory of Schoenberg and Mur [1989] has the advantage, for seismology applications, that the same mathematical formalism is used for both microbeds and fractures. At present, there appear to be no dynamic microbedding theories which yield elastic coefficients, although much work has been done on the relation between microbedding and apparent Q . Menke [1983a] has shown how to predict the apparent attenuation of a Goupillaud medium, at vertical incidence, from the root-mean-square sound speed fluctuation. Menke [1983b] showed that P -SV coupling due to microbeds decreases the apparent Q_p more than the apparent Q_s and that the apparent sound speed of the SV wave is increased. Menke and Dubendorff [1985] showed that normal incidence transmission data could be inverted for both intrinsic Q and scattering Q if intrinsic attenuation is mainly due to shear. Burridge *et al.* [1988] considered acoustic propagation in a Goupillaud medium and derived an integrodifferential equation governing the evolution of the seismic pulse as it propagates through the medium. Burridge and Chang [1989] consider P wave propagation in a micro-layered elastic medium and derive an integrodifferential equation governing propagation in the limit as interlayer reflection coefficients approach zero, but they do not consider equivalent media.

The method outlined in this paper can be used to generate dynamic elastic constants for both microlayered and fractured media. It thus addresses two of the gaps in the literature cited above. Section 2 gives the main ideas, and subsequent sections give the theory applicable to useful special cases.

2. MICROBEDDED ROCKS

There are many situations in which it is desirable to generate elastic coefficients for a microbedded rock. For example, suppose that we have a sediment core 5–10 m long

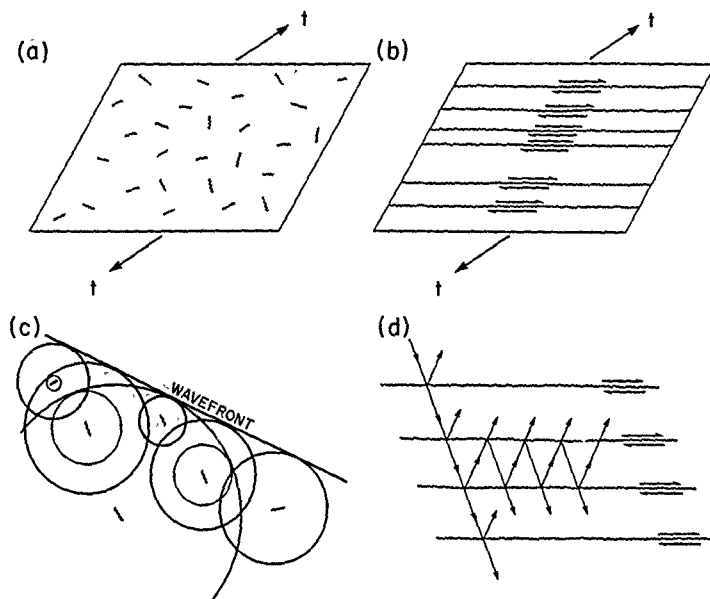


Fig. 1. (a) Static crack theories: the macroscopic stress on the rock is partly relieved by displacement jumps across crack boundaries. The apparent constitutive relation is perfectly elastic. (b) Static fracture theories: macroscopic stress is partly relieved by displacement jumps across fracture boundaries in accordance with a (static) fracture constitutive relation. (c) Dynamic crack theories: a plane wave passing through the medium is composed of a primary wave and secondary waves generated by interaction of the primary wave with the microcracks. The macroscopic plane wave decays with distance because of backscatter. (d) Dynamic fracture theory: plane waves passing through the medium are reflected and refracted at each fracture. Frequency-dependent phase shifts are induced by the fractures themselves, even if they absorb no energy, and by interbed multiples.

and we wish to predict the effect of the core sediments on seismic waves with wavelengths several hundred meters long. Conceivably, we could measure the thickness and properties of each microbed in the core (there might be several thousand of these) and put each microbed into our seismic model. As the cost of seismic modeling is linear with the number of beds, this will be expensive. Also, it does not address the question of how to model sediments beneath the core, sediments quite likely to be seismically similar to those in the core. If the core is homogeneous at length scale λ , then much time could be saved by finding a few elastic constants that predict its behavior for seismic waves of wavelength λ .

Logically, the method consists of three steps: in step 1 a sample realization of the microbedded rock is generated from the statistics of the microbedding; in step 2 a few plane waves are propagated through the realization using exact two-way wave theory; in step 3 the two-way synthetic data are inverted using one-way theory for elastic waves. In practice, it may be numerically efficient to combine steps 1 and 2 so that microbeds can be discarded as soon as they are used.

A sample realization of the microbedded rock can be generated in many different ways. *Krumbein and Dacey*

[1969], *Schwarzacher* [1972], *Godfrey et al.* [1980], and *Velzeboer* [1981] model sedimentary sequences as M state Markov chains, where M is the number of distinct lithologies. (A Markov chain is a random sequence of states for which the probability of being in a certain state depends only on the previous state.) Of course, if a core is available, then whatever model is used should have the same statistics as the core; that is, the core must be a likely realization of the model.

To make the discussion more concrete, consider a simple sand-shale sequence. Suppose that cores or other field observations indicate that the thickness s of the sand beds has the exponential distribution, $p(s) = \bar{s}^{-1} \exp(-s/\bar{s})$, where \bar{s} is the mean sand thickness. Similarly, the thickness t of the shale beds has the distribution $p(t) = \bar{t}^{-1} \exp(-t/\bar{t})$, where \bar{t} is the mean shale thickness. The two parameters \bar{s} and \bar{t} can be inferred by measurement on a core or outcrop. To generate a realization of the rock in the computer, we alternately sample from the two thickness distributions. A standard technique for sampling from an arbitrary distribution in the computer is to map the computer-supplied uniform random number generator into the cumulative probability density (cpd) function of the desired distribution. The

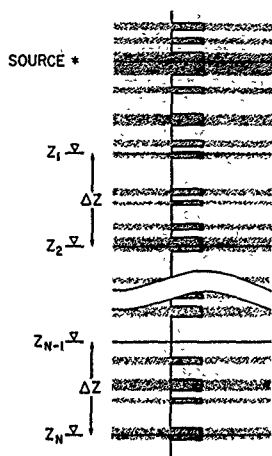


Fig. 2. A realization of the microbedded medium. Receivers are all beneath the source and Δz apart.

cpd function of the exponential distribution for the sand thickness is $p_c(s) \propto 1 - \exp(-s/\lambda)$.

The method of this paper requires that only a few waves be propagated through the material, so if a core were available, one might wish to use the core itself as the realization. However, in order for the seismic model inferred from the core to be generally valid, it is necessary that virtually all realizations give the same seismic response. Thus, in theory, there is no particular virtue in using the core for modeling; its only use is to estimate the statistics of the sedimentary process. In practice, one cannot know exactly all the statistics of the sedimentary process; so, if one is fortunate enough to have a long enough core, then using that core as a realization is a tedious but sensible thing to do.

Having gotten a realization of the random sedimentary sequence and knowing the sound speeds and densities of each of the microbeds in the sequence, one proceeds to step 2. As shown in Figure 2 a source is embedded in the realization, and exact two-way seismic wave theory is used to calculate the resulting motions at various depths beneath the source. The synthetic source emits only one monochromatic plane wave at a time so the only distances that matter are distances normal to the bedding planes. Each receiver should be separated from its neighbors by less than a seismic wavelength. The source must generate both PSV and SH motions. An example of such a source is a point force with equal components in the three coordinate directions. It does not matter in which type of bed the source is located because the source washes out of the inversion. Neither does it matter in which type of bed a receiver is located, because the physical variables being synthesized are all continuous across interfaces and the beds are much thinner than a wavelength. Of course, for frequencies at which bed thicknesses are an appreciable fraction of a wavelength it does matter in which type of bed a receiver is located. At such

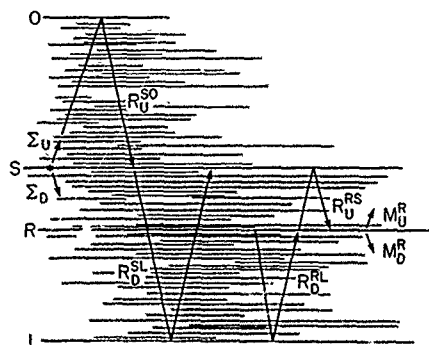


Fig. 3. Synthesis of exact two-way plane wave data in the realization of the microbedded medium. The realization is made infinite by adding beds above the source until R_U^{SO} converges and by adding beds beneath the deepest receiver until R_D^{SL} converges.

frequencies the concept of an equivalent medium begins to lose its usefulness. This matter is discussed in greater detail in section 7.

The propagation step can be carried out using either Kennett's (1974, 1983) method or the global matrix method [Chin et al., 1984; Schmidt and Jensen, 1984; Schmidt and Tango, 1986]. It is important that there be enough microbeds both above the source and below the deepest receiver, so that the realization is effectively infinite. With the Kennett method this is easily achieved by generating the realization coeval with the propagation. As shown in Figure 3, beds are generated upward from the source until R_U^{SO} , the upward looking reflection coefficient from the source, converges to a limit. This limit must exist because the motion is less affected by far beds than by near beds. Similarly, beds are added beneath the deepest receiver until R_D^{SL} , the downward looking reflection coefficient from the receiver, converges to its limit. Thus beds can be discarded soon after being generated.

Assume that each microbed is azimuthally isotropic (AI), i.e., hexagonally symmetric with a vertical axis of symmetry. Two-way propagation modeling in a material consisting of homogeneous AI layers can be made very rapid by use of the formulas of Fryer and Frazer (1987, section 4.3). One calculates the response of the model for two or more plane waves at a single frequency f . The reason at least two plane waves are needed will become clear below.

Now take the synthetic data calculated using an exact two-way method for the microbedded medium and invert it using one-way wave theory for a homogeneous medium. A derivation of the one-way elastic wave equations for plane waves is given in section 5. Here it is necessary to know only that for downward PSV propagation of plane waves, whose wave fronts are parallel to the y axis, the wave equation is

$$\partial_z u = i\omega H \cdot u \quad (1)$$

in which $u = [u, \tau_{zz}]^T$, u_x is the x component of velocity, τ_{zz} is the zz component of stress, and H is the 2×2 "Hamiltonian" matrix whose components we wish to recover. The

entries of H_V are functions of the elastic constants and the plane wave slowness p_x . Their parametric forms are given below. Similarly, for downward SH propagation the governing one-way wave equation is

$$\partial_z v_y = i\omega H_H v_y \quad (2)$$

in which v_y is the y component of velocity and H_H is the "SH Hamiltonian" which depends on the elastic constants and p_x .

Now the components of H_V and H_H are recovered numerically from the synthetic data for a particular plane wave. As shown in Figure 2, the motions u and v_y have been synthesized at $N \approx 3$ "receiver" depths beneath the source. Receivers are separated in depth by Δz . Let the synthesized value of v_y at depth j be denoted by $(v_y)_j$. If an equivalent homogeneous medium exists, then the synthetic SH data at adjacent depths must satisfy

$$(v_y)_{j+1} = \exp(i\omega \Delta z H_H)(v_y)_j \quad (3)$$

Therefore the numerical value of H_H is recovered from any two adjacent receivers in the form

$$H_H = \frac{1}{i\omega \Delta z} \ln \left(\frac{(v_y)_{j+1}}{(v_y)_j} \right) \quad (4)$$

and one can expect to get a better estimate of H_H by averaging over all $N - 1$ pairs of adjacent receivers.

For the PSV system denote the synthesized value of u at depth j by $(u)_j$. Now form two $2 \times (N - 1)$ data matrices, A and B . The columns of A are $(u)_1, \dots, (u)_2$; and the columns of B are $(u)_{N-1}, \dots, (u)_1$. If an equivalent homogeneous medium exists, then these two matrices of synthetic data must be related by

$$A = \exp(i\omega \Delta z H_V)B \quad (5)$$

Accordingly, one can recover the numerical value of H_V as

$$H_V = \frac{1}{i\omega \Delta z} \ln (AB^{-1}) \quad (6)$$

in which B^{-1} is a generalized inverse of B . The matrix logarithm here is just $E^{-1} \text{diag}(\ln \lambda_1, \ln \lambda_2) E$, where $E^{-1} \text{diag}(\lambda_1, \lambda_2) E$ is any diagonalization of B . If the computer supplied $[-\pi, \pi]$ branch of $\ln(\cdot)$ is used, then receivers must be separated by less than half a seismic wavelength, but if the $[0, 2\pi]$ branch is used, then receivers can be separated by nearly a full seismic wavelength. Thus the $[0, 2\pi]$ branch is better. Vertically travelling waves ($p_x = 0$) are most prone to aliasing because the effective vertical wavelength of each wave type increases with p_x .

It can be seen that in order to generate the data matrices A and B , only three receiver depths are necessary. Extra receiver depths add precision to the estimate of H_V , and they also permit an estimate of the error in H_V . For example, suppose six receiver depths are used. Then there are four three-receiver groups with 50% overlap and two three-receiver groups with no overlap. Consider the groups with no overlap. Propagation within a group is affected much more by beds within the group than by beds outside of it. As the beds within a group have no correlation with those in a nonoverlapping group, each group sees a different realization of the medium. The change in H_V between different

realizations is the error in H_V . If this error is relatively large then there is no equivalent homogeneous medium.

As tensor densities have been found in equivalent media for perfectly periodic fluid-fluid media [Schoenberg and St 1983] and periodic fluid-solid media [Schoenberg, 198] they can also be expected to be necessary in solid-solid media. For an AI medium the density tensor must be invariant under rotations about the z axis, and so ρ $\text{diag}(\rho_{xx}, \rho_{xx}, \rho_{zz})$.

Equations (4) and (6) are used to recover the numerical values of H_V and H_H for several values of p_x . H_V and H_H are then squared; then we use the following formulas for I and H_H^2 to extract the elastic constants of the equivalent homogeneous medium.

$$H_H^2 = I + Jp_x^2 \quad I = \rho_{11}C_{44}^{-1}$$

$$J = C_{44}^{-1}(C_{12} - C_{11})/2$$

$$(H_V^2)_{11} = C + Dp_x^2 \quad C = \rho_{11}C_{44}^{-1}$$

$$D = C_{13}C_{33}^{-1} - C_{44}^{-1}(C_{11} - C_{13}C_{33}^{-1})$$

$$(H_V^2)_{12} = Gp_x$$

$$G = C_{33}^{-1}(1 + C_{13}C_{44}^{-1})$$

$$(H_V^2)_{21} = Mp_x + Np_x^3$$

$$M = \rho_{11} + \rho_{33}C_{13}C_{33}^{-1}$$

$$N = C_{13}^2C_{33}^{-1} - C_{11}$$

$$(H_V^2)_{22} = S + Tp_x^2$$

$$S = \rho_{33}C_{33}^{-1} \quad T = C_{13}C_{33}^{-1} \quad (7)$$

Least squares fitting of these formulas for at least two values of p_x yields the quantities I, J, C, D, G, M, N, S , and T . The elastic coefficients are recovered from them as follows.

$$C_{44} = N(D - T)^{-1}$$

$$\rho_{11} = C_{44}I = C_{44}C$$

$$\rho_{33} = (M - \rho_{11})T^{-1}$$

$$C_{33} = \rho_{33}S^{-1} \quad (8)$$

$$C_{13} = C_{44}(GC_{33} - 1) = C_{33}(M - \rho_{11})\rho_{33}^{-1} = C_{33}(D - NC_{44}^{-1})$$

$$C_{11} = -N + C_{13}^2C_{33}^{-1} = C_{44}(C_{13}C_{33}^{-1} - D) + C_{13}^2C_{33}^{-1}$$

$$C_{12} = -C_{11} - 2C_{44}J$$

The C_{IJ} and ρ_{ij} are complex quantities which depend on the single frequency at which the two-way synthetic data were generated. In order to see the frequency dependence of these quantities we must generate synthetic data at a number of different frequencies. The Q of each C_{IJ} is usually defined by the relation [O'Connell and Budiansky, 1978]

$$Q_{C_{IJ}}^{-1} = -\frac{\Im(C_{IJ})}{\Re(C_{IJ})} \quad (9)$$

where the minus sign on the right-hand side appears because we are assuming a forward Fourier transform $\mathcal{F} = \int_{-\infty}^{\infty} dt e^{i\omega t}$. A Q defined in this way may not be immediately useful because it cannot be directly compared with a Q determined in the laboratory from physical propagation measurements. A Q defined in terms of sound speed may be more useful.

ly large,

at media
and Sen,
1984),
solid must be
so $\rho =$

umerical
and H_H
is for H_V
quivalent

$C_{13}^2 C_{33}^1$)

~ 1
33 (7)

wo values
nd T. The
llows:

(8)

$-NC_{44}^{-1}$)

I_1

end on the
data were
ce of these
number of
defined by

(9)

ars because
 $\bar{r} = \int_{-\infty}^{\infty} dt$
ately useful
determined
measurements.
ore useful.

For example, let Q_{av} be the Q of vertically travelling compressional waves and let Q_{bv} be the Q of vertically travelling shear waves. Natural definitions of these quantities are

$$Q_{av}^{-1} = 2 \frac{\Re[(\rho_{33}/C_{33})^{1/2}]}{\Re[(\rho_{33}/C_{33})^{1/2}]} \quad (10)$$

$$Q_{bv}^{-1} = 2 \frac{\Re[(\rho_{44}/C_{44})^{1/2}]}{\Re[(\rho_{44}/C_{44})^{1/2}]}$$

The modulus Q of equation (9) will be numerically equivalent to a sound speed Q when the imaginary part of density is small, compared to its real part, and Q is greater than about 50.

There is a way of improving the estimate of H_V that has not yet been discussed. In the course of generating the two-way synthetic data for $u = [u_x, u_z]^T$ and v_y , one can also generate synthetic data for $w = [\tau_{xz}, v_z]^T$ and τ_{yz} . The downward propagation of w is also governed by equation (1), and the downward propagation of τ_{yz} is governed by equation (2). Thus these synthetic data can also be used to determine H_V and H_H . Estimates of H_H from v_y data and from τ_{yz} data can be averaged, but for H_V it is probably better to combine the w data with the u data at an earlier stage. The simplest way to do this is to augment the data matrices A and B with columns of w data: the matrix A acquires the extra columns $(w)_N, \dots, (w)_2$, while the matrix B acquires the extra columns $(w)_{N-1}, \dots, (w)_1$. In theory, these extra columns carry no new information, but numerically, their inclusion is likely to improve the estimate of H_V . It may seem strange at first that only one realization of a random microbedding or fracturing process is needed in order to learn everything about the equivalent medium. One explanation is that the random process is stationary. Thus, to the extent a group of receivers is separated from another group, the two groups see different realizations. Furthermore, both groups had better give nearly the same equivalent medium or else the notion of an equivalent medium is not a useful one at that frequency.

3. A SINGLE FRACTURE

Before treating fracture systems we derive generally valid reflection and transmission coefficients for the linear slip fracture model of Schoenberg (1980). The procedures for treating fracture systems, introduced in the next section, are not limited to this model, but the data and analysis of Pyrak-Nolte *et al.* [1987], who refer to it as the displacement discontinuity model, indicate that it works very well for P waves normally incident on a natural fracture in quartz monzonite. The single-fracture reflection coefficients are needed to compute exact two-way synthetic seismograms for a fractured solid by the Kennett [1983] method.

In the linear slip model the fracture displacement jump Δs is related to the fracture traction t and the symmetric 3×3 fracture compliance matrix η through the relation $\Delta s = \eta t$. For a fracture parallel to the xy plane we write this in terms of components as

$$\begin{bmatrix} \Delta s_x \\ \Delta s_y \\ \Delta s_z \end{bmatrix} = \begin{bmatrix} \eta_{xx} & \eta_{xy} & \eta_{xz} \\ \eta_{yx} & \eta_{yy} & \eta_{yz} \\ \eta_{zx} & \eta_{zy} & \eta_{zz} \end{bmatrix} \begin{bmatrix} t_x \\ t_y \\ t_z \end{bmatrix} \quad (11)$$

Notice that reversing the order of the components in both Δs and t causes the components of η to be transposed across the lower left to upper right diagonal. If a fracture of finite thickness Δz is filled by material with compliance coefficients $\tilde{\eta}_{ij}$, then the elastic stress-strain relation for the infilling material gives directly

$$\begin{bmatrix} \Delta s_x / \Delta z \\ \Delta s_y / \Delta z \\ \Delta s_z / \Delta z \end{bmatrix} = \begin{bmatrix} \tilde{\eta}_{33} & \tilde{\eta}_{34} & \tilde{\eta}_{35} \\ \tilde{\eta}_{34} & \tilde{\eta}_{44} & \tilde{\eta}_{45} \\ \tilde{\eta}_{35} & \tilde{\eta}_{45} & \tilde{\eta}_{55} \end{bmatrix} \begin{bmatrix} \tau_{zz} \\ \tau_{yz} \\ \tau_{zx} \end{bmatrix} + O[(\Delta z)^2] \quad (12)$$

This shows that a horizontal zero-thickness fracture is just the limiting case of a fracture with thickness Δz , whose infilling material has compliance coefficients $\tilde{\eta}_{ij}$ given by

$$\begin{bmatrix} \tilde{\eta}_{33} & \tilde{\eta}_{34} & \tilde{\eta}_{35} \\ \tilde{\eta}_{34} & \tilde{\eta}_{44} & \tilde{\eta}_{45} \\ \tilde{\eta}_{35} & \tilde{\eta}_{45} & \tilde{\eta}_{55} \end{bmatrix} = \frac{1}{\Delta z} \begin{bmatrix} \eta_{zz} & \eta_{yz} & \eta_{zx} \\ \eta_{yz} & \eta_{yy} & \eta_{xy} \\ \eta_{zx} & \eta_{xy} & \eta_{xx} \end{bmatrix} \quad (13)$$

For a vertical fracture parallel to the yz plane the correspondence is

$$\begin{bmatrix} \tilde{\eta}_{11} & \tilde{\eta}_{15} & \tilde{\eta}_{16} \\ \tilde{\eta}_{55} & \tilde{\eta}_{56} & \tilde{\eta}_{66} \end{bmatrix} = \frac{1}{\Delta z} \begin{bmatrix} \eta_{xx} & \eta_{xz} & \eta_{xy} \\ \eta_{xz} & \eta_{zz} & \eta_{yz} \\ \eta_{xy} & \eta_{yz} & \eta_{yy} \end{bmatrix} \quad (14)$$

In some papers the fracture stiffness matrix k is used instead of the compliance matrix η . Then $t = k \Delta s$ and k is just the matrix inverse of η . The relations between the elastic stiffnesses of an infilling material \tilde{C}_{ij} and the stiffness coefficients of the fracture k_{ij} are the same as in equations (13)–(14) except that $1/\Delta z$ is replaced by Δz .

In the next section we consider horizontal orthorhombic fractures whose planes of symmetry are parallel to the coordinate planes. For such fractures, $\eta = \text{diag}(\eta_{xx}, \eta_{yy}, \eta_{zz})$. When an isotropic medium is fractured with orthorhombic fractures the resulting medium is orthorhombic. When an AI medium is fractured by horizontal orthorhombic fractures, the resulting medium is orthorhombic. A special case of the orthorhombic fracture is the transversely isotropic (TI) fracture. For a horizontal TI fracture, $\eta_{xx} = \eta_{yy}$. When an AI medium is fractured by vertical TI fractures, or by vertical orthorhombic fractures with a horizontal symmetry plane, the resulting medium is orthorhombic.

Now we derive reflection and transmission coefficients for a horizontal fracture between two solids. The solids may have any anisotropy and may be different from each other. The fracture may have any complex compliance matrix η . The first order system for plane wave propagation in the upper and lower solids may be written as

$$\partial_z \begin{bmatrix} v \\ t \end{bmatrix} = i\omega D A D^{-1} \begin{bmatrix} v \\ t \end{bmatrix} \quad (15)$$

in which $v = [v_x, v_y, v_z]^T$ is velocity, $t = [\tau_{xz}, \tau_{yz}, \tau_{zx}]^T$ is horizontal traction, A is a diagonal matrix, and D has the form

$$D = \begin{bmatrix} M^u & M^d \\ N^u & N^d \end{bmatrix} \quad (16)$$

This notation implies that the first three columns of D represent upgoing waves and the last three columns represent downgoing waves. No special normalization of the columns is assumed here nor is any assumption made about

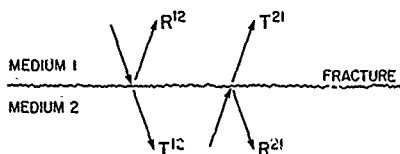


Fig. 4 Reflection and transmission at a fracture between dissimilar media.

the ordering of wave types within the upgoing and downgoing groups. The order may be unknown, and it may be different for the upper and lower solids. In a generally anisotropic medium it is sometimes difficult to distinguish the two kinds of S waves, and sometimes it is even difficult to distinguish P waves from S waves, but if there is any attenuation, then upgoing and downgoing solutions can always be distinguished by the signs of the imaginary parts of their associated eigenvalues.

The notation for the 3×3 matrices of reflection and transmission coefficients is shown in Figure 4. For example, R^{12} is the downward reflection matrix from medium 1 to medium 2. Imposition of the fracture boundary conditions gives

$$\begin{bmatrix} M_1^u & M_1^d \\ N_1^u & N_1^d \end{bmatrix} \begin{bmatrix} T^{21} & R^{12} \\ 0 & I \end{bmatrix} - \begin{bmatrix} M_2^u & M_2^d \\ N_2^u & N_2^d \end{bmatrix} \begin{bmatrix} I & 0 \\ R^{21} & T^{12} \end{bmatrix} \\ = (-i\omega) \begin{bmatrix} \eta N_1^u T^{21} & -\eta N_2^d T^{12} \\ 0 & 0 \end{bmatrix} \quad (17)$$

In this equation the first row imposes the condition that the jump in velocity across the fracture be given by $-i\omega\eta t$, and the second row imposes the condition that traction be continuous across the fracture. The first column imposes these conditions for the case of waves incident from below (medium 2), and the second column imposes them for waves incident from above (medium 1).

Solving for the downgoing transmission and reflection matrices yields

$$T^{12} = \{M_2^d - [(-i\omega)\eta + M_1^u(N_1^u)^{-1}N_2^d]^{-1} \\ \cdot [M_1^d - M_2^u(N_1^u)^{-1}N_2^d]\} \quad (18)$$

and

$$R^{12} = (N_1^u)^{-1}[N_2^d T^{12} - N_1^d] \quad (19)$$

For the upgoing reflection and transmission coefficients the results are

$$T^{21} = \{M_1^u - [(-i\omega)\eta + M_2^d(N_2^d)^{-1}N_1^u]^{-1} \\ \cdot [M_2^u - M_1^d(N_2^d)^{-1}N_1^u]\} \quad (20)$$

and

$$R^{21} = (N_2^d)^{-1}[N_1^u T^{21} - N_2^u] \quad (21)$$

For a horizontal TI fracture between two AI solids these formulas reduce to similar 2×2 matrix formulas for PSV , and similar scalar formulas for SH . If medium 1, medium 2, and the fracture have infinite Q , then all quantities in

equation (17) are real except for i . Thus the reflection and transmission coefficients for the fracture are always complex and frequency-dependent.

4 FRACTURED ROCKS

In this section a fracture system consisting of plane parallel orthorhombic fractures is embedded in an azimuthally isotropic (AI) background rock. The background rock may have been generated using the procedure given above for microbedding. The case of horizontal fractures is treated first, then the case of vertical fractures.

For horizontal fractures the procedure is similar to the procedure given above for a microbedded sediment. First, sample from the statistical distributions for the fracture compliances, and for the interfracture distance, to generate a realization of the fractured medium. For example, one could use the same compliance matrix η for each fracture but assume that the interfracture distance h has the exponential distribution $p(h) = h^{-1} \exp(-h/h_0)$. Then place a source in the realization and generate synthetic plane wave data at $N \approx 4$ depths beneath the source.

Generation of the synthetic two-way data can be carried out by the Kennett [1983] method using the reflection and transmission coefficients derived in the last section. The formulas for D , A , etc., for an AI medium are given in section 4.3 of Fryer and Frazer (1987). The formulas there are for isotropic density, but the modifications needed for AI density are straightforward. Use of an AI density will be appropriate if the AI medium was generated from microbeds by the procedures of the last section. As the fractured medium will be orthorhombic, synthetic data are needed for at least two values of x slowness p_x and two values of y slowness p_y . For example, one could generate synthetic data for the four plane waves with slownesses $\{(p_x)_1, (p_y)_1\}$, $\{(p_x)_2, (p_y)_2\}$, $\{(p_x)_3, (p_y)_3\}$, and $\{(p_x)_4, (p_y)_4\}$. These synthetic data are then inverted using the one-way wave equation for vertical propagation in an orthorhombic solid. This part of the procedure will be the same for vertical fractures as for horizontal fractures. Discussion of it begins below, at the paragraph containing equation (25).

For vertical fractures, shown in Figure 5d, the background AI medium is first rotated by 90° about the y axis, so that its axis of symmetry is parallel to the x axis. Denoting the elastic stiffness coefficients of the original AI medium by C_{IJ} and the coefficients of the rotated medium by \hat{C}_{IJ} we have [Fryer and Frazer, 1987, section 4.2]

$$\begin{aligned} \hat{C}_{11} &= C_{33} & \hat{C}_{12} &= C_{13} & \hat{C}_{13} &= C_{13} \\ \hat{C}_{22} &= C_{11} & \hat{C}_{23} &= C_{12} & \hat{C}_{33} &= C_{11} \\ \hat{C}_{44} &= C_{66} & \hat{C}_{55} &= C_{44} & \hat{C}_{66} &= C_{44} \end{aligned} \quad (22)$$

with all other \hat{C}_{IJ} being equal to zero. These relations are obtained from the stress-strain relation for an AI medium [e.g., Fryer and Frazer, 1987, equation 4.5] by transposing each 3×3 submatrix of the 6×6 matrix (C_{IJ}) about its lower left, upper right diagonal. The effect is to interchange indices 1 and 3, to interchange indices 4 and 6, and to leave indices 2 and 5 unchanged. The derivation of equations (22) also uses the fact that the unrotated medium is AI, so that many of the C_{IJ} are the same.

If the AI medium was generated using the procedure given in section 2, then it will have tensor density which must also

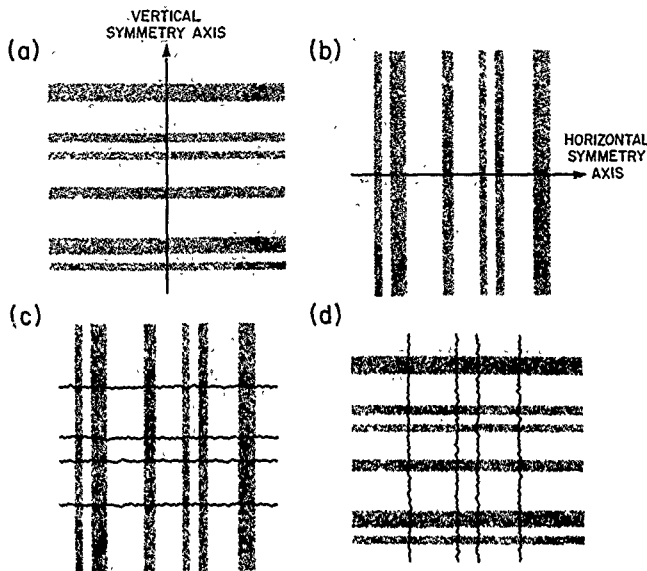


Fig. 5. Vertical fractures in an AI-background: (a) original interfraction rock; (b) rotated fractured rock; (c) exact two-way synthetic data are generated for rock (Figure 5c) and inverted to find an equivalent medium. The equivalent medium for rock (Figure 5c) is rotated to give the equivalent medium for rock (Figure 5d).

be rotated. Denoting the density components of the unrotated AI medium by $\bar{\rho}_u$ and the density components of the rotated AI medium by $\bar{\rho}_H$, we have

$$\bar{\rho}_{xx} = \bar{\rho}_{zz} \quad \bar{\rho}_{yy} = \bar{\rho}_{xx} \quad \bar{\rho}_{zz} = \bar{\rho}_{xx} \quad (23)$$

The fractures must also be rotated before insertion into the interfraction material. Denoting the compliance components of the unrotated fractures by η_u and the compliance components of the rotated fractures by η_H , we have

$$\eta_{xx} = \eta_{zz} \quad \eta_{yy} = \eta_{yy} \quad \eta_{zz} = \eta_{xx} \quad (24)$$

As with horizontal fractures, the next step is to generate a realization of the fracture process. For example, one could assume η_{xx} , η_{yy} , and η_{zz} to be constant and generate the fracture spacings by sampling from a distribution $p(h) = h^{-1} \exp(-h/h)$. One could also assume statistics for the η_u and sample from their distributions.

Now that the fractures are horizontal the synthetic two-way data for the realization of the fractured rotated medium are computed by the Kennett [1983] method using the fracture reflection and transmission coefficients derived in the last section. Formulas for D , A , etc., in a hexagonal medium with a horizontal symmetry axis are given in section 4.2 of Fryer and Frazer [1987]. These formulas are for isotropic density but the modifications needed for tensor density are straightforward. Generation of D , A , etc., can also be carried out using the more general, but possibly slower procedures of Frazer and Fryer [1989].

Next we invert the synthetic two-way data using one-way wave theory. This step is the same for horizontal fractures as for (the originally) vertical fractures. The one-way plane wave equation for downward propagation in an orthorhombic medium with symmetry planes parallel to the coordinate planes is

$$\partial_z u = i\omega H u \quad (25)$$

in which H is the 3×3 "Hamiltonian" matrix whose entries depend on the values of the C_{ij} , ρ_x and ρ_y ; $u = [v_x, \tau_{xz}, v_z]^T$, where v_x and v_z are the x and y components of velocity; and τ_{xz} is the zz component of stress. The one-way equation for $w = [\tau_{xz}, v_x, \tau_{yz}]^T$ is the same. The procedure for recovery of P is similar to that for H_V given earlier. For each plane wave one forms the data matrices A and B . The matrix A has columns $(u)_N, \dots, (u)_2, (w)_N, \dots, (w)_2$; and the matrix B has columns $(u)_{N-1}, \dots, (u)_1, (w)_{N-1}, \dots, (w)_1$. The Hamiltonian matrix H is recovered numerically for each plane wave as

$$H = \frac{1}{i\omega \Delta z} \ln \left[\frac{AB^{-1}}{2} \right] \quad (26)$$

in which B^{-1} is a generalized inverse of B , Δz is the receiver depth spacing, and ω is the radian frequency at which the plane wave data were generated.

The formulas for the components of H^2 in an orthorhombic medium are

$$(H^2)_{11} = C + Dp_x^2 + Ep_y^2 \quad (27a)$$

in which $C = \rho_{11}C_{33}^{-1}$, $E = -C_{66}C_{33}^{-1}$, and $D = C_{13}C_{33}^{-1} - C_{35}^{-1}(C_{11} - C_{13}C_{33}^{-1})$;

$$(H^2)_{12} = Gp_x \quad (27b)$$

in which $G = C_{33}^{-1}(1 + C_{13}C_{33}^{-1})$;

$$(H^2)_{13} = Fp_x p_y \quad (27c)$$

in which $F = C_{23}C_{33}^{-1} - C_{33}^{-1}(C_{66} + C_{12} - C_{13}C_{23}C_{33}^{-1})$;

$$(H^2)_{21} = Mp_x + Np_y^2 + Op_x p_y^2 \quad (27d)$$

in which $M = \rho_{11} + \rho_{33}C_{13}C_{33}^{-1}$, $N = C_{13}^2C_{33}^{-1} - C_{11}$, and $O = C_{13}C_{23}C_{33}^{-1} - 2C_{66} - C_{12}$;

$$(H^2)_{22} = S + Tp_x^2 + Up_y^2 \quad (27e)$$

in which $S = \rho_{33}C_{33}^{-1}$, $T = C_{13}C_{33}^{-1}$, and $U = C_{23}C_{33}^{-1}$;

$$(H^2)_{23} = Pp_y + Qp_y^3 + Rp_x^2 p_y \quad (27f)$$

in which $P = \rho_{22} + \rho_{33}C_{23}C_{33}^{-1}$, $Q = C_{23}^2C_{33}^{-1} - C_{22}$, and $R = C_{13}C_{23}C_{33}^{-1} - 2C_{66} - C_{12}$;

$$(H^2)_{31} = Hp_x p_y \quad (27g)$$

in which $H = C_{13}C_{33}^{-1} - C_{44}^{-1}(C_{66} + C_{12} - C_{13}C_{23}C_{33}^{-1})$,

$$(H^2)_{32} = Lp_y \quad (27h)$$

in which $L = C_{33}^{-1}(1 + C_{23}C_{44}^{-1})$; and

$$(H^2)_{33} = I + Jp_x^2 + Kp_y^2 \quad (27i)$$

in which $I = \rho_{22}C_{44}^{-1}$, $J = -C_{66}C_{44}^{-1}$, and $K = C_{23}C_{33}^{-1} - C_{44}^{-1}(C_{22} - C_{23}C_{33}^{-1})$.

The derivation of these expressions is given in section 5. Note that for an orthorhombic medium, ρ must be of the form $\text{diag}(\rho_{xx}, \rho_{yy}, \rho_{zz})$ with all other components of ρ equal to zero. This is the most general second-order tensor that is invariant under inversion of each coordinate axis. Numerical values of the coefficients C, D, \dots, J , and K are recovered from the numerical value of H^2 using least squares and four or more plane waves. Then the numerical values of the ρ_{ij} and the C_{IJ} in the equivalent medium are obtained by the relations

$$\begin{aligned} C_{55} &= N(D - T)^{-1} & C_{44} &= Q(K - U)^{-1} \\ \rho_{11} &= C_{55}C & \rho_{22} &= C_{44}I \\ \rho_{33} &= (M - \rho_{11})T^{-1} & &= (P - \rho_{22})U^{-1} \\ C_{33} &= \rho_{33}S^{-1} & C_{66} &= -C_{44}J = -C_{55}E \\ C_{13} &= C_{33}T & &= (M - \rho_{11})C_{33}\rho_{33}^{-1} \\ C_{23} &= C_{33}U & &= (P - \rho_{22})C_{33}\rho_{33}^{-1} \\ C_{11} &= -N + C_{13}^2C_{33}^{-1} \\ C_{22} &= -Q + C_{23}^2C_{33}^{-1} \\ C_{12} &= -C_{55}(F - C_{23}C_{33}^{-1}) - C_{66} + C_{13}C_{23}C_{33}^{-1} \\ &= -C_{44}(H - C_{13}C_{33}^{-1}) - C_{66} + C_{13}C_{23}C_{33}^{-1} \end{aligned} \quad (28)$$

For horizontal fractures we are now done. In the case of fractures which were originally vertical the fractured medium must now be rotated back into its original orientation. This reverses the rotation performed earlier. Denoting the coefficients of the vertically fractured medium by C_{IJ} we have

$$\begin{aligned} \hat{C}_{11} &= C_{33} & \hat{C}_{12} &= C_{23} & \hat{C}_{13} &= C_{13} \\ \hat{C}_{22} &= C_{22} & \hat{C}_{23} &= C_{12} & \hat{C}_{33} &= C_{11} \\ \hat{C}_{44} &= C_{66} & \hat{C}_{55} &= C_{55} & \hat{C}_{66} &= C_{44} \end{aligned} \quad (29)$$

with all other \hat{C}_{IJ} equal to zero. Density must also be rotated back. The density components of the vertically fractured rock are given by

$$\hat{\rho}_{xx} = \rho_{33} \quad \hat{\rho}_{yy} = \rho_{22} \quad \hat{\rho}_{zz} = \rho_{11} \quad (30)$$

These are the elastic coefficients and densities of a rock whose interfracture material is AI (with elastic coefficients \hat{C}_{IJ} and densities $\hat{\rho}_{ij}$), and whose fractures are parallel to the yz plane with fracture compliance matrix $\text{diag}(\eta_{xx}, \eta_{yy}, \eta_{zz})$.

5. ONE-WAY WAVE EQUATIONS

In this section the one-way elastic wave equations used above are derived. For an elastic medium the linearized momentum equation is

$$-\omega^2 \rho_{ij} u_j = \partial_j \tau_{ij} + f_i \quad (31)$$

in which ω is temporal radian frequency, u_j is displacement, τ_{ij} is stress, and f_i is the body force per unit volume. Here we are anticipating a medium with microstructure by letting the inertial mass density be a symmetric tensor ρ_{ij} instead of the usual scalar. The linearized constitutive relation is

$$\tau_{ij} = c_{ijkl} \partial_k u_l \quad (32)$$

in which (c_{ijkl}) is the fourth-order elastic stiffness tensor. Both the constitutive relation and the momentum equation are frequency domain relations, so that, in general, all terms in each equation are complex and ω -dependent. For an orthorhombic medium with symmetry planes parallel to the coordinate planes these equations can be rearranged as

$$\begin{aligned} \partial_z \begin{bmatrix} u_x \\ \tau_{zz} \\ u_y \\ \tau_{xz} \\ u_z \\ \tau_{yz} \end{bmatrix} &= - \begin{bmatrix} 0 & 0 & 0 & a_{14} & a_{13} & a_{15} \\ 0 & 0 & 0 & a_{64} & a_{63} & a_{65} \\ 0 & 0 & 0 & a_{24} & a_{23} & a_{25} \\ a_{41} & a_{46} & a_{42} & 0 & 0 & 0 \\ a_{31} & a_{36} & a_{32} & 0 & 0 & 0 \\ a_{51} & a_{56} & a_{52} & 0 & 0 & 0 \end{bmatrix} \begin{bmatrix} u_x \\ \tau_{zz} \\ u_y \\ \tau_{xz} \\ u_z \\ \tau_{yz} \end{bmatrix} + \begin{bmatrix} 0 \\ -f_z \\ 0 \\ -f_x \\ 0 \\ -f_y \end{bmatrix} \end{aligned} \quad (33)$$

with wave- and \mathbf{f} Opt. ogy. / that c_{ij} an N

re case of
tured me-
mentation:
giving the
by C_{IJ} we

(29)

be rotated
y fractured

(30)

s of a rock
coefficients
parallel to the
 x, y, z

sations used
ie linearized

(31)

displacement,
me. Here we
by letting the
instead of the
on is

(32)

Iness tensor.
tum equation
eral, all terms
dent. For an
parallel to the
ranged as

a_{15}
 a_{15}
 a_{25}
0
0
0

0
 f_z
0
 f_x
0
 f_y

in which ∂_x stands for $\partial/\partial x$, and the components of the first-order system matrix on the right-hand side are

$$\begin{aligned} a_{14} &= -C_{55}^{-1} & a_{13} &= \partial_x \\ a_{64} &= \partial_x & a_{63} &= \rho_{33} \omega^2 \\ a_{24} &= 0 & a_{23} &= \partial_y \\ a_{41} &= \rho_{11} \omega^2 + \partial_x Y_{11} \partial_x + \partial_y C_{66} \partial_y & a_{46} &= \partial_x X_1 \\ a_{31} &= X_1 \partial_x & a_{36} &= -C_{33}^{-1} \\ a_{51} &= \partial_y Y_{21} \partial_x + \partial_x C_{66} \partial_y & a_{56} &= \partial_y X_2 \end{aligned}$$

$$a_{15} = 0$$

$$a_{65} = \partial_y$$

$$a_{25} = -C_{44}^{-1}$$

$$a_{42} = \partial_x Y_{12} \partial_y + \partial_y C_{66} \partial_x$$

$$a_{32} = X_2 \partial_y$$

$$a_{52} = \rho_{22} \omega^2 + \partial_y Y_{11} \partial_y + \partial_x C_{66} \partial_x$$

in which

$$X_I = C_{I3} C_{33}^{-1} \quad \text{for } I = 1, 2$$

and

$$Y_{IJ} = C_{IJ} - C_{I3} C_{33}^{-1} \quad \text{for } I, J \in \{1, 2\}$$

With some obvious changes in notation we rewrite equation (33) as

$$\partial_z \begin{bmatrix} \tilde{u} \\ \tilde{w} \end{bmatrix} = - \begin{bmatrix} 0 & \mathcal{K} \\ \mathcal{L} & 0 \end{bmatrix} \begin{bmatrix} \tilde{u} \\ \tilde{w} \end{bmatrix} + \begin{bmatrix} \tilde{g} \\ \tilde{h} \end{bmatrix} \quad (35)$$

Applying ∂_z to both sides of the above equation and substituting for $\partial_z \begin{bmatrix} \tilde{u} \\ \tilde{w} \end{bmatrix}$ in the result, yields the second-order system

$$\partial_z^2 \begin{bmatrix} \tilde{u} \\ \tilde{w} \end{bmatrix} = \begin{bmatrix} \mathcal{K}\mathcal{L} & 0 \\ 0 & \mathcal{L}\mathcal{K} \end{bmatrix} \begin{bmatrix} \tilde{u} \\ \tilde{w} \end{bmatrix} + \begin{bmatrix} -\mathcal{K}\tilde{g} + \partial_z \tilde{g} \\ -\mathcal{L}\tilde{h} + \partial_z \tilde{h} \end{bmatrix} \quad (36)$$

Note that this equation is valid even when $c_{\mu\mu}$ and $\rho_{\mu\mu}$ depend on x, y , and z . All we have assumed is that the medium is orthorhombic with symmetry planes parallel to the coordinate planes. Each component of $\mathcal{L}\mathcal{K}$ is the negated operator transpose of the corresponding component of $\mathcal{K}\mathcal{L}$. For example, the 12-component of $\mathcal{K}\mathcal{L}$ is $-C_{55}^{-1} \partial_x X_1 - \partial_x C_{33}^{-1}$ and the 21-component of $\mathcal{L}\mathcal{K}$ is $-X_1 \partial_x C_{33}^{-1} - C_{33}^{-1} \partial_x$. We now assume that $c_{\mu\mu}$ and $\rho_{\mu\mu}$ are independent of z , so that upgoing and downgoing waves are decoupled. Then the second-order operators in equation (36) can be factored into the product of two first-order operators, one of which annihilates upgoing waves and the other of which annihilates downgoing waves. Outside the source region the motion is governed by

$$0 = (\partial_z - i\mathcal{K}\partial_z)^+ = (\partial_z + i\mathcal{K}\partial_z)^- \quad (37)$$

(with similar relations for \tilde{w}^+ and \tilde{w}^- . Here \tilde{u}^+ and \tilde{w}^+ are waves travelling in the $+z$ direction (downward) direction and \tilde{u}^- and \tilde{w}^- are $(-\mathcal{K}\mathcal{L})^{1/2}$.

Operators like \mathcal{K} are not very familiar objects in seismology. A useful (and correct) way to think of \mathcal{K} is to imagine that each operator component of $\mathcal{K}\mathcal{L}$ has been discretized as an $N \times N$ matrix. Then $\mathcal{K}\mathcal{L}$ is just a $3N \times 3N$ matrix whose

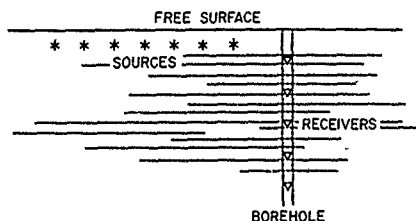


Fig. 6. Multioffset VSP geometry. Each surface source is recorded by at least three borehole geophones.

square root can be calculated by well known numerical methods. The main difference between the square root of a scalar and the square root of an $N \times N$ matrix is that the former has $2 = 2^1$ branches, whereas the latter has 2^N branches. In the forward modeling of seismic waves it is necessary to construct \mathcal{K} from assumed density and elastic profiles. Construction of \mathcal{K} from synthetic data, as in this paper, is a much simpler problem.

In a homogeneous medium, Fourier transformation of the above equations replaces ∂_x by ik_x , and ∂_y by ik_y . Then it is convenient to replace the displacements u_x and u_z , in the definitions of \tilde{u} and \tilde{w} , by the velocities $-i\omega u_x$ and $-i\omega u_z$, respectively. With the Fourier transformation and the change from displacements to velocities the variables of this section become the variables introduced above in section 4. Thus \tilde{u} becomes u , \tilde{w} becomes w , and both $\mathcal{K}\mathcal{L}$ and $\mathcal{L}\mathcal{K}$ turn into $-\omega^2 H^2$, where the components of H^2 are given by equations (27). Equation (36) becomes

$$\partial_z^2 \begin{bmatrix} u \\ w \end{bmatrix} = -\omega^2 \begin{bmatrix} H^2 & 0 \\ 0 & H^2 \end{bmatrix} \begin{bmatrix} u \\ w \end{bmatrix} + \begin{bmatrix} -Kh + \partial_z \tilde{g} \\ -Lg + \partial_z \tilde{h} \end{bmatrix} \quad (38)$$

where the components of K and L are obtained from (34). Factorization of (38) gives the one-way plane wave equation (25). In an AI medium, H is block diagonal, and the full one-way equation (25) decouples into the one-way PSV relation (1) and the one-way SH relation (2).

6. CORES AND VERTICAL SEISMIC PROFILES

One of the goals of the microbedding theory of section 2 is to resolve the discrepancy between sound speeds inferred from velocity logs, or cores, and those inferred from seismic data. The path to this goal is necessarily indirect: bed thicknesses from cores are used to make synthetic two-wave data; these data are inverted for an equivalent medium; seismic sound speeds of the equivalent medium are compared with sound speeds inferred from seismic data. However, there is one situation in which a more direct comparison is possible.

Consider the multioffset vertical seismic profile (VSP) geometry shown in Figure 6. For each source, upgoing and downgoing waves are easily separated by filtering in the $\omega-k_z$ domain. Then for each receiver the upgoing and downgoing waves can be Fourier transformed into the $\omega-p_x$ domain. If the sediments are AI, then for each p_x the downgoing wave data at successive depths are related by the one-way SH equation (2) and the one-way PSV equation (1). Equations (6)–(8) can therefore be used to recover the medium from the

VSP data. A minor problem occurs because the recorded PSV data consist not of v_x and τ_{xz} but of v_x and v_z . To get τ_{xz} from v_x and v_z , assume initial values of C_{11} and C_{33} . Then use the stress strain relation

$$\tau_{xz} = \frac{1}{-i\omega} (C_{11}\partial_x v_x + C_{33}\partial_z v_z) \quad (39)$$

Here $\partial_x v_x$ is given by $i\omega p_x v_x$, and $\partial_z v_z$ is obtained as $\mathcal{F}_z^{-1} i k_z \mathcal{F}_z v_z$, where \mathcal{F}_z is Fourier transformation along the borehole. Then use equations (6)–(8) to get improved estimates of C_{11} and C_{33} . Then update τ_{xz} using (39). A few iterations of this procedure must recover density and C_{IJ} from the VSP data. In the absence of noise, these ought to be the same as the densities and C_{IJ} generated from core bed-thickness data.

7. DISCUSSION AND CONCLUSIONS

Data analyses using the theory will be presented in future papers. Such analyses should answer such interesting questions as whether tensor frequency-dependent density is really required for modelling microbedded or fractured materials or whether real scalar density is a good enough approximation. Other issues can only be addressed by extensive numerical testing. For example, results obtained using the method of this paper must tend, as frequency approaches zero, to the static results of Schoenberg and Douma [1988]. One would like to know, for typical sediments, the frequencies below which a static approximation is acceptable.

The main disadvantage of the theory above is that the microbeds and fractures are assumed to be planar and parallel. For many rocks this is a poor approximation. Another disadvantage is that it can only be utilized with the aid of a computer. Computer programs based on the theory may provide physical insights, but the theory itself provides no insight. This is due, at least in part, to the completeness of the physics. For example, all interbed and interface multiples are included in the generation of the synthetic two-way data. If a more approximate two-way theory were used, say one which incorporated just a few multiples, then it might be possible to invert analytically for the equivalent medium. I have not attempted to do this, partly because any results obtained using such an approach will generally require checking by the full method given above.

In regard to fractures, one of the advantages of the method of this paper is that it is not tied to any particular fracture model. Although reflection and transmission coefficients were derived above for the displacement discontinuity model, these need not be used, instead, fractures can be modeled as sequences of layers, with high strength material for the outer layers and weak material for the inner layers.

A limitation of the theory, in its present state, is that it does not allow one to generate a medium equivalent to nonparallel sets of vertical fractures. An AI background rock so fractured is monoclinic with a horizontal plane of symmetry. However, in the method of this paper, in order to incorporate the second set of fractures the equivalent medium containing the first set must be rotated so that the second set will be horizontal when inserted. Thus neither the background medium, containing only the first set, nor the resulting equivalent medium, containing both sets, has a

horizontal plane of symmetry. Exact two-way modeling for such a background is straightforward [Mallick and Frazer, 1990], but so far I have not derived one-way wave equations for a material without a horizontal plane of symmetry.

In the multioffset VSP application, if a grid of surface sources is recorded instead of a line, then one can invert for an orthorhombic material using equations (26)–(28). The VSP data must first be rotated [e.g., Alford et al., 1986] so that the symmetry planes of the medium are parallel to the coordinate planes. This does not require much knowledge of the medium; it is only necessary to assume that the medium is orthorhombic with one of its symmetry planes parallel to the xy plane. Also, for multioffset VSP, there is no limitation to a single set of vertical fractures. If the data area is known to have nonparallel sets of vertical fractures in an AI background, then it can be inverted using one-way theory for a monoclinic medium with a horizontal plane of symmetry. The appropriate one-way equation is straightforward to derive by the method of section 5 because a horizontal plane of symmetry always gives a first-order system like (33) with blocks of zeros on its diagonal.

Earlier the remark was made that as bed thicknesses (or interfracture distances) approach a significant fraction of a seismic wavelength, the concept of an equivalent medium begins to lose its usefulness. Physically, what happens is that the displacement function appears to be discontinuous on the scale of a wavelength. In a fractured medium, for example, the displacements are always discontinuous across fractures, but if there are enough fractures within a seismic wavelength, then the magnitude of each jump is relatively small compared to the total displacement. If there are few fractures within a wavelength and the fracture compliance is low compared to the interfracture rock, then the displacement jump across a fracture will be quite noticeable. The situation is similar for a microbedded sediment with the role of the fracture being played by the most compliant type of microbed. The tractions τ_{xz} , τ_{yz} , and τ_{zz} are always much smoother than displacements, as can be seen by considering the linearized momentum equation (31). If density is constant in (31), then continuity of displacement at an interface implies that even the spatial derivatives of stress must be smooth across that interface.

Even when frequency is so large that an equivalent medium becomes a dubious concept, we may still wish to find an equivalent medium. The best way to do this would be to take advantage of the smoothness of the stresses and to invert for the equivalent medium using a one-way equation for the stresses alone. I have not been able to derive such a one-way equation. However, there are three ways in which the procedures above can be modified to approach this goal. The first and simplest way is to generate synthetic data at a large number of receivers so that the number of columns in the data matrices A and B becomes very large. A second way is to smooth the synthetic displacements over some fraction of a wavelength before forming A and B. This requires the generation of synthetic data at many more receiver depths. A third way is to take advantage of the smoothness of the tractions and to synthesize a smoothed displacement from these tractions, putting this displacement into A and B. This must be done iteratively as displacement and stress are related by density, and the density of the equivalent medium is not known. To simplify matters, consider only PSV

S
w
th
ro
an
co

Alfr
D
E
Baci
tal
Bud
sol
Bum
pro
231
Bum
proj
19-4

Chin,
in s
483-

Frazer,
matn
phys
Fryer,
trop
system
Jodfrey
with
toeng,
Solids
Iudson,
Cambri
Iudson,

odeling for
nd Frazer,
equations
netry.
of surface
n invert for
(28). The
il., 1986) so
rallel to the
nowledge of
the medium
s parallel to
no limitation
area is known
es in an AI
way theory for
of symmetry.
ghtforward to
onizational plane
n like (33) with

thicknesses (or
nt fraction of a
valent medium
t happens is that
is continuous on
ed medium, for
ontinuous across
within a seismic
imp is relatively
If there are few
ure compliance is
then the displace-
ment with the role
compliant type of
are always much
een by considering
If density is con-
nent at an interface
s of stress must be

that an equivalent
ve may still wish to
y to do this would be
f the stresses and to
s a one-way equation
able to derive such a
three ways in which
to approach this goal.
ate synthetic data at a
number of columns in
ry large. A second way
nts over some fraction
d B. This requires the
more receiver depths.
the smoothness of the
hed displacement from
ment into A and B. This
cement and stress are
f the equivalent medium
s, consider only PS

propagation and suppose that scalar density is a good approximation for the equivalent medium. Let ρ_e be a first guess at this density, and let τ_{xz} and τ_{zz} be the tractions synthesized by the two-way method. Then from the momentum equation (31) we estimate the z displacement of the equivalent medium in the form

$$u_{ze} = \frac{-1}{\rho_e \omega^2} (\partial_x \tau_{xz} + \partial_z \tau_{zz}) \quad (40)$$

In this relation, $\partial_x \tau_{xz}$ is given by $i\omega \rho_x \tau_{xz}$, and $\partial_z \tau_{zz}$ will be obtained by differencing. The matrices A and B are now constructed from u_{ze} and τ_{zz} and processed in the usual way to generate a temporary equivalent medium with a better estimate for ρ_e . Iterating in this fashion, until ρ_e converges, will give the best equivalent medium.

Acknowledgments. This research was supported by National Science Foundation grant EAR-8721152. Earlier ONR support for work on one-way wave equations is also gratefully acknowledged. I thank Michael Schoenberg for his Honolulu lecture series on anisotropy. Also Peter Leary and Tom McEvilly for organizing the recent anisotropy Chapman conference. Hawaii Institute of Geophysics contribution 2244.

REFERENCES

- Alford, R. M., Shear data in the presence of Azimuthal anisotropy: Dilley, Texas, paper presented at 56th Annual Meeting, Soc. of Explor. Geophys., Houston, Tex., 1986.
- Backus, G. E., Long wave elastic anisotropy produced by horizontal layering, *J. Geophys. Res.*, **67**, 4427-4440, 1962.
- Budiansky, B., and R. J. O'Connell, Elastic moduli of a cracked solid, *Int. J. Solids Struct.*, **12**, 81-97, 1976.
- Burridge, R., and H.-W. Chang, Multimode one-dimensional wave propagation in a highly discontinuous medium, *Wave Motion*, **11**, 231-244, 1989.
- Burridge, B., B. White, and G. Papanicolaou, One-dimensional wave propagation in a highly discontinuous medium, *Wave Motion*, **10**, 19-44, 1988.
- Chin, R. C. Y., G. W. Hedstrom, and L. Thigpen, Matrix methods in synthetic seismograms, *Geophys. J. R. Astron. Soc.*, **77**, 483-502, 1984.
- Frazer, L. N., and G. J. Fryer, Useful properties of the system matrix for a homogeneous anisotropic visco-elastic solid, *Geophys. J.*, **97**, 173-177, 1989.
- Fryer, G. J., and L. N. Frazer, Seismic waves in stratified anisotropic media, II, Elastodynamic solutions for some anisotropic systems, *Geophys. J. R. Astron. Soc.*, **91**, 73-101, 1987.
- Jodrey, R., F. Muir, and F. Rocca, Modeling seismic impedance with Markov chains, *Geophysics*, **45**, 1351-1372, 1980.
- Toenig, A., Elastic moduli of a non-randomly cracked body, *Int. J. Solids Struct.*, **15**, 137-154, 1979.
- Judson, J. A., Overall properties of a cracked solid, *Math. Proc. Cambridge Philos. Soc.*, **88**, 371-384, 1980.
- Judson, J. A., Wave speeds and attenuation of elastic waves in material containing cracks, *Geophys. J. R. Astron. Soc.*, **64**, 133-150, 1981.
- Kennett, B. L. N., Reflections, rays and reverberations, *Bull. Seismol. Soc. Am.*, **64**, 1685-1696, 1974.
- Kennett, B. L. N., *Seismic Wave Propagation in Stratified Media*, Cambridge University Press, New York, 1983.
- Krumbein, W. C., and M. F. Dacey, Markov chains and embedded Markov chains in geology, *J. Math. Geol.*, **1**, 79-96, 1969.
- Mallick, S., and L. N. Frazer, Computation of synthetic seismograms for stratified azimuthally anisotropic media, *J. Geophys. Res.*, (submitted), 1989.
- Menke, W., A formula for the apparent attenuation of acoustic waves in randomly layered media, *Geophys. J. R. Astron. Soc.*, **75**, 541-544, 1983a.
- Menke, W., On the effect of P-S coupling on the apparent attenuation of elastic waves in randomly layered media, *Geophys. Res. Lett.*, **12**, 1145-1147, 1983b.
- Menke, W., and B. Dubendorf, Discriminating intrinsic and apparent attenuation in layered rock, *Geophys. Res. Lett.*, **12**, 721-724, 1985.
- Nishizawa, O., Seismic velocity anisotropy in a medium containing oriented cracks—Transversely isotropic case, *J. Phys. Earth*, **30**, 331-347, 1982.
- O'Connell, R. J., and B. Budiansky, Measures of dissipation in viscoelastic media, *Geophys. Res. Lett.*, **5**, 5-8, 1978.
- O'Doherty, R. F., and N. A. Anstey, Reflections on amplitudes, *Geophys. Prospect.*, **19**, 430-458, 1971.
- Pyrak-Nolte, L. J., L. R. Myer, and N. W. G. Cook, Seismic visibility of fractures, *Proc. U.S. Symp. Rock Mech.*, **28th**, 47-56, 1987.
- Schmidt, H., and F. B. Jensen, An efficient numerical solution technique for wave propagation in horizontally stratified environments, *Rep. SM-173*, SACLANT ASW Res. Cent., La Spezia, Italy, 1984.
- Schmidt, H., and G. Tango, Efficient global matrix approach to the computation of synthetic seismograms, *Geophys. J. R. Astron. Soc.*, **84**, 331-360, 1986.
- Schoenberg, M., Elastic wave behaviour across linear slip interfaces, *J. Acoust. Soc. Am.*, **68**, 1516-1521, 1980.
- Schoenberg, M., Reflection of elastic waves from periodically stratified media with interfacial slip, *Geophys. Prospect.*, **31**, 265-292, 1983.
- Schoenberg, M., Wave propagation in alternating solid and fluid layers, *Wave Motion*, **6**, 303-320, 1984.
- Schoenberg, M., and J. Douma, Elastic wave propagation in media with parallel fractures and aligned cracks, *Geophys. Prospect.*, **36**, 571-590, 1988.
- Schoenberg, M., and F. Muir, A calculus for finely layered media, *Geophysics*, **54**, 582-590, 1989.
- Schoenberg, M., and P. N. Sen, Properties of a periodically stratified acoustic half-space and its relation to a Biot fluid, *J. Acoust. Soc. Am.*, **73**, 61-67, 1983.
- Schwarzacher, W., The semi-Markov process on a general sedimentation model, in *Mathematical Models in Sedimentary Processes*, edited by D. F. Merriam, pp. 247-268, Plenum, New York, 1972.
- Velzeboer, C. J., The theoretical seismic reflection response of sedimentary sequences, *Geophysics*, **46**, 843-853, 1981.

L. N. Frazer, Hawaii Institute of Geophysics, University of Hawaii at Manoa, 2525 Correa Road, Honolulu, HI 96822

(Received April 3, 1989,
accepted July 7, 1989)

Computation of Synthetic Seismograms for Stratified Azimuthally Anisotropic Media

SUBHASHIS MALLICK AND L. NEIL FRAZER

Hawaii Institute of Geophysics, University of Hawaii, Honolulu

We outline a method of computing synthetic seismograms for stratified, azimuthally anisotropic, viscoelastic earth models. This method is an extended form of the Kennett algorithm that is efficient for multioffset vertical seismic profiling. The model consists of a stack of homogeneous plane layers, and the response is computed iteratively by successive inclusion of deeper layers. In each layer, the 6×6 system matrix A is diagonalized numerically; this permits treatment of triclinic materials, i.e., those with the lowest possible symmetry. Jacobi iteration is an efficient way to diagonalize A because the entries of A change little from one wavenumber to the next. When the material properties are frequency dependent, the wavenumber loops are inside the frequency loop, and the computation is slow even on a supercomputer. When the material parameters are frequency independent, it is better to make frequency the deepest loop, with diagonalization of A outside the loop, in which case vectorization gives a relatively rapid computation. Temporal wraparound is avoided by making use of complex frequencies, and spatial aliasing is avoided by using a generalized Filon's method to evaluate both the wavenumber integrals. Various methods of generating anisotropic elastic constants from microlayers, cracks, and fractures and joints are discussed. Example computations are given for azimuthally isotropic and azimuthally anisotropic (AA) earth models. Comparison of computations using single and double wavenumber integrations for a realistic AA model shows that single wavenumber integration often gives incorrect answers especially at near offsets. Errors due to use of a single wavenumber integration are explained heuristically by use of wave front diagrams for point and line sources.

INTRODUCTION

Until recently, most seismic data have been analyzed and interpreted assuming wave propagation through an isotropic earth. This assumption was adequate for explaining most features of seismograms. But with the increased use of three component seismometers and large arrays, seismic signal to noise ratios have improved to the point where anisotropic effects are often seen in data, especially shear wave data. Hence there is a growing awareness that the assumption of isotropy is often incorrect and that we must develop the means to analyze and interpret data on the basis of more general anisotropic earth models.

Anisotropy has been widely detected in the crust and in the upper mantle [e.g., Fuchs, 1977; Stephen, 1981; Anderson and Dzewinski, 1982; Shimamura, 1984; Anderson and Regan, 1983; Johnston, 1986; Becker and Perelberg, 1986; Lynn and Thomsen, 1986; Alford, 1986; Willis et al., 1986; Majer et al., 1988], and laboratory measurements imply that it is common in both crystalline and sedimentary rocks [Bachman, 1979; Christensen and Salisbury, 1979; Babuska, 1981; Rai and Hanson, 1986]. Anisotropic behavior of earth materials may be inherent; that is, it may be due to the anisotropy of the crystals from which a rock is formed, or it may be induced by thin layering, by fractures, or by cracks. Crampin et al. [1984] review the many different causes of anisotropy. Thomsen [1988] reviewed the effects of azimuthal anisotropy on surface seismic reflection data. Though anisotropy has been detected and its presence is now thought to be widespread, there have been very few available data of the type needed to compute realistic anisotropic models. Recently, Christensen [1984] has esti-

mated the magnitude of upper mantle anisotropy, based on laboratory measurements. Calculations of equivalent elastic moduli for an isotropic medium containing cracks have been given by Hudson [1981] and Nishizawa [1982]. Calculations of the equivalent transversely isotropic elastic moduli for a medium composed of thin periodic isotropic layers were given by Schoenberg [1983]. Schoenberg and Douma [1988] extended the procedure of Schoenberg [1983] to obtain the equivalent elastic moduli for a medium composed of thin, periodic, arbitrarily anisotropic layers with sets of oriented cracks. Their procedure can handle multiple intersecting crack systems, and they relate their crack model to the crack models of Hudson [1981] and Nishizawa [1982].

As realistic values for anisotropy within the Earth become available, there is now a growing need to be able to compute accurate synthetic seismograms for a stratified anisotropic medium. Seismic modeling capability for azimuthally anisotropic (AA) media has been relatively slow to develop both because of the complexity of the mathematics and because of a lack of the necessary computer power. The mathematics of surface wave propagation in stratified AA media were treated by Crampin [1970] and Smith and Dahlen [1973] and were extended to include body waves by Keith and Crampin [1977a, b]. The first synthetics were the simple plane wave seismograms of Keith and Crampin [1977c]. Booth and Crampin [1983a, b] constructed synthetics for point sources using a single wavenumber integration. This gives exact solutions for azimuthal isotropy (AI), and approximate solutions for azimuthal anisotropy, good only when the azimuthal anisotropy is very weak. Fryer and Frazer [1984] described an exact method for computing the synthetic seismograms for a stratified anisotropic medium, using Kennett's [1974, 1983] imbedding algorithm. Subsequently, Fryer and Frazer [1987] gave analytical expressions for the eigenvectors and eigenvalues of the system matrix A (de-

Copyright 1990 by the American Geophysical Union

Paper number J01B00091.
0148-0227/90/J01B-00091\$05.00

finer below) for media with a horizontal plane of symmetry. Thus, for example, the expressions of *Fryer and Frazer* [1987] can be used to calculate synthetic seismograms for a layered model with multiple intersecting sets of vertical fractures, but they cannot be used to treat a model with even a single set of dipping fractures. To overcome this restriction, *Frazer and Fryer* [1989] developed two numerical methods of diagonalizing A in the general triclinic case. Their results were used by *Van der Hijden* [1987] in his extension of the Cagniard-de Hoop method [*de Hoop*, 1960] to anisotropic models; but the Cagniard-de Hoop method is inadequate for multilayered earth models when a complete response is needed. *Gajewski and Pšenčík* [1987] used ray theory to compute high-frequency synthetic seismograms in laterally inhomogeneous anisotropic media. *Chapman and Shearer* [1988] showed that ray theory is difficult in AA media because of the coupling between different types of shear waves. *Taylor* [1987] has shown how to choose an optimal contour for the single wavenumber integral computation of synthetics in AA media by the reflectivity method.

This paper describes how the numerical techniques of *Frazer and Fryer* [1989] for diagonalizing A are incorporated into the vertical seismic profiling (VSP)-efficient Kennett algorithm of *Mallick and Frazer* [1988] to give a method for the computation of synthetic seismograms in stratified media with arbitrary anisotropy.

BASIC THEORY

Here we briefly review the theory of wave propagation in a stratified anisotropic medium and show how synthetic seismograms can be computed. We work in a Cartesian coordinate system x, y, z (or x_1, x_2, x_3) with the z (or x_3) axis pointing vertically downward.

As we work in Cartesian coordinates, we identify the displacement vector u with the column vector $[u_x, u_y, u_z]^T$. We use t to denote the scaled vertical traction vector $(t/\omega)[\tau_{xz}, \tau_{yz}, \tau_{zz}]^T$ in which τ_{xz} , τ_{yz} , and τ_{zz} are components of the stress tensor τ .

The constitutive relation is

$$\tau = c : \epsilon$$

or

$$\tau_{ij} = c_{ijkl} \epsilon_{kl} \quad (1)$$

This equation relates the components of the stress tensor τ_{ij} to the components of the strain tensor ϵ_{kl} through the components of the fourth-order elastic tensor c_{ijkl} . The elastic tensor c has the symmetries (due to the symmetry of the stress and strain tensors),

$$c_{ijkl} = c_{jikl} = c_{ijlk}$$

Thus, of the 81 components of the elastic tensor, only 36 are distinct. The six independent components of the stress tensor can be related to the six independent components of the strain tensor through these 36 components by a (6×6) matrix C :

$$\sigma = C \cdot \epsilon \quad (2)$$

where

$$\sigma = (\tau_{xx}, \tau_{yy}, \tau_{zz}, \tau_{yz}, \tau_{xz}, \tau_{xy})^T$$

$$C = \begin{pmatrix} c_{xxxx} & c_{xxyy} & c_{xxzz} & c_{xxyz} & c_{xxzx} & c_{xxxy} \\ c_{yyxx} & c_{yyyy} & c_{yyzz} & c_{yyxz} & c_{yyzx} & c_{yyxy} \\ c_{zzxx} & c_{zzyy} & c_{zzzz} & c_{zzxz} & c_{zzzx} & c_{zzxy} \\ c_{yzxx} & c_{zyxy} & c_{yzxz} & c_{yzzy} & c_{yzxz} & c_{yzxy} \\ c_{zxxx} & c_{xzyy} & c_{zxzz} & c_{zxzx} & c_{zxzx} & c_{zxxy} \\ c_{xyxx} & c_{xyyy} & c_{xyzz} & c_{xyxz} & c_{xyzx} & c_{xyxy} \end{pmatrix}$$

and

$$\epsilon = (\epsilon_{xx}, \epsilon_{yy}, \epsilon_{zz}, 2\epsilon_{yz}, 2\epsilon_{xz}, 2\epsilon_{xy})^T$$

Then, assuming the existence of a strain energy function, it can be shown that $c_{ijkl} = c_{klij}$ [e.g., *Aki and Richards*, 1980, pp. 20-23]. This means that the (6×6) matrix C in equation (2) is symmetric and there are only 21 independent elastic constants in the most general anisotropic medium, satisfying equation (1).

Besides the constitutive relation, we need the momentum equation

$$\rho u = \nabla \cdot \tau + f$$

or

$$\rho u_{i,t} = \tau_{ij,j} + f_i \quad (3)$$

where f denotes the external body force per unit volume.

We now apply a triple Fourier transform to our variables. For any function g we define

$$\hat{g}(k_x, k_y, z, \omega) = \iiint g(x, y, z, t) \cdot \exp[i(\omega t - k_x x - k_y y)] dx dy dt$$

and

$$\hat{g}(x, y, z, t) = 1/(8\pi^3) \iiint \hat{g}(k_x, k_y, z, \omega) \cdot \exp[i(k_x x + k_y y - \omega t)] dk_x dk_y d\omega$$

in which all integrations are from $-\infty$ to ∞ . For calculations, it is more convenient to work with the slowness components $p_x = k_x/\omega$ and $p_y = k_y/\omega$ rather than the wave vector components k_x and k_y .

In the transformed domain, it can be shown [e.g., *Woodhouse*, 1974] that the constitutive relation (1) and the momentum equation (3) may be written together in the form

$$\partial_z b = i\omega A \cdot b + F \quad (4a)$$

in which $\partial_z \equiv \partial/\partial z$,

$$b = [u^T, t^T]^T \quad (4b)$$

$$F = \omega^{-1}[0, 0, 0, i\tau_z, i\tau_y, i\tau_x]^T \quad (4c)$$

and A is a (6×6) matrix whose elements are functions of the elastic coefficient matrix C , frequency ω , slownesses p_x, p_y , and the density ρ . This matrix has the form

$$A = \begin{pmatrix} T & B \\ \vdots & \vdots \\ S & T^T \end{pmatrix} \quad (4d)$$

where T , B , S are all (3×3) matrices, S and B being symmetric. If it happens that the medium has infinite Q and that p_x and p_y are real, then A will be real.

Let D denote the local eigenvector matrix of the matrix A . Thus each column of D is an eigenvector of A and

$$AD = DA \quad (5)$$

where $A = \text{diag}(\lambda_1, \lambda_2, \lambda_3, \lambda_4, \lambda_5, \lambda_6)$ is the matrix of eigenvalues. The wave vector v is then defined by

$$v = D^{-1}b \quad (6)$$

where b is the vector of physical variables in equation (4) and D^{-1} is the inverse of the eigenvector matrix D . The components of the wave vector can be regarded as the amplitudes of the six plane waves which propagate independently in any homogeneous region. The eigenvalues, $\lambda_1 \dots \lambda_6$, are the vertical components of the wave vectors associated with these plane waves. The columns of D are ordered so that the three upgoing solutions come first, followed by the three downgoing wave solutions. This ordering is necessary for the Kennett algorithm where reflection and transmission coefficients are calculated. It is not necessary to know which columns are P and which are S . Columns corresponding to upgoing waves are easily distinguished from those of downgoing waves by the signs of the imaginary parts of their associated eigenvalues.

All plane layer algorithms for synthetic seismograms make use of the quantities introduced above. The particular method used to compute the examples of this paper is the Kennett (invariant imbedding) algorithm discussed by Fryer and Frazer [1984] and extended to the VSP case by Mallick and Frazer [1988]. Essentially, this algorithm computes the response for a stack of homogeneous plane layers iteratively by successive inclusion of deeper and deeper layers. For each layer we obtain the eigenvalues and the eigenvectors of the elastic system matrix A by diagonalizing A numerically. This permits the treatment of triclinic materials, i.e., those with the lowest possible symmetry. A is a function of C , ρ , and the slownesses p_x and p_y . Since the entries of A change little from one p_x (or p_y) to the next, Jacobi iteration [Golub and Van Loan, 1983, pp. 295-301] is an efficient way to diagonalize A . Before diagonalizing A it is convenient to symmetrize A [Frazer and Fryer, 1989] by means of the similarity transformation

$$A' = S^{-1}AS \quad (7)$$

in which

$$S = \frac{e^{i\pi/4}}{2^{1/2}} \begin{pmatrix} 1 & i \\ i & 1 \end{pmatrix} \quad (8)$$

and i is the 3×3 identity matrix. Then A can be diagonalized using the algorithm of Eberlein [1971] for complex symmetric matrices. In practice, rather than symmetrizing A at each step, we work with the transformed first-order system

$$\partial_z b' = i\omega A' b' + S^{-1}F \quad (9)$$

The new vector of physical variables $b' = S^{-1}b$ is continuous at an interface between two solids, so reflection and transmission coefficients can be calculated just as with the original unsymmetrized system. It is only necessary to go back to the original system via the relation

$$D = SD' \quad (10)$$

at source and receiver depths. Here D' is the matrix of eigenvectors of A' . One of the advantages of working in the symmetrized system is that the columns of D' are orthogonal in the Euclidean inner product, whereas the columns of D are K orthogonal for

$$K = \begin{pmatrix} 0 & I \\ I & 0 \end{pmatrix} \quad (11)$$

I being a 3×3 identity matrix. This means (see Frazer and Fryer [1989] for the details) that the inverse D^{-1} of D is given by

$$D^{-1} = D'^T K \quad (12)$$

whereas the inverse $(D')^{-1}$ of D' is given by

$$(D')^{-1} = (D')^T \quad (13)$$

in which superscript T denotes the usual matrix transpose.

When the elastic tensor is frequency dependent, the p_x and p_y loops must be inside the frequency loop. Then, A must be diagonalized for each p_x , p_y , and ω . However, if the elastic tensor is frequency independent then the ω loop can be made the deepest loop, with diagonalization of A outside that loop. Therefore, even on a nonvector computer, frequency independent models are much more rapidly computed than frequency dependent models. On vector computers that difference in speed is magnified because the code for diagonalization of A contains numerous branches and is therefore difficult to vectorize over p_x and p_y .

To avoid time aliasing (wraparound), we use complex frequencies following the procedure outlined by Mallick and Frazer [1987], and to avoid spatial aliasing, we use the trapezoidal Filon method [Frazer, 1977; Frazer and Gettrust, 1984] to evaluate the integrals over p_x and p_y . Our slowness contours are straight lines at small angles to the $\text{Re}(p_x)$ and $\text{Re}(p_y)$ axes. With the slowness loops outside the frequency loop the same two slowness contours are used for all frequencies. If ω has a constant imaginary part (to avoid wraparound), then each frequency has slightly different contours in the complex k_x and k_y planes. At low frequencies, where the real part of ω is small, the k_x and k_y contours will be far from the real k_x and k_y axes, respectively, and numerical problems can result. Good results can be obtained by choosing the angle of the p_x contour to the $\text{Re}(p_x)$ axis so that k_x is real on that contour for ω in the middle of its band. However, if the frequency band is wide then $\text{Im}(\omega)$ should be kept small; that is, one should not attempt to attenuate wrapped around energy by more than a factor of 10. Band limiting of wavenumber and frequency integral transforms was done with Hanning windows (see Mallick and Frazer [1987] for details). For an AA medium, we first compute the reflectivity function in (p_x, p_y, ω) space and then use a triple Fourier transform to obtain the time domain synthetics. However, when the medium is azimuthally isotropic (AI), the reflectivity function depends only on radial slowness $p_r = (p_x^2 + p_y^2)^{1/2}$ and on frequency ω . Then the transform from (p_r, ω) space to (r, ω) space is carried out by the familiar Bessel transform, and the time domain synthetics are obtained using a Fourier transform.

GENERATION OF ELASTIC CONSTANTS

When we think of anisotropic earth models we do not usually think in terms of 21 elastic constants. More often we

think in terms of anisotropy due to fractures or joints or anisotropy due to sequences of thin layers, such as sand and shale. Thus it is convenient to have some method of generating equivalent constants for fractured media, thin-layered media, and fractured thin-layered media. This convenience becomes a necessity when it is recalled that the main use of synthetic seismograms is to model effects seen in data, and from this modeling to infer the values of meaningful Earth parameters. For example, if the goal of modeling is to infer the direction of fractures in a certain area, then it is necessary to specify fracture direction and fracture compliance as input parameters, rather than elastic constants.

There are a number of current theories for generating equivalent elastic constants for fractured media, and new theories are being developed. Researchers dismayed at the thought of having to become experts in this area simply to find which way the fractures are pointing can take comfort from two observations: First, there is some evidence that at least two very different theories give practically identical results. Second, our experience has been that at least one of these theories is straightforward to understand and to apply. Finally, for the case of weak anisotropy Thomsen [1986] showed that only three parameters are necessary to characterize the anisotropy, and he tabulated measured values of these parameters for 46 sedimentary rocks.

In Hudson's [1980, 1981] theory for generating the elastic coefficients of a cracked rock, the cracks are assumed to be small in the sense that $\nu a^3 \ll 1$, where ν is the number of cracks per unit volume and a is the mean radius of the cracks. Furthermore, the radii and separation distances of the cracks are assumed to be small compared to a wavelength, and the interaction between cracks is assumed to be small. Using a second-order scattering theory of Keller [1964], Hudson [1980] derives an integral equation for the mean field in such a cracked medium. When this mean field is taken to be a plane wave the resulting integral equation can be manipulated into the form of an elastodynamic equation for an equivalent medium whose elastic constants are given in terms of the crack parameters and the elastic constants of the original uncracked medium. The effect of the cracks is to perturb the elastic tensor c . Hudson [1981] has also derived frequency dependent expressions for the anisotropic variation of dissipation, and Crampin [1984] has recast these expressions into the imaginary components of the elastic tensor c . More recently, Hudson has extended his method to the case of multiple sets of cracks aligned in different directions [Hudson, 1986] and to the case of partially saturated cracks [Hudson, 1988]. For cracks, the advantage of the Hudson theory over the Schoenberg theory, discussed below, is that the Hudson theory is dynamic; that is, it gives the frequency dependence and imaginary part of the perturbed elastic tensor.

Nishizawa [1982] has attempted to overcome the limitation of low crack density by an iterative approach. New elastic constants are calculated for a medium with a very low crack density. The resulting equivalent medium is then cracked with a very low crack density, and so forth until the desired crack density is reached. So far, Nishizawa's [1982] approach has been applied only to cracks of circular cross section in an isotropic material. It is not yet known whether this approach correctly models crack-crack interactions, however, Schoenberg and Douma [1988] have shown that the Nishizawa model agrees with the Hudson microcrack

model and with the joint model (discussed below) for microcracks with aspect ratios as large as 0.3. In this context "agreement between models" means that different crack parameters in different models can be chosen so that the resulting elastic tensor components agree to within a few percentage points.

Schoenberg and Douma [1988] show how to generate the elastic tensor for a homogeneous medium containing fractures, i.e., parallel "microcracks" of infinite aspect ratio. The material between the fractures can have any anisotropy. In Schoenberg's [1980] linear slip model of fracturing, traction is continuous across a fracture, but displacement is discontinuous there with a jump proportional to the traction. In the quasi-static approximation to such fractures the components of stress normal to the fractures, and the components of strain tangent to the fractures, are assumed to be constant over a wavelength. Other components are replaced by their average values. However, propagation through rock containing linear slip fractures is inherently dispersive because of the reflection and transmission that occur at each fracture, and this effect is not modeled by the Schoenberg and Douma [1988] procedure. Schoenberg [1980, 1983] has derived exact reflection coefficients for the interface between a fractured medium and an unfractured medium, and Pyrak-Nolte et al. [1987] have shown that the equivalent dynamic modulus for compressional wave propagation normal to a single fracture gives good agreement with experimental results at high frequencies. Schoenberg and

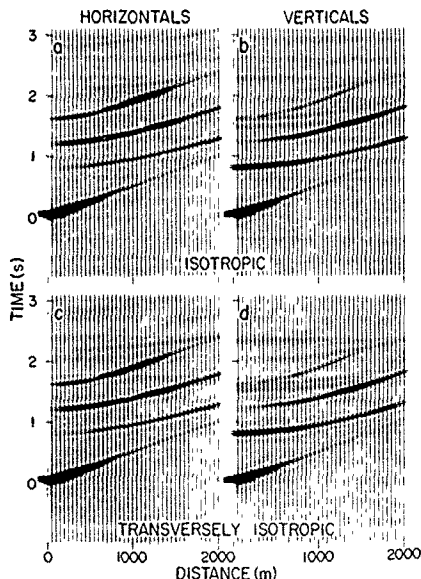


Fig. 1. (a) and (b) Horizontal and vertical components of motion computed using the isotropic model shown in Table 1 (c) and (d) Same as Figures 1a and 1b, but for the transversely isotropic model shown in Table 2

DEPTH (km)

Douma [1988] the One of equiv of the same berg and thin layer group; as the group parallel to that fracture group ele fractures practical [1988] has crust has horizontal

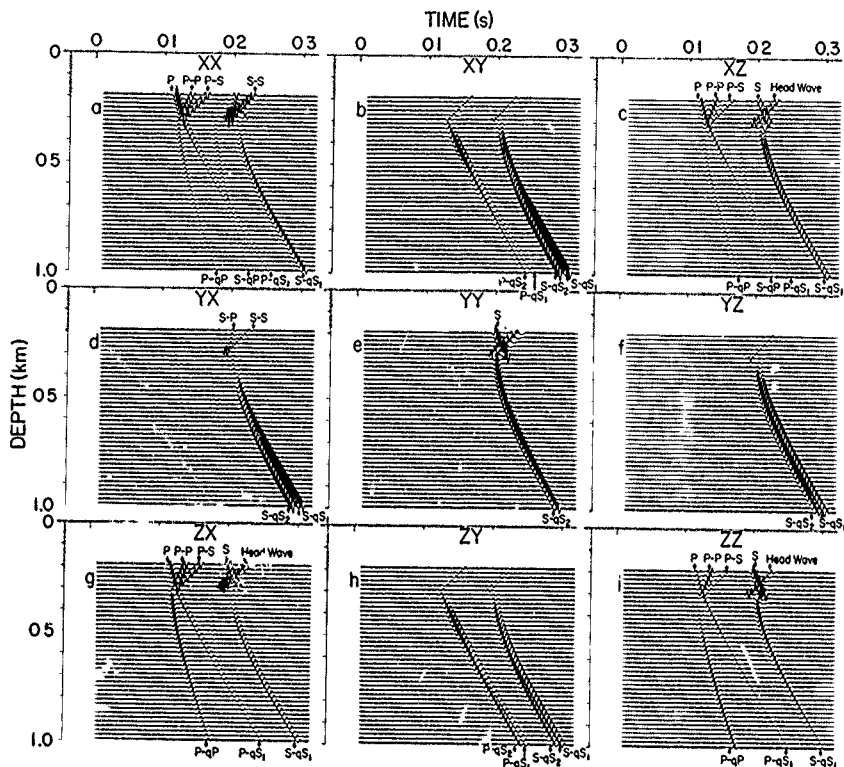


Fig. 2. (a), (b), and (c) The x , y , and z components of displacement for a source polarization in the x direction. Computed using the model shown in Table 3. (d), (e), and (f) Same as Figures 2a, 2b, and 2c but for a source in the y direction. (g), (h), and (i) same as Figures 2a, 2b, and 2c but for a source in the z direction.

Douma [1988] find that flat microcracks in an isotropic background material can be modeled equally well by the Hudson [1981] theory and by their quasi-static approximation.

One of the advantages of the Schoenberg and Douma [1988] quasi-static treatment is that the method of calculating of equivalent elastic constants for a thin layered medium is the same as that for a fractured medium. Recently, Schoenberg and Muir [1989] have shown how the constituents of a thin layered composite map to elements of a commutative group; adding the group elements of the constituents gives the group element corresponding to the composite. Set of parallel fractures are also represented as group elements so that fracturing a rock corresponds to the addition of the group element for the rock and the group element for the fractures. This group formulation of anisotropy has some practical features. For example, Hood and Schoenberg [1988] have used it to show how an orthorhombic oceanic crust has a unique resolution into vertical fractures and horizontal fractures.

Frazer [1990] has outlined how frequency dependent elastic moduli might be obtained both for fractures systems and for microlayering by the use of two-way and one-way elastic wave equations. Exact two-way methods of synthetic data generation are applied to a medium consisting of many thin layers, or fractures, then the resulting synthetic data are inverted using the one-way equations for propagation in the equivalent homogeneous medium. Frazer [1990] also gives exact expressions for the reflection and transmission coefficients at a linear slip fracture between different media of arbitrary anisotropy.

At the present time, generation of equivalent elastic constants for fractured or thin layered media can be summarized as follows: (1) The Schoenberg quasi-static approach is easy to use, provides a uniform treatment of fractured and thin layered media, and, in the case of cracks, gives substantially the same results as the Hudson microcrack theory, however, (2) the quasi-static approach does not give the anisotropic frequency dependent dissipation that comes out of the

TABLE 1. Parameters of the Isotropic Model Used to Compute the Synthetics Shown in Figures 1a and 1b

Layer	Elastic Coefficient Matrix c , 10^9 N/m ²	Density ρ , kg/m ³	Q	Thickness h , m
1	$\begin{pmatrix} 4 & 2 & 2 & 0 & 0 & 0 \\ 2 & 4 & 2 & 0 & 0 & 0 \\ 2 & 2 & 4 & 0 & 0 & 0 \\ 0 & 0 & 0 & 1 & 0 & 0 \\ 0 & 0 & 0 & 0 & 1 & 0 \\ 0 & 0 & 0 & 0 & 0 & 1 \end{pmatrix}$	1000	500	1800
2	$\begin{pmatrix} 18 & 5.04 & 5.04 & 0 & 0 & 0 \\ 5.04 & 18 & 5.05 & 0 & 0 & 0 \\ 5.04 & 5.04 & 18 & 0 & 0 & 0 \\ 0 & 0 & 0 & 6.48 & 0 & 0 \\ 0 & 0 & 0 & 0 & 6.48 & 0 \\ 0 & 0 & 0 & 0 & 0 & 6.48 \end{pmatrix}$	2000	500	1000
3	$\begin{pmatrix} 48 & 0.96 & 0.96 & 0 & 0 & 0 \\ 0.96 & 48 & 0.96 & 0 & 0 & 0 \\ 0.96 & 0.96 & 48 & 0 & 0 & 0 \\ 0 & 0 & 0 & 23.52 & 0 & 0 \\ 0 & 0 & 0 & 0 & 23.52 & 0 \\ 0 & 0 & 0 & 0 & 0 & 23.52 \end{pmatrix}$	3000	500	half-space

Hudson microcrack theory; and (3) theories exist for generating exact frequency dependent moduli for systems of linear slip fractures and for microlayers, but these theories have not been sufficiently tested to warrant routine use in seismic modeling codes. For modeling the weak anisotropies seen in most earth materials, quasi-static approximations appear to be adequate.

EXAMPLES

The first set of examples, shown in Figure 1, is a comparison of isotropic and transversely isotropic models. The second set of examples, shown in Figure 2, is for comparison with Van der Hijden's [1987] results from the Cagniard-de Hoop method. Later examples illustrate the use of our

method in computing synthetic seismograms for realistic AA earth models.

The model used to compute Figures 1a and 1b consists of three isotropic layers described in Table 1. The source time function was an impulse, band limited by a frequency domain Hanning window with a minimum frequency of 10 Hz and a maximum frequency of 60 Hz. A constant Q of 500 was used for each elastic modulus.

The model used to compute Figures 1c and 1d is described in Table 2. It also has three layers. Layers 1 and 3 have the same elastic properties as the isotropic model of Table 1, but layer 2 has been replaced by a weakly transversely isotropic medium. The transverse isotropy of layer 2 was assumed to be due to periodic stratification of two isotropic materials

TABLE 2. Parameters of the Transversely Isotropic Model Used to Compute the Synthetics Shown in Figures 1c and 1d

Layer	Elastic Coefficient Matrix c , 10^9 N/m ²	Density ρ , kg/m ³	Q	Thickness h , m
1	$\begin{pmatrix} 4 & 2 & 2 & 0 & 0 & 0 \\ 2 & 4 & 2 & 0 & 0 & 0 \\ 2 & 2 & 4 & 0 & 0 & 0 \\ 0 & 0 & 0 & 1 & 0 & 0 \\ 0 & 0 & 0 & 0 & 1 & 0 \\ 0 & 0 & 0 & 0 & 0 & 1 \end{pmatrix}$	1000	500	1800
2	$\begin{pmatrix} 19.351 & 4.887 & 4.495 & 0 & 0 & 0 \\ 4.887 & 19.351 & 4.495 & 0 & 0 & 0 \\ 4.495 & 4.495 & 15.431 & 0 & 0 & 0 \\ 0 & 0 & 0 & 5.129 & 0 & 0 \\ 0 & 0 & 0 & 0 & 5.129 & 0 \\ 0 & 0 & 0 & 0 & 0 & 7.232 \end{pmatrix}$	2000	500	1000
3	$\begin{pmatrix} 48 & 0.96 & 0.96 & 0 & 0 & 0 \\ 0.96 & 48 & 0.96 & 0 & 0 & 0 \\ 0.96 & 0.96 & 48 & 0 & 0 & 0 \\ 0 & 0 & 0 & 23.52 & 0 & 0 \\ 0 & 0 & 0 & 0 & 23.52 & 0 \\ 0 & 0 & 0 & 0 & 0 & 23.52 \end{pmatrix}$	3000	500	half-space

TABLE 3. Parameters of the Azimuthally Anisotropic Model Used to Compute the Synthetic VSP Responses in Figure 2

Layer	Elastic Coefficient Matrix c , 10^9 N/m ²	Density ρ , kg/m ³	Q	Thickness h , m
1	$\begin{pmatrix} 62.5 & 23.3 & 23.3 & 0 & 0 & 0 \\ 23.3 & 62.5 & 23.3 & 0 & 0 & 0 \\ 23.3 & 23.3 & 62.5 & 0 & 0 & 0 \\ 0 & 0 & 0 & 19.6 & 0 & 0 \\ 0 & 0 & 0 & 0 & 19.6 & 0 \\ 0 & 0 & 0 & 0 & 0 & 19.6 \end{pmatrix}$	2500	5000	300
2	$\begin{pmatrix} 260.78 & 80 & 80 & 0 & 0 & 0 \\ 80 & 200.77 & 72.99 & 0 & 0 & 0 \\ 80 & 72.99 & 200.77 & 0 & 0 & 0 \\ 0 & 0 & 0 & 63.89 & 0 & 0 \\ 0 & 0 & 0 & 0 & 72.9 & 0 \\ 0 & 0 & 0 & 0 & 0 & 72.9 \end{pmatrix}$	3300	5000	half-space

The x axis is the axis of symmetry.

with $\alpha_1 = 2.5$ km/s, $\beta_1 = 1.4$ km/s, $\rho_1 = 1700$ kg/m³, $h_1 = 0.5$ and $\alpha_2 = 3.5$ km/s, $\beta_2 = 2.2$ km/s, $\rho_2 = 2300$ kg/m³, and $h_2 = 0.5$ (here h_1 and h_2 are the fractional thicknesses of the two materials). The equivalent elastic moduli for the resulting layer were computed following the procedure given by Schoenberg (1983). In all the synthetic examples in Figure 1, the source was assumed to be embedded 20 m below the free surface and the receivers were 10 m below the free surface. Computation of the synthetics in Figure 1 required about a minute of CPU time on a Cray-2. Apart from using Bessel functions in the slowness transforms, no special advantage was taken of the vertical axis of symmetry. The matrix A was diagonalized using the general trilinear procedure mentioned above.

The next example, shown in Figure 2, is a vertical seismic profile (VSP) for the model of Table 3, an isotropic layer over an AA half-space. In this example, we computed the x , y , and z components of motion for source polarizations in the x , y , and z directions. The source was located 10 m below the top of the first layer, and the receivers were at a horizontal offset of 500 m and at depths from 190 to 990 m in steps of 20 m. The source time functions were impulse responses, band limited by a frequency domain Hanning window with a minimum frequency of 10 Hz and a maximum frequency of 300 Hz. The anisotropic medium in Table 3 is of hexagonal type with the x axis as the axis of symmetry. Such a medium

can be regarded as having sets of parallel fractures perpendicular to the x axis. We rotated the medium through an angle of -73° about the z axis, so that the surface line between the source and the borehole makes an angle of $+73^\circ$ with the fractures. These synthetics were computed using 256 frequencies, 300 values of p_y , and 300 values of p_z . The model shown in Table 3 is the same as that used by Van der Hijden [1987], and our Figures 2a-2f correspond to his Figures 7.2-7.7, respectively. Slight differences between Van der Hijden's results and ours are due to his inclusion of frequencies up to 750 Hz, his use of a Blackman-Harris window instead of a Hanning window, and the omission of multiples from his calculation.

In Figure 2, the labels P and S denote the P and S waves, respectively, in the top isotropic layer, whereas qP , qS_1 , and qS_2 denote quasi- P , quasi- S_1 , and quasi- S_2 waves respectively, in the lower AA half-space. Many of these arrivals are characteristics of wave propagation in an AA medium. For example, the XY , YX , YZ , and ZY components (Figure 2b, 2d, 2f, and 2h) would be zero if the medium were AI. The splitting of the shear arrivals marked $P-qS_1$ and $P-qS_2$ and $S-qS_1$ and $S-qS_2$ in Figures 2b, 2d, 2f, and 2h is another characteristic feature of wave propagation in an AA medium where the two shear waves, qS_1 and qS_2 , travel at different speeds.

The next example is a surface seismic record for the model given in Table 4. This is a 17-layer model consisting of isotropic and anisotropic layers. The anisotropic layers are of hexagonal type with the y axis as the axis of symmetry.

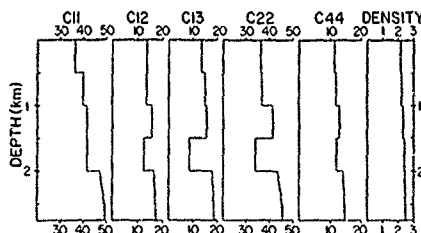


Fig. 3. Five independent elastic constants (C_{11} , C_{12} , C_{13} , C_{22} , and C_{44}) and density as a function of depth for the model described in Table 4. The elastic constants are in units of 10^9 N/m² and the density is in units of g/cm³.

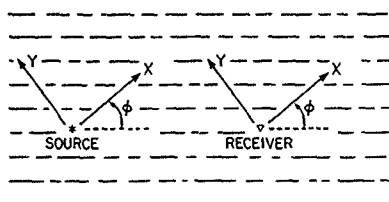


Fig. 4. Orientation of the fractured medium for the seismic profiles shown in Figures 5-8

TABLE 4. Parameters of the Azimuthally Anisotropic Model Used to Compute the Synthetics Shown in Figures 5-9

Layer	Elastic Coefficient Matrix c , 10^9 N/m ²	Density ρ , kg/m ³	Q	Thickness h , m
1	$\begin{pmatrix} 36.327 & 13.617 & 13.617 & 0 & 0 & 0 \\ 13.617 & 36.327 & 13.617 & 0 & 0 & 0 \\ 13.617 & 13.617 & 36.327 & 0 & 0 & 0 \\ 0 & 0 & 0 & 11.355 & 0 & 0 \\ 0 & 0 & 0 & 0 & 11.355 & 0 \\ 0 & 0 & 0 & 0 & 0 & 11.355 \end{pmatrix}$	2151	250	500
2	$\begin{pmatrix} 39.932 & 13.575 & 15.113 & 0 & 0 & 0 \\ 13.575 & 36.887 & 13.575 & 0 & 0 & 0 \\ 15.113 & 13.575 & 39.932 & 0 & 0 & 0 \\ 0 & 0 & 0 & 11.886 & 0 & 0 \\ 0 & 0 & 0 & 0 & 12.409 & 0 \\ 0 & 0 & 0 & 0 & 0 & 11.886 \end{pmatrix}$	2232	250	500
3	$\begin{pmatrix} 41.552 & 15.684 & 15.684 & 0 & 0 & 0 \\ 15.684 & 41.552 & 15.684 & 0 & 0 & 0 \\ 15.684 & 15.684 & 41.552 & 0 & 0 & 0 \\ 0 & 0 & 0 & 12.934 & 0 & 0 \\ 0 & 0 & 0 & 0 & 12.934 & 0 \\ 0 & 0 & 0 & 0 & 0 & 12.934 \end{pmatrix}$	2314	250	500
4	$\begin{pmatrix} 41.588 & 12.486 & 8.518 & 0 & 0 & 0 \\ 12.486 & 33.978 & 12.486 & 0 & 0 & 0 \\ 8.518 & 12.486 & 41.588 & 0 & 0 & 0 \\ 0 & 0 & 0 & 12 & 0 & 0 \\ 0 & 0 & 0 & 0 & 16.535 & 0 \\ 0 & 0 & 0 & 0 & 0 & 12 \end{pmatrix}$	2395	250	500
	varying from			
5	$\begin{pmatrix} 47.193 & 16.389 & 17.867 & 0 & 0 & 0 \\ 16.389 & 43.536 & 16.389 & 0 & 0 & 0 \\ 17.867 & 16.389 & 47.193 & 0 & 0 & 0 \\ 0 & 0 & 0 & 14.045 & 0 & 0 \\ 0 & 0 & 0 & 0 & 14.663 & 0 \\ 0 & 0 & 0 & 0 & 0 & 14.045 \end{pmatrix}$	varying from 2425 at the top to the layer 6 value at the bottom	250	500
	at the top to layer 6 values at the bottom			
6	$\begin{pmatrix} 49.459 & 17.271 & 18.732 & 0 & 0 & 0 \\ 17.271 & 45.621 & 17.271 & 0 & 0 & 0 \\ 18.732 & 17.271 & 49.454 & 0 & 0 & 0 \\ 0 & 0 & 0 & 14.71 & 0 & 0 \\ 0 & 0 & 0 & 0 & 15.361 & 0 \\ 0 & 0 & 0 & 0 & 0 & 14.713 \end{pmatrix}$	2477	250	half-space

The five independent elastic constants and the density of this model are shown in Figure 3, and the orientation of the fractures with respect to the seismic lines in terms of the azimuthal angle ϕ is given in Figure 4. For this model, synthetic seismograms were computed at three different azimuthal angles as shown in Figures 5-7. The source time functions were impulse responses, band limited by a frequency domain Hanning window between 10 and 60 Hz. The sources and receivers in these examples were embedded 20 and 10 m, respectively, beneath the free surface. The synthetics were computed using 256 frequencies, 400 values of p_x , 400 values of p_y , and a slowness aperture such that the minimum phase velocity was 2.3 km/s. Computation of all nine responses required 6.5 hours of CPU time on a single CPU of a Cray X-MP. Although the synthetics in Figures 5-7 are complicated, the characteristic features of seismic wave propagation in AA media are clearly evident. For example, note the splitting of the refracted shear wave arrival on the XX , XZ , YY , ZX , and ZZ profiles. This particular arrival, marked by an arrow on each record section, is earlier on the

YY section (Figures 5-7e) than on the others. This is due to the fact that the quasi- S_2 wave is faster than the quasi- S_1 wave, for the model given in Table 4. Also the XY , YX , YZ , and ZY sections for the 45° line (Figures 6b, 6d, 6f, and 6h) would have been zero if the entire medium were AI.

Our final example is a 500 m offset-VSP for the model of Table 4 at an azimuthal angle $\phi = 45^\circ$. The VSP synthetics, shown in Figure 8, were computed with 256 frequencies, 250 values of p_x , 250 values of p_y , and a minimum phase velocity of 2.3 km/s. The CPU time was 8 hours on a Cray X-MP. The source time functions and the source locations for these synthetics are the same as for those shown in Figures 5-7. The slowness sampling interval was increased for the VSP because the VSP offset of 500 m was smaller than the 2.5-km maximum offset of the surface seismic. The minimum phase velocity could also have been increased for the VSP for a greater saving in CPU time, though this was not done here. For VSPs the computational overhead incurred by having receivers at many depths is compensated for by a smaller slowness aperture and a larger

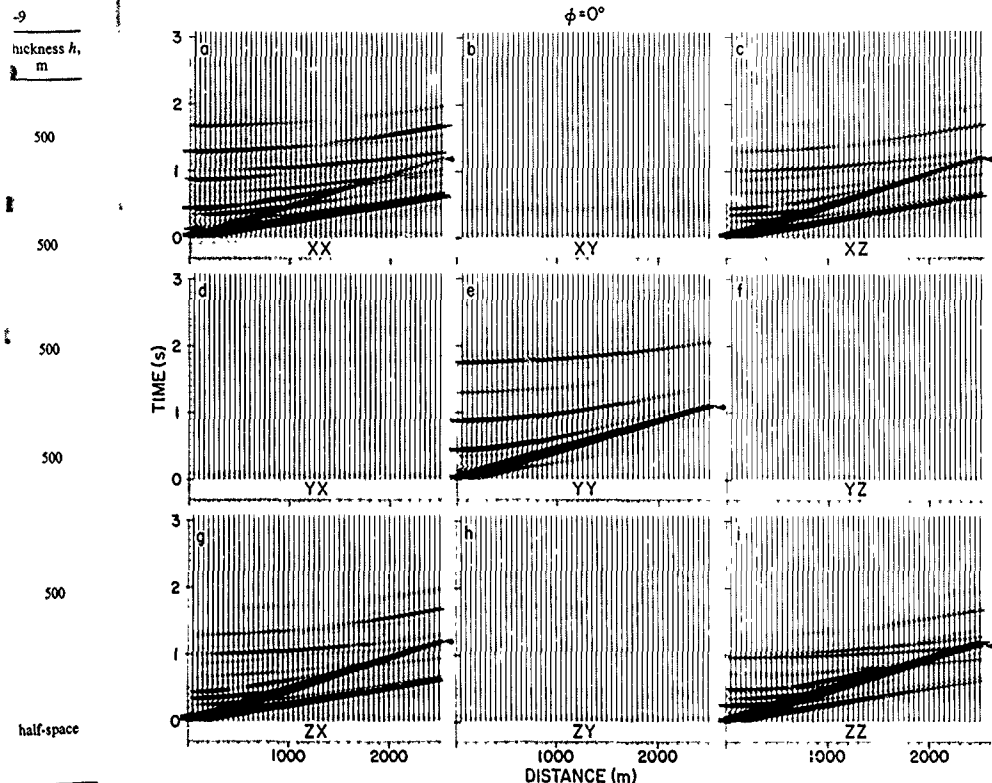


Fig. 5. (a), (b), and (c) The x , y , and z components of displacement for a source polarization in the x direction, computed using the model of Table 4. The seismic line is along the strike of the fractures. (d), (e), and (f) same as Figures 5a, 5b, and 5c but for a source in the y direction. (g), (h), and (i) same as Figures 5a, 5b, and 5c but for a source in the z direction.

This is due to the quasi- S_1 in the XY , YX , YZ , d , $6f$, and $6h$) are AI for the model of 3P synthetics, frequencies, 250 phase velocity one CPU of a and the source e as for those g interval was t of 500 m was of the surface also have been ; in CPU time, computational many depths is are and a larger

slowness sampling. Our experience has been that VSPs and surface seismic require almost the same amount of computation time.

DISCUSSION

The computations shown above indicate that it is now feasible to generate synthetic seismograms for realistic AA models. The reason for the higher CPU time required to compute synthetic seismograms for AA media is that, to be sure of accuracy in the AA case, one must compute the reflectivity matrix as a function of frequency ω and two wavenumbers p_x and p_y . If computing an AI model with 256 frequencies and 250 wavenumbers requires 1.5 min of CPU time, then computing a similar AA model will require 256 frequencies, 250 p_x , and 250 p_y , and the computation time will be approximately $(250 \times 1.5) \text{ min} = 6.25 \text{ hours}$.

Nevertheless, our experience has been that it is often necessary to do two wavenumber integrations for AA models. To demonstrate this point, Figure 9 shows synthetics for the same model and geometry as Figure 6 but computed with a single wavenumber integration. Comparison of Figures 6 and 9 reveals that the amplitudes of certain reflected events are much lower with a single integration (Figure 9) than with a double integration (Figure 6), especially at near offsets. Furthermore, although arrival times in both figures are nearly the same, some phases present in Figure 6 are absent from Figure 9. For example, the phases marked M_1 and M_2 on Figure 6e are the qP head wave and the qS_2 - qP reflection respectively, from the top of layer 2 in Table 4. M_1 and M_2 are completely absent from Figure 9e. We suspect that other such phases are also missing or weak in Figure 9, and that it is the absence or relative weakness of these phases that

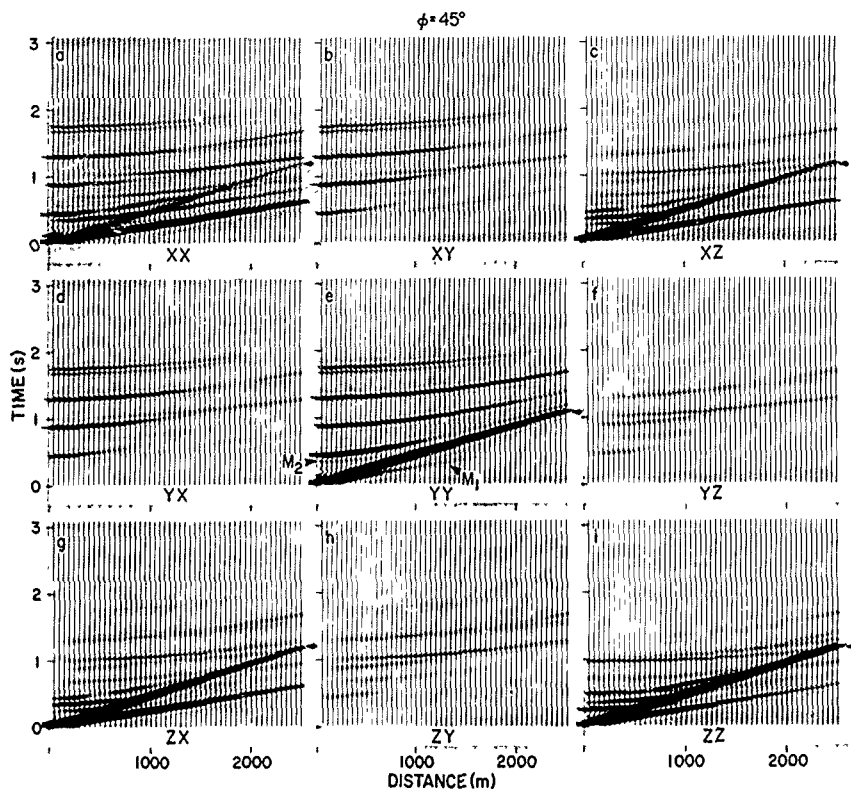


Fig. 6. Same as Figure 5, except that the seismic line makes an azimuthal angle of 45° with respect to the strike of the fractures. The phases marked M_1 and M_2 on section in Figure 6e are missing from the single k integral of Figure 9, below.

lowers the amplitudes of some multiple-wave type reflection events. In this regard, note that the amount of azimuthal anisotropy in the model used to compute the synthetics in Figures 6 and 9 is fairly small (Table 4), so that the two shear waves qS_1 and qS_2 travel with almost the same speed. As a result, a shear wave reflection will in general consist of the four reflections: qS_1 - qS_1 , qS_1 - qS_2 , qS_2 - qS_1 , and qS_2 - qS_2 . If the single wave number integration correctly computes, say, the qS_1 - qS_1 and qS_2 - qS_2 reflection amplitudes, but fails to compute correctly qS_1 - qS_2 and qS_2 - qS_1 , then the cumulative shear reflection event will have incorrect amplitude. It is disturbing that those phases which suffer lowered amplitude in a single integration are most weakened at near offsets, since near offsets are widely used in exploration. Note that many reflection events do not show this effect. Originally, we had hoped that the amplitude reductions were an artifact of the particular numerical scheme that we used for the Fourier-Bessel quadrature in the single integration. How-

ever, extensive testing appears to indicate that such is not the case: near-offset amplitude errors and missing phases seem to be inherent in the single integration approximation.

Although it is not evident from the examples presented here, travel times are often faster for a single integration than for a double integration. Note that synthetic seismograms computed for an AA medium by a single integration are not synthetics for an associated AI medium; if that were the case, then the XY , YX , ZY , and YZ sections of Figure 9 would be identically zero, and travel times would always be faster for a double integration than for a single integration because the former permits propagation outside the sagittal plane (vertical plane containing the source and receivers), whereas the latter does not.

To understand why, for an AA medium, a single integration will often give incorrect results, recall that a single integration gives the travel times of a line source even when Bessel functions are used as the kernels of the integral

trans
expo
the p
times
point
dimen
wave
a poin
the poi
is para
wave
source
integra
but oth
do not
arrivals
of the
azimuth.

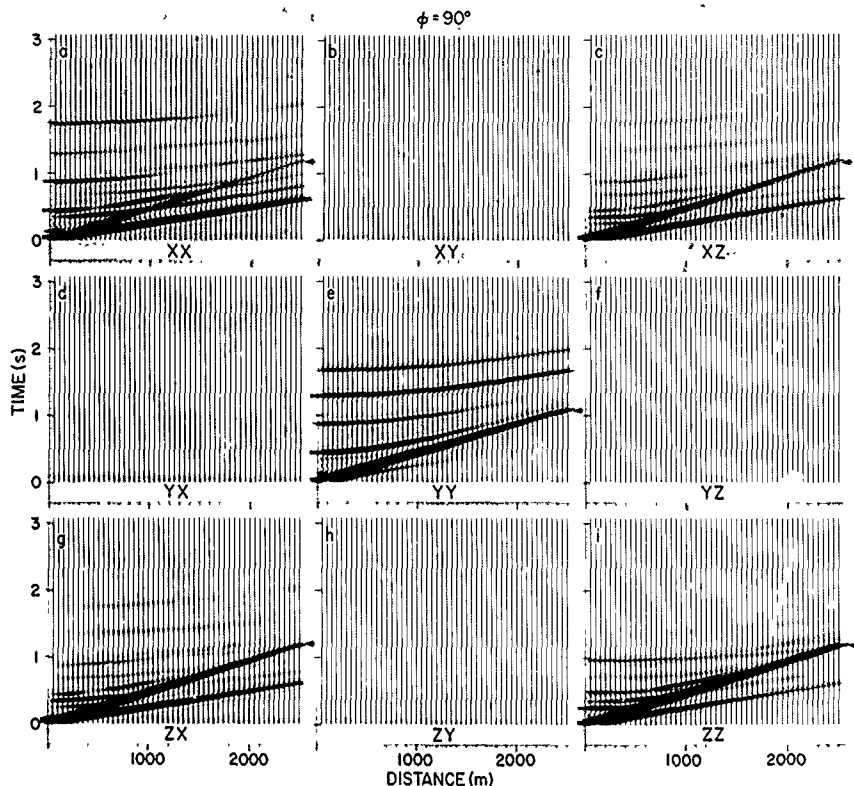


Fig. 7 Same as Figure 5, except that the seismic line makes an azimuthal angle of 90° with respect to the strike of the fractures.

like of
Figure

that such is not missing phaser approximation plies present integration than ic seismograms egration are not f that were the ons of Figure 9 would always be ngle integration tside the sagittal and receivers).

a single integra- all that a single ource even when s of the integral

transforms. Use of Bessel function kernels instead of an exponential kernel changes the amplitudes of arrivals and the phase shift of wavelets, but it does not change arrival times. The difference between line source arrival times and point source arrival times can be seen from the two-dimensional wave front surfaces shown in Figure 10. The wave front of a line source is obtained from the wave front of a point source by projection parallel to the line source. On the point source wave front, only points at which the tangent is parallel to the line source will contribute to the line source wave front. It can be seen that in two dimensions if the source and receiver lie in a plane of symmetry, then a single integration will give correct travel times for some arrivals, but other arrivals may be absent. If the source and receiver do not lie in a plane of symmetry, then not only may some arrivals be missing, but also the travel times and amplitudes of the main arrivals will be incorrect. Of course, if the azimuthal anisotropy is very weak, then these errors will be

very small. Also, the two-dimensional wave front surfaces of Figure 10 are a gross oversimplification of the actual situation in three dimensions, where propagation is vertical as well as horizontal (A quantitative study of these effects for realistic AA media is presently being carried out by B Nolte.) Since one can never be sure that a single integration will give correct travel times, amplitudes, and phases, it is always advisable to check final results for AA earth models by using two wavenumber integrations.

In view of the computation time it is appropriate to consider alternative faster methods of seismogram synthesis. Geometrical acoustics methods will run faster than the reflectivity approach demonstrated here. However, Chapman and Shearer [1988] and Shearer and Chapman [1988] have shown that it is difficult to apply ray theory to AA models with gradient zones. In AA media the qS polarizations twist along ray paths through gradient zones causing frequency dependent coupling between the qS waves. As

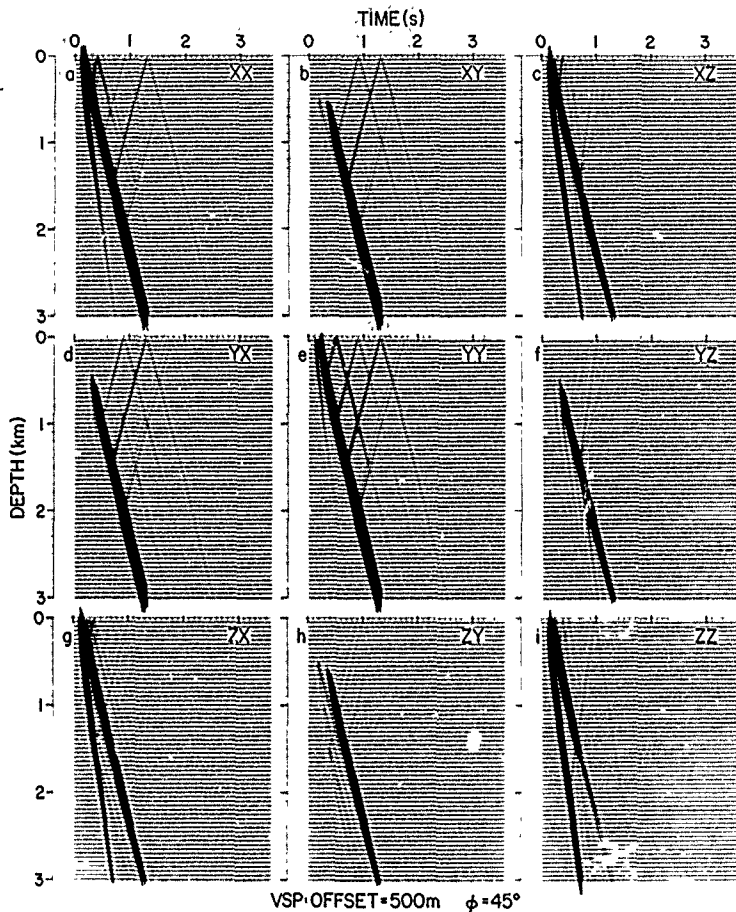


Fig. 8. Same as Figure 5 but now in VSP geometry and for the seismic line making an azimuthal angle of 45° with respect to the strike of the fractures

this coupling is much stronger than the analogous coupling between the P and SV waves in isotropic gradients, ray-tracing results for the qS wave polarizations are typically valid only at relatively high frequencies and do not converge to the isotropic results in the limit of infinitely weak anisotropy [Chapman and Shearer, 1988]. As a result, applications of ray theory to AA media are limited at present to relatively simple models [e.g., Gajewski and Pšenčík, 1987].

Another alternative to computation of synthetic seismograms for azimuthally anisotropic media is the Cagniard-de Hoop method as extended to AA media by Van der Hyden [1987]. If no gradient zones are present and multiple phases

are not important so that only a few generalized rays are needed, then Cagniard-de Hoop may be preferable to the reflectivity approach used here. However, Cagniard computer codes, even for isotropic models, generally demand of their users considerable skill. In AA media much more expertise is required because of the complicated nature of the Cagniard contours. The reflectivity method became the most widely used method for isotropic models because of its ease of use (the same contours of integration work for all models) and its automatic inclusion of multiples. It seems likely that as computers become faster the reflectivity method will also become the method of choice for AA models.

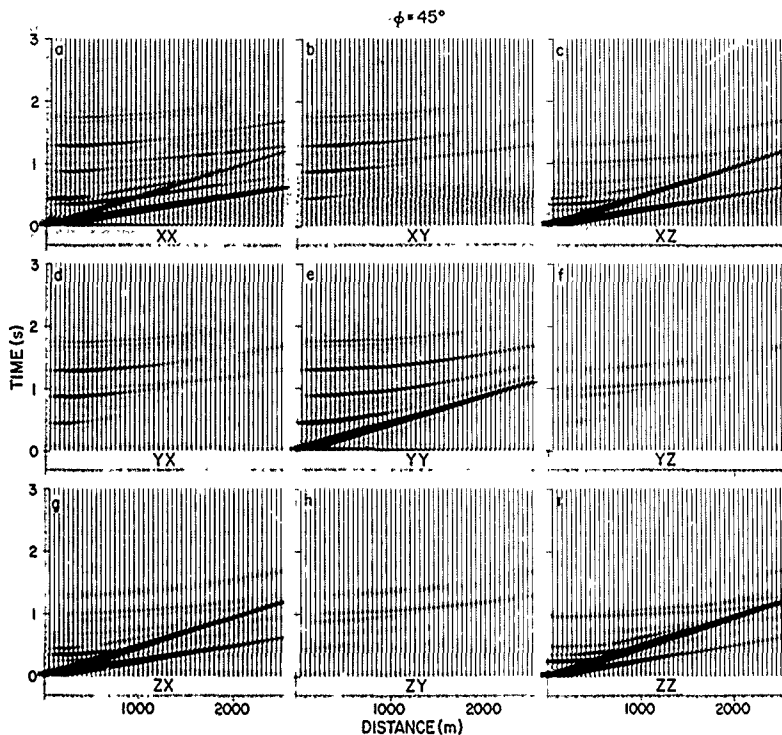


Fig. 9. Same as Figure 6, except that here all the synthetics were computed with a single wave number integration.

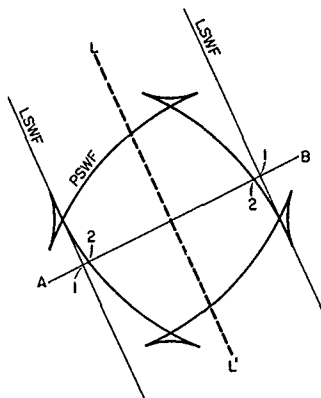


Fig. 10. A horizontal slice through wavefronts from a point source and a line source in a strongly anisotropic medium. PSWF, point source wave front; LL', line source, AB, line of receivers; LSWF, line source wave front. The wave fronts of the line source are obtained by parallel projection of points where the tangent to the wave front is parallel to the line of sources.

Acknowledgments. We are grateful to Cray Research for time on a Cray-2 and a Cray X-MP and to Schlumberger-Doll Research for time on a Cray-1. Ralph Wiggins encouraged us to begin this work in 1983. Stimulating discussions with Bertram Nolte improved our understanding of the differences between single and double integrations. The model of Table 4 was suggested by Leon Thomsen at Amoco. We thank Geo-Pacific Corporation for use of the ANIVEC synthetic seismogram software and for permission to publish this paper. Support of earlier theoretical work by NSF and ONR is also gratefully acknowledged. Hawaii Institute of Geophysics contribution 2270.

REFERENCES

- Aki, K., and P. G. Richards, *Quantitative Seismology*, vol. 1, W. H. Freeman, New York, 1980.
- Alford, R. M., Shear data in the presence of azimuthal anisotropy, paper presented at 56th Annual International Meeting, Soc. of Exp. Geophys., Houston, Tex., 1986.
- Anderson, D. L., and A. M. Dziewonski, Upper mantle anisotropy: Evidence from free oscillations, *Geophys. J. R. Astron. Soc.*, **69**, 383-404, 1982.
- Anderson, D. L., and J. Regan, Upper mantle anisotropy and the oceanic lithosphere, *Geophys. Res. Lett.*, **10**, 841-844, 1983.
- Babuska, V., Anisotropy of V_p and V_s in rock forming minerals, *J. Geophys.*, **50**, 1-6, 1981.
- Bachman, R. T., Acoustic anisotropy in marine sediments and sedimentary rocks, *J. Geophys. Res.*, **84**, 7661-7663, 1979.
- Becker, D. F., and P. I. Perelberg, Seismic detection of subsurface

- fractures, paper presented at 56th Annual International Meeting, Soc. of Exp. Geophys., Houston, Tex., 1986.
- Booth, D. C., and S. Crampin, The anisotropic reflectivity technique: Theory, *Geophys. J. R. Astron. Soc.*, **72**, 755-766, 1983a.
- Booth, D. C., and S. Crampin, The anisotropic reflectivity technique: Anomalous reflected arrivals from an anisotropic upper mantle, *Geophys. J. R. Astron. Soc.*, **72**, 767-782, 1983b.
- Chapman, C. H., and P. M. Shearer, Ray tracing in azimuthally anisotropic media, 2, Quasi-shear wave coupling, *Geophys. J.*, **96**, 65-83, 1988.
- Christensen, N. I., The magnitude, symmetry and origin of upper mantle anisotropy based on fabric analyses of ultramafic tectonites, *Geophys. J. R. Astron. Soc.*, **76**, 89-111, 1984.
- Christensen, N. I., and M. H. Salisbury, Seismic anisotropy in the oceanic upper mantle: Evidence from the Bay of Islands ophiolite complex, *J. Geophys. Res.*, **84**, 4601-4610, 1979.
- Crampin, S., The dispersion of surface waves in multilayered anisotropic media, *Geophys. J. R. Astron. Soc.*, **21**, 387-402, 1970.
- Crampin, S., Effective anisotropic elastic constants for wave propagation through cracked solids, *Geophys. J. R. Astron. Soc.*, **76**, 135-145, 1984.
- Crampin, S., E. M. Chesnokov, and R. G. Hipkin, Seismic anisotropy—The state of the art, II, *Geophys. J. R. Astron. Soc.*, **76**, 1-16, 1984.
- de Hoop, A. T., Modification of Cagniard method for solving seismic pulse problems, *Appl. Sci. Res.*, **38**, 349-356, 1960.
- Eberlein, P. J., On the diagonalization of complex symmetric matrices, *J. Inst. Math. Appl.*, **7**, 377-383, 1971.
- Frazer, L. N., Synthesis of shear coupled-PL, Ph.D. thesis, Princeton Univ., Princeton, N. J., 1977.
- Frazer, L. N., Dynamic elasticity of microbedded and fractured rocks, *J. Geophys. Res.*, **93**, 4821-4831, 1990.
- Frazer, L. N., and G. J. Fryer, Useful properties of the system matrix for a homogeneous anisotropic viscoelastic medium, *Geophys. J.*, **97**, 173-177, 1989.
- Frazer, L. N., and J. F. Gettrust, On a generalization of Filon's method and the computation of the oscillatory integrals of seismology, *Geophys. J. R. Astron. Soc.*, **76**, 461-481, 1984.
- Fryer, G. J., and L. N. Frazer, Seismic waves in stratified anisotropic media, *Geophys. J. R. Astron. Soc.*, **78**, 691-710, 1984.
- Fryer, G. J., and L. N. Frazer, Seismic waves in stratified anisotropic media, II, Elastodynamic eigensolutions for some anisotropic systems, *Geophys. J. R. Astron. Soc.*, **91**, 73-101, 1987.
- Fuchs, K., Seismic anisotropy of the subcrustal lithosphere as evidence for dynamical processes in the upper mantle, *Geophys. J. R. Astron. Soc.*, **49**, 167-179, 1977.
- Gajewski, D., and I. Pšenčík, Computation of high frequency seismic wavefields in 3-D laterally inhomogeneous anisotropic media, *Geophys. J. R. Astron. Soc.*, **91**, 383-411, 1987.
- Golub, G. H., and C. F. Van Loan, *Matrix Computations*, Johns Hopkins University Press, Baltimore, Md., 1983.
- Hood, J. A., and M. Schoenberg, Decoupling vertical fracture parameters from background transverse isotropy in an orthorhombic oceanic crust, *Eos Trans. AGU*, **69**, 1331, 1988.
- Hudson, J. A., Overall properties of a cracked solid, *Math. Proc. Cambridge Philos. Soc.*, **88**, 371-384, 1980.
- Hudson, J. A., Wave speeds and attenuation of elastic waves in material containing cracks, *Geophys. J. R. Astron. Soc.*, **64**, 133-150, 1981.
- Hudson, J. A., A higher order approximation to the wave propagation constants for a cracked solid, *Geophys. J. R. Astron. Soc.*, **87**, 265-274, 1986.
- Hudson, J. A., Seismic wave propagation through material containing partially saturated cracks, *Geophys. J.*, **92**, 33-37, 1988.
- Johnston, D. H., VSP detection of fracture induced velocity anisotropy, paper presented at 56th Annual International Meeting, Soc. of Exp. Geophys., Houston, Tex., 1986.
- Keith, C. M., and S. Crampin, Seismic body waves in anisotropic media, reflection and refraction at a plane interface, *Geophys. J. R. Astron. Soc.*, **49**, 181-208, 1977a.
- Keith, C. M., and S. Crampin, Seismic body waves in anisotropic media: Propagation through a layer, *Geophys. J. R. Astron. Soc.*, **49**, 209-223, 1977b.
- Keith, C. M., and S. Crampin, Seismic body waves in anisotropic media: Synthetic seismograms, *Geophys. J. R. Astron. Soc.*, **49**, 225-243, 1977c.
- Keller, J. B., Stochastic equations and wave propagation in random media, *Proc. Symp. Appl. Math.*, **16**, 145-170, 1964.
- Kennaeth, B. L. N., Reflections, rays, and reverberations, *Bull. Seismol. Soc. Am.*, **64**, 1685-1696, 1974.
- Kennaeth, B. L. N., *Seismic Wave Propagation in Stratified Media*, Cambridge University Press, New York, 1983.
- Lynn, H. B., and L. A. Thomsen, Reflection shear-wave data along the principal axes of azimuthal anisotropy, paper presented at 56th Annual International Meeting, Soc. of Exp. Geophys., Houston, Tex., 1986.
- Majer, E. L., T. V. McEvilly, F. S. Eastwood, and L. R. Myer, Fracture detection using P-wave and S-wave vertical seismic profiling at The Geysers, *Geophysics*, **53**, 76-84, 1988.
- Mallick, S., and L. N. Frazer, Practical aspects of reflectivity modeling, *Geophysics*, **52**, 1355-1364, 1987.
- Mallick, S., and L. N. Frazer, Rapid computation of multi-offset vertical seismic profile synthetic seismograms for layered media, *Geophysics*, **53**, 479-491, 1988.
- Nishizawa, O., Seismic velocity in a medium containing oriented cracks—Transversely isotropic case, *J. Phys. Earth*, **30**, 331-347, 1982.
- Pyrak-Nolte, L. J., L. R. Myer, and N. G. W. Cook, Seismic visibility of fractures, *Proc. U.S. Symp. Rock Mech.*, **28th**, 47-56, 1987.
- Rai, C. S., and K. E. Hanson, Shear-wave birefringence: A laboratory study, paper presented at 56th Annual International Meeting, Soc. of Exp. Geophys., Houston, Tex., 1986.
- Schoenberg, M., Elastic wave behavior across linear slip interfaces, *J. Acoust. Soc. Am.*, **68**, 1516-1521, 1980.
- Schoenberg, M., Reflection of elastic waves from periodically stratified media with interfacial slip, *Geophys. Prospect.*, **31**, 265-292, 1983.
- Schoenberg, M., and J. Douma, Elastic wave propagation in media with parallel fractures and aligned cracks, *Geophys. Prospect.*, **36**, 571-590, 1988.
- Schoenberg, M., and F. Muir, A calculus for finely layered anisotropic media, *Geophysics*, **54**, 581-589, 1989.
- Shearer, P. M., and C. H. Chapman, Ray tracing in azimuthally anisotropic media, I, Results for models of aligned cracks in the upper crust, *Geophys. J.*, **96**, 51-64, 1988.
- Shimamura, H., Anisotropy in the oceanic lithosphere of the northwestern Pacific Basin, *Geophys. J. R. Astron. Soc.*, **76**, 253-260, 1984.
- Smith, M. L., and F. A. Dahlen, The azimuthal dependence of Love and Rayleigh Wave propagation in a slightly anisotropic medium, *J. Geophys. Res.*, **78**, 3321-3333, 1973.
- Stephen, R. A., Seismic anisotropy observed in upper oceanic crust, *Geophys. Res. Lett.*, **8**, 865-868, 1981.
- Taylor, D. B., Double contour integration for transmissions from point sources through anisotropic layers as used in ROCAPAC software, *Geophys. J. R. Astron. Soc.*, **91**, 373-381, 1987.
- Thomsen, L., Weak elastic anisotropy, *Geophysics*, **51**, 1954-1966, 1986.
- Thomsen, L., Reflection seismology over azimuthally anisotropic media, *Geophysics*, **53**, 304-313, 1988.
- Van der Huden, J. H. M. T., *Propagation of Transient Elastic Waves in Stratified Anisotropic Media*, North-Holland, New York, 1987.
- Willis, H. A., G. L. Rethford, and E. Bielanski, Azimuthal anisotropy occurrence and effect on shear-wave data quality, paper presented at 56th Annual International Meeting, Soc. of Exp. Geophys., Houston, Tex., 1986.
- Woodhouse, J. H., Surface waves in laterally varying layered structure, *Geophys. J. R. Astron. Soc.*, **37**, 461-490, 1974.

L. N. Frazer and S. Mallick, Hawaii Institute of Geophysics, University of Hawaii, 2525 Correa Road, Honolulu, HI 96822

(Received April 3, 1989,
revised November 7, 1989,
accepted November 12, 1989)

RESEARCH NOTE

Useful properties of the system matrix for a homogeneous anisotropic visco-elastic solid

L. Neil Frazer and Gerard J. Fryer

University of Hawaii at Manoa, Hawaii Institute of Geophysics, 2525 Correa Road, Honolulu, HI 96822, USA

Accepted 1988 October 7. Received 1988 October 7, in original form 1986 July 30

SUMMARY

For the computation of synthetic seismograms in a generally anisotropic layered earth it is necessary to find the eigenvectors and eigenvalues of the first order elastic system matrix \mathbf{A} for many values of wavenumber and frequency. The analytical formulas used to construct the eigenvectors of \mathbf{A} in the isotropic case are not available in the general anisotropic case so one must use numerical methods whose speed often depends on an efficient use of the properties of \mathbf{A} . First we review the symmetries of \mathbf{A} and the conditions under which \mathbf{A} is not semi-simple. Then we construct a perturbation theory for the eigenvectors of \mathbf{A} . Finally we show how to make \mathbf{A} symmetric so that special techniques for symmetric matrices, such as Jacobi iteration, can be used. All the results given here remain valid when the medium is attenuating, i.e. when the elastic coefficients are complex.

Key words: elastic system matrix, perturbation theory

1 REVIEW

As the elastic system matrix is discussed in many other papers and books we include here only a bare outline of its derivation and a few details that will be needed below. For general anisotropy it is convenient to use Cartesian coordinates (x_1, x_2, x_3) with x_3 as the depth coordinate. The constitutive equation relating the stress tensor τ and the displacement vector \mathbf{u} is then

$$\tau_{ij} = c_{ijkl} * u_{k,l} \quad (1)$$

in which $*$ denotes time convolution and repeated subscripts imply summation. The momentum equation is

$$\rho \partial_t^2 u_i = \tau_{ij,j} + f_i \quad (2)$$

in which ρ is mass density, t is time and \mathbf{f} is body force per unit volume. To remove derivatives in x_1, x_2 and t from these equations we take a triple Fourier transform:

$$g(p_1, p_2, \omega) = \int_{-\infty}^{\infty} dx_1 \int_{-\infty}^{\infty} dx_2 \times \int_{-\infty}^{\infty} dt \exp[i\omega(t - p_1 x_1 - p_2 x_2)] g(x_1, x_2, t) \quad (3)$$

After some algebraic manipulations one then obtains the first order system in the form

$$\partial_3 \mathbf{b} = i\omega \mathbf{A} \mathbf{b} - \frac{i}{\omega} \begin{pmatrix} 0 \\ \mathbf{f} \end{pmatrix} \quad (4)$$

in which

$$\mathbf{b} = \begin{pmatrix} u \\ t \end{pmatrix} \quad (5)$$

is the vector of motions, $\mathbf{u} = [u_1, u_2, u_3]^T$, and scaled tractions, $\mathbf{t} = (i/\omega)[\tau_{13}, \tau_{23}, \tau_{33}]^T$. One reason for scaling the tractions is that it makes the components of \mathbf{A} real when the medium is lossless, which is useful in certain kinds of computations. The system matrix \mathbf{A} has the form

$$\mathbf{A} = \begin{pmatrix} \mathbf{T} & \mathbf{C} \\ \mathbf{S} & \mathbf{T}^T \end{pmatrix} \quad (6)$$

where \mathbf{T} , \mathbf{S} , and \mathbf{C} are 3×3 submatrices and \mathbf{C} and \mathbf{S} are symmetric. Note that \mathbf{A} has this same form and these same symmetries even if any or all of ω , p_1 , p_2 , or the c_{ijkl} are complex. Thomson, Clarke & Garmann (1986) have summarized the symmetries of \mathbf{A} that result from various definitions of \mathbf{b} , including our equation (5), and from not factoring $i\omega$ out of \mathbf{A} . It is straightforward to translate the results of this paper into forms consistent with these other definitions.

2 ISOTROPY AND ANISOTROPY

For an isotropic medium one can calculate explicit formulas for the eigenvectors of \mathbf{A} by the use of potentials (e.g. Aki & Richards 1980, p. 166). These formulas show that the eigenvectors of \mathbf{A} have the following properties:

(a) \mathbf{A} is diagonalizable and the eigenvectors of \mathbf{A} span the

six-dimensional complex space C^6 except on the set of measure zero, MZ , in which $p = \sqrt{p_1^2 + p_2^2}$ is equal either to α^{-1} or to β^{-1} , where α and β are the P- and S-wave speeds, respectively.

(b) Eigenvectors of A with different eigenvalues are K -orthogonal, i.e. they are orthogonal in the inner product (\cdot, \cdot) defined by

$$(a, b) = a^T K b, \quad (7)$$

in which K is the 6×6 matrix given by

$$K = \begin{pmatrix} 0 & I \\ I & 0 \end{pmatrix}, \quad (8)$$

and I is the 3×3 identity matrix.

(c) Except on MZ , there is a matrix D and a diagonal matrix A such that $D^{-1} = D^T K$ and $AD = DA$. In other words, where A is diagonal, there is a basis for C^6 consisting of eigenvectors of A which are K -orthogonal but not K -null. (Vectors a and b are K -orthogonal if $(a, b) = 0$ and a vector a is said to be K -null if $(a, a) = 0$.)

These three properties hold for complex values of ω , p_1 , p_2 , α and β . Property (a) is a consequence of the physics that led to A ; when $p = \alpha^{-1}$ say, then the upgoing P-wave and the downgoing P-wave become the same horizontally travelling P-wave. Properties (b) and (c) will be shown below to follow directly from the symmetry properties in equation (6). Property (c) is a very powerful statement: it guarantees that each degenerate eigenvalue has enough K -orthonormal eigenvectors to span its subspace. This does not mean that K -null eigenvectors do not exist; in fact they are easy to construct: let u_H and u_V be two K -orthonormal eigenvectors with the same eigenvalue; then $u_H + iu_V$ is a K -null eigenvector.

Property (c) is useful because it enables one to quickly compute the inverse of the matrix of eigenvectors (Fryer & Frazer 1984) and thus construct the propagator solution of equation (4). The construction is as follows: let $B = [b_1, b_2, \dots, b_6]$ be the matrix whose columns are the eigenvectors of A obtained algebraically by the use of potentials. We divide each column b_i of B , by its K -norm $(b_i, b_i)^{1/2}$ and call the resulting matrix D ; then the inverse of D is $D^T K$. Letting A denote the diagonal matrix of eigenvalues of A , we then have the propagator of the system (4) in the form

$$P(x_3, x_3') = D \exp[i\omega(x_3 - x_3')] A D^T K \quad (9)$$

The construction just given is so familiar for isotropy that we take it for granted. In the case of anisotropy we expect to find a similar situation. As we will show below, properties (b) and (c) hold unchanged in the case of general anisotropy; however, property (a) requires modification because the set MZ , on which A is not diagonal, is now much more complicated. For a medium with a horizontal plane of symmetry the structure of MZ can be deduced from analytical formulas. For example, in the monoclinic case, MZ is just the locus of the zeroes and, branch points, of λ_1 , λ_2 and λ_3 given by equations (3.4) of Fryer & Frazer (1987). Although formulas for the eigenvalues and eigenvectors of A are not yet available in the general (triclinic) case, it is possible to give a general description of MZ in terms of the slowness surface (Synge 1957), a good discussion of which

may be found in Garmany (1983). Briefly, the slowness surface is the locus of solutions of the dispersion relation,

$$\det[p\delta_{jk} - p_j p_k c_{ijkl}] = 0,$$

which can be obtained from the momentum equation and the usual elastic constitutive equation in a few steps (e.g. Auld 1973, p. 212). This dispersion relation holds even when the c_{ijkl} are complex, provided p_1 , p_2 and p_3 are also allowed to be complex. Even if the c_{ijkl} are real, at least one of p_1 , p_2 , and p_3 must be allowed to be complex if evanescent solutions are to be included.

When the c_{ijkl} are real the solutions of the dispersion relation lie along a three-sheeted surface in R^3 called the slowness surface. At points where two sheets intersect, or are tangent to each other, A will be degenerate (have repeated eigenvalues) but it need not be defective (non-diagonal). In general, A is defective at any point (p_1, p_2) for which the line drawn through (p_1, p_2) , parallel to the p_3 -axis, is tangent to one or more sheets. MZ is the set of such points.

There is a slightly more general way of expressing this, which also holds in the evanescent case, and in the case of complex c_{ijkl} . Solutions of the dispersion relation still form, as before, a three-sheeted two-dimensional manifold; however, this manifold is now a complex submanifold of C^3 . Let $p = (p_1, p_2)$ be any point in C^2 and let $q = (p_1, p_2, p_3)$ be any solution of the dispersion relation corresponding to p . Let S be the sheet on which q is located. If there is no neighbourhood of q , on S , for which the projection map $(p_1, p_2, p_3) \rightarrow (p_1, p_2)$ is one-to-one, then A is defective at p . MZ is the set of such p . Physically, the reason that A is defective on MZ and not necessarily defective at points, for example, where two sheets intersect, is that in the latter case the degenerate eigenvectors of A correspond to plane waves with the same phase velocity but with different group velocity. It is only at points in MZ that the group velocities are also the same.

It is worth noting that although the structure of MZ is of theoretical interest one needs to know very little about MZ to compute accurate synthetic seismograms by frequency-wavenumber integration methods. Contours of integration which avoid MZ are given below.

3 PROPERTIES OF A

Garmany (1983) gives a good discussion of the symmetries of A but his results are valid only for perfectly elastic media. All of the results given in this paper are valid for visco-elastic media. Our first goal is to show that property (b) follows from the symmetries of A as expressed by equation (6). Since (6) holds generally, so then will (b). First it is convenient to define, for any matrix B , the K -transpose of B

$$B^K = K B^T K^T. \quad (10)$$

This definition is motivated by the requirement that $(B^K u, v) = (u, Bv)$ for all u and v in C^6 , whenever K is orthogonal ($KK^T = I$). A matrix B is said to be K -symmetric if $B^K = B$. It is easy to verify that the system matrix A given by (6) is K -symmetric for K defined by (8).

Now let u and v be two eigenvectors of A with

eigenvalues μ and ν , respectively. Then $v(u, v) = vu^T K v = u^T K A v = (u, A v) = (A^T u, v) = (A u, v) = \mu(u, v)$. Hence $(u, v) = 0$ if $\mu \neq \nu$, which shows that property (b) holds in general.

Our next goal is to prove property (c), above. Proof is needed because the inner product (\cdot, \cdot) is improper, and so we have no *a priori* way of knowing that the eigenvectors of A are not K -orthogonal to themselves. Recall that an $N \times N$ matrix is said to be semi-simple (non-defective) if it has N independent eigenvectors. A matrix K is said to be involutive if $K^2 = I$.

THEOREM

Let A be a semi-simple complex 6×6 matrix satisfying $KA^T K = A$ for some symmetric involutive matrix K . Then A may be written in the form $A = DAD^T K$ where the columns of D are the eigenvectors of A , A is the diagonal matrix of eigenvalues of A , and the inverse of D is $D^T K$.

PROOF

Since A is semi-simple there is a basis $\{u_i\}_{i=1}^6$ for C^6 consisting of eigenvectors of A . This basis has a dual basis $\{v_i\}_{i=1}^6$ normalized so that $v_i^T u_j = \delta_{ij}$, where the superscript 't' denotes transposition followed by complex conjugation. (Existence of the dual basis follows from the fact that the Hermitian inner product $(u, v) = u^T v$ is a proper inner product.) Now for $i = 1, \dots, 6$, define $z_i = K v_i^T$ where ' \cdot ' denotes complex conjugation. Since $K^2 = I$, we have $v_i^T = z_i^T K$. Therefore $z_i^T K u_j = \delta_{ij}$. Let λ_i be the eigenvalue associated with u_i , so that $A u_i = \lambda_i u_i$. We may write

$$z_i^T K A u_j = z_i^T K \lambda_j u_j = \lambda_j \delta_{ij} = \lambda_i \delta_{ij} = \lambda_i z_i^T K u_j$$

so that

$$(z_i^T K A - \lambda_i z_i^T K) u_j = 0.$$

Since the u_j span C^6 this means that $z_i^T K A = \lambda_i z_i^T K$, from which, taking the transpose, and multiplying on the left by K , we get $KA^T K z_i = \lambda_i z_i$. Since A is K -symmetric this means that z_i is also an eigenvector of A with eigenvalue λ_i . First suppose that A has no repeated eigenvalues; then $z_i = \alpha_i u_i$ for some complex α_i . Since $1 = z_i^T K u_i = \alpha_i u_i^T K u_i$ we may absorb the factor $\alpha_i^{1/2}$ into u_i and then have $z_i = u_i$. We have shown that, when the eigenvalues of A are distinct, C^6 has a basis $\{u_i\}_{i=1}^6$ of eigenvectors of A that satisfy $u_i^T K u_j = \delta_{ij}$. Writing $D = (u_1, u_2, \dots, u_6)$ it follows that $D^{-1} = D^T K$ and $A = DAD^T K$.

Now suppose that A has repeated eigenvalues: we may still write

$$A = \sum_{i=1}^6 \lambda_i u_i u_i^T = \sum_{i=1}^6 \lambda_i u_i z_i^T K.$$

Let A' be any matrix obtained from A by changing the eigenvalues so that no two are the same:

$$A' = \sum_{i=1}^6 \lambda'_i u_i z_i^T K.$$

The argument just given shows that we can normalize the u_i so that $A' = D A' D^T K$ where $D^{-1} = D^T K$. Since the only difference between A' and A is in the eigenvalues we may

now replace A' by A to get $A = DAD^T K$. This completes the proof. Note that the only properties of A used in the proof were diagonality and the K -symmetry. Thus the result holds when any or all of ω , p_1 , p_2 and c_{ijk} are complex.

The theorem shows the relations between A , K , and the matrix of eigenvectors, D , but it does not tell us how to compute D . Two methods for computing D are given in the following sections.

4 PERTURBATION THEORY FOR A

In computing synthetic seismograms we need to find the eigenvectors of A for a dense array of values of p_1 and p_2 . Here we briefly outline how to use perturbation theory to rapidly update the eigenvectors and eigenvalues when A is changed by a small amount. Our notation is adapted from Pease (1965, chapter 10). As above, we assume only that A is diagonality and K -symmetric; thus the perturbation formulas derived below remain valid when any or all of ω , p_1 , p_2 and c_{ijk} are complex.

Suppose we have A_0 with known eigenvector matrix $D = (u_1, \dots, u_6)$ and known eigenvalue matrix $A = \text{diag}(\lambda_1, \dots, \lambda_6)$ and we want to find these same quantities for $A = A_0 + \delta A$. From the eigenvectors of A we can generate the K -dyads E_{ij} defined by

$$E_{ij} = u_i u_j^T K. \quad (11)$$

It is easy to show that the K -dyads have the properties

$$E_{ij} E_{kl} = E_{ij} \delta_{jk} \quad (12)$$

and

$$I = \sum_{i=1}^6 E_{ii}. \quad (13)$$

The matrix A may be expanded as

$$A = \sum_{i=1}^6 \lambda_i E_{ii}. \quad (14)$$

and an arbitrary matrix B may be expanded as

$$B = \sum_{i=1}^6 \sum_{j=1}^6 b_{ij} E_{ij}, \quad b_{ij} = u_i^T K B u_j, \quad (14a, b)$$

To obtain these last relations multiply B on the right and left by I , substitute from (13), and then make use of (11). When the matrix δA is added to A_0 let the resulting change in the j th eigenvalue be $\delta \lambda_j$ and the change in the j th eigenvector be

$$\delta u_j = \sum_i b_{ij} u_i. \quad (15)$$

The eigenvector equation for A becomes

$$(A_0 + \delta A)(u_j + \delta u_j) = (\lambda_j + \delta \lambda_j)(u_j + \delta u_j) \quad (16)$$

Using the K -dyad expansions of A_0 and δA and neglecting quantities that are second order in δA we find

$$\delta \lambda_j = u_j^T K \delta A u_j \quad (17a)$$

The coefficient b_{ij} is taken to be zero if $j = i$ and is otherwise given by

$$b_{ij} = \frac{u_i^T K \delta A u_j}{\lambda_j - \lambda_i} \quad (17b)$$

Formulas (17) assume that λ_j has only one eigenvector and that $\lambda_j + \delta\lambda_j$ is not numerically close to another eigenvalue. If such is not the case then we must use degenerate perturbation theory. Suppose λ_j has the two eigenvectors u_j and u_k . We write $w = u_j + \alpha u_k$ where α is a constant to be determined. Now let the perturbation to w be

$$\delta w = \sum_{i \neq j, k} b_i u_i$$

and the perturbation to λ_j be $\delta\lambda_j$, and substitute into the equation

$$(A_0 + \delta A)(w + \delta w) = (\lambda_j + \delta\lambda_j)(w + \delta w). \quad (18)$$

Neglecting quantities of second order in δA we find the two solutions:

$$\alpha_{\pm} = \frac{c-a}{2b} \pm \sqrt{1 + \left(\frac{c-a}{2b}\right)^2} \quad (19a)$$

$$\delta\lambda_{j\pm} = a + b\alpha_{\pm} \quad (19b)$$

in which

$$a = u_j^T K \delta A u_j; \quad b = u_j^T K \delta A u_k;$$

$$\text{and } c = u_k^T K \delta A u_k. \quad (19c, d, e)$$

The perturbations to the eigenvectors w_{\pm} are given by

$$b_{i\pm} = \frac{u_i^T K \delta A w_{\pm}}{(\lambda_j - \lambda_i)} \quad i \neq j, k. \quad (20)$$

While eigenvalues are the same only at shear-wave singularities (Fryer & Frazer 1987), they are more often numerically close in the sense that the perturbations to the eigenvalues may be greater than their difference. When that is the case we use quasi-degenerate perturbation theory (e.g. Messiah 1962, p. 111). This consists of altering the unperturbed matrix A_0 so as to make the nearby eigenvalues identical. Suppose λ_j and λ_k are numerically close. Then we replace A_0 by

$$A'_0 = 1/2(\lambda_j + \lambda_k)(E_{jj} + E_{kk}) + \sum_{i \neq j, k} \lambda_i E_{ii} \quad (21)$$

and we replace δA by

$$\delta A' = \delta A + 1/2(\lambda_j - \lambda_k)E_{jj} + 1/2(\lambda_k - \lambda_j)E_{kk}. \quad (22)$$

Notice that $A'_0 + \delta A' = A_0 + \delta A$ but that A'_0 has the repeated eigenvalue $(\lambda_j + \lambda_k)/2$ so that we can now use degenerate perturbation theory.

The corrections to the eigenvalues and eigenvectors that perturbation theory gives us are not exact but we can find exact corrections by iterating. Suppose we have just used one of the above methods to calculate new approximate eigenvectors, $u'_i = u_i + \delta u_i$, and eigenvalues, $\lambda'_i = \lambda_i + \delta\lambda_i$. We K -orthogonalize the u'_i using Gram-Schmidt, and then normalize them to unit K -length; call these new vectors u''_i . The expressions derived above can be used to show that the u''_i are K -orthogonal to first order in δA and that K -orthonormalization changes them by quantities which are only second order in δA ; therefore the u''_i are eigenvectors of A correct to first order in δA . Using the u''_i and the λ_i , we form the reference matrix

$$A'_0 = \sum_{i=1}^6 \lambda'_i u''_i u''_i^T K. \quad (23)$$

and the new perturbation

$$\delta A' = A - A'_0. \quad (24)$$

Since the u''_i and the λ'_i are exact eigenvectors and eigenvalues of A'_0 we can now use perturbation theory again. Updating the reference matrix is important for numerical work because it allows one to diagonalize a long sequence of matrices, the last member of which may be very different from the first.

Parts of the theory of this section have been utilized by Van der Hijden (1988) in the computation of synthetic seismograms for azimuthally anisotropic media by the Cagniard-de Hoop method.

5 JACOBI ITERATION

The procedures of the last section are straightforward but they are unsuitable for use on a vectorizing computer because of the large number of 'if' statements required. An alternative procedure for calculating eigenvalues and eigenvectors, which takes advantage of the fact that these are approximately known, is Jacobi iteration (e.g. Golub & Van Loan 1983, p. 295). In order to use Jacobi iteration we must first transform the system matrix A into a symmetric matrix. With reference to equation (5) we introduce a new vector of physical variables b' which is related to b by

$$b = S b'. \quad (25)$$

Then equation (5) becomes

$$\partial_3 b' = i \omega A' b' - \frac{i}{\omega} S^{-1} \begin{pmatrix} 0 \\ f \end{pmatrix} \quad (26)$$

in which

$$A' = S^{-1} A S. \quad (27)$$

We want to choose S so that $(A')^T = A'$. We also want to choose S so that our K -product becomes the Euclidean product, i.e. if $u = Su'$ and $v = Sv'$ then

$$u^T K v = (u')^T v'. \quad (28)$$

Substitution for u' and v' in this last equation yields

$$S^{-T} S^{-1} = K. \quad (29)$$

For our K , defined by equation (8), this last equation is solved by $S = K^{-1/2}$ where $K^{1/2}$ is given by

$$K^{1/2} = \frac{\exp(-i\pi/4)}{\sqrt{2}} \begin{pmatrix} 1 & iI \\ iI & 1 \end{pmatrix}, \quad (29a)$$

with inverse

$$K^{-1/2} = \frac{\exp(i\pi/4)}{\sqrt{2}} \begin{pmatrix} 1 & -iI \\ -iI & 1 \end{pmatrix}. \quad (29b)$$

To verify that A' is symmetric for $S = K^{-1/2}$, substitute for S in equation (27), take the transpose of both sides, and recall that A is K -symmetric so that $A^T = KAK$. The eigenvectors of A transform like other vectors so that if D' is the eigenvector matrix of A' and D is the eigenvector matrix of A then

$$D' = K^{1/2} D \quad (30)$$

The transformation preserves the orthonormality of the eigenvectors:

$$(D')^T D' = D'^T K^{1/2} K^{1/2} D' = D'^T K D' = I, \quad (24)$$

although this orthonormality is now with respect to the Euclidean inner product instead of the K -product. Note that our symmetrization procedure used only the K -symmetry of A ; thus it works even when any or all of ω , p_1 , p_2 and the c_{ijk} are complex.

Now that we have transformed A into a symmetric matrix we can use standard methods to compute the eigenvectors. Suppose we have found the matrix D' of eigenvectors of A' , and we wish to find the eigenvectors of $A' + \delta A'$. The matrix

$$A + M = (D')^T (A' + \delta A') D' \quad (31)$$

has off-diagonal components which are of order δA . Jacobi iteration iteratively reduces the sum of the squares of the off-diagonal elements of $A + M$ in a manner that converges very rapidly if the off-diagonal elements are small to begin with. It finds a complex orthogonal matrix R such that A' is diagonal where

$$A' = R^T (A + M) R = R^T (D')^T (A' + \delta A') D' R. \quad (32)$$

Thus the matrix of eigenvectors of $A' + \delta A'$ is $D'R$. An efficient Jacobi iteration for complex symmetric matrices was given by Eberlein (1971). Anderson & Loizou (1973) show that Eberlein's method converges rapidly when the off-diagonal elements are small; an ALGOL implementation of the algorithm can be found in Anderson & Loizou (1976).

The theory of this section has been used extensively by Mallick & Frazer (1989) for the computation of synthetic seismograms for azimuthally anisotropic visco-elastic media by the Kennett (1983) algorithm. They found that, for models with attenuation typical of earth materials, integration along the $\text{Re}(p_1)$ -axis and the $\text{Re}(p_2)$ -axis avoids the set MZ . For models with unrealistically high Q 's, integration along the contours $\arg(p_1) = -\epsilon$ and $\arg(p_2) = -\epsilon$, where $\epsilon = 0.1$, avoids MZ . When a complex temporal frequency is used to avoid wrap-around (Mallick & Frazer, 1987) then the contours $\arg(p_1) = -\epsilon - \arg(\omega)$ and $\arg(p_2) = -\epsilon - \arg(\omega)$ should be used so as to keep the wavenumbers k_1 and k_2 near their real axes. These double

contours are analogous to the single contours that have been used on isotropic models for many years.

ACKNOWLEDGMENTS

Contributions of the first and second authors were with support of, respectively, the Geo-Pacific Corporation, US Office of Naval Research, Contract No. N0001-0181 and Hawaii Institute of Geophysics Contribution 2107.

REFERENCES

- Aki, K. & Richards, P. G., 1980. *Quantitative Seismology*, W. H. Freeman, San Francisco.
- Anderson, P. & Loizou, G., 1973. On the quadratic convergence of an algorithm which diagonalizes a complex symmetric matrix. *J. Inst. Math. Appl.*, **12**, 261-271.
- Anderson, P. & Loizou, G., 1976. A Jacobi method for complex symmetric matrices. *Numer. Math.*, **25**, 347-363.
- Auld, B. A., 1973. *Acoustic Fields and Waves in Solids*, Wiley, New York.
- Craven, B. D., 1969. Complex symmetric matrices. *J. Aust. Soc.*, **10**, 341-354.
- Eberlein, J. J., 1971. On the diagonalization of complex symmetric matrices. *J. Inst. Math. Appl.*, **7**, 377-383.
- Fryer, G. J. & Frazer, L. N., 1984. Seismic waves in stratified media. *Geophys. J. R. astr. Soc.*, **78**, 691-710.
- Fryer, G. J. & Frazer, L. N., 1987. Seismic waves in stratified media - II. Elastodynamic eigensolutions for anisotropic systems. *Geophys. J. R. astr. Soc.*, **91**, 73-101.
- Garmany, J., 1983. Some properties of elastodynamic eigenfunctions in stratified media. *Geophys. J. R. astr. Soc.*, **565**-569.
- Golub, G. H. & Van Loan, C. F., 1983. *Matrix Computations*, Johns Hopkins University Press, Baltimore, Maryland.
- Kennett, B. L. N., 1983. *Seismic Wave Propagation in Stratified Media*, Cambridge University Press.
- Mallick, S. & Frazer, L. N., 1987. Practical aspects of reflection modeling. *Geophys. Res.*, **52**, 1355-1364.
- Mallick, S. & Frazer, L. N., 1989. Computation of synthetic seismograms in layered media with arbitrary anisotropy. *Geophys. Res.*, submitted.
- Messiah, A., 1962. *Quantum Mechanics*, vol. II, North-Holland, Amsterdam.
- Pease, M. C., 1965. *Methods of Matrix Algebra*, Academic Press, New York.
- Thomson, C., Clarke, T. & Garmany, J., 1986. Observation of seismic wave equation and reflection coefficient synthetic stratified media. *Geophys. J. R. astr. Soc.*, **86**, 675-686.
- van der Hijden, J. H. M. T., 1988. *Propagation of Transient Elastic Waves in Stratified Anisotropic Media*, North-Holland, Amsterdam.
- Woodhouse, J. H., 1974. Surface waves in a laterally variable layered structure. *Geophys. J. R. astr. Soc.*, **37**, 461-490.

(29a)

(29b)

(30)

Contract: N00014-87-K-0181
Seismology & Acoustics

**Theoretical and Computational Studies
in Marine Seismology**

L. Neil Frazer

Sediment shear Q from airgun OBS data

P. D. Bromirski, L. N. Frazer and F. K. Duennebieber

School of Ocean and Earth Sciences, University of Hawaii, Honolulu, HI 96822, USA

Accepted 1992 March 17. Received 1992 March 17; in original form 1991 October 30

SUMMARY

Direct measurement of the sediment shear-wave quality factor, Q_β , has been hindered by the lack of an effective shear-wave source. We show that if a satisfactory horizontal component ocean bottom seismometer (OBS) is available, then sediment Q_β can be determined directly by using spectral ratios of converted shear-wave reflections. Spectral ratios are formed with the PS reflection from the sediment/basement interface and the $PSSS$ multibounce sediment shear-wave reflection. As a check, we also computed Q_β from the peak amplitudes of PS and $PSSS$.

We applied the spectral ratio method to airgun OBS data collected over 356 m of primarily high-porosity biosiliceous clay in 5467 m of water in the northwest Pacific at 43°55.44'N, 159°47.84'E (DSDP Site 581). An average sediment shear-wave velocity of about 0.2 km s⁻¹ was obtained from the PS traveltime. Effective Q_β for the sediment column was found to be 97 ± 11 ($\alpha = 0.281 \pm 0.032$ dB λ^{-1}) in the frequency band 3–18 Hz.

We tested the methods by applying them to reflectivity synthetic seismograms computed for various velocity profiles with both frequency-dependent Q and frequency-independent Q . The Q_β estimate obtained from synthetic seismograms was within 15 per cent of the true Q_β for each velocity profile. Q_β estimates within 25 per cent of the true Q were obtained with the addition of up to 6.5 per cent signal-generated noise, whereas the addition of only 3 per cent signal-generated noise energy makes estimates of the frequency dependence of Q unreliable using spectral ratios. We conclude that the two-octave band of the data is not wide enough to determine the frequency dependence of Q_β .

Tests on synthetic seismograms, computed from models containing alternating layers of high impedance contrast with realistic velocities, indicated that apparent attenuation due to intrabed multiples does not significantly affect the spectral ratio Q_β estimates, although a shift in spectral content to higher frequencies for PS and $PSSS$ phases and a delay in the apparent arrival time of $PSSS$ were observed. However, the alternative peak amplitude ratio method gave Q_β estimates more than 25 per cent lower than the true Q for multilayer sediment models. We also tested the methods on synthetic data subjected to hard and soft clipping. Spectral ratio estimates of Q_β , from synthetic data with PS clipped up to 50 per cent, were within 25 per cent of the true Q_β .

Key words: converted shear-wave reflections, horizontal geophone OBS data, sediment attenuation, spectral ratios.

1 INTRODUCTION

When corrected for geometric spreading, seismic body waves decay in amplitude like $e^{-\alpha x}$, where x is the source–receiver distance and α is the attenuation

Attenuation is thus a property of the material through which the waves propagate. In discussions of rock properties or of propagation loss, it is sometimes more convenient to speak of the quality factor Q , given by $Q = \pi f / \alpha c$, where f is frequency and c is the seismic velocity. Attenuation includes

both intrinsic losses due to anelastic heating and apparent losses resulting from scattering. Although neither the mechanism nor the exact mathematical description of attenuation is precisely known, most *in situ* measurements imply that Q is frequency-independent (Hamilton 1976a, Kanamori & Anderson 1977), whereas most theories suggest some form of frequency dependence (e.g. Strick 1967).

The determination of the attenuation characteristics of seismic waves in marine sediments has been the focus of numerous studies (e.g. Hamilton 1976a, b; Jacobson, Shor & Dorman 1981; Jensen & Schmidt 1986). Stratification within the sediments may result in significant scattered energy and associated interference of seismic signals that can make attenuation measurements extremely difficult. Attempts to separate effective compressional-wave attenuation into its components and to determine its frequency dependence (e.g. Jacobson 1987) have not been conclusive. There is still no conclusive evidence of the frequency dependence of Q within the seismic band between 1 and 100 Hz, although some studies (e.g. Stoll 1985; Jensen & Schmidt 1986) have presented evidence which suggests that α varies as f^a , with B between 1 and 2.

The effect of sediment shear-wave parameters on acoustic propagation loss in the ocean has been examined by Vidmar (1980a, b), Harrison & Cousins (1985) and Hughes *et al.* (1990). Sediment attenuation can be useful in identifying sediment type (Hamilton 1980), and changes in attenuation with depth can indicate the degree of lithification (Hamilton 1976a; Jacobson *et al.* 1981). Reflectively modelling of the oceanic crust can give erroneous results for crustal Q_p if incorrect assumptions are made about sediment Q_p .

Ocean bottom sediment compressional-wave properties can be measured directly due to the ease of generating and detecting compressional signals (e.g. Hamilton 1976a; Jacobson *et al.* 1981). Although the shear-wave properties of ocean sediments can be determined using Scholte-waves (Jensen & Schmidt 1986), numerical modelling shows that Scholte-waves propagate only in the topmost portion of the sediments. For shallow water sediments, Jensen & Schmidt found a relatively steep gradient in both shear-wave velocity, c_s , and Q_s between the sea-floor and 60 m depth.

Direct measurement of sediment Q_s has been limited by the absence of high quality sediment shear-wave data. This is due largely to the lack of satisfactory ocean bottom S-wave sources, but is also related to problems in ocean bottom seismometer (OBS) design (Sutton & Duennebie 1987). Here we circumvent the source problem by analysing converted shear-wave reflections from the top of the crust (basement) recorded by an OBS. The detection and identification of multiply-reflected basement-converted shear waves allows us to make the first direct measurement of effective Q_p for the entire sediment column at a deep water site.

We first present the OBS data that motivated the shear-wave analysis and discuss the key phases. We briefly review propagation parameters and alternative descriptions of attenuation. Then, using synthetic seismograms, we show that spectral ratios and peak amplitude ratios can be used to determine Q_p from converted S-wave reflections. A variety of velocity profiles are tested, with and without clipping, with and without added noise, and with the use of a realistic multipulse source function. Finally, we apply our methods

to horizontal-component OBS data.

2 DATA

The OBS data used in this study were obtained in conjunction with the Ocean Sub-bottom Seismometer IV Experiment on DSDP Leg 88 (Duennebie *et al.* 1987). The experiment site (Hole 581C) is located in ~110 Ma crust about 40 km south of the Hokkaido Trough in the northwest Pacific basin at 43°55.44'N, 159°47.84'E. Typical water depth in the area is 5500 m. Single-channel reflection data show pelagic sediments roughly 350 m thick, smoothly draped over basaltic crust. Holes drilled at Site 581 on Legs 86 and 88 encountered continuous pelagic siliceous clays; chert bands beginning about 70 m above basement become numerous near the base of the sediments. Core data indicate a low-velocity zone at a depth of about 200 m below sea bottom.

The data used in this study were recorded by a Hawaiian Institute of Geophysics isolated sensor ocean bottom seismometer, OBS Y-220, (Byrne *et al.* 1983) from a 30 litre airgun towed across the site in an approximately north-south direction by Soviet research vessel *Dimitri Mendeleev* (Duennebie *et al.* 1987). The airgun was towed at a depth of 20 m and operated at a pressure of about 2000 psi with a repetition rate of 1 min. More than 300 shots were recorded at horizontal ranges between 0 and 55 km, with nominal spacing of about 0.17 km. The analogue data were digitized at 80 samples s⁻¹. Ship track, gain and $R^{0.66}$ spreading corrections were applied.

2.1 Data analysis

Fig. 1 shows the unfiltered OBS horizontal geophone (a) and hydrophone (b) record sections. Horizontal geophones are sensitive to motion along their axis in the horizontal plane; this motion can be due to either non-vertical compressional-waves, to shear waves, or, sometimes, to tilting of the instrument package. In contrast, pressure sensors detect only compressional-wave energy and are insensitive to shear-wave energy and tilt. Comparing the pressure data with the horizontal data, we see that only the direct water wave is common to both, thus the phases observed on the horizontal component must be near-vertical travelling shear waves.

Using the 2.00 ± 0.02 s $P+S$ traveltime from the horizontal geophone data and the sediment thickness of 356 m from drilling, we estimate an average sediment shear-wave velocity, \bar{c}_s , between 0.195 and 0.204 km s⁻¹, assuming the average sediment compressional-wave velocity, \bar{c}_p , is between 1.8 and 1.5 km s⁻¹. Basement compressional and shear-wave velocities of 2.45 and 4.35 km s⁻¹, respectively, were obtained from the slopes of the PSS and PPS refraction branches, in general agreement with other studies (e.g. Spudich & Orcutt 1980; White & Stephen 1980; Duennebie *et al.* 1987). As it is difficult to locate precisely where these phases emerge from the converted basement reflection, or to determine their slope at that point, the actual velocities at the top of the crust may be somewhat lower than these measurements. The limited dynamic range of the instrument, which clipped some high amplitude signals, precludes amplitude versus offset analysis

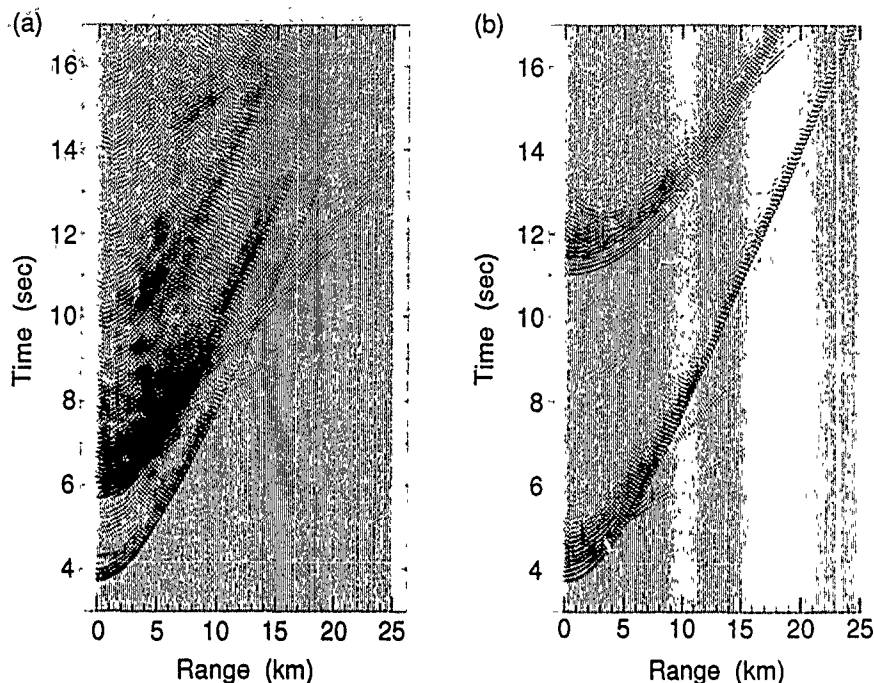


Figure 1. (a) Unfiltered horizontal OBS refraction data. (b) Unfiltered OBS pressure record section. Amplitudes in each record section are scaled relative to the maximum amplitude in the nearest trace.

to identify the critical distances for the refraction phases and thereby constrain the uppermost crustal velocities.

This paper will focus on the first 12 s of the horizontal data (Fig. 2). A reduction velocity of 2.25 km s^{-1} was applied in order to separate phases and to facilitate identification of the sediment shear-wave reflections. The traveltimes shown in Fig. 2 were generated by tracing rays for converted and multiply-reflected S phases using a one-layer sediment model with $c_0 = 1.55 \text{ km s}^{-1}$, $c_H = 0.198 \text{ km s}^{-1}$, and a sediment thickness of 356 m. The PS phase travels down through the sediment column as P and converts to S at the sediment/basement interface. The $PSSS$ phase transits the sediment column four times, once as P and three times as S . The $PSSS$ multiple shear-wave reflection from basement was the motivation for the sediment Q_B analysis in this paper.

Fig. 3 shows the horizontal component data from selected traces at less than 2 km horizontal range, with each trace normalized to the same maximum amplitude. The water wave, WW , an intrasediment reflection IPS , and the PS and $PSSS$ converted basement reflections are identified. The

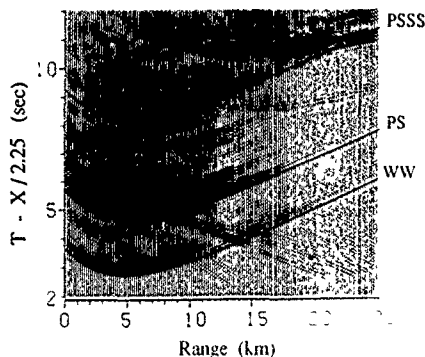


Figure 2. Part of the horizontal data in Fig. 1(a) reduced at 2.25 km s^{-1} with traveltimes identifying the key converted shear reflections.

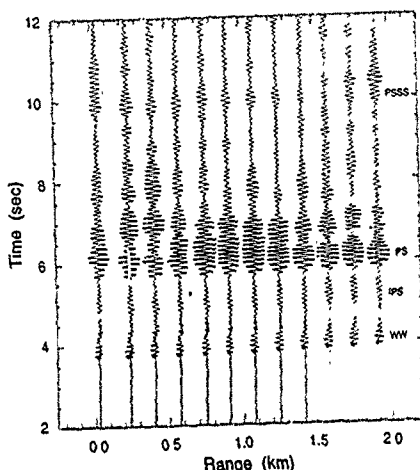


Figure 3. Selected trace-normalized horizontal data at distances to 2 km. The water-wave, WW, intrasediment converted reflection, IPS, and the PS and PSSS converted basement (crustal) reflections are identified. (Same data as portion of Fig. 2.)

phase IPS is identified as a converted S-wave reflection from within the sediment column by its arrival time between the WW and PS phases and by the similarity of its coda to that of the other S-wave reflections. Phases appearing between PS and PSSS that have approximately the same moveout are the result of multipathing within the sediment column.

Fig. 4 shows the spectra of 2 s of OBS 'noise' prior to the first arrival, and of 2 s of 'signal' starting at 5.67 s, which includes the PS reflection for the trace at 0.41 km in Fig. 3. Noise levels are a combination of background noise and signal generated noise from earlier shots. The amplitude spectrum (solid line in Fig. 4) of the horizontal data has a dominant frequency of about 9 Hz. The signal level is generally at least 10 dB above the noise level between 5 and

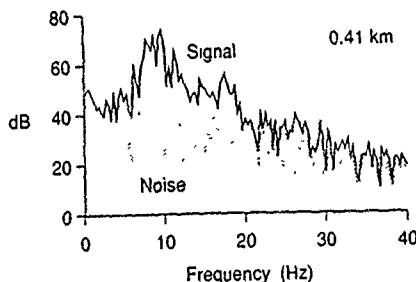


Figure 4. Amplitude spectra of 2 s of noise (dotted) and signal (solid) data starting at 1.5 and 5.67 s, respectively, for the trace at 0.41 km in Fig. 3.

18 Hz. Spectral estimates in this paper are referenced to 1 (digital unit)/V/Hz.

The 9 Hz dominant frequency gives a shear wavelength in the sediments of about 22 m, compared to about 190 m for compressional waves. This difference results in a finer sampling of the sediment structure using shear waves than is possible with compressional waves for this source. The sensitivity of short-wavelength shear waves to fine scale structure may explain some of the reverberation observed in the horizontal data.

2.2 Path differences

Snell's Law shows that the shear legs for PS and PSSS reflections are near vertical for an average sediment shear-wave velocity $c_s = 0.2 \text{ km s}^{-1}$ and for any reasonable choice of sediment c_p . The extreme case, where the incident P-wave is horizontal at the sediment/basement boundary, and $c_p = 1.5 \text{ km s}^{-1}$, gives a shear-wave incident angle at the receiver of $\theta_s = 7.7^\circ$. As Fig. 5 shows schematically, the PS arrival, S_1 , and the PS branch of the PSSS reflection, S'_1 , have different paths and consequently different ray parameters. In order to estimate Q_p , we compare the amplitudes and the spectra of S_1 and S_2 , assuming that S'_1 and S_1 are the same. The amplitudes of S'_1 and S_1 depend in part on phase conversion at the sediment/basement interface and the downward path-length, with associated compressional losses, which are both angle dependent. We need to show that S'_1 samples the same portion of the sediment column as S_1 . As all S paths are nearly vertical, and as S_1 and S_2 have the same source and receiver, this will be true if the downward P paths for S_1 and S'_1 at range X are approximately the same, i.e. if their ray parameters, p , are not very different.

Assuming horizontal layers, the total horizontal distance X_T between source and receiver can be expressed as

$$X_T(p) = X_w(p) + X_a(p) + N_\beta X_\beta(p), \quad (1)$$

where X_w is the horizontal water distance, N_β is the number of sediment shear paths, and X_a and X_β are the horizontal sediment compressional and shear-wave distances, respectively. For a stratified medium with homogeneous sediment layers, (1) may be written in the form

$$X_T(p) = H_w \left(\frac{pc_w}{\sqrt{1-p^2c_w^2}} \right) + H_{sed} \left(\frac{pc_p}{\sqrt{1-p^2c_p^2}} + N_\beta \frac{pc_s}{\sqrt{1-p^2c_s^2}} \right), \quad (2)$$

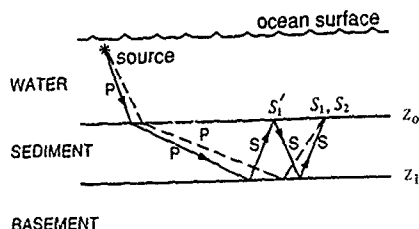


Figure 5. Schematic of the $S_1 = PS$ (dashed) and $S_2 = PSSS$ (solid) ray paths for a uniform sediment layer over basement.

where H_w is the thickness of the water column between the source and the ocean bottom, H_{sed} is the sediment thickness, c_w is the water velocity, and c_p and c_s are the sediment compressional and shear-wave velocities. We choose a real reference distance X_T corresponding to the OBS range of interest and solve (2) for complex p_1 (PS phase with $N_B = 1$) and complex p_2 (PSSS phase with $N_B = 3$). We find that the real parts of p_1 and p_2 differ by less than 2 per cent with $H_w = 5.467$ km and $H_{sed} = 0.356$ km, and that the sediment path-length and the traveltime of PS(p_1) differ from those of PSSS(p_2) by less than one metre and 0.01 s, respectively. Thus the P paths and associated losses, as well as the incident angles at the basement and associated P -to- S conversion, are effectively identical for PS and PSSS.

3 PROPAGATION PARAMETERS

In a homogeneous medium, seismic wave propagation is determined by the phase velocity c and the specific quality factor Q , which is a dimensionless measure of the internal friction or anelasticity of the medium. Johnston & Toksöz (1981) present various definitions of Q and their interrelationships. A definition that relates Q to wave amplitude A is given by

$$\frac{1}{Q} = \frac{1}{\pi} \frac{\Delta A}{A}, \quad (3)$$

in which ΔA is the amplitude loss per cycle. From (3) the amplitude decay due to attenuation is given by

$$A(X) = A_0 \exp\left(-\frac{\omega X}{2cQ}\right), \quad (4)$$

where A_0 is the initial amplitude, X is the path-length in the attenuating medium, c is the phase velocity, and ω is the angular frequency. The attenuation factor α is given in terms of ω or frequency f by

$$\alpha = \omega/2cQ \quad \text{or} \quad \alpha(f) = \frac{\pi f}{c(f)Q(f)}. \quad (5)$$

Attenuation can also be expressed by the power-law relation

$$\alpha(f) = k_0 f^B, \quad (6)$$

where $0 < B < 1$ and k_0 is the attenuation coefficient (Strick 1967). In order to satisfy the Paley-Weiner causality condition, a precisely linear frequency dependence ($B = 1$) is not possible (Papoulis 1962). Combining the expressions for $\alpha(f)$ in (5) and (6) gives

$$Q(f) = \frac{f}{f^B k_0 c(f)}. \quad (7)$$

It can be seen that if k_0 and Q are constant and $B \neq 1$, then the velocity of propagation must be dependent on frequency. To model seismic data accurately it is important to know the frequency dependence of Q and c . We investigate the dispersion relations of Strick (1967, 1970), Liu, Anderson & Kanamori (1976) and Kjartansson (1979) in a later section.

3.1 Effective attenuation

Attenuation measured from field data is termed effective attenuation (α_E) as it includes contributions from both intrinsic (α_i) and apparent (α_A) attenuation. This can be expressed in terms of α or Q as

$$\alpha_E = \alpha_i + \alpha_A \quad \text{or} \quad Q_E^{-1} = Q_i^{-1} + Q_A^{-1}. \quad (8)$$

Both Q_i and Q_A may be frequency dependent, although *in situ* measurements indicate that Q_E is effectively frequency independent in the seismic band (Kanamori & Anderson 1977).

Some mechanisms to account for intrinsic α_i losses are presented in Toksöz & Johnston (1981). Included are friction and frame anelasticity (Walsh 1966), pore fluid movement between cracks (Mavko & Nur 1973; O'Connell & Budiansky 1978), and fluid flow relative to the mineral matrix (Biot 1956). Stoll & Bryan (1970) and Stoll (1974) predict a non-linear frequency dependence of the attenuation factor α for propagation of acoustic waves in saturated sediments, known as the Biot-Stoll model. Several studies suggest that Q increases with depth in sediments and may follow a power law (f^B) (Hamilton 1980; Stoll 1985; Jensen & Schmidt 1986).

Apparent attenuation is the amplitude decay of a seismic pulse resulting from the scattering of energy by heterogeneities such as microbeds (O'Doherty & Anstey 1971; Schoenberger & Levin 1974, 1978; Spencer, Edwards & Sonnad 1977; Spencer, Sonnad & Butler 1982; Richards & Menke 1983; Menke 1983; Banik, Lerche & Shuey 1985; Menke & Dubendorf 1985; Lerche & Menke 1986). In apparent attenuation, energy is redistributed to other parts of the coda, unlike intrinsic attenuation where energy is removed from the coda. However, its effect on spectral content is difficult to distinguish from intrinsic losses. Note that Q_A^{-1} includes all non-intrinsic losses.

4 METHODS TO ESTIMATE Q

4.1 Spectral ratios

The spectral ratio (SR) method uses the ratio of the amplitude spectra of different arrivals to estimate Q . Variations of the spectral ratio method have been used by Janssen, Voss & Theilen (1985) and Jacobson (1987) to determine compressional Q_p in marine sediments. We chose the spectral ratio method since the PS and PSSS reflections are observed for the same source and receiver, and the shear-wave ray paths are virtually the same. When the ratio of the amplitude spectra of these phases is taken, source and receiver effects cancel.

We use the PS reflection (the dashed ray path in Fig. 5) at the reference depth, z_0 , as our reference signal, with associated amplitude spectrum $S_1(\omega)$. The amplitude spectrum $S_2(\omega)$ of the PSSS phase (solid ray path in Fig. 5) is related to $S_1(\omega)$ by

$$|S_2(\omega)| = |S_1(\omega)| \mathcal{R} \exp[-2\alpha(z_1 - z_0)],$$

where \mathcal{R} is a ratio of geometrical spreading terms and \mathcal{R} contains reflection and transmission coefficients, assumed independent of frequency. Here z_0 is the depth at the water/sediment interface and z_1 is the depth at the sediment

basement interface. Taking the natural log of the ratio of the two spectra gives

$$\ln SR(\omega) = \ln \left| \frac{S_2(\omega)}{S_1(\omega)} \right| = \ln |\mathcal{R}| - 2\alpha(z_1 - z_0). \quad (10)$$

Letting $2(z_1 - z_0) = T\bar{\epsilon}_p$ where T is the traveltime difference between successive shear multiples and $\bar{\epsilon}_p$ is the average shear-wave velocity in the sediments, and substituting for α with (5) we have

$$\ln SR(\omega) = \text{const} - \left(\frac{T}{2} Q^{-1} \right) \omega, \quad (11)$$

in which const is a term independent of ω that includes spreading and transmission/conversion losses. This last expression differs from the expression obtained by Jannsen *et al.* (1985) only in the constant term. Note that if Q is independent of ω , then equation (11) describes a straight line with slope $a_1 = -(T/2)Q^{-1}$. Below we determine the value of a_1 by a least-squares fit to the spectral ratios. From this slope we obtain an effective frequency-independent Q^{-1} .

A similar procedure is used if Q is frequency dependent. Then we expand $Q^{-1}(\omega)$ in a Taylor series about a reference frequency ω_0

$$Q^{-1}(\omega) \approx Q^{-1}(\omega_0) + (\omega - \omega_0) \frac{dQ}{d\omega}. \quad (12)$$

Substituting (12) into (11) we get

$$\ln SR(\omega) = \text{const} - \frac{T}{2} \left[Q^{-1}(\omega_0) - \omega_0 \frac{dQ}{d\omega} \right] \omega - \frac{T}{2} \left(\frac{dQ}{d\omega} \right) \omega^2, \quad (13)$$

which is quadratic in ω . This gives a frequency-dependent Q^{-1} at ω_0 as

$$Q^{-1}(\omega_0) = -\frac{2}{T} (a_1 + \omega_0 a_2), \quad (14)$$

where a_1 and a_2 are the coefficients of ω and ω^2 , respectively. The coefficients a_1 and a_2 are estimated by a least-squares quadratic fit to the spectral ratios. It can be seen that when $a_2 = 0$, (14) reduces to the constant Q estimate obtained from (11).

The PS and $PSSS$ reflections in the OBS data contain noise. If the noise power is constant, and S_1 and S_2 are the noise free signal spectra and S_n is the noise spectrum, then

$$\frac{S_2 + S_n}{S_1 + S_n} > \frac{S_2}{S_1},$$

since S_2 is less than S_1 . In general, the magnitude of this inequality will increase with frequency since S_2 decreases with frequency faster than S_1 . This reduces the slope of the SR curve, giving a Q estimate that is larger than the true Q . Consequently, we subtracted the noise power from both PS and $PSSS$ prior to taking the ratios as

$$|S(\omega)| = [S_{s,n}^2(\omega) - S_n^2(\omega)]^{1/2},$$

where $S_{s,n}(\omega)$ is the wavelet spectrum that includes noise. We used a portion of the data prior to the first arrival, with the same length as the signal window, for the noise estimate

It is important to note that the Q estimated from data in this manner is an effective Q , which includes intrinsic attenuation, apparent attenuation due to scattering and intrabed multiples, interference and leakage to other paths. The relative importance of these mechanisms will vary with sediment type and the complexity of the velocity structure in the sediment column.

As we are comparing phases for the same source and receiver, source and receiver directivity factors will not affect the relative amplitudes. From (10) we see that the slope of the SR plot is independent of the reflection/transmission factor \mathcal{R} and of the spreading term \mathcal{G} . The intercept, I_{SR} , of the least-squares fit to the SR plot gives an estimate of $\ln |\mathcal{R}|$. Below we use synthetic data to examine how closely I_{SR} matches the true value of $\ln |\mathcal{R}|$.

4.2 Peak amplitude ratios

Sediment Q_p can also be estimated from the ratio of the time domain amplitude, s_1 , of PS to the amplitude, s_2 , of $PSSS$ (Fig. 5). In order to estimate Q_p in this fashion, we need to correct s_1 and s_2 for losses due to transmission and phase conversion. For a perfectly elastic medium,

$$s_1 = G_1 R_1 s_0 \quad \text{and} \quad s_2 = G_2 R_2 s_0,$$

in which s_0 is the source amplitude, and R and G are the reflection/transmission coefficient and spreading terms, with subscripts 1 and 2 referring to the PS and $PSSS$ phases, respectively. As we have shown above that the difference between the ray parameters p_1 and p_2 for PS and $PSSS$, respectively, is negligible, the water paths are nearly identical and can be neglected. Then R_2 , corresponding to the $PSSS$ reflection in Fig. 5, has the form

$$R_2 = T_{pP}^d R_{pS}^d R_{SS}^u R_{SS}^d, \quad (15)$$

where T_{pP}^d and R_{SS}^u are the transmission and reflection coefficients at the water/sediment interface, and R_{pS}^d and R_{SS}^d are the reflection coefficients at the sediment/basement interface. The superscripts refer to the direction of propagation, whereas the left subscript denotes the incident phase and right subscript denotes the resultant phase.

The amplitudes, s_1 and s_2 , are the maxima of the envelope functions for the PS and $PSSS$ wavelets. The envelope function is computed by taking the square root of the sum of the squared time series and its squared Hilbert transform. Since only the last leg is constrained to be S , $PSSS$ also includes contributions from the $SPSS$ and $SSPS$ phases. This gives the ratio of the peak amplitudes of the sediment shear reflections for nearly vertical P and S ray paths as

$$\frac{s_2}{s_1} = \left| \frac{G_2}{G_1} \right| \left| \frac{(R_2 + R_3 + R_4)}{R_1} \right| \frac{e^{-(\alpha_P + 3\alpha_S)}}{e^{-(\alpha_P + \alpha_S)}}, \quad (16)$$

where the subscripts P and S refer to P and S -waves, R_1 , R_2 , R_3 and R_4 correspond to the reflection/transmission coefficients for the PS , $PSSS$, $SPSS$ and $SSPS$ phases, respectively, and the α terms are the attenuation factors where those terms associated with s_2 are identified by primes. Note that the left-hand side of (16) is a ratio of time domain amplitudes whereas the right-hand side has terms in α_P , α_S etc. which depend on frequency. We give meaning to

(16) by specifying that the frequency to be used in evaluating α_p and α_s is f_1 , the centroid of the spectrum of PS , and that the frequency to be used in evaluating α_p' and α_s' is f_2 , the centroid of the spectrum of $PSSS$. Substituting for α using (5) and rearranging gives

$$\frac{1}{Q_s} = \frac{1}{\pi f_2 \Delta T / 2} \ln \left| \frac{s_2}{g R_{s1}} \right| + \left(\frac{f_2 - f_1}{f_1} \right) \left(\frac{\bar{c}_s}{\bar{c}_p Q_p} \right), \quad (17)$$

where ΔT is the traveltime difference $t_{PSSS} - t_{PS}$, $f_3 = f_1 - 3f_2$, $R_s = (R_2 + R_3 + R_4)/R_1$, $g = G_2/G_1$ and \bar{c}_s and \bar{c}_p are the average S -wave and P -wave velocities in the sediments. Note that $\ln |g R_{s1}|$ corresponds to the intercept in (11). For synthetic traces, we use model parameters to compute the frequency-dependent velocities with the dispersion relation used in reflectivity computations. The ray parameters, p , for the PS and $PSSS$ phases are determined from (2). To compute R_s , we obtain the reflection/transmission coefficients from equations (5.39) of Aki & Richards (1980). g is obtained from the ratio of $\cos \theta(p)$ ($dA/d\Omega$)^{-1/2} for the two phases, in which the horizontal sensor directivity term, $\cos \theta(p)$, associated with the shear-wave velocity, β , at the receiver is given by $\cos \theta(p) = \sqrt{1 - p^2 \beta^2}$, dA is the cross-sectional area of the ray tube at the receiver, and $d\Omega$ is the solid angle of the ray tube at the source. We compute $dA/d\Omega$ as

$$dA/d\Omega = \frac{X(dX/dp)}{pc_w^2} \sqrt{1 - p^2 c_w^2} \sqrt{1 - p^2 \beta^2},$$

where X is the horizontal range, and c_w is the water velocity at the source. For a multilayered model, dX/dp is given by

$$\frac{dX}{dp} = \sum_{j=1}^n \frac{h_j c_j}{(1 - p^2 c_j^2)^{3/2}},$$

with h_j and c_j the thickness and phase velocity in the j th sediment layer. The directivity terms $\cos \theta(p)$ have negligible effect since the rays are nearly vertical and $p_1 \approx p_2$. If the sediment shear-wave velocity is significantly less than the compressional-wave velocity and f_2 is not too different from f_1 , the second term on the right-hand side of (17) is small and can be neglected in a first-order approximation of Q . These formulae are used below.

5 DISPERSION RELATIONS

Anelasticity in earth materials results in the dispersion of seismic waves. Attenuation, characterized by the intrinsic quality factor Q , causes a wavelet to broaden and flatten during propagation. In reflectivity modelling, attenuation is introduced by making the seismic velocities complex. Depending on the dispersion relation, the specification of a reference velocity and a reference Q , as well as additional parameters, are generally required. However, improper selection of the additional parameters can cause either $c(\omega)$ or $Q(\omega)$ as calculated for synthetic seismograms to be significantly different from the reference values away from the reference frequency. In order to make synthetic tests for testing a method of extracting Q from data, we need to examine first the variation of c and Q with ω .

Based on a variety of assumptions, methods and approximations, several investigators have derived nearly

identical dispersion relations for band-limited nearly constant Q using a standard linear solid for their viscoelastic model (e.g. Futterman 1962; Liu *et al.* 1976; Kanamori & Anderson 1977). In a different approach, Strick (1967, 1970) used the power law (6) to obtain an expression for $c(\omega)$ that does not require bandwidth specification. Both the band-limited and the Strick relations require the selection of parameters that affect the frequency dependence of c and of Q , and the resulting waveforms.

In contrast to these nearly constant Q models, Kjartansson (1979) gives a linear description of attenuation with Q exactly independent of frequency, attenuation is completely specified by c_0 , the phase velocity at a reference frequency f_0 , and by Q . Kjartansson's model requires the phase velocity to be slightly dependent on frequency.

We review several dispersion relations to examine their potential differences and the influence of parameter selection. Here it is useful to have Q defined in terms of complex seismic phase velocity, $c(\omega)$, by

$$Q(\omega) = 0.5 \frac{\Re \{1/c(\omega)\}}{\Im \{1/c(\omega)\}}. \quad (18)$$

This definition, from O'Connell & Budiansky (1978), is nearly equivalent to definition (3) for body waves, but it is more convenient than (3) because neither the change in amplitude nor the cycle length needs to be determined.

• Absorption Band (ABQ) rule (Liu *et al.* 1976), modified from Mallick & Frazer (1987):

$$c(\omega) = c_0 \left\{ 1 + \frac{1}{\pi Q_m} \ln \left[\frac{\omega_2(\omega_1 - i\omega)}{\omega_1(\omega_2 - i\omega)} \right] \right\}. \quad (19)$$

Here ω_1 , ω_2 , c_0 , and Q_m are input parameters. The radian frequencies ω_1 and ω_2 are intended to be chosen so that $\omega_1 \ll \omega \ll \omega_2$ in the band of interest. The reference velocity c_0 is the velocity of the medium both at $\omega \rightarrow 0$ and $\omega \rightarrow \infty$. Note that the $Q(\omega)$ given by this rule is not equal to the parameter Q_m : $Q(\omega) > Q_m$ for all ω , but $Q(\omega)$ is only slightly greater than Q_m for $\omega_1 \ll \omega \ll \omega_2$. Notice that $Q(\omega) \rightarrow \infty$ both in the limit $\omega \rightarrow 0$ and in the limit $\omega \rightarrow \infty$.

• Power Law (PLQ) rule (Strick 1967, 1970), a modified version of Strick's Power Law as presented in Mallick & Frazer (1987):

$$\frac{1}{c(\omega)} = \frac{1}{c_w} + \frac{k_0}{\sin \left(\frac{\sigma \pi}{2} \right)} \frac{1}{(\varepsilon - i\omega)^\sigma} \quad (20)$$

Here c_w , k_0 , ε , and σ are the input parameters. However, it is usually more convenient to define k_0 by the relation $k_0 = |\omega_0|^\sigma / 2c_w Q_m$ and then to regard c_w , ω_0 , Q_m , ε , and σ as input parameters. In consequence of the above definition of k_0 , equation (20) implies that for $\omega \gg \varepsilon$

$$Q(\omega) \approx \left| \frac{\omega}{\omega_0} \right|^\sigma Q_m + \frac{1}{2} \cot(\sigma \pi / 2).$$

Notice that $Q(\omega)$ is greater than Q_m whenever $\omega > \omega_0$. Substituting the expression for k_0 into (20) gives

$$\frac{1}{c(\omega)} = \frac{1}{c_w} \left\{ 1 + \frac{1}{2Q_m} \frac{|\omega_0|^\sigma}{\sin \left(\frac{\sigma \pi}{2} \right)} (c - i\omega)^\sigma \right\}$$

It can be seen that c_∞ is the seismic velocity in the limit as $\omega \rightarrow \infty$.

The parameter ε was introduced by Mallick & Frazer (1987) to remove the velocity singularity at $\omega=0$; for body waves, ε should be chosen so that $\varepsilon \ll \omega$ in the band of interest; we use $\varepsilon=0.001$. Following Strick (1970), we use $\sigma=0.1$, thought to be suitable for most earth materials.

- Constant Q (CQ) rule (Kjartansson 1979):

$$c(\omega) = c_0 \left(\frac{i\omega}{\omega_0} \right)^\gamma \quad (21)$$

Here c_0 , ω_0 and γ are the input parameters. However, it is often more convenient to define γ by $\gamma = (1/\pi) \tan^{-1}(1/Q_m)$ and c_0 by $c_0 = c_m / \cos(\pi\gamma/2)$ so that c_m , ω_0 and Q_m are the input parameters. With this dispersion relation it is easy to see that Q is independent of ω . However, like the ABQ rule and the PLQ rule, the CQ rule gives a seismic velocity that increases with frequency.

For testing our procedures, we require synthetic seismograms computed both with a frequency-independent Q and with a frequency-dependent Q . We chose $f_0 = 1$ Hz for the reference frequency, with $\omega_0 = 2\pi f_0$. Fig. 6 shows $c(\omega)$ and $Q(\omega)$ for three dispersion relations. Clearly the Q and c given by these relations can differ significantly from the input parameter Q_m and c_m away from the reference frequency. In selecting values for the parameters ω_1 and ω_2 in the ABQ, and σ in the PLQ relations, there is a trade-off between constant Q and $c(\omega)$. Keeping Q nearly constant away from ω_0 causes $c(\omega)$ to diverge more from the reference phase velocity, and vice versa. Although the shapes of the phase velocity curves in Fig. 6(a) are similar, we found that improper selection of the other input parameters can cause the PLQ and ABQ curves to differ significantly from the CQ curve. For the ABQ it was necessary to increase the bandwidth to $\omega_1 = 0.01$ and $\omega_2 = 10000$ (the dashed curves in Fig. 6) in order for $Q(\omega)$ to be effectively constant over the frequency band 3 to 18 Hz (Fig. 6b) and maintain $c(\omega)$ relatively constant, compared with $\omega_1 = 0.1$ and $\omega_2 = 1000$ (dotted). For the ABQ relation, as ω_1 decreases, $c(\omega)$ increases. Examination of (19) and Fig. 6(a) indicates that ABQ increases the propagation velocity of a pulse, whereas PLQ gives the delay generally expected in a dispersive medium. However, we see in Fig. 6(b), obtained from $c(\omega)$ using (18), that PLQ gives $Q(\omega)$ considerably greater than Q_m for $\omega > \omega_0$.

To see the differences in the resulting waveforms, we computed the plane wave solutions for the reference model using $c_0 = c_m = c_\infty = 1.0 \text{ km s}^{-1}$ and $Q_m = 50$ at $x = 10 \text{ km}$. As Fig. 6(c) shows, the waveforms are similar in shape although the arrival times differ from the 10 s time expected for the model parameters. The differences become more pronounced as Q_m decreases. As Q_m increases, the waveforms approach the same amplitude and their arrival times approach x/c . Note that the input velocity and Q_m can be adjusted so that the three dispersion relations give similar results in a given frequency range. And it may be possible to choose k_0 in the PLQ model and Q_m in the ABQ model such that the $Q(\omega)$ and $c(\omega)$ curves are closer together. However, it is unclear what values of k_0 and Q_m to use for unconsolidated sediments and whether these parameters

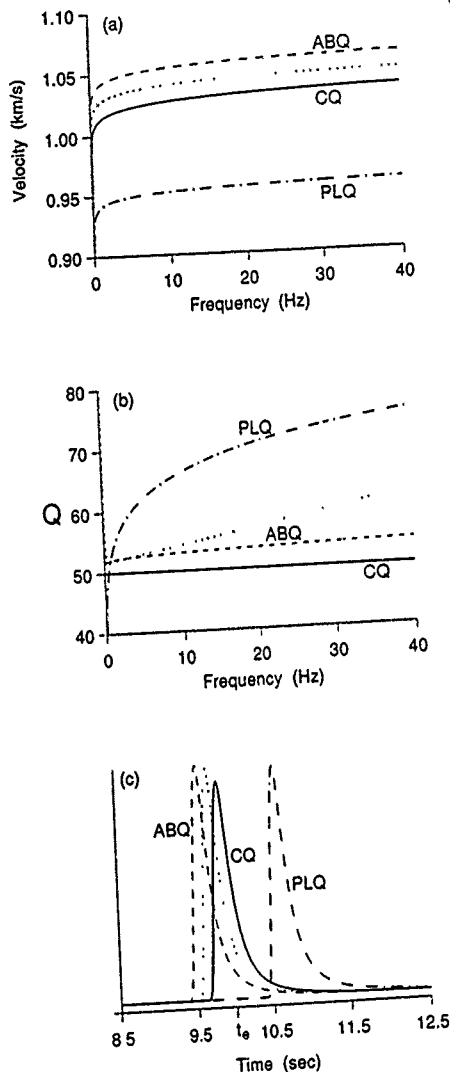


Figure 6. Results from various dispersion relations. (a) velocity, (b) $Q(\omega)$ calculated using (18), and (c) impulse response for plane wave propagation through 10 km of medium at a reference velocity of 1 km s^{-1} and a reference Q of 50. t_0 is the expected arrival time of 1 km s^{-1} . The curves in each plot were computed using Constant Q (solid), Power Law Q (dot-dash) with $\sigma=0.1$ and $\varepsilon=0.001$, and Absorption Band Q (dotted) with $\omega_1=0.1$, $\omega_2=1000$ and (dashed) with $\omega_1=0.01$, $\omega_2=10000$. For all computations, $f_0=1$ Hz.

should vary with material type. Since the modelling of seismic data involves the matching of traveltimes and amplitudes, it is clear that different dispersion relations can require distinctly different input models to obtain similar synthetic seismograms. The differences in the $Q(\omega)$ and $c(\omega)$ curves emphasize the importance, in modelling studies, of explicitly stating the dispersion relation and its input parameter values.

6 NUMERICAL TESTS ON SYNTHETIC DATA

Reflectivity synthetic seismograms were computed using both the CQ and PLQ dispersion relations. We used $f_0 = 1$ Hz as the reference frequency for both relations. For the PLQ computations, we used $\sigma = 0.1$ and $\epsilon = 0.001$, with c_m and Q_m the reflectivity model velocity and model Q , respectively. For the CQ computations, c_m and Q_m are the reflectivity model parameters. The code used to generate the synthetic seismograms was developed by Mallick & Frazer (1987, 1988). In this study, a variety of sediment models were used to test the accuracy of the spectral ratio (SR) and peak amplitude ratio (PAR) methods for Q_n estimation. SR and PAR give effective Q_n , equation (8), as the reflectivity synthetics include all multiples and converted phases.

From single-channel reflection data and core logs from drilling (Duennebieer *et al.* 1987), it is certain that the actual sediment column at Hole 581C has vertical heterogeneity. Hence we require a definition of intrinsic Q for an n -layer sediment profile. A natural definition is obtained by considering the effect of the intrinsic Q of each layer on a vertically travelling seismic wave. The amplitude loss of the wave in layer j due to intrinsic attenuation can be expressed as $\exp(-\omega h_j / 2c_j Q_j)$, in which h_j , c_j , and Q_j are the thickness, phase velocity, and Q in layer j , and ω is the angular frequency. The loss for a stack of n layers, L_n is then

$$L_n = \exp \left[-\omega \left(\frac{h_1}{2c_1 Q_1} + \frac{h_2}{2c_2 Q_2} + \dots + \frac{h_n}{2c_n Q_n} \right) \right]. \quad (22)$$

Next, we define δ to be the total thickness of the stack, $h_T = \sum_{j=1}^n h_j$, divided by the total traveltime; thus

$$c = h_T \left[\sum_{j=1}^n \frac{h_j}{c_j} \right]^{-1}. \quad (23)$$

Finally we define Q_1 , the effective intrinsic Q of the stack, by writing

$$L_n = \exp \left[-\frac{\omega h_T}{2c Q_1} \right]. \quad (24)$$

Solving (22) and (24) for Q_1 then yields

$$Q_1 = \frac{h_T}{c} \left[\sum_{j=1}^n \frac{h_j}{c_j Q_j} \right]^{-1}. \quad (25)$$

In these equations the c_j and Q_j are frequency-dependent quantities computed using the dispersion relation for the j th layer. For the multilayer sediment models in this study, we refer to Q_1 in (25) as the true Q . In discussing our tests on synthetic data, we will say that a method gave the correct result if the Q recovered by the method was equal to Q_1 given by (25).

6.1 Synthetic data

Here we discuss the synthetic record sections used to develop and test our SR and PAR methods for extracting Q_n . Recall that in the SR method we must first estimate the spectrum of PS and the spectrum of $PSSS$. Q_n is then obtained from the slope of the ratio of these two spectra. The synthetic traces were computed with a Nyquist frequency of 40 Hz, consistent with the OBS data sampling interval of 0.0125 s. We used 55 point windows for PS and $PSSS$ in order to match the length of the PS coda in the OBS data at 0.41 km (Fig. 3). Prior to transforming to the frequency domain, the mean was removed and a 10 per cent Hanning taper was applied to the windowed phases. Tests showed that 256 point windows padded with zeros gave the best results. Although tapering the window is unnecessary for synthetic data from simple models free of noise, we include the taper in our tests since the OBS data may contain other phases and noise arriving close to the PS and $PSSS$ wavelets.

The argon source function and the theoretical instrument response were included in our modelling to facilitate direct comparison of synthetics to the OBS data. At first glance it might be surmised that the source and the instrument functions should be self-cancelling in both the SR and PAR methods. In theory they are not exactly self-cancelling in the SR method because a long source-instrument wavelet may cause the tails of the PS and $PSSS$ arrivals to be outside their respective windows, they are not exactly self-cancelling in the PAR method because of the possible interference of other phases with PS and $PSSS$. Accordingly, in the synthetic seismograms used below to test our methods for estimating Q_n , we included a source and instrument response similar to those of the data. However, we also tested our SR and PAR methods with a variety of other source-instrument wavelets, including the unit (delta function) wavelet. We found that both methods were relatively insensitive to the source-instrument wavelet; the other factors discussed below such as noise, clipping, and interference had much larger effects.

The HIG OBS horizontal component instrument velocity response is relatively flat between 3 and 20 Hz (Sutton *et al.* 1980) where most of the energy in the data is found (Fig. 4). The instrument response was computed with the formula in Table IV of Sutton *et al.* (1981) using $\tau_1 = 0.035$. The Soviet argon source was modelled using a modified form of the explosive source function presented in Spudich & Orcutt (1980). The spectral content of the argon source wavelet is a function of the argon volume, chamber pressure, and depth. The source function parameters that control the bubble pulse decay were estimated by comparing the amplitude spectrum of the source wavelet convolved with the instrument response with the water wave from OBS hydrophone data at about 13 km, where the water wave is not severely clipped as in the near traces (Fig. 7). The peaks in the amplitude spectra of the convolved wavelet and the OBS water wave at about 9 Hz match reasonably well (Fig. 7), as does the fall-off in the spectral estimates between the first and third peaks. Since the water wave in real data is contaminated by the sediment basement P reflections, as well as by refracted phases and surface waves not included in the convolved wavelet, we can only approximate the

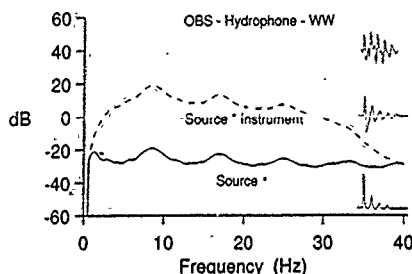


Figure 7. Amplitude spectra for the source wavelet, source convolved with the instrument response, and water wave from the OBS hydrophone data at about 13 km. The wavelets giving these spectra are shown at the right.

shape of its spectrum. To match the water wave spectrum, we need an accurate sediment model and an accurate transfer function between the instrument and the sediments in which it rests.

Spikes or holes in the spectral ratios can be caused by other arrivals in the same time window. Holes in either of the spectra due to time series discretization can also cause the SR curve to be irregular. When the spectral estimate of $PSSS$ is greater than that of PS at the same frequency, or when the PS and $PSSS$ spectra are significantly dissimilar in shape, interference with another phase or with noise is the likely cause. The longer the source-receiver wavelet and the more complicated the sediment structure, the greater the chance that interference effects will be encountered. As interference is likely in real data, we smoothed the amplitude spectra using a $\frac{1}{2}$, $\frac{1}{3}$, $\frac{1}{4}$ smoothing function before taking the spectral ratios. The degree of acceptable smoothing was established with tests on simple models where apparent attenuation would not be a factor, and we could ensure that the trend of the SR curve was not distorted. We found that five passes through the smoothing function gave minimal distortion of the SR curve. The bandwidth for least-squares estimation was restricted to those frequencies where the general trend of the SR curve was approximately the same as that near the dominant frequency. The difference between the true Q and the estimated Q is the measure of error.

6.2 Tests on one- and two-layer sediment models

The application of the spectral ratio (SR) method to synthetic seismograms computed using the Constant Q rule for one-layer sediment models with Q_B of 50, 100 and 150 (Table 1) recovered the intrinsic model Q_B with an error less than 5 per cent. The spectral ratio curves for these models are virtually linear and are consequently not shown.

Table 1. Input parameters for one-layer sediment models with velocities c_s , c_p in km s^{-1} and density ρ in g cm^{-3}

	c_s	c_p	$Q_B(a)$	$Q_B(b)$	$Q_B(c)$	ρ	$h(\text{km})$
water	1.49	5000	0.0	0	0	1.0	5.467
sediment	1.77	50	0.198	50	100	1.80	0.356
basement	4.25	300	2.25	250	275	—	—

Although, as noted above, the source and instrument are not exactly self-cancelling in the SR method, our tests of SR for these models with and without the source and instrument functions gave results that were insignificantly different. The peak amplitude ratio (PAR) method Q_B estimates were between 10 and 20 per cent below the model Q . To assess the sensitivity of the PAR method to the frequency parameters in equation (17), we also computed Q_B from (17) by substituting, in turn, $-2f_1$, $-2f_2$, and $\bar{f} = -2(f_1 + f_2)/2$, in place of f_3 . These substitutions were motivated by the expectation that f_2 would not be too different from f_1 .

The most accurate PAR results for both low- and high- Q models were obtained with \bar{f} in place of f_3 , although $-2f_1$ and $-2f_2$ in place of f_3 gave smaller errors for high- and low- Q , respectively. The PAR results using \bar{f} in place of f_3 were within 5 per cent of the model Q . This improvement may result from \bar{f} compensating for the band-limited nature of the source spectrum. We use \bar{f} in place of f_3 for the remainder of the PAR tests unless otherwise stated.

The spectral ratio intercept I_{SR} from equation (10) gives an estimate of the shear-to-shear reflection coefficient at the sediment/basement interface R_{SS}^d as

$$|R_{SS}^d| \approx |R_s| = \exp(I_{SR} - \ln|\mathcal{Q}|). \quad (26)$$

Note that the PS reflection coefficients in R_1 and R_2 , equation (16), essentially cancel because $p_1 \approx p_2$ and because R_3 and R_4 make only small contributions to \mathcal{R} . Also, the spreading ratio \mathcal{S} is easily computed if the sediment thickness is known. Equation (26) gives a lower bound for R_{SS}^d since layering within the sediment column and conversion of S-to-P at the water bottom will make $|R_s| < |R_{SS}^d|$. In general, R_{SS}^d will be negative since we expect a significant increase in c_s , c_p and ρ at the sediment/basement interface.

For the one-layer models in Table 1, (26) gave R_{SS}^d within 5 per cent of the model value. In addition, increasing the sediment Q_s and the basement Q_b and Q_B had an insignificant effect on the accuracy of the SR and PAR results for these models. This indicates that Q_B determined by these methods is effectively independent of other attenuation parameters.

To test the robustness of SR and PAR for more complicated sediment structures, horizontal component synthetic seismograms were computed, for both low and high Q_B , with a relatively strong impedance boundary within the sediment column. Table 2 gives two two-layer models that differ from each other only in the Q_B of the two sediment layers. The parameters in Table 2 serve as the input model parameters to the dispersion relations of the reflectivity code. Table 3 gives the actual velocities, at 9 Hz, of the models in Table 2, computed by the CQ rule (21), and the actual Q_s , at 9 Hz, computed using the O'Connell &

Table 2. Input parameters c_s and Q_B used in computing the synthetic traces in Fig. 8. Velocities are in km s^{-1} and densities are in g cm^{-3} . Actual velocities at 9 Hz are given in Table 3

	c_s	Q_B	c_p	$Q_B(a)$	$Q_B(b)$	ρ	$h(\text{km})$
water	1.5	10000	0.0	0	0	1.0	5.467
sediments	1.15	30	0.160	45	190	1.35	0.200
	1.15	30	0.295	70	225	1.75	0.156
basement	4.25	300	2.25	250	2.65	—	—

Table 3. Computed velocity and Q at 9 Hz determined from the input parameters c_m and Q_m in Table 2, using the Constant Q dispersion relation. The resulting intrinsic Q , given by equation (25), is 50 for sediment column (a) and 200 for sediment column (b), using $c_p = 0.2 \text{ km s}^{-1}$.

	c_p	Q_m	$c_p(a)$	$c_p(b)$	$Q_p(a)$	$Q_p(b)$	ρ	$h(\text{km})$	
water	1.5	10000	0.0		0		1.0	5.467	
sediments	L1a	162	30	0.165	0.161	45	191	1.35	0.200
	L1b	1.83	30	0.300	0.297	70	226	1.75	0.156
basement	4.27	301	2.26		* 251		2.65		

Table 4. Input parameters c_m and Q_m used in computing the Power Law synthetic trace in Fig. 7. Velocities are in km s^{-1} and densities are in gm cm^{-3} . Actual values of velocity and Q at 9 Hz, computed by the PLQ dispersion relation, are identical to those of Table 3.

		c_p	Q_p	$c_p(a)$	$c_p(b)$	$Q_p(a)$	$Q_p(b)$	ρ	$h(\text{km})$
water		1.5	10000	0.0	0.0	0	0	1.0	5.467
sediments	L1a	1.80	21.5	0.179	0.164	33	150	1.35	0.200
	L1b	2.05	21.5	0.315	0.301	53	178	1.75	0.156
basement		4.31	238	2.29		198	2.65		

Budiansky relation (18). The intrinsic Q_p of the sediment column, given by substituting Table 3 values into equation (25), is 50 in case (a) and 200 in case (b). Note that the Table 3 values are also obtained from the PLQ rule at 9 Hz, using the input parameters c_m and Q_m given in Table 4. The non-linear nature of the PLQ dispersion relation required adjustment of the velocities as well as Q in order to match the sediment Q_p , Q_s , c_p , and c_s in Table 3. Using the model parameters in Table 4, (20) gives velocities and layer Q within 1 per cent of the values in Table 3. Note the significant difference between the CQ (Table 2) and PLQ (Table 4) model Q_p necessary to obtain the same values of Q_1 and Q_2 for the sediment column; this difference was noted earlier in the curves for $Q(\omega)$ and $c(\omega)$ in Fig. 6.

Fig. 8 shows the traces computed for these models at a range of 0.41 km, corresponding to trace 3 in the OBS data (Fig. 3). Fig. 9 shows the ray paths of the major arrivals identified on the bottom trace in Fig. 8. In Fig. 9, all ray paths not labelled P are S , and phases resulting from reflection/conversion at the intrasediment boundary are dashed. Additional layers significantly increase the multipathing and the complexity of the seismic trace, with the number and amplitude of phases observed depending on the magnitude of the impedance contrast between the layers. The seismogram for the PLQ model with intrinsic $Q_p = 200$ is also plotted in Fig. 8. As expected, very little difference can be seen between the traces for the CQ and PLQ models. The close similarity of these traces demonstrates that identical synthetic seismograms can be obtained from significantly different input models when different dispersion relations are used. The amplitude spectra for the CQ and PLQ models also show only slight differences (Fig. 10a). The PLQ trace for intrinsic $Q_p = 50$ is omitted because it is similarly indistinguishable from the corresponding CQ trace and amplitude spectrum [case (a), Table 2].

Fig. 10(a) shows the smoothed amplitude spectra of the PS and PSSS wavelets in Fig. 8. The resulting spectral ratio curves are shown in Fig. 10(b). The differences between these models can readily be seen in the relative amplitudes of the PS and PSSS phases, their amplitude spectra, and the slope of the SR curves. Assuming constant Q_p , a straight

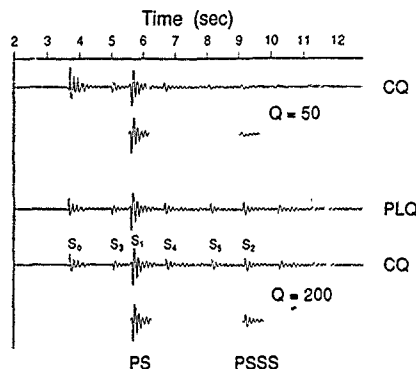


Figure 8. Reflectivity synthetic traces for the two-layer sediment models of Table 3 showing the wavelets selected for Q analysis for the CQ models. Ray paths for the arrivals identified on the lower trace are shown in Fig. 9. The PL trace for $Q = 50$ is omitted because it is indistinguishable from the CQ trace for $Q = 50$.

line was fitted to each spectral ratio curve and equation (11) was used to estimate Q_p . We obtained $Q_p = 52 \pm 1$, in the band [3, 15] Hz, and $Q_p = 198 \pm 3$, in the band [3, 25] Hz, for the low- and high- Q CQ models, respectively. The \pm refers to 95 per cent confidence limits for the least-squares fit to the spectral ratios. Recovered Q_p varied less than 10 per cent from the true Q_p for both CQ models in Table 2 using bandwidths of at least 10 Hz that included the dominant frequency of 9 Hz. Estimates without tapering the wavelets differed from these results by less than 5 per cent. The error for the high- Q model increases slightly as the bandwidth decreases, with $Q_p = 208 \pm 10$, in the band [3, 15] Hz. The general trend of the low- Q SR curve in Fig. 10(b) changes at about 15 Hz, restricting the useable

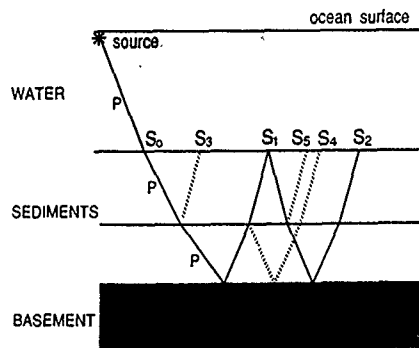


Figure 9. Ray paths for the arrivals identified on the bottom trace (CQ, $Q = 200$) in Fig. 8. The downgoing P -wave legs are labelled P . All other legs are S -waves, the dashed legs result from reflection/conversion at the intrasediment (IPS) boundary.

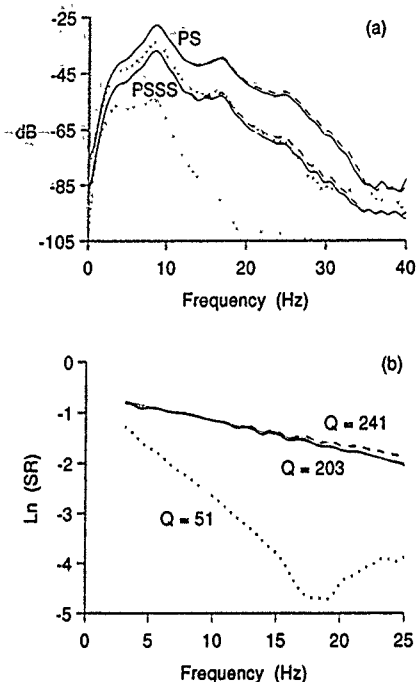


Figure 10. PS and PSSS amplitude spectra (a) and associated spectral ratio (SR) curves and Q estimates (b) of the CO (solid, $Q = 200$, dotted, $Q = 50$) and PLQ (dashed, $Q = 200$) traces in Fig. 8. The thin lines in (b) are the least-squares fits for the band in which the SR Q estimate was obtained

bandwidth for the low- Q model. This is because the spectral estimates at frequencies greater than about 15 Hz (lower dotted curve in Fig. 10a) approach the numerical noise level, related to a combination of the source function spectral content and the low Q . The accuracy of these SR Q estimates suggests that layering and S-to-P conversion do not present problems for the SR method.

We also used the quadratic least-squares procedure, equations (13) and (14), to estimate Q from traces computed using the PLQ dispersion relation. The quadratic least-squares Q procedure is much more sensitive to bandwidth than the linear least-squares procedure. The most accurate Q estimates were obtained for the band where the significance of the second-order term in the quadratic least-squares fit was a minimum, as determined by standard F -test techniques (Hines & Montgomery 1980). However, the quadratic least-squares results of $Q = 54 \pm 0.1$, in the band [3, 15] Hz, and $Q = 241 \pm 2$, in the band [3, 18] Hz, for the low- and high- Q PLQ models, respectively, are still within 25 per cent of the true Q values. The \pm refers to the average deviation of the high

and low estimates obtained from 95 per cent confidence limits for the least-squares coefficients a_1 and a_2 in (14). The Q estimates for the high- Q model have greater than 25 per cent error for bands with the upper limit less than 18 Hz, e.g. $Q = 267$ in the band [3, 15] Hz. The error for the high- Q model decreases as the bandwidth increases, with $Q = 222$, in the band [3, 25] Hz.

The quadratic least-squares Q estimates from PLQ synthetic seismograms (Fig. 10b) do not recover the true Q as accurately as the linear least-squares procedure applied to Constant Q synthetics. This is probably due to averaging effects over the band for which the quadratic least-squares estimate is obtained. For some bands, the quadratic least-squares procedure applied to PLQ synthetics gave errors greater than 50 per cent whereas the linear least-squares procedure, applied to the same PLQ synthetics, gave Q estimates within 10 per cent of the true Q at 9 Hz. For example, for the low- Q PLQ model in the [3, 15] Hz band, we obtained $Q = 150$ with the quadratic fit and $Q = 54$ with the linear fit. For the high- Q PLQ synthetics, quadratic fit SR Q estimates are generally within 40 per cent of the true Q . However, for most bands a linear fit gave Q estimates within 25 per cent of the true Q at 9 Hz, significantly better than the quadratic fit estimates. These results indicate that any frequency dependence of Q will be very difficult to extract from our OBS data.

To determine the usefulness of the PAR method on real data, where the sediment column is likely to be heterogeneous, we also applied the PAR method to the traces in Fig. 8. When estimating Q using the peak amplitude ratio (PAR) method for multilayer sediment structures, the reflection coefficient term, R , in equation (17), must be modified to include the S-wave transmission coefficients, T_{SS}^d and T_{SS}^u . The expression for the PSSS reflection-transmission factor R_2 , equation (15), then becomes

$$R_2 = T_{PP}^d R_{PS}^d T_{SS}^u R_{SS}^d T_{SS}^d R_{SS}^u T_{SS}^u$$

For the low- Q two-layer model, PAR results using both the spectral ratio intercept, I_{SR} , and model parameters to estimate Q , gave Q estimates within 10 per cent of the true Q . However, the estimates for the two-layer high- Q models are about 30 per cent below the true Q using the model Q , whereas substituting $\exp(I_{SR})$ for Q in (17) resulted in less than 5 per cent difference between the estimated and true Q . These results suggest that interference between phases resulting from conversion at, and reflections from, the IPS boundary causes a reduction in the peak amplitude of the PSSS reflection, and that these interference effects are included in the SR intercept. This surprising in that interference is a frequency-dependent phenomenon while I_{SR} should contain only frequency-independent components. In addition, the interference effect on I_{SR} does not affect the spectral ratio results.

6.3 Noise

Real data can be influenced by factors not usually included in synthetic seismograms such as noise and signal 'clipping' due to limited recording dynamic range. To determine the sensitivity of the SR and PAR methods to these factors, we

applied different levels of signal clipping and noise to the synthetic data.

To determine the accuracy of the SR method in the presence of noise, we added different levels of noise energy to the high- Q_B wavelets. Noise was incorporated in the synthetic wavelets by taking a portion of the corresponding OBS data trace preceding the water wave as the noise estimate and adding it to both the PS and PSSS wavelets prior to transforming to the frequency domain. Such added noise has a greater effect on the spectral estimates of the lower amplitude PSSS wavelet than it does on the higher amplitude PS. We also generated random, or white, noise in the frequency domain by fixing the noise modulus at unity and randomizing the phase, transforming to the time domain, and adding the result to the synthetic trace. We express the percentage of noise energy as $100 \log_{10}$ of the ratio of the variance of the noise amplitudes to the variance of the signal + noise amplitudes for the PSSS wavelet. When obtaining spectral noise estimates, we windowed the noise with the same taper used on the signal.

Subtracting the noise power from the spectral power estimates steepens the slope of the spectral ratios and consequently has the effect of lowering the Q_B estimate. If noise power is not subtracted from the signal power spectra before the spectral ratio is taken, then the Q_B estimate may be higher than the true value. The high- Q_B models are more sensitive to noise since a slight change in slope can result in a significant error in the Q_B estimate. Accordingly, for our noise analysis, we use the high- Q CQ model in Table 2 with $Q_B = 200$.

A linear least-squares fit to the spectral ratios was made using the frequency band in which spectral estimates for the PS phase were at least 3 dB greater than those of the PSSS wavelet and the spectral estimates for both phases were at least 3 dB above the noise level. These acceptance criteria can reduce the useable bandwidth significantly and exclude certain frequencies within that band. Fig. 11(a) shows the wavelet spectra after adding about 5.5 per cent data noise energy to the hi- Q CQ model trace in Fig. 8. For the PS phase, very little difference can be seen between the amplitude spectra with noise added (solid) and without noise for frequencies less than 30 Hz. However, for PSSS, near 15 Hz and above 19 Hz there are noticeable differences between the amplitude spectra with noise and without noise. These small differences significantly affect the spectral ratio curve. The SR curve becomes considerably more irregular (solid, Fig. 11b). But the Q_B estimate obtained with the noise power subtracted as discussed above, using those frequencies in the [3, 25] Hz band that meet our acceptance criteria, was 216 ± 38 , still within 10 per cent of Q_1 . In Fig. 11(b), the short linear portion of the SR curve near 15 Hz shows the frequencies not used in the fit. Although not subtracting the noise power does not appear to change the shape of the SR curve significantly (dotted, Fig. 11b), it results in a Q_B estimate of 248 ± 40 for the same band; thus the bias in the Q estimate increased from 10 to 25 per cent when noise was not subtracted. Data noise gave larger errors in the Q_B estimates than did random noise, so we used data noise for the remainder of our tests.

As noise levels increase, the useable bandwidth narrows and the portion of the amplitude spectrum above noise level becomes smaller and more distorted. The associated SR

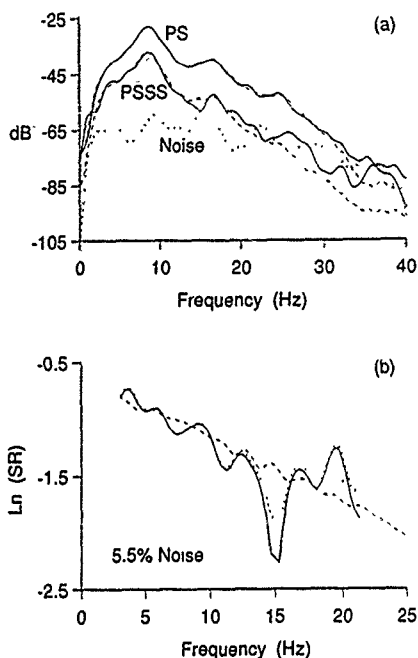


Figure 11. (a) Amplitude spectra of the PS and PSSS wavelets in Fig. 8 with about 5.5 per cent noise energy added (solid) for the CQ model with $Q = 200$. Also shown are the noise free spectra (dashed) and the noise estimate (dotted). (b) Spectral ratio (SR) curves for the spectra in (a) with the noise power removed (solid), not removed (dotted) and the noise free case (dashed).

curves are more irregular with more frequencies excluded. Subtracting the noise power compensates for both the reduction in slope of the SR curve and the associated downward shift in the spectral ratio intercept. We obtain less than 25 per cent error between measured and true Q_B with the addition of up to 6.5 per cent noise to the synthetic data for the high- Q CQ model. For the one-layer sediment models in Table 1, and for multilayer sediment models with lower impedance contrast or with Q_B less than 150, we find better than 25 per cent accuracy for as much as 8 per cent noise energy added. These results differ somewhat from those reported by Janssen *et al.* (1985) and Tonn (1991) who obtained greater than 25 per cent error for the addition of more than 5 per cent noise energy. The improved accuracy we obtained may be due to the lack of downgoing S-waves through the water column, the nearly perfect S-wave reflection at the water/sediment interface, the subtraction of the noise power from the spectral estimates prior to taking the ratios, or a combination of the above.

For the PLQ $Q_B = 200$ synthetics, the addition of about 5 per cent noise energy causes Q_B estimates to be more than

25 per cent different from the true Q . We found that the linear least-squares procedure gave much better estimates than the quadratic fit for PLQ models when more than 3 per cent noise energy was added. For example, for the $Q_B = 200$ PLQ model with 5 per cent noise, we obtained Q_B estimates of 144 and 213 using the quadratic and linear least-squares procedures, respectively. These results indicate that, when noise is present in narrow-band data, a linear approximation to the spectral ratios gives the most reliable Q_B estimate for both frequency-dependent and frequency-independent Q . We also infer that, from our real data, which undoubtedly include noise and interference effects, it will be very difficult to determine any frequency dependence of Q_B .

The peak amplitude ratio (PAR) method was also tested with noise for the one-layer $Q_B = 150$ model (b) in Table 1. The PAR method gave better results than the SR method as the noise levels increased above about 8 per cent, where the SR slope became negative. The PAR estimates of Q_B were within 10 per cent of the model Q of 150 with up to 25 per cent noise energy added using the model \mathcal{R} , in (17). This means that if we are sure the sediment column is nearly homogeneous, if we know the sediment thickness, and if we can make a good estimate of \mathcal{R} , then sediment Q_B can be determined accurately even in the presence of considerable noise by comparing peak amplitudes of selected phases.

6.4 Clipping

Clipping due to restricted instrument dynamic range affects primarily the PS reflection for the near traces. The gain in the OBS record section used in this study was set automatically according to the RMS voltage for the previous minute, resulting in clipping of the highest amplitude signals in each trace. To test the impact of clipping on the SR Q_B results, we applied 'hard' and 'soft' clipping to CQ synthetic data for the two-layer model with $Q_B = 200$. In both cases the clipping level was set to a percentage of the maximum amplitude of the PS wavelet. For hard clipping, all amplitudes greater than the clipping level were set to the clipping level. We limited clipping of PS to levels at which PSSS was not clipped. As can be seen in Fig. 12(a), hard clipping results in a shift of energy to higher frequencies, increasing the centroid frequency of the PS spectrum. In Fig. 12(b), it is clear that increased clipping causes greater distortion of the SR curves between 3 and 20 Hz.

For soft clipping, the wavelets were first scaled by $\sinh(1.0)/(\text{clipping level})$. We took the \sinh^{-1} of the scaled amplitudes to obtain the soft clipped wavelets shown in Fig. 13(a). Comparing Figs 12(a) and 13(a), we see that hard clipping shifts more energy to higher frequencies than does soft clipping. In Fig. 13, we see that as the amount of clipping increases, more energy shifts to the higher frequencies, the SR curves become more distorted, and their intercepts become more positive. However, the SR method still yields estimates within 25 per cent of the model Q with up to 50 per cent hard or soft clipping applied to the wavelets.

Application of the PAR method to data with the PS phase clipped will give an upper bound for Q_B if we have a reasonably good estimate of \mathcal{R} . As expected, the PAR method is sensitive to clipping and gives a much higher Q_B estimate than the true Q . However, using $-2f_1$ and

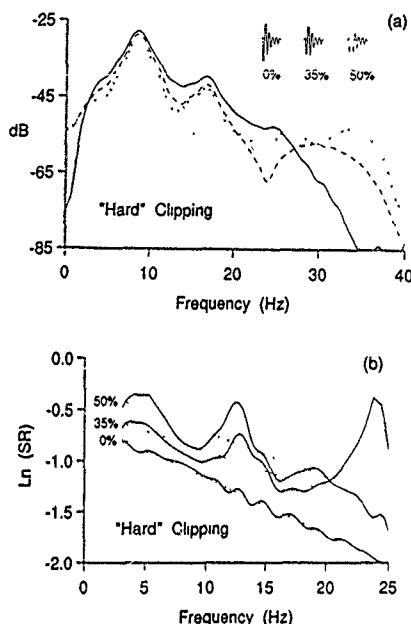


Figure 12. (a) Amplitude spectra for the PS wavelet in Fig. 8 with 0 (solid), 35 (dashed), and 50 per cent (dotted) 'hard' clipping applied. (b) Spectral ratio curves for the spectra in (a), with the spectrum of PSSS in Fig. 10, gave estimates for Q_B of 201 ± 5 , 281 ± 36 , and 252 ± 44 for 0, 35, and 50 per cent clipping, respectively. The dashed lines are the least-squares fits over the band in which the Q_B estimate was obtained.

$\exp(l_{GR})$, in place of f_3 and the model \mathcal{R} , respectively, in (17), gave results close to the true Q . In addition, as clipping increases above 35 per cent, the centroid frequency increases; then using twice the dominant frequency for the PS reflection, $-2f_{1D}$, in place of f_3 in (17), gives Q_B estimates closer to the true Q than using either f_3 , f_1 , or $-2f_1$. For the source function employed, the difference between f_1 and f_{1D} is an indication of the amount of clipping present in the data. These results show that the amplitude spectrum below 20 Hz is not greatly affected by moderate amounts of clipping, and that clipping effects are mostly confined to the SR intercept.

6.5 Apparent attenuation

Here we consider the effects of apparent attenuation on our procedures for estimating Q_B . In particular, for multilayered models, we wish to know whether our procedures tend to estimate the Q given by equation (25), or whether they recover an effective Q containing a strong component of apparent attenuation. First, notice that if Q_A is large, then (8) reduces to $Q_E = Q_1$. If Q_A is small, then the Q_C

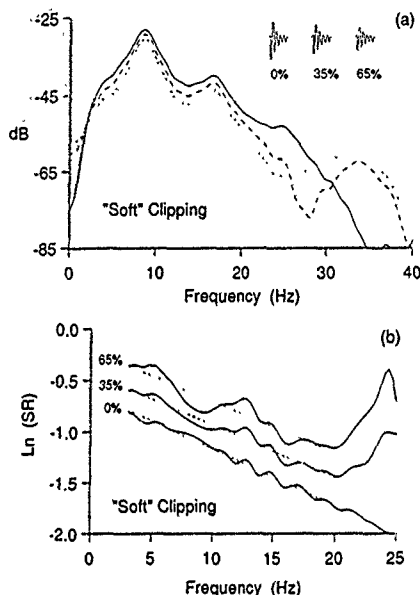


Figure 13. (a) Amplitude spectra for the PS wavelet in Fig. 8 with 0 (solid), 35 (dashed), and 65 per cent (dotted) 'soft' clipping applied. (b) Spectral ratio curves for the spectra in (a), with the spectrum of P555 in Fig. 10, gave estimates for Q_B of 201 ± 5.4 , 216 ± 10 , and 221 ± 19 for 0, 35, and 65 per cent clipping, respectively. The dashed lines are the least-squares fits over the band in which the Q_B estimate was obtained.

estimated by the SR method will be less than the true Q_1 . We decided to hold Q_1 fixed at a relatively high value and see how Q_B estimated by the SR and PAR methods differs from the true Q_1 .

Synthetic seismograms were computed for sediment models with realistic velocities containing alternating layers with high impedance contrast. These models were designed to maximize the magnitude and frequency of impedance contrasts while maintaining total $P+S$ sediment traveltime of about 200 s for a sediment thickness of 356 m. The vertical traveltime through each sediment layer was held constant for velocities computed with the Constant Q rule. These sediment models (Table 5) have layer thicknesses of $1, \frac{1}{2}, \frac{1}{3}, \frac{1}{4}$ and $\frac{1}{5} \lambda_B$ at 10 Hz, respectively, while holding shear $Q_1 = 150$ fixed. In Table 5, the number of sediment layers having the same density, velocity and Q in that layer is in parentheses, e.g. model A5 has 142 sediment layers. Residual fractions of layers were distributed equally between the top and bottom layers. Fig. 14 shows synthetic traces computed at 0.41 km with the Constant Q rule, with the $Q_B = 200$ CQ two-layer model from Table 2 at the top included for comparison.

As the synthetics shown in Fig. 14 are horizontal motion, virtually all of the energy is in shear. In particular, the energy between WW and PS consists of intrasubmarine P -to- S converted arrivals. Note that the amplitude of the water wave is approximately the same for all models. In model A2 (Fig. 14), the amplitude of the converted S phases decreases with time as more energy is removed from the downgoing P -wave. The amplitude reduction is also partly due to the upgoing S -waves losing energy to reverberations, reversion, and absorption in the sediment column.

Interference of the converted S phases occurs where the thickness of successive layers sums to an integer multiple of $\frac{1}{2} \lambda_B$, giving the characteristic pattern observed for the arrivals between WW and PS. A resonance condition exists when the sediment thickness is an odd multiple of $\frac{1}{4} \lambda_B$. The resonance frequency, f_r , is given by

$$f_r = \frac{c_B m}{4 H_{sed}} \quad (m = 1, 3, 5, \dots),$$

where H_{sed} is the thickness of the sediments. Applying this expression to the individual layers in model A4 gives $f_r = 10$ Hz with $m = 1$ for each of the contrasting layers, corresponding to the fundamental resonance frequency for the stack of layers. Consequently, we associate the peak at

Table 5. Alternating sequence of sediment model parameters used in computing the synthetic seismograms for models A1–A5 with sediment layer thickness of $1, \frac{1}{2}, \frac{1}{3}, \frac{1}{4}$ and $\frac{1}{5} \lambda_B$, respectively, at 10 Hz. In parentheses are the number of sediment layers having the same density (ρ , gm cm $^{-3}$), velocity (c , km s $^{-1}$) and Q . Total sediment thickness is approximately 356 m.

	c_0	Q_0	c_B	Q_B	ρ	h (m)				
						A1	A2	A3	A4	A5
water	1.51	10000	0.0	0	1.0			5467		
sediments	1.55	100	0.150	150	1.45	15.0	7.5	5.625	3.75	1.875
	1.85	100	0.250	150	1.75	25.0	12.5	9.395	6.25	3.125
	1.55	100	0.150	150	1.45	15.0	7.5	5.625	3.75	1.875
	1.85	100	0.250	150	1.75	25.0	12.5	9.395	6.25	3.125
	1.55	100	0.150	150	1.45	15.0 (9)	7.5 (17)	5.625 (24)	3.75 (36)	1.875 (71)
	1.85	100	0.250	150	1.75	25.0 (9)	12.5 (17)	9.395 (24)	6.25 (36)	3.125 (71)
basement	4.25	300	2.35	250	2.65			170		
	Gradient - 6 layers							170 m each		
	6.1	500	3.5	300	2.4			10000		

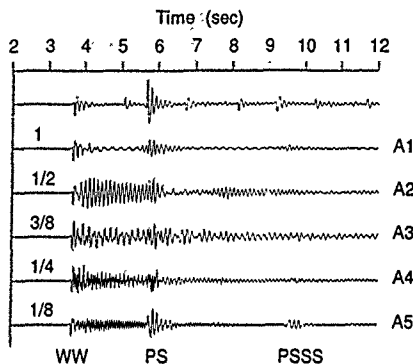


Figure 14. Synthetic data traces at 0.41 km for models A1-A5 with alternating sediment layer thicknesses of $1, \frac{1}{2}, \frac{3}{8}$ and $\frac{1}{4}\lambda_p$ (see Table 5). The trace at the top is for the constant Q two-layer high- Q model.

10 Hz in models A1-A4 in Fig 15 with the acoustic propagation loss maximum determined by Hughes *et al.* (1990) for one-layer sediment models.

The arrivals between WW and PS increase in frequency from about 10 Hz for model A2 to about 18 Hz in model A4. As the layer thickness decreases, the layers become increasingly transparent to the downgoing P-wave resulting in less P-to-S conversion. In model A5 (Fig. 15e), the $\frac{1}{4}\lambda_p$ layer thickness is small enough to allow the 9 Hz peak in the source spectrum (Fig. 7) to control the location of the dominant frequency of the PS and PSSS spectra, as opposed to the 10 Hz dominant frequency in the spectra of models A1-A3. The 10 Hz peak matches the frequency used to determine the layer thicknesses. For model A4, the pronounced peak in the spectrum near 18 Hz is likely due to phases that include odd numbers of multiple ray paths in both layers. In general, the sediment layers act as a strongly peaked bandpass filter whose zeros are related to the thicknesses and velocities of the layers in the sequence.

The wavelet arrival times for models A1-A5 were computed by ray theory. All models have a time-average sediment S-wave velocity of 0.201 km s^{-1} with arrival times for PS and PSSS of 5.61 and 9.14 s. Since thin-bed layering delays the arrival of some of the energy, we used a larger window, 1.0 s, for the spectral ratio analysis compared with the 0.69 s window in the analyses of the two-layer sediment models above. The phases PS and PSSS still arrive at the computed times, but their amplitudes can be significantly reduced (Fig. 14). The delay of energy is clearest in model A5 where the apparent PSSS arrival occurs at about 9.42 s, 0.29 s later than the ray theoretical arrival time. The window positions for spectral estimation were not adjusted to compensate for these delays. To reduce the possible effect of other arrivals near PS and PSSS within the 1 s windows, we applied a 10 per cent Hanning taper to the wavelets. The upper bound of the band in the SR tests was 20 Hz because the spectral estimates approached the numerical noise level above this limit. The lower bound was set at 3 Hz except for

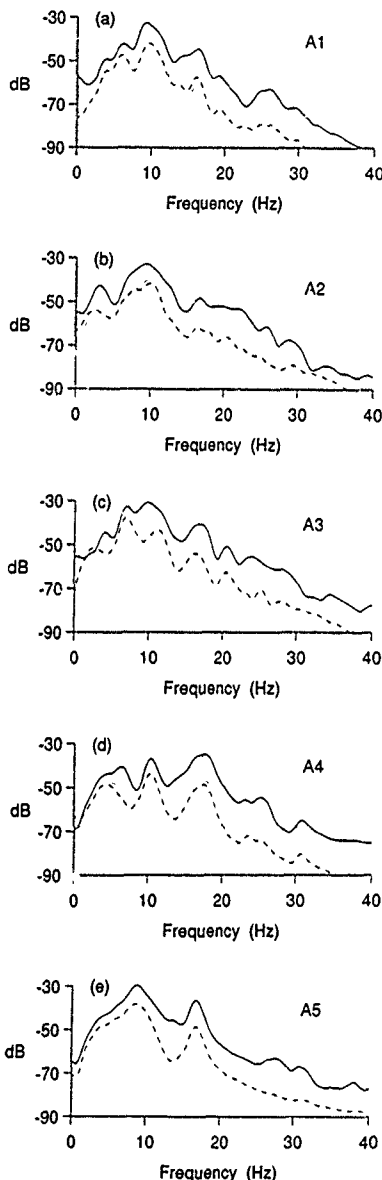


Figure 15. Amplitude spectra (a)-(e) for the PS (solid) and PSSS (dashed) wavelets from the traces for models A1-A5 shown in Fig 14.

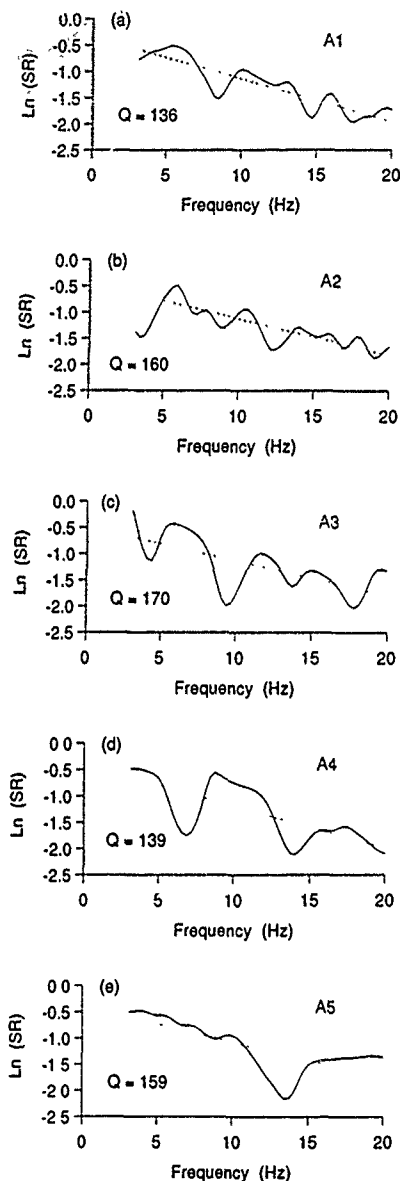


Figure 16. Spectral ratio curves for the amplitude spectra in Fig. 15 for models A1–A5 (a)–(e). The dashed lines are the least-squares fits over the band in which the Q_B estimate was obtained

model A2 in which it was set to 5 Hz. Below 5 Hz, the SR curve for model A2 was greatly distorted, probably because of interference.

As expected, the *PS* and *PSSS* phases for these models have much more irregular amplitude spectra and SR curves (Figs 15 and 16) than those of the noise free two-layer models (Fig. 10). The spectrum of model A4 (Fig. 15d) clearly shows a significant shift in the dominant frequency of the wavelets to about 18 Hz with a corresponding reduction in the peak at 10 Hz. The linear least-squares SR method for models A1–A5 gives Q_B estimates within 25 per cent of the true Q of 150 with 95 per cent confidence limits between ± 26 and ± 47 . These results could have been improved by shifting the time windows to compensate for the layering delay and by increasing the percentage of the wavelets tapered. We conclude that spectral ratio estimates of Q_E will not be significantly affected by apparent attenuation due to intrabed multiples resulting from thin, horizontal bedding within the sediment column in the [3, 20] Hz band. In our analysis of the OBS data, we expect that the Q_H recovered will be close to the intrinsic Q defined for multilayer models by equation (25).

In addition to estimating the importance of Q_A , the long codas for these models also test the sensitivity of the SR method to source function and window length. Interference may explain why the 95 per cent confidence limits for the Q_H estimates for models A1–A5 are significantly larger than those for the two-layer models of Table 2

7 APPLICATION TO OBS DATA

After the extensive tests on synthetic data discussed above, we applied the SR and PAR methods to the OBS horizontal data from DSDP Hole 581C. The position and length of each wavelet window was adjusted to obtain as smooth an amplitude spectrum as possible. After the mean was removed from the wavelets, the 10 per cent time-domain Hanning taper and smoothing functions were applied in the same way as for the synthetic data. For noise estimates needed in the SR method, we selected the portion of the data prior to the first arrival starting at 2.0 s after the origin time for the shot, with the same length as the wavelets used for the spectral ratios. The noise power was subtracted from the spectral power estimates after smoothing.

We restricted our analysis to offsets less than 1.0 km. Since the shear waves take a nearly vertical path, the near traces are least contaminated by scattered energy or by refracted crustal phases. Fig. 17(a) shows the horizontal component OBS data at 0.41 km and the *PS* and *PSSS* wavelets selected for spectral ratio analysis. The intrasediment converted reflection, *IPS*, and the direct water wave, *WW*, are also identified. The phases arriving between *PS* and *PSSS* are shear waves that probably result from multipathing within the sediment column. Noise levels restrict the useable band for the SR method to about 3–18 Hz. The noise energy estimate for this trace is 4.7 per cent of the *PSSS* wavelet, corresponding to a signal-to-noise ratio of 21, well within the 25 per cent SR accuracy range in the presence of noise energy determined from the tests on synthetic data above. We conclude that signal generated noise does not significantly reduce the accuracy in determining Q_B by either the SR or PAR methods from

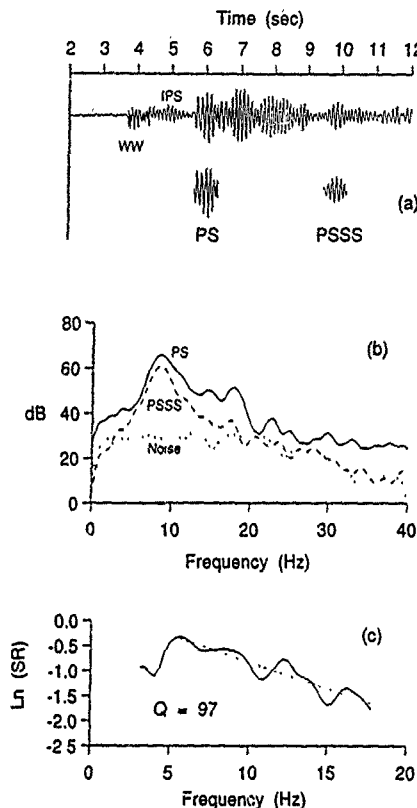


Figure 17. (a) Horizontal geophone OBS data at 0.41 m with the PS and PSSS wavelets for SR and PAR analysis. The water wave, WW and the intrasediment reflection IPS are also identified; (b) amplitude spectra of the wavelets in (a) and of the noise estimate, and (c) spectral ratio curve for the spectra in (b).

these OBS data. Fig. 17(b) shows that the shapes of the signal spectra are roughly similar to those for the two-layer synthetic data shown in Fig. 11(a); thus interference and clipping are probably not significant for this trace.

The horizontal geophone is contained in a cylindrical OBS instrument package. Coupling through soft sediments can modify the instrument response to ground motion, with the coupling resonance frequency related to the shape and mass of the instrument package and the properties of the sediments (Sutton *et al.* 1981). Coupling effects include instrument package rocking induced by shear waves, resulting in enhancement of the spectra near the resonance frequency. To have complete confidence in our estimates of sediment Q_B from horizontal geophone OBS data, we need to know that the effects of coupling resonance are linear for the coda amplitude and spectral content of PS and PSSS. Linear effects will not bias our estimated Q_B because our numerical experiments showed that the source wavelet is practically self-cancelling in both the SR and PAR methods. Cross-coupling from vertical seismic motion to horizontal geophone signals may also affect the Q_B estimates, although Sutton *et al.* (1981) determined that this is not a problem for this instrument. High amplitude signals will be more strongly affected if the resonance effect is non-linear, with soft clipping of the signal the most likely result. However, the similarity of the spectra of PS and PSSS noted above leads us to conclude that the coupling effects are linear within the dynamic range of the instrument. In any case, our clipping experiments on synthetic data indicate that soft clipping effects should not significantly affect the Q_B estimates.

In Fig. 17(b), the fall-off in energy at frequencies less than 5 Hz may be due to interference by Scholte-waves generated by earlier shots, gradient induced shear-compressional wave coupling (Fryer 1981), or source characteristics. The divergence of the PS and PSSS spectra below 5 Hz results in distortion of the spectral ratio curve (Fig. 17c), consequently we do not use that portion of the SR curve in our least-squares estimate for this trace. A linear least-squares estimate of Q_B was obtained using frequencies within the [5, 18] Hz band that met the 3 dB acceptance criteria discussed above.

In Table 6 we list the SR and PAR results for OBS data traces 1–7 from Fig. 3. We believe these traces are relatively free of interference and clipping effects. Fig. 18 shows the

Table 6. Results of spectral ratio and peak amplitude ratio analysis of OBS data traces 1–7. BW is the bandwidth in which the least-squares spectral ratio Q_B estimate (Q_{SR}), with associated intercept I_{SR} , was obtained; t_{PS} and t_{PSSS} are the arrival times of the respective phases, and \bar{f} is the average of the centroids of their spectra between 3 and 20 Hz used in obtaining the peak amplitude ratio Q_B estimates (Q_{PAR}). At the bottom are the results for the spectral average of the nearest five traces.

Range (km)	t_{PS} (s)	t_{PSSS} (s)	Window (s)	BW (Hz)	\bar{f} (Hz)	Q_{PAR}	I_{SR}	Q_{SR}
0.027	5.68	9.59	0.69	3.1, 17.8	10.0	163	0.121	110 ± 20
0.238	5.67	9.59	0.56	6.2, 17.5	10.7	143	0.332	105 ± 25
0.405	5.67	9.49	0.69	5.0, 17.8	9.7	100	0.351	97 ± 10
0.576	5.68	9.49	0.63	3.1, 15.0	10.4	141	-0.027	100 ± 17
0.747	5.68	9.50	0.50	5.9, 17.8	10.0	136	0.053	102 ± 15
0.906	5.70	9.62	0.50	3.1, 13.8	11.3	310	-0.443	135 ± 31
1.077	5.70	9.68	0.50	6.2, 17.5	11.4	206	-0.075	133 ± 23
Spectral Average				3.1, 17.2	10.0	122	0.245	97 ± 11

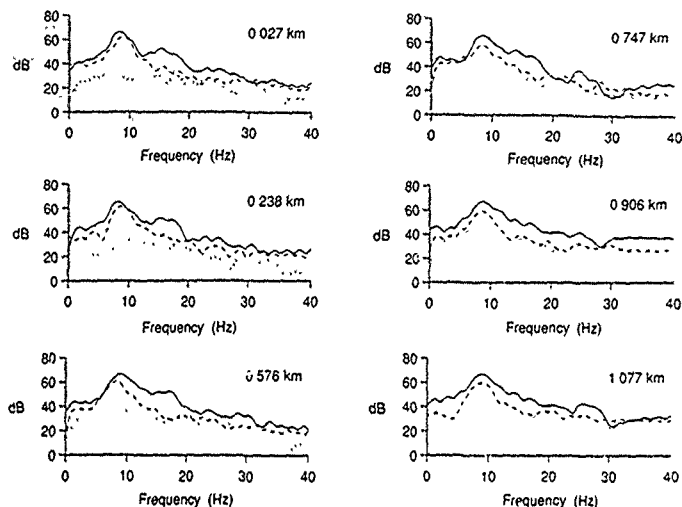


Figure 18. Amplitude spectra of the PS (solid), PSSS (dashed), and noise estimate (dotted) wavelets for the OBS data.

wavelet spectra for these traces, and Fig. 19 shows their SR curves. Variations in the arrival time of PSSS in Fig. 3 may be due to slightly different slant paths for the downward P and upward S , possibly caused by non-horizontal layering within the sediments or basement topography. Interference, clipping, or an increase in signal generated noise energy was

inferred wherever the spectral estimates for PSSS are greater than for PS. These spectral bands (the flat, truncated segments of the SR curves in Fig. 19) were excluded from the SR curves and thus from the least-squares estimation of Q_n . Window length and position were adjusted to obtain PSSS spectra with approximately the

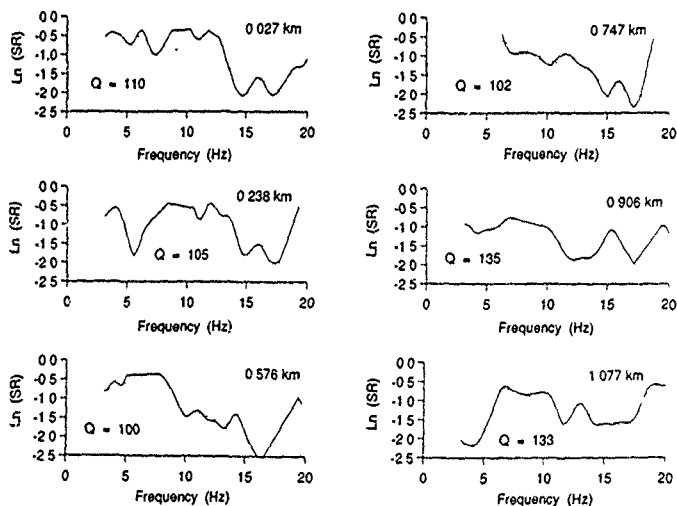


Figure 19. Spectral ratio curves for the spectra in Fig. 18. The dashed lines are the least-squares fits over the band in which the Q_n estimate was obtained.

same shape as the *PS* spectra. In the peak amplitude ratio analysis, we estimated Q_B with $\exp(I_{SR})$, and used \bar{f} for f_p in equation (17) while neglecting the second term on the right-hand side of (17).

Some trace-to-trace variation is seen in the linear least-squares SR Q_B estimates of Table 6. Although the degree of signal clipping in the data is unknown, the spectral ratio tests on synthetic data above indicate that relatively large amounts of clipping will not affect the SR estimates in the [3, 18] Hz band used in this analysis. The efficiency of *P*-to-*S* conversion generally increases with range up to the sediment/basement shear-wave critical angle, increasing the amplitude of the *PS* arrival and generally resulting in more severe clipping of that phase as the range increases. Consequently, we reduced the length of the time window at greater offsets in an effort to exclude the most severely clipped pulses in the *PS* coda. Not surprisingly, we still obtained significantly higher Q_B estimates from the two farthest traces in Table 6 than from the five nearest traces. The increase in \bar{f} at 0.906 km also suggests greater signal clipping. Holes in the spectra of *PSSS*, such as those seen at about 5 Hz in Figs 18(b) and (f), are probably caused by interference; they result in holes in the *SR* curves (Figs 19b and f) which we exclude from the least-squares estimates. These interference and clipping effects may account for the variation observed in the spectral ratio results for the five nearest traces in Table 6. Also, as the spectra in Fig. 18 show, the noise energy varies from trace to trace. If the in-trace noise variability is as great as its trace-to-trace

variability, then the noise estimate may not accurately represent the noise level in the windows selected.

To average these effects and thus lower the statistical variance of the spectral estimates, we computed arithmetic (Fig. 20a) and median averages of the spectral estimates for the nearest five traces in Table 6 prior to taking their ratios. Both averaging methods gave similar results, although the median average spectra and spectral ratios were noticeably less smooth. We obtained $Q_B = 97 \pm 11$ over the [3, 17.2] Hz band for the arithmetic spectral average in Fig. 20(b) using the linear least-squares procedure.

The peak amplitude ratio results, Q_{PAR} in Table 6, are consistently higher than the Q_{SR} estimates, as would be expected if *PS* were clipped. The spectral average Q_{PAR} estimate of $Q_B = 122$ can be considered an upper bound. Note that there is little difference between Q_{SR} and Q_{PAR} at 0.405 km, suggesting that clipping for this trace is not as severe as the other traces, and that this trace probably gives the most reliable individual estimate of sediment Q_B .

8 CONCLUSIONS

We have shown that spectral ratio and peak amplitude ratio methods can give accurate estimates of sediment Q_B from converted shear-wave reflections on horizontal component synthetic seismograms. Tests on synthetic data suggest that moderate amounts of noise and signal clipping do not introduce significant error in spectral ratio estimates of Q_B . Q_B estimates within 25 per cent of the model can be obtained with the addition of up to 7 per cent noise energy. However, the frequency dependence of sediment Q_B cannot be determined by spectral methods for narrow bandwidth data when a small amount of noise is present.

Our methods were applied to horizontal component OBS data collected over soft sediments at a deep water site in the northwest Pacific. The spectral ratio method gave Q_B estimates between 97 and 110 (corresponding to an attenuation, α , between 0.281 and 0.248 dB λ^{-1}) using the linear least-squares procedure. The spectral average of these traces yields a Q_B estimate of 97 ± 11 . We suggest that the spectral ratio method can give effective Q_B estimates for the entire sediment column with better than 10 per cent accuracy from converted shear-wave reflections for broadband horizontal component OBS data in areas where *PS* and *PSSS* are observed. This accuracy is not greatly degraded by modest amounts of noise and signal clipping.

ACKNOWLEDGMENTS

We thank the Office of Naval Research for financial support and Eduard Berg for reading the manuscript.

REFERENCES

- Aki, K. & Richards, P. G., 1980 *Quantitative Seismology*, vol. I, W. H. Freeman & Company, San Francisco.
- Bank, N. C., Lerche, I. & Shuey, R. T., 1985 Stratigraphic filtering. Part I: Derivation of the O'Doherty-Anstey formula. *Geophysics*, **50**, 2768-2774.
- Biot, M. A., 1956 Theory of propagation of elastic waves in a fluid-saturated porous solid I. Low frequency range. *J. acoust. Soc. Am.*, **28**, 168-178.
- Byrne, D. A., Sutton, G. H., Blackinton, J. G. & Duennebieer, F.

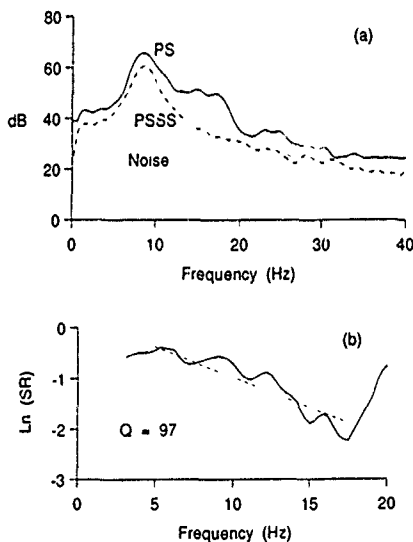


Figure 20. (a) Spectral average of the *PS* (solid), *PSSS* (dashed), and noise estimate (dotted) wavelets for the five nearest OBS data traces. (b) Spectral ratio curve for the spectra in (a).

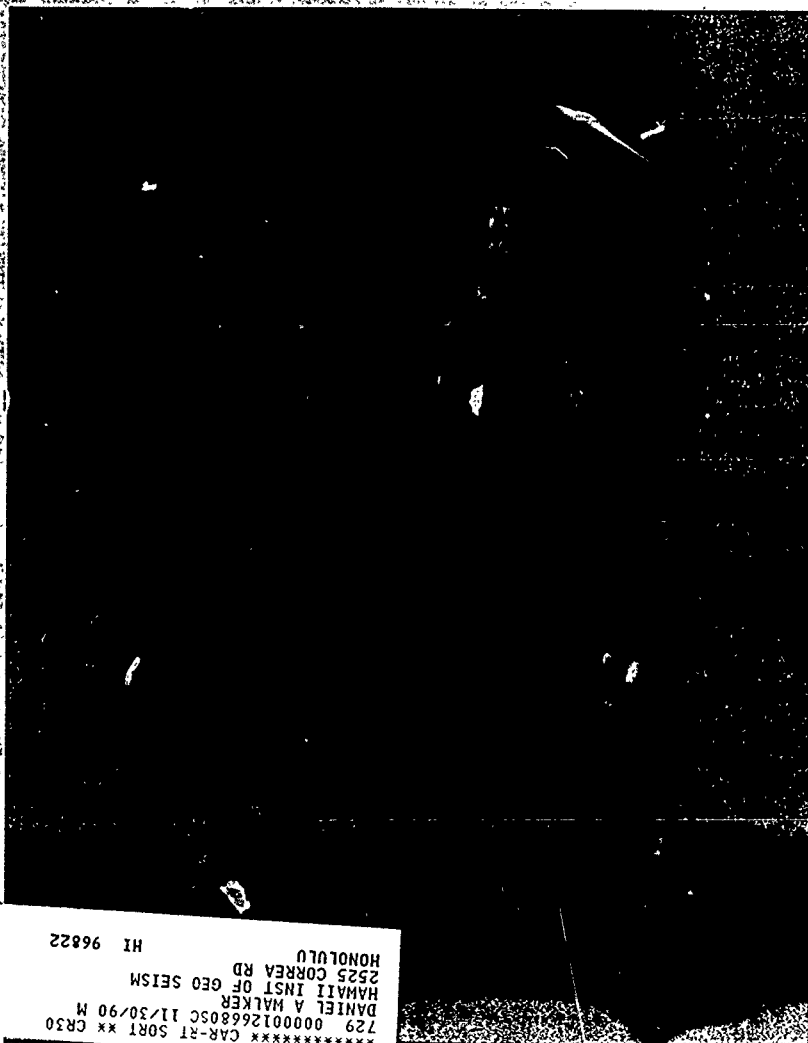
- K., 1983. Isolated sensor ocean bottom seismometer, *Mar geophys Res.*, 5, 437-449.
- Duennebieber, F. K., Lienert, B., Cessaro, R., Anderson, P. & Mallick, S., 1987. Controlled-source seismic experiment at Hole 581-C, in *Int. Repts. DSDP*, 88, pp. 105-125, eds Duennebieber, F. K., Stephen, R., Gettrust, J. F., et al., Washington (US Government Printing Office).
- Fryer, G. J., 1981. Compressional-shear wave coupling induced by velocity gradients in marine sediments, *J. acoust. Soc. Am.*, 69, 647-660.
- Futterman, W. I., 1962. Dispersive body waves, *J. geophys. Res.*, 67, 5279-5291.
- Hamilton, E. L., 1976a. Sound attenuation as a function of depth in the sea floor, *J. acoust. Soc. Am.*, 59, 528-535.
- Hamilton, E. L., 1976b. Attenuation of shear waves in marine sediments, *J. acoust. Soc. Am.*, 60, 334-338.
- Hamilton, E. L., 1980. Geoacoustic modeling of the sea floor, *J. acoust. Soc. Am.*, 68, 1313-1340.
- Harrison, C. H. & Cousins, P. L., 1985. A study of propagation loss dependence on sediment layer thickness using the Fast Field Program, in *Ocean Seismo-Acoustics: Low Frequency Underwater Acoustics*, pp. 139-148, eds Akal, T. & Berkson, J. M., Plenum Press, New York.
- Hines, W. W. & Montgomery, D. C., 1980. *Probability and Statistics in Engineering and Management Science*, John Wiley & Sons, New York.
- Hughes, S. J., Ellis, D. D., Chapman, D. M. F. & Staal, P. R., 1990. Low frequency acoustic propagation loss in shallow water over hard-rock seabeds covered by a thin layer of elastic-solid sediment, *J. acoust. Soc. Am.*, 88, 281-297.
- Jacobson, R. S., 1987. An investigation into the fundamental relationships between attenuation, phase dispersion, and frequency using seismic refraction profiles over sedimentary structures, *Geophysics*, 52, 72-87.
- Jacobson, R. S., Shor, G. G., Jr & Dormin, L. M., 1981. Linear inversion of body wave data—Part II: Attenuation versus depth using spectral ratios, *Geophysics*, 46, 152-162.
- Jannsen, D., Voss, J. & Theilen, F., 1985. Comparison of methods to determine Q in shallow marine sediments from vertical reflection seismograms, *Geophys. Prosp.*, 33, 479-497.
- Jensen, F. B. & Schmidt, H., 1986. Shear properties of ocean sediments determined from numerical modeling of Scholte-wave data, in *Ocean Seismo-Acoustics: Low Frequency Underwater Acoustics*, pp. 683-692, eds Akal, T. & Berkson, J. M., Plenum Press, New York.
- Johnston, D. H. & Toksöz, M. N., 1981. Seismic wave attenuation—definition and terminology, in *Seismic Wave Attenuation*, pp. 1-5, eds Toksöz, M. N. & Johnston, D. H., SEG Geophysics reprint series No. 2, Tulsa.
- Kanamori, H. & Anderson, D. L., 1977. Importance of physical dispersion in surface wave and free oscillation problems: Review, *Rev. Geophys. Space Phys.*, 15, 105-112.
- Kjartansson, E., 1979. Constant Q -wave propagation and attenuation, *J. geophys. Res.*, 84, 4737-4748.
- Lerche, I. & Menke, W., 1986. An inversion method for separating intrinsic and apparent attenuation in layered media, *Geophys. J. R. astr. Soc.*, 87, 333-347.
- Liu, H.-P., Anderson, D. L. & Kanamon, H., 1977. Velocity dispersion due to anelasticity, Implications for seismology and mantle composition, *Geophys. J. R. astr. Soc.*, 47, 41-58.
- Mallick, S. & Frazer, L. N., 1987. Practical aspects of reflectivity modeling, *Geophysics*, 52, 1355-1364.
- Mallick, S. & Frazer, L. N., 1988. Rapid computation of multi-offset vertical seismic profile synthetic seismograms for layered media, *Geophysics*, 53, 479-491.
- Mayko, G. M. & Nur, A., 1979. Wave attenuation in partially saturated rocks, *Geophysics*, 44, 161-178.
- Menke, W., 1983. A formula for the apparent attenuation of acoustic waves in randomly layered media, *Geophys. J. R. astr. Soc.*, 75, 541-554.
- Menke, W. & Dubendorff, B., 1985. Discriminating intrinsic and apparent attenuation in layered rock, *Geophys. Res. Lett.*, 12, 721-724.
- O'Connell, R. J. & Budiansky, B., 1978. Measures of dissipation in viscoelastic media, *Geophys. Res. Lett.*, 5, 5-8.
- O'Doherty, R. F. & Anstey, N. A., 1971. Reflections on amplitudes, *Geophys. Prosp.*, 19, 430-458.
- Papoulis, A., 1962. *The Fourier Integral and its Applications*, McGraw-Hill, New York.
- Richards, P. G. & Menke, W., 1983. The apparent attenuation of a scattering medium, *Bull. seism. Soc. Am.*, 73, 1005-1021.
- Schoenberg, M. & Levin, F. K., 1974. Apparent attenuation due to intrabed multiples, *Geophysics*, 39, 278-291.
- Schoenberg, M. & Levin, F. K., 1978. Apparent attenuation due to intrabed multiples. II, *Geophysics*, 43, 730-737.
- Spencer, T. W., Edwards, C. M. & Sonnad, J. R., 1977. Seismic wave attenuation in nonresolvable cyclic stratification, *Geophysics*, 42, 939-949.
- Spencer, T. W., Sonnad, J. R. & Butler, T. M., 1982. Seismic Q Stratigraphy or dissipation?, *Geophysics*, 47, 16-24.
- Spudich, P. K. P. & Orcutt, J. A., 1980. Petrology and porosity of an oceanic crustal site. Results from wave form modeling of seismic refraction data, *J. geophys. Res.*, 85, 1409-1433.
- Stoll, R. D., 1974. Acoustic waves in saturated sediments, in *Physics of Sound in Marine Sediments*, pp. 9-39, ed Hampton, L., Plenum Press, New York.
- Stoll, R. D., 1983. Marine sediment acoustics, *J. acoust. Soc. Am.*, 77, 1789-1799.
- Stoll, R. D. & Bryan, G. M., 1970. Wave attenuation in saturated sediments, *J. acoust. Soc. Am.*, 47, 1440-1447.
- Strick, E., 1967. The determination of Q , dynamic viscosity and transient creep curves from wave propagation measurements, *Geophys. J. R. astr. Soc.*, 13, 197-218.
- Strick, E., 1970. A predicted pedestal effect for pulse propagation in constant- Q solids, *Geophysics*, 35, 387-403.
- Sutton, G. H. & Duennebieber, F. K., 1987. Optimum design of ocean bottom seismometers, *Mar. geophys. Res.*, 9, 47-65.
- Sutton, G. H., Duennebieber, F. K., Iwataki, B. & Tuthill, J. D., 1981. An overview and general results of the Lopez Island OBS Experiment, *Mar. geophys. Res.*, 5, 3-34.
- Sutton, G. H., Lewis, B. T. R., Ewing, J., Duennebieber, F. K., Iwataki, B., Tuthill, J. D. et al., 1980. *Lopez Island Ocean Bottom Seismometer Intercomparison Experiment*, Hawaii Inst. of Geophys. Tech. Rep. HIG-80-4, Hawaii Inst. Geophys., Honolulu.
- Toksöz, M. N. & Johnston, D. H., eds, 1981. *Seismic Wave Attenuation*, SEG Geophysics reprint series No. 2, Tulsa.
- Toon, R., 1991. The determination of seismic quality factor Q from VSP data: A comparison of different computational methods, *Geophys. Prosp.*, 39, 1-27.
- Vidmar, P. J., 1980a. The effect of sediment rigidity on bottom reflection loss in a typical deep sea sediment, *J. acoust. Soc. Am.*, 68, 634-638.
- Vidmar, P. J., 1980b. Ray path analysis of sediment shear wave effects on bottom reflection loss, *J. acoust. Soc. Am.*, 68, 639-648.
- Walsh, J. B., 1966. Seismic attenuation in rock due to friction, *J. geophys. Res.*, 71, 2591-2599.
- White, R. S. & Stephen, R. A., 1980. Compressional to shear wave conversion in oceanic crust, *Geophys. J. R. astr. Soc.*, 63, 547-565.

AMERICAN
ASSOCIATION FOR THE
ADVANCEMENT OF
SCIENCE

SCIENCE

21 SEPTEMBER 1990
VOL. 249 ■ PAGES 1349-1472

\$3.50



***** CAR-RT SORT ** CR30
729 000001266805C 11/30/90 M
DANIEL A WALKER
HAMMILL INST OF GEO SEISM
2525 CORREA RD
HONOLULU HI 96822

ent, that is, in the afterburn region. The afterburn region is consistent with visual observation of the brightness of the burned sample being sustained for over 30 s and confirms an earlier report by Boldyrev *et al.* (5), who deduced the formation of two intermediates from their TR diffraction experiments in the second time regime.

It is clear from Fig. 3A that most of the observed scattering in the TR diffraction patterns was recorded in the 2θ region of 43° to 46°. In Fig. 4, the integrated intensity in this 2θ region is plotted as a function of time. This plot summarizes the TR diffraction events in the combusting Al-Ni system. It is characterized by a very sharp and high-intensity peak, peak A, at 5.4 s with a number of low-intensity peaks on either side. With decreased slit size, the number of these low-intensity peaks decreased as a result of a smaller number of grains correctly oriented to scatter the incident x-ray. This result lends credence to the effect of grain orientation or grain motion, or both, at high temperature on the multiplex features observed with the geometric resolution of our diffraction setup. After 20 s or so, broader peaks such as the one labeled B are observed. Beyond 50 s, the plot becomes almost featureless in accordance to a mere shift of the AlNi(110) product peak to high 2θ as a result of thermal contraction. Both features at A and B are reproducible in a number of Al + Ni samples repeatedly combusted under identical experimental conditions. Because grain orientation or random motions for individual grains at high temperature would not reproduce the same intensity peaks at the same time in successive scans, the sharp and high-intensity feature observed at 5.4 s is most likely due to an intermediate phase formed before the formation of the final AlNi product.

The technique of TR-XRD with synchrotron radiation is a very powerful and perhaps unique method for following phase transformations and chemical dynamics of solid combustion reactions in situ at high temperature. When temperature profile and wave-front velocity are measured synchronously and correlated with the TR diffraction scans, then all participating phases may be identified as a function of time and temperature. Intrinsic, real-time kinetic data of this sort are needed to allow critical testing of existing theoretical models of solid combustion and to provide the basis for developing new theories. In the case of the Al-Ni systems, there is a great interest in understanding the phase transformation and combustion dynamics as a function of the composition of the starting materials at various stoichiometric as well as off-stoichiometric compositions across the binary sys-

tem (27). Finally, with brighter and higher flux synchrotron sources available currently at wiggler beamlines (~10¹² photons per second) or next generation storage rings such as those of the Advanced Light Source (ALS) at Berkeley and the Advanced Photon Source (APS) at Argonne (10¹⁶ photons per second), higher spatial resolution should allow a "closer look" at the combustion front in this interesting class of high-temperature solid-state reactions.

REFERENCES AND NOTES

1. This is evident from the volume of articles published in *Combustion and Flame* since 1957.
2. Z. A. Munir, *Ceram. Bull.* 27, 342 (1988).
3. P. Novikov, I. P. Borovinskaya, A. G. Merzhanov, in *Progress in Chemical Engineering and Metallurgy*, A. G. Merzhanov, Ed. (Chernogolovka, 1975), pp. 174-188.
4. Z. A. Munir and U. Anselmi Tamburini, *Mater. Sci. Rep.* 3, 277 (1989).
5. V. V. Boldyrev *et al.*, *Dokl. Akad. Nauk SSSR* 259, 1127 (1981).
6. A. G. Merzhanov, *Arch. Processu Spalenia* 5, 17 (1974).
7. *Arch. Combust.* 1, 23 (1981).
8. S. M. Gruner, *Science* 238, 305 (1987).
9. G. Zorn, E. Hellstern, H. Gobel, L. Schultz, *Adv. X-Ray Anal.* 30, 483 (1987).
10. J. R. Schoonover and S. H. Lin, *J. Solid State Chem.* 76, 143 (1988).
11. M. Sutton *et al.*, *Phys. Rev. Lett.* 62, 288 (1988).
12. R. Clark and P. Hernandez, *ibid.*, p. 1768.
13. E. M. Larson, P. A. Waide, J. Wong, *Rev. Sci. Instrum.*, in press.
14. A. S. Rogachev, V. M. Shkuro, I. D. Chauskava, M. V. Sivtsov, *Fiz. Goreniya Vozdukh* 24 (no. 6), 89 (1987).
15. Yu. S. Nisiborodenko and V. I. Iun, *ibid.* 11, 343 (1975).
16. *ibid.*, p. 734.
17. E. A. Nakazov, V. K. Smolyakov, Yu. M. Maksimov, *ibid.* 17, 39 (1981).
18. A. G. Merzhanov *et al.*, *Povoshk. Metall.* 10, 50 (1981).
19. K. A. Philpott, Z. A. Munir, J. B. Holt, *J. Mater. Sci.* 22, 159 (1987).
20. J. B. Holt and Z. A. Munir, *ibid.* 21, 151 (1986).
21. A. Bearden and A. F. Burr, *Rev. Mod. Phys.* 39, 125 (1966).
22. N. F. Gurur, W. Thonstun, S. M. White-DePace, *NSLS User's Manual: Guide to the XUV and X-ray Beamlines* (Brookhaven National Laboratory, Upton, NY, ed. 3, 1989).
23. S. D. Dunnead, D. W. Readey, C. E. Semler, J. B. Holt, *J. Am. Ceram. Soc.* 72, 2318 (1990).
24. R. P. Elliott, *Constitution of Binary Alloys* (McGraw-Hill, New York, 1965), p. 233.
25. V. P. Aleksandrov and M. A. Korzhagin, *Fiz. Goreniya Vozdukh* 23, 55 (1987).
26. V. S. Touloukian, Ed., *Thermophysical Properties of High Temperature Solid Materials* (Macmillan, New York 1967), vol. 1, p. 704.
27. J. Wong, P. A. Waide, J. B. Holt, B. Rupp, E. M. Larson, in preparation.
28. We acknowledge experimental assistance from L. Faresia, J. Scrofano, G. Lambie, S. M. Heald, M. Wilt, and L. Summers. Technical discussions with F. W. Lytle, A. Larson, and L. Tanner are appreciated. This work is supported under the auspices of the U.S. Department of Energy (DOE) by the Lawrence Livermore National Laboratory under contract W-7408-ENG-48. We are also grateful for the support of DOE, Division of Materials Sciences, under contract DE-AS05-80-ER10742, for its role in the development and operation of Beam Line X-11 at the NSLS. The NSLS is supported by DOE, divisions of Materials Sciences and Chemical Sciences, under contract DE AC02-76CH00016.

13 March 1990, accepted 21 June 1990

Rapid Determination of the Critical Temperature in Simulated Annealing Inversion

ATANU BASU AND L. NEIL FRAZER*

Knowledge of the critical temperature, T_c , the temperature at which a phase change occurs, greatly improves the efficiency of simulated annealing when used for optimization or inversion. A numerical method of accurately determining T_c in a relatively short computation time has been developed. This method is used to recover the seismic soundspeed profile from wavefield data, a problem in which cycle skipping causes many local minima of the energy function and the averaging of the medium by finite length waves results in many states with similar energies. Computations indicate that it is cost-effective to spend about 80 percent of the computing budget looking for T_c , instead of annealing, and that in the course of finding T_c , many states with energies near the global minimum will also be found. The a posteriori probability distribution of the solution has been constructed from trial solutions generated at T_c .

SIMULATED ANNEALING (SA) WAS INVENTED independently by Kirkpatrick, Gelatt, and Vecchi (1) and by Cerny (2). SA makes use of the principle that for a system of particles having random configura-

tions at a fixed temperature T the probability of finding the system in state j with energy E_j is given by the Gibbs distribution

$$g_j = \exp(-E_j/T)/Z \quad (1)$$

in which the partition function Z is given by a sum over all possible states

$$Z = \sum_j \exp(-E_j/T) \quad (2)$$

Hawaii Institute of Geophysics, University of Hawaii at Manoa, Honolulu, HI 96822

*To whom correspondence should be addressed

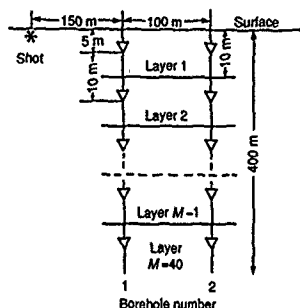


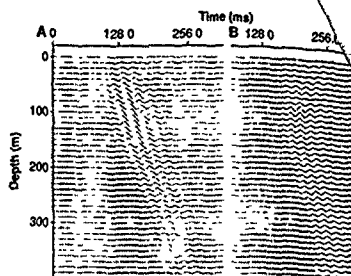
Fig. 1. Geometry of the model. Two boreholes are located 100 m apart with 40 geophones, spaced 10 m apart, in each borehole. The shot is located just beneath the surface 150 m to the left of borehole 1.

When SA is used for optimization, the unknown parameters are regarded as particles, and the allowed values of a parameter correspond to the allowed states of its associated particle. The energy E in Eq. 1 is the cost function, and the temperature is lowered very slowly so that the system of particles eventually freezes into the global minimum of E . In our experiments, we used the heat bath algorithm (3). The Metropolis algorithm (4) is mathematically equivalent to the heat bath algorithm (5), but the heat bath algorithm may be more efficient than the Metropolis algorithm for inversion problems (6).

In the heat bath algorithm, each particle is visited in sequence. Visiting the i th particle, one fixes the states of other particles and calculates the system energy for each allowed state of particle i . These energies are used to generate a Gibbs distribution for particle i , from which a new state for particle i is chosen by sampling once. After each particle in the system has been visited once (this cycle is called a sweep), the temperature T is lowered by a small amount and then each particle is visited again. After many sweeps, the system will be in equilibrium at a low temperature, frozen into a global energy minimum. An M -particle system requires M random numbers per sweep.

The conditions under which SA can be proved to converge to the global minimum of E are often unacceptable because they require so much computer time. Thus, progress in SA depends on experiment as well as theory; experiments are generally used to select a cooling (annealing) schedule, a prescription for lowering T over time. A cooling schedule includes the starting temperature T_0 , the rate of cooling, the amount of time to be spent at each temperature, and the time at which to stop. Theoretical ap-

Fig. 2. (A) Wavefield observed in borehole 1; (B) wavefield observed in borehole 2.



proaches to the design of cooling schedules are given in (7-9). Rothman (6) found the global minimum in a seismic inversion problem by starting at a high temperature and then cooling slowly to just below T_c , the temperature at which a phase change occurs. He determined T_c by trial and error, that is, by repeated runs for different assumed values of T_c .

In our problem, theoretical cooling schedules (7, 8) gave poor results, and a trial and error determination of T_c required prohibitive amounts of computer time. Hence we developed a method to rapidly determine T_c . While finding T_c , our method also finds many good solutions; thus, the issue of cooling schedules became far less important. We applied SA to an inverse problem (10), the problem of determining the soundspeed versus depth profile $c(z)$ of a layered earth from motions recorded in a borehole. As shown in Fig. 1, a seismic source is located 150 m away from the first of two boreholes and the resulting motion is recorded by geophones in both boreholes. In a stratified earth, the resulting data are identical to data recorded in a single borehole from two sources at different horizontal distances.

We chose this problem to experiment with SA, because the Green's functions necessary for its solution are more economical to compute than those of most other seismic inversion problems. All the other difficult characteristics of wavefield inversion problems are present, however, making SA inversion an appropriate method. Our soundspeed-depth profile has $M = 40$ layers, and each layer can have one of $N = 5$ possible soundspeeds, so the number of possible solutions is $N^M \approx 10^{28}$. Enormous computational time would be needed to examine this number of profiles even if geologically unlikely models are excluded. Furthermore, many geologically acceptable profiles differ greatly from each other, so traditional inversion methods that require linearization cause the final solution profile to be highly dependent on the starting profile. SA is

independent of starting profile, and its efficiency relative to other methods increases rapidly with M , the number of unknowns. As our main purpose was to investigate we used for the "observations" in the boreholes synthetic data computed by an exact method (11).

The wavefield observations (Fig. 2) in first and second boreholes are $U_1(t, z)$ and $U_2(t, z)$, respectively, in which t is time and z is receiver depth. We calculate a theoretical borehole 2 data set \hat{U}_2 using U_1 at all depths and an assumed soundspeed profile c . This process is called migration. If the migrated data \hat{U}_2 agree perfectly with

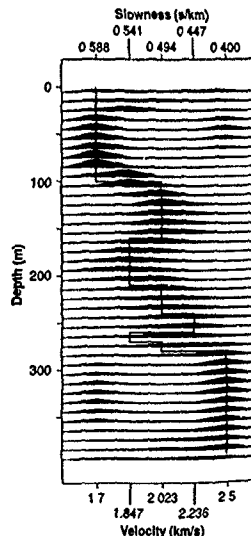


Fig. 3. A posteriori probability distribution (PPDs) for soundspeed at each depth. The profile is indicated by the solid line. The PPDs were computed by a procedure called weighted graph binning, explained in the text.

observed borehole 2 data U_2 , then $c(z)$ is the true profile. We use SA to find that $c(z)$ which gives the best agreement between U_2 and U_1 . For convenience, we assume a layered earth with the layer boundaries halfway between the receivers as shown in Fig. 1. Then $c(z)$ is piecewise constant and is represented as an array $c = (c_1, \dots, c_M)$ where $c_i = c(z_i)$ is the soundspeed of the i th layer. We restrict the soundspeed in each layer to five possible values, thus $c_i \in \{\gamma_1, \dots, \gamma_5\}$.

Our algorithm for migration is a Kirchhoff-Fermat method similar to that used by Carter and Frazer (12). The $U_1(t, z)$ are weighted, time-shifted, and summed to generate $\hat{U}_2(t, z)$ according to the relation

$$\hat{U}_2(t, z_j) = \sum_k a_{jk} U_1(t - t_{jk}, z_k) + b_{jk} \hat{U}_1(t - t_{jk}, z_k) \quad (3)$$

in which \hat{U}_1 is the temporal Hilbert transform of U_1 , a_{jk} and b_{jk} are weights, k is the depth index in borehole 1, j is the depth index in borehole 2, and t_{jk} is the time shift. The weights a_{jk} and b_{jk} are independent of $c(z)$ and depend only on the difference $j - k$ except near the tops and bottoms of the boreholes. The travel time t_{jk} is the integral of $1/c(z)$ along the straight line from depth z_k in borehole 1 to depth z_j in borehole 2.

Agreement of the zero-mean time series \hat{U}_2 and U_2 is measured by the correlation

$$\varphi(\hat{U}_2, U_2) = \frac{1}{N_2} \sum_{j=1}^{N_2} \left(\frac{\sum_{i=1}^{N_1} \hat{U}_2(t, z_j) U_2(t, z_j)}{\left[\sum_{i=1}^{N_1} \hat{U}_2(t, z_j)^2 \right]^{1/2} \left[\sum_{i=1}^{N_1} U_2(t, z_j)^2 \right]^{1/2}} \right) \quad (4)$$

in which N_1 is the number of points in each time series and N_2 is the number of receivers. The correlation would be 1.0 if the soundspeed profile used in migration were the true profile and our migration algorithm were perfect. In practice, our imperfect migration algorithm yields a correlation whose maximum approaches 0.92, a value that varies with the true profile. To apply SA, we define the energy E as the negative correlation, plus a small penalty term to discriminate against highly oscillatory profiles:

$$E(c) = -\varphi(\hat{U}_2, U_2) + \epsilon P(c) \quad (5)$$

If we ignore the penalty term, $E \in [-1, 1]$. The penalty term is given by

$$P(c) = \frac{\sum_{i=1}^{N_2-1} 1/(c_{i+1} - 2c_i + c_{i-1})}{2(N_2 - 2)(1/c_{\min} - 1/c_{\max})} \quad (6)$$

where c_{\max} is the largest permitted sound-

speed and c_{\min} is the minimum permitted soundspeed. The maximum possible value of $P(c)$ is 1.0, realized only when c oscillates between c_{\max} and c_{\min} in successive layers. For most realistic profiles, $P(c)$ is less than 0.1. In the experiments presented below, the value of ϵ in Eq. 5 was fixed at 1.0.

The acoustic wavefields shown in Fig. 2 were used as observations in our numerical experiments. These observations had been synthesized elsewhere by an exact method based on the use of the true soundspeed profile indicated by the line in Fig. 3. As the wavelet of the seismic source was strongly peaked at 50 Hz, side lobes of the correlation function gave a high percentage of states with relatively low energies but inaccurate sound speed profiles. This is called cycle skipping.

To describe our method for determining T , we first introduce the concept of a short run. A short run is a run at fixed temperature T that begins with a random soundspeed profile c , and consists of 25 sweeps requiring a set R of 25M random numbers. At the end of each sweep, we save the energy E . The energies of the 25 sweeps in the short run are averaged to give $\bar{E}_{25} = \bar{E}_{25}(T, c, R)$. We make other short runs at temperatures between 10^{-3} and 10^1 , beginning with the same c , and the same R . As shown in Fig. 4A, these short runs give the graph of $-\bar{E}_{25}(T, c, R)$ (solid line) versus $\log_{10} T$.

To reduce the dependence of \bar{E}_{25} on c and R , we make this series of runs five times with five different c , and five different R . The results are shown as solid lines in Fig. 4, A through E. The five different graphs of $\bar{E}_{25}(T, c, R)$ versus $\log_{10} T$ are averaged to give the graph of $\bar{E}_{25}(T)$ shown in Fig. 4F; thus

$$\bar{E}_{25}(T) \approx \frac{1}{5} \sum_{(c, R)} \bar{E}_{25}(T, c, R) \quad (7)$$

We define T_c to be the temperature at which $-\bar{E}_{25}(T)$ attains its maximum. From Fig. 4F, $\log_{10} T_c$ was estimated as -2.0 ± 0.2 . We refer to T_c as the critical temperature because in the short runs at $T = T_c$, E usually dropped sharply within 10 to 20 sweeps. To show the effect of the penalty function in Eq. 6, Fig. 4 includes the graph of $\varphi_{25}(T)$ (dashed lines), computed at the same time as $-\bar{E}_{25}(T)$.

The curves in Fig. 4 are low at low T because the system is too cold to find its way out of the local energy minimum nearest to the starting model; they are low at high T because, at high T , high- E states are as acceptable as low- E states. The peak temperature T_c represents a balance point at which low- E states are preferred, but the system is warm enough to tunnel between such states.

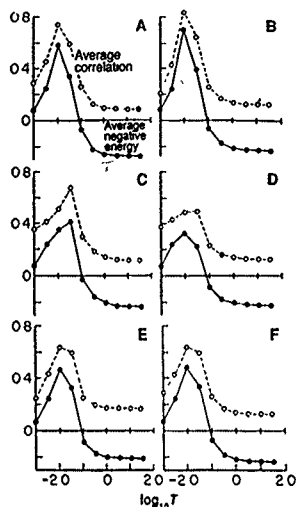


Fig. 4. Curves plotted in (A) show average correlation (dashed line) and average negative energy (solid line), for 25 sweeps at a fixed temperature. At each temperature, a 25 sweep run was made with the same set of 25M random numbers and the same random starting model. We computed the curves in (B), (C), (D), and (E) as for (A) but used different sets of 25M random numbers and different random starting models. The curves in (F) are the averages of the curves in (A) through (E). The temperature at the peak of the average energy curve in (F) is defined to be T_c .

We repeated the experiment described here for a variety of true soundspeed profiles, with similar results. We found that T_c is different for different true soundspeed profiles and that it also changes with the value of ϵ , the penalty weight in Eq. 5. Any change in the definition of E or any change in the ω -a set $\{U_1, U_2\}$ changes T_c . This behavior is analogous to that of a melt whose freezing point is sensitive to small changes in the proportions of minor components.

We also explored alternative definitions of average short-run energy. For example, at each temperature, instead of making five runs with five sets of 25M random numbers, we made a single run with one set of 125M random numbers. The difference is that with five shorter runs the system is set to the starting model five times instead of once. The resulting graphs of $-\bar{E}(T)$ were higher than those in Fig. 4F, but the peak was at the same temperature. We obtained slightly smoother graphs for $\bar{E}(T)$ by using the same set of random numbers at each temperature rather than different sets at different tem-

***Po/So* synthetics for a variety of oceanic models and their implications for the structure of the oceanic lithosphere**

S. Mallick and L. N. Frazer

Hawaii Institute of Geophysics, University of Hawaii, 2525 Correa Road Honolulu, HI 96822 USA

Accepted 1989 July 24. Received 1989 July 15; in original form 1987 December 16

SUMMARY

Po/So synthetic seismograms were computed for a variety of oceanic structures in order to model data from an $m_b = 5.7$ earthquake, recorded during the OSS IV seismic experiment. Satisfactory modelling of *Po/So* waveshapes and frequency content was achieved with no lateral heterogeneity, but with a small random vertical heterogeneity in the mantle, superimposed on a mean velocity structure which is consistent with seismic refraction data. The random heterogeneity in the *P* and *S* velocities appears to be about 2 per cent with a scale length of 5 km. This kind of heterogeneity is easily achieved by varying slightly the major mineral components in either the peridotite or eclogite mantle mineralogy and can be another cause of observed upper mantle anisotropy.

Using a step-function source time behaviour, our numerical modelling also indicates that in the upper mantle Q_p is roughly proportional to $f^{0.22}$, rising from about 450 at $f = 1$ Hz to about 800 at $f = 15$ Hz, and that Q_s is roughly proportional to $f^{0.25}$, rising from about 900 at $f = 1$ Hz to about 1800 at $f = 15$ Hz. A slight decrease in Q_s from these values in any small zone of the upper mantle reduces *So* amplitudes drastically and we believe this is why *So* is sometimes missing from observed seismograms.

The computed synthetic record sections were also used to examine the relation between intrinsic Q and the apparent Q inferred from data in earlier studies. Apparent Q was found to be lower than intrinsic Q below about 5 Hz and higher than intrinsic Q above 5 Hz. When these differences are accounted for, the mantle Q 's of this study agree with the mantle Q 's of Butler *et al.* (1987) to within 10 per cent. There can no longer be any doubt that oceanic upper mantle Q 's are very large, above 5 Hz, and that Q_s is about twice as large as Q_p .

Key words: oceanic models, synthetic seismograms.

1 INTRODUCTION

Po and *So* are the high-frequency guided waves with long coda that travel with great efficiency in the crust and the uppermost mantle underlying the world's oceans. They have fairly constant first arrival speeds of about 8.0 and 4.6 km s⁻¹, respectively. These phases, which were observed as early as 1935 and whose exact mode of propagation has not been well understood, have been called *Pn/Sn*, *oceanic Pn/Sn*, or *long range Pn/Sn* over the past fifty years. In order to avoid ambiguity between these well-defined arrivals observed in the oceans and the well-known *Pn/Sn* phases observed in the continents, Walker (1982) proposed the names *ocean P*/*ocean S* or simply *Po/So*.

Recognition and analysis of *Po/So* played an important role in the understanding of plate tectonics in the sixties. An account of this can be found in Molnar & Oliver (1969). In fact, the anomalous propagation of *Po/So* across the mid-oceanic ridges and across the trenches was one of the pieces of evidence which suggested that the uppermost mantle is weaker at the ridge crests and at the trenches, and that the relatively stronger lithospheric plates originating from the ridge crests spread away from each other and ultimately subduct into the deep mantle at the trenches (Oliver & Isacks 1967, Molnar & Oliver 1969).

Since the first reported observations by Linnhan (1940), in the north Atlantic, *Po/So* has been found in the north, western and central Pacific, the Gulf of Mexico, the

Philippine Sea and many other parts of the deep ocean basins. References to most of these studies may be found in Molnar & Oliver (1969), Walker (1977), Talandier & Bouchon (1979), McCreery (1981), Ouchi (1981), Ouchi, Nagumo & Koresawa (1981), Bibee (1983) and Butler (1986). It is now generally believed that these phases travel very efficiently throughout the laterally homogeneous geophysical provinces of the world oceans, such as the deep ocean basins. However, their propagation is quite inefficient across ocean ridge systems, trenches and island arcs. So far *Po* and *So* have been recorded at least to distances of 3680 and 3660 km, respectively (Walker & Sutton, 1971).

Po/So phases are unusual in comparison to other seismic phases. First, they are much more prominent, and have much higher signal-to-noise ratios, than the direct *P* or *S* phases. Second, their frequency content is much higher than that of other phases. At 2000 km distance, the observed frequencies of *Po* and *So* are as high as 30 and 35 Hz, respectively, and at 3300 km, they are as high as 15 and 20 Hz, respectively. Third, although *So* has a slightly higher frequency content than *Po*, the former is often completely absent and the *Po* wavetrain is usually much longer than the *So* wavetrain. Fourth, observations suggest that *Po/So* velocities depend on lithospheric age. An account of these observations may be found in Walker (1977, 1981, 1982, 1984), Sutton & Walker (1972), Walker *et al.* (1978), Walker, McCreery & Sutton (1983), Walker & McCreery (1985, 1987) and McCreery (1981). Recent observations also suggest anisotropic propagation velocities in *Po/So* (Shimamura & Asada 1983, Shimamura 1984, Butler 1985).

Some attempts to explain the generation and propagation of *Po/So* have been made through qualitative studies and quantitative computer modelling. The nearly constant propagation velocity and low attenuation of these phases led scientists to regard *Po/So* as guided waves in the high-*Q* lithosphere, overlying the low-*Q* and low-velocity asthenosphere (Shurbet 1962, 1964; Bath 1966; Oliver & Isacks 1967; Molnar & Oliver 1969; Mitronovas, Isacks & Seaber 1969; Walker & Sutton 1971; Sutton & Walker 1972; Barazangi, Isacks & Oliver 1972; Hart & Press 1973; Talandier & Bouchon 1979). Kind (1974) used the reflectivity method of Fuchs & Müller (1971) to generate phases similar to *Po/So*, simply by assuming that the lower part of the lithosphere consists of alternating high- and low-velocity layers. Fuchs & Schultz (1976) used the same technique to explain that such phases could be generated if the lower part of the lithosphere consists of thin high-velocity layers and overlies a low-velocity asthenosphere. Stephens & Isacks (1977) showed that the Earth's sphericity creates an effective waveguide for *SH* above the low-velocity zone of the upper mantle. They also showed that modes with group velocity maxima greater than 4.7 km s^{-1} (the group speed of *So*) have substantial displacements in the low-velocity zone for periods above 1.5 seconds, but not for periods of less than this. They suggested that this *sphericity waveguide* permits high frequency propagation up to a distance of 4500 km. Mantovani *et al.* (1977) carried out similar computations to show that *So* could be generated both with or without low-velocity zones and that in the case of models without low-velocity zones, the later part of the *So* wavetrain samples structure as deep as the 420-km discontinuity

Menke & Richards (1980) interpreted *Po* as a sum of whispering gallery waves for models similar to those of Stephens & Isacks (1977). All these efforts explained some of the features exhibited by *Po/So* in terms of their velocities and arrival times. However none could successfully model the long coda duration that characterizes these phases. Gettrust & Frazer (1981) first used the reflectivity technique to correctly model the traveltime as well as the first 15–20 s of the *Po* wavetrain up to a distance of 900 km, for a typical oceanic model obtained from seismic refraction studies in the Pacific. Though their computation was over-simplified, as they included only one free surface multiple, it matched the data well. Menke & Chen (1984), from their studies of acoustic wave propagation in a randomly layered medium, suggested that *Po/So* might consist predominantly of forward scattered coda off a randomly layered mantle. Sereno & Orcutt (1985) used a model similar to that used by Gettrust & Frazer (1981) and computed synthetics for both *Po* and *So* up to a distance of 1000 km and a frequency of 6.4 Hz. Their analysis of both real and synthetic *Po/So* signals showed that multiple reverberations within the sediment and the water column can explain many features of the *Po/So* spectra. However, all the conclusions of Sereno & Orcutt (1985) were based on a single velocity model, the same model used by Gettrust & Frazer (1981). Moreover, Sereno & Orcutt (1985) did not try to match their synthetics with real *Po/So* data in the time domain or the time-frequency domain. A comparison of synthetics with actual *Po/So* data shows that the Gettrust & Frazer (1981) model does not give the very long codas characteristic of *Po/So*. In more recent work, Sereno & Orcutt (1987) improved upon the Gettrust & Frazer (1981) model with a more appropriate frequency-dependent *Q* structure in the lithosphere to model *Po/So* data collected from the 1983 Ngendei Seismic Experiment in the southwest Pacific. Their modelling showed that the characteristic shapes of *Po/So* spectra are due to water-sediment reverberation. The modelling experiments presented in this paper (discussed below), indicate that although water-sediment reverberation is important in lengthening the *Po/So* coda, the fine-scale vertical structure in the oceanic lithosphere is equally important. The fine-scale lithospheric structure homogenizes the *Po/So* coda in the time domain, spreading coda energy into the gaps between the water-sediment reverberations.

So far, there has been no oceanic velocity model that is able to fit the observed *Po/So* wavetrain in the time domain, or in the time-frequency display often used to display *Po/So* observations. Computer runs using more realistic models than that used by Gettrust & Frazer (1981) and Sereno & Orcutt (1985, 1987) up to much higher frequencies and greater distances are required for this purpose. Unfortunately, the cost of computing such synthetics is large even for stratified models, partly because of the large source-receiver distances, measured in wavelengths, and partly because of the observed frequency dependence of *Po* and *So* *Q*'s. It is known that reflectivity codes can be vectorized if the frequency dependence of velocities is neglected (Phinney, Odom & Fryer 1988, Odegard, M. E., personal communication). However, as the *Q*, and the fall-off rate, of *Po/So* appear to vary with frequency (Brandsdottir 1986, Novelo-Casanova & Butler

1986, Sereno & Orcutt 1987) it seems desirable to take account of the frequency dependence of seismic velocities. Recently, Mallick & Frazer (1986, 1988) showed how reflectivity codes can be made to vectorize even when the seismic velocities are frequency dependent. Applications of their method to the modelling of marine seismic refraction data were given in Duennebie *et al.* (1985), Duennebie *et al.* (1987), and Sen *et al.* (1988). In this paper their method is used to synthesize Po/So seismograms for a variety of oceanic models for comparison with Po/So data recorded during the OSS IV experiment (Cessaro & Duennebie 1987).

2 A REFLECTIVITY CODE FOR MODELLING Po/So

Computation of Po/So synthetic seismograms with present hardware requires a relatively efficient reflectivity code. The factors which affect the speed of computation are:

- (1) the reflectivity function must be adequately sampled in wavenumber, in order to avoid distance aliasing on transformation into the offset domain,
- (2) often a time series much longer than the signal of interest must be computed in order to avoid time aliasing,
- (3) velocity gradient zones are often approximated by many thin layers.

The experience of many workers, reviewed and summarized by Mallick & Frazer (1985, 1987), has shown that:

- (1) the use of a generalized Filon's method (e.g. Frazer 1978; Frazer & Gettrust 1984) for wavenumber integration allows a larger step size in wavenumber,
- (2) the use of complex frequencies (Phinney 1965) avoids computing a time-series longer than the signal of interest,
- (3) the careful use of phase integrals in gradient zones enhances the computation speed without loss of accuracy

Mallick & Frazer (1986, 1988) have also shown that if the wavenumber loop is made the innermost loop and the frequency loop is made the outermost loop, with the layer loop intermediate to these two loops, then reflectivity codes can be efficiently vectorized on a CRAY X-MP system, even when frequency-dependent velocities are used. The speed and efficiency of this type of code make it suitable for modelling Po/So wavetrains

3 MODELLING OF Po/So DATA RECORDED AT OSS IV

In this section, we present a series of numerical experiments using the reflectivity code described above. Our objective was to model the Po/So signal recorded from an earthquake during the OSS IV seismic experiment. The details of this seismic experiment have been reported elsewhere (see Duennebie *et al.* 1987; Cessaro & Duennebie 1987) but are briefly summarized here for completeness.

The ocean sub-bottom seismometer (OSS IV) was employed by HIG scientists at hole 581 C, following DSDP Leg 88. The hole drilled through 356 m of sediment and about 22 m of basalt. The instrument package, which consisted of a vertical 4.5 Hz geophone stack and two

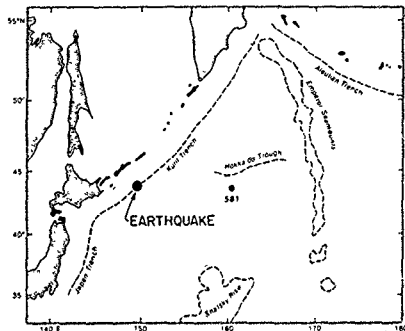


Figure 1. Location map for the OSS IV area, indicating the hole and the earthquake locations.

orthogonal horizontal 4.5 Hz geophone pairs, was clamped about 20 m above the basalt. During a period of 64 days, from 1982 September 11 to 1982 November 17, OSS IV recorded 660 earthquakes, of which 59 were reported by the National Earthquake Information Service (NEIS). Many of these earthquakes generated distinct Po/So arrivals. Fig. 1 shows a location map of the OSS IV site. The data, originally recorded on analogue magnetic tapes, were later digitized at a rate of 80 samples s^{-1} . Fig. 2(a) shows the vertical response recorded by OSS IV from one of the earthquake events stated above. This event was reported by NEIS: origin time, 1982 November 4, 09 29.53 Z UT, $m_b = 5.7$, latitude; 44 04'S, longitude; 148.04'E, depth, 39 km, best double couple, $M_0 = 9.3 \times 10^{23}$ NPI: strike = 204°, dip = 19°, slip = 50° NP2: strike = 66°, dip = 76°, slip = 103°. The reported epicentre lies at a distance of 8.47° (~941 km) and at an azimuth of 274.9° from the OSS IV site. This data trace is of extremely good quality and many of the numerical experiments described below were made in an attempt to model this Po/So trace. Since the recorded horizontal motions were clipped and relatively noisy for this earthquake, as well as for the other earthquakes whose focal mechanisms solutions are reliably known, we restricted our modelling to the vertical geophone response only. In Fig. 2(b-f), this vertical response is replotted after filtering with frequency-domain Hanning windows of 0-25 Hz, 0-12.8, 0-6.4, 0-3.2 and 0-1.6 Hz [see Mallick & Frazer (1987) for the details of the Hanning window]. This allowed us to determine approximately the maximum frequency content of the data and the frequency window within which Po and So are clearly observed. A comparison of the raw data and the data filtered with different windows shows that there is little energy above noise beyond 25 Hz and that 6 Hz energy must be included in order to observe distinct So arrivals. We therefore computed synthetics for all the trial models up to 6.4 Hz, convolved the computed response with the OSS IV instrument response function (Fig. 3 shows the instrument response function with formula), filtered with a 0-6.4 Hz Hanning window, and compared the results with the observed data filtered in the same way. For the model which best fits the data up to 6.4 Hz, synthetics were computed to

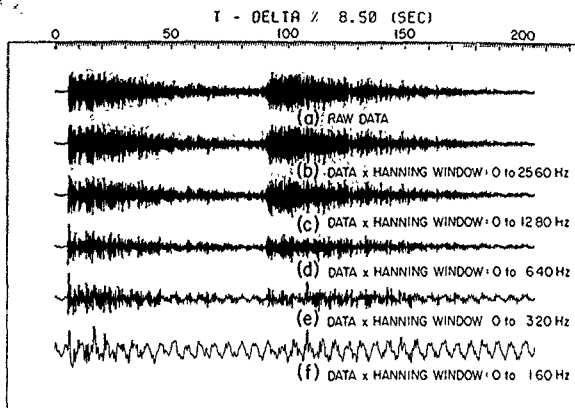


Figure 2. OSS IV data filtered with different Hanning windows, as indicated

higher frequencies. Unless otherwise specified, all the synthetics shown are scaled so that each trace has the same maximum amplitude.

We now review some earlier seismic velocity models for the area of the OSS IV site. The model used by Gettrust & Frazer (1981) to compute P_0 synthetics was consistent with

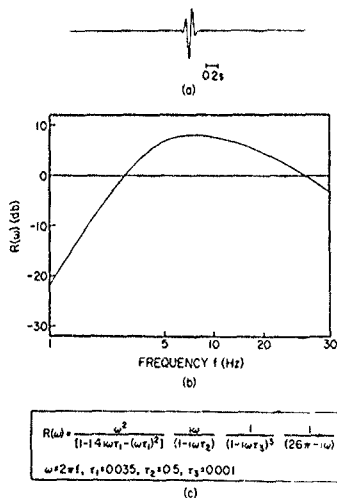


Figure 3. OSS IV instrument response function with formula (a) Response in time domain, filtered with a 0–15 Hz Hanning window, (b) response in frequency domain and (c) response-function formula

prior refraction studies in this area. As very little information about Q was available at that time, Gettrust & Frazer (1981) used a constant Q_p of 5000 and Q_s of 2500 throughout the crust and lithosphere. Sereno & Orcutt (1985) modified the model of Gettrust & Frazer (1981) to include different Q 's for water, sediment, basement and upper mantle. Their model will be referred to here as the Gettrust & Frazer (Sereno & Orcutt Q) model, or simply the GF(SOQ) model. Asada & Shimamura (1976), from the longshot seismic experiments, obtained a best-fit model for the crust and the upper mantle of this area. This model is referred to here as the Asada & Shimamura model or the AS model. Dziewonski & Anderson (1981), from the inversion of seismic data on a global scale, obtained a preliminary reference earth model (PREM), which is an average model for the whole Earth. Finally, Duennebie *et al.* (1987), studied the OSS IV refraction data and nearby OBS data obtained from the Soviet argon shots and obtained a crustal model for the OSS IV area (Fig. 4). Even the fine-scale features of the OSS IV model of Duennebie *et al.* (1987) were very strongly constrained by the data, and so the OSS IV model shown in Fig. 4 is thought to be an accurate model for the crust in this area. This model also used a frequency-dependent Q structure, using a generalized Strick's power law with a reference frequency of 1 Hz, $\sigma = 0.1$ and $\epsilon = 0.001$. A detailed account of these parameters may be found in Strick (1967, 1970) and Mallick & Frazer (1987). It was therefore thought reasonable to fix the OSS IV model for the crust and to vary the mantle structures, from GF(SOQ), PREM and AS models, in our preliminary trials. These three preliminary models are shown in Fig. 5(a), (b) and (c) and a comparison of the observed data with the synthetics computed using these models is shown in Fig. 6. It can be seen that none of these models generates enough S_0 amplitude. Even though the velocity gradient in the PREM mantle was extended to great depth, there is not much difference between the P_0 coda

OSSIV CRUSTAL MODEL

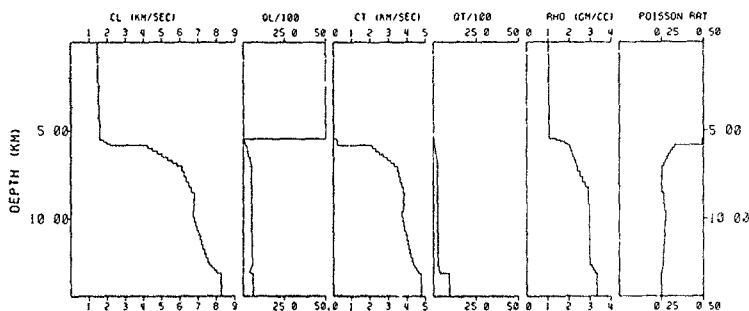
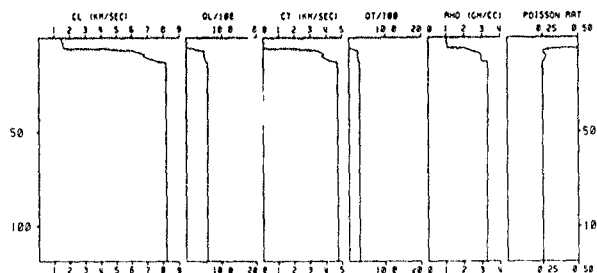
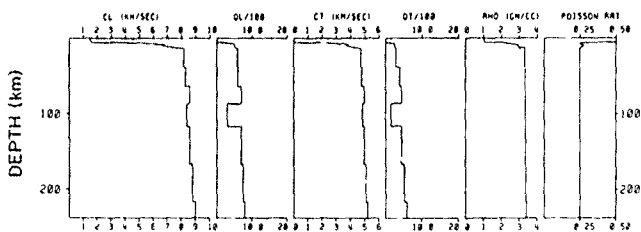


Figure 4. P-wave velocity (CL), P-wave Q (QL), S-wave velocity (CT), S-wave Q (QT), density (RHO) and Poisson's ratio (POISSON RAT) as a function of depth for the OSSIV crustal model Q values shown are at a reference frequency of 1 Hz.

(a) OSSIV CRUST, GF(SOO) HANTLE MODEL



(b) OSSIV CRUST, ASADA & SHIMAMURA HANTLE MODEL



(c) OSSIV CRUST, PREM HANTLE

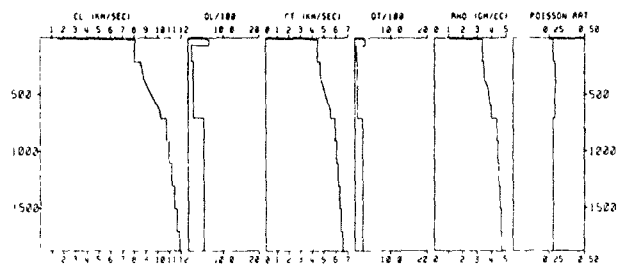


Figure 5. P-wave velocity (CL), P-wave Q (QL), S-wave velocity (CT), S-wave Q (QT), density (RHO) and Poisson's ratio (POISSON RAT) as a function of depth for (a) GF(SOO), (b) AS, and (c) PREM models

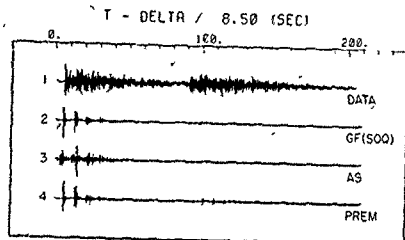


Figure 6. OSSIV data compared with synthetics computed using models GF(SOQ), AS and PREM, up to a maximum frequency of 6.4 Hz

obtained from the GF(SOQ) mantle and that from the PREM mantle, with the indication that only the first few hundred kilometres of the mantle are involved in the propagation of Po/So . Neither the GF(SOQ) nor the PREM mantle gives a long enough Po coda. The AS model

gives a longer Po coda, but its traveltimes are inconsistent with the data. The longer Po coda obtained from the AS model suggests that the upper mantle structure given by this model may be more correct, although the velocities must be changed in order to match the traveltimes correctly. The relatively low amplitude ratio of So to Po suggests that the ratio of Q_S to Q_P in the lithosphere may be too low in all three models. In all the above models, a frequency dependence of Q similar to that of the OSSIV crustal model was assumed, with Q_P and Q_S set at 600 and 300, respectively, at the reference frequency of 1 Hz. In the AS model, where there is a low-velocity zone, Q_P and Q_S of 200 and 100, respectively, were used with a similar frequency dependence.

In the next modelling attempt the frequency dependence remained the same, but Q_P and Q_S were raised at the reference frequency to 1000 and 800, respectively, except in the LVZ, where Q_P and Q_S were raised to 600 and 300, respectively. After a few trials we obtained model NM-1, shown in Fig. 7, which improved the quality of the Po and

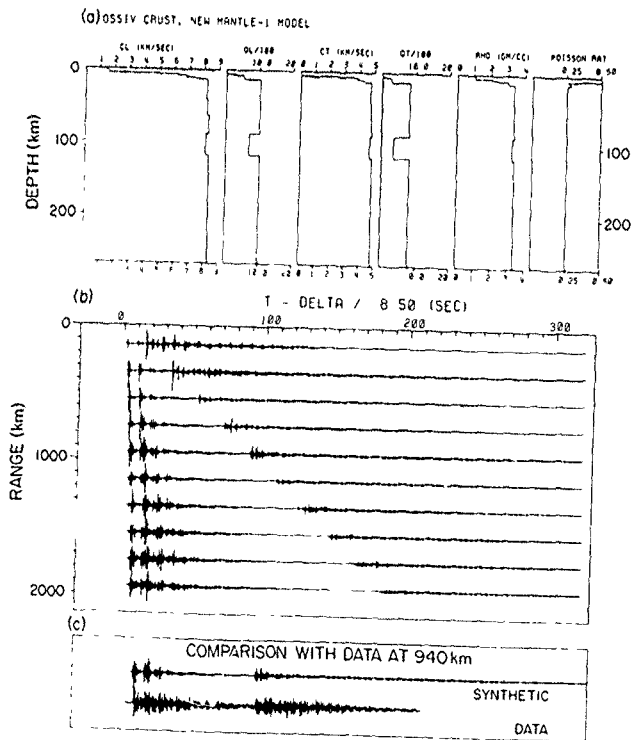


Figure 7. Synthetic seismograms, computed using model NM-1 (a) the model, (b) synthetic record section for vertical particle velocity at ranges from 141 km to 194 km in steps of 20 km and (c) comparison of the observed data with the synthetic seismogram at 940 km. Synthetics were computed up to a maximum frequency of 6.4 Hz.

So coda, although the agreement of data and synthetic is far from perfect. The traveltimes of *Po* and *So* arrivals are reasonably good but the *Po* and *So* codas from this model are still far too small and too short in duration.

A possible explanation for the long coda duration of *Po/So* was first given by Fuchs & Schultz (1976). Their computation suggested that such coda could be generated if the lower part of the lithosphere consists of thin high-velocity layers overlying a low-velocity asthenosphere. Wenzel, Sandmeier & Wäldle (1987) explained the complex nature of the seismic reflection and refraction data by using thin random layers in the lower crust. In order to improve upon the coda, we hypothesize that upper mantle velocities are random, with a certain standard deviation from mean velocity-depth functions; this randomness is due to a variable intermixing of two mineral assemblages with velocities at the upper and the lower limits of the randomness. This means that a uniform probability density function for velocity variations is more appropriate than a Gaussian distribution. Furthermore, because temperature and pressure gradients in the mantle are nearly vertical, the scale length of mantle heterogeneity is likely to be much larger in the horizontal direction than in the vertical direction. Thus our model of the mantle consists of many thin horizontal layers, which behave like thin lenses, with aspect ratios greater than about fifty. Technically the seismic response of such a mantle cannot be modelled with a reflectivity code because the code assumes the layers to be infinite in length. However, scattering studies using random layers (Menke 1983; Menke & Chen 1984; Menke, W., personal communication) have shown that a surprisingly small number of layers is needed before one random velocity process gives the same seismic response as another such process. This being the case, a reflectivity code may safely be used to model the thin lens medium described above providing the vertical scale length of the heterogeneity, i.e. the thickness of the lenses, does not change with x . To understand this point, consider the velocity function beneath the source and the velocity function beneath the receiver. In general their random components will be different, but, as both random components give the same seismic response, just one of them may be used at both the source and the receiver and the same seismogram will still be obtained.

The probability density function used here for the random component of velocity in each mantle layer is

$$p(v_1) = \begin{cases} \frac{1}{2\sqrt{3}d} & \text{if } -\sqrt{3}d \leq v_1 \leq \sqrt{3}d \\ 0 & \text{if } |v_1| > \sqrt{3}d \end{cases} \quad (1)$$

in which v_1 is the variation of velocity in per cent and d is the standard deviation of the distribution $p(v_1)$. For example, if V_p in a layer is 8.1 and a value of v_1 is drawn from the distribution $p(v_1)$ then the value of V_p used in place of 8.1 is

$$8.1(1 + v_1/100)$$

As V_p and V_s are assumed to be correlated, the same value of v_1 is used for both. Therefore two parameters are supplied to the computer. (i) the standard deviation, d , from the mean velocity value (in per cent) and (ii) the

thickness of each layer having random velocities, i.e. the vertical scale length of the randomness. A random model is generated from a given mantle background velocity model by introducing thin layers with thicknesses equal to the vertical scale length, and with velocities randomly distributed about the mean given by the background model velocities. When *P*- and *S*-wave velocities are random the density is also expected to be random. However, any such randomness in density is expected to be too small to affect the computed synthetics. Therefore, the density was not randomized.

The vertical scale length was finally fixed at 5 km after various scale lengths had been tried, and subsequently only the percentage of randomness was changed. To the model NM-1 shown in Fig. 7, $d = 1$ per cent randomness was introduced in the mantle, and the result is shown in Fig. 8. This gave only a small increase in the coda from that of the equivalent non-random model. Fig. 9 shows the results of increasing the randomness to $d = 2$ per cent in model NM-1. Although it still decays too rapidly, the *Po* coda of the synthetic now resembles the *Po* coda of the data to a much greater extent. The *So* coda of the synthetic still contains far less energy than the *So* of the data. Earlier modelling experience, with non-random models, suggested that changing the behaviour of Q as a function of frequency could be used to improve the *So* amplitude. Changes in Q that were uniform across the frequency band gave incorrect relative amplitudes of *Po* to *So*. Moreover, as mentioned earlier, model NM-1 does not give very accurate *Po* and *So* arrival times. Either model NM-1 must be modified or we must begin with a different model that gives better arrival times. Inspection of the GF(SOQ) model (Fig. 5a) and the synthetics computed using this model (Fig. 6) shows that even though this model does not generate good coda, it does give fairly accurate arrival times. The result of randomizing GF(SOQ) is shown in Fig. 10. The randomized GF(SOQ) has good codas and arrival times. However, a careful look at the record section plot, (Fig. 10b), reveals that the randomized GF(SOQ) mantle has a new phase, travelling with a velocity greater than 8.5 km s^{-1} . As this high-velocity phase is not present in the data, we rejected the GF(SOQ) mantle and continued work on NM-1.

To improve the arrival times and amplitudes, both the mantle velocities and the Q structure of NM-1 were modified. The resulting model is referred to as NM-2. The Q structure for NM-2 was taken from the recent observational work of Butler *et al.* (1987) who used *Po/So* data from the Wake Island array to estimate mantle Q_p and Q_s as a function of frequency. They found that mantle Q_p is roughly proportional to $f^{0.7}$ (f = frequency) and rises from 300 at 2.5 Hz to 1500 at 17.5 Hz. Mantle Q_s on the other hand was reported to be roughly proportional to $f^{1.1}$, rising from about 400 at 2.5 Hz to about 3000 at 22.5 Hz. In order to treat frequency-dependent attenuation it is convenient to make use of some attenuation law, e.g. the absorption band law (Liu *et al.* 1976) or Strick's power law (Strick 1967, 1970) and to choose parameters such that Q_p and Q_s come out as desired. For example, Butler *et al.* (1987) fitted an absorption band model to data from the western Pacific. As in our earlier computations, we used an extended Strick's power law and found that the choices $\sigma = 0.7$, $\epsilon = 0.001$, and $Q_p = 300$ (at $f = 2.5 \text{ Hz}$) for *P*-waves and $\sigma = 1.1$,

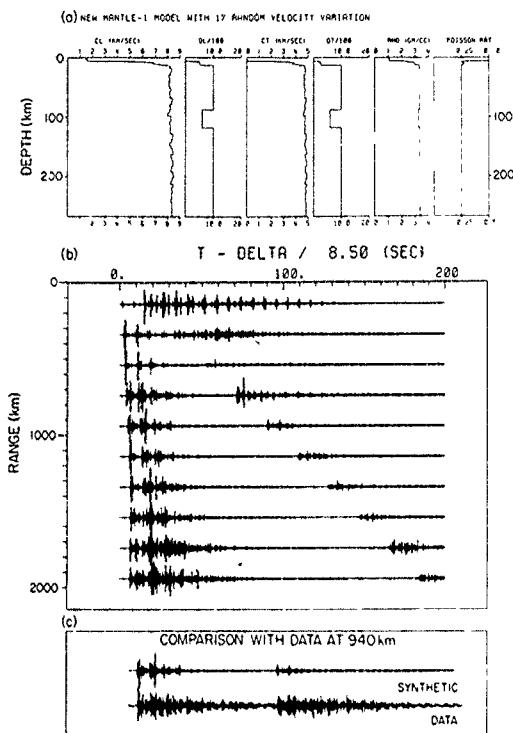


Figure 8. Same as Fig. 7, but now using the model NM-1 whose mantle velocities have been randomized with a standard deviation of 1 per cent and vertical scale length of 5 km.

$\epsilon = 0.001$, and $Q_s = 400$ (at $f = 2.5$ Hz) for S -waves [see Mallick & Frazer, (1987) for the details of these parameters] matched the observed attenuation curves of Butler *et al.* (1987). The synthetic seismograms for model NM-2 with $d = 2$ per cent randomness are shown in Fig. 11. The arrival times are now improved and the Po coda is fairly good but the So coda has not improved at all. (This lack of agreement with Butler's results is due to the fact that the Q 's obtained by Butler *et al.* 1987, are apparent Q 's whereas our Q values are intrinsic Q 's. See Discussion section below.) After a long series of trials we obtained the best-fit model NM-3, shown in Fig. 12(a) with randomness, and in Fig. 13(a) without randomness. The synthetics in Figs 12(b) and (c) were computed up to a maximum frequency of 15 Hz. The essential features of model NM-3 may be summarized as follows.

(1) The crustal velocities, densities, Q_P and Q_S are exactly the same as that of Duenneber *et al.* (1987).

(2) Mantle velocities are random with $d = 2$ per cent randomness and a 5-km vertical scale length.

(3) From the Moho down to a depth of about 60 km, the

mean velocities rise gently with depth. The mean V_P rises from 8.1564 to 8.1807 km s^{-1} over this depth range, whereas the mean V_S rises from 4.7144 to 4.7233 km s^{-1} . (The extra digits in these speeds are included for the use of anyone who wishes to compute the exact seismogram). Q_P and Q_S are frequency dependent in this zone. Q_P is roughly proportional to $f^{0.22}$, rising from about 450 at $f = 1$ Hz to about 800 at $f = 15$ Hz. Q_S on the other hand is roughly proportional to $f^{0.25}$, rising from about 900 at $f = 1$ Hz to about 1800 at $f = 15$ Hz. This zone of the upper mantle can be regarded as the lid of the oceanic lithosphere.

(4) At around 60 km below Moho, V_P and V_S drop to 8.0065 and 4.5796 km s^{-1} , respectively. Q_P in this zone varies from 100 at $f = 1$ Hz to about 180 at $f = 15$ Hz whereas Q_S varies from 50 at $f = 1$ Hz to about 100 at $f = 15$ Hz. For P , this low-velocity low- Q zone extends down to 85 km, whereas for S it continues to 160 km below Moho (see Fig. 13a for details).

(5) Below the LVZ, V_P and V_S increase gently with depth, at a rate which is difficult to infer from the Po/So data. Q_P and Q_S in this zone seem to have a frequency dependence similar to that of the LID. Modelling indicates

Figure

that t
observ

The
perfect
the ot
Fig 12
there is
that the
vertical
show t
observ
While
that con
which k
Orcutt
column
Drilling
sediment
high-velo
mainly by
layers mig

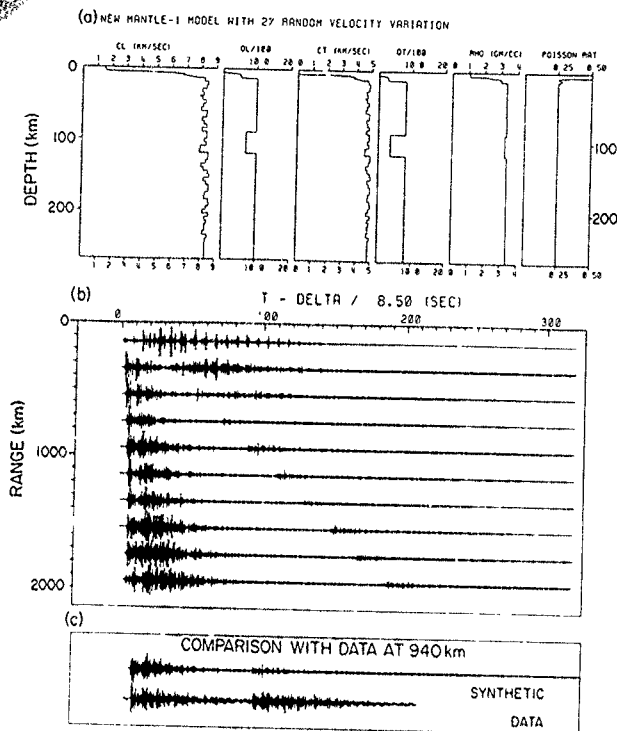


Figure 9. Same as Fig. 8, but here mantle velocities have been randomized with a standard deviation of 2 per cent

that the gentle gradient in this zone is required by the observations.

The agreement of data and synthetic in Fig. 12, while not perfect, is significantly better than the agreement in any of the other figures. Fig. 14 shows the data and synthetic of Fig. 12c in the time-frequency domain and the agreement there is also very good. While the modelling does not prove that the characteristic codas of *Po* and *So* are caused by vertical heterogeneity in a high-*Q* upper mantle, it does show that such a mantle is consistent with *Po/So* observations.

While there are undoubtedly many kinds of heterogeneity that contribute to *Po/So* coda waves it is of interest to know which kinds of heterogeneity contribute the most. Sereno & Orcutt (1985) showed that the sediment and the water column play a significant role in the generation of *Po/So*. Drilling results at hole 581C suggest that the ocean sediments there contain 2 per cent thin (~10 cm) high-velocity chert layers and, that if *Po/So* were controlled mainly by the water column and the sediment, these chert layers might have a significant effect on its coda. Also, it was

suggested that *Po/So* might be generated by a randomly layered lower crust. In order to investigate these possibilities, we first computed synthetics for model NM-3 with a non-random upper mantle. These are shown in Fig. 13. We then introduced chert layers ($V_p = 6 \text{ km s}^{-1}$, $V_s = 3.5 \text{ km s}^{-1}$) of 10-cm thickness randomly distributed as 2 per cent of the sediment. To do this, the entire sediment column was first sub-divided into 5-m thick zones. Each 5-m zone was then divided into 50 layers, each having a thickness of 10 cm. Then, by generating a random number between one and 50, one 10-cm layer in each 5-m zone was randomly selected as a chert layer. Fig. 15(b) shows the computed synthetic seismograms for this model. Comparison of Fig. 15(b) with Fig. 13(c) indicates that *Po/So* codas are not caused by scattering from chert layers within the sediment column.

The lower crustal velocities were then randomized with a standard deviation of $d = 5$ per cent. To do this, each layer of the lower crust (see Fig. 4) was randomized using the probability density function given by equation (1). The synthetics for this random lower crust are shown in Fig. 15(c). Comparison of Fig. 13(c) (non-random crust and

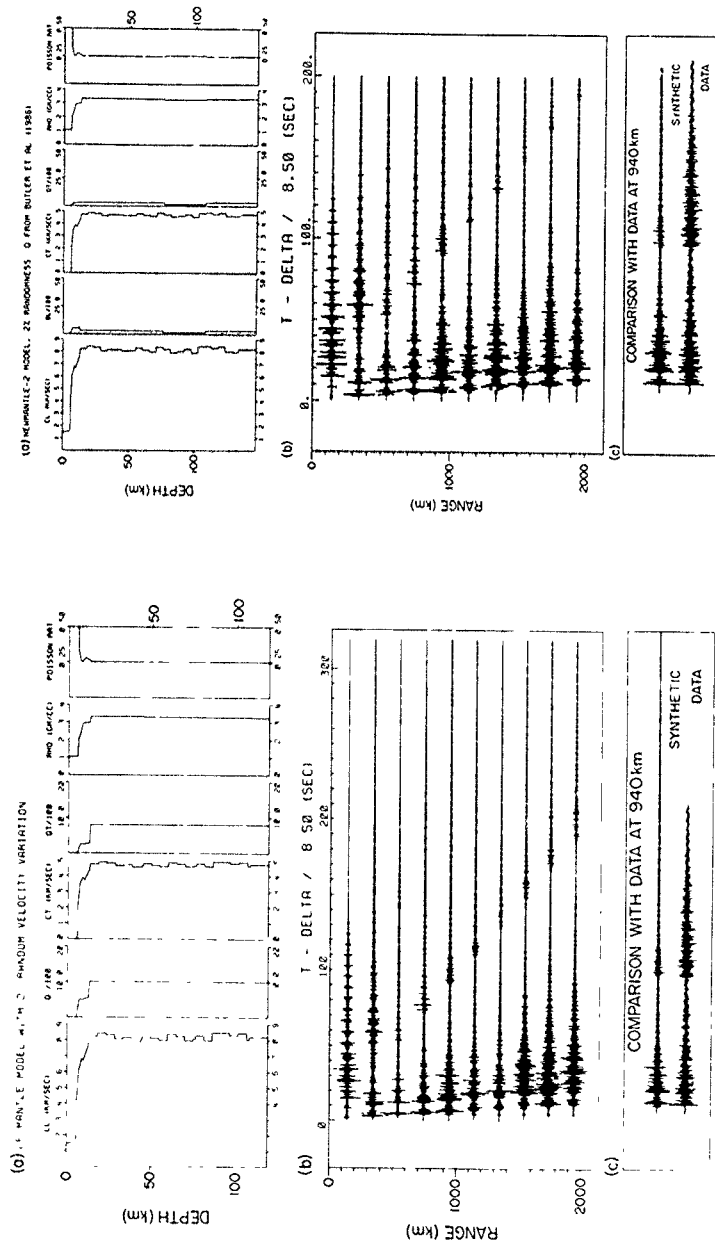


Figure 10. Synthetic seismograms using GF(500) model with 2 per cent randomness in mantle velocities, otherwise similar to Fig 8

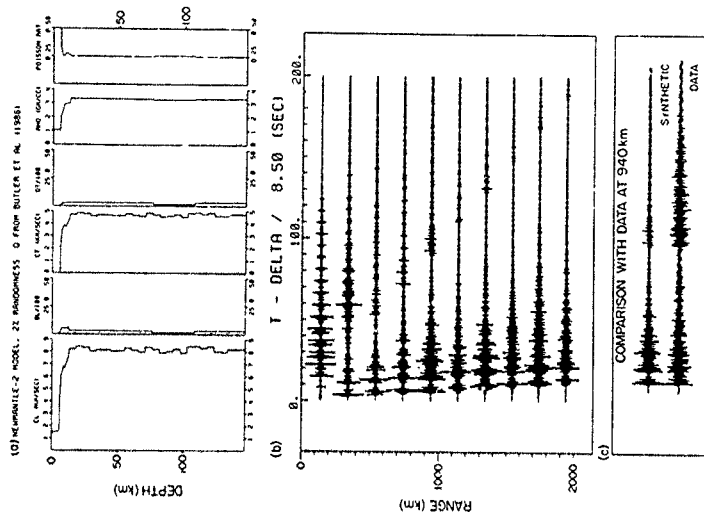


Figure 11. Synthetic seismograms using model NM-2 with 2 per cent randomness in mantle velocities and values of $Q_p(f)$ and $Q_s(f)$ in the mantle from Butler *et al.* (1987). Otherwise similar to Fig 8

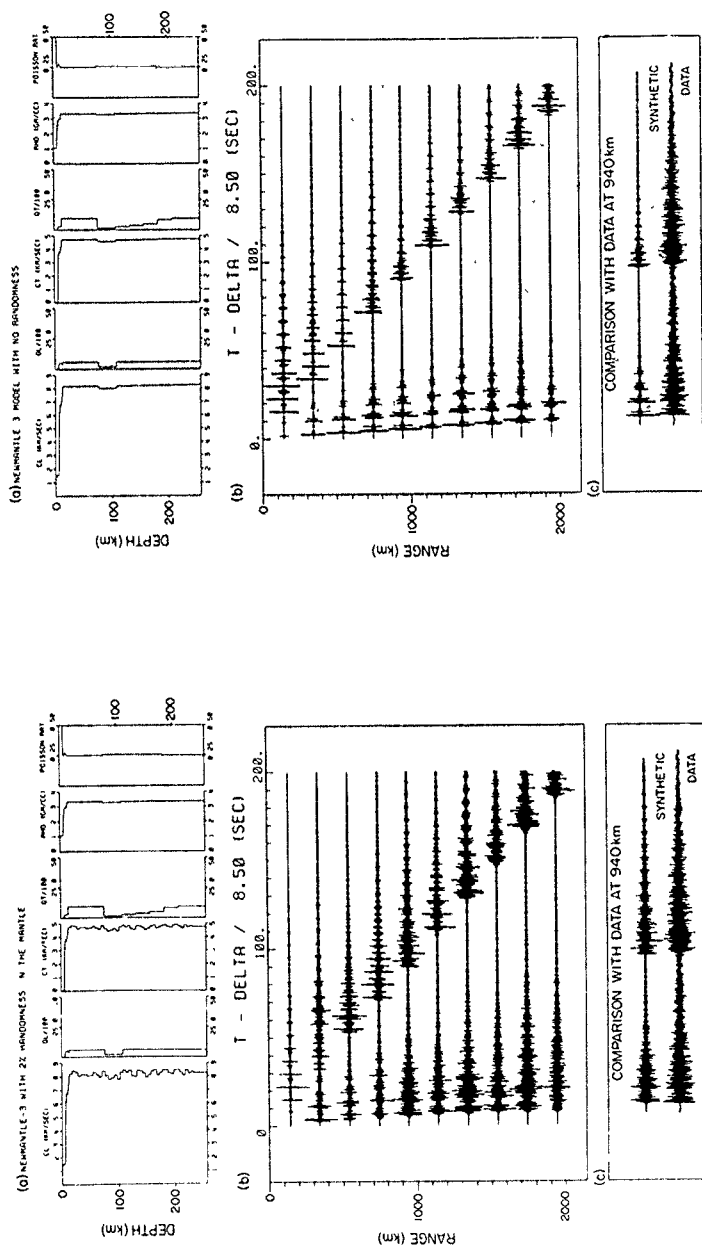


Figure 12. Synthetic seismograms using model NM-3, up to a maximum frequency of 15 Hz, otherwise similar to Fig. 9

Figure 13. Same as Fig. 12, but with a non-random mantle

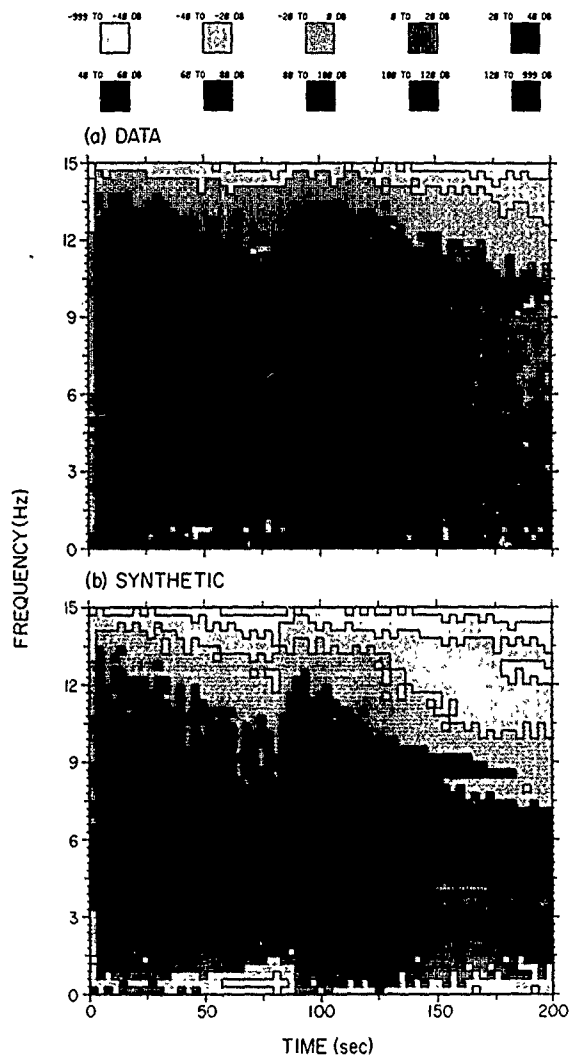


Figure 14. Comparison of the *Po/So* data and the synthetics in the time-frequency domain (a) data, (b) synthetics computed with model NM-3

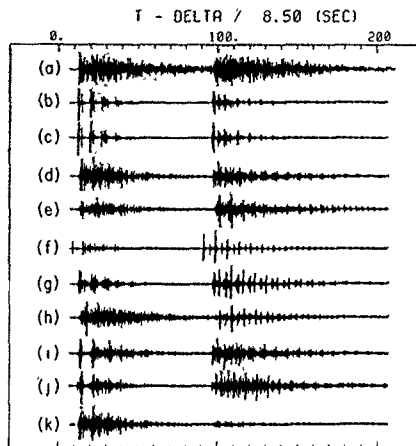


Figure 15. (a) OSSIV *Po/So* data. (b) Synthetic computed with non-random NM-3 mantle and with 2 per cent of the sediments composed of randomly distributed, 10-cm thick chert layers. (c) Same as (b), but with no chert in the sediment and a random $d = 5$ per cent lower crust. (d) Same as Fig. 12(c), but with another choice of the random mantle velocities. (e) Same as Fig. 12(c), but with a vertical scale length of 2.5 km. (f) Same as Fig. 12(c), but with a vertical scale length of 10 km. (g) Same as Fig. 12(c), but with $d = 1$ per cent randomness. (h) Same as Fig. 12(c), but with $d = 4$ per cent randomness. (i) Same as Fig. 12(c), but the model is terminated at the top of the LVZ with a homogeneous half-space. (j) Same as Fig. 12(c), but the model here does not have any LVZ, the gradients above LVZ were continued through the mantle. (k) Same as Fig. 12(c), except that the top 20 km of the mantle have now a Q_2 slightly lower than Q_1 .

mantle) with Fig. 15(c) (random crust, non-random mantle) indicates that *Po/So* codas are probably not generated by scattering from vertical heterogeneity within the lower crust.

The fact that there is almost no difference in the computed seismograms presented in Figs 13(c), 15(b) and (c), but there is a drastic improvement in *Po/So* coda in the synthetics shown in Fig. 12(c), indicates that it is the heterogeneity of the upper mantle and not that of the sediment or the lower crust which plays the most significant role in the generation of the characteristic *Po/So* wavetrains. The crust and the water column lengthen the duration of *Po/So* wavetrains, but without mantle heterogeneity these wavetrains still do not resemble the data. The synthetics shown in Figs 13, 15(b) and 15(c) were computed up to a maximum frequency of 10 Hz.

The calculations discussed above indicate that a randomly layered mantle is consistent with our observations of *Po/So* coda, but many questions remain. Do two processes of the same mean mantle velocity model generate synthetics that are exactly alike? Are the *Pc* and *So* codas sensitive to the value chosen for the scale length of the upper mantle heterogeneity? What effect does the degree of randomness have on the *Po/So* coda? In our best-fit model of Fig. 12,

what happens to the *Po/So* coda if the model at the top of the LVZ is terminated or the LVZ removed altogether? Does the mantle randomness needed to account for the *Po/So* coda affect the waveshapes of long-period body wave phases? What are the effects of errors in the focal mechanism of the source and the time behaviour of the source? How would our conclusions be affected if the data were clipped? The calculations shown in Figs 15(d)–(j) and 16 address these questions. Unless specified, the synthetics shown in the following figures were computed up to a maximum frequency of 10 Hz.

Figure 15(d) shows the computed synthetic seismogram up to 15 Hz for another version (different set of random layers) of the model NM-3 of Fig. 12(a). Since the synthetics of Figs 12(c) and 15(d) are nearly alike, it may be concluded that, for the calculation of synthetic seismograms, one choice of our random velocity is as good as another; in particular, then, the same version may be used for all distances between the source and receiver.

Figures 15(e) and (f) show the effect of using vertical scale lengths of 2.5 and 10 km respectively and a randomness of $d = 2$ per cent, with model NM-3. A comparison of Figs 12(c), 15(e) and 15(f) suggests that the synthetics computed with a 5-km vertical scale length of randomness match the data better than those computed with a vertical scale length of 2.5 km or 10 km. Though the result with a 2.5-km vertical scale length (Fig. 15e) is reasonable, especially for *Po*, a 10-km vertical scale length (Fig. 15f) gives a very poor match of the synthetic to the data. Computations using these and other vertical scale lengths, not included here, suggest that the best estimate of vertical scale length is 5 ± 1.5 km. However, our estimate of vertical scale length is based on modelling up to a frequency of 15 Hz. Since the data contain energy up to 25 Hz (see Fig. 2), modelling to higher frequencies might have resulted in a lower estimate of the vertical scale length or possibly have required a distribution of scale lengths. Figs 15(g) and (h) show results using model NM-3, with a 5-km vertical scale length and randomness values of $d = 1$ per cent and $d = 4$ per cent respectively. Comparison of Figs 12(c), 15(g) and 15(h) suggests that a randomness of $d = 2$ per cent matches the data better than $d = 1$ per cent or $d = 4$ per cent although the result of using $d = 4$ per cent (Fig. 15h) is reasonable. Computations using other randomness, not included here, suggest that our best estimate of mantle randomness is $2 \leq d \leq 4$ per cent.

Figure 15(i) shows the synthetic seismogram for model NM-3, homogeneous below the top of the low-velocity, low- Q zone of the upper mantle, and Fig. 15(j) shows the synthetic for the same model with the low-velocity, low- Q zone completely removed by continuing the lid velocity gradients down through the mantle. In both synthetics we used the same upper mantle randomness (2 per cent, 5 km) as in model NM-3 of Fig. 12. Comparison of Figs 12(c) and 15(i) suggests that when the model is terminated at the top of the LVZ, the quality of the *Po* coda is poor, but *So* does not change significantly. Again, comparison of Figs 12(c) and 15(j) suggests that when the LVZ is removed from our model by continuing the gradient down to greater depths the agreement of the *Po* synthetic with the data is significantly degraded. As the overall match of synthetics to the observed data is better in Fig. 12(c) than in Figs 15(i) and (j), it

appears that we can neither terminate the model at the top of the LVZ, nor remove the LVZ altogether, and still get the same synthetics as in Fig. 12. The LVZ is a necessary part of the earth model for *Po/So* modelling.

In order to investigate the sensitivity of our results to errors in the earthquake focal mechanism the strike of the source was varied by $\pm 5^\circ$, and the dip of the source by $\pm 5^\circ$. Synthetics (not shown here) for these four sources were slightly different from the NEIS-supplied source. Since the stereographic plot of our earthquake source and receiver locations on a focal sphere (not shown here) does not indicate that we are near a nodal plane, we do not believe that the uncertainties in focal mechanism could strongly affect most of our conclusions regarding the mantle velocity structure and the *Q*. As the time function of this earthquake is not known, a unit step was used as our time domain source function. This gives a far-field wavefront with a δ -function displacement behaviour. If, as seems likely, the actual source were more complicated as a result, say, of multiple smaller events, then the effect would be to make the coda of our synthetics slightly more dense and to improve the agreement of the synthetic and the observation in Fig. 12.

Finally, the similarity in synthetics up to 0.2 Hz computed with the non-random and random versions of NM-3 shown in Figs 16(a) and (b), respectively, shows that the randomness required to explain the *Po/So* coda does not significantly affect the shapes of long-period body waves.

The *Po/So* data used in this study were carefully tested for signs of hard clipping and soft clipping but no evidence of clipping could be found. However, to see how unknown clipping would affect our conclusions, look again at the comparison of synthetic with observation at the bottom of Fig. 12. If we had clipped the high amplitudes off the synthetic and then rescaled it so that its maximum amplitudes were the same as the observation then *Po* and *So* codas of the synthetic would be larger and denser and decay more slowly. In short, the clipped synthetic would resemble the observation much better than the unclipped synthetic. We conclude that the effect of unknown clipping would be an increase in the apparent randomness, and that the correct degree of randomness is within the error bounds of our estimate, $2 \leq d \leq 4$ per cent.

If the characteristic *Po/So* codas are caused by a vertically heterogeneous upper mantle then *Po/So* data give an estimate of this heterogeneity, not in a deterministic sense but rather in a statistical sense of standard deviation in percent, from a mean velocity-depth function. Both *Po* and *So* contain direct as well as converted forward scattered phases off the randomly layered mantle. For *Po*, *P* to *S* converted arrivals tend to stretch the coda to longer duration. For *So*, on the other hand, *S* to *P* converted arrivals tend to shorten the coda duration. As a result, on the seismograms, it is expected that *Po* will have a longer coda duration than the *So* (this is usually the case, even though this is not indicated by the data we have modelled). In order to match the observed *Po* and *So* amplitudes satisfactorily, it was necessary that, in the mantle, the frequency-dependent Q_S be higher than Q_P . Thus it is not surprising that the *So* signal contains higher frequencies than the *Po* signal. Our modelling experiments also suggest that the *So* coda is very sensitive to Q_S in the mantle. As an

example, in Fig. 15(k), synthetic seismograms are shown for a model similar to NM-3 of Fig. 12(a), except that in the top 20 km of the mantle Q_S is slightly less than Q_P . The poor quality of the *So* coda in Fig. 15(k) indicates that *So* is very sensitive to Q_S . A slight decrease of Q_S in a small zone of the lithosphere significantly reduces *So* amplitudes. We believe that this is the reason why *So* is often missing from seismograms.

4 PETROLOGICAL INTERPRETATION

In the previous section it was shown that *Po/So* can be modelled fairly well when the mantle is taken to be vertically heterogeneous with a 2 per cent random velocity variation. Apart from this fine structure, our velocity models are not remarkably different from other velocity models of the oceanic crust and lithosphere. The obvious question therefore arises: how can we petrologically account for such a random velocity variation in the upper mantle?

Present knowledge on the composition of the upper mantle is based on two possible mineral assemblages: (1) peridotite and (2) eclogite. Constraints on upper mantle velocity, anisotropy and density, from observations in ophiolite complexes and kimberlite pipes, tend to favour the peridotite upper mantle composition over the eclogite (e.g. Ringwood 1975). On the other hand, observed velocity jumps at the 400-km seismic discontinuity and the nearly isotropic behaviour of the upper mantle below 220 km are better explained by an eclogite assemblage (Bass & Anderson 1984; Estey & Douglas 1986). Controversy still exists regarding the possible composition of the upper mantle and we therefore consider each of the above two compositions separately. The calculations in the following paragraphs are based on isotropic (randomly oriented minerals) velocities of peridotitic and eclogitic mineral assemblages; however, our conclusions on mantle randomness would be the same if each assemblage were anisotropic due to preferentially oriented minerals.

Peridotite is mainly an olivine- and orthopyroxene-bearing rock with some garnet, clinopyroxene and other minor constituents. A typical mantle composition, garnet lherzolite, is 57 per cent olivine, 17 per cent orthopyroxene, 12 per cent clinopyroxene (diopside) and 14 per cent garnet (Bass & Anderson, 1984). Using the *P*- and *S*-wave velocities of these minerals for typical upper mantle conditions by extrapolating the experimentally determined curves in fig. 1 of Bass & Anderson (1984), the above composition yields *P*- and *S*-wave velocities of about 8.0 and 4.59 km s⁻¹ respectively. If we now use a composition of 57 per cent olivine, 10 per cent orthopyroxene and 33 per cent garnet, which is still a valid peridotitic composition, garnet harzburgite, and follow a similar procedure, we get *P* and *S* velocities of about 8.3 and 4.8 km s⁻¹ respectively. These two sets of V_P and V_S are, respectively, 2 per cent lower and higher than our mean velocities of 8.1654 and 4.7233 km s⁻¹. Therefore for a peridotite upper mantle, a 2 per cent variation in V_P and V_S can easily be achieved by varying slightly the relative proportion of its constituents.

Eclogite is a garnet-clinopyroxene-bearing rock with some olivine and orthopyroxene and other minor minerals. A composition which may be typical of upper mantle is olivine 16 per cent, orthopyroxene 3 per cent, garnet 37 per

cent, diopside 23 per cent and jadeite 21 per cent. Following the procedure described in the previous paragraphs, this composition yields $V_P = 8.16 \text{ km s}^{-1}$ and $V_S = 4.72 \text{ km s}^{-1}$ under the conditions of the upper mantle. If this composition is changed to olivine 16 per cent, orthopyroxene 3 per cent, garnet 30 per cent, diopside 30 per cent and jadeite 21 per cent then V_P and V_S drop by 2 per cent, whereas if the composition is changed to olivine 16 per cent, orthopyroxene 3 per cent, garnet 44 per cent, diopside 16 per cent and jadeite 21 per cent, then V_P and V_S rise by 2 per cent.

It can be seen that randomness in mantle velocities is easily achieved by slightly varying the mineral composition of either a peridotite or an eclogite upper mantle model. Such a variation is quite probable (Anderson, D. L., personal communication). Conventional seismic methods used so far in the study of the structure of the upper mantle will fail to detect this fine-scale structure because of their relatively low resolving power.

It is generally believed that upper mantle anisotropy is due to preferentially aligned olivine and orthopyroxene crystals. Can the random layering, suggested by our studies, be another cause of upper mantle anisotropy? A method for the calculation of long-wavelength anisotropic elastic constants from periodic sequences of thin isotropic layers was given by Schoenberg (1983). The most anisotropic version of our random mantle model that is possible with a 2 per cent standard deviation is a periodic sequence of two thin layers having velocities $2\sqrt{3}$ per cent less and $2\sqrt{3}$ per cent more, respectively, than the mean mantle velocities. Calculations following Schoenberg (1983) indicate that this maximum anisotropy is about 0.2 per cent and that to obtain the long-wavelength anisotropy of 2 per cent observed by Anderson & Regan (1983), it is necessary to have a randomness at least as high as $d = 6$ per cent in the upper mantle. As noted earlier, our best estimate of mantle randomness is $2 \leq d \leq 4$ per cent. Using a similar procedure with $d = 4$ per cent randomness, the maximum anisotropy is about 1 per cent. Thus the random layering required to satisfy Po/So observations also contributes to upper mantle anisotropy in a small but significant way.

5 DISCUSSION

In the previous sections, it has been shown that the Po/So can be well modelled using an upper mantle with a small random component of velocity. We have also noted that such randomness in the upper mantle is petrologically feasible, either from a peridotite or an eclogite mantle mineralogy. Our model NM-3, which gives the best match of the synthetics to the observed data is characterized by a high-velocity, high- Q lithosphere with a gentle gradient in the P and S velocities, followed by a low-velocity, low- Q zone, followed by a high-velocity, high- Q mantle (Fig. 13a). While the LVZ for P -waves extends from 60 km below Moho down to about 85 km, for S -waves it continues further down to a depth of 160 km below Moho. It has been a common observation from surface-wave studies and other studies that there exists a global LVZ below the oceans and sometimes below the continents, and that this LVZ is generally better developed for S -waves than for P -waves. It has also been observed that this zone is usually present from

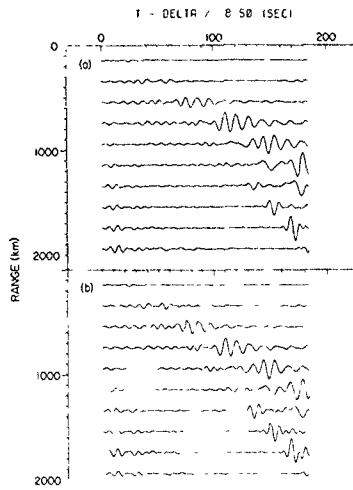


Figure 16. Synthetic seismograms up to a frequency of 0.2 Hz using (a) non-random model NM-3 and (b) random model NM-3.

60 to 200 km below the Moho. Descriptions of the LVZ can be found in Dorman, Ewing & Oliver (1960), Burdick & Helmberger (1978), Given & Helmberger (1980) and Bott (1982). In view of the above, the model NM-3 does not contradict what is normally observed globally. The only departure of the model from more standard earth models is the upper mantle randomness, required to explain the Po/So coda. As we have seen earlier (see Fig. 16), the long-period waves used to obtain the structure of the Earth's deep interior would fail to detect such fine structure except indirectly as an apparent transverse isotropy. However Po/So waves, because of their high frequency content, are able to directly sense this detailed structure.

The fine-scale vertical variation in mantle velocities can be different at different ranges, but if the statistics of the variation are range independent then a single version may be used for all ranges. The error inherent in this procedure is the lack of scattering from one ray parameter into another. Rays travelling near the horizontal in a mantle containing thin-lens heterogeneities will be deflected away from the horizontal into lower values of ray parameter and non-minimum time paths. These deflected rays, and the energy they carry, are missing from all our synthetics. Their absence may be the reason that the codas of the Po/So synthetic in Fig. 12(c) fall off more rapidly than the codas in the data trace. Also, a 3-D scattering structure might produce the same amount of scattered energy with less than a 2 to 4 per cent velocity variation.

In all our computations a unit step was used as our time domain source function. This gives a far-field wavefront with a delta function displacement behaviour. But, it is likely that the time behaviour of the actual source is far more complicated. How will such complicated source-time

behaviour affect our conclusions? If the source duration is about 1–5 s long, such a source will make the coda of our synthetic slightly denser, which will improve the agreement of the synthetic with the data. If the source duration is 10–30 s long, then the *Po/So* coda will be long even if the mantle is smooth. Near-source observations on land using short-period instruments indicate that the source duration at high frequencies can sometimes be as long as 30 s. Although source complexity and near-source scattering undoubtedly make some contribution to *Po/So* codas, this contribution must be small in comparison to the contribution of scattering effects along the path of propagation. If source complexity were the dominant effect then *Po* and *So* codas would not exhibit the characteristic build-up and decay rates observed for many different source mechanisms in different regions of the world (Brandsdottir 1986). Furthermore if *Po/So* codas were due largely to source complexity then the coda build-up and decay rates would not decrease with increasing source distance, which they are observed to do.

Another point which must be noted regarding the behaviour of the source is its spectral characteristics. In all our computations, we assumed that the far-field amplitude spectrum of our earthquake source was flat within the band of interest. However it is known (see e.g. Kasahara 1981) that the amplitude spectrum of an earthquake source is flat only below a certain frequency, known as the corner frequency (Brune 1970). Beyond this corner frequency the amplitude spectrum decays rapidly with increasing frequency. This behaviour of the source will affect our estimates of Q_p and Q_s as functions of frequency. Because of the corner frequency effect, the source used in our computations probably contains more energy at higher frequencies than the actual source. As a result, the Q 's which give the best fit of the synthetic to the observed data will be lower than the true Q 's for frequencies above the corner frequency and larger than the true Q 's for frequencies below the corner frequency. At first glance, this appears to explain why our estimates of Q are higher, at low frequency, and lower, at high frequency, than those obtained by Butler *et al.* (1987). However, our estimates of Q , when corrected for a corner frequency of 1 Hz, appear to be much higher, at high frequency, than those obtained by Butler *et al.* (1987). In fact, these differences are well explained by comparing the apparent Q 's of our synthetic record sections with the apparent Q 's measured from data by Butler *et al.* (1987).

Although many researchers have believed that the apparent Q 's estimated from the data are close to the intrinsic Q 's, it has never been established that this is indeed the case. As for each model we always computed a full synthetic record section out to offsets of 2000 km (e.g. Fig. 12b), instead of a single seismogram at the distance of interest, we were able to estimate apparent Q 's from our synthetic record sections and compare these apparent Q 's with the intrinsic Q values used to compute them. To do this, we corrected each record section for geometrical spreading, filtered the spreading corrected record section with a narrow-band Hanning window centred at the frequency of interest, and then computed the envelope function of the filtered output (Fig. 17a). Next, the amplitude of the envelope was estimated as a function of range for different group velocities. For example, the lines

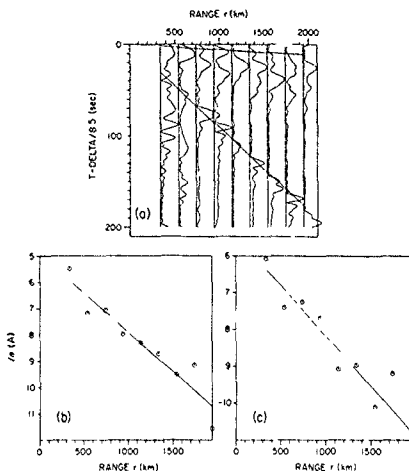


Figure 17. (a) Envelope functions for a frequency $f = 2$ Hz, computed from the record section of Fig. 12(b). The lines correspond to the arrival times for 8.1 and 4.7 km/s⁻¹ group velocities. (b) $\ln(A)$ versus r plot, where A is the amplitude and r is the range, for a group velocity of 8.1 km/s⁻¹. (c) Similar to (b) but for a group velocity of 4.7 km/s⁻¹.

drawn across Fig. 17(a) correspond to group velocities of 8.1 and 4.7 km/s⁻¹. To estimate the amplitudes corresponding to different group velocities, the envelope function was averaged at each range over ten samples centred around the sample number closest to the arrival time of the particular group velocity. Having obtained the amplitude, A , as a function of range, r , and group velocity, v , for a frequency, f , we used the relation $A \propto \exp(-\pi f r / Qv)$ to compute the apparent Q for that group velocity and frequency from the slope of the $\ln(A)$ versus r plot (Figs 17b and c). To estimate Q_p , we averaged the Q values from group velocities in the range of 8.2–7.5 km/s⁻¹ and to estimate Q_s , we averaged the Q values from group velocities in the range of 4.8–4.6 km/s⁻¹. Comparison of our estimates of apparent Q_p and Q_s with the intrinsic Q_p and Q_s used to compute the record sections indicates the following:

- (1) For all models, apparent Q 's and intrinsic Q 's vary together, that is, apparent Q_p and Q_s increased when the intrinsic Q_p and Q_s used in computing the synthetic seismograms were increased.
- (2) For the best models, such as model NM-3, apparent Q_p and Q_s are lower, below $f = 5$ Hz, and higher, above $f = 5$ Hz, than the intrinsic Q_p and Q_s of the lid. For example, at 2 Hz, $Q_p^{\text{app}} = \frac{1}{2} Q_p^{\text{int}}$ and $Q_s^{\text{app}} = \frac{1}{3} Q_s^{\text{int}}$. On the other hand, at 12 Hz, $Q_p^{\text{app}} = 2 Q_p^{\text{int}}$ and $Q_s^{\text{app}} = 1.3 Q_s^{\text{int}}$.
- (3) Apparent Q_p and Q_s estimated from our best model NM-3 (Fig. 12) agree with Q_p and Q_s obtained by Butler *et al.* (1987), to within 10 per cent throughout the 2 to 12 Hz band. Where differences approached 10 per cent our Q 's were higher.

Not surprisingly, our results indicate that apparent Q is not intrinsic Q . The fact that the apparent Q 's obtained from our best model NM-3 agree so well with the Q 's obtained by Butler *et al.* (1987) suggests that our intrinsic Q values are probably correct.

This last point is important, for without a relation between intrinsic and apparent Q our conclusions would be based on the analysis of a single seismogram. For example, in our best model, NM-3 of Fig. 12(a), if we change the mantle C_p and Q_s so that the relative Po to So amplitudes are preserved, then we may still get a good fit of the synthetic to the data for a model with a completely different Q structure than that of model NM-3. To see this in more detail, note that the amplitude ratio A_p/A_s , for P- and S-wave displacement fields at a range r and at a frequency f is given by

$$\frac{A_p}{A_s} = \exp \left[-\pi f r \left(\frac{1}{Q_p V_p} - \frac{1}{Q_s V_s} \right) \right], \quad (2)$$

where V_p and V_s stand for the P- and S-wave velocities, respectively. In order to have A_p/A_s constant at a range r , so that we get the same Po/So amplitude on our computed seismogram, we must have

$$\frac{1}{Q_p V_p} - \frac{1}{Q_s V_s} = \text{constant}, \quad (3)$$

which means

$$dQ_s = \frac{1}{\sqrt{3}} \frac{Q_s^2}{Q_p^2} dQ_p, \quad (4)$$

assuming a Poisson solid with $V_p/V_s = \sqrt{3}$. Thus, from our estimates of Q_p and Q_s , we can generate a new set of Q_p and Q_s from equation (3) above and still preserve the relative Po/So amplitude at our distance of interest. When we did this by cutting Q_p in half, and adjusting Q_s in our model NM-3, the computed synthetic (not shown here) did not agree as well with the data in Fig. 12(c). Although it is possible that some other set of mantle velocities and Q structures would model our single seismogram, we have not been able to find other structures that give record sections whose apparent Q 's agree so well with Butler *et al.*'s (1987) measurements of apparent Q . Nevertheless, in order to improve upon our estimates, it would be desirable to directly model with synthetic seismograms the same data set used by Butler *et al.* That data set was gathered in 1981 by Walker & McCreery (1987) using a 1500-km linear hydrophone array and a magnitude (m_b) 6.6 earthquake at a distance of 2740 km from the nearest array element. The work summarized in this paper started as a feasibility study for the analysis of this larger data set, for the reason that 15-Hz synthetic seismograms are far more economical to compute for source-receiver offsets of 1000 km than for source-receiver offsets of 3000 km. Modelling of this larger data set will almost certainly improve the precision of our estimates of mantle velocities, Q structure and heterogeneity.

ACKNOWLEDGMENTS

We are grateful to Fred Duennel for providing us with the OSS IV data, to Dan Walker for many helpful

conversations about Po/So, and to Don Anderson for helpful discussions of mantle velocities and their variability. Rhett Butler, Fred Duennel, Joe Gettrust, John Orcutt, Paul Richards, Tom Sereno, and an anonymous reviewer gave many helpful comments on the original manuscript. Development of the software used in this project was supported by ONR. The computations were carried out at the San Diego Supercomputer Center with support from NSF contracts EAR 85-18146 and EAR 86-07460. The gap between submission and acceptance dates is the responsibility of the authors, not *GJI*, nor the editor, whose patience is gratefully acknowledged. Hawaii Institute of Geophysics contribution no. 2201.

REFERENCES

- Anderson, D. L. & Regan, J., 1983. Upper mantle anisotropy and the oceanic lithosphere, *Geophys. Res. Lett.*, **10**, 841-844.
- Asada, T. & Shumamura, H., 1976. Observations of earthquakes and explosions at the bottom of the Western Pacific: structure of oceanic lithosphere revealed by longshot experiment, *AGU Geophys. Mono.*, pp. 135-153, eds Sutton, G. H., Manghant, M. H. & Moberly, R., AGU, Washington, DC.
- Bass, J. & Anderson, D. L., 1984. Composition of the upper mantle: Geophysical tests of two petrological models, *Geophys. Res. Lett.*, **11**, 237-240.
- Bath, M., 1966. Propagation of Sn and Pn to teleseismic distances, *Pure appl. Geophys.*, **64**, 19-30.
- Barazangi, M., Isacks, B. & Oliver, J., 1972. Propagation of seismic waves through and beneath the lithosphere that descends under the Tonga Island Arc, *J. geophys. Res.*, **77**, 952-958.
- Bibee, L., 1983. Propagation studies in the West Philippine Sea. A long line refraction experiment; Ocean Acoustics Program summary for FY82, ed McKisic, J. M., 88-89, Environmental Sciences Directorate, Office of Naval Research, Washington D C.
- Brandsdottir, B., 1986. Precise measurements of coda buildup and decay rates of western Pacific P, Po and So phases and their relevance to lithosphere scattering, *MSc thesis*, Oregon State University, Corvallis, Oregon.
- Bott, M. H. P., 1982. *The interior of the earth: its structure, constitution and evolution*, Elsevier, Amsterdam.
- Brune, J. N., 1970. Tectonic stress and the spectra of seismic shear waves from earthquakes, *J. geophys. Res.*, **75**, 4997-5009.
- Burdick, L. J. & Helmberger, D. V., 1978. The upper mantle P velocity structure of the western United States, *J. geophys. Res.*, **83**, 1669-1712.
- Butler, R., 1985. Anisotropic propagation of P- and S-waves in the western Pacific lithosphere, *Geophys. J. R. astr. Soc.*, **81**, 89-101.
- Butler, R., 1986. Regional seismic observations of the Ontong Java plateau and east Mariana Basin, *Mar. geophys. Res.*, **8**, 27-38.
- Butler, R., 1987. A seismic absorption band in the western Pacific lithosphere, *Bull. seism. Soc. Am.*, **77**, 266-269.
- Butler, R., McCreery, C. S., Frazer, L. N. & Walker, D. A., 1987. High frequency seismic attenuation of oceanic P- and S-waves in the Western Pacific, *J. geophys. Res.*, **92**, B2, 1383-1396.
- Cessaro, R. K. & Duennel, F., 1987. Regional earthquakes recorded by ocean bottom seismometers (OBS) and an ocean sub-bottom seismometer (OSS IV) on leg 88, *Int. Rep. DSDP*, Washington, **88**, 129-145.
- Dorman, J., Ewing, M. & Oliver, J., 1960. Study of shear-velocity distribution in the upper mantle by mantle Rayleigh waves, *Bull. seism. Soc. Am.*, **50**, 87-115.
- Duennel, F. & Mallick, S., 1985. High quality OBS refraction data modelled by reflectivity synthetics, (abstract), *EOS, Trans. Am. geophys. Un.*, **66**, 956.

- Duënniebert, F., Lienert, B., Cessaro, R., Anderson, P. & Mallick, S., 1987. Controlled source seismic experiment at hole 581-C. *Int. Rep. DSDP*, Washington, **88**, 105-125.
- Dziewonski, A. M. & Anderson, D. L., 1981. Preliminary reference earth model, *Phys. Earth planet. Inter.*, **25**, 297-356.
- Estey, L. & Douglas, B. J., 1986. Upper mantle anisotropy: a preliminary model, *J. geophys. Res.*, **91**, 11393-11406.
- Frazer, L. N., 1978. Synthesis of shear coupled PL, *PhD thesis*, Princeton University.
- Frazer, L. N. & Gettrust, J. F., 1984. On a generalization of Filon's method and the computation of the oscillatory integrals of seismology, *Geophys. J. R. astr. Soc.*, **76**, 461-481.
- Fuchs, K. & Müller, G., 1971. Computation of synthetic seismograms with the reflectivity method and comparison with observations, *Geophys. J. R. astr. Soc.*, **23**, 417-433.
- Fuchs, K. & Schultz, K., 1976. Tunneling of low frequency waves through the subcrustal lithosphere, *J. Geophys.*, **42**, 175-190.
- Gettrust, J. F. & Frazer, L. N., 1981. A computer model study of the propagation of the long range Pn phase, *Geophys. Res. Lett.*, **8**, 749-752.
- Given, J. W. & Helmberger, D. V., 1980. Upper mantle structure of northwestern Eurasia, *J. geophys. Res.*, **85**, 7183-7194.
- Hart, R. & Press, F., 1973. Sn velocities and the composition of the Lithosphere in the regionalized Atlantic, *J. geophys. Res.*, **78**, 707-711.
- Kasahara, K., 1981. *Earthquake mechanics*, Cambridge University Press, Cambridge, UK.
- Kind, R., 1974. Long range propagation of seismic energy in the lower Lithosphere, *J. Geophys.*, **40**, 189-502.
- Linahan, D., 1940. Earthquakes in the West Indian region, *EOS, Trans. Am. geophys. Un.*, **21**, 229-232.
- Liu, H.-P., Anderson, D. L., & Kanamori, A., 1976. Velocity dispersion due to anelasticity: implications for seismology and mantle composition, *Geophys. J. R. astr. Soc.*, **47**, 41-58.
- Mallick, S. & Frazer, L. N., 1985. Practical aspects of reflectivity modeling, (abstract), *EOS, Trans. Am. geophys. Un.*, **66**, 981.
- Mallick, S. & Frazer, L. N., 1986. Po/Po synthetics for a variety of oceanic models, (abstract), *EOS, Trans. Am. geophys. Un.*, **67**, 1082.
- Mallick, S. & Frazer, L. N., 1987. Practical aspects of reflectivity modeling, *Geophysics*, **52**, 1355-1364.
- Mallick, S. & Frazer, L. N., 1988. Rapid computation of multi-offset vertical seismic profile synthetic seismograms for layered media, *Geophysics*, **53**, 479-491.
- Mantovani, E., Schwab, F., Liao, H. & Knopoff, L., 1977. Telesismic Sn: a guided wave in the mantle, *Geophys. J. R. astr. Soc.*, **51**, 709-726.
- McCreery, C. S., 1981. High frequency Pn, Sn phases recorded by ocean bottom seismometers on the Cocos Plate, *Geophys. Res. Lett.*, **8**, No. 5, 489-492.
- Menke, W. & Richards, P. G., 1980. Crust-Mantle whispering gallery phases: a deterministic model of teleseismic Pn wave propagation, *J. geophys. Res.*, **85**, 5416-5422.
- Menke, W., 1983. A formula for the apparent attenuation of acoustic waves in randomly layered media, *Geophys. J. R. astr. Soc.*, **75**, 741-744.
- Menke, W. & Chen, R., 1984. Numerical studies of the coda falloff rate of multiply scattered waves in randomly layered media, *Bull. seism. Soc. Am.*, **74**, 5, 1605-1621.
- Mitronovas, W., Isacks, B. & Seeber, L., 1969. Earthquake locations and seismic wave propagation in the upper 250 km of the Tonga Island arc, *Bull. seism. Soc. Am.*, **59**, 1115-1135.
- Molnar, P. & Oliver, J., 1969. Lateral variations of attenuation in the upper mantle and discontinuities in the Lithosphere, *J. geophys. Res.*, **74**, 2648-2682.
- Novello-Casanova, D. A. & Butler, R., 1986. High frequency seismic coda and scattering in the Northwestern-Pacific, *Bull. seism. Soc. Am.*, **76**, 617-626.
- Oliver, J. & Isacks, B., 1967. Deep earthquake zones, anomalous structure in the upper mantle and the lithosphere, *J. geophys. Res.*, **72**, 4259-4275.
- Ouchi, T., 1981. Spectral structure of high frequency P and S phases observed by OBS's in the Mariana Basin, *J. Phys. Earth*, **29**, 305-326.
- Ouchi, T., Nagumo, S. & Koresawa, S., 1981. Ocean bottom seismometer study on the seismic activity in the Mariana Island arc region, *Bull. Earth Res. Inst. Tokyo Univ.*, **56**, 43-65.
- Phinney, R. A., 1965. Theoretical calculations of the spectrum of first arrivals in layered elastic mediums, *J. geophys. Res.*, **70**, 5107-5123.
- Phinney, R. A., Odom, R. J., & Fryer, G. J., 1988. Rapid generation of synthetic seismograms in layered media by vectorization of the algorithm, *Bull. seism. Soc. Am.*, **77**, 2218-2226.
- Ringwood, A. E., 1975. *Composition and petrology of the earth's mantle*, McGraw-Hill, New York.
- Schoenberg, M., 1983. Reflection of elastic waves from periodically stratified media with interfacial slip, *Geophys. Prosp.*, **31**, 265-292.
- Sen, M. K., Frazer, L. N., Mallick, S. & Chapman, N. R., 1988. Analysis of multipath sound propagation in the ocean near 49°N 128°W, *J. acoust. Soc. Am.*, **83**, 588-597.
- Sereno, T. & Orcutt, J., 1985. Synthesis of realistic oceanic Pn wavetrains, *J. geophys. Res.*, **90**, 12755-12776.
- Sereno, T. & Orcutt, J., 1987. Synthetic Pn and Sn phases and the frequency dependence of Q of oceanic lithosphere, *J. geophys. Res.*, **92**, 3541-3566.
- Shumamura, H., 1984. Anisotropy in the oceanic lithosphere of the Northwestern Pacific basin, *Geophys. J. R. astr. Soc.*, **76**, 253-260.
- Shumamura, H. & Asada, T., 1953. Velocity anisotropy extending over the entire depth of the oceanic lithosphere, in *Geodynamics of the Western Pacific Indonesian region*, Geodyn. Ser., Vol. 11, pp. 121-125 eds Hilde, T. W. C. & Uyeda, S., AGU, Washington, DC.
- Shurbet, D. H., 1962. The high frequency P and S waves from the West Indies, *Bull. seism. Soc. Am.*, **52**, 957-962.
- Shurbet, D. H., 1964. The high frequency S phase and structure of the Upper Mantle, *J. geophys. Res.*, **59**, 2065-2070.
- Stephens, C. & Isacks, B. L., 1977. Towards an understanding of Sn normal modes of Love waves in an oceanic structure, *Bull. seism. Soc. Am.*, **67**, 69-78.
- Strick, E., 1967. The determination of Q, dynamic viscosity, and transient creep curves from wave propagation measurements, *Geophys. J. R. astr. Soc.*, **13**, 197-218.
- Strick, E., 1970. A predicted pedestal effect for pulse propagation in constant Q solids, *Geophysics*, **35**, 387-403.
- Sutton, G. H. & Walker, D. A., 1972. Oceanic mantle phases recorded on seismographs in the Northwestern Pacific at distances between 7° and 40°, *Bull. seism. Soc. Am.*, **62**, 631-655.
- Talander, J. & Bouchon, M., 1979. Propagation of high frequency Pn waves at great distances in the Central and South Pacific and its implications for the structure of the lower lithosphere, *J. geophys. Res.*, **84**, 5613-5619.
- Walker, D. A., 1977. High frequency Pn and Sn phases recorded in the Western Pacific, *J. geophys. Res.*, **82**, 3350-3360.
- Walker, D. A., 1981. High frequency Pn, Sn velocities: some comparisons for the Western, Central and South Pacific, *Geophys. Res. Lett.*, **8**, 207-209.
- Walker, D. A., 1982. Oceanic Pn/Sn phases: a qualitative explanation and reinterpretation of the T-phase, *Hawaii Inst. Geophys. rep.*, **HIG-82-6**.
- Walker, D. A., 1984. Deep ocean seismology, *EOS, Trans. Am. Geophys. Un.*, **65**, 2-3.
- Walker, D. A. & Sutton, G. H., 1971. Oceanic mantle phases

recorded on hydrophones in the North Western Pacific at distances between 9 and 40, *Bull. seism. Soc. Am.*, **61**, 65-78

Walker, D. A., McCreery, C. S., Sutton, G. H. & Dunnebie, F. K., 1978. Spectral analyses of high frequency *Pn* and *Sn* phases observed at great distances in the western Pacific, *Science*, **199**, 1333-1335.

Walker, D. A., McCreery, C. S. & Sutton, G. H., 1983. Spectral characteristics of high frequency *Pn*, *Sn* phases in the Western Pacific, *J. geophys. Res.*, **88**, 4289-4298.

Walker, D. A. & McCreery, C. S., 1985. Significant unreported earthquakes in aseismic regions of the western Pacific, *Geophys. Res. Lett.*, **12**, 433-436.

Walker, D. A. & McCreery, C. S., 1987. Po/So phases propagation velocity across a 1500-km-long, deep ocean hydrophone array, *J. Phys. Earth*, **35**, 111-126.

Wenzel, F., Sandmeier, K. & Wäde, W., 1987. Properties of the lower crust from modeling refraction and reflection data, *J. geophys. Res.*, **92**, 11575-11583.

Maximizing Matched Field Processing Output Used in a New Approach to Ocean Acoustic Tomography

A. Tolstoy
Acoustics Division
Naval Research Laboratory
Washington, DC 20375

L. N. Frazer
Hawaii Institute of Geophysics
University of Hawaii
Honolulu, Hawaii 96822

Abstract: A new approach to ocean acoustic tomography uses matched field processing for narrow band, low frequency sources distributed around the region perimeter and detected on widely distributed vertical arrays. A key component to the success of this new approach is an algorithm to compute "the global maximum" of the processor outputs over the very large set of candidate environments. In this paper we present an algorithm based on the "back propagation" algorithms used in medical tomography but modified to allow for non-uniform values along each source-receiver path and weighted according to the length of the path segment of interest. Computational results to date show that the algorithm can result in very accurate and efficient tomographic solutions but can also stall unpredictably.

1. INTRODUCTION

Ocean acoustic tomography is a technique involving the transmission of acoustic fields through an ocean region and subsequently inferring the 3-D sound-speed profiles of the region by examining those fields. Over the last decade ocean tomography experiments have shown that examination of the acoustic multipath arrivals interpreted in terms of ray theoretic models can be highly effective (Munk and Wunsch, 1979; Behringer et al., 1982; Cornuelle et al., 1989). However, such an approach requires "high" frequency signals (above 100 Hz), and so results will be degraded by such factors as uncertainties in the source/receiver locations, internal waves and tides, rough surface scattering, etc. The measurement process itself can be extremely time-consuming requiring weeks at sea to navigate the perimeter and send signals through the region. In addition, the use of high frequencies which attenuate rapidly as a function of range limits the size of the regions which can be sampled. More generally, working with data in the time domain requires high time resolution receivers to distinguish arrivals and to detect changes in those arrivals which result

from sound-speed variability. Our new technique examines interference patterns across vertical arrays of hydrophones for single frequency (not time domain) low frequency data (10-30 Hz) modeled by highly accurate normal mode methods. The sources will be explosive shots dropped from an airplane flying around the perimeter, and so experimental time will decrease from weeks to days. The new technique will effectively transfer the burden from intense oceanographic surveys to intense computer demands.

2. APPROACH

The essence of the new approach is to find the family of sound-speed profiles which maximizes the matched field processing (MFP) power computed for each vertical array receiving signals from the known shot sources. That is, signals received at the arrays are cross-correlated with modeled signals which have propagated through candidate environments, and we seek to maximize those correlations. If the problem is properly posed, i.e., if we impose sufficient constraints, then the maximum MFP power will occur only for the true environment. (See Bucker, 1976, and Fizzell, 1987) for details about MFP.)

The first stage of the process is to characterize the environment in as few parameters as possible. Oceanographers have developed a method for deriving efficient basis functions, known as empirical orthogonal functions (EOFs), from measured data (Davis, 1976). Consequently, an ocean region might be very accurately described in terms of only 2 or 3 EOFs. The simulated "double eddy" environment and their associated (modified) EOFs used for the results in this paper are described in detail in Tolstoy et al., 1991.

The next stage is to grid the ocean region into cells where each cell corresponds to one sound speed profile, i.e., 2 or 3 EOF coefficients. We also need to consider the geometry of our problem: how many vertical arrays will we use and where will we deploy them? how many sources will we use and where will we drop them? For the results to be discussed here we will use four vertical arrays and 36 sources distributed as shown in Fig 1. Each array will have 28 phones spaced at 37.5 m for processing 20 Hz signals. The first phone will be just below the surface of the water and thus span the upper 1000 m of water where all the sound-speed variability is found. We assume that the sound-speed profiles at the source and array cells have been measured and their EOF coefficients are known. The complete values of the dominant EOF coefficients are shown in Fig 2.

Finally, we need an algorithm to perform the inversion, i.e., to compute the unknown EOF coefficients which maximize the MFP power at the array for all the source signals.

nes interference patterns across
time domain) low frequency data
thods. The sources will be
he perimeter, and so experimental
ue will effectively transfer the
puter demands

nily of sound-speed profiles which
mputed for each vertical array
ginals received at the arrays are
gated through candidate
is. If the problem is properly
maximum MFP power will occur
izell, 1987) for details about MFP.)

environment in as few parameters
deriving efficient basis functions,
measured data (Davis, 1976).
described in terms of only 2 or 3
ir associated (modified) EOFs used
oy et al., 1991.

where each cell corresponds to
e also need to consider the
we use and where will we deploy
drop them? For the results to be
ces distributed as shown in Fig
rocessing 20 Hz signals. The first
span the upper 1000 m of water
e that the sound-speed profiles at
OF coefficients are known. The
wn in Fig 2

rsion, i.e., to compute the
for the array for all the source

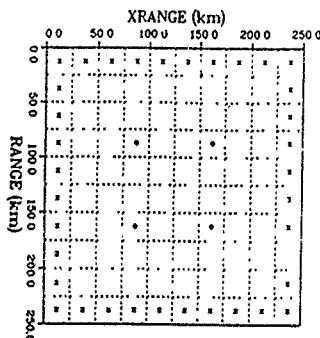


Fig. 1. Distribution of 4 arrays (indicated by •) and 36 sources at 100 m depth (indicated by *) for 10 by 10 grid covering 250 by 250 km²

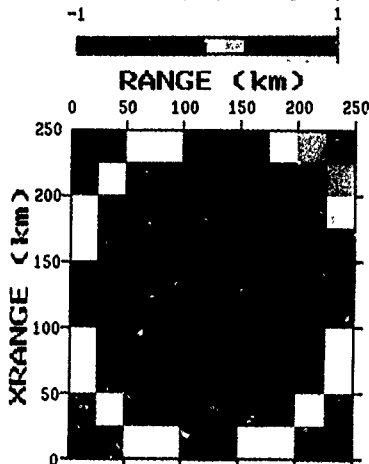


Fig 2 Plot of the dominant EOF coefficient $\beta_1(ij)$ as a function of range and cross-range. The scale has been normalized so that negative values range from -1 to 0, positive values from 0 to +1

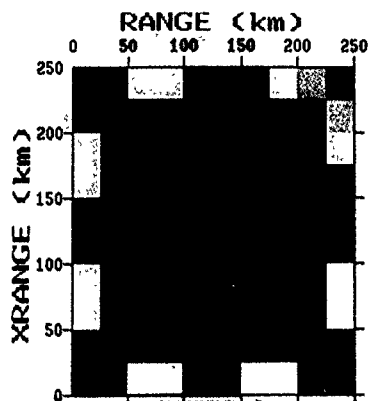


Fig. 3. Initial estimates for EOF coefficient $\hat{\beta}_1(ij)$ as a function of range and cross-range. The coefficients around the perimeter (where the sources are located) and at the arrays are known; otherwise, $\hat{\beta}_1 \approx \text{constant}$.

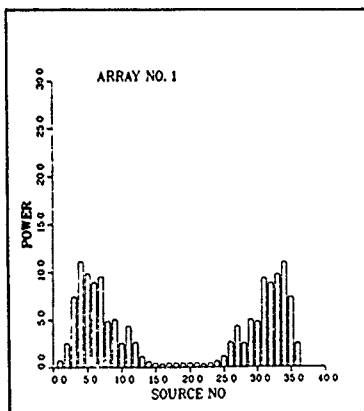


Fig. 4. Initial estimates for MFP power P_{rs} at array $r = 1$ for each source s given initial environment of Fig. 3



a function of range and
are the sources are located)
= constant.



3. THE ALGORITHM

First, we initialize our algorithm with a simple test environment. In particular, we will assume that we know the range of possible values for the EOF coefficients throughout our region and then use their mid-range values as a first estimate for all the unknown values (see Fig. 3). We know that this estimate is not very good because the MFP power computed at each array for each source is very low. In Fig. 4 we see a plot of MFP power P_{rs} for each receiver-source path for $r = 1$. The maxima should be about 28 (the number of phones).

Let $\beta_1(ij)$, $\beta_2(ij)$ denote the true EOF coefficients for the i^{th} cell. Consider the j^{th} cell, and iterate through all possible values of the EOF coefficient β_1 . Let $P_{rs}^*(ij)$ denote the maximum power found for the path from source s to array r intersecting the j^{th} cell (all other coefficients along the path are fixed), i.e.,

$$P_{rs}^*(ij) = \max_{\beta_1} P_{rs}.$$

Let $\beta_{1,rs}^*(ij)$ be the corresponding coefficient, and $\Delta_{rs}(ij)$ be the length of the path through the cell. Then, define the new coefficient estimate by

$$\hat{\beta}_1(ij) = \frac{\sum_{rs} \beta_{1,rs}^*(ij) \Delta_{rs}(ij)}{\sum_{rs} \Delta_{rs}(ij)}$$

Next, consider β_2 and repeat the procedure. Then, proceed to the next cell. When all cells have been processed (one sweep), repeat from the first cell (note that all the cells may have changed their coefficients and so path contributions from the non j^{th} cell will have changed). For the results presented here, the process was stopped when the total power $P_{\text{total}} = \sum_{rs} P_{rs}$ was no longer increasing.

For the example discussed, we obtained excellent results for 31 sweeps with a maximum sound-speed error everywhere of less than 0.2 m/sec. However, there were other array configurations for which the algorithm stalled, i.e., stopped before giving good results. So, we also considered variations of the algorithm by selecting the $\beta_{1,rs}^*(ij)$ which simply maximize $\sum_{rs} P_{rs} \Delta_{rs}$, $\sum_{rs} \sqrt{P_{rs}} \Delta_{rs}$, or $\sum_{rs} P_{rs} \Delta_{rs}^2$. In general, we found that these variations sometimes improved results over the original but sometimes did not, and were also prone to stalling.

4. CONCLUSIONS

We conclude that efficient characterization of the environment, i.e., through the use of (modified) empirical orthogonal functions, plus careful source/array geometry, can result in highly accurate estimates of the 3-D sound speed environment (Fig. 5).

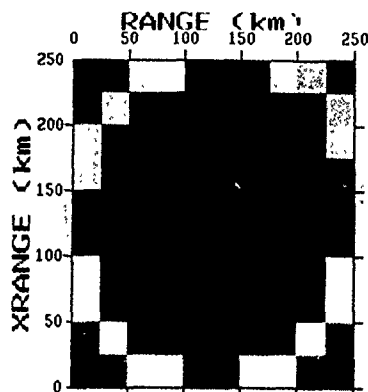


Fig 5 Final estimates for EOF coefficient $\hat{\beta}_1(i)$ as a function of range and cross range. Compare to Fig 2

In particular, we saw that 4 vertical arrays spanning the upper 1000 m of water and placed in the interior of the region of interest with shots distributed every 25 km along the perimeter resulted in maximum errors less than 0.2 m/sec for our 250 km per side square region and for the frequency 20 Hz. However, the algorithm and variations on it developed for the inversion can stall. We are presently working to find a remedy for this difficulty.

REFERENCES

- [1] Behringer, D., Birdsall, T., Brown, M., Cornuelle, B., Heinmiller, R., Knox, R., Metzger, K., Munk, W., Spiesberger, J., Spindel, R., Webb, D., Worcester, P., and Wunsch, C., A demonstration of ocean acoustic tomography, *Nature*, vol. 299, 1982, pp. 121-125.
- [2] Buckner, H. P., Use of calculated sound fields and matched field detection to locate sound sources in shallow water, *J. Acoust. Soc. Am.*, vol. 59, 1976, pp. 368-373.
- [3] Cornuelle, B., Munk, W., and Worcester, P., Ocean acoustic tomography from ships, *J. Geophys. Res.*, vol. 94, 1989, pp. 6232-6250.
- [4] Davis, R. E., Predictability of sea surface temperature and sea level pressure anomalies over the North Pacific Ocean, *J. Phys. Ocean.*, vol. 6, 1976, pp. 249-266.
- [5] Fizeff, R. G., Application of high resolution processing to range and depth estimation using ambiguity function methods, *J. Acoust. Soc. Am.*, vol. 82, 1987, pp. 606-613.
- [6] Munk, W. H., and Wunsch, C., Ocean acoustic tomography: a scheme for large scale monitoring, *Deep Sea Res.*, vol. 26A, 1979, pp. 123-161.
- [7] Tolstoy, A., Duchook, O., and Frazer, L. N., Acoustic tomography via matched field processing, *J. Acoust. Soc. Am.*, vol. 89, 1991, pp. 1119-1127.

SEDIMENT Q_β FROM SPECTRAL RATIOS OF CONVERTED SHEAR REFLECTIONS

Peter D. Bromirski, L. Neil Frazer, and Fred K. Duennebieer
GG/SOEST/University of Hawaii at Manoa
2525 Correa Road
Honolulu, HI 96822

ABSTRACT. Spectral ratios of the basement-converted shear reflections PS and PSSS on refraction seismograms are used to estimate the sediment shear quality factor Q_β . The spectral ratio method is tested on a variety of synthetic seismograms computed using the constant- Q dispersion relation of Kjartansson (1979). Q_β estimates from synthetic seismograms were within 15% of the true Q_β for all sediment models tested, both in the presence of added noise, and with the use of a complicated source function. Tests on synthetic seismograms computed from realistic sediment models, composed of alternating layers with high impedance contrast between them, indicate that apparent attenuation due to intrabed multiples is not a significant loss mechanism between 5 and 15 Hz. The method is applied to 9 Hz horizontal component airgun-OBS refraction data collected over 356 m of primarily high-porosity biosiliceous clay in 5467 m of water near 44°N, 160°E. Effective Q_β for the sediment column was found to be 107 ± 15 ($\alpha = 0.255 \pm 0.03$ dB/λ) at 9 Hz.

1. Introduction

The importance of sediment shear parameters on acoustic propagation loss in the ocean has been identified by several studies (e.g. Vidmar, 1980; Hughes et al., 1990). Direct measurement of sediment shear attenuation parameters has been limited by the lack of satisfactory ocean bottom shear sources and by problems in ocean bottom seismometer (OBS) design (Sutton and Duennebieer, 1987). Here the shear source problem is circumvented by analysing converted shear reflections from the top of the crust (basement) observed on OBS horizontal component refraction seismograms.

The OBS data used in this study were obtained in conjunction with the OSS IV Experiment on DSDP Leg 88 near Hole 581C. The data were recorded by an Hawaii Institute of Geophysics isolated sensor ocean bottom seismometer, OBS Y-220, from a large (30-liter) airgun towed by Soviet research vessel Dimitri Mendeleev at a depth of 20 m. Single-channel reflection data show pelagic sediments smoothly draped over ocean crust with a 2-way travel time of about 0.35 s. Holes drilled at Site 581 encountered roughly 350 m thick continuous pelagic siliceous clays with occasional chert bands becoming numerous near basement (Duennebieer et al., 1987).

The $P + S$ travel time through the sediments is about 2.00 ± 0.02 s obtained from the

PS reflection on the horizontal data (Figure 1a). The time and distance constraints give an average sediment compressional velocity \bar{c}_p of about 1.7 km/s and an average shear velocity \bar{c}_s of 0.20 ± 0.01 km/s. The identification of the *PSSS* multiple shear reflection (Figure 1a) was the motivation for this study. The spectral ratio method was used since the *PS* and *PSSS* reflections are observed for the same source and receiver, and the shear paths are virtually the same. When the ratio of the amplitude spectra of these phases are taken, source and receiver effects cancel.

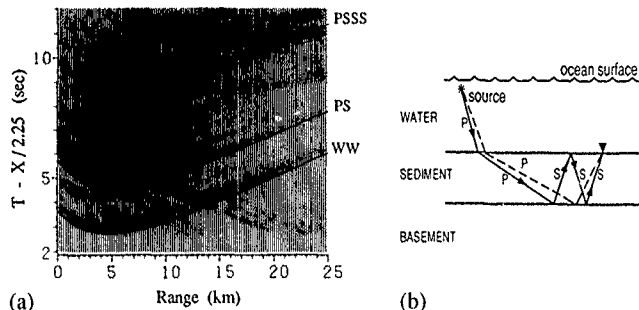


Figure 1 (a) Horizontal component OBS refraction data reduced to 2.25 km/s with travel-time curves for the water wave *WW* and the *PS* and *PSSS* reflections for a 1-layer average sediment model. (b) Raypath diagram for the *PS* (dashed) and *PSSS* (solid) reflections.

2. Effective Attenuation

Attenuation measured from field data is termed effective attenuation (α_E) as it includes contributions from both intrinsic (α_I) and apparent (α_A) attenuation. This can be expressed in terms of α or Q as

$$\alpha_E = \alpha_I + \alpha_A \quad \text{or} \quad Q_E^{-1} = Q_I^{-1} + Q_A^{-1} \quad (1)$$

Either Q_I or Q_A may be frequency-dependent. In-situ measurements indicate that Q_E is frequency-independent in the seismic band (Kanamori and Anderson, 1977).

Some attenuation mechanisms to account for intrinsic losses were presented in Toksoz and Johnston (1981). Intrinsic α_I is attributed to friction mechanisms and frame anelasticity while apparent α_A is the amplitude decay of a seismic pulse resulting from the scattering of energy by heterogeneities such as microbeds (O'Doherty and Anstey, 1971; Schoenberger and Levin, 1978; Menke, 1983). In apparent attenuation, energy is redistributed to other parts of the coda unlike α_I where energy is removed from the coda. However, its affect on spectral content is difficult to distinguish from intrinsic losses.

The time and distance constraints give an α of 1.7 km/s and an average shear velocity \bar{c}_s . The Q ratio method was used since the PS source and receiver, and the shear paths PS and SS multiple shear reflection (Figure 1b) are taken, and the shear paths PS and SS multiple shear reflection (Figure 1b) are taken, and the shear paths PS and SS multiple shear reflection (Figure 1b) are taken.

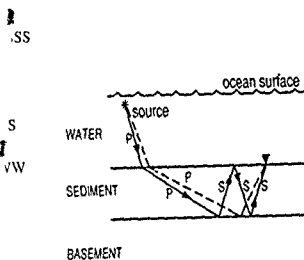


Figure 1b. Action data reduced to 2.25 km/s with travel-time corrections for PS and SS reflections for a 1-layer average Q (dashed) and PS (solid) reflections.

termed effective attenuation (α_E) as it includes parent (α_A) attenuation. This can be expressed

$$Q_E^{-1} = Q_A^{-1} + Q_I^{-1} \quad (1)$$

dent. In-situ measurements indicate that Q_E is independent of frequency (Kanamori and Anderson, 1977). The Q ratio method was used since the PS source and receiver, and the shear paths PS and SS multiple shear reflection (Figure 1b) are taken, and the shear paths PS and SS multiple shear reflection (Figure 1b) are taken, and the shear paths PS and SS multiple shear reflection (Figure 1b) are taken.

3. Spectral Ratios

The spectral ratio (SR) method uses the ratio of the amplitude spectra of different arrivals to estimate Q . Variations of the spectral ratio method have been used by Jacobson et al (1981) and Janssen et al (1985) to determine compressional Q in marine sediments. The amplitude spectrum of a vertically traveling signal multiply reflected between $z = z_0$ and at $z = z_1$ (Figure 1b) is given by

$$|A_1(\omega)| = |A_0(\omega)G(z)R| \exp[-2\alpha(z_1 - z_0)]$$

where $G(z)$ is the geometrical spreading and R contains reflection and transmission coefficients, assumed independent of frequency. In this case z_0 is the depth at the water/sediment interface and z_1 is the depth at the sediment/basement interface. We use a vertically incident converted shear phase at z_0 as our reference amplitude $A_0(\omega)$ corresponding to the PS reflection (the dashed raypath in Figure 1b) while $A_1(\omega)$ corresponds to the SS reflection. Thus, $A_0(\omega)$ includes source, receiver, and noise contributions which we assume are constant for each trace. We take the natural log of the ratio of the two spectra, and letting $2(z_1 - z_0) = T\bar{c}_s$ where T is the travel time difference between successive multiples, \bar{c}_s is the average shear wave velocity in the sediments, and $\alpha = \omega/2\bar{c}_s Q$, we have

$$\ln \left[\frac{A_1(\omega)}{A_0(\omega)} \right] = \text{const} - \left(\frac{T}{2} Q^{-1} \right) \omega \quad (2)$$

in which const is a term independent of ω that includes contributions from spreading and from reflection and transmission coefficients. Note that if Q is independent of ω , then equation (2) describes a straight line with slope $m = -\frac{T}{2} Q^{-1}$. The value of m can be determined by a least squares fit to the spectral ratios. From this slope one obtains an effective Q for any successive pair of reflected shear multiples.

Using Snell's Law for $c_p = 0.2$ km/s and $c_s = 1.5$ km/s, the shear-wave incident angle at the water/sediment interface is less than 5° , resulting in a less than 1% increase in path length from vertical and negligible S to P conversion. Note that S to P conversion affects only the const term in (2). Also, our tests with synthetic data computed by an exact method (Mallick and Frazer, 1987) recover Q_I exactly.

4. Numerical Tests on Synthetic Data

Since the data we are examining have a narrow bandwidth and since it has been widely observed that Q depends very little upon frequency within the range of frequencies observed in seismic investigations (e.g., Strick, 1967; Kanamori and Anderson, 1977), we assume Q to be independent of frequency and use the constant Q dispersion relation of Kjartansson (1979) in the computation of reflectivity synthetic seismograms.

A variety of multi-layer sediment models were used to test the accuracy of the spectral ratio method. Intrinsic Q_I for an n -layer constant- Q sediment model is given by

$$Q_I = \frac{Z_T}{\bar{c}} \left[\sum_{j=1}^n \frac{z_j}{c_j Q_j} \right]^{-1} \quad j = 1, n \quad (3)$$

where Z_T is the total thickness, \bar{c} is the average velocity for the stack of layers, and z_j , c_j , and Q_j are the thickness, phase velocity, and Q , respectively, of the j^{th} layer

Test parameters. The synthetic traces were computed with a Nyquist frequency of 40 Hz matching the OBS data sampling interval of 0.0125 s. We selected 55-point wavelets to match the length of the *PS* phase coda in the OBS data. A 10% Hanning taper was applied prior to transforming to the frequency domain. Tests showed that a 256 point window padded with zeros gave the best results. In all spectra shown, zero dB is relative to 1 (digital unit)²/Hz.

We smoothed the amplitude spectra before taking the spectral ratios using a $\frac{1}{2}, \frac{1}{2}, \frac{1}{2}$ smoothing function keeping the endpoints fixed. The argon source was modeled using a modified form of the explosive source function presented in Spudich and Orcutt (1980). All tests were performed on synthetic traces at range 0.41 km to compare with data trace 3. Sediment thickness was 356 m

TABLE 1 Model parameters used in computing the synthetic traces in Figures 2a and 2b

		c_a	Q_a	c_b	Q_b (2a)	Q_b (2b)	ρ	h (km)
water		1.5	10000	0.0	0	0	1.0	5.467
sediments	L1a	1.55	30	0.160	190	45	1.35	0.200
	L1b	1.75	30	0.295	225	70	1.75	0.156
basement		4.25	300	2.25	250	250	2.65	

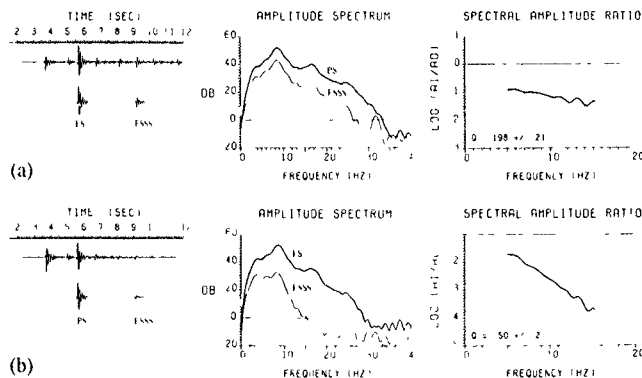


Figure 2 Synthetic traces with selected wavelets, their associated amplitude spectra and spectral ratio curves for model Q_T of (a) 200 and (b) 50

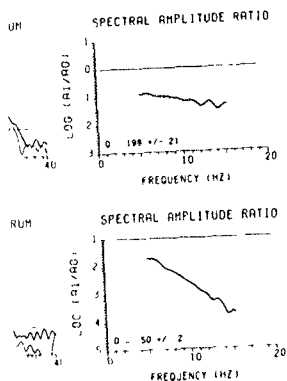
by for the stack of layers, and z_j , c_j , ρ_j , respectively, of the j^{th} layer.

ted with a Nyquist frequency of 40 25 s. We selected 55-point wavelets BS data. A 10% Hanning taper was in Tests showed that a 256 point all spectra shown, zero dB is relative

ig the spectral ratios using a $\frac{1}{2}$, $\frac{1}{2}$, $\frac{1}{2}$ o argun source was modeled using a ed in Spudich and Orcutt (1980). All 11 km to compare with data trace 3.

computing the synthetic traces in

Q_β (2a)	Q_β (2b)	ρ	h (km)
0	0	1.0	5.467
190	45	1.35	0.200
225	70	1.75	0.156
250	250	2.65	—



their associated amplitude spectra and b) 50

2-layer sediment model. Horizontal component synthetic seismograms (Figure 2a,b) were computed to test the accuracy of the method for high and low Q_β for two 2-layer models (Table 1) that differ only in Q_β . These models give $Q_\beta \approx 200$ and $Q_\beta \approx 50$ using (3). The smoothed amplitude spectra of the wavelets selected for the SR tests along with their spectral ratios are shown in Figure 2. The \pm refers to 95% confidence limits for the least squares fits to the spectral ratios, which give Q_β estimates within 5% of the model values. The differences between the two models can readily be seen in the relative amplitudes of the PS and PSSS phases, their amplitude spectra, and the slope of the spectral ratio curves. The accuracy of these SR Q_β estimates suggests that the implicit assumption of vertical raypaths is acceptable. These results also imply that layering and S to P conversion do not pose problems for this method.

Apparent attenuation. The importance of intrabed multiples in the apparent Q_A^{-1} term in (1) can be estimated by making Q_I large, which gives $Q_E^{-1} = Q_A^{-1}$. If apparent attenuation is small, then Q_A is large and (1) reduces to $Q_E = Q_I$. Synthetic seismograms were computed for realistic models containing alternating layers of high impedance contrast with layer thicknesses of $\frac{1}{2} \lambda_\beta$, for an oscillating sediment velocity structure of $c_\beta = 150$ m/s and 250 m/s with a constant shear $Q_I = 150$. This model was designed to maximize the frequency of impedance contrasts while maintaining the travel-time and path-length constraints and the average $c_\beta = 200$ m/s. If apparent attenuation is significant, the measured Q_E will be less than the model Q_I . The synthetic trace for this model is shown in Figure 3. Although the 95% confidence limits are larger than in the previous tests, the least squares fit to the spectral ratios gives a Q_β estimate within 12% of the model value. This suggests that apparent attenuation from intrabed multiples is not significant at 9 Hz and that the Q we are measuring is Q_I .

In addition to estimating the importance of Q_A , the long codas for this model also test the sensitivity of the method to interference problems due to source function length. This may explain why the 95% confidence limits are significantly larger than for the previous 2-layer sediment model tests.

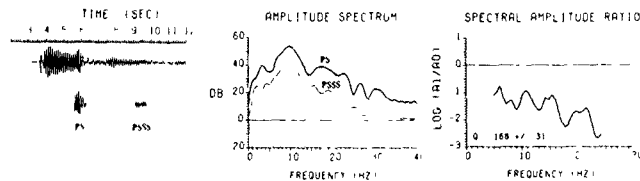


Figure 3 Synthetic trace with selected wavelets, their associated amplitude spectra and spectral ratio curve for a model with layer thickness of $1/2$ a shear wavelength

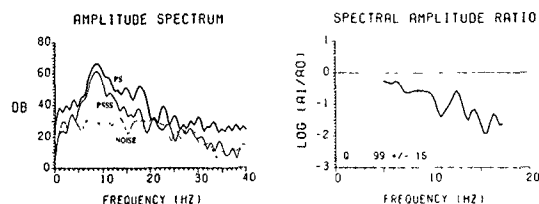


Figure 4. Amplitude spectra and spectral ratio curve for the wavelets selected in Figure 5 for data trace 3 at 0.41 km.

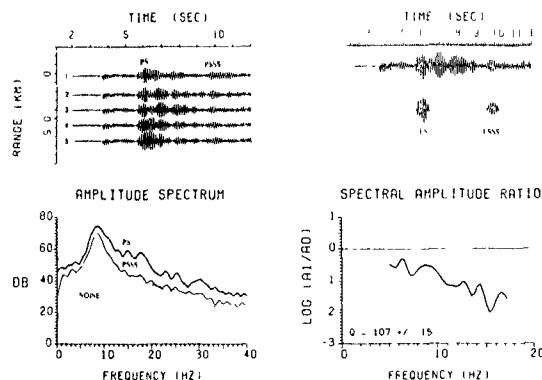
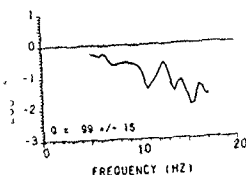


Figure 5. Lower figures are the average spectra and spectral ratio curve for the data traces 1-5 (upper left). Upper right is data trace 3 at 0.41 km with selected wavelets

TABLE 2. Results of spectral ratio analysis of data traces 1-5

Range (km)	Travel Time (s)	Bandwidth (Hz)	Q_β
0.027	3.84	[2,17]	155 ± 45
0.238	3.92	[3.5,17]	134 ± 35
0.405	3.82	[5,17]	99 ± 15
0.576	3.82	[2,13]	101 ± 32
0.747	3.83	[3,13]	63 ± 14

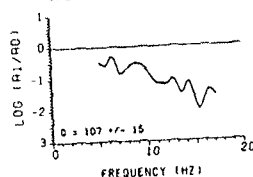
SPECTRAL AMPLITUDE RATIO



for the wavelets selected in Figure 5



SPECTRAL AMPLITUDE RATIO

1 spectral ratio curve for the data traces
1 km with selected wavelets

analysis of data traces 1-5.

width (Hz)	Q_β
[2,17]	155 ± 45
[3,5,17]	134 ± 35
[5,17]	99 ± 15
[2,13]	101 ± 32
[3,13]	63 ± 14

5. Application to OBS Refraction Data

Next our method was applied to the OBS refraction data. Each wavelet window, position and length, was adjusted in order to obtain as smooth an amplitude spectrum as possible. After the mean was removed from the wavelets, the time-domain Hanning taper and smoothing functions were applied in the same way as for the synthetics. We selected the portion of the data prior to the first arrival starting at 2.0 s, with the same length as the wavelets used for the spectral ratios, as the noise estimate. We subtracted the noise power from the spectral power estimates after smoothing. If noise is included in the spectral ratios, then the Q_β estimate will be higher than the true value.

We restricted our analysis to offsets less than 1.0 km. Since the S-rays have a near vertical path, the near traces are least contaminated by scattered energy and interference effects. The amplitude spectra of the wavelets selected for trace 3 at 0.41 km (Figure 4) show that the data have a dominant frequency of about 9 Hz and that noise levels restrict the useable bandwidth to about 5-15 Hz. A linear least squares fit to the spectral ratios was made for frequencies at which the spectral estimates for the *PS* and *PSSS* wavelets were at least 3 dB above the noise level. We obtained an effective $Q_\beta = 99 \pm 15$ for this trace.

Table 2 shows that, although there is considerable variation from trace to trace in the results for Q_β , the 95% confidence intervals of the first four traces overlap. To average path irregularities and possible interference effects, we took an arithmetic average of the spectral estimates for the 5 traces in Table 2 prior to obtaining the spectra and ratios seen in Figure 5. These gave $Q_\beta = 107 \pm 15$. Although it is not evident for the traces analysed, interference is probably present in these data to some degree and we suspect that interference of the crustal S refraction with the *PSSS* coda for the trace at 0.747 km is the reason this Q_β estimate is significantly lower than the other traces. Synthetic seismograms computed for a single sediment layer using $Q_\beta = 100$ match the amplitude decay of the *PS* and two successive shear multiples observed in the data.

6. Conclusions

Our spectral average $Q_\beta = 107 \pm 15$, corresponding to an attenuation of about 0.255 ± 0.03 dB/ λ , is consistent with results from Scholte-wave studies (Jensen and Schmidt, 1986). Since we are assuming a minimum sediment travel path, i.e. perfectly vertical shear raypaths, and the actual path is somewhat longer, and since the reflection profiling indicates subhorizontal layering, and both interference and noise tend to steepen the slope of the spectral ratio curves, the spectral ratio method gives a lower bound for Q_β . We conclude that sediment Q_β can be obtained to a precision of $\pm 15\%$ or better in areas where there is significant P to S conversion at the sediment/basement interface and sediment thickness allows separation of shear-wave arrivals.

7. References

- Duennebie, F.K., Lienert, B., Cessaro, R., Anderson, P., and Mallick, S. (1987) 'Controlled-source seismic experiment at Hole 581-C', In Duennebie, F.K., Stephen, R., Get-

- trust, J.F., et al., eds., *Init. Repts DSDP, 88*, Washington (U.S. Govt. Printing Office), 105-125.
- Hamilton, E.L. (1980) 'Geoacoustic modeling of the sea floor', *J. Acoust. Soc. Am.*, 77, 1789-1799.
- Hughes, S.J., Ellis, D.D., Chapman, D.M.F., and Staal, P.R. (1990) 'Low frequency acoustic propagation loss in shallow water over hard-rock seabeds covered by a thin layer of elastic-solid sediment', *J. Acoust. Soc. Am.*, 88, 283-297.
- Jannsen, D., Voss, J. and Theilen, F. (1985) 'Comparison of methods to determine Q in shallow marine sediments from vertical reflection seismograms', *Geophys. Prosp.*, 33, 479-497.
- Jacobson, R.S., Shor, G.G., Jr., and Dorman, L.M. (1981) 'Linear inversion of body-wave data - Part II: Attenuation versus depth using spectral ratios', *Geophysics*, 46, 152-162.
- Jensen, F.B. and Schmidt, H. (1986) 'Shear properties of ocean sediments determined from numerical modeling of Scholte-wave data', In Akal, T. and Berkson, J.M., eds., *Ocean Seismo-Acoustics: Low Frequency Underwater Acoustics*, Plenum Press, New York, 683-692.
- Kanamori, H. and Anderson, D.L. (1977) 'Importance of physical dispersion in surface wave and free oscillation problems: Review', *Rev. of Geophys. and Space Phys.*, 15, 105-112.
- Kjartansson, E. (1979) 'Constant Q-wave propagation and attenuation', *J. Geophys. Res.*, 84, 4737-4748.
- Mallick, S. and Frazer, L.N. (1987) 'Practical aspects of reflectivity modeling', *Geophysics*, 52, 1355-1364.
- Menke, W. (1983) 'A formula for the apparent attenuation of acoustic waves in randomly layered media', *Geophys. J. Roy. Astr. Soc.*, 75, 541-554.
- O'Doherty, R.F. and Anstey, N.A. (1971) 'Reflections on amplitudes', *Geophys. Prosp.*, 19, 430-458.
- Schoenberger, M. and Levin, F.K. (1978) 'Apparent attenuation due to intrabed multiples, II', *Geophysics*, 43, 730-737.
- Spudich, P.K.P. and Orcutt, J.A. (1980) 'Petrology and porosity of an oceanic crustal site: Results from wave form modeling of seismic refraction data', *J. Geophys. Res.*, 85, 1409-1433.
- Strick, E. (1967) 'The determination of Q, dynamic viscosity and transient creep curves from wave propagation measurements', *Geophys. J. Roy. Astr. Soc.*, 13, 197-218.
- Sutton, G.H. and Duennebie, F.K. (1987) 'Optimum design of ocean bottom seismometers', *Mar. Geophys. Res.*, 9, 47-65.
- Toksoz, M.N. and Johnston, D.H., eds. (1981) *Seismic Wave Attenuation*, SEG Geophys. cs reprint series No. 2, Tulsa.
- Vidale, R.J. (1980) 'Ray path analysis of sediment shear wave effects on bottom reflection loss', *J. Acoust. Soc. Am.*, 68, 639-648.

Single-hydrophone localization

L. Neill Frazer and Peter I. Pechols

Hawaii Institute of Geophysics, University of Hawaii at Manoa, 2525 Correa Road, Honolulu, Hawaii 96822

(Received 17 February 1989; accepted for publication 29 March 1990)

It is shown that Clay's single-hydrophone time-domain localization algorithm is a member of a large class of algorithms $\{\chi_n^m\}$ that require exact knowledge of the source time function $w(t)$. The single-hydrophone Clay algorithm is χ_1^2 ; however, χ_1^2 often localizes better than χ_1^2 . Next, five new families of single-hydrophone localization algorithms are introduced. The first of these, $\{\mu_n^m\}$, also requires a knowledge of $w(t)$, and is introduced mainly to emphasize that Clay localization is the ratio of norms. The four new localizer families, $\{\varphi_n^m\}$, $\{\theta_n^m\}$, $\{\beta_n^m\}$, and $\{\nu_n^m\}$, require almost no knowledge of $w(t)$. These new algorithms actually yield an estimate of the source spectrum $W(\omega)$, as well as the location of the source. The localizers φ , θ and ν work best when $|W(\omega)|$, the amplitude spectrum of the source, is smooth, although $w(t)$ need not be a pulse. The β localizers work best when $w(t)$ is a pulse. If it happens that an estimate of $W(\omega)$ is available, then φ , θ , β , and ν can use this information and their performance is enhanced. A similar enhancement is obtained when two hydrophones are available.

PACS numbers: 43.30.Wi, 43.60.Gk, 43.60.Pt

INTRODUCTION

By "localization" we mean the problem of determining the location of a source of sound in the ocean by use of hydrophone data. Single-hydrophone localization methods are those that use data from only one hydrophone. Serious research in localization may be said to have begun with Buckner's matched-field technique¹ in 1976, although as Clay² has pointed out, experiments by Parvulescu and Clay³⁻⁵ had shown, a decade earlier, that localization was a feasible problem.

Most research in localization has, following Buckner,¹ used continuous wave (cw) sources, whereas the Parvulescu-Clay experiments led to techniques that are perhaps more easily understood in the time domain. The literature of cw localization is now quite large, and a review of the subject is beyond the scope of this paper. Interesting recent cw work, incorporating sophisticated signal-processing techniques, is presented by Fize⁶ and Bagge⁷ *et al.* Here, we are most concerned with the time-domain single-hydrophone technique of Clay² as implemented by Li and Clay.⁸

In the sequel, lower-case Roman letters are used for time-dependent quantities, and upper-case letters are used for their Fourier transforms. Thus we often write f , instead of $f(t)$, and F instead of $F(\omega)$. Exceptions are source positions, denoted by \hat{X} , X , X_1 , etc. In our numerical experiments, functions were sampled in both domains and transforms were carried out with an FFT.

1. CLAY'S METHOD

The principle underlying Clay's time-domain localization algorithm is that, for given source and receiver loca-

tions, the best signal detector is the time-reversed Green's function of the medium. Let the Green's function of the medium be $g(X, t)$ in which X is source location and the dependence of g on the fixed hydrophone location has been suppressed. Let the unknown location of the actual source be \hat{X} ; let the time signal emitted by the source be $w(t)$; and let the time signal recorded by the hydrophone be $d(t)$. The sources used in this study are shown in Figs. 1 and 2. In Clay's scheme $w(t)$ is assumed to be known, and it is convenient to introduce the function $h(X, t) = g(X, t) * w(t)$, where "*" is the usual time-domain convolution. Then the most probable source location is the value of X that maximizes the Clay localizer:

$$\sup_X |h(X, -t) * d(t)| / \|h(X, t)\|_2 \|d\|_2. \quad (1)$$

In this expression, we have used the notation

$$\|f\|_p = \left(\int_{-\infty}^{\infty} dt |f(t)|^p \right)^{1/p}, \quad (2)$$

for the time domain L^p norm, and \sup , denotes the supremum over t .

To see why the localizer works, notice that since \hat{X} is the true source location, $d(t) = g(\hat{X}, t) * w(t)$. As convolution is associative, we have that

$$h(X, -t) * d(t) = g(X, -t) * g(\hat{X}, t) * w(-t) * w(t) \quad (3)$$

To a good approximation, $g(X, t)$ is a random sequence of spikes, one spike for each different ray arrival. As the random sequence is different for each X , the quantity $g(X, -t) * g(\hat{X}, t)$ resembles $\delta(t)$ when $X = \hat{X}$ and is approximately equal to zero otherwise. Thus the numerator of the Clay localizer is approximately zero when $X \neq \hat{X}$.

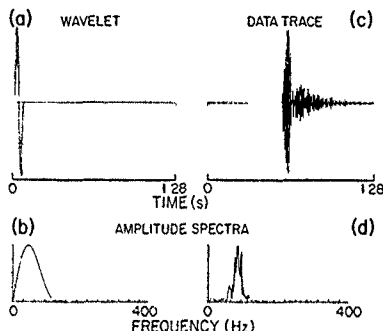


FIG 1 The source signal used in Figs 3-11. (a) Source waveform, (b) source spectrum, (c) hydrophone data waveform, (d) hydrophone data spectrum

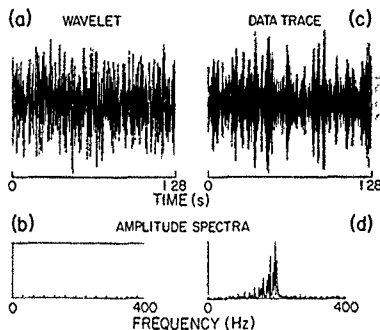


FIG 2 The white noise source signal used in Fig 12. (a) Source waveform, (b) source spectrum, (c) hydrophone data waveform, (d) hydrophone data spectrum

II. TWO FAMILIES OF CLAY-LIKE LOCALIZERS

Notice that the numerator of the Clay localizer is actually a norm, the L^∞ norm. This leads us to introduce the family of localizers $\{\chi_n^m\}$ defined by

$$\chi_n^m = \|h(X) * d\|_m / [\|h(X)\|_n \|d\|_n]. \quad (4)$$

In this notation, the Clay localizer of the last section is seen to be χ_2^2 .

To determine which values of m and n give the best localization, we carried out numerical experiments, discussed in greater detail below, for several hydrophone depths, a grid of source locations, and a number of source waveforms. These experiments showed that, in most cases, the higher the ratio m/n , the higher the resolution of the localization. In particular, χ_2^2 often localizes better than χ_2^2 . However, this is not always the case: For the source location used to compute Figs. 3 and 4, χ_2^2 localizes slightly better than χ_2^2 .

Another family of localizers, simpler than $\{\chi_n^m\}$, is the family $\{\mu_n^m\}$ given by

$$\mu_n^m = \|h(X) * d\|_m / \|h(X) * d\|_n. \quad (5)$$

Our numerical experiments indicate that μ_n^m , shown in Fig 5, does not work as well as χ_n^m , shown in Fig 4. The only difference between χ and μ is in the denominator, where in χ the norm of $h(X) * d$ has been split into the product of the norms of $h(X)$ and d . This suggests that for long source waveforms, the performance of χ might be improved if the norm of $h(X)$, in the denominator of χ , were replaced by the product of the norms of $g(X)$ and w . We have not investigated this, as several of the localizers introduced below work much better than χ without requiring a knowledge of w .

Neither the χ nor μ localizer families work well if $h(X)$ is replaced by $g(X)$ in Eqs. (4) and (5). Thus the source waveform w must be known

III. LOCALIZATION AS DECONVOLUTION

The family $\{\mu_n^m\}$ is reminiscent of the MED deconvolution algorithm of Wiggins.^{9,10} When regarded in this light, the localizers χ_n^m and μ_n^m are seen to be deconvolutions in which the inverse of an operator is approximated by the adjoint of that operator. In most deconvolution problems, there are good reasons for such an approximation. The inverse of a time series may be singular, or of infinite length, especially if the original time series is corrupted by noise. However, we will see that in the localization problem these instabilities work to our advantage.

Before introducing our new localization algorithms, we Fourier transform our hydrophone data $d(t)$ and Green's function $G(X, t)$ into the temporal frequency domain to get $D(\omega)$ and $G(X, \omega)$, respectively. Thus, in the absence of noise, $D = G(X)W$, where W is the Fourier transform of the unknown source time function w ; L^2 norms in the frequency domain will be indicated by writing $\|D\|_p$ for $[\int_{-\infty}^{\infty} d\omega |D(\omega)|^p]^{1/p}$. Consider the quantity $G(\hat{X})/G(X)$. In general $G(X)$ has zeros near the $\Re(\omega)$ axis. The locations of these near zeros will vary rapidly with X so that $G(\hat{X})/G(X)$ will generally have singularities near the $\Re(\omega)$ axis unless $X = \hat{X}$. For similar reasons, $D/G(X)$ will also have singularities near the $\Re(\omega)$ axis. Evidently the frequency series $|D/G(X)|$ will tend to be relatively "spiky" for all $X \neq \hat{X}$ and relatively smooth for $X = \hat{X}$.

In view of the above, we introduce the localizer family $\{\varphi_n^m\}$ given by

$$\varphi_n^m = [\|D\|_m / \|G(X)\|_m] / \|D/G(X)\|_n. \quad (6)$$

It can be seen that, when $m < n$, φ_n^m provides a measure of the smoothness of the frequency series $|D/G(X)|$. In the absence of noise, the maximum of φ_n^m will always be at the point $X = \hat{X}$.

Notice that the φ_n^m localizers require no knowledge of

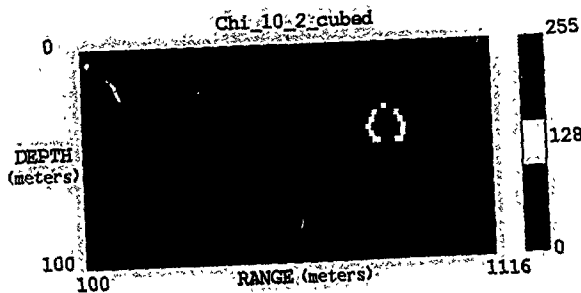


FIG 3 Ambiguity surface of the Clay localizer, χ_T^* given by Eq. (1). For clarity, the topography of the ambiguity surface has been exaggerated by cubing all the ambiguity values and then rescaling. With this localizer, the source time waveform must be known.

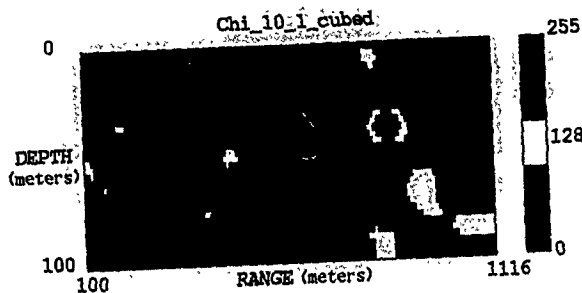


FIG 4 Ambiguity surface of another Clay localizer, χ_T^* given by Eq. (4). The ambiguity values have been cubed and rescaled. For many source-receiver geometries, χ_T^* localizes better than the original Clay localizer χ_T^* , however, for this geometry, χ_T^* is better.

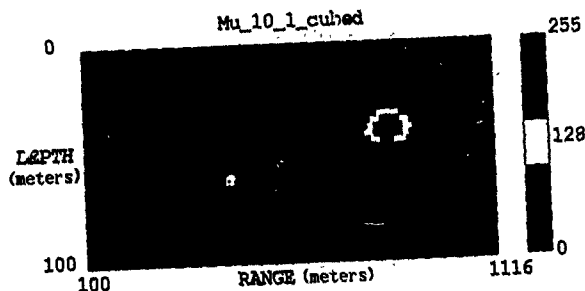


FIG 5 Ambiguity surface of the localizer μ_T^* given by Eq. (5). Ambiguity values have been cubed and rescaled. This localizer is simply the ratio of two time-domain norms. Like the Clay localizers, it requires knowledge of the source time function.

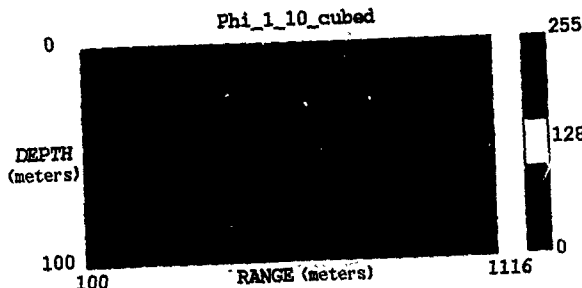


FIG 6 Ambiguity surface of the new localizer ϕ_L^* given by Eq. (6). Ambiguity values have been cubed and rescaled. For this localizer, the source time function is not required.

the source function W . In fact, they yield an estimate of the source function because, after \hat{X} has been found, we can recover W as $D/G(\hat{X})$.

An example of φ^1 is shown in Fig. 6. Numerical examples for a number of hydrophone depths, a grid of source locations, and several source waveforms show that φ^1 localizes better than any of the χ or μ localizers.

Another localizer family that works almost as well as φ^1 is the family θ^1 given by

$$\theta^1 = \|D/G(X)\|_\infty / \|D/G(X)\|_1 \quad (7)$$

An example of θ^1 is shown in Fig. 7. The fact that θ does not work as well as ϕ is not surprising since we found that μ did not work as well as χ . Both μ and θ take the same computational shortcut.

Although we have written the definitions of φ^1 and θ^1 in the frequency domain, they should still be regarded as time-domain methods because they require knowledge of D in a band of frequencies and we must compute $G(X)$ within this band. Thus, if the source has power only in a very narrow band, then the φ^1 cannot be expected to localize very well.

For consistency with the Clay-type localizers, we have defined the φ^1 so that they are a maximum, rather than a minimum, at the point $X = \hat{X}$. If $G(X)$ has zeros on the $\Re(\omega)$ axis, then it is possible that numerical problems will result. One method for avoiding this problem is to replace $D/G(X)$ in the numerator of Eq. (6) and in both the numerator and denominator of Eq. (7) by $DG^*(X)/(|G|^2 + \epsilon)$, where ϵ is a positive number much smaller than $\|G(X)\|_2$ and G^* is the complex conjugate of G . A second method is to replace $G(X, \omega)$ in Eqs. (6) and (7) by $G(X, \omega + i\epsilon)$. If $G(X)$ is to be generated in the frequency domain, then $G(X, \omega + i\epsilon)$ can be computed directly; and if $G(X)$ is computed in the time domain, then $G(X, \omega)$ can be analytically continued away from the $\Re(\omega)$ axis by multiplying $g(X, t)$ by $\exp(-\epsilon t)$ before taking the numerical Fourier transform. A third method is to zero certain bands in the spectrum of D so that these bands are excluded from the norms. All three methods are known signal-processing procedures. They did not seem to be needed in the numerical experiments presented here except for the β localizer (see below), which worked slightly better when small values of $D(\omega)$ were zeroed.

The family θ^1 has an associated time-domain localizer family β^1 given by

$$\beta^1 = \|d * g(X)^{-1}\|_\infty / \|d * g(X)^{-1}\|_1 \quad (8)$$

In this equation, $d * g(X)^{-1}$ is the inverse Fourier transform of $D/G(X)$. Examples of β^1 localization are shown in Figs 8 and 9.

Our experiments show that β^1 localizes better than θ^1 for the source time function of Fig. 2 (Note that this is not obvious from comparison of Figs 7 and 9 because the ambiguity surface in Fig. 7 has been cubed and rescaled.) This is because that source is very local in the time domain. Its spectrum is smooth compared to the spectrum of the Green's function, so the φ and θ localizers also work well, they do not work as well as β because the smoothness of $|W|$ here is outweighed by the "localness" of w . For the random u of

Fig. 2, which is very nonlocal in the time domain, the β localizers do not work at all, but the φ and θ localizers work better than before because the random w of Fig. 2 has a spectrum W that is smoother than the W of Fig. 1.

Our final single-hydrophone frequency domain localizer family is v^1 given by

$$v^1 = [\|d_\omega^2 D\|_\infty / \|d_\omega^2 G(X)\|_\infty] / \|d_\omega^2 D/G(X)\|_\infty \quad (9)$$

Here, d^2 stands for $d^2/d\omega^2$, $|D|$ is the modulus of D , and $|G(X)|$ is the modulus of $G(X)$. An example of v^1 localization is shown in Fig. 10.

The v family of localizers is similar to φ and θ except that, with v , the smoothness of the frequency series $|D/G(X)|$ is measured much more directly by the reciprocal norm $\|d_\omega^2 D/G(X)\|_\infty^{-1}$. In the φ and θ localizers, the smoothness of $|D/G(X)|$ is obtained indirectly, as the ratio of two L^p norms with different p 's. One would expect the effectiveness of the v^1 to be nearly independent of the values of m and n , and our numerical experiments seem to bear this out. For each source waveform we tried, v^1 for any value of m worked much better than any other localizer. However, for two sources of similar strength with the same waveform, v was inferior to every other localizer.

IV. NUMERICAL EXAMPLES

For convenience in computing time-domain Green's functions, we have used a 100-m-deep ocean model with a constant sound-speed profile of 1.5 km/s. At the top of the model was a slightly lossy pressure-release surface with an angle-independent reflection coefficient of -0.98 . The bottom reflection coefficient R varied linearly with $\cos^2(\phi)$, where ϕ is grazing angle, from $R = 0.9$ at $\phi = 0^\circ$ to $R = 0.1$ at $\phi = 90^\circ$. Geometrical acoustics was used to compute the Green's functions, and propagation in the subbottom was neglected. Synthetic hydrophone data were generated by convolving the source time function with the Green's function for the source location.

In the computations shown here, the hydrophone was located at a depth of 73 m and the source was located at depth 39 m and range 768 m. Each localization formula was tested over a grid of source locations for a number of hydrophone depths. None of the localizers worked significantly better or worse for hydrophone depths and source locations other than the ones shown here.

The simple propagation model used here is realistic only for propagation in shallow water with a moderately hard bottom and homogeneous subbottom. However, it seems clear that the results of this paper are applicable to other ocean models, provided only that the computed Green's functions are consistent with the actual propagation. In general, the goodness of localization can be expected to increase with the complexity of the Green's function, so that in areas where subbottom propagation is significant, localization will be improved. Conversely, in areas where the propagation is not bottom limited, we expect localization to be degraded, especially at large ranges where the sound field is dominated by a few modes.

Following Clay,¹ the source time function $w(t)$ was (ex-

ain, the β
izers work
2 has a
l.
ain loca-

$X) \|_{\infty}$
(9)

of D , and
localiza-

θ except
ries $|D|$ /
ciprocal
zers, the
the ratio
pect the
ie values
bear this
value of
(owever,
veform,

Green's
with a
of the
with an
he bot-
 ϕ^2 ,
 $\epsilon = 0.1$
ute the
gn was
ted by
func-

ie was
ted at
gn was
ydro-
cantly
ations

only
hard
eems
other
een's
gen-
rease
reas
i will
on is
ided,
ated

[ex-

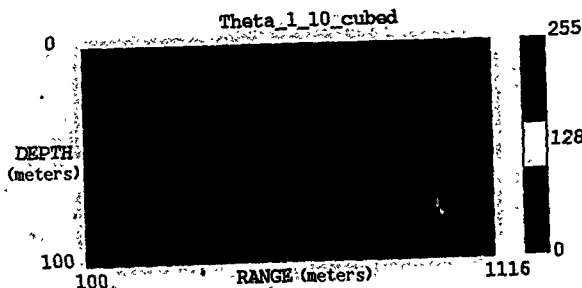


FIG. 7 Ambiguity surface of the new localizer θ_1 . Ambiguity values have been cubed and rescaled. The source time function was not used in localization. To see the effects of cubing and rescaling, compare this figure with Fig. 11.

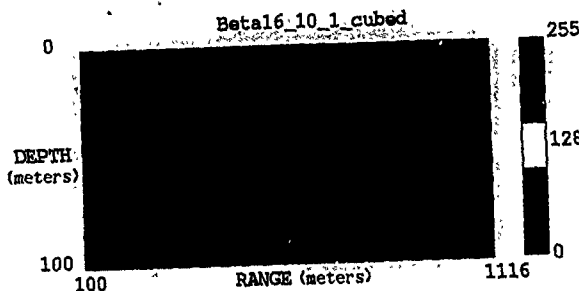


FIG. 8. Ambiguity surface of the new time-domain localizer β given by Eq. (8). Ambiguity values have been cubed and rescaled for comparison with earlier figures. In the Fourier version to the time domain, the frequency band used was that for which $|D(\omega)|$ was greater than $1/16$ th of its peak value. The source function was not used in localization.

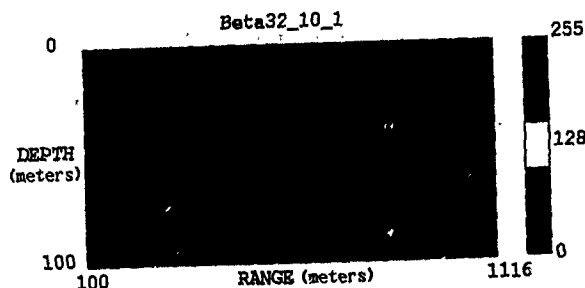


FIG. 9 As in Fig. 8 except that the frequency band used was that for which $|D(\omega)|$ was greater than $1/32$ nd of its peak value. Not ambiguity values have not been cubed and rescaled.

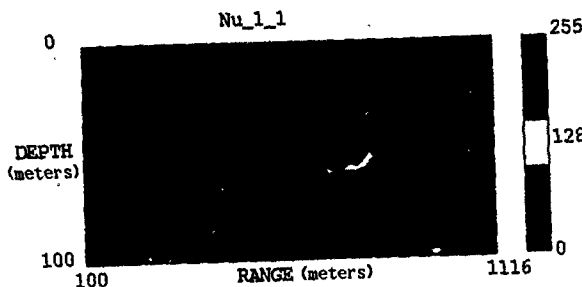


FIG. 10 Ambiguity surface of the new frequency-domain localizer ν_1 given by Eq. (9) that ambiguity values have not been cubed and rescaled, and the source function was not used in localization.

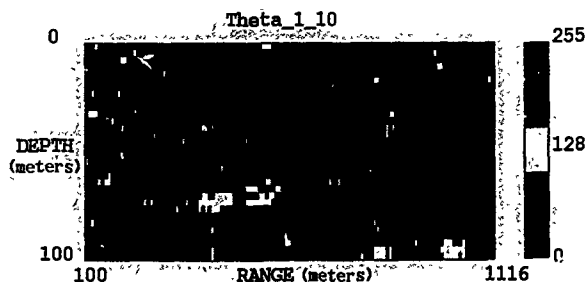


FIG 11. Ambiguity surface of θ^1_+ for the original source time function of Fig. 1. This ambiguity surface is the same as the one shown in Fig. 1 except that here the ambiguity values have not been cubed or rescaled.

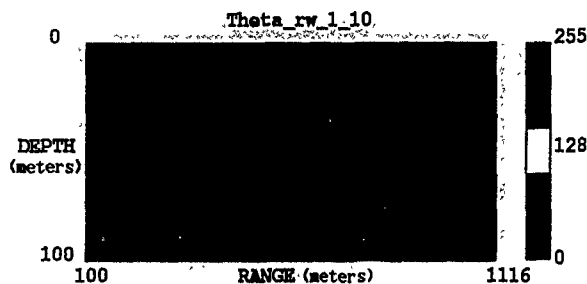


FIG 12. Ambiguity surface of θ^1_+ for the random source time function of Fig. 2. Ambiguity values have not been cubed or rescaled.

cept in Fig. 12) a single cycle of a sine wave. Figure 1 shows this time function and its amplitude spectrum along with the synthetic hydrophone data trace and its spectrum. In the experiments shown here, the number of frequencies used was 128 and the number of time samples in each time series was 256. A few experiments were conducted with 256 frequencies and 512 time points; in general, localizers that worked for 128 frequencies worked slightly better for 256 frequencies.

In order to show that the effectiveness of φ , θ , and ν depends only on the smoothness of $|W|$ relative to the smoothness of $G(X)$, and not on the localness of w in the time domain, tests were also conducted with the random source time function shown in Fig. 2. This source function is perfectly white, each Fourier amplitude being equal to unity but with a phase randomly distributed on the interval $[-\pi, \pi]$. Note that although this function has a white amplitude spectrum, it is not at all local in the time domain. Figure 11 shows an example of θ^1_+ localization with the time-local source waveform of Fig. 1 while Fig. 12 shows an example of localization with the white noise waveform of Fig. 2. The ambiguity surface of Fig. 11 has not been cubed and rescaled so it appears to have more features than the ambiguity surface of Fig. 7.

V. DISCUSSION

It is significant that, although φ , θ , β , and ν do not require a knowledge of the source spectrum W , their performance can certainly be improved if an estimate of W is available. To improve them we would just replace $G(X)$ by $G(X)W$ in Eqs. (6), (7), and (9). It does not matter if the phase of W is not available since the right-hand sides of these equations are independent of the phases of D and $G(X)$. An estimated source spectrum $|W|_{est}$ need not be highly accurate for localization to improve, all that is necessary is that the ratio $|W|_{true}/|W|_{est}$ be smoother than $|W|_{true}$.

The β localizers are not so easily enhanced, for Eq. (8) shows that they are ratios of time-domain norms. In order to replace $g(X)$ by $g(X)w$ in Eq. (8) we need to know w , which means that we need to know the phase of W .

The possibility of localization with a single hydrophone is surprising at first since most localization schemes make use of large arrays of hydrophones. The methods introduced here show that, at least to some extent, there is a trade-off between hydrophone array size and bandwidth. Even more surprising, at first, is that single-hydrophone localization is possible without knowing the source function w . Here, it must be admitted that the new localizers φ , θ and ν work

well only if the source amplitude spectrum $|W|$ is smoother than the Green's function amplitude spectrum $|G(X)|$. This will be the case for many sources of underwater sound, but not all. Similarly, the localizer β works well only if w is local in time, i.e., fairly short in duration. So some knowledge of the source is being assumed, although this knowledge is very limited.

An interesting question is whether localizers can be deliberately deceived. For the single-hydrophone localizers of this paper, the answer is "yes." To see how this could be done, suppose a source located at \hat{X} wishes to deceive a hydrophone (whose location it knows) into believing it is located at X' . In order to deceive the localizers φ , θ , and ν , the source should deliberately radiate any waveform with amplitude spectrum $|FG(X')/G(\hat{X})|$, where $|F|$ is any smooth function. Recall that φ , θ , and ν localize by finding the X for which the frequency series $D/G(X)$ is smoothest. For the deceitful source, the hydrophone will record data with spectrum $|D| = |FG(X')|$; thus $|D/G(X)|$ will be smoothest when $X = X'$.

The β localizer is more difficult to deceive because it uses phase information; the deceitful source must radiate a time waveform equal to the inverse Fourier transform of $G(X')/G(\hat{X})$. Localizers that make use of multiple hydrophones will also be more difficult to deceive because the deceitful source must radiate a different waveform to each hydrophone. In principle, this could be accomplished using source directivity, but the multiplicity of paths between the source and each hydrophone makes it a difficult problem.

Although the numerical experiments shown here are for 2-D localization, there is no reason a single hydrophone cannot be used to localize in 3-D. Single-hydrophone localization in 2-D is possible because the ocean waveguide assigns each range and depth a unique Green's function. Similarly, single-hydrophone localization in 3-D is feasible whenever the ocean waveguide is laterally heterogeneous so that each range, depth, and azimuth has a different Green's function. Perkins *et al.*¹¹ refer to this principle as environmental symmetry breaking (ESB) in their demonstration that localization in range and azimuth is possible with a single vertical array.

If multiple hydrophones are available, then the methods introduced here can be extended in a number of ways. The least sophisticated method is "stacking," in which ambiguity surfaces for different hydrophones are averaged. For an example of a more sophisticated extension, suppose that just two hydrophones are available. Let D_1 and D_2 be the Fourier transformed data from the two hydrophones and let $G_1(X)$ and $G_2(X)$ be their respective Green's functions. At the true source location, D_1/G_1 and D_2/G_2 will both be equal to the source spectrum W and so their ratio $(D_1/G_1)/(D_2/G_2)$ will be unity at all frequencies. A new φ localizer, modified from Eq. (6), is

$$\varphi_w^m = \frac{||D_1||_m ||G_2(X)||_m}{||D_2||_m ||G_1(X)||_m} \quad (10)$$

Numerical tests show that the two-hydrophone φ_w^2 works well for any unknown source spectrum W , i.e., it is not necessary for $|W|$ to be smooth. Ambiguity surfaces for the

two-hydrophone φ_w^2 are always as sharp as the surface shown in Fig. 10.

New two-hydrophone θ , β , and ν localizers are obtained in a similar manner. To change a single-hydrophone method into a two-hydrophone method, the modification principle that $D_2/G_2(X)$ is used as an estimate of W . This estimate W is used to remove W from D_1 . Thus a two-hydrophone localizer with no knowledge of W is equivalent to a single-hydrophone localizer with complete knowledge of W . A Green's function is unique in the sense

$$X_1 \neq X_2 \Rightarrow (\exists \omega_1, \omega_2) G(X_1, \omega_1) \neq G(X_2, \omega_2),$$

it follows that two hydrophones can always localize and one hydrophone can always localize if W is known. However, the computations above demonstrate more. They show that a single hydrophone can often localize when W is not known.

An important issue is the robustness of the new localizers in the presence of multiple sources and/or non-multiple sources of comparable strength are present, these have different unknown source time functions, the performance of all our localizers is degraded. The reason for this is that our localizers are frequency coherent or nearly so. The φ , θ , and ν localizers use the relative amplitudes of adjacent frequencies within a band while the θ and β localizers use not only the relative amplitudes of adjacent frequencies, but also their relative phases.

Although single-hydrophone localization is not practically practical, the calculations presented above show it is certainly possible. In a heterogeneous ocean containing dominant source, one broadband hydrophone gains enough information to locate that source. Additional information about the source, such as an approximate amplitude spectrum, is easily incorporated to improve the localization.

ACKNOWLEDGMENTS

The work presented here is part of a larger project on localization in an unknown environment, supported by ONR. Hawaii Institute of Geophysics Contribution 2298

¹¹ H. P. Buckner, "Use of calculated sound fields and matched-field data to locate sound sources in shallow water," *J. Acoust. Soc. Am.* **59**, 373 (1976).

¹² C. S. Clay, "Optimum time domain signal transmission and source location in a waveguide," *J. Acoust. Soc. Am.* **81**, 660-664 (1987).

¹³ A. Parvulescu, "Signal detection in a multipath medium by MESS," *J. Acoust. Soc. Am.* **33**, 1674 (1961).

¹⁴ A. Parvulescu and C. S. Clay, "Reproducibility of signal transmission in the ocean," *Radio Eng. Electron.* **29**, 223-228 (1965).

¹⁵ I. Tolstoy and C. S. Clay, *Ocean Acoustics* (American Institute of Physics, New York, 1966). The Parvulescu-Clay experiment is described in p. 7.

¹⁶ R. G. Fizzle, "Application of high-resolution processing to range depth estimation using ambiguity function methods," *J. Acoust. Soc. Am.* **82**, 606-613 (1987).

¹⁷ A. B. Baggeroer, W. A. Kuperman, and H. Schmidt, "Matched field processing: Source localization in correlated noise as an optimum parameter estimation problem," *J. Acoust. Soc. Am.* **83**, 571-587 (1988).

¹⁸ S. Li and C. S. Clay, "Optimum time domain signal transmission: source location in a waveguide. Experiments in an ideal wedge,"

guide," *J. Acoust. Soc. Am.* 82, 1409-1417 (1987)

⁹R. A. Wiggins, "Minimum entropy deconvolution," in *Proceedings of the International Symposium on Computer Aided Seismic Analysis and Discrimination*, Falmouth, MA (IEEE Computer Society, Falmouth, MA, 1977), pp 7-14.

¹⁰R. A. Wiggins, "Entropy guided deconvolution," *Geophysics* 50, 2720-2726 (1985)

¹¹J. S. Perkins, W. A. Kuperman, and F. Ingenito, "Environmental symmetry breaking: An application of 3-D matched-field processing," *J. Acoust. Soc. Am. Suppl.* 1 83, S87 (1988)

Acoustic tomography via matched field processing

A. Tolstoy and O. Diachok

Acoustics Division, Naval Research Laboratory, Washington, DC 20375

L. N. Frazer

Hawaii Institute of Geophysics, University of Hawaii, Honolulu, Hawaii 96822

(Received 8 August 1990, accepted for publication 19 November 1990)

This paper suggests a new approach based on narrow-band, low-frequency data using air-deployed shots recorded on widely distributed large aperture vertical arrays. This approach uses fast, cheap, and high S/N data. Results to date with a simulated three-dimensional (3-D) eddy environment show that efficient characterization of the environment plus careful selection of the source/array geometry can lead to highly accurate estimates of the 3-D sound-speed profiles, e.g., maximum errors less than 0.2 m/s.

PACS numbers: 43.30.Pc

INTRODUCTION

Tomography is properly defined as the cross-sectional imaging of an object from either transmission or reflection data collected by illuminating the object from many different directions (Kak and Slaney, 1987). Here, the term will be used to describe a technique involving transmission of acoustic fields through an ocean region and subsequently inferring the 3-D sound-speed profiles by examining those fields. The primary objective of this study is to demonstrate a new approach to deep water ocean tomography.

Over the last decade ocean tomography experiments have shown that remote sensing of ocean mesoscale structures is highly effective at ranges up to 300 km using "high" frequencies (above 100 Hz) where sound-speed structure is inverted through comparison of measured with predicted times of arrival of rays/multipaths propagating to a receiver from a pulsed source (Munk and Wunsch, 1979; Behringer *et al.*, 1982; Cornuelle *et al.*, 1985). More recently larger regions, e.g., 1000×1000 km, have also been considered (Cornuelle *et al.*, 1989). These approaches use either moored source/receivers, or moving source/receivers, or some combination of each. The moored tomography technique, in particular, requires resolution on the order of 10 ms (Spiesberger *et al.*, 1980) to detect the effects of environmental changes, and this demands broadband coded source signals with accurate synchronization of transmission and recordings. The data must be collected over long periods of time to counter fluctuations due to internal waves and tides. Furthermore, the method requires that the relative source location be known to within a fraction of an acoustic wavelength, however, absolute location will not and need not be as well known resulting in small overall biases in sound-speed estimation (J. Lynch, 1990). One major drawback of the moored approach is that it will always suffer from a sparsity of deployment [number of paths = $n(n-1)/2$, where n is the number of moorings]. On the other hand, moving source/receiver tomography efforts at large scale ocean

monitoring (covering thousands of square kilometers) with at least one ship will always be very time consuming and thus very costly. Moreover, high-precision mapping requires their source and receiver positions to be known with 10-m accuracy (Cornuelle *et al.*, 1989). By contrast, the new technique will use air-deployed shots (fast, cheap, and good S/N) and will require position locations known only to within a few wavelengths. In particular, at 20 Hz this is about 150 m (the width of the processor peak is usually considerably broader than this so that position errors of a few wavelengths result in very small processor power degradations). The new technique¹ examines interference patterns across an array for single-frequency (not time domain), low-frequency data (10–30 Hz) modeled by highly accurate normal mode methods. The lower frequencies will propagate with less attenuation and will not be as sensitive to internal wave fluctuations as the higher frequencies, so time averaging should not be required (scaling of high-frequency fluctuation data at long range, e.g., Stanford, 1974, indicates that at 20 Hz, phase errors will be less than a tenth of a wavelength, and thus within generally accepted bounds for coherent addition of signals on hydrophone arrays). The new technique will transfer the burden from intense oceanographic surveys to intense computer processing demands.

1. APPROACH

Given vertical arrays of hydrophones and sources at known ranges and depths, the essence of the approach is to find the family of profiles for the front or eddy that maximizes the matched field power at the known source locations as seen at the arrays. For a discussion of the technique of matched field processing (MFP), see the papers by Bucker (1976) and Fizell (1987). Results to be discussed here used the Capon, a.k.a. maximum likelihood or minimum variance, processor (with S/N = 10 dB), which has been shown to be sensitive to sound-speed profiles depending upon the

source frequency and depth, and upon the array configuration and depth (Tolstoy, 1989a).²

The first stage of the process is to characterize the environment in as few parameters as possible. Oceanographers have developed a method for deriving efficient basis functions, known as empirical orthogonal functions (EOFs), for measured sound-speed profiles (Davis, 1976). This method is described briefly in Sec. II. In an effort to speed up program calculations, a perturbation method has been used to estimate modal wave numbers from an initial set of wave numbers and perturbations in the environmental parameters. As a result, the standard EOF method needed to be modified. This is discussed in Sec. II as well. In Section III, we have applied the modified EOF approach to simulated acoustic "data" propagating through a simulated environment. This environment describes a deep water (bottom at 4500 m) "double eddy" by means of a standard background sound-speed profile plus two offset perturbations [each perturbation is Gaussian in range and depth as in Shang (1989)], which introduce anisotropic range and depth dependence. The details of the environment are presented in Sec. III. Subsequently, we have gridded the surface of the environment into square cells in order to discretize the problem. Each cell will be characterized by one sound-speed profile, and propagation through the environment will be modeled by means of adiabatic normal mode theory (Porter and Reiss, 1984, 1985; Shang, 1989), where we consider only the waterborne modes. The standard model of Porter and Reiss, i.e., the KRAKEN model, was used to generate mode functions and wave numbers at the source and receiver locations (and for the mean AXBT profile) while a perturbation scheme was used to determine the wave numbers for all intervening path regions (see Appendix). We shall assume that bottom interacting energy has been mode filtered or time gated out (including such energy decreases MFP sensitivity to sound-speed profile changes and would increase computer run times significantly). It should be noted that our propagation model will not allow for full three-dimensional (3-D) effects, i.e., horizontal refraction will not be accurately described. Rather, our effects will be limited to "2.5-D" effects where the propagation will be range- and depth-dependent along each 2-D source-receiver path, and these paths will each vary substantially as they cross through the environment. Early studies by Baer (1980, 1981) have shown that full 3-D modeling through ocean eddies is very accurately approximated by the 2.5-D approach.

Finally, we have examined array placements, source distributions, and numerical methods for finding the MFP maxima as a function of the environmental parameters. Those results are presented in Sec. IV.

II. EFFICIENT CHARACTERIZATION OF THE ENVIRONMENT

In an effort to reduce the parameter search space, one can describe a sound-speed profile as a sum of EOFs (Kundu *et al.*, 1975; LeBlond and Middleton, 1980; Rizzoli *et al.*, 1985). The EOFs are defined as the eigenfunctions $f(z) = (f_1(z), f_2(z), \dots, f_K(z))$ (actually eigenvectors since we

sample at K discrete depths z_1, \dots, z_K) of the covariance matrix R , where for N sample profiles

$$Rf = \lambda f,$$

$$R_{ij} = \frac{1}{N} \sum_{n=1}^N \{c_n(z_i) - \bar{c}(z_i)\} \cdot \{c_n(z_j) - \bar{c}(z_j)\},$$

with $\lambda_j = \lambda_j \delta_{ij}$, and λ_j the eigenvalues, and where $c_n(z_i)$ is the sound-speed of the n th profile at the i th depth and \bar{c} is the average sample profile. The N sample profiles can come either from archival data or more accurately from measurements, e.g., from AXBT data. The results in this paper use profiles sampled every 25 km about 1/4 the perimeter of the region as indicated by the circles in Fig. 1. Then, the sound speed $c(x, y, z_i)$ at any point (x, y, z_i) in the region is given by

$$c(x, y, z_i) = \bar{c}(z_i) + \sum_{k=1}^K \alpha_k(x, y) f_k(z_i).$$

Since we used a perturbation scheme to determine modal wave numbers for a perturbed environment (see Appendix), we needed to modify the aforementioned EOF procedure. In particular, the entries of R have become

$$R_{ij} = \frac{1}{N} \sum_{n=1}^N \left(\frac{1}{c_n^2(z_i)} - \frac{1}{c_{mean}^2(z_i)} \right) \cdot \left(\frac{1}{c_n^2(z_j)} - \frac{1}{c_{mean}^2(z_j)} \right),$$

where

$$\frac{1}{c_{mean}^2(z_i)} = \frac{1}{N} \sum_{n=1}^N \left(\frac{1}{c_n^2(z_i)} \right).$$

That is, $c(z)$ has been replaced everywhere by $1/c^2(z)$. We shall denote the new EOFs by $g_k(z_i)$.

The EOF basis functions have the advantageous feature that they are the most efficient basis functions [in a least-squares sense, see Davis (1976)] for an expansion of the sound-speed profiles. In general, only two or three such

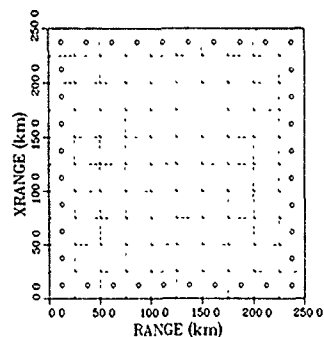


FIG. 1. Region of interest for tomographic study gridded into cell blocks. \odot indicates AXBT.

functions are necessary for a highly accurate representation of a profile. That is,

$$c(x,y,z) \approx \bar{c}(z) + \sum_{k=1}^3 \alpha_k(x,y) f_k(z).$$

Similarly,

$$\frac{1}{c^2(x,y,z)} \approx \frac{1}{c_{mean}^2(z)} + \sum_{k=1}^3 \beta_k(x,y) g_k(z).$$

Thus our parameter search space has been reduced to finding two or three coefficients $\{\beta_k\}$ per sound-speed profile rather than finding all the values of the sound-speed profile as a function of depth. Of course, pathological profiles, i.e., those whose character differs significantly from the profiles generating the EOFs, may require more than two or three terms for their expansions. The series expansion is referred to in the signal processing literature as the Karhunen-Loève expansion (Van Trees, 1968).

III. THE SIMULATED ENVIRONMENT

The environment selected simulates a deep water north Pacific region and consists of a background sound-speed profile $c_0(z)$ taken from archival data (from the NODC, 1968) and shown as the solid curve in Fig. 2, plus two offset Gaussian perturbations applied to depths from 0 to 900 m. For all x,y , we have $c(1000 \text{ m}) = 1480.4 \text{ m/s}$ and $c(4500 \text{ m}) = 1530 \text{ m/s}$ with a simple linear fit between the two depths. At the point (x,y,z) , we have

$$c(x,y,z) = c_0(z) + \Delta C_1(x,y,z) + \Delta C_2(x,y,z),$$

where

$$\Delta C_1(x,y,z) = \Delta_1 \exp\left\{-\left(r_1/R_1\right)^2 - \left[(z-z_1)/Z_1]^2\right\},$$

$$r_1 = \sqrt{(x-x_1)^2 + (y-y_1)^2},$$

where $\Delta_1 = -10 \text{ m/s}$, $\Delta_2 = -5 \text{ m/s}$, $(x_1, y_1) = (125 \text{ km}, 125 \text{ km})$, $(x_2, y_2) = (175 \text{ km}, 175 \text{ km})$, $R_1 = 100 \text{ km}$, $R_2 = 50 \text{ km}$, $z_1 = 500 \text{ m}$, $z_2 = 200 \text{ m}$, $Z_1 = 500 \text{ m}$, $Z_2 = 200 \text{ m}$.

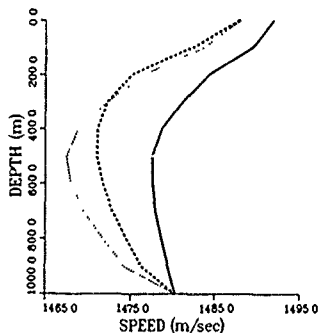


FIG 2 Sound speed profiles as function of depth (0-1000 m only). Solid curve corresponds to profile with no eddy perturbations. Dotted curve gives profile at center of large perturbation, i.e., at (125 km, 125 km). Dashed curve gives profile at center of small perturbation, i.e., at (175 km, 175 km).

Thus the maximum change in sound speed as a function of (x,y) occurs at $z = 500 \text{ m}$, will be approximately -10 m/s , and occurs between profiles at the region perimeter and those near the region center. Sample region profiles are shown in Fig. 2.

Having simulated a 3-D sound-speed environment, we next computed the EOFs $\{g_k(z)\}$ given the 36 profiles $c_n(z)$ sampled about the perimeter as shown in Fig. 1. Earlier work (Tolstoy, 1989b) has shown the lower-order/major EOFs to be surprisingly robust, i.e., insensitive, to how the environment is sampled. In general, the first two EOFs themselves change slightly with different sampling, e.g., through the perturbation regions versus along the perimeter, although their coefficients can change quite a bit. The efficiency of the EOFs can be improved by good sampling. The two major EOFs $g_1(z)$, $g_2(z)$, $i = 1, 2$ are shown in Fig. 3 with corresponding normalized eigenvalues $\lambda_1 = 1$, $\lambda_2 = 0.04$. The higher-order eigenvalues are of order 10^{-7} , and their significantly smaller values indicate their reduced contribution to the expansions. That is, the vast majority of the environmental variability can be described by only two EOFs. Indeed, fits to our environment indicate that errors in sound speed are less than 0.1 m/s if only two EOFs are used.

Having determined the (modified) EOFs for our simulated eddy region, we next computed their coefficients as a function of (x,y) throughout the region. For the discretized area of Fig. 1 (10×10 grid over $250 \times 250 \text{ km}$ area), we show their values in Fig. 4. These will be the parameters that we will attempt to find in our tomography program.

IV. RESULTS

Consider four vertical arrays distributed in the interior of the region of interest as shown in Fig. 5, with sources distributed around the perimeter at the centers of those cells

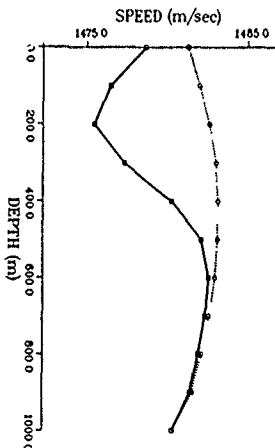


FIG 3 Modified EOFs $\{g_k(z)\}$, $k = 1, 2$ multiplied by 50×10^{-10} and added to 1480. The dotted curve corresponds to g_1 with a maximum at 500 m while the solid curve corresponds to g_2 with a maximum at 200 m.

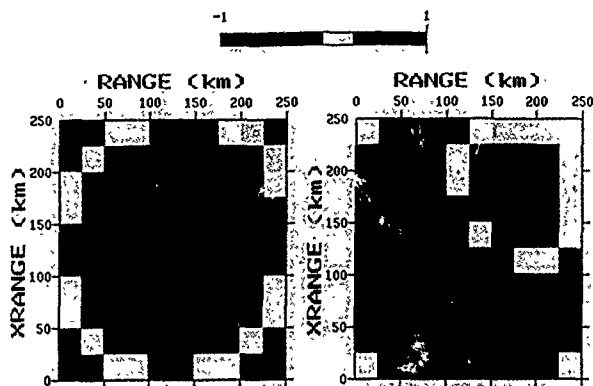


FIG 4 Modified EOF coefficients as a function of (x, y) . Normalized scale indicated above pictures. Part (a) displays the β_1 coefficient values (normalized from -1 to 0 , 0 to $+1$, actual values from -135×10^{-10} to 0 , 0 to 25×10^{-10}) and part (b) displays the β_2 coefficient values (normalized from -1 to 0 , 0 to $+1$, actual values from -10×10^{-10} to 0 , 0 to 30×10^{-10}).

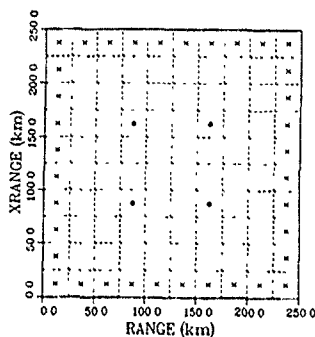


FIG 5 Distribution of four arrays (indicated by \bullet) and 36 sources at 100 m depth (indicated by $*$) for 10×10 grid covering 250×250 square km

For the results of this paper, we shall assume that the source and array locations are known exactly (recent work indicates that errors in source locations can be largely corrected by adding source coordinates as parameters for iteration). We shall assume that, along with the sources/shots and arrays, we will also distribute AXBTs and/or CTDs so that we will know the sound-speed profiles, i.e., EOF coefficients β_1 , β_2 , for those cells. We also estimate the range of values (we shall suppress the factor 10^{-10}) that those coefficients can achieve in the interior, i.e., $-135 < \beta_1 < 25$, $-10 < \beta_2 < 30$. Thus the simplest initialization of the coefficient values is to select mid values, i.e., $\beta_1 = -55$, $\beta_2 = 10$, as shown in Fig 6.

The frequency selected will be 20 Hz, and the arrays will each have 28 phones spaced every 37.5 m (half-wavelength spacing) in depth with the first phone just below the surface. Thus the arrays span the upper 1000 m of the water. Previous work (Tolstoy, 1989a) has shown (not surprisingly) that shallow arrays are most sensitive to sound-speed

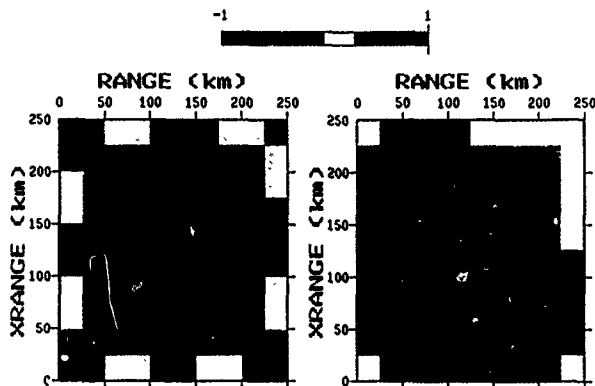


FIG 6 Itera's estimates for modified EOF coefficients as a function of (x, y) . Note that scales are identical to those of Fig 4, and that the coefficients around the perimeter (where the sources are located) and at the arrays are known: other wise, $\beta_1 = -55$, $\beta_2 = 10$.

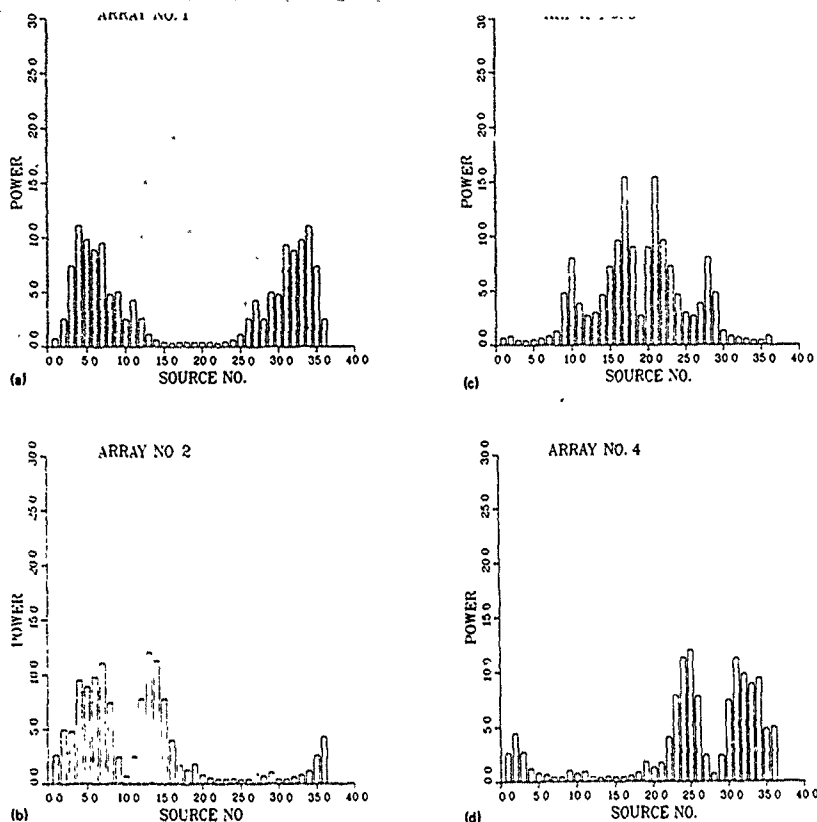


FIG. 7. Initial estimates for MFP power P_n at each receiving array r for each source s given the environment of Fig. 6

changes in the upper water depths, and so we shall locate our arrays there.

We begin by examining the MFP power P_n at each array r for each source s given the environment of Fig. 6 and the source/array distribution of Fig. 5. This power is shown in Fig. 7, and we note that the power is generally low, indicating that the environment is in error (maximum value is approximately 28).

We considered a number of numerical schemes to iterate through the environment in the hopes of finding the solution environment. First, a simulated annealing scheme (see Metropolis *et al.*, 1953; Kirkpatrick *et al.*, 1983; Kirkpatrick, 1984, and most readable of all, Press *et al.*, 1986) was implemented with "temperature" T set to zero. This was

equivalent to attempting to climb to the global maximum assuming the solution space was convex, i.e., that there were no local maxima to stall the procedure. This did not work. Next, the algorithm was used for various values of T in an effort to find the critical temperature. In general, the algorithm was very time-consuming. In an effort to shortcut the computations, another approach was finally used: "Beta backpropagation." This method was motivated by the early "backpropagation" schemes used in medical tomography (see Brooks and Di Chiro, 1976). Our method can be described as follows.

Consider the y th cell, and iterate through all possible values of the EOF coefficient β_y . Let $P_n^*(y)$ denote the maximum power found for the path from source s to array r

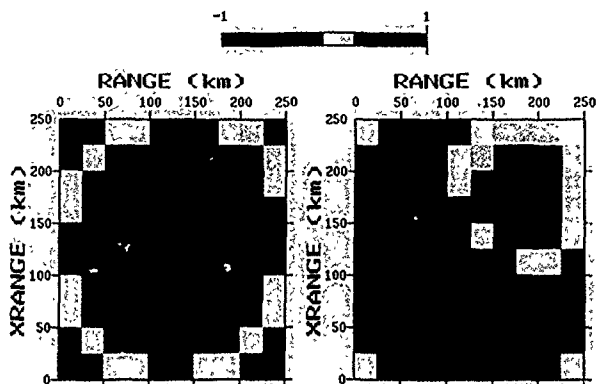


FIG 8 Final estimates for modified EOF coefficients as a function of (x, y) . Compare to Fig 4

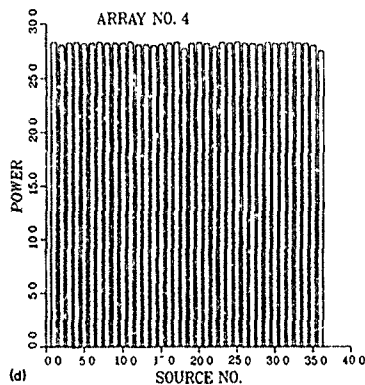
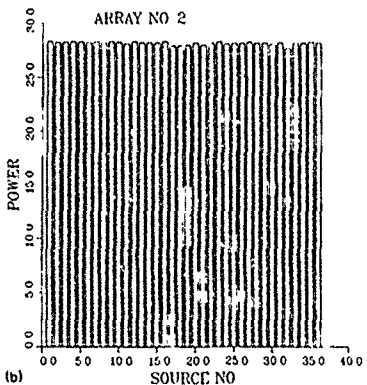
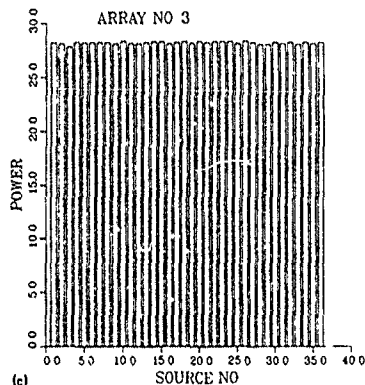
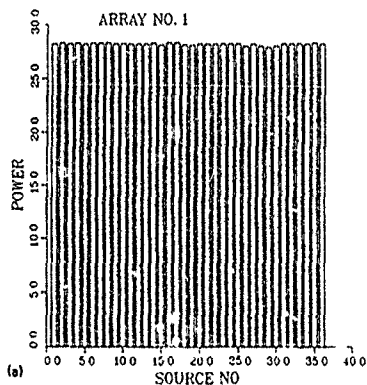


FIG 9 Final estimates for MFP power P_m at each receiving array r for each source s given environment of Fig 8. Compare to Fig 7

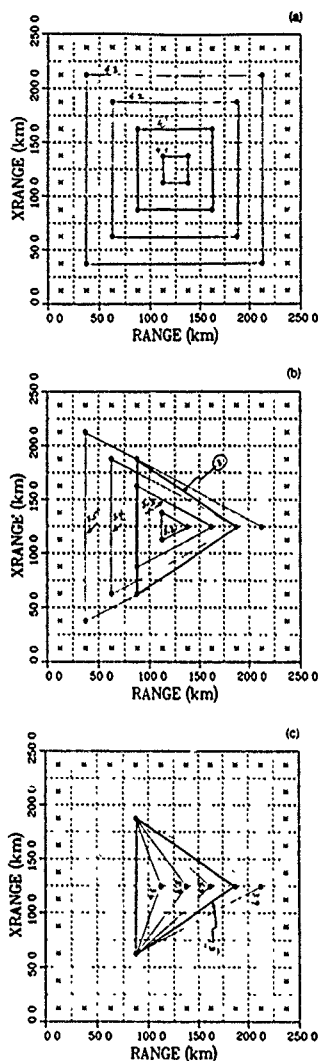


FIG 10 Configuration designs considered for three and four arrays (a) four-array squares, (b) three array triangles with two or three vertices changing location, (c) three-array triangles with one vertex changing location

intersecting the i th cell (all other coefficients along the path are fixed), i.e.,

$$P_n^*(ij) = \max_{\beta_i} P_n.$$

TABLE I. Results with four arrays.

Design ID	4 1	4	4 2	4 3
Max error β_1	53.9	3.0	4.7	38.2
Av error β_1	15.4	1.1	1.2	7.2
Max error β_2	3.9	1.6	2.1	5.4
Av error β_2	1.4	0.5	0.7	1.4
No. sweeps	33	31	26	18

Let $\beta_{1,n}^*(ij)$ be the corresponding coefficient, and $\Delta_n(ij)$ be the length of the path through the cell. Then, define the new coefficient estimate by

$$\hat{\beta}_1(ij) = \sum_n \beta_{1,n}^*(ij) \Delta_n(ij) \left(\sum_n \Delta_n(ij) \right)^{-1}.$$

Next, consider β_2 and repeat the procedure. Then, proceed to the next cell. When all cells have been processed (one sweep), repeat from the first cell (note that all the cells may have changed their coefficients and so path contributions from the non- i th cell will have changed). For the results presented here, the process was stopped when the total power $P_{total} = \sum_n P_n$ was no longer increasing.

For the example discussed, we obtained excellent results for 31 sweeps as shown in Figs. 8 and 9, with a maximum sound-speed error everywhere of less than 0.2 m/s.

Next, we considered other configurations of three and four arrays, and Fig. 10 illustrates the ones examined so far. We found that the four-array design outperformed the three-array design, and that the best results corresponded to designs that were neither very widespread nor very compactly concentrated in the region. When comparing designs, we considered the maximum EOF coefficient errors and the average coefficient errors obtained at the conclusion of the beta backpropagation computation and presented in Tables I and II. The best configuration for three arrays (design ID 3) resulted in a maximum sound-speed error of 1.0 m/s.

V. CONCLUSIONS

We conclude that efficient characterization of the environment, i.e., through the use of empirical orthogonal functions, plus careful source/array geometry, can result in highly accurate estimates of the 3-D sound-speed environment. In particular, we saw that four vertical arrays spanning the upper 1000 m of water and placed in the interior of the region of interest with shots distributed every 25 km along the pe-

TABLE II. Results with three arrays

Design ID	3	3 2	3 3	3 4	3 5	3 6	3 7	3 8	3 9
Max error β_1	13.6	58.0	22.0	22.6	27.2	23.8	14.2	32.7	11.1
Av error β_1	4.8	24.9	6.0	6.1	6.1	4.8	3.1	6.3	3.3
Max error β_2	6.5	7.8	3.7	8.2	6.9	15.1	2.7	3.4	8.6
Av error β_2	1.6	2.4	1.1	2.1	2.0	2.5	0.7	0.9	1.7
No. sweeps	15	7	23	23	27	30	40	17	46

rimeter resulted in maximum errors less than 0.2 m/s for our 250-km-per-side square region and for the frequency 20 Hz. Configurations with fewer arrays resulted in less accuracy, and arrays placed too near the perimeter or too close together in the center of the region resulted in poorer performance.

VI. FUTURE WORK

Our results so far involve simulation "data" in a simulated eddy environment. Even for these ideal conditions, many issues remain to be resolved, such as how does the number of cells relate to the number of sources required for a desired sound-speed resolution (for the examples discussed here we had many paths through each cell resulting in an overdetermined system)? How finely does the environment have to be gridded in order for the adiabatic assumption to remain "valid"? Will some form of interpolation through the environment be necessary to counteract the abrupt cell boundaries (requiring a horizontal correlation scale parameter) and what will the effect be? Can we suggest an optimal geometry for a given number of arrays and sources? What range limitations will be encountered by this technique and why? Are there better algorithms for finding the global MFP maxima? Additional questions will arise with measured data, such as will there be difficulties FFT processing shot data at the frequencies of interest, i.e., 10 to 30 Hz, with subsequent problems inverting the cross-spectral matrix? Will consideration of additional frequencies introduce more useful information? How will removal of bottom interacting energy via mode filtering affect our computations? What will be the cumulative effects of errors/uncertainties in source locations, array deformations, environmental measurements, and smoothings? These issues will be addressed in future work.

APPENDIX

Let $\phi = p/\sqrt{\rho}$, where p is pressure and ρ is density. Let the unperturbed eigenfunctions $\phi_i(z)$ satisfy

$$(L + V)\phi_i = \lambda_i \phi_i,$$

where $\lambda_i = k_i^2$, k_i is the i th modal wave number, $V = \omega^2/c_0^2(z)$, and $L = \rho^{1/2} \partial_z \rho^{-1/2} \partial_z \rho^{1/2}$. Let the perturbed eigenfunctions $\tilde{\phi}_i$ satisfy

$$(L + V + \delta V)\tilde{\phi}_i = \tilde{\lambda}_i \tilde{\phi}_i,$$

where $\delta V = \omega^2(1/c^2(z) - 1/c_0^2(z))$, and $\tilde{\lambda}_i$ is the perturbed eigenvalue. Let $\tilde{\phi}_i = \sum_j a_{ij} \phi_j$. Then

$$(L + V + \delta V) \sum_j a_{ij} \phi_j = \tilde{\lambda}_i \sum_j a_{ij} \phi_j.$$

Applying $\langle \phi_m | = \int_0^\infty \phi_m(z) dz$ to both sides and recalling that

$$\langle \phi_m | \phi_n \rangle = \delta_{mn}$$

gives

$$a_{im} \lambda_m + \sum_j a_{ij} \langle \phi_m | \delta V | \phi_j \rangle = \tilde{\lambda}_i a_{im}.$$

Setting $a_{ii} = 1$ and discarding terms of $O(|\delta V|^2)$ while noting that $a_{ij} = O(|\delta V|)$ we have, for $i = m$,

$$\tilde{\lambda}_i - \lambda_i = \langle \phi_i | \delta V | \phi_i \rangle = \delta \lambda_i.$$

Let $\delta V = \omega^2 \sum_j \beta_j \phi_j(z)$. Then

$$\delta \lambda_i = \omega^2 (\beta_1 A_{i1} + \beta_2 A_{i2} + \dots),$$

where

$$A_{ij} = \langle \phi_i | \phi_j(z) | \phi_i \rangle.$$

Thus, given the EOFs $\{\phi_j(z)\}$, the unperturbed eigenfunctions $\{\phi_i(z)\}$, eigenvalues $\{\lambda_i\}$ (computed from the mean AXBT sound-speed profile), and coefficients $\{\beta_j\}$, we can rapidly (and accurately) compute the perturbed eigenvalues $\{\tilde{\lambda}_i\}$ from which we can obtain the new modal wave numbers.

¹ The use of MFP for environmental inverse problems has been suggested elsewhere (Tolstoy, 1987; Livingston and Diachok, 1989).

² The authors have recently begun investigating the linear processor and found it to produce similar results to those presented in this section.

³ AXBT stands for air-deployed expendable bathythermograph, which measures temperature as a function of depth. These measurements are then converted to sound speeds.

⁴ Recent investigations using low-frequency (15 Hz) shot data (see Karangelan and Diachok, 1990; Fizzell et al., 1990) have not shown any difficulties for sources at approximately 50-km range although diagonal loading was necessary, as expected.

Baer, R. N. (1980). "Calculations of sound propagation through an eddy," *J. Acoust. Soc. Am.* 67, 1180-1185.

Baer, R. N. (1981). "Propagation through a three-dimensional eddy including effects on an array," *J. Acoust. Soc. Am.* 69, 70-75.

Behringer, D., Birdsall, T., Brown, M., Cornuelle, B., Heinmiller, R., Knox, R., Metzger, K., Munk, W., Spiesberger, J., Spindel, R., Webb, D., Worcester, P., and Wunsch, C. (1982). "A demonstration of ocean acoustic tomography," *Nature* 299, 121-125.

Brooks, R. A., and Di Chiro, G. (1976). "Principles of computer assisted tomography (CAT) in radiographic and radioisotopic imaging," *Phys. Med. Biol.* 21, 689-732.

Bucker, H. P. (1976). "Use of calculated sound fields and matched-field detection to locate sound sources in shallow water," *J. Acoust. Soc. Am.* 59, 368-373.

Cornuelle, B., Munk, W., and Worcester, P. (1989). "Ocean acoustic tomography from ships," *J. Geophys. Res.* 94, 6232-6250.

Cornuelle, B., Wunsch, C., Behringer, D., Birdsall, T., Brown, M., Heinmiller, R., Knox, R., Metzger, K., Munk, W., Spiesberger, J., Spindel, R., Webb, D., and Worcester, P. (1985). "Tomographic maps of the ocean mesoscale Part I: Pure acoustics," *J. Phys. Oceanogr.* 15, 133-152.

Davis, R. E. (1976). "Predictability of sea surface temperature and sea level pressure anomalies over the North Pacific Ocean," *J. Phys. Oceanogr.* 6, 249-266.

Fizzell, R. G. (1987). "Application of high-resolution processing to range and depth estimation using ambiguity function methods," *J. Acoust. Soc. Am.* 82, 606-613.

Fizzell, R. G., Dicus, R. L., and Diachok, O. I. (1991). "Experimental applications of matched field processing in the North Pacific," *J. Acoust. Soc. Am.* (to be submitted).

Kak, A. C., and Slaney, M. (1987). *Principles of Computerized Tomographic Imaging* (IEEE, New York).

Karangelan, C., and Diachok, O. (1991). "Sound speed determination using matched field processing techniques," *J. Acoust. Soc. Am.* (to be submitted).

Kirkpatrick, S. (1984). "Optimization by simulated annealing: quantitative studies," *J. Stat. Phys.* 34, 975-986.

Kirkpatrick, S., Gelatt, C. D., Jr., and Vecchi, M. P. (1983). "Optimization by simulated annealing," *Science* 220, 671-680.

Kundu, P. K., Allen, J. S., and Smith, R. L. (1975). "Modal decomposition of the velocity field near the Oregon coast," *J. Phys. Oceanogr.* 5, 683-704.

- LeBlanc, L. R., and Middleton, F. M. (1980) "An underwater acoustic sound velocity data model," *J. Acoust. Soc. Am.* 67, 2055-2062.
- Livingston, E., and Diachok, O. (1989) "Estimation of average under-ice reflection amplitudes and phases using matched field processing," *J. Acoust. Soc. Am.* 86, 1909-1919.
- Lynch, J. (1990). Personal communication.
- Metropolis, N., Rosenbluth, A. W., Rosenbluth, M. N., Teller, A. H., and Teller, E. (1953). "Equation of state calculations by fast computing machines," *J. Chem. Phys.* 21, 1087-1092.
- Munk, W. H., and Wunsch, C. (1979) "Ocean acoustic tomography: a scheme for large scale monitoring," *Deep Sea Res.* 26 A, 123-161.
- NODC (1968) "The variation of sound velocity and temperature in the North Pacific," Vol II, National Oceanographic Data Center, Washington, DC 20390.
- Porter, M. B., and Reiss, E. L. (1984) "A numerical method for ocean acoustic normal modes," *J. Acoust. Soc. Am.* 76, 244-252.
- Porter, M. B., and Reiss, E. L. (1985) "A numerical method for bottom interacting ocean acoustic normal modes," *J. Acoust. Soc. Am.* 77, 1760-1767.
- Press, W. H., Flannery, B. P., Teukolsky, S. A., and Vetterling, W. T. (1986) *Numerical Recipes* (Cambridge U.P., Cambridge, MA).
- Rizzoli, P. M., Spiesberger, J. L., and Chaves, M. (1985) "Gulf Stream variability for acoustic tomography," *Deep Sea Res.* 32, 237-250.
- Shang, E. C. (1989) "Ocean acoustic tomography based on adiabatic mode theory," *J. Acoust. Soc. Am.* 85, 1531-1573.
- Spiesberger, J. L., Spindel, R. C., and Metzger, K. (1980) "Stability and identification of ocean acoustic multipaths," *J. Acoust. Soc. Am.* 67, 2011-2017.
- Stanford, G. E. (1974) "Low frequency fluctuations of a cw signal in the ocean," *J. Acoust. Soc. Am.* 55, 968-977.
- Tolstoy, A. (1987) "Matched field estimation of environmental parameters," in *21st Annual Congress of the Canadian Meteorological and Oceanographic Society* June 1987 (Publisher, City).
- Tolstoy, A. (1989a) "Sensitivity of matched field processing to sound-speed profile mismatch for vertical arrays in a deep water Pacific environment," *J. Acoust. Soc. Am.* 85, 2394-2404.
- Tolstoy, A. (1989b) "Low frequency acoustic tomography using matched field processing," *J. Acoust. Soc. Am. Suppl.* 186, S7.
- Van Trees, H. L. (1968) *Detection, Estimation, and Modulation Theory* (Wiley, New York).

Multifold phase space path integral synthetic seismograms

Mrinal K. Sen¹ and L. Neil Frazer²

¹Institute for Geophysics, The University of Texas at Austin, Austin, Texas 78759, USA

²Hawaii Institute of Geophysics, Honolulu, Hawaii 96822, USA

Accepted 1990 September 19 Received 1990 September 17, in original form 1990 May 10

SUMMARY

We consider a medium consisting of homogeneous layers separated by curved interfaces. In order to evaluate the response of a single generalized ray, the source and receiver wavefields are expanded in a series of plane waves. The coupling of these plane waves at each point of the surfaces of material discontinuity is determined by means of a Kirchhoff integral using generalized reflection and transmission coefficients. The resulting integral, called the multifold phase space path integral (PSPI) consists of a series of integrals over ray parameters and over interfaces touched by the generalized ray on its way from the source to the receiver. This approach is a generalization of the multifold configuration space path integral (CSPI) to which it reduces by successive application of the stationary phase point method over the ray-parameter integrals.

The PSPI like the CSPI automatically includes diffractions from corners. In addition classical head waves are included, although for curved interfaces the head waves are only approximate. 2-D synthetic seismograms are converted to equivalent approximate point-source responses by assuming cylindrical symmetry about source and/or receiver. The waveforms and amplitude of PSPI synthetic seismograms compare well with those computed by generalized ray theory for a 1-D model, and with finite difference synthetics for a 2-D model.

Key words: diffractions, head waves, Kirchhoff, phase space, synthetic seismograms.

1 INTRODUCTION

Kirchhoff–Helmholtz (KH) integrals, especially ray-Kirchhoff formulations, have been used both in their acoustic (Troyer 1977, Hilterman 1970, 1975) and elastic forms (Frazer & Sen 1985, Sen & Frazer 1985) for computing reflection and refraction seismograms in laterally inhomogeneous media. Rays are traced from both source and receiver to a surface of material discontinuity and the KH theory is applied to determine the coupling between each source ray and each receiver ray at the interface. The assumption inherent in the KH formulation is the *tangent plane approximation* which assumes that at the point of intersection wavefronts are locally plane and the interface is planar, allowing the use of plane wave reflection and transmission coefficients. However, real sources are finite and actual wavefronts at the interface are spherical. Brekhovskikh (1960) established a relation between the spherical and plane wave reflection coefficients and showed that the error term grows in the post-critical region. Thus, the Kirchhoff formulation will be in error for near and past critical reflections.

The ray-Kirchhoff formulation is valid even when the receiver is located at a caustic and the diffractions from any corner on the surface of integration are automatically included. However, caustics of the source and receiver wavefields caused on the surface of integration are not correctly treated, head waves are not included, and the diffractions from corners at intermediate interfaces are not included.

Recently, Zhu (1988) developed a ray-Kirchhoff formulation that avoids the singularity at the caustics by using a modified Eikonal equation to derive the geometrical ray theory Green's functions. This approach gives a solution that is regular even when there are caustics on the surfaces of integration. However, as the ray-field becomes multivalued (due to multipathing) on the surface of integration, the integration has to be carried out for each branch of the ray-field. This gives rise to diffraction like phases from each endpoint of the surface of integration (Frazer & Sinton 1984, Sen & Frazer 1985).

A generalization of the Kirchhoff–Helmholtz procedure which overcomes some of these problems is the multifold configuration space path integral (CSPI) (Frazer 1987, Sen &

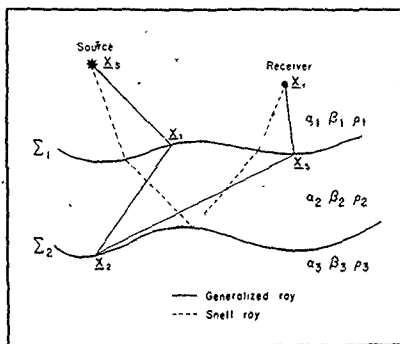


Figure 1. Formulation of a CSPI. Summing over all paths from source to the receiver via the interfaces reduces to Snell ray path at the high-frequency limit

Frazer 1987). Here we briefly review the CSPI, for completeness. Consider a medium consisting of two layers over a half-space. The response of a single generalized ray (Fig. 1) can be written as

$$u(x_r) \approx \int dx_1 \int dx_2 \left\{ dx_3 f(x_s, x_1, x_2, x_3, x_r) \right. \\ \left. \times \exp[i\omega T(x_s, x_1, x_2, x_3, x_r)] \right\}, \quad (1)$$

which is derived using the elastic KH integral iteratively. The function f contains geometrical spreading terms, generalized reflection/transmission coefficients, etc. and T is the traveltime of a ray from the source to the receiver via the interfaces. The CSPI makes use of geometrical acoustics, generalized plane wave reflection and transmission coefficients and an elastodynamic form of the KH integral. Thus the approximations made are those used in geometrical ray theory and the tangent plane approximation. In essence a CSPI is a multiple Huygen's construction and the resulting integral resembles the Feynman configuration space path integral (Schulman 1981). A true Feynman path integral solves the Schrodinger equation (factorized Helmholtz equation, in the seismological context) in terms of an infinite dimensional integral, which when evaluated by stationary phase methods, gives the classical path. Thus, our CSPI given by equation (1) is not a true Feynman path integral, for the derivation of (1) is based on an entirely different context and assumptions. First, separation of the elastic wave equation into two exact one-way Schrodinger type equations has not been made. Second, we integrate only over surfaces of material discontinuity where the boundary conditions are explicit. Our integral contains the contribution of all possible paths which are piecewise straight with vertices at the interfaces, hence the name *configuration space path integral*. Successive application of the stationary phase method to equation (1) yields the classical or Snell ray paths.

The CSPI avoids the problem of caustics and multipathing of rays on surfaces of integration and includes diffractions from corners at any intermediate interface. However, head

waves and certain tunnelled waves are not included, and a layer pinchout will give rise to a singularity in the integrand for a ray transmitted through the pinched-out layer. Such singularities are integrable, but near the layer-pinchouts the curvature of the wavefront is so great that the Kirchhoff approximation is no longer valid. To address these problems we introduce below a generalization of the CSPI called the multifold phase space path integral (PSPI)

2 SCALAR KH INTEGRAL

Here for completeness we derive a frequency domain version of the scalar KH integral which will be needed in the sequel for the derivation of the PSPI. As shown in Fig. (2) we consider a volume V with boundary ∂V and an outward pointing unit normal \mathbf{n} and consider two scalar wave equations given by

$$\left(\nabla^2 + \frac{\omega^2}{\alpha^2}\right)\phi_1 = f_1, \quad \left(\nabla^2 + \frac{\omega^2}{\alpha^2}\right)\phi_2 = f_2, \quad (2)$$

where ω is the angular frequency, α is the wave velocity and f_1 and f_2 have support at points x_1 and x_2 , respectively. Thus the function f_1 vanishes inside V and on ∂V and f_2 vanishes outside V and on ∂V . The scalar fields ϕ_1 and ϕ_2 can be used to represent displacement or velocity potentials in an elastic medium or pressure in an acoustic medium. By the divergence theorem, we have

$$\int_{\partial V} \mathbf{n} \cdot (\phi_1 \nabla \phi_2 - \phi_2 \nabla \phi_1) dA = \int_V (\phi_1 \nabla^2 \phi_2 - \phi_2 \nabla^2 \phi_1) dV \\ = \int_V \phi_1 f_2 dV. \quad (3)$$

Note that the surface integral reduces to a line integral in 2-D. Letting $f_2 = \delta(x - x_2)$ this integral reduces to

$$\phi_1(x_2) = \int_{\partial V} \mathbf{n} \cdot (\phi_1 \nabla \phi_2 - \phi_2 \nabla \phi_1) dA. \quad (4)$$

Thus the scalar wavefield ϕ_1 at point x_2 due to a source f_1 outside of V is expressed as an integral of the scalar fields ϕ_1 , ϕ_2 and their normal derivatives over the surface ∂V . For correct use of (4) ϕ_1 must be due to a source with support exterior to V and the scalar field ϕ_2 must be associated with a point-source at x_2 of the type $f_2 = \delta(x - x_2)$. In the derivation of the CSPI (Frazer & Sen 1985), the integrand of the scalar KH integral is evaluated by using geometrical ray theory Green's functions. To

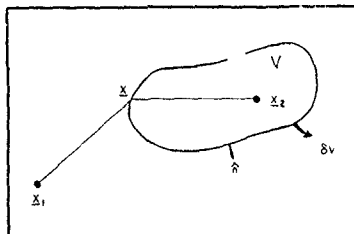


Figure 2. The scalar Kirchhoff-Helmholtz formulation

derive the PSPI, we will instead use the ray-parameter expansions of the source and receiver wavefields given in the next section.

3 P-INTEGRAL REPRESENTATION OF SCALAR WAVEFIELDS IN 2-D HOMOGENEOUS, ISOTROPIC MEDIA

The frequency-domain vector wave equation for displacement \mathbf{u} in a homogeneous, isotropic, elastic medium is given as

$$(\lambda + 2\mu)\nabla(\nabla \cdot \mathbf{u}) - \mu\nabla \times \nabla \times \mathbf{u} + \rho\omega^2\mathbf{u} = \mathbf{f}. \quad (5)$$

Decomposing \mathbf{u} into Helmholtz potentials as

$$\mathbf{u} = \nabla\phi - \nabla \times \mathbf{A} \quad (6)$$

with

$$\nabla \cdot \mathbf{A} = 0$$

gives

$$\nabla \cdot \mathbf{u} = \nabla^2\phi \quad (7)$$

and

$$\nabla \times \mathbf{u} = \nabla \times \nabla \times \mathbf{A}$$

Thus from (5) and (6) we obtain

$$\nabla[(\lambda + 2\mu)\nabla^2\phi + \rho\omega^2\phi] - \nabla \times (\rho\omega^2\mathbf{A} + \mu\nabla \times \nabla \times \mathbf{A}) = \mathbf{f}. \quad (8)$$

The source term \mathbf{f} can also be expressed in terms of Helmholtz potentials as

$$\mathbf{f} = \nabla p_0 - \nabla \times \mathbf{L}_0. \quad (9)$$

For a purely compressional source, $\mathbf{f} = \nabla p_0$, and $\mathbf{L}_0 = 0$, so that (8) reduces to

$$(\nabla^2 + \frac{\omega^2}{\alpha^2})\phi = \frac{p_0}{(\lambda + 2\mu)} = P_0. \quad (10)$$

We now apply a spatial Fourier transform given by

$$\tilde{\phi}(p, z) = \int_{-\infty}^{\infty} \exp(-i\omega p x) \phi(x, z) dx \quad (11)$$

for $\omega > 0$, with inverse

$$\phi(x, z) = \frac{\omega}{2\pi} \int_{-\infty}^{\infty} \exp(i\omega p x) \tilde{\phi}(p, z) dp \quad (12)$$

From (10) and (11), we have

$$\partial_z^2 \tilde{\phi} + \omega^2 \left(\frac{1}{\alpha^2} - p^2 \right) \tilde{\phi} = \tilde{P}_0 \quad (13)$$

Homogeneous solutions of (13) can be written as $\tilde{\phi} = \exp(\pm i\omega q z)$, where $q = \sqrt{(1/\alpha^2 - p^2)}$ is the vertical slowness. In order to obtain the inhomogeneous solutions, which are determined uniquely by the source term on the right-hand side of (13), further transformation is necessary. Applying the following transformation

$$\tilde{\phi} = \int_{-\infty}^{\infty} \tilde{\phi} \exp(-i\gamma z) dz \quad (14)$$

we obtain

$$(-\gamma^2 + \omega^2 q^2) \tilde{\phi} = \tilde{P}_0$$

or

$$\tilde{\phi} = \frac{\tilde{P}_0}{(-\gamma^2 + \omega^2 q^2)} \quad (15)$$

which can be evaluated after we evaluate \tilde{P}_0 . This is given as

$$\tilde{P}_0 = \int_{-\infty}^{\infty} \int_{-\infty}^{\infty} dx dz \exp(-i\omega p x - i\gamma z) P_0(x, z) \quad (16)$$

For a point explosion source,

$$\mathbf{f} = \nabla \delta(\mathbf{x} - \mathbf{x}_s) \quad (17)$$

and we have

$$P_0 = \frac{\rho_0}{\rho \alpha^2}$$

Without loss of generality we can take $\mathbf{x}_s = \mathbf{z}_s = 0$ so that

$$\tilde{P}_0 = \frac{1}{\rho \alpha^2} \int_{-\infty}^{\infty} \int_{-\infty}^{\infty} dx dz \exp(-i\omega p x - i\gamma z) \delta(x) \delta(z)$$

Then substitution for \tilde{P}_0 in (15) gives

$$\tilde{\phi} = \frac{1}{\rho \alpha^2} \left(\frac{1}{-\gamma^2 + \omega^2 q^2} \right), \quad \tilde{\phi} = \frac{1}{2\pi} \int_{-\infty}^{\infty} \exp(i\gamma z) \tilde{\phi} dz, \quad (18)$$

$$\tilde{\phi} = \frac{1}{2\pi \rho \alpha^2} \int_{-\infty}^{\infty} \frac{\exp(i\gamma z)}{(\omega^2 q^2 - \gamma^2)} d\gamma \quad (19)$$

We now use residue theorem to evaluate (19) and apply inverse Fourier transform to obtain ϕ . This is given as

$$\phi = \frac{i\omega}{2\pi \rho \alpha^2} \int_{-\infty}^{\infty} \frac{\exp[i\omega(pz + qz)]}{(2\omega q)} dp,$$

$$\phi = \frac{i}{2\pi \rho \alpha^2} \int_{-\infty}^{\infty} \frac{\exp(i\omega \mathbf{P} \cdot \mathbf{X})}{(2q)} dp, \quad (20)$$

where $\mathbf{P} = \mathbf{x}p + \mathbf{z}q$ is the slowness vector. Equation (20) expresses the P -wave displacement potential due to an explosion source in a 2-D homogeneous, isotropic medium as an integral over ray-parameter p .

4 POINT-FORCE IN A 2-D MEDIUM

The elastic equations of motion for a line force acting in an infinite medium can be written as (e.g., Piliant, 1979)

$$\alpha^2 \nabla(\nabla \cdot \mathbf{u}) - \beta^2 \nabla \times \nabla \times \mathbf{u} + \omega^2 \mathbf{u} = -\mathbf{a} \frac{\delta(r)}{\rho 2\pi r} \quad (21)$$

where α and β are compressional and shear wave velocities, ρ is the density, $r = \sqrt{(x^2 + z^2)}$ and \mathbf{a} is a unit vector in the direction of the point-force. First, we write

$$\mathbf{u} = \nabla(\nabla \cdot \mathbf{A}_p) - \nabla \times (\nabla \times \mathbf{A}_s), \quad (22)$$

where we have introduced a scalar potential $(\nabla \cdot \mathbf{A}_p)$ and a vector potential $(\nabla \times \mathbf{A}_s)$ (e.g., Piliant 1979). We also have the identity

$$\mathbf{a} \frac{\delta(r)}{\rho 2\pi r} = \nabla \nabla \cdot \left(\frac{\mathbf{a} \ln(r)}{2\pi \rho} \right) - \nabla \times \nabla \times \left(\frac{\mathbf{a} \ln(r)}{2\pi \rho} \right) \quad (23)$$

Thus from (21), (22) and (23), we obtain

$$(\nabla^2 + k_p^2)A_p = -\mathbf{a} \frac{\ln(r)}{2\pi\rho\alpha^2}, \quad (24)$$

$$(\nabla^2 + k_s^2)A_s = -\mathbf{a} \frac{\ln(r)}{2\pi\rho\beta^2}, \quad (25)$$

where

$$k_p^2 = \frac{\omega^2}{\alpha^2}, \quad k_s^2 = \frac{\omega^2}{\beta^2}.$$

Notice that, as \mathbf{a} is a constant vector, equations (24) and (25) show that A_p and A_s are parallel to \mathbf{a} . Dotting \mathbf{a} into both sides of (24) and (25) and letting $A_p = \mathbf{a} \cdot A_p$ and $A_s = \mathbf{a} \cdot A_s$, we obtain

$$(\partial_z^2 + \partial_r^2)A_p + k_p^2 A_p = -\frac{\ln(r)}{2\pi\rho\alpha^2}, \quad (26)$$

$$(\partial_z^2 + \partial_r^2)A_s + k_s^2 A_s = -\frac{\ln(r)}{2\pi\rho\beta^2}, \quad (27)$$

which are the scalar wave equations for the P and S potentials. In order to solve (26) and (27) by transform methods we first determine the Fourier transform, with respect to x , of $\ln(r)/2\pi$. Recall that $\ln(r)/2\pi$ is the solution of

$$\nabla^2 \psi = \delta(x) \delta(z),$$

which approaches zero as r goes to infinity. Taking a Fourier transform in x yields

$$(\partial_z^2 - K_x^2)\tilde{\psi} = \delta(z),$$

which gives the x -transform of $\ln(r)/2\pi$ as

$$\tilde{\psi} = \frac{\exp(-|K_x||z|)}{-2|K_x|} \quad (28)$$

where $| \cdot |$ represents the modulus. As the procedures for solving (26) and (27) are the same we consider equation (26) only. We take a Fourier transform in x of (26) and substitute for the Fourier transform of $\ln(r)/2\pi$ the expression given in the right-hand side of equation (28). This gives

$$(\partial_z^2 + \gamma^2)\tilde{A}_p = \frac{1}{\rho\alpha^2} \frac{\exp(-|K_x||z|)}{(-2|K_x|)} \quad (29)$$

where

$$\gamma^2 = K_p^2 - K_x^2.$$

We know that the solution of $(\partial_z^2 + \gamma^2)\phi = \delta(z)$ is given by $\exp(i\gamma|z|)/(2i\gamma)$. Therefore, the solution of equation (29) is given by the following convolution

$$\tilde{A}_p = \frac{1}{\rho\alpha^2} \int_{-\infty}^{\infty} d\xi \frac{\exp(-|K_x||z-\xi|) \exp(i\gamma|\xi|)}{(-2|K_x|)} \quad (30)$$

Taking the inverse Fourier transform of this equation, we obtain

$$A_p(x, z) = -\frac{1}{8\pi\rho\alpha^2} \int_{-\infty}^{\infty} dK_x \exp(iK_x x) \times \int_{-\infty}^{\infty} d\xi \frac{\exp(-|K_x||z-\xi|) \exp(i\gamma|\xi|)}{(|K_x|\gamma)}$$

Now we set $z=0$ and $x=r$ to obtain

$$A_p(r) = -\frac{1}{4\pi\rho\alpha^2} \int_{-\infty}^{\infty} \frac{dK_x \exp(iK_x r)}{|K_x|\gamma} \times \int_0^{\infty} d\xi \exp[-\xi(|K_x| - i\gamma)],$$

or

$$A_p(r) = -\frac{1}{4\pi\rho\alpha^2} \int_{-\infty}^{\infty} dK_x \frac{\exp(iK_x r)}{\gamma |K_x| (|K_x| - i\gamma)}. \quad (31)$$

Substituting $K_x = \omega p$ in equation (31), we express A_p as an integral over ray-parameter p . Thus equation (31) represents the scalar P -wave potential due to a point-force in a 2-D elastic medium

5 REFLECTION FROM AN IRREGULAR INTERFACE

In order to evaluate reflections from a curved interface (Fig. 3), we follow the procedure outlined in Frazer & Sen (1985). The surface of material discontinuity Σ is made coincident with a part of the surface of integration such that the volume V contains both points \mathbf{x}_1 and \mathbf{x}_2 . We will use equation (4) and the point \mathbf{x}_1 and \mathbf{x}_2 used in equation (4) will be replaced by \mathbf{x}_s and \mathbf{x}_r respectively. Now, we replace ϕ_1 by its equivalent scattered field appearing to emanate from points outside volume V . Although the physical source point is inside V , the virtual source region is not inside V , and so none of the assumptions used in the derivation above is violated. Thus we have

$$\phi_s(\mathbf{x}_r) = \int_{\Sigma} \mathbf{n} \cdot (\phi_r' \nabla \phi_r - \phi_r \nabla \phi_r') dA, \quad (32)$$

where the superscript 'r' stands for the reflected field at the interface and the subscripts 'r' and 's' for the receiver and source wavefields, respectively. The symbol $\phi_s(\mathbf{x}_r)$ represents the field reflected from Σ , measured at the point \mathbf{x}_r due to a source at \mathbf{x}_s .

In our earlier approach we assumed that the wavefronts and the interface are locally planar and used the plane wave reflection coefficient to evaluate the scattered field. Here, we will make assumptions that are less severe. Both the fields ϕ_1 and ϕ_2 will be expressed as integrals over ray parameters and then we will use the plane wave reflection coefficient to express the reflected field at the interface

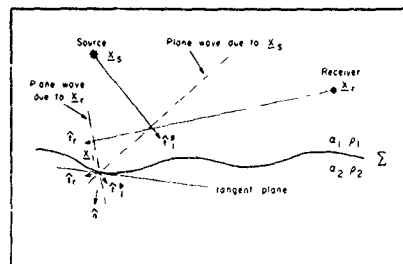


Figure 3. PSPI for reflection from a curved interface

Thus, the wavefronts are actually planar although the interfaces are assumed to be locally plane ignoring the interaction of the wavefield between neighbouring points of the interfaces. At the interface, the incident scalar field due to an explosion source (equation 20) ϕ_s can be written as

$$\phi_s(x_1) = \frac{i}{2\pi\rho\alpha_1^2} \int dp_s \frac{\exp[i\omega \mathbf{P} \cdot (\mathbf{x}_1 - \mathbf{x}_s)]}{(2q_s)}, \quad (31)$$

where \mathbf{P} is the slowness vector, q_s is the vertical slowness such that $\mathbf{P} = xp_s + zq_s$ and \mathbf{x}_1 is a point on the interface. Now $\mathbf{P} = (1/\alpha_1)t_1^p$, where t_1^p is the unit vector normal to the plane wavefront. Therefore,

$$\phi_s(x_1) = \frac{i}{2\pi\rho\alpha_1^2} \int dp_s \frac{\exp\{(i\omega/\alpha_1)t_1^p \cdot (\mathbf{x}_1 - \mathbf{x}_s)\}}{(2q_s)}, \quad (32)$$

In order to calculate the reflected field at point \mathbf{x}_1 , we apply Snell's law at that point. For each plane wave appearing in the above equation we calculate the angle of incidence with respect to the normal \mathbf{n} at \mathbf{x}_1 and then apply Snell's law to obtain the reflected field. Let t_1^{rp} be the direction of the reflected wavefield; then following Frazer & Sen (1985), we have

$$t_1^{rp} = t_1^p \cdot (1 - 2nn)$$

where \mathbf{i} is the unit dyadic. Thus, the reflected field on the upper surface of Σ will be given as

$$\phi'_s(x_1) = \frac{i}{2\pi\rho\alpha_1} \int dp_s R_{pp} \frac{\exp\{(i\omega/\alpha_1)t_1^{rp} \cdot (\mathbf{x}_1 - \mathbf{x}_s)\}}{(2q_s)}, \quad (33)$$

where R_{pp} is the plane wave reflection coefficient (for potentials) computed for the local slowness at the interface. Also, since the medium is homogeneous above the interface, $\alpha_1 = \alpha_s$. The incident wavefield at \mathbf{x}_1 due to the receiver can be written as

$$\phi_r(x_1) = \frac{i}{2\pi\rho\alpha_1^2} \int dp_r \frac{\exp\{(i\omega/\alpha_1)t_r \cdot (\mathbf{x}_1 - \mathbf{x}_r)\}}{(2q_r)}, \quad (34)$$

Therefore, using (32), (35), and (36), we have

$$\phi_s(x_r) = \frac{-i\omega}{(2\pi\rho_1\alpha_1^2)(2\pi\rho_1\alpha_1^2)} \int dp_s \int_x dx_1 \int dp_r \frac{R}{(2q_s)(2q_r)} \times \exp\left\{\frac{i\omega}{\alpha_1} [t_1^{rp} \cdot (\mathbf{x}_1 - \mathbf{x}_s) + t_r \cdot (\mathbf{x}_1 - \mathbf{x}_r)]\right\}, \quad (35)$$

where

$$R = R^{pp}(\mathbf{n} \cdot \mathbf{t}_r - \mathbf{n} \cdot \mathbf{t}_1^{rp})/\alpha_1, \quad (36)$$

Equation (37) gives the reflected wavefield at the receiver point \mathbf{x}_r in terms of a three fold integral. Replacing the integrals over p_s and p_r with their stationary phase values, yields the CSPI result. Note that we used equation (20) to evaluate the source wavefield. Therefore, the resulting equation (37) represents the PP (displacement potential) measured at the receiver point due to an explosion source. The integrals for $P-S$, $S-P$ and $S-S$ reflections can be derived in the same manner and need not be given here. The expression for calculating the pressure response due to an explosion source in an acoustic medium will be very similar to equation (37). If, however, we need to calculate the PP reflection at the receiver point due to a unidirectional point force at \mathbf{x}_s we need to substitute (31) for

ϕ_s in (32) and follow the same procedure outlined above. In order to derive the equation for the transmitted field at the receiver point in a situation where \mathbf{x}_s and \mathbf{x}_r are separated by a material discontinuity, we simply replace the reflection coefficient term in (37) with its associated transmission coefficient term (Frazer & Sen 1985).

6 MULTILAYERED MEDIUM

We now consider a medium consisting of three layers as shown in Fig. 4. We wish to calculate the reflected wavefield at the receiver at point \mathbf{x}_r for the generalized ray path shown by the dashed line in the figure. Different parameters and symbols used in the following derivation are shown in Fig. 4. The derivation is carried out in the following steps. First we write the incident wave field at \mathbf{x}_1^- (the upper part of the interface S_1) as

$$\phi_s(x_1^-) = \frac{i}{2\pi\rho_1\alpha_1^2} \int dp_s \frac{\exp\{(i\omega/\alpha_1)t_1 \cdot (\mathbf{x}_1 - \mathbf{x}_s)\}}{(2q_s)}, \quad (37)$$

Next, to calculate the field at \mathbf{x}_1^+ (the lower side of S_1), we transmit each plane wave given by the above equation using the local Snell's law and plane wave transmission coefficients. We define (Frazer & Sen 1985):

$$t_1 = \mathbf{i} - \mathbf{nn}, \quad \sigma = \frac{1}{\alpha_1} t_1^p \cdot \mathbf{l}_1,$$

$$t_1^{tp} = \alpha_2 \sigma \sigma + \sqrt{(1 - \alpha_2^2 \sigma^2)} \mathbf{n}$$

Thus, we have

$$\phi_s(x_1^+) = \frac{i}{2\pi\rho_1\alpha_1^2} \int dp_s PP_{12} \frac{\exp\{(i\omega/\alpha_1)t_1^{tp} \cdot (\mathbf{x}_1 - \mathbf{x}_s)\}}{(2q_s)}, \quad (38)$$

where PP_{12} is the downward looking transmission coefficient for the potential. Next we use a KH surface integral over the surface S_1 and an integral over ray-parameter p_1 (Fig. 4) to compute the field at \mathbf{x}_2^- . The result is

$$\phi_s(x_2^-) = \frac{(i)^2 i \omega}{(2\pi\rho_1\alpha_1^2)(2\pi\rho_2\alpha_2^2)} \times \int dp_s \int_{S_1} dx_1 \int dp_1 T_{12} \times \frac{\exp\{i\omega[\mathbf{P}_s \cdot (\mathbf{x}_1 - \mathbf{x}_s) + \mathbf{P}_1 \cdot (\mathbf{x}_2 - \mathbf{x}_1)]\}}{(2q_s)(2q_1)}, \quad (39)$$

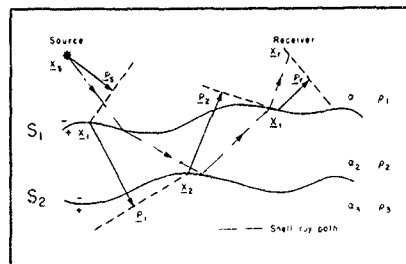


Figure 4. PSPI for a multilayered medium

where

$$T_{12} = -PP_{12} \left(\frac{1}{\alpha_1} \frac{\mathbf{n}_1 \cdot \mathbf{v}_1''}{\alpha_1} \right) \quad (42)$$

In the next step, the reflected field at \mathbf{x}_1^+ is given by

$$\phi_s(\mathbf{x}_1^+) = \frac{1}{(2\pi)^2} \frac{(i\omega)^2}{\alpha_1^2 (2\pi p_2 \alpha_2)^2} \int_{\mathbf{x}_1} d\mathbf{x}_1 \int_{\mathbf{x}_2} d\mathbf{x}_2 \int_{\mathbf{x}_3} d\mathbf{x}_3 \frac{T_{12} R_{23}}{(2q_1)(2q_2)(2q_3)} \exp(i\omega[\mathbf{P}_s \cdot (\mathbf{x}_1 - \mathbf{x}_s) + \mathbf{P}_1 \cdot (\mathbf{x}_1 - \mathbf{x}_1^+) + \mathbf{P}_2 \cdot (\mathbf{x}_2 - \mathbf{x}_2^+)]) \quad (43)$$

where

$$R_{23} = PP_{23} \left(\frac{1}{\alpha_2} \frac{\mathbf{n}_2 \cdot \mathbf{v}_2''}{\alpha_2} \right) \quad (44)$$

and

$$\mathbf{v}_i'' = \mathbf{v}_i' \cdot (1 - \mathbf{n}_i \cdot \mathbf{n}_i) \quad (45)$$

Continuing in this manner, the field at the receiver is given by

$$\phi_s(\mathbf{x}_r) = \frac{1}{(2\pi)^2} \frac{(i\omega)^2}{\alpha_1^2 (2\pi p_2 \alpha_2)^2} \int_{\mathbf{x}_1} d\mathbf{x}_1 \int_{\mathbf{x}_2} d\mathbf{x}_2 \int_{\mathbf{x}_3} d\mathbf{x}_3 \frac{T_{12} R_{23} T_{34}}{(2q_1)(2q_2)(2q_3)} \exp(i\omega[\mathbf{P}_s \cdot (\mathbf{x}_1 - \mathbf{x}_s) + \mathbf{P}_1 \cdot (\mathbf{x}_1 - \mathbf{x}_1^+) + \mathbf{P}_2 \cdot (\mathbf{x}_2 - \mathbf{x}_2^+) + \mathbf{P}_3 \cdot (\mathbf{x}_3 - \mathbf{x}_3^+) + \mathbf{P}_4 \cdot (\mathbf{x}_4 - \mathbf{x}_r)]) \quad (46)$$

where

$$T_{ij} = -PP_{ij} \left(\frac{1}{\alpha_i} \frac{\mathbf{n}_i \cdot \mathbf{v}_i''}{\alpha_i} \right) \quad (47)$$

Thus, the response of the generalized ray shown in Fig. 4 is given by the generalized ray integral as in equation (46) above. The response of a generalized ray with many branches can easily be written out as a sum of such integrals. Such integrals will be referred to as ray integrals (PSPI). These integrals have many similarities with the ray integrals used in the Born phase space path integrals used in quantum mechanics. In this formulation, the contribution of each ray is summed to evaluate the total response. As explained in Fig. 4, each ray is converted from the source and receiver are coupled by means of a scalar product. Note that a generalized ray touches the interface at $(2n+1)$ points, where n is the number of folds. Note that the power of the ray is seldom needed and that a reduced fold number can be derived directly, without the use of the ray method.

7 SYNTHETIC SEISMOGRAMS

It is known that the response can be computed more rapidly in the frequency domain. However, in the frequency domain, the attenuation in the medium can be included by making the velocities frequency dependent. We discuss here only the

frequency-domain calculation of the single interface P-P reflection problem considered earlier.

The PSPI synthetic seismograms are calculated in two steps. The first step involves calculation of wavenumber (ray parameter) integrals and the second step involves the computation of surface integrals. Since the ray-parameter integrals are oscillatory, they can be evaluated rapidly by using a generalized Filon method (GFM) quadrature formula (Frazer & Gettrust 1984). Frequency-dependent sampling intervals are chosen to avoid spatial aliasing and the ray-parameter integrals are tapered at endpoints using Hanning windows to avoid truncation phases. The ray parameter p is converted to local slowness at the interface for the evaluation of the generalized reflection and transmission coefficients. Complex angles of incidence are allowed in order to include the evanescent regime. For example, referring to Fig. 5, we note that for a ray with ray parameter p_s , we have

$$p_s = \frac{\sin(\theta_s)}{\alpha}, \quad q_s = \frac{\cos(\theta_s)}{\alpha},$$

$$p_1 = \frac{\sin(\theta_1)}{\alpha}, \quad q_1 = \frac{\cos(\theta_1)}{\alpha},$$

and

$$\theta_1 = \theta_s - \psi_1.$$

The above relations hold even in the evanescent regime and by substitution for θ_1 in the expression for p_1 and q_1 we obtain

$$p_1 = p_s \cos(\psi_1) - q_s \sin(\psi_1)$$

and

$$q_1 = q_s \cos(\psi_1) + p_s \sin(\psi_1)$$

These equations can be used to calculate the local slowness at each point along the interface. Having computed the slowness integrals, the surface integrals can be carried out simply by the method explained in Sen & Frazer (1985).

Our first numerical example is a two-layered acoustic medium consisting of an acoustic layer (P-wave velocity = 1.0 km s⁻¹, density = 1.0, thickness = 2.0 km) over an acoustic half-space (P-wave velocity = 2.0 km s⁻¹, density = 1.0). We calculate the primary reflection (pressure response

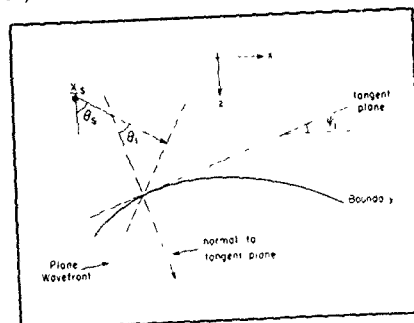


Figure 5. Conversion of ray parameter values to the local slowness at the interface.

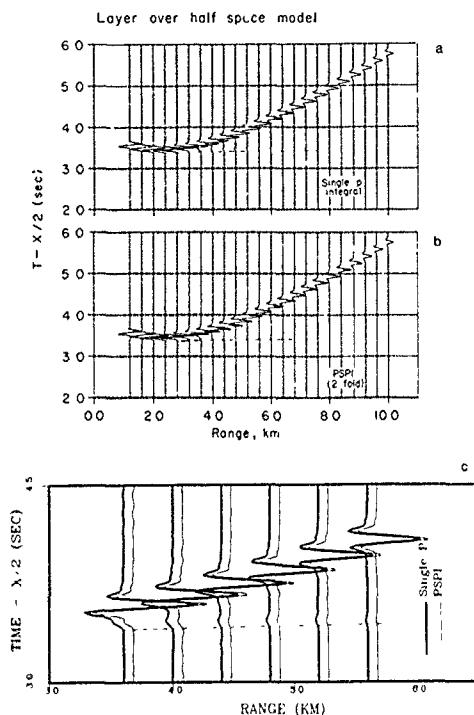


Figure 6. Synthetic seismograms for a layer over half-space model computed (a) by a single ray-parameter integral, (b) by twofold PSPI (see text for details) and (c) an expanded plot of single- p and PSPI seismograms in the range 3.6–5.6 km for comparison. The head wave is marked by a dashed line.

from an explosion source) from the interface, recorded at the surface receivers. This can be easily evaluated by a single ray-parameter integral (Aki & Richards 1980). Evaluating this by means of a PSPI will require using a threefold integral similar to the one given by equation (37). Our numerical experiments (Sen & Frazer 1988) showed that we do not need to use a full threefold integral and that a twofold PSPI gives identical results. We, therefore, used a twofold integral obtained by replacing the receiver ray-parameter integral (p_r) by its equivalent geometrical acoustics Green's function. In Fig. 6(a), we show the synthetic seismograms computed by using a single p -integral for this model. Similarly, Fig. 6(b) shows the profile computed by using a twofold PSPI. Fig. 6(c) shows an expanded plot of single- p and PSPI seismograms in the range 3.6–5.6 km for better comparison. The match between these two sets of synthetics is excellent. We notice that the post-critical reflection (both amplitude and phase) and head waves are modelled very well by PSPI. This confirms the accuracy of the PSPI formulation for the 1-D model.

Next, we consider a two-layered acoustic medium as shown in Fig. 7(a). In this example, we calculate the primary reflection (pressure response) from a truncated reflector. The source-receiver geometry is shown in Fig. 7(a). The reflected ray path shows a shadow zone beyond a range of 40 km ($p_c = 0.707$ s km $^{-1}$). A fairly common mistake is to calculate the response for this model as a single p -integral, truncated at the ray parameter corresponding to the ray from the source to the corner, such a calculation is shown in Fig. 7(b). We also evaluate this using a twofold PSPI (Fig. 7c) and a fourth-order acoustic finite-difference algorithm (Fig. 7d). The free surface was treated as an absorbing boundary for the finite difference calculation and the line source synthetics were converted to approximate point-source solutions (Vidale & Helmberger 1987). The PSPI models the diffractions and reflections very well. The match of amplitude, phase and traveltimes is excellent between the PSPI and finite difference seismograms. As expected, the synthetics shown in Fig. 7(b) computed by a single ray-parameter integral are in error. For example, we see a truncation phase arriving with a phase velocity of

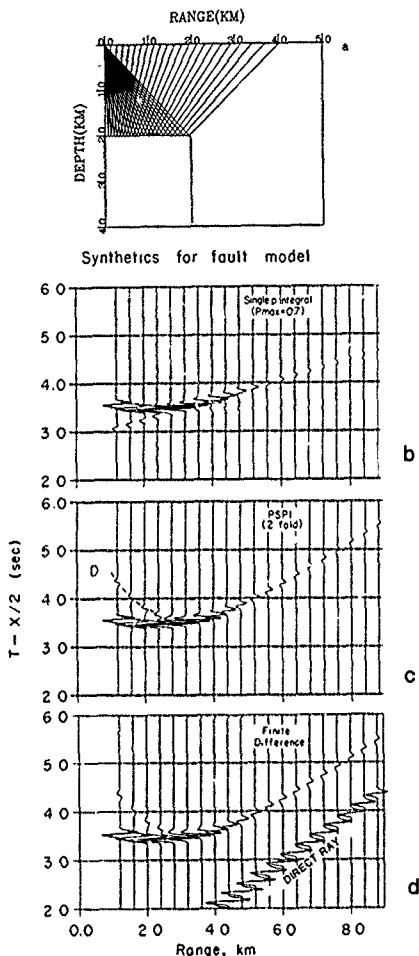


Figure 7. (a) A fault model and the source-receiver geometry (b) Synthetic seismograms computed by a single- p integral. Note the truncation phase in the seismograms (c) Synthetic seismograms computed by a PSPI (d) Synthetic seismograms computed by a fourth-order finite difference code. The first arrivals at ranges greater than 4 km in the finite-difference seismograms are the direct arrivals

0.707 km s^{-1} instead of the diffraction branch. Any method based on a single p -integral such as the Gaussian beam method will have similar errors (George, Vineux & Madanaga 1987). This validates the usefulness of PSPI over Gaussian beam or WKBJ/Maslov (Chapman & Drummond 1982; Frazer & Phinney 1980; Maslov 1965) methods.

8 DISCUSSION AND CONCLUSIONS

In this paper we have demonstrated the usefulness of the PSPI method over other ray-based methods. The tangent plane approximation used in the PSPI is more accurate than the usual tangent plane approximation, since the wavefronts are actually planar, although the interfaces are still assumed to be locally plane. The use of ray-parameter integrals in the KH integrand enables us to include classical head waves, although the head waves from curved interfaces are only approximate and the whispering gallery head waves will not be included. The angles of incidence are allowed to be complex and thus the evanescent regime is also included. Although the full PSPI formulation requires evaluation of a series of integrals, a careful examination of the Snell rays often enables one to reduce the fold by replacing many of the integrals with this stationary phase point values.

ACKNOWLEDGMENTS

We thank Don Helmberger for many helpful discussions, Richard Stead for the use of the finite difference code and Steve Cardmona for critically reading the manuscript. The University of Texas Institute for Geophysics contribution no. 827.

REFERENCES

- Aki, K. & Richards, P. G., 1980 *Quantitative Seismology*, Academic Press, New York.
- Brekhovskikh, L. M., 1960 *Waves in Layered Media*, Academic Press, New York.
- Chapman, C. H. & Drummond, R., 1982. Body-wave seismograms in inhomogeneous media using Maslov asymptotic theory, *Bull. seism. Soc. Am.*, **72**, S277-S317.
- Frazer, L. N., 1987. Synthetic seismograms using multifold path integrals—Part I Theory, *Geophys. J. R. astr. Soc.*, **88**, 621-646.
- Frazer, L. N. & Phinney, R. A., 1980. The theory of finite frequency body wave synthetic seismograms in inhomogeneous elastic media, *Geophys. J. R. astr. Soc.*, **63**, 691-713.
- Frazer, L. N. & Gettrust, J. F., 1984. On a generalization of Filon method and computation of the oscillatory integrals of seismology, *Geophys. J. R. astr. Soc.*, **76**, 461-481.
- Frazer, L. N. & Sinton, J. B., 1984. A Kirchhoff method for the computation of finite-frequency body wave synthetic seismograms in laterally inhomogeneous media, *Geophys. J. R. astr. Soc.*, **78**, 413-429.
- Frazer, L. N. & Sen, M. K., 1985. Kirchhoff-Helmholtz reflection seismograms in a laterally inhomogeneous multi layered elastic medium, Part I Theory, *Geophys. J. R. astr. Soc.*, **80**, 121-147.
- George, Th., Vineux, J. & Madanaga, R., 1987. Seismic wave synthesis by Gaussian beam summation, *Geophysics*, **52**, 1065-1073.
- Hilterman, F. J., 1970. Three-dimensional seismic modeling, *Geophysics*, **35**, 1020-1037.
- Hilterman, F. J., 1975. Amplitude of seismic waves—a quick look, *Geophysics*, **40**, 745-762.
- Maslov, V. P., 1965 *Theory of Perturbation and Asymptotic Methods*, 1st MGU, Moscow (in Russian).
- Pilant, W. L., 1979 *Elastic Waves in the Earth*, Elsevier, Amsterdam.
- Schulmann, L. S., 1981 *Techniques and applications of path integrations*, Wiley, New York.

- Sen, M. K. & Frazer, L. N., 1985 Kirchhoff-Helmholtz reflection seismograms in a laterally inhomogeneous multi-layered elastic medium, Part II: Computations, *Geophys. J. R. astr. Soc.*, **82**, 415-437.
- Sen, M. K. & Frazer, L. N., 1987 Synthetic seismograms using multifold path integrals—II: Computations, *Geophys. J. R. astr. Soc.*, **88**, 647-671.
- Sen, M. K. & Frazer, L. N., 1988. Multifold phase space path integral synthetic seismograms, *SEG Expanded Abstracts*, V.11,

- 1050-1052.
- Trorey, A. W., 1977 A simple theory for seismic diffractions, *Geophysics*, **35**, 762-786
- Vidale, J. E. & Helmberger, D. V., 1987 Path effects in strong motion seismology, in *Strong Motion Synthetics*, ed Bolt, B. A., Academic Press, New York.
- Zhu, T., 1988. A ray-Kirchhoff method for body-wave calculations in inhomogeneous media Theory, *Geophys. J. R. astr. Soc.*, **92**, 181-193

of the
tangent
ite than
Jeffreys
are still
parameter
classical
interfaces
ad waves
owed to
included.
tion of a
inell rays
many of
s

discussions,
code and
script. The
contribution

Seismology.

Academic
seismograms
theory, *Bull*

multifold path
str. Soc., **88**,

ory of finite
homogeneous
-713.
ization of Filon
y integrals of
481

method for the
synthetic seismo-
phys. J. R. astr.

nholtz reflection
n layered elastic
astr. Soc., **80**,

7 Seismic wave
Geophysics, **52**.

ismic modeling

es—a quick look

and Asymptot

Earth, Elsevier

applications

Seismogram synthesis for azimuthally anisotropic media with a single slowness integration

Bertram Nolte, L. Neil Frazer and Subhashis Mallick

School of Ocean and Earth Science and Technology, University of Hawaii at Manoa, 2525 Correa Road, Honolulu, HI 96822, USA

Accepted 1992 April 14 Received 1992 April 7, in original form 1991 May 28

SUMMARY

The computation of exact synthetic seismograms for azimuthally anisotropic (AA) models with a frequency–slowness integration method requires two horizontal slowness integrations. However, a single slowness integration that is exact for azimuthally isotropic media requires much less computation time, and has therefore been considered for the AA case as well. As a single slowness integration leads to traveltimes and amplitude errors, it should be used for AA media only if these errors are negligible. In this paper we discuss the errors, and outline how they can be estimated. The main contribution to the single-integration traveltimes error comes from incorrect group (ray) velocities in the single-integration case. The single-integration group velocities are always greater than or equal to the true group velocities, causing traveltimes to be too small. If there are cusps in the group-velocity surface, not only may the traveltimes be wrong, but there may also be arrivals missing from the seismograms. In layered AA media a minor contribution to the single-integration error arises from not allowing the ray to leave the sagittal plane. The resulting traveltimes error is opposite in sign, but much smaller than the traveltimes error caused by incorrect group velocities. Amplitudes may be incorrect even though traveltimes are accurate. However, this can only be the case for certain isolated sagittal planes, such as symmetry planes; in other sagittal planes amplitude errors and traveltimes errors go together. To decide whether single-integration amplitudes will be accurate one should compute the sagittal velocity curves for single and double integration for a range of azimuths. If the velocity errors are insignificant, then the amplitudes will be accurate for all sagittal planes.

Key words: azimuthal anisotropy, reflectivity, seismic modelling.

INTRODUCTION

This paper necessarily uses many special terms from the area of seismic anisotropy. Winterstein (1990) gives definitions of all these terms, as well as a good introduction to the whole subject. More detailed treatments of the theory have been given by Musgrave (1970), Auld (1973) and Helbig (1991). Auld (1973) is much easier reading than Musgrave (1970), while Helbig (1991) also gives material that is of special interest to reflection seismologists.

With the increasing interest in seismic anisotropy in recent years, techniques which are useful for the modelling of wave propagation in isotropic media have been extended to anisotropic media. Among these techniques are frequency–wavenumber (or frequency–slowness) integration methods such as the reflectivity method (Fuchs & Muller 1971, Kennett 1983), recently extended to azimuthally anisotropic

media by Mallick & Frazer (1990, 1991). The main advantage of reflectivity methods is that they compute the exact wavefield. A disadvantage is that the model must be stratified, meaning that the model parameters must be independent of the horizontal coordinates. Other methods that do not require stratified models either compute an approximate wavefield, as ray theoretical methods (e.g. Červený, Molotkov & Pšenčík 1977), or they require too much computation time at large offsets and high frequencies, as finite difference and finite element techniques.

With vector computers the reflectivity method becomes very efficient for isotropic models, and even models with hundreds of layers can be treated. This is because it is possible to take advantage of the cylindrical symmetry about the vertical axis containing the source. If cylindrical coordinates are used, then only one slowness integration is

required. For anisotropic media, however, cylindrical symmetry only exists if the medium is transversely isotropic with a vertical symmetry axis (azimuthally isotropic), and a single slowness integration is exact only in this case. In all other cases, the exact solution requires two slowness integrations (Fryer & Frazer 1984, 1987; Mallick & Frazer 1990, 1991). This increases the computation time by a large factor so that exact modelling studies are presently feasible only for AA models with at most a few tens of layers.

Booth & Crampin (1983) suggested that a single integration gives results that are a good approximation for weak anisotropy. Although a single integration has been used for seismogram synthesis for AA media since then (e.g. Crampin 1987) it remains unclear whether this usage is a justifiable approximation. The main advantage of reflectivity techniques is, as mentioned before, the exact computation of the wavefield. Introducing an approximation such as single integration into the method forfeits this exactness and is therefore justifiable only if the error can be shown to be so small that single-integration seismograms are indistinguishable from double-integration seismograms. In this paper we show how to decide for a given model whether single integration will be a good approximation.

THEORY

Consider a stratified elastic medium, i.e. a structure in which the elastic properties vary only with depth z but are independent of the horizontal coordinates r and ϕ . Let this medium be composed of homogeneous azimuthally isotropic layers. At any depth z a displacement vector $\tilde{u}(p_r, m, z, \omega)$ in the frequency-slowness domain can be calculated by well-known techniques such as the Kennett algorithm (Kennett 1974; Kennett & Kerry 1979), and the vector $\tilde{u}(r, \phi, z, t)$ in the time-distance domain is obtained by a Fourier-Hankel transform and a finite Fourier transform. The vertical component of the displacement vector becomes (Kennett 1983)

$$u_z(r, \phi, z, t) = \frac{1}{2\pi} \int_{-\infty}^{\infty} d\omega \omega^2 \exp(-i\omega t) \\ \times \int_0^{\infty} dp_r p_r \sum_m \tilde{u}_z(p_r, m, z, \omega) J_m(\omega p_r r) \\ \times \exp(im\phi), \quad (1)$$

where J_m denotes the Bessel function of m th order. Similar expressions are obtained for the horizontal components. For symmetry reasons the summation can be restricted to azimuthal orders $|m| < 2$ for point sources consisting of force and dipole components (Kennett 1983). Here cylindrical coordinates are used in order to take advantage of the axial symmetry about the z -axis.

In the case of azimuthal anisotropy it is preferable to use Cartesian coordinates (Fryer & Frazer 1984; Mallick & Frazer 1990). Then the Fourier-Hankel transform of equation (1) is replaced by a 3-D Fourier transform

$$u(x, y, z, t) = \frac{1}{8\pi^3} \iiint dp_x dp_y d\omega \omega^2 \tilde{u}(p_x, p_y, z, \omega) \\ \times \exp[-i\omega(t - p_x x - p_y y)] \quad (2)$$

This equation yields exact results even in the most general case of triclinic symmetry since the integration is carried out for both horizontal components of the slowness vector.

Equation (1) can be computed much faster than equation (2), because only one slowness integration is performed. Integrations are carried out numerically as summations. If a model requires the computation of the integrand at n (≈ 500) values of p_r , when equation (1) is used then, for the same model, equation (2) will require the computation of the integrand at $2n \times 2n$ values, because, first, it has to be computed both at positive and at negative values, and, second, the range of integration should be the same in p_x and p_y . Numerical experiments have shown that sometimes even more values may be needed in the double integration, because the sampling interval δp may need to be smaller off the p_x -axis, than on it. A smaller sampling interval is equivalent to an increased number of slownesses if the range of integration is the same.

In view of the above, we would like to use equation (1) for AA media rather than equation (2). However this results in errors both in the traveltimes and in the amplitudes of various arrivals in the synthetic seismograms. We now discuss these errors, and show how they can be estimated.

Recall that the elastic behaviour of a homogeneous solid (e.g. Musgrave 1970, section 6.5) can be described with reference to four characteristic three-sheeted surfaces, which can all be constructed from each other as shown in Fig. 1. The first of these is the group-velocity surface, G , which is the locus of the wavefront at unit time after a disturbance at the origin. The group-velocity surface is sometimes called the ray surface, the ray-velocity surface, the wave surface, or the wavefront surface. Note that we use G to indicate the position vector of a particular point on the group-velocity surface, and G to denote the surface itself. One should beware of the notational confusion that can arise when a surface such as G is given in the form of a scalar function $G(x_1, x_2, x_3) = 0$ for then of course $G(x_1, x_2, x_3)$ is unequal to $|G|$, the length of G . For this reason we always denote the length of G by $|G|$.

The second important surface is the velocity surface, V . As shown in Fig. 1, the point $V \in V$, corresponding to the

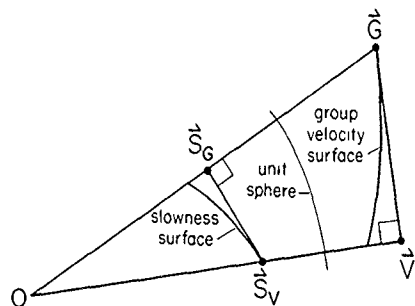


Figure 1. Relations between the four surfaces. Corresponding position vectors on the group-velocity surface G , the (phase) velocity surface V , the group-slowness surface S_G , and the (phase) slowness surface S_V are labelled G , V , S_G , and S_V , respectively.

point $G \in G$, is the point where a straight line from the origin intersects normally the plane tangent to G at G . Accordingly, V is called the pedal point, or footpoint, of G and the surface V is called the pedal surface, or footpoint surface, of G . One constructs G from V by drawing, for each $V \in V$, the plane through the endpoint of V that is normal to V . The surface G is the caustic or envelope of all such planes. Accordingly, the surface G is called the envelope of the surface V . The velocity surface V is sometimes referred to as the normal surface or the phase-velocity surface.

The third important surface is the slowness surface, S_V . The point S_V corresponding to the point V is given by the relation $S_V = V/|V|^2$. In other words S_V is the inverse of V in the unit sphere, as shown in Fig. 1. The inverse of the pedal of a surface is called the polar reciprocal of that surface, consequently S_V is the polar reciprocal of G . The geometric method used to construct V from G and S_V from V shows that corresponding points on G and S_V satisfy the relation

$$G \cdot S_V = 1$$

The slowness surface is sometimes called the inverse velocity surface or the phase-slowness surface.

The fourth surface is the group-slowness surface, S_G . Each point $S_G \in S_G$ is the pedal of its corresponding point $S_V \in S_V$. In other words S_G is constructed from S_V in exactly the same way that V is constructed from G . As S_G is the pedal of S_V , S_V is the envelope of S_G . It follows from the definitions of V , S_V and S_G that the surface S_G can also be constructed directly from G by inversion in the unit sphere. In other words, the point $S_G \in S_G$ corresponding to the point $G \in G$ is given by the relation $S_G = G/|G|^2$. As S_G is the inverse of G , and S_V is the envelope of S_G , we see that the polar reciprocal of a surface is the envelope of the inverse of that surface. The group-slowness surface S_G is sometimes called the ray-slowness surface or the inverse wave surface. Notice that the velocity and group-velocity surfaces are defined in a velocity space with Cartesian coordinates v_x, v_y and v_z , whereas the slowness and group-slowness surfaces are defined in a slowness space with Cartesian coordinates p_x, p_y and p_z due to the different dimensions of slowness and velocity.

The error that is caused by the single-integration approximation is most easily treated by considering synthetic seismograms for a homogeneous anisotropic whole-space. We will assume that both the source and the receivers are located in the x - z plane in the Cartesian coordinate system of equation (2), and that, with respect to this system, the cylindrical coordinate system of equation (1) is oriented so that the azimuthal coordinate ϕ is zero for both source and receivers, and that the r - and the z -axis of the cylindrical system are parallel to the x - and the z -axis, respectively, of the Cartesian system.

In order to calculate seismograms from equation (1) or (2) it is necessary to compute the integrand as a function of the horizontal components of the slowness vector. The computation of the integrand involves the computation of the corresponding vertical components of the slowness vectors, which are obtained as the eigenvalues of the system matrix (e.g. Fryer & Frazer 1984, Frazer & Fryer 1989). When double integration is used, this computation is carried

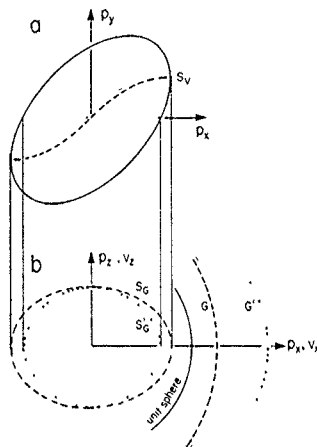


Figure 2. (a) View of S_V down the p_x -axis. Planes parallel to the p_y -axis are tangent to S_V along the dashed curve. The dotted curve is the intersection of S_V with the $p_y = 0$ plane. (b) Sagittal section of the true group-slowness surface S_G , and true group-velocity surface G given by double integration. Single integration gives the incorrect group-slowness curve S'_G and group-velocity curve G' . Traveltimes are observed along a radial line in (b).

out for an array of values $\{p_x, p_y\}$. This is equivalent to the computation of the whole three-dimensional slowness surface S_V . Fig. 2(a) shows one sheet of S_V viewed from a direction parallel to the p_x -axis. The direction of energy propagation is given by the group-velocity vector G , or by the group-slowness vector S_G , both of which must lie in the sagittal plane. As the group-slowness surface S_G is the pedal of the slowness surface S_V , each point of S_G can be constructed by dropping a perpendicular from the origin to the tangent plane at the corresponding point of S_V . The dashed line in Fig. 2(a) shows the point of tangency on S_V , and the dashed lines in Fig. 2(b) show the corresponding cross-sections of S_G and G through the sagittal ($p_y, v_y = 0$) plane.

For a single integration with equation (1) only slowness vectors in the plane $p_y = 0$ are calculated and the slowness surface S_V is assumed to be axially symmetric about the p_x -axis. Then the points of tangency on S_V are assumed to be in the $p_y = 0$ plane, along the dotted line in Fig. 2(a). The sagittal plane sections of the resulting effective group-slowness surface S'_G , and effective group-velocity surface G' , are indicated by dotted lines in Fig. 2(b). The difference in length between the vectors S_G and S'_G , multiplied by the distance from the source to the receiver, gives the difference in traveltime between single and double integration in a homogeneous medium. Clearly single-integration traveltimes will always be greater than or equal to those for double integration.

In the foregoing discussion we have regarded the slowness surface as fundamental, subject to the provision that the observed group-velocity vector must lie in the sagittal plane.

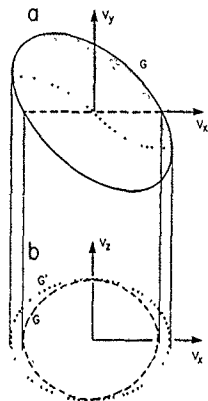


Figure 3. (a) View of the true group-velocity surface G down the v_y -axis. Planes parallel to the v_y -axis are tangent to G along the dotted curve. The dashed curve is the intersection of G with the sagittal plane. (b) The dashed curve is the sagittal section of G given by double integration. Single integration gives the incorrect sagittal section G' . Often G has cusps and then the sagittal sections of G and G' are much more complicated.

An alternative way of understanding the difference between single and double integration is to begin with the group-velocity surface G , as shown in Fig. 3(a). The intersection of G with the sagittal plane $v_y = 0$ gives the group-velocity curve for double integration, shown dashed in Fig. 3(b). Now recall that, for single integration, traveltimes are the same for a point source as for a line source along the y -axis. The group-velocity surface for such a line source is the cylinder generated by translation of G parallel to the v_y -axis. For a point source, the group-velocity surface given by single integration is therefore generated by rotating the $v_y = 0$ section of this cylinder about the v_z -axis. The intersection of the line-source group-velocity cylinder with the $v_y = 0$ plane is the dotted curve labelled G' in Fig. 3(b), this is the group-velocity curve for single integration. Like Fig. 2, Fig. 3 shows clearly that traveltimes for a single integration will always be greater than or equal to those for a double integration. Note that the true G very often has cusps. Then the sagittal sections of G and G' will be much more complicated, and different in shape, than is the case in Fig. 3(b). A numerical example of such a case is given later.

In order to get the velocities that represent single and double integration as functions of the direction, we must compute the sagittal sections of G and G' . For reference below we denote the sagittal section of the j th sheet of G by \mathcal{G}_j , and we denote the sagittal section of the j th sheet of G' by \mathcal{G}'_j . To find \mathcal{G}_j we generate G from V as described by Musgrave (1970). His equation (7.4.10) gives Cartesian coordinates $\xi_{k(j)}$ for the point on the j th sheet of G corresponding to the point on the j th sheet of V , specified

by direction cosines n_i :

$$\xi_{k(j)} = \frac{1}{2\rho v_{(j)}} \left(\frac{p_{k(j)}^2}{\alpha_k^2} \right) \left[(\rho v_{(j)}^2 - A_k) \frac{\partial \alpha_k}{\partial n_i} + \alpha_k^2 \frac{\partial A_k}{\partial n_i} \right], \quad (3)$$

where summation is implied only over the subscript k . The curves \mathcal{G}_j are obtained by computing a sufficiently dense set of points $\xi_{k(j)}$ and finding those points with $\xi_z = 0$.

As Musgrave did not define all the terms in equation (3) we give the definitions here. All quantities are defined with reference to the symmetric 3×3 Christoffel matrix $\Gamma_{\alpha\gamma}$ given by

$$\Gamma_{\alpha\gamma} = c_{\alpha\beta\gamma\delta} n_\beta n_\delta,$$

in which $c_{\alpha\beta\gamma\delta}$ is the fourth-order tensor of elastic stiffness coefficients. The quantity $v_{(j)}$ is the positive square root of the j th eigenvalue of the matrix $\rho^{-1}\Gamma_{\alpha\gamma}$, where ρ is the mass density; it is also the distance from the origin to the j th sheet of V in the direction of n_i . The quantity $p_{k(j)}$ is the k th component of the j th eigenvector of $\rho^{-1}\Gamma_{\alpha\gamma}$, i.e. the j th polarization vector. In equation (3) the polarization vectors are assumed to have been normalized to unit amplitude so that $\sum_{k=1}^3 p_{k(j)}^2 = 1$ for $j = 1, 2, 3$. The quantity A_k is given, for $k = 1, 2, 3$, by $A_k = \Gamma_{kk}$. The α_k are given by $\alpha_1 = \sqrt{\Gamma_{12}\Gamma_{31}/\Gamma_{23}}$, $\alpha_2 = \sqrt{\Gamma_{21}\Gamma_{31}/\Gamma_{32}}$, and $\alpha_3 = \sqrt{\Gamma_{23}\Gamma_{31}/\Gamma_{12}}$. The relations for the A_k and α_k were obtained by noting that any symmetric 3×3 matrix Γ can be written in terms of a vector α and a vector A as

$$\Gamma = \alpha\alpha^T + \text{diag}(A_1 - \alpha_1^2, A_2 - \alpha_2^2, A_3 - \alpha_3^2),$$

and then solving for the A_k and the α_k in terms of the components of Γ .

The curves \mathcal{G}'_j are obtained by evaluating equations (3) for G along all directions $(n_1, 0, n_3)$. Note that $\xi_{2(j)}$ is not evaluated but set to zero, it must vanish identically because the effective single-integration velocity surface is axially symmetric about the vertical. In homogeneous media the curves \mathcal{G}_j and \mathcal{G}'_j permit the errors in traveltimes that result from single integration to be calculated exactly for all three wave types propagating in any direction. The error is $\Delta t = \ell/|\mathcal{G}'_j| - \ell/|\mathcal{G}_j|$, where ℓ denotes the length of the ray path and $|\mathcal{G}'_j|$ and $|\mathcal{G}_j|$ are the distances from the origin to the points on the curves \mathcal{G}'_j and \mathcal{G}_j , respectively, along the same straight ray.

Synthetic seismograms computed with a single integration may also give wrong amplitudes. The amplitude of a wave propagating in a particular direction is a function of the Gaussian curvature of the slowness surface at the point related to this direction of propagation (Lighthill 1960). Single integration will introduce an error in both the location of this point on the slowness surface and in the Gaussian curvature. As we know how to estimate the traveltimes error we would like some assurance that the amplitude error will be sufficiently small when the traveltimes error is found to be sufficiently small. We showed above that the traveltimes error depends on the group velocities $|\mathcal{G}'_j|$ and $|\mathcal{G}_j|$. Also, when the difference between $|\mathcal{G}'_j|$ and $|\mathcal{G}_j|$ in some direction is small, the slowness vector for double integration that is related to wave propagation in this particular direction has a negligible p_z -component, i.e. it lies in the sagittal plane, and the slowness surface intersects the sagittal plane at nearly a right angle at this point. Therefore

(3)

The
se setin (3)
with
C_{ray}iffness
not of
mass
sheet
e kth
e yth
ectors
ide so
given,
n by
α_i =
ained
ritten

of the

is (3)
is not
cause
axially
a the
resultthree
or is
ie ray
ing to
ig theation
wave
if the
point
1960)
i the
n the
the
the
time
e that
/1 and
g) in
double
this
it lies
is the
reore

the slowness vectors for double and single integration will be almost identical. If this holds for every direction in the sagittal plane then the normal vectors to both the slowness surface and the group-velocity surface at every point on the curves \mathcal{G}_d lie in the sagittal plane, and the slowness vectors for double and single integration are almost identical for waves propagating in every direction in the sagittal plane.

The Gaussian curvature, however, could still be wrong in the single-integration case. For example, if the sagittal plane is a symmetry plane of the medium, then the curves \mathcal{G}_d and \mathcal{G}_s coincide exactly, but the curvatures of their respective slowness surfaces may be very different. However, if we compute the curves \mathcal{G}_d and \mathcal{G}_s for a series of sagittal planes at increasing azimuths, and we find that \mathcal{G}_d and \mathcal{G}_s match at each azimuth, then we can conclude that the group-velocity surface and, thus, the slowness surface is nearly axially symmetric, hence, the amplitudes obtained by single integration will be accurate. If the slowness surface was not nearly axially symmetric it would not intersect all of these different sagittal planes at right angles and, hence, the p_z -components of the slowness vectors related to the group-velocity vectors in these sagittal planes would not be nearly zero everywhere. Then the curves \mathcal{G}_d and \mathcal{G}_s would also differ from each other. The fact that the amplitudes are accurate for single integration if the curves \mathcal{G}_d and \mathcal{G}_s match for a series of increasing azimuths has been confirmed by our numerical experiments, an example of which is given below.

The above discussion suggests the following method for determining whether single integration gives the correct amplitudes. Compute the curves \mathcal{G}_d and \mathcal{G}_s for a series of increasing azimuths. If these curves match for all azimuths then the amplitudes will be correct for all azimuths, too. In multilayer models this condition must hold for all anisotropic layers.

MULTILAYER MODELS

So far we have assumed that the waves propagate in an homogeneous whole-space, so that the ray paths are always straight lines. In layered media the rays will change their directions due to reflection and transmission. In AA media this will generally make the rays leave the sagittal plane. Double integration automatically incorporates this effect, while, as we have seen, single integration forces the ray to remain in the sagittal plane. This is illustrated in Fig. 4 for the case of two anisotropic half-spaces with a source located in the lower half-space and a receiver located in the upper one. Fig. 4(a) shows the projection of the ray paths onto the xz -plane, and Fig. 4(b) shows their projections onto the xy -plane. We call the actual ray path P^D and the single integration ray path P^S .

To quantify completely the difference in traveltime between single and double integration in a layered medium it will be necessary to trace rays. However, we can use Fermat's principle to infer that the traveltime effect of the departure from the sagittal plane is opposite in sign to the traveltime effect of the velocity change and much smaller. Although Fermat's principle is usually applied to perturbations in the spatial structure of velocity it is equally applicable to perturbations in the directional structure of velocity. In the present case we consider the three

PROJECTION OF RAY PATH ONTO

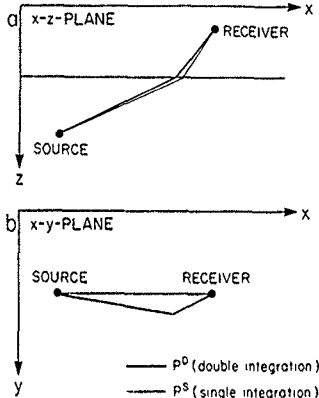


Figure 4. Schematic illustration of the projection of a ray path onto the xz -plane (a) and onto the xy -plane (b). The double integration ray path is marked as P^D and the single integration ray path as P^S . The projection of P^S onto the xy -plane is a straight line.

traveltimes $t(P^D, G)$, the traveltime over the path P^D using the true group-velocity structure, $t(P^S, G)$, the traveltime over the path P^S using the true group-velocity structure, and $t(P^S, G')$, the traveltime over the path P^S using the single-integration group-velocity structure G' . Fermat's principle states that the time difference due to path,

$$(\delta t)_p = t(P^S, G) - t(P^D, G)$$

is of second order in the perturbation $G \rightarrow G'$ whereas the time difference due to velocity,

$$(\delta t)_G = t(P^S, G') - t(P^S, G)$$

is of first order in the perturbation $G \rightarrow G'$. Notice that if P^D is a minimum time path (the usual case), then $(\delta t)_p$ must be positive. Furthermore, we have seen that the sagittal section of G is always interior to the sagittal section of G' , which means that $(\delta t)_G$ must be negative. As $(\delta t)_p$ is opposite in sign to $(\delta t)_G$, the total time difference,

$$\delta t = (\delta t)_p + (\delta t)_G$$

must be bounded below by $(\delta t)_G$. Except for maximum time phases, which are uncommon in reflection work, double-integration traveltimes will always be greater than or equal to single-integration traveltimes, and we can estimate a limit for the traveltime error by ignoring the departure of the ray from the sagittal plane.

For a given multilayer earth model, and a given source-receiver geometry, how can one decide in advance whether or not a single slowness integration is sufficiently accurate? Using the principles discussed above one can invent numerous methods for making this decision. We outline two such methods here.

For the first method, begin by generating sagittal group velocity curves \mathcal{G}_i and \mathcal{G}_r for each layer of the model. For the arrival of interest let p be the horizontal component of phase slowness in the sagittal plane, i.e. the x -component, and let $\mathcal{G}(p, i)$ and $\mathcal{G}(p, r)$ be the sagittal single- and double-integration group-velocity curves, respectively, for layer i . Next, using the $\mathcal{G}(p, i)$, trace rays from the source to the receiver. This is most simply done by a shooting method, as follows: (1) pick a p , (2) trace the ray of slowness p by noting that in layer i the tangent to the ray is $\mathcal{G}(p, i)/|\mathcal{G}(p, i)|$ and that p is preserved during reflection and transmission, (3) if the ray passes through the receiver depth before (after) the receiver then increase (decrease) p and shoot again. A ray path found in this way is a single-integration ray path. To get a bound for the traveltime error use Fermat's principle in accordance with the discussion above; integrate the quantity $1/|\mathcal{G}| - 1/|\mathcal{G}|$ along the ray. If the error is less than one eighth of the shortest period in the source wavelet then single integration will give excellent traveltimes. This method has the advantage that explicit generation of the curves \mathcal{G} and \mathcal{G} reveals whether \mathcal{G} has cusps that are not present in \mathcal{G} . Later we show an example of a traveltime computation using this method.

The second method consists of rapidly calculating exact traveltimes for both single and double integration using subroutines already present in the reflectivity code. For simplicity, suppose we are interested in the traveltime of the P - P reflection from a layer at depth z , for a surface source and a surface receiver. First we compute the double-integration traveltimes. Here it is convenient to denote the x -component of slowness by p , the y -component of slowness by q , the vertical component of slowness for a downgoing wave by ψ^d , and the vertical slowness of an upgoing wave by ψ^u . We also use \mathbf{p} to denote the horizontal projection of the slowness vector, thus $\mathbf{p} = (p, q)$. In this notation the traveltime of a plane wave of slowness \mathbf{p} is given by

$$T(\mathbf{p}) = \mathbf{p} \cdot \mathbf{x} + \tau(\mathbf{p}),$$

in which $\tau(\mathbf{p})$ is given by

$$\tau(\mathbf{p}) = \int_0^z d\zeta [\psi^d(\mathbf{p}, \zeta) - \psi^u(\mathbf{p}, \zeta)] = \sum_i [\psi_i^d(\mathbf{p}) - \psi_i^u(\mathbf{p})]z_i$$

Here ψ_i^d , ψ_i^u and z_i are the vertical slownesses and thickness, respectively, of the i th layer in the stack of layers above depth z .

Group arrivals are given by the condition

$$\frac{\partial T}{\partial \mathbf{p}} = 0$$

With our choice of coordinate axes the sagittal plane is the $y = 0$ plane, so this condition becomes the two equations

$$0 = x + \frac{\partial \tau}{\partial p}$$

and

$$0 = \frac{\partial \tau}{\partial q}$$

Numerically, our task is to find the points \mathbf{p}_* , at which these equations are satisfied for a given sequence of sagitta receiver positions $(x_i, 0)$. Then the double-integration traveltimes will be given by

$$T_d(x_i) = x_i p_{*i} + \tau(\mathbf{p}_{*i}) \quad (4)$$

To do this we first compute τ over a dense grid of point (p_k, q_k) in the vicinity of the p -axis. By numerical differentiation we also generate $\partial\tau/\partial p$ and $\partial\tau/\partial q$ on a similar grid. Then, for each fixed p_k , we search in the q -direction, as shown in Fig. 5, to find the point $q(p_k)$ at which $\partial\tau/\partial q = 0$. This sequence $\{p_k, q(p_k)\}$ samples the contour in the \mathbf{p} -plane along which $\partial\tau/\partial q = 0$. For each point in the sequence $\{p_k, q(p_k)\}$ we have an $\tau(p_k)$ given by

$$x(p_k) = -\frac{\partial \tau}{\partial p}[p_k, q(p_k)]$$

Interpolating in the derived sequence $\{p_k, x(p_k)\}$ gives the values p_{*i} associated with the given receiver positions x_i . Interpolation also gives the values q_{*i} and the value $\tau_{*i} = \tau(p_{*i}, q_{*i})$ needed to compute the traveltime by equation (4).

To compute the single-integration traveltimes the procedure is similar, except that the contour on which $\partial\tau/\partial q = 0$ is replaced by the p -axis. From the double-integration procedure we already have values of τ on a grid over a grid in the \mathbf{p} -plane. On the line of that grid which coincides with the p -axis, we have the sequence $\{p_k, x(p_k)\}$ where $x(p_k) = -[\partial\tau/\partial p](p_k, 0)$. We interpolate in this sequence to find the points p_{*i} corresponding to the given receiver locations x_i , and the values $\tau(p_{*i})$ needed to compute the single-integration traveltime $T_s(x_i) = p_{*i}x_i + \tau(p_{*i}, 0)$. Note that p_{*i} has a different meaning in the single-integration and double-integration cases. The traveltime error is given by the difference $T_d(x_i) - T_s(x_i)$. In most cases, computation of the traveltime errors will be several orders of magnitude faster than

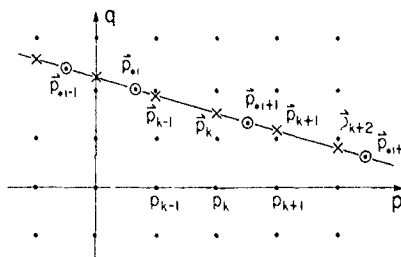


Figure 5. Computation of double integration traveltimes prior computing synthetics. The solid line is the contour along which $\partial\tau/\partial q = 0$, points indicated by 'x' sample this contour. Interpolation gives the points indicated by 'o' which are horizontal slownesses p_{*i} of group arrivals at given receiver locations $(x_i, 0)$. For single-integration traveltimes no search is made for the contour on which $\partial\tau/\partial q$ vanishes instead $\partial\tau/\partial q$ assumed to vanish on the p -axis.

computation of the synthetic seismograms by double integration.

NUMERICAL EXAMPLES

To illustrate the effects discussed above we have computed synthetic seismograms for some anisotropic models. All the seismograms have been computed with the ANIVEC™ program of Mallick & Frazer (1990).

Our first model is an anisotropic whole-space. The material is transversely isotropic with a horizontal symmetry axis. This symmetry might result from an isotropic background material containing vertically aligned cracks or fractures (Hudson 1981; Schoenberg & Douma 1988). The elastic stiffnesses are those of medium 1 in Table 1. We chose a material of rather high anisotropy in order to illustrate the effect more clearly. In the vertical plane containing the symmetry axis the group-velocity curves \mathcal{G}_1 and \mathcal{G}_2 are identical. In a vertical plane at an angle of 45° to the symmetry axis, the sagittal group-velocity curves \mathcal{G}'_1 (Fig. 6b) differ from the curves \mathcal{G}_1 (Fig. 6a). The greatest difference is for the *P*-wave, because its group-velocity surface deviates most from axial symmetry about the vertical axis. This difference is greatest for horizontal paths. For the faster *S*-wave the difference is considerably smaller, and there is no difference for the slower *S*-wave, due to the axial symmetry of its group-velocity surface.

From these curves we computed traveltimes for the source-receiver configuration shown in Fig. 7. The receivers are located 1000 m above the source, and the horizontal offsets extend from 100 to 2000 m with a spacing of 100 m.

Table 1. Elastic stiffnesses for the materials used in our modelling. The stiffnesses are given in condensed notation. They are specified in a coordinate system in which the *x*-axis is the symmetry axis. The density is 2.4 g cm^{-3} for all four media.

	Elastic Stiffesses [10^9 N/m^2]							
	11	22	33	12	13	23	44	55
Medium 1	11.36	4.46	4.46	0	0	0	0	0
	4.46	27.62	8.02	0	0	0	0	0
	4.46	8.02	27.62	0	0	0	0	0
	0	0	0	9.80	0	0	0	0
	0	0	0	0	6.73	0	0	0
Medium 2	0	0	0	0	0	6.73	0	0
	0	0	0	0	0	0	6.73	0
	29.40	9.80	9.80	0	0	0	0	0
	9.80	29.40	9.80	0	0	0	0	0
	9.80	9.80	29.40	0	0	0	0	0
Medium 3	0	0	0	9.80	0	0	0	0
	0	0	0	0	6.58	0	0	0
	0	0	0	0	0	6.58	0	0
	29.40	9.80	9.80	0	0	0	0	0
	9.80	29.40	9.80	0	0	0	0	0
Medium 4	9.80	9.80	29.40	0	0	0	0	0
	0	0	0	9.80	0	0	0	0
	0	0	0	0	8.70	0	0	0
	0	0	0	0	0	8.70	0	0
	18.38	6.13	6.13	0	0	0	0	0
Medium 5	6.13	28.18	8.58	0	0	0	0	0
	6.13	8.58	28.18	0	0	0	0	0
	0	0	0	9.80	0	0	0	0
	0	0	0	0	7.98	0	0	0
	0	0	0	0	0	7.98	0	0

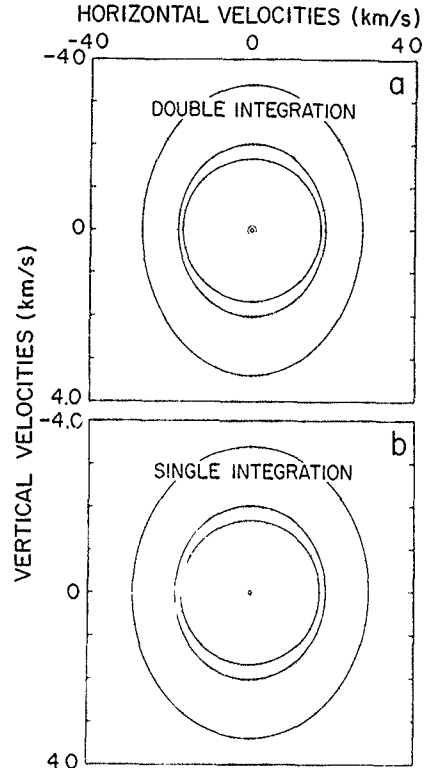


Figure 6. Curves $\mathcal{G}_1(a)$ and $\mathcal{G}'_1(b)$ for medium 1 in Table 1, in a vertical plane at an angle of 45° to the vertical symmetry planes. The greatest difference between \mathcal{G}_1 and \mathcal{G}'_1 occurs in the horizontal direction for the *P*-wave.

The traveltime plots (Fig. 8) show the arrival times expected for synthetic seismograms computed with double and single integration. We expect single-integration arrival times that are too small at larger offsets, especially for the *P*-wave. Figs 9(a) and (b) show the synthetic *x*-component motions.

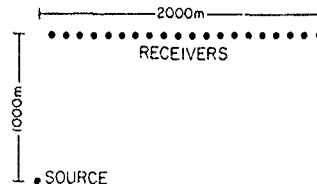


Figure 7. Source-receiver geometry for the computations of Fig. 8 and 9.

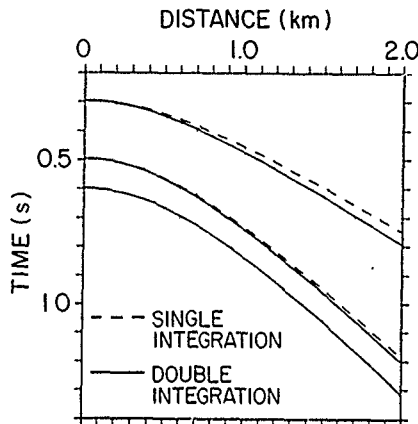


Figure 8. Time-distance diagrams for the double- and the single-integration seismograms. The diagrams are calculated from the curves in Fig. 6 and the source-receiver geometry in Fig. 7. At higher offsets the differences become quite large for the P -wave, due to the near-horizontal incidence and the longer ray paths.

computed by double and single integration, respectively. The source was a point force source in the x -direction. The source spectrum was a Hanning window between 10 and 80 Hz. The arrival times match those of Fig. 8 exactly, as expected.

Our second model is also a transversely isotropic medium with a horizontal symmetry axis, but for this model the group-velocity surface has cusps. The elastic stiffnesses are those of medium 2 in Table 1. Fig. 10 shows the

group-velocity curves in the vertical plane containing the symmetry axis. Notice the cusps in the curve for the faster S -wave. Fig. 11 shows the group-velocity curves \mathcal{G}_1 and \mathcal{G}_2 in a vertical plane at an angle of 45° to the symmetry axis. At higher incidence angles one of the curves \mathcal{G}_1 shows a branch that is missing in the corresponding curve \mathcal{G}_2 . Fig. 12 shows the traveltime curves for this medium with a source-receiver configuration similar to that of Fig. 7, except that for Fig. 12 the source-receiver offsets extend up to 3000 m. In the double-integration case, shown in Fig. 12(a), there is an arrival, due to the cusps, which is the second arrival at large offsets. This arrival is missing in the single-integration case.

For medium 2 we also computed synthetic seismograms for a source oriented in the y -direction. Fig. 13 shows the y -components of motion for double and single integration. As expected, the arrival that originates from the cusp is present in the double-integration seismograms but absent from the single-integration seismograms, and the arrival times match those predicted in Fig. 12. The P -wave is not evident in these seismograms, because its amplitude on the y -component is so much weaker than those of the S -waves. Figs 12 and 13 make it clear that single integration should never be used in off-symmetry planes for media with cusps in the group-velocity surface. Now we will show that it should be avoided in symmetry planes, as well.

We again computed seismograms for medium 2 in Table 1, but this time we placed the source and the receivers in the vertical plane containing the symmetry axis, so that the curves \mathcal{G}_1 and \mathcal{G}_2 are identical. Fig. 14 shows the double- and single-integration z -component seismograms for a source oriented in the x -direction. The arrival times of the double and single integration are identical, as expected. However, single integration gives wrong amplitudes for the S -wave sheet of the group-velocity surface containing the cusps. (This is the only S -wave that appears in the seismogram. The other S -wave is polarized in the y -direction.) At offsets less than the offset at which the arrival from the cusp begins,

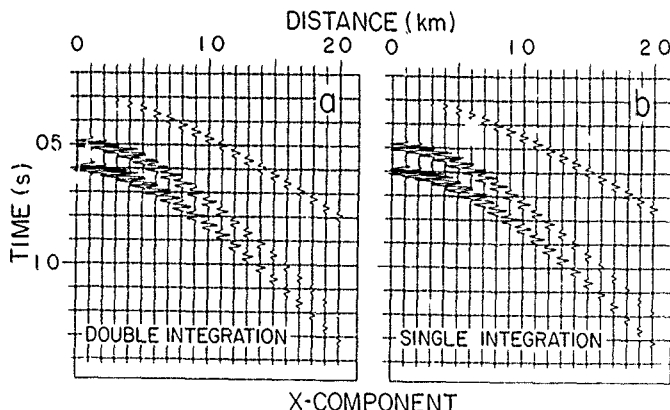


Figure 9. Synthetic seismograms for the same model used in Fig. 8. The source was oriented in the x -direction, and the z -component is shown here. Panel (a) shows the double- and panel (b) shows the single-integration seismograms. The arrival times match those predicted in Fig. 8.

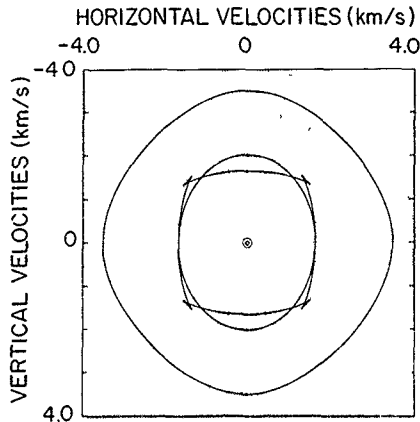


Figure 10. Group velocity curves for medium 2 in Table 1, for propagation in the vertical plane that contains the symmetry axis. The picture represents both S_1 and S_2 , since these curves are identical in symmetry planes.

the single-integration amplitudes are too low, and at higher offsets they are too large. This computation illustrates our earlier remarks to the effect that if the sagittal plane is near a symmetry plane then amplitudes may be wrong even though traveltimes are correct. Therefore single integration should never be used for seismogram synthesis for strongly anisotropic media, even if the sagittal plane is a symmetry plane.

Next, we show an example of weak anisotropy. We

choose a model that will give accurate single-integration traveltimes, and we demonstrate how to verify that the amplitudes are accurate, as well. The elastic stiffnesses are those of medium 3 in Table 1. Note that they are identical to those of medium 2, with the exception of C_{44} and C_{66} , whose values have been changed from $6.58 \times 10^9 \text{ N m}^{-2}$ to $8.70 \times 10^9 \text{ N m}^{-2}$ which is closer to the value of $9.80 \times 10^9 \text{ N m}^{-2}$ that would make the medium isotropic. The group-velocity surface for this medium does not have cusps. The group-velocity curves S_1 and S_2 for double and single integration are shown in Figs 15(a)–(c) for three off-symmetry planes at different azimuths to the vertical symmetry plane orthogonal to the symmetry axis. These azimuths are (a) 15° , (b) 30° , and (c) 45° . For all azimuths the difference between the curves S_1 and S_2 is negligible. This is also true for other azimuths (not shown here) which leads us to expect that we will obtain accurate amplitudes with a single integration, for sagittal planes at any azimuth.

In Figs 16 and 17 we show double- and single-integration seismograms for two planes. One is the symmetry plane containing the symmetry axis (Figs 16a and b). The second one is a plane at an angle of 30° to the first plane (Figs 17a and b). The source–receiver geometry is that of Fig. 7. The seismograms show z-motion for a source oriented in the x-direction. At both azimuths, amplitudes and traveltimes are accurate for single integration, as expected. Our numerical experiments (not all of which are shown here) confirm that the amplitude error is negligible if the traveltimes are accurate. Even in the seismograms in Figs 9(a) and (b), where there is a considerable traveltimes error, the amplitude error is very small.

For our last model we chose a material similar to medium 1, but we introduced a five-layer gradient zone between the source and the receivers to make the rays leave the sagittal plane. At the receiver level the stiffnesses are those of medium 1 and at the source level the elastic stiffnesses are

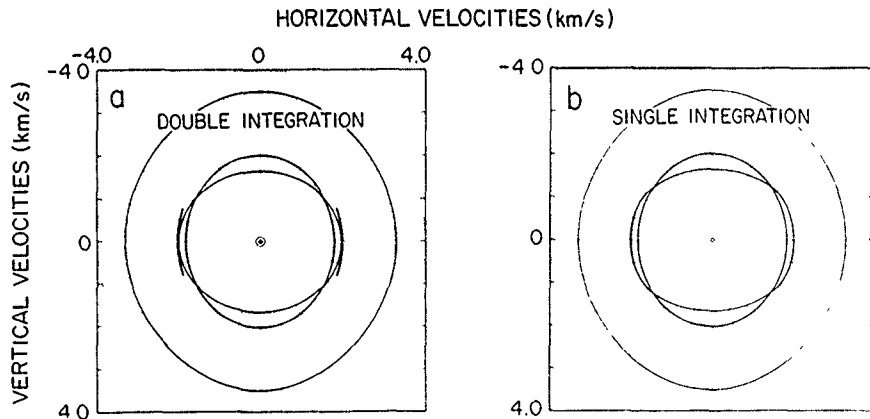


Figure 11. Group velocity curves for the same material as in Fig. 10, but here for propagation in a plane at 45° with the symmetry planes. At directions that are close to the horizontal, the curves S_1 in (a) show branches that are not present in the curves S_1 in (b).

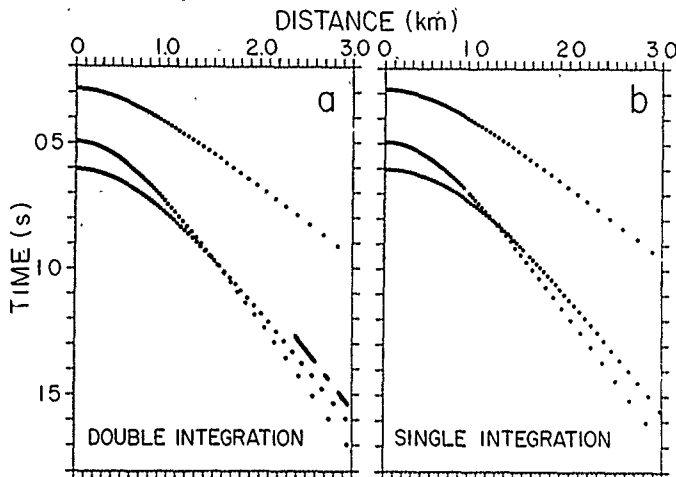


Figure 12. Traveltimes calculated from the curves in Fig. 11 for a geometry as in Fig. 7, but with horizontal offsets up to 3000 m. At large offsets an arrival is present in the double-integration plots (a) that is absent from the single-integration plots (b).

those of medium 4, given in Table 1. The elastic stiffnesses of the layers in the gradient zone were obtained by linear interpolation between the stiffnesses of the upper and lower half-spaces. The anisotropy decreases with depth and therefore increases from source to receiver level. The seismograms for this model are shown in Fig. 18. The source and the receivers are oriented in the x -direction. As

expected, the arrival times in the single-integration seismograms are still too small, because, as shown above, the traveltime error introduced by neglecting the departure of a ray from the sagittal plane is much smaller than the traveltime error caused by the use of incorrect group velocities.

We computed traveltimes for this model (Fig. 19),

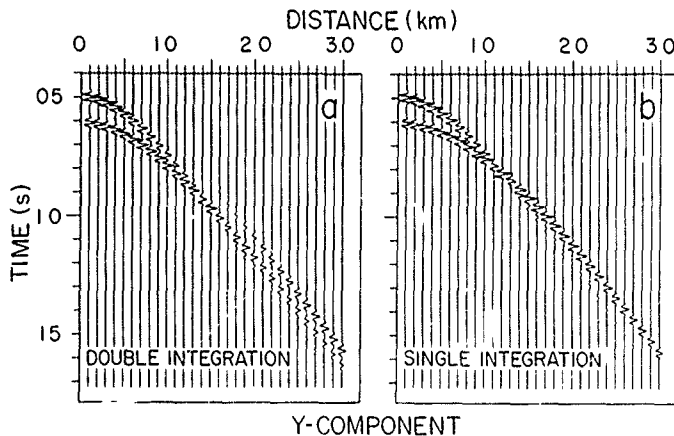


Figure 13. Synthetic seismograms for the same model as in Fig. 12. The source was oriented in the y direction and the y component is shown here. P waves are not visible because their amplitudes are relatively small. The arrival from the cusp is prominent in the double integration seismograms (a), where it is the first arrival at large offsets. It is missing in the single-integration seismograms (b). All arrival times match those in Fig. 12.

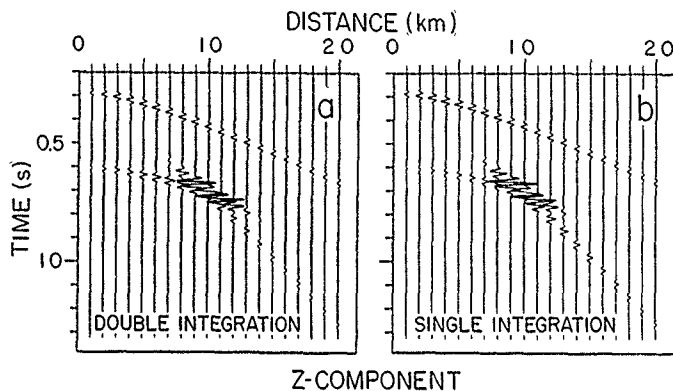


Figure 14. Seismograms computed for medium 2 of Table 1 for wave propagation in the symmetry plane that contains the symmetry axis. The corresponding group-velocity curves are those of Fig. 10. The source was oriented in the x direction, and the z -component is shown here. The slower S -wave does not appear on this component. The cusp in the group velocity surface causes triplication of the S arrival. Although the arrival times are identical in the double (a) and single (b) integration seismograms, the amplitudes differ.

applying the first method for multilayered media that was described above. This method gives the exact single-integration traveltimes and an upper limit for the double-integration traveltimes. We only get an upper limit for the latter because the traveltimes are computed along the single-integration ray path in the sagittal plane. However, comparison of Fig. 19 with Fig. 18 shows that both the single- and the double-integration arrival times match those of the synthetic seismograms perfectly. This demonstrates that the effect of the ray leaving the sagittal plane is a minor one.

CONCLUSIONS

Computing synthetic seismograms for AA media with a single integration can result in errors in both traveltimes and amplitudes. If the traveltimes are inaccurate, they will be too small, since single-integration group velocities are greater than or equal to double-integration group velocities. If the group-velocity surface on the medium has cusps and the sagittal plane is not a symmetry plane then some arrivals might be missing from the single-integration seismograms. Single integration should not be used for these kinds of models.

For multilayer models the traveltime error inherent in single integration can be regarded as the sum of two terms: one term due to the use of an effective group-velocity curve \mathcal{G} that is incorrectly large, and another term due to neglect of the fact that the true ray leaves the sagittal plane. The first error term is relatively large and negative while the second term is relatively small and positive. Therefore it is possible to estimate an upper bound for the error by considering only the error arising from the wrong velocities. We described a method that takes advantage of this fact.

Comparison of the traveltimes computed with this method with synthetic seismograms showed that the error introduced by the neglect of the ray leaving the sagittal plane appears to be negligible even for strongly anisotropic media, so that the estimated upper bound for the error is very close to the error itself. We also outlined an alternative method for computing the traveltime error prior to the computation of the synthetic seismograms.

The amplitude error can be estimated from the sagittal group velocity curves \mathcal{G}_s and \mathcal{G} . We showed that if these curves match for sagittal planes at a number of increasing azimuths then the amplitudes will be accurate at any azimuth. Generally, amplitudes appear less likely to be in error than traveltimes. However, one can have accurate traveltimes and wrong amplitudes in case of strong anisotropy if, for example, the sagittal plane is near a symmetry plane. Therefore, one should always use double integration for seismogram synthesis for strongly anisotropic media, even if the sagittal plane is a symmetry plane. As a safe method, we suggest using single integration in symmetry planes only for those models for which single integration can also be used in off-symmetry planes.

In most cases of weak anisotropy one finds that single integration gives sufficiently exact results for traveltimes and amplitudes so that it is not necessary to use double integration. The model used to make Figs 15–17 is a typical (in that respect) instance of weak anisotropy.

ACKNOWLEDGMENTS

We thank the Office of Naval Research for research support, Cray Research for computer time, the Geo-Pacific Corporation for the use of ANIVECTM, and Joe Dellinger for many useful discussions. SOEST Contribution No. 2843.

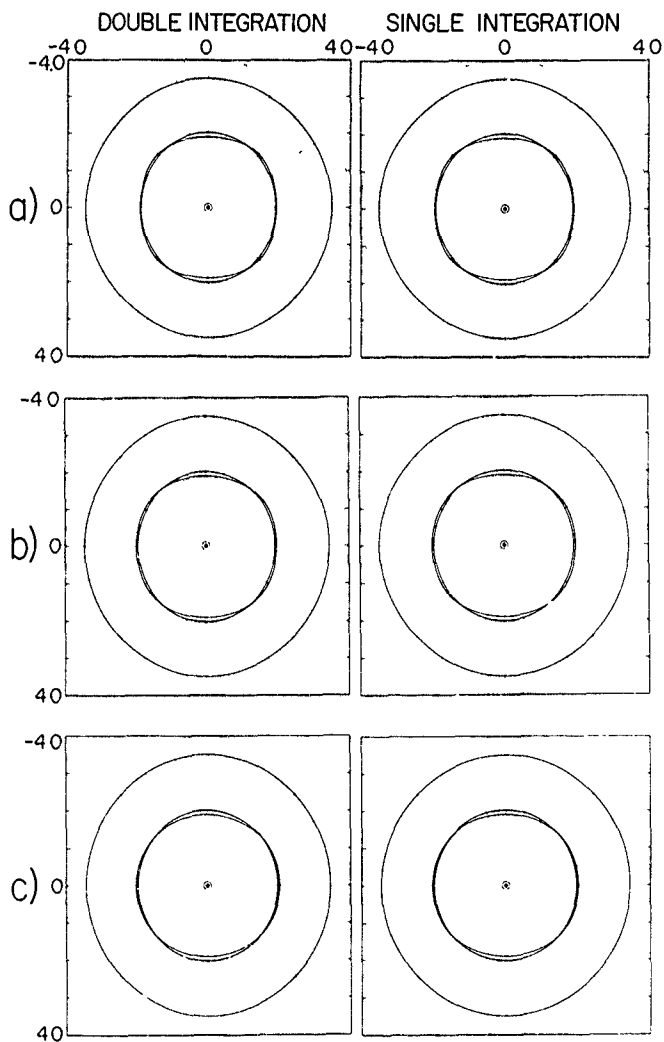


Figure 15 Curves \mathcal{C}_1 and \mathcal{C}_2 for medium 3 of Table 1 for off-symmetry planes at different angles to the vertical plane containing the symmetry axis: (a) 15° , (b) 30° and (c) 45° . The curves \mathcal{C}_1 (left) and \mathcal{C}_2 (right) are identical in all cases.

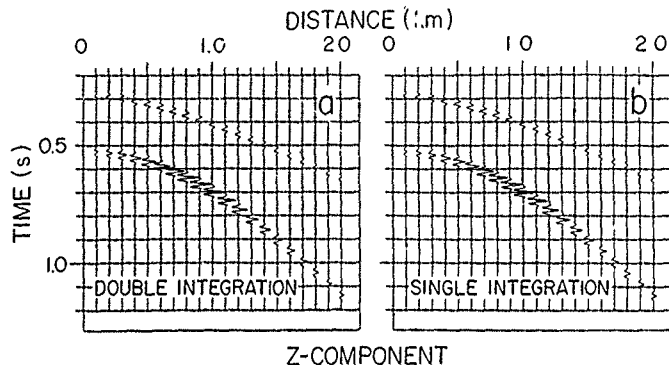


Figure 16. Synthetic seismograms (z-component) for a whole-space composed of medium 3 of Table 1. The source-receiver geometry is that of Fig. 7. The source was oriented in the x-direction. The sagittal plane is the vertical plane containing the symmetry axis. As expected, the single-integration amplitudes are accurate.

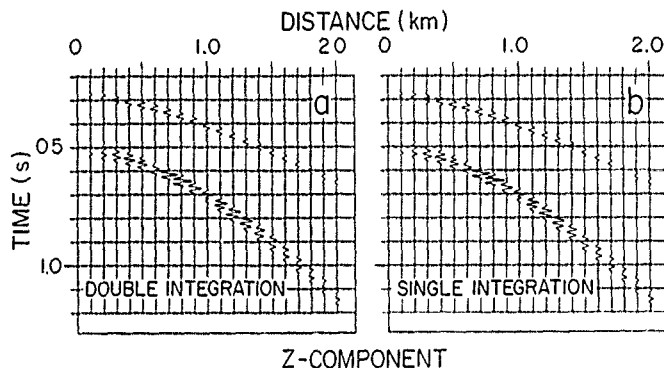


Figure 17. Synthetic seismograms for the same model as in Fig. 16 for a sagittal plane at an azimuth of 30° to the sagittal plane of Fig. 16. Again, single-integration amplitudes are accurate.

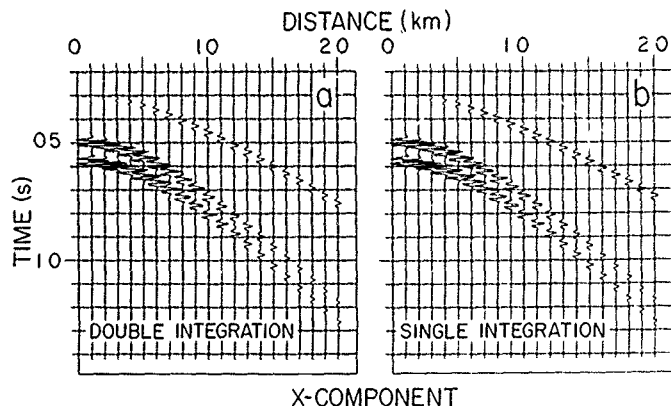


Figure 18. Synthetic seismograms for a model with a vertical gradient. The anisotropy decreases with depth. The elastic stiffnesses at the source depth are those of medium 4 in Table 1, and the elastic stiffnesses at the receiver depth are those of medium 1 in Table 1. The source-receiver geometry is that of Fig. 7. The source was oriented in the x-direction and the x-component is shown here. The arrival times are still too early in the single-integration seismograms (b).

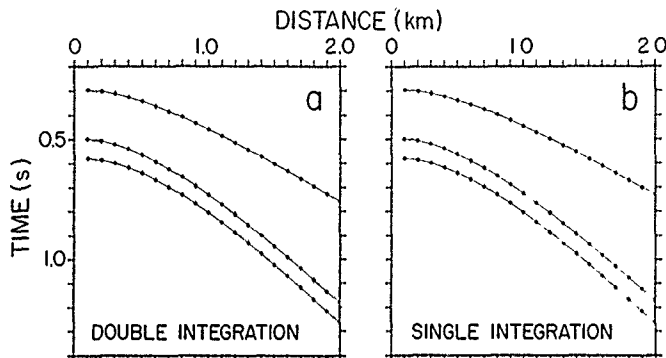


Figure 19. Time-distance plots for the same model as in Fig. 18, computed along the single-integration ray path as explained in the text. Computed points are marked by filled circles. Both the double-integration (a) and the single-integration (b) arrival times match those in Fig. 18, even though the departure of the ray from the sagittal plane was ignored in the computation of (a).

REFERENCES

- Auld, B. A., 1973 *Acoustic Fields and Waves in Solids*, vol. 1, John Wiley & Sons, New York.
- Booth, D. C. & Crampin, S., 1983 The anisotropic reflectivity technique: theory, *Geophys. J. R. astr. Soc.*, **72**, 755-766.
- Červený, V., Molotkov, I. A. & Pšenčík, I., 1977 *Ray Method in Seismology*, Praha. Univerzita Karlova.
- Crampin, S., 1987 Crack porosity and alignment from shear wave VSPs, in *Shear-wave exploration*, eds Danbom, S. H. & Domenico, S. N., Geophysical Developments, SEG Special Publ., **1**, 227-251.
- Frazer, L. N. & Fryer, G. J., 1989 Useful properties of the system matrix for a homogeneous anisotropic elastic solid, *Geophys. J. R. astr. Soc.*, **97**, 173-177.
- Fryer, G. J. & Frazer, L. N., 1984 Seismic waves in stratified anisotropic media, *Geophys. J. R. astr. Soc.*, **78**, 691-710.
- Fryer, G. J. & Frazer, L. N., 1987 Seismic waves in stratified anisotropic media—II. Elastodynamic eigensolutions for some anisotropic systems, *Geophys. J. R. astr. Soc.*, **91**, 73-101.
- Fuchs, K. & Müller, G., 1971 Computation of synthetic seismograms with the reflectivity method and comparison with observations, *Geophys. J. R. astr. Soc.*, **23**, 417-433.
- Helbig, K., 1992 *Seismic Anisotropy*, Pergamon Press.
- Hudson, J. A., 1981 Wave speeds and attenuation of elastic waves in material containing cracks, *Geophys. J. R. astr. Soc.*, **64**, 133-150.
- Kennett, B. L. N., 1974 Reflections, rays, and reverberations, *Bull. seism. Soc. Am.*, **64**, 1685-1696.
- Kennett, B. L. N., 1983 *Seismic Wave Propagation in Stratified Media*, Cambridge University Press.
- Kennett, B. L. N. & Kerry, N. J., 1979 Seismic waves in a stratified half space, *Geophys. J. R. astr. Soc.*, **57**, 557-583.
- Lighthill, M. J., 1960 Studies on magneto-hydrodynamic waves and other anisotropic wave motions, *Phil. Trans. R. Soc. Lond. A*, **252**, 397-430.
- Mallick, S. & Frazer, L. N., 1990 Computation of synthetic seismograms for stratified azimuthally anisotropic media, *J. geophys. Res.*, **95**, 8513-8526.
- Mallick, S. & Frazer, L. N., 1991 Reflection/transmission coefficients and azimuthal anisotropy in marine seismic studies, *Geophys. J. Int.*, **105**, 241-252.
- Musgrave, M. J. P., 1970 *Crystal Acoustics*, Holden-Day.
- Schoenberg, M. & Douma, J., 1988 Elastic wave propagation in media with parallel fractures and aligned cracks, *Geophys. Prosp.*, **36**, 571-590.
- Winterstein, D. F., 1990 Velocity anisotropy terminology for geophysicists, *Geophysics*, **55**, 1070-1088.

WORKSTATION COMPUTATION OF SYNTHETIC SEISMOGRAMS FOR VERTICAL AND HORIZONTAL PROFILES: A FULL WAVEFIELD RESPONSE FOR A TWO-DIMENSIONAL LAYERED HALF-SPACE

ALBERT J. RUDMAN,¹ SUBHASHIS MALLICK,² L. NEIL FRAZER,³ and PETER BROMIRSKI¹

¹Department of Geological Sciences, Indiana University, Bloomington, IN 47405, ²Western Geophysical, P.O. Box 2469, Houston, TX 77252-2469, and ³Department of Geology and Geophysics, 2525 Correa Road, Honolulu, HI 96822, U.S.A.

(Received 31 August 1992, accepted 6 October 1992)

Abstract—FORTRAN code for generation of full wavefield synthetic seismograms is presented for two-dimensional horizontally layered models bounded by a free surface and a half space. Model layers are user defined by compressional and shear velocities, Q factors, densities and thicknesses. The algorithm is based on the reflectivity method and uses the propagator matrix approach. Explosion (point) and double couple (fault) sources are generated with a moment tensor representation. As evaluation of the slowness integrals involves time consuming numerical Harkel transforms, these computations are made with a generalized Filon method that saves computational time. The architecture of the program is unusual because the outermost loop is over temporal frequency and the innermost loop is over slowness. This permits the use of frequency-dependent seismic velocities, necessary for causality, while giving a factor of seven speed-up from vectorization. The codes are applicable for both vector computers and workstations.

Two test cases demonstrate successful applications of the codes for both horizontal seismic profiles (receivers at one depth at successively larger offsets) and for vertical seismic profiles (receivers arranged in a vertical array at any offset). Receivers and source may be positioned within any layer. The seismograms display direct, refracted, reflected, and head-wave arrivals and their multiples. Mode converted events of compressional and shear propagation are generated and identified. The code generates seismograms for pressure, vertical and horizontal displacement sensors and for models combining acoustic and elastic layers.

Key Words: Synthetic seismogram, Reflectivity method, Propagator matrix, Full wavefield response, Vertical seismic profile (VSP)

INTRODUCTION

Most geophysical problems are studied using either the forward (direct) modeling approach or an inverse method approach. In seismology, the *inverse* problem may involve determining the velocity model from the observed arrival times of elastic waves at a set of seismograph stations. Given the velocity model, origin time, location, and dynamics of the source, the computation of a seismogram displaying the wave forms of all possible seismic events expected at a specific location is a classic *forward* problem. Specifically, the response of a stratified half space to a general source as recorded by a sensor is known as a *synthetic seismogram*. Analysis of observed differences between synthetic and recorded seismograms provides insight into either the velocity (geologic) structure or the nature of the seismic source, and is of fundamental importance in both exploration and earthquake studies.

In this paper we present an algorithm for the computation of synthetic seismograms using the

codes REFLSYNF and REFLSYNT (Appendix 1). These codes generate seismograms recorded either on a set of sensors at increasing horizontal distances x from the source, termed a horizontal seismic profile (HSP) or on a set of sensors at increasing vertical depths, termed a vertical seismic profile (VSP) (Fig. 1). The codes compute a full wavefield response for a medium consisting of plane horizontal isotropic layers bounded above by a free surface and below by a half-space (Fig. 2). Each layer is described by its compressional (longitudinal) velocity α and shear (transverse) velocity β (CL and CT respectively in the code), its quality factors QL and QT, and density ρ (RHO). Although codes for generation of seismograms for the situation of *vertically* incident plane waves are available widely (Frazer, Bates, and Rudman, 1985), this is not the situation for codes that are applicable to workstations and that generate both HSP and VSP full wave synthetics. The next generation of synthetic seismogram codes are now being developed for anisotropic layers (e.g. Mallik and Frazer, 1990b, 1991).

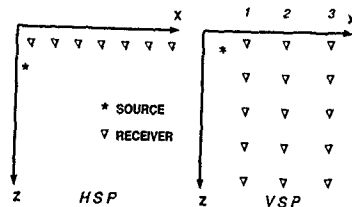


Figure 1 Source-receiver geometries for program REFLSYN. For horizontal seismic profile (HSP) receivers are at equal increment spacing at one depth. Sources may be above or below receiver. For vertical seismic profiles (VSP) receivers are at various specified depths at common offset (x) distance. Several source to receiver offsets may be obtained from one computation.

THEORY

Let capital bold letters denote matrices and lower case bold letters denote vectors. In a homogeneous medium, a seismic wavefield can be described by the solution of the simple wave equation

$$\frac{\partial^2 \phi}{\partial x^2} = \frac{1}{c^2} \frac{\partial^2 \phi}{\partial t^2} \quad (1)$$

where ϕ is a potential function of the elastic displacement vector u , c is the phase velocity, x represents space coordinates, and t is time. Solutions to the wave equation are given many places (e.g. Aki and Richards, 1980). However, for more realistic earth models the seismic wavefield is best developed by first reformulating the wave equation in terms of the momentum equation

$$-\rho \omega^2 u = \nabla \tau + f \quad (2)$$

$$\frac{\partial}{\partial z} \begin{bmatrix} U \\ V \\ M \\ N \end{bmatrix} = \omega \begin{bmatrix} 0 & p(1-2\beta^2/\alpha^2) & (\rho\alpha^2)^{-1} & 0 \\ -p & 0 & 0 & (\rho\beta^2)^{-1} \\ -\rho & 0 & 0 & p \\ 0 & \rho(v\rho^2-1) & -\rho(1-2\beta^2/\alpha^2) & 0 \end{bmatrix} \begin{bmatrix} U \\ V \\ M \\ N \end{bmatrix} + \begin{bmatrix} 0 \\ 0 \\ g_z \\ g_r \end{bmatrix} \quad (5)$$

and the constitutive relation

$$\tau = C:\epsilon \quad (3)$$

where ω is radian temporal frequency, f is the body force density, C is the fourth-order elastic tensor, and τ and ϵ are the second-order stress and strain tensors, respectively.

Matrix solutions to Equations (2) and (3) are based on continuity of normal stresses and displacements at layer boundaries. Thomson (1950) and Haskell (1953) represented a vertically inhomogeneous medium as a stack of homogeneous layers and described up and down going waves with a matrix representation. Their approach was a special situ-

ation of the Gilbert and Backus (1966) systemat development using a 'Propagator Matrix' between successive layers in the stratified medium. The mathematics for the various methods have been summarized carefully and reviewed by Chir, Hedstrom, and Thigpen (1984).

We use cylindrical coordinates x (offset), z (depth) and ϕ (azimuth) with source on the z axis and receivers on the $\phi = 0$ plane. The algorithm is based on the reflectivity method introduced by Fuchs and Muller (1971) and developed extensively by Kennel (1983) and others into a matrix representation in the frequency-wavenumber domain. The process involves transforming out the dependence of Equations (2) and (3) on the horizontal coordinate (x) and time (t) using Hankel and Fourier transforms respectively to obtain a set of equations of the form

$$\hat{C}_i(b) = -i\omega Ab + g \quad (4)$$

where b is a stress-displacement vector of physical variables referred to as the reflectivity function $i = \sqrt{-1}$. A is either a 2×2 matrix for an SH system (shear waves with motion transverse to the propagation direction and confined to a horizontal plane) or a 4×4 matrix for a P/SV system [coupled compressional (P) and shear wave (SV) propagation in a vertical plane], and g is the source function. In our code the point source g is described by a moment tensor to simulate either an explosion or a double couple (earthquake) system. The algorithm presented here does not include the SH wave computation.

Equation (4) takes a convenient form if expressed in terms of horizontal slowness $p = k_x/\omega$, where k_x is the horizontal wavenumber. Thus for P/SV waves we have (Kennett, 1983, eq. 2.24)

where U and V are scalar transforms of displacement, M and N are scalar transforms of stress, and $v = 4\rho\beta^2(1-\beta^2/\alpha^2)$. Unique solutions of Equation (5) are obtained by imposing the boundary conditions of vanishing normal stress at the free surface and of outgoing radiation in the lower halfspace. To obtain the ω - x domain solution, one evaluates the inverse Hankel transforms; for example, the vertical component \hat{U} is expressed as

$$\hat{U}(x, z, \omega) = \int dp \omega^2 p \hat{U}(p, z) H_0^1(\omega p, x) \quad (6)$$

where H_0^1 is the Hankel function of type 1 and order 0. $\hat{U}(p, z)$ is one of the components of b obtained by

the reflectivity method. Continuity of displacement and stress across layer boundaries yields expressions for a system of reflection and transmission coefficients, R and T , used to compute $\underline{U}(x, z)$.

where $f(p) = (\omega^2/2) p H_0^1(\omega p, x) e^{-\log p} U(\omega, p)$, $S = i\omega x$, and $g(p) = p$. After some arithmetic, Frazer (1988) obtains the GFM analog of the trapezoidal rule of integration in the form

$$\int_a^b f(p) e^{Sg(p)} dp = \left\{ \frac{\delta p}{S \delta g} \left[\delta(f e^{Sg}) - \left\{ \delta(f) \delta(e^{Sg}) / S \delta g \right\} \right] \right. \\ \left. \left\{ \delta p / 2 \right\} [f(a) e^{Sg(a)} + f(b) e^{Sg(b)}] \right\} \quad \begin{matrix} \delta g \neq 0 \\ \delta g = 0 \end{matrix} \quad (9)$$

Explicit forms for R and T are given in Aki and Richards (1980, chap. 5). Final computation of the seismogram involves Fourier transformation of $\underline{U}(x, z, \omega)$ from frequency into the time domain by

$$u(x, z, t) = 1/2\pi \int d\omega \underline{U}(x, z, \omega) e^{-i\omega t}, \quad (7)$$

where u is the vertical displacement seismogram.

Computation of the slowness integral [Eq. (6)] is obtained with a numerical Hankel transform for a large range of slownesses and iteratively over all frequencies up to the Nyquist. Rapid oscillation of the Hankel function kernel indicates that standard quadrature methods require a large number of steps (δp is inversely proportional to ωx). In order to reduce the computation time, we use the generalized Filon quadrature method (GFM) described by Frazer (1988). The Filon method allows the step size to be proportional to $(\omega x)^{-1/2}$ and, for a given step size, computations may yield a time savings of up to 80%. We rewrite Equation (6) in the GFM form

$$\int f(p) e^{Sg(p)} dp \quad (8)$$

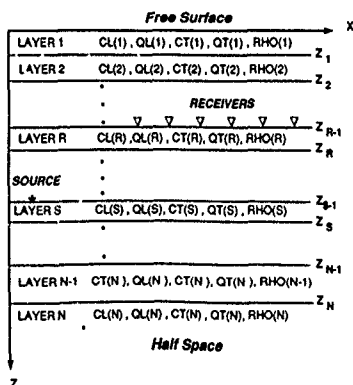


Figure 2 Two-dimensional layer model for program FEF-FLSYNF. Parameter inputs for each layer are compressional velocity (CL), compressional Q (QL), shear velocity (CT), shear Q (QT), density (RHO), and layer thickness ($z_{i+1} - z_i$). Receivers and source depth are located at top of layers selected by layer number

where δ refers to the interval $b - a$, and δf means $f(b) - f(a)$.

Attenuation is introduced by making each seismic velocity $c(\omega)$ a complex, frequency-dependent function dependent on seismic Q . We use a modified version of Strick's power law (Strick, 1970).

$$\frac{1}{c(\omega)} = \frac{1}{c(\omega_0)} + \frac{\kappa_0}{\sin(\pi/2)(\epsilon - i\omega)^{\kappa_0}} \quad (10)$$

where $c(\omega)$ = complex velocity, $c(\omega_0)$ the velocity at infinite frequency, $\sigma = 0.1$ for earth materials, $\kappa_0 \approx \omega_0^2 / [2c(\omega_0)Q(\omega_0)]$ and ω_0 is a reference frequency, $Q(\omega_0)$ is the model Q and $\epsilon = 0.001$

MATRIX SOLUTIONS

The displacement components of the reflectivity functions, \underline{U} and \underline{V} , are computed from the reflection and transmission matrices R and T . The matrices R and T for different regions are the fundamental building blocks of the Kennett solution to Equation (5). These blocks are assembled in different ways depending on whether the receiver is above the source or vice versa. The following brief introduction to the matrix approach draws primarily from Kennett's book (1983). For plane waves in a layer, let v_{PU} , v_{PS} be the displacement potentials of the upgoing compressional and shear waves, respectively. Similarly, let v_{PD} and v_{SD} represent the downgoing waves. We write

$$\underline{v}_U = \begin{bmatrix} v_{PU} \\ v_{PS} \end{bmatrix} \quad \text{and} \quad \underline{v}_D = \begin{bmatrix} v_{PD} \\ v_{SD} \end{bmatrix} \quad (11)$$

At each depth we define a reflection matrix R_D relating amplitudes of up and downgoing waves \underline{v}_U and \underline{v}_D , respectively, for elastic and fluid layers

$$\underline{v}_U = R_D \underline{v}_D, \\ R_D = \begin{pmatrix} R_{PP}^E & R_{PS}^E \\ R_{SP}^E & R_{SS}^E \end{pmatrix} \quad (\text{ELASTIC})$$

and

$$R_D = R_{DL}^F \quad (\text{LIQUID}) \quad (12)$$

where, for example, R_{PP}^E is the reflection coefficient of the downward travelling incident compressional wave (P) reflected as a shear wave (S). Corresponding definitions similar to Equation (12) may be developed for R_U and for the transmission matrices T_D and T_U .

For n layers sandwiched between two half spaces, we have a matrix representation of upgoing and

systematic
Matrix between
dium. The math-
ve been summar-
Hedstrom and

offset), z (depth),
the z axis and
algorithm is based
ed by Fuchs and
ively by Kennett
resentation in the
ic process involves
of Equations (2)
te (x) and time (t)
rms respectively to
orm

(4)

vector of physical
flectivity function,
for an SH system
erse to the propa-
horizontal plane)
tem (coupled com-
v) propagation in a
ce function. In our
ied by a moment
losion or a double
algorithm presented
ive computation.

at form if expressed
= k_z/ω , where k_z is
s for P/SV waves we

$$\begin{bmatrix} 0 \\ 0 \\ s_z \\ s_x \end{bmatrix} \quad (5)$$

rms of displacement,
rms of stress, and
lutions of Equation
boundary conditions
free surface and of
halfspace. To obtain
evaluates the inverse
le, the vertical com-

$$p, z) H_0^1(\omega p, x) \quad (6)$$

n of type 1 and order
nents of b obtained by

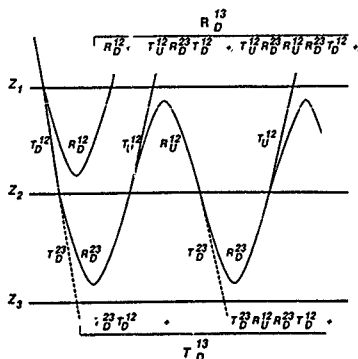


Figure 3. Physical significance of reflection coefficient matrix R^{12} and transmission coefficient matrix T^{12} showing interaction of regions '12' and '23' [Eq. (17)]. Modified from Kennett (1983, fig 6.1)

downgoing wavefields. In layer 1, U_1 and D_1 are given by

$$\begin{pmatrix} U_1 \\ D_1 \end{pmatrix} = Q \begin{pmatrix} U_{N+1} \\ D_{N+1} \end{pmatrix} \quad (13)$$

where Q is a wave propagator matrix related to a matrix of the total reflection and transmission coefficients R and T as follows

$$Q = \begin{pmatrix} T_U - R_D T_D^{-1} R_U & R_D T_D^{-1} \\ -T_D^{-1} R_U & T_D^{-1} \end{pmatrix} \quad (14)$$

To illustrate the physical meaning of the total reflection and transmission matrices, consider an inhomogeneous region $z_1 < z < z_3$ subdivided by a horizontal plane at $z = z_2$ (Fig. 3). The overall response for the '13' region is

$$\begin{aligned} R_B^{13} &= R_B^{12} + T_B^{12} R_B^{22} [I - R_B^{12} R_B^{22}]^{-1} T_B^{12}, \\ T_B^{13} &= T_B^{12} [I - R_B^{12} R_B^{22}]^{-1} T_B^{12}, \\ R_B^{23} &= R_B^{22} + T_B^{22} R_B^{33} [I - R_B^{22} R_B^{33}]^{-1} T_B^{22}, \\ T_B^{23} &= T_B^{22} [I - R_B^{22} R_B^{33}]^{-1} T_B^{22} \end{aligned} \quad (15)$$

where I is the identity matrix. The notation used here again follows Kennett (1983). An incident downward travelling wave at some layer z_1 gives rise to a series of reflection and transmission terms. The reflection series R_B^{12} is the reflection matrix for the '12' region in isolation. The matrix inverse in Equation (15) may be expanded as a power series

$$[I - A]^{-1} = I + A + A^2 + \dots \quad (16)$$

Therefore, line 1 of Equation (15) may be written as

$$R_B^{13} = R_B^{12} + T_B^{12} R_B^{22} T_B^{12} + T_B^{12} R_B^{22} R_B^{22} T_B^{12} + \dots \quad (17)$$

Figure 3 shows the travel path of each term in Equation (17). R_B^{12} represents the reflection from the z_2 interface. $T_B^{12} R_B^{22} T_B^{12}$, reading right to left, rep-

resents a transmission down from interface z_1 through interface z_2 , reflection from interface z_3 , followed by transmission up from interface z_2 to interface z_1 . The third term includes another internal reverberation (multiple). The reflection/transmission matrices containing the bracketed quantities of Equation (15), termed the reverberation operator, includes all phases and multiples within the two layers.

R and T may be calculated by adding a layer at each computational stage, beginning at the bottom of the stack of layers. The reflection and transmission coefficients given here contain phase shifts due to the travel time in each layer. When these depth intervals are homogeneous layers, it is convenient to write the phase shift terms explicitly. Thus, R_B^{12} is obtained from

$$R_B^{12} = E R^{12} E \quad (18)$$

where R^{12} is the reflection coefficient for the interface at depth z_1 , and

$$E = \begin{pmatrix} e^{i q_1 z_1} & 0 \\ 0 & e^{-i q_1 z_1} \end{pmatrix} \quad (19)$$

where $q_1 = (\alpha^2 - p^2)^{1/2}$, $q_2 = (\beta^2 - p^2)^{1/2}$, and $z = z_3 - z_2$. The phase matrix E accounts for the distance travelled in the corresponding layer ($z_3 - z_2$) in terms of the phase velocities α and β in the layer and the horizontal slowness p .

For VSP, when there may be receivers above the source and many receivers below the source, a somewhat complicated use of R and T yields a rapid computation. Such topics are beyond the scope of this paper but the interested reader can obtain a detailed treatment in Mallick and Frazer (1988). All the examples in that paper were computed with REFLSYNF.

ALGORITHM

Two separate codes are presented in this paper: REFLSYNF and REFLSYNT. The main code, REFLSYNF implements Equation (6) and computes file WXP (binary), the synthetic seismogram equivalent in the frequency-distance domain at specified offsets x and depths z for the pressure, horizontal displacement, and vertical displacement components of the wavefield. REFLSYNT implements Equation (7) and Fourier transforms WXP to the time-distance domain. This code uses a standard FFT and will not be discussed further.

REFLSYNF is summarized in a brief flowdiagram (Fig. 4). It requires two input files, MODEL and RESP.MODEL gives the velocity model parameters and RESP specifies computational parameters (details are in the code comments). Within REFLSYNF subroutine EXECUT contains the bulk of the computations discussed in the earlier sections on Theory and Matrix Representation. After opening files, initializing arrays and setting flags to identify the source and receiver types, the frequency loop begins. The frequency domain response is computed for all NW

PROGRAM REFLSYNF

```

MAIN PROGRAM
  Open files. Call Subroutines
SUBROUTINE MODLIN
  Initialize. Read in model parameters. Generate default parameters
  If necessary, interpolate layers and introduce earth flattening
SUBROUTINE RESPIN
  Read in program control parameters. Set source parameters
SUBROUTINE EXECUT
  Open files. Initialize. Set flags for source/receiver properties.
  Generate headers for output files.
  Begin Calculations
    Frequency loop (for all frequencies up to Nyquist)
      Calculate p loop controls
      Layer loop
        p loop
          Iteration equations to compute the reflection/transmission coefficients
        End p loop
      If source layer then
        p loop
          Store reflection/transmission coefficients to this point.
          Reset reflection coefficients to 0 and transmission coefficients to 1.
        End p loop
      If receiver layer then
        p loop
          Store reflection/transmission coefficients to this point.
        End p loop
      End layer loop
      Receiver loop
        p loop
          Compute displacement response using appropriate formula for receiver
          above or below source
        End p loop
      x loop
        Filter integrate over p to transform p to x
      End x loop
      End receiver loop
      Write response for this frequency
      End frequency loop
    End calculations.
  SUBROUTINE BUFOUT
    Write binary output for input to REFLSYNT (which Fourier transforms to time domain)

```

Figure 4. Flowdiagram for program REFLSYNF (see Appendix).

interface
face, z_1 to
internal
transmission
quantities of
operator,
in the two

ng a layer at
the bottom of
transmission
is due to the
length intervals
nt to write the
is obtained

(18)

or the interface

(19)

$p^2)^{1/2}$, and $z =$
for the distance
($z_1 - z_2$) in terms
he layer and the

ceivers above the
source, a some-
T yields a rapid
and the scope of
der can obtain a
Frazer (1988) All
re computed with

nted in this paper.
The main code, RE-
6) and computes file
smogram equivalent
in at specified offsets
horizontal displace-
t components of the
ents Equation (7) and
he time-distance do-
J FFT and will not be

in a brief flowdiagram
at files, MODEL and
city model parameters
tional parameters (de-
s) Within REFLSYNF
is the bulk of the com-
puter sections on Theory
After opening files, ini-
g to identify the source
frequency loop begins The
is computed for all NW

frequencies up to the Nyquist frequency. The layer and receiver loops are within the frequency loop. Within the layer loop, the reflection/transmission coefficients are computed for each interface for all ray parameters and are stored separately for the special situations of source and receiver layers. Iteration generates the reflection/transmission coefficient matrix for the entire stack of layers. The receiver loop, which follows the layer loop, includes a transformation to space coordinates [evaluation of Eq. (6)]. Computations differ depending on the relative positions of receiver and source. Both the layer and receiver loops contain p loops that vectorize. Having the outer loop over frequency and the inner loop over slowness permits use of frequency-dependent seismic velocities. This unusual vector architecture reduces the time for computations on a Cray Y-MP by a factor of seven. The code also has been tested successfully on a workstation (Sun Sparcstation2) with run

times that are 50-60 times longer than on the Cray for relatively simple models.

Two distinct array-source geometries are available. HSP is the conventional exploration configuration with receivers extended along a horizontal line, usually at equal increments (offsets) for the source (Fig. 1A). Source and receiver depths are selected by the user, although receivers usually are placed just below the free surface. VSP is associated with down-hole logging with receivers in a vertical array at specified intervals at fixed horizontal offsets from the source (Fig. 1B), arbitrary source and receiver depths again are selected by the user. Further specifics on running of the program, available options and variable names and their significance are given in the program listing.

The advantage of the reflectivity method is that it includes all possible generalized rays within the model, the principal disadvantage is that compu-

tation may require extensive computer time. Computations are slowed by the need to (1) adequately sample the reflectivity function in wavenumber (slowness) space to avoid spatial aliasing on transforming into the offset domain, (2) use many frequencies to avoid wraparound in the time domain, (3) compute a time series longer than the interval of interest to

avoid time aliasing, and (4) include numerous thin layers in the models to represent velocity gradients. Although computing time is not dependent strongly on the number of offsets requested, it is proportional to the number of frequencies, layers and wavenumbers (or slowness) samples used in the integration of Equation (6). Variations in speed and accuracy for

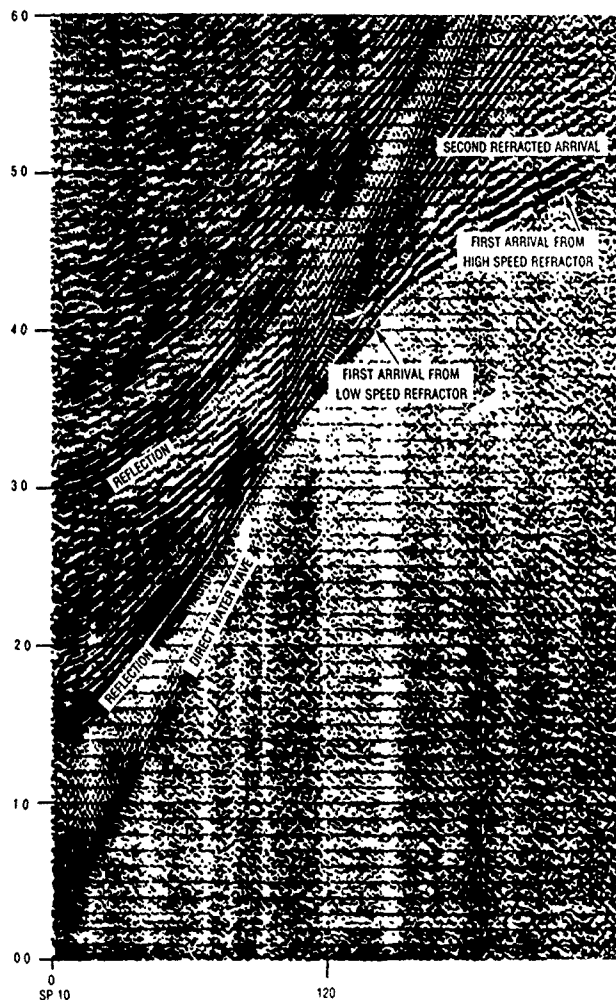


Figure 5. Sonobuoy seismogram profile from 10° recording line. Modified from Dobson and Saxton (1981).

Table 1 Model parameters for Figure 6—liquid layer over elastic layer over elastic half space

LAYER	THICKNESS(KM)	CL (KMS)	QL	CT (KMS)	QT	RHO (GM/CC)
1	1.15	150	5000	0	0	1.0
2	2.00	250	200	1.44	100	2.5
3	HALF SPACE	6.00	300	3.46	150	3.0

different algorithms have been studied by Mallick and Frazer (1987). They have discussed the advantages of the use of (1) a generalized Filon's method (Frazer and Gettrust, 1984) for including larger step sizes in the slowness integration of Equation (6), (2) complex frequencies (Phinney, 1965) for reducing the time-series length, (3) careful use of phase integrals in gradient zones for computational speed, and (4) complex velocities to incorporate Q dependence. All of these techniques are applied in the algorithm presented here.

As may be the situation, there may be some computational pitfalls that the user may encounter. For example, there is a linear event that seems related to the integration window defined by the variable PMAX. If necessary, the event may be minimized with a careful choice of frequencies NW and integration window parameters P1, P2, P3, and P4. Another computational problem is related to near offset distances. The integration involving the Hankel function [Eq. (6)] is not applicable for near zero offsets. In consequence at the near offsets arrival times of events are correct, but true amplitudes are larger than predicted. At this time no other problems are known to the authors. Although numerous models were run, time and space considerations limit our presentation to two test cases.

TEST CASES

Horizontal seismic profile

We demonstrate the code operation for an HSP with a simple model consisting of two layers over a half space and then compare it to a real seismic profile. Figure 5 shows a sonobuoy profile modified from the introductory geophysics text of Dobrin and Savit (1988, fig. 11-17). The text describes the profile as a ship recording extending for a horizontal distance of 50,000 ft. The geology in the region of this profile is not given, but there are several labeled events that are identified. For example, the 'direct water wave' from source to receivers and two arrivals from a 'low-speed' and a 'high-speed' velocity refractor (also termed head waves) are identified on the figure. Two prominent reflections are evident at zero offset arrival times of approximately 0.15 and 0.29 sec. In addition to noise superimposed on the recording, there are numerous other unidentified events. These probably are related to reflections, refractions, and multiples from a layered geologic section. In our model we presume that the profile was generated by a point source within the first (oceanic) layer. Although sonobuoys record only pressure arrivals, we anticipate that some events on the profile may involve intervening S-wave mode conversions, e.g. a PSP headwave phase from the top of layer 2. Therefore, a realistic synthetic seismogram must include the full solution to the wave equation, including multiple arrivals and mode converted phases.

We have used REFLSYNF to try to generate the more prominent features displayed on Figure 5 and thereby demonstrate the program's versatility in seismic modeling. Although the geology is unknown, the presence of the two prominent refractions led us to select a simple model consisting of an acoustic (ocean) layer over an elastic layer over an elastic half space. Table 1 lists the model parameters of layer thicknesses, velocities, Q values and densities. These parameters are read in to REFLSYNF from file MODEL (Table 2). Note that shear velocities and Q factors for layer 2 and the half space are not read in directly, but were computer generated by REFLSYNF as default values.

Computational parameters are from file RESP (Table 2). A record length of TSEC = 30 sec was computed in combination with 512 frequencies (NW). Integration was based on a step size of DP =

Table 2 Input files used to generate HSP synthetic seismogram (Fig. 6). Code is run with *reflsynf model resp*

MODEL
0.0750 0.0,2
15.5000,0.0,0.0,1.0,0.1
15.5000,0.0,0.0,1.0,0.1
15.5000,0.0,0.0,1.0,1.13
25.200,-1.0,-1.0,2.5,2.0
6.0,300,-1.0,-1.0,3.0,1000
RESP
Sonobuoy model
512,1.30,0.1,0.002
3
0.15,25
0.0,0.0,0
D
0.0,0.0

ous thin
gradients
nt strongly
proportional
wavenum-
integration of
accuracy for

240

tance of 50,000 ft

0.002 to a maximum slowness of $p = 1.0$ sec/km. A point source was located 100 m below the free surface and 60 receivers were positioned 200 m below the free surface at 0.25 km intervals horizontally from the source. The maximum frequency NW selected by the user controls the characteristic appearance of the signal. One tries to pick the lowest maximum frequency and record length (TSEC) that generates a seismogram that displays readable events in the time frame of interest. In summary, input files MODEL AND RESP described in REFLSYNF comments generate an output file WXP which is the frequency-space domain seismogram. REFLSYNT uses WXP and a single line parameter file PARAM to generate

the ASCII file plotted as a synthetic seismogram (Fig. 6)

With both source and receiver in the water layer, we have opted to generate an HSP synthetic seismogram for a pressure receiver. Although the synthetic seismogram (Fig. 6) was generated from just two layers over a half space, it displays numerous events. For example, model velocities allow us to identify the direct water wave (D) and the refracted arrivals (head waves) from the top of the second layer (H1) and from the top of the half space (H2). The normally incident reflection from the bottom of the water layer (R1) arrives at zero offset at 1.53 sec, with multiples (M1 and M2) at regular 1.53 sec intervals

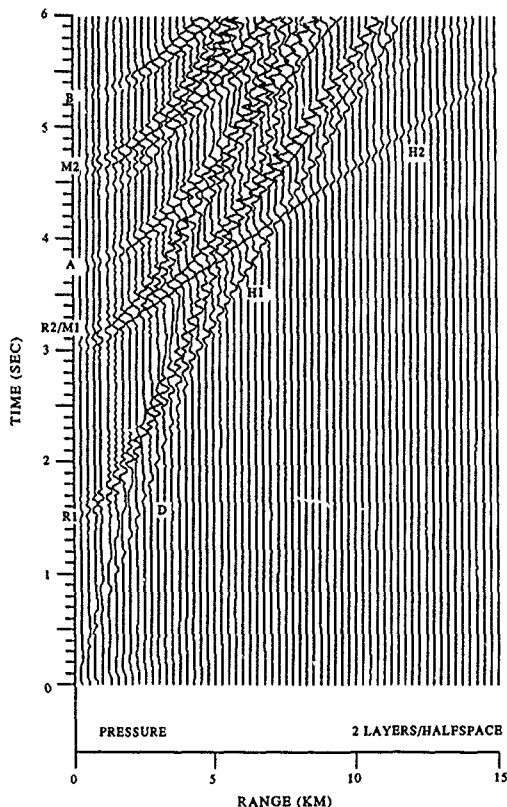


Figure 6 HSP test case pressure synthetic seismogram for liquid layer over elastic layer over elastic half space (Table 1). Seismogram simulates sonobuoy profile of Figure 5. Prominent events identified by apparent velocity and curvature are: D (direct water wave), H1 and H2 (head waves), R1 and R2 (primary reflections), M1 and M2 (multiple reflections), and A and B (mixed mode events).

seismogram

water layer, synthetic seismogram through the synthetic layer from just above the numerous layers allow us to see the refracted second layer (H2). The bottom of the trace is 1.53 sec, with 0.3 sec intervals.

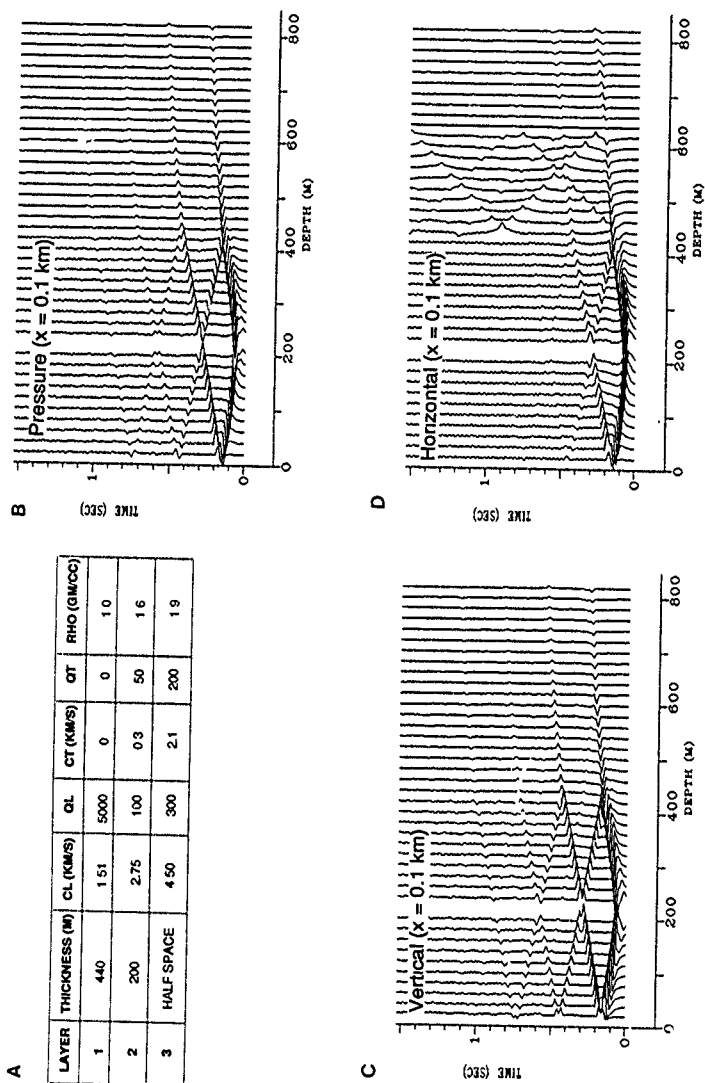


Figure 7 VSP test case A—Table of layer parameters, B-D—seismograms at a common offset of 0.1 km

VCB

15

over elastic half
space identified by
and R2 (primary
events)

the first 10 receivers with a moveout velocity of 1.51 km/sec and arrives at receiver 1 at 0.13 sec. It then is reflected from the free surface with a polarity change and continues as a downgoing wave. Simultaneously, the downgoing wave from the source arrives at the top of layer 2 (receiver 20) at 0.13 sec and then is reflected as an upgoing wave toward the free surface without a polarity change. These up and downgoing waves generate a chevron pattern of reverberating reflections within the first layer as observed on receivers 1–20. Because this is an acoustic layer no pure shear modes are present.

As each downgoing wave encounters layer 2 (receiver 21), a portion of the wave continues downward into the second (elastic) layer as a compressional wave and as a shear wave. The downgoing waves next encounter the top of the elastic half-space at 660 m (receiver 30). Again a portion of the energy is reflected as a compressional and shear wave, and a portion is refracted (never to return) into the half-space as compressional and shear waves. The reverberating events in layer 2 are displayed on receivers 21–30 as a chevron pattern with an apparent compressional velocity of 2.75 km/sec. The downgoing linear patterns in the half-space (receivers 31–40) exhibit a compressional velocity of 4.50 km/sec characteristic of the half-space.

The vertical component seismogram (Fig. 7C) should display displacements of both compressional and shear modes. In this situation, the vertical component of the shear mode is too small in amplitude at 0.1 km offset to be apparent on the seismograms. Therefore, the vertical seismogram is similar to the pressure component seismogram.

The horizontal seismogram (Fig. 7D) contains both compressional and shear arrivals. Within the acoustic layer (receivers 1–20), the horizontal component is small and gains for all traces were adjusted relative to trace 11. Some of the small oscillations present on these traces are valid arrivals, but some are computational noise enhanced by the gains. Within layer 2 (elastic), the horizontal displacements of both compressional and shear modes are evident and recognizable by their respective velocities of 2.75 and 0.3 km/sec. As expected on a horizontal seismogram, the dominant event is the chevron pattern related to

the shear mode. Within the underlying half-space (receivers 31–40) the major energy transmitted is related to the compressional mode (as determined by the reflection/transmission coefficients). The observation that the low velocity chevron pattern in layer 2 consists mainly of shear wave reflections can be verified by running the model with the CT values set equal to zero. This generates an acoustic model that shows no shear wave velocities and the horizontal synthetic at 0.1 km offset shows an absence of the pattern in layer 2.

We consider next the vertical component VSP seismograms generated at offsets of 0.1 (Fig. 7C), 0.6 km (Fig. 8A) and 1.1 km (Fig. 8B). Comparison of the seismograms at these three different offsets shows the effect of refraction due to vertical velocity heterogeneity. The most significant differences involve the presence of arrivals prior to events taking the direct source–receiver path in layer 1. This is explained by recognizing that a combination of a refracted path and headwave path sees the higher velocities in layer 2 and in the half-space. For example, the direct wave from source to receiver A (Fig. 9) would travel at 1.51 km/sec. The headwave along layer 2 travels at 2.75 km/sec and eventually arrives before the direct path. Similarly, the headwave along the half-space travels at 4.50 km/sec and eventually arrives before the other events. Finally, the headwaves exhibit an offset and low-frequency waveform similar to that predicted by theory and field observations (Helmberger, 1968).

CONCLUSIONS

Synthetic seismograms computed with the reflectivity method and implemented by the matrix approach of Kennett (1983) are applicable to both vector computers (CRAY) and workstation (SUN) computation. REFLSYNF and REFLSYNT (Appendix) have been tested extensively for both horizontal and vertical profiles. Full-wave synthetic seismograms have been generated successfully for a variety of models. Other examples are shown in Mallick and Frazer (1987, 1988, 1990a). The authors have verified the program behavior in terms of shape and polarity of waveforms, relative amplitudes, generation of mode converted phases, effect of attenuation factors (Q), and the presence of multiple events, headwaves, and surface waves. Generation of synthetic seismograms that closely compare to observed seismograms requires the user to make iterative model changes in layer thickness, velocity, density, and Q . The reflectivity codes presented here lend themselves to rapidly making these changes to match relative amplitudes and arrival times of phases of interest.

Acknowledgments—A portion of this work was carried out on the Cray at the Illinois Supercomputer Center with support from NCSA contracts EAR910002N and EAR 910003N. The first author is grateful to SOEST at the University of Hawaii for his 1992 summer appointment as Visiting Scientist while completing this manuscript.

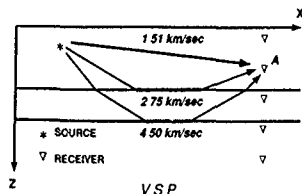


Figure 9. Schematic of direct and refracted head wave paths from source to common receiver, using velocity model of Figure 7.

lying half-space transmitted by the earth. The observed pattern in layer effects can be the CT values set out in the model that and the horizontal in absence of the

component VSP of 0.1 (Fig. 7C, 8B). Comparison of different offsets to vertical velocity ant differences in or to events taking in layer 1. This is combination of a path sees the higher the half-space. For source to receiver A 1/sec. The headwave 1/sec and eventually. Similarly, the head- is at 4.50 km/sec and er events. Finally, the low-frequency wave- by theory and field

8)

ONS
uted with the reflectiv-
the matrix approach
able to both vector
station (SUN) compu-
EFLSYNT (Appendix)
or both horizontal and
synthetic seismograms
sfully for a variety of
shown in Mallick and
the authors have verified
ns of shape and polarity
plitudes, generation of
ct of attenuation factors
multiple events, headwaves,
tion of synthetic seismo-
to observed seismograms
terative model changes in
sity, and Q . The reflectiv-
nd themselves to rapidly
natch relative amplitudes
s of interest

a of this work was carried
t Supercomputer Center with
cts EAR910002N and EAR-
is grateful to SOEST at the
1992 summer appointment as
lecting this manuscript

REFERENCES

- Aki, K., and Richards, P. G., 1980, Quantitative seismology: W. H. Freeman & Co., San Francisco, 2 vol., 932 p.
- Balch, A. H., and Lee, M. W., 1984, Vertical seismic profiling techniques, applications and case histories Intern. Human Res. Dev. Corp., unpaginated.
- Chin, R. C. Y., Hedstrom, G. W., and Thigpen, L., 1984, Matrix methods in synthetic seismograms Geophys. Jour. Roy. Astro. Soc., v. 77, no. 2, p. 483-502.
- Dobrin, M. D., and Savit, C. H., 1988, Introduction to geophysical prospecting (4th ed.) McGraw-Hill Book Co., New York, 867 p.
- Frazer, L. N., 1988, Quadrature of wavenumber integrals (seismological algorithms) Academic Press Ltd., New York, p. 279-290.
- Frazer, L. N., and Gettrust, J. F., 1984, On a generalization of Filon's method and the computation of oscillatory integrals of seismology Geophys. Jour. Roy. Astro. Soc., v. 76, no. 2, p. 461-481.
- Frazer, L. N., Bates, D. L., and Rudman, A. J., 1985, Generation of vertically incident seismograms Indiana Geol. Survey Occasional Paper 49, 62 p.
- Fuchs, K., and Muller, G., 1971, Computation of synthetic seismograms with the reflectivity method and comparison with observations Geophys. Jour. Roy. Astro. Soc., v. 23, no. 4, p. 417-433.
- Gilbert, F., and Backus, G. E., 1966, Propagator matrices in elastic wave and vibration problems Geophysics, v. 31, no. 2, p. 326-332.
- Haskell, N. A., 1953, The dispersion of surface waves on multilayered media Bull. Seism. Soc. America, v. 43, no. 1, p. 17-34.
- Helmberger, D., 1968, The crust-mantle transition in the Bering sea Bull. Seism. Soc. America, v. 58, no. 1, p. 179-214.
- Kennett, B. L. N., 1983, Seismic wave propagation in stratified media Cambridge Univ. Press, New York, 342 p.
- Mallick, S., and Frazer, L. N., 1987, Practical aspects of reflectivity modeling Geophysics, v. 52, no. 10, p. 1355-1364.
- Mallick, S., and Frazer, L. N., 1988, Rapid computation of multioffset vertical seismic profile synthetic seismograms for layered media Geophysics, v. 53, no. 4, p. 479-491.
- Mallick, S., and Frazer, L. N., 1990a, Po/So synthetics for a variety of oceanic models and their implications for the structure of the oceanic lithosphere Geophys. Jour. Intern., v. 100, no. 2, p. 235-253.
- Mallick, S., and Frazer, L. N., 1990b, Computation of synthetic seismograms for stratified azimuthally anisotropic media Jour. Geophys. Res., v. 95, no. B6, p. 8513-8526.
- Mallick, S., and Frazer, L. N., 1991, Reflection/transmission coefficients and azimuthal anisotropy in marine seismic studies Geophys. Jour. Intern., v. 105, no. 2, p. 241-252.
- Phinney, R. A., 1965, Theoretical calculations of the spectra of first arrivals in layered elastic mediums Jour. Geophys. Res., v. 70, no. 20, p. 5107-5123.
- Strick, E., 1970, A predicted pedestal effect for pulse propagation in constant Q solids Geophysics, v. 35, no. 3, p. 387-403.
- Thomson, W. T., 1950, Transmission of elastic waves through a stratified solid medium Jour. Appl. Phys., v. 21, no. 2, p. 89-93.

Appendix overleaf

[illegible][illegible]

[illegible]

CALL BUFOUT(MATLEN, NPHC)

[illegible]

[illegible]

END LOOP

[illegible]

[illegible]

WRN012-EWIGH11 B1BUN19202

[illegible]


```

TDR11(PP=TDNR11(LK))
TDR12(PP=TDNR12(LK))
TDR13(PP=TDNR13(LK))
TDR14(PP=TDNR14(LK))
TDR15(PP=TDNR15(LK))
TDR16(PP=TDNR16(LK))
TDR17(PP=TDNR17(LK))
TDR18(PP=TDNR18(LK))
TDR19(PP=TDNR19(LK))
TDR20(PP=TDNR20(LK))
TDR21(PP=TDNR21(LK))
TDR22(PP=TDNR22(LK))
TDR23(PP=TDNR23(LK))
TDR24(PP=TDNR24(LK))
TDR25(PP=TDNR25(LK))
TDR26(PP=TDNR26(LK))
TDR27(PP=TDNR27(LK))
TDR28(PP=TDNR28(LK))
TDR29(PP=TDNR29(LK))
TDR30(PP=TDNR30(LK))
TDR31(PP=TDNR31(LK))
TDR32(PP=TDNR32(LK))
TDR33(PP=TDNR33(LK))
TDR34(PP=TDNR34(LK))
TDR35(PP=TDNR35(LK))
TDR36(PP=TDNR36(LK))
TDR37(PP=TDNR37(LK))
TDR38(PP=TDNR38(LK))
TDR39(PP=TDNR39(LK))
TDR40(PP=TDNR40(LK))
TDR41(PP=TDNR41(LK))
TDR42(PP=TDNR42(LK))
TDR43(PP=TDNR43(LK))
TDR44(PP=TDNR44(LK))
TDR45(PP=TDNR45(LK))
TDR46(PP=TDNR46(LK))
TDR47(PP=TDNR47(LK))
TDR48(PP=TDNR48(LK))
TDR49(PP=TDNR49(LK))
TDR50(PP=TDNR50(LK))
TDR51(PP=TDNR51(LK))
TDR52(PP=TDNR52(LK))
TDR53(PP=TDNR53(LK))
TDR54(PP=TDNR54(LK))
TDR55(PP=TDNR55(LK))
TDR56(PP=TDNR56(LK))
TDR57(PP=TDNR57(LK))
TDR58(PP=TDNR58(LK))
TDR59(PP=TDNR59(LK))
TDR60(PP=TDNR60(LK))
TDR61(PP=TDNR61(LK))
TDR62(PP=TDNR62(LK))
TDR63(PP=TDNR63(LK))
TDR64(PP=TDNR64(LK))
TDR65(PP=TDNR65(LK))
TDR66(PP=TDNR66(LK))
TDR67(PP=TDNR67(LK))
TDR68(PP=TDNR68(LK))
TDR69(PP=TDNR69(LK))
TDR70(PP=TDNR70(LK))
TDR71(PP=TDNR71(LK))
TDR72(PP=TDNR72(LK))
TDR73(PP=TDNR73(LK))
TDR74(PP=TDNR74(LK))
TDR75(PP=TDNR75(LK))
TDR76(PP=TDNR76(LK))
TDR77(PP=TDNR77(LK))
TDR78(PP=TDNR78(LK))
TDR79(PP=TDNR79(LK))
TDR80(PP=TDNR80(LK))
TDR81(PP=TDNR81(LK))
TDR82(PP=TDNR82(LK))
TDR83(PP=TDNR83(LK))
TDR84(PP=TDNR84(LK))
TDR85(PP=TDNR85(LK))
TDR86(PP=TDNR86(LK))
TDR87(PP=TDNR87(LK))
TDR88(PP=TDNR88(LK))
TDR89(PP=TDNR89(LK))
TDR90(PP=TDNR90(LK))
TDR91(PP=TDNR91(LK))
TDR92(PP=TDNR92(LK))
TDR93(PP=TDNR93(LK))
TDR94(PP=TDNR94(LK))
TDR95(PP=TDNR95(LK))
TDR96(PP=TDNR96(LK))
TDR97(PP=TDNR97(LK))
TDR98(PP=TDNR98(LK))
TDR99(PP=TDNR99(LK))
TDR100(PP=TDNR100(LK))
TDR101(PP=TDNR101(LK))
TDR102(PP=TDNR102(LK))
TDR103(PP=TDNR103(LK))
TDR104(PP=TDNR104(LK))
TDR105(PP=TDNR105(LK))
TDR106(PP=TDNR106(LK))
TDR107(PP=TDNR107(LK))
TDR108(PP=TDNR108(LK))
TDR109(PP=TDNR109(LK))
TDR110(PP=TDNR110(LK))
TDR111(PP=TDNR111(LK))
TDR112(PP=TDNR112(LK))
TDR113(PP=TDNR113(LK))
TDR114(PP=TDNR114(LK))
TDR115(PP=TDNR115(LK))
TDR116(PP=TDNR116(LK))
TDR117(PP=TDNR117(LK))
TDR118(PP=TDNR118(LK))
TDR119(PP=TDNR119(LK))
TDR120(PP=TDNR120(LK))
TDR121(PP=TDNR121(LK))
TDR122(PP=TDNR122(LK))
TDR123(PP=TDNR123(LK))
TDR124(PP=TDNR124(LK))
TDR125(PP=TDNR125(LK))
TDR126(PP=TDNR126(LK))
TDR127(PP=TDNR127(LK))
TDR128(PP=TDNR128(LK))
TDR129(PP=TDNR129(LK))
TDR130(PP=TDNR130(LK))
TDR131(PP=TDNR131(LK))
TDR132(PP=TDNR132(LK))
TDR133(PP=TDNR133(LK))
TDR134(PP=TDNR134(LK))
TDR135(PP=TDNR135(LK))
TDR136(PP=TDNR136(LK))
TDR137(PP=TDNR137(LK))
TDR138(PP=TDNR138(LK))
TDR139(PP=TDNR139(LK))
TDR140(PP=TDNR140(LK))
TDR141(PP=TDNR141(LK))
TDR142(PP=TDNR142(LK))
TDR143(PP=TDNR143(LK))
TDR144(PP=TDNR144(LK))
TDR145(PP=TDNR145(LK))
TDR146(PP=TDNR146(LK))
TDR147(PP=TDNR147(LK))
TDR148(PP=TDNR148(LK))
TDR149(PP=TDNR149(LK))
TDR150(PP=TDNR150(LK))
TDR151(PP=TDNR151(LK))
TDR152(PP=TDNR152(LK))
TDR153(PP=TDNR153(LK))
TDR154(PP=TDNR154(LK))
TDR155(PP=TDNR155(LK))
TDR156(PP=TDNR156(LK))
TDR157(PP=TDNR157(LK))
TDR158(PP=TDNR158(LK))
TDR159(PP=TDNR159(LK))
TDR160(PP=TDNR160(LK))
TDR161(PP=TDNR161(LK))
TDR162(PP=TDNR162(LK))
TDR163(PP=TDNR163(LK))
TDR164(PP=TDNR164(LK))
TDR165(PP=TDNR165(LK))
TDR166(PP=TDNR166(LK))
TDR167(PP=TDNR167(LK))
TDR168(PP=TDNR168(LK))
TDR169(PP=TDNR169(LK))
TDR170(PP=TDNR170(LK))
TDR171(PP=TDNR171(LK))
TDR172(PP=TDNR172(LK))
TDR173(PP=TDNR173(LK))
TDR174(PP=TDNR174(LK))
TDR175(PP=TDNR175(LK))
TDR176(PP=TDNR176(LK))
TDR177(PP=TDNR177(LK))
TDR178(PP=TDNR178(LK))
TDR179(PP=TDNR179(LK))
TDR180(PP=TDNR180(LK))
TDR181(PP=TDNR181(LK))
TDR182(PP=TDNR182(LK))
TDR183(PP=TDNR183(LK))
TDR184(PP=TDNR184(LK))
TDR185(PP=TDNR185(LK))
TDR186(PP=TDNR186(LK))
TDR187(PP=TDNR187(LK))
TDR188(PP=TDNR188(LK))
TDR189(PP=TDNR189(LK))
TDR190(PP=TDNR190(LK))
TDR191(PP=TDNR191(LK))
TDR192(PP=TDNR192(LK))
TDR193(PP=TDNR193(LK))
TDR194(PP=TDNR194(LK))
TDR195(PP=TDNR195(LK))
TDR196(PP=TDNR196(LK))
TDR197(PP=TDNR197(LK))
TDR198(PP=TDNR198(LK))
TDR199(PP=TDNR199(LK))
TDR200(PP=TDNR200(LK))
TDR201(PP=TDNR201(LK))
TDR202(PP=TDNR202(LK))
TDR203(PP=TDNR203(LK))
TDR204(PP=TDNR204(LK))
TDR205(PP=TDNR205(LK))
TDR206(PP=TDNR206(LK))
TDR207(PP=TDNR207(LK))
TDR208(PP=TDNR208(LK))
TDR209(PP=TDNR209(LK))
TDR210(PP=TDNR210(LK))
TDR211(PP=TDNR211(LK))
TDR212(PP=TDNR212(LK))
TDR213(PP=TDNR213(LK))
TDR214(PP=TDNR214(LK))
TDR215(PP=TDNR215(LK))
TDR216(PP=TDNR216(LK))
TDR217(PP=TDNR217(LK))
TDR218(PP=TDNR218(LK))
TDR219(PP=TDNR219(LK))
TDR220(PP=TDNR220(LK))
TDR221(PP=TDNR221(LK))
TDR222(PP=TDNR222(LK))
TDR223(PP=TDNR223(LK))
TDR224(PP=TDNR224(LK))
TDR225(PP=TDNR225(LK))
TDR226(PP=TDNR226(LK))
TDR227(PP=TDNR227(LK))
TDR228(PP=TDNR228(LK))
TDR229(PP=TDNR229(LK))
TDR230(PP=TDNR230(LK))
TDR231(PP=TDNR231(LK))
TDR232(PP=TDNR232(LK))
TDR233(PP=TDNR233(LK))
TDR234(PP=TDNR234(LK))
TDR235(PP=TDNR235(LK))
TDR236(PP=TDNR236(LK))
TDR237(PP=TDNR237(LK))
TDR238(PP=TDNR238(LK))
TDR239(PP=TDNR239(LK))
TDR240(PP=TDNR240(LK))
TDR241(PP=TDNR241(LK))
TDR242(PP=TDNR242(LK))
TDR243(PP=TDNR243(LK))
TDR244(PP=TDNR244(LK))
TDR245(PP=TDNR245(LK))
TDR246(PP=TDNR246(LK))
TDR247(PP=TDNR247(LK))
TDR248(PP=TDNR248(LK))
TDR249(PP=TDNR249(LK))
TDR250(PP=TDNR250(LK))
TDR251(PP=TDNR251(LK))
TDR252(PP=TDNR252(LK))
TDR253(PP=TDNR253(LK))
TDR254(PP=TDNR254(LK))
TDR255(PP=TDNR255(LK))
TDR256(PP=TDNR256(LK))
TDR257(PP=TDNR257(LK))
TDR258(PP=TDNR258(LK))
TDR259(PP=TDNR259(LK))
TDR260(PP=TDNR260(LK))
TDR261(PP=TDNR261(LK))
TDR26
```

CAGEO 193- L

[illegible]

[illegible]

[illegible]

[illegible]

MAY 19 1988

070
Mal
Vec
Ph.D.

A VECTOR REFLECTIVITY ALGORITHM AND
SYNTHESIS OF P_0/S_0

RETURN TO
HAWAII INSTITUTE OF GEOPHYSICS
LIBRARY ROOM

A DISSERTATION SUBMITTED TO THE GRADUATE DIVISION OF THE
UNIVERSITY OF HAWAII IN PARTIAL FULFILLMENT
OF THE REQUIREMENTS FOR THE DEGREE OF

DOCTOR OF PHILOSOPHY

IN GEOLOGY AND GEOPHYSICS
DECEMBER 1987

RETURN TO
HAWAII INSTITUTE OF GEOPHYSICS
LIBRARY ROOM

By
Subhashis Mallick

Dissertation Committee:
L. Neil Frazer, Chairman
Gerard J. Fryer
Frederick K. Duennebiele
Daniel A. Walker
Pui K. Lam

A complete copy of this thesis is
available from University Microfilms

SEDIMENT SHEAR Q
FROM HORIZONTAL COMPONENT
AIRGUN OBS DATA

A DISSERTATION SUBMITTED TO THE GRADUATE DIVISION OF
THE UNIVERSITY OF HAWAII IN PARTIAL FULFILLMENT OF
THE REQUIREMENTS FOR THE DEGREE OF

DOCTOR OF PHILOSOPHY

IN

GEOLOGY AND GEOPHYSICS

DECEMBER 1993

By

Peter D. Bromirski

Dissertation Committee

L. Neil Frazer, Chairperson

Eduard Berg

Frederick K Duennebier

Roy H Wilkens

Eric Firing

A complete copy of this thesis is available from
University Microfilms

STUDIES IN GEOPHYSICAL INVERSION

A DISSERTATION SUBMITTED TO THE GRADUATE DIVISION OF THE
UNIVERSITY OF HAWAII IN PARTIAL FULFILLMENT OF THE
REQUIREMENTS FOR THE DEGREE OF

DOCTOR OF PHILOSOPHY

IN

GEOLOGY AND GEOPHYSICS

AUGUST 1994

By

Atanu Basu

Dissertation Committee:

L. Neil Frazer, Chairperson

Eduard Berg

Frederick K. Duennebier

Roy H. Wilkens

Narendra K. Saxena

Contract: N00014-87-K-0181
Marine Geology & Geophysics

**Correction and Quantitative Analysis
of SeaMARC II Sonar**

T. Reed



received
18 November 1993

Oceanic Imaging Consultants

Manoa Innovation Center

2800 Woodlawn Dr., Suite 147 Honolulu, HI 96822

(808) 539-3708, reed@kilauea.soest.hawaii.edu

Peter V. Garrod, Acting Dir Res
Office of Research Administration
Univ of Hawaii at Manoa
Honolulu, HI 96822

November 16 1993

Dear Sir

I'm responding to your notices requesting final project reports for my ONR contract "A Layered Approach to Analysis and Classification of Ocean Bottom Data", award no N00014-90-J-1497. In March of this year, I resigned from the University, and formed my own consulting company. Per attached letters to the Office of Naval Research, I have converted the above referenced grant to a contract, now administered and serviced by my new company, Oceanic Imaging Consultants.

The grant was converted with both the consent and assistance of ONR and their local resident representative, Ms. Carlena Leufroy. Apparently your offices were not informed in writing of these changes.

The contract is currently active, and reports are being delivered to both scientific officers and our new administrative officer, Ms. Mildred McGinnis at DCMAO.

Should you have any further questions, please feel free to contact me at the above address.

Sincerely,


Dr. Thomas B. Reed IV,

President, OIC

CC file, Ms. Judy Rubano, SOEST Contracts/Grants office



DEFENSE LOGISTICS AGENCY
DEFENSE CONTRACT MANAGEMENT COMMAND INTERNATIONAL
DEFENSE CONTRACT MANAGEMENT AREA OPERATION RESIDENCY-HONOLULU
BOX 64110
CAMP H M SMITH HI 96861-4110

IN REPLY
REFER TO DCMCI-GJH

21 Oct 93

SUBJECT: Contract N00014-93-C-0184

TO: Oceanic Imaging
Manoa Innovation Center Suite 147
2800 Woodlawn Drive
Honolulu HI 96822

1. Contract N00014-93-C-0184 has been delegated to this office for administration. The Administrative Contracting Officer (ACO) is identified below:

NAME: Mildred E. McGinnis

ADDRESS: DCMAOR Honolulu
Box 64110
Camp H. M. Smith, HI 96861-4110

TELEPHONE: (808)477-3712

FAX: (808)477-3391

2. Please furnish name(s) and title(s) of managerial personnel who will be my contact(s).


MILDRED E. MCGINNIS
Administrative Contracting Officer

cc: Genesta S. Belton, PCO
Dr. Moshen Baidey, Scientific Engineer
DCMAO Japan (w/copy of contract)

Oceanic Imaging

Manoa Innovation Center, Suite 147

2800 Woodlawn Drive

Honolulu, HI 96822

(808) 539-3708 , reed@kawe.soest.hawaii.edu

July 8, 1993

TO Office of Naval Research

Code 1513 TMM

Ballston Tower 1

800 N Quincy St

Arlington, VA 22217-5660

Fax 703-696--0993

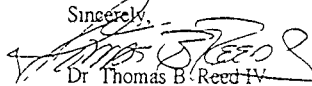
Dear Sirs

I am writing to inform you that TRV Consulting has been dissolved and subsumed by our new company, Oceanic Imaging, under my leadership. All the staff of TRV Consulting continues on with Oceanic Imaging, and some new members will join as well.

As a result of this dissolution, Oceanic Imaging will take responsibility for the execution of the proposal submitted to your offices previously by TRV Consulting entitled "A Layered Approach to Analysis and Classification of Seafloor Data (cont)" We anticipate no changes in budget or timing of completion of the project.

We anticipate this will cause you no administrative difficulties, and thank you for your continued support.

Sincerely,



Dr. Thomas B. Reed IV

President, Oceanic Imaging

TRIV pt

fax (808) 539-3710

On the Determination of Depth from Overlapping Side-Scan Sonar Images

THOMAS BECKETT REED IV

The Pacific Mapping Center
Honolulu, Hawaii 96822

Abstract A method for obtaining depth determinations from overlapping side-scan sonar is presented. The technique is analogous to the photogrammetric method of deriving topographic measurements from aerial photographic stereo pairs. In the aerial case, image overlap is in the along-track direction and topographic measurements are based on image parallax. The overlap of the sonar images is in the across-track sense, and the look directions of the two images are opposed. In terrains where slope is the controlling factor of image intensity, the opposite look directions may yield radically distinct images, thus invalidating traditional photogrammetric measurement techniques. We present a new approach based on matching image edge features rather than image intensities. The algorithm is tested on synthetic imagery generated from a bathymetric model and the results are excellent. Application to actual imagery yielded viable depth determinations consistent with trend and ancillary data.

Introduction

SeaMARC II is a 12 KHZ shallow-towed side-scan sonar system that provides simultaneous acoustic imagery and swath map bathymetry. For a complete system description, see Blackinton, Hussong, and Kosalos (1983). In all oceanic depths, the system yields a 10-km-wide side-scan image swath and interferometric bathymetry from nadir to 60°. In water depths greater than 2.9 km the bathymetric swath will cover the full cross-track range of the acoustic image. In shallower water depths, there will be a gap. An investigator wishing to conduct a survey in waters shallower than this depth has two choices:

- (1) Conduct the survey with track lines sufficiently close to allow complete bathymetric coverage, thereby significantly increasing the number of tracks necessary and thus the survey time.
- (2) Conduct the survey with nominal overlap of the side scan and suffer the bathymetric data gaps.

An alternative is presented.

Opposing tracks often contain up to 2 to 3 km of overlapping side-scan data. As we can calculate the slant range to each pixel through knowledge of the nadir depth and sequential arrival time, an unambiguous solution for the three-dimensional position of any reflector can be acquired from two opposing looks (provided we neglect the possibility that the reflector is located above the water) through coregistration of matching features in the two opposite look directions. Clearly this technique will be dependent on the ability to coregister data from opposing tracks digitally.

Overlapping imagery holds the potential for depth determination via matching of similar features in a fashion similar to that used in analysis of aerial stereo photo pairs. Traditional stereoscopic methods rely on the parallax error in the location of similar objects in images taken from distinct perspectives to calculate object height. In the usual case with aerial photography, the overlap is in the along-track direction and the sensor-object geometries from the stereo pair have only one degree of freedom. Constancy of object appearance allows use of the geometric displacement due to the shift in perspective to determine height. For side-scan imagery, object appearance (intensity) is largely due to incidence angle. Consequently, overlapping images from opposite look directions are often negatives (see Figures 1a and b). Fault scarps illuminated from one perspective are shadowed from the opposite look direction. Object matching is therefore nontrivial, and photogrammetric methods may fail because of this increase in the number of degrees of freedom.

Stereoscopic Side Scan

Our approach has been to shift our attention from the image intensity to the nature of the edges in the image. For uniform surfaces, edges result from changes in view-to-surface geometries. For a fixed view location, the edge (i.e., a pixel-to-pixel change in image



Figure 1 (a) Side-scan image of a shadowed fault (white linear feature)

th determination via matching of
 analysis of aerial stereo photo pairs
 error in the location of similar
 calculate object height. In the usual
 ing-track direction and the sensor-
 degree of freedom. Constancy of
 ement due to the shift in perspec-
 t appearance (intensity) is largely
 ages from opposite look directions
 s illuminated from one perspective
 t matching is therefore nontrivial,
 increase in the number of degrees

image intensity to the nature of the
 from changes in view-to-surface
 a pixel-to-pixel change in image



fault (white linear features)



(b)

Figure 1 (Continued) (b) Side scan image from an opposite look direction illuminating fault scarp

amplitude) is the result of a change in the surface normal (a slope break). As the existence of this edge is a function only of the surface, and not the look direction, its presence in the image is independent of view direction. Therefore, the presence of edges can be used as the matching feature. Further refinement in the matching process can be made by noting that for uniform, continuously differentiable surfaces (among which the seafloor must qualify) inflections (resulting in edges) are of only two types: concave and convex.

In the profile shown in Figure 2 depicting schematically a depth profile across a graben structure, the inflection point at A is convex upward, while that at point B is concave upward. If we let shadows and weak reflectors be light and strong reflectors dark, as we do when presenting SeaMARC II acoustic imagery, then a dark to light edge transition will always represent a concave-upward surface, and a light to dark transition will always represent a convex upward break, irrespective of the look direction. We may therefore match features on both the existence and type of edges.

Admittedly, the foregoing presumes that all image edge features are the result of changes in slope. Clearly, this is not the case. Adjacent surfaces of distinct acoustic impedance or surface roughness will equally well generate image edge structures, with change polarity with a change in the direction from which they are viewed.

as the images are discrete, by definition all nonidentical pixel transitions will yield image edge features. However, by limiting our application of this edge-matching technique to regions where the assumption of surface uniformity is viable, and by setting an edge strength threshold that any candidate edge must exceed to winnow out the digitization discontinuities, we can safely treat all edge features as indicative of breaks in surface slope.

Our final criterion for matching edge features is depth. Although this is the quantity we were solving for, it is also an effective discriminant. Like all side-scanning systems, SeaMARC II produces nominally corrected imagery by assuming the terrain is flat athwartships and at a depth equal to that beneath the towfish. The cross-track pixel position is derived by the system from the nadir depth, the slant-range travel time, and the Pythagorean theorem. We can, therefore, for any edge at some cross-track pixel location X , invert for the actual slant range to that edge. The possibility of (unknown)

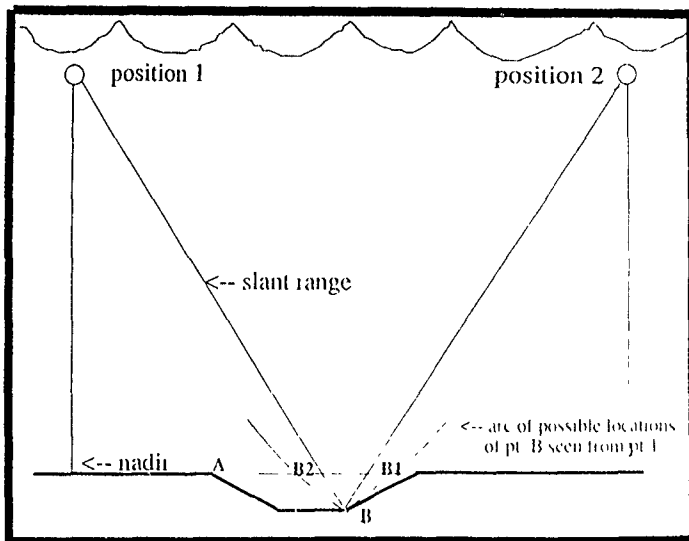
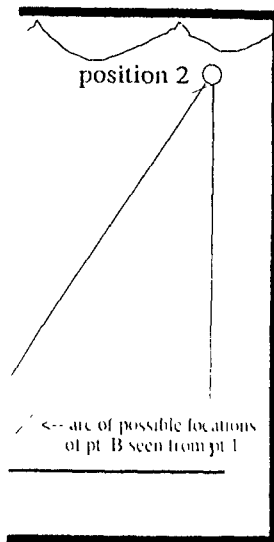


Figure 2. Schematic illustration of logic used in reconstructing bathymetry from overlapping, distorted side-scan images. Because of the flat bottom assumptions of the data acquisition system (Blackinton et al., 1982), images of any topographic features such as this graben will be distorted. Point B will be imaged at point B1 when the system is at position 1 and at point B2 when the system views the feature from the opposite look direction at point 2. Knowledge of nadir depth on a ping-by-ping basis allows exact recalculation of the true slant range to any reflector. Any qualifying feature is swung along an arc of possible locations, yielding the correct depth and cross-track position at only the match point. Matching is based on edge detection and type, as described in the text, thus resolving the look direction ambiguity illustrated in Figure 1.

pixel transitions will yield image this edge-matching technique to viable, and by setting an edge to winnow out the digitization indicative of breaks in surface

Although this is the quantity Like all side-scanning systems, by assuming the terrain is flat towfish The cross-track pixel slant-range travel time, and edge at some cross-track pixel The possibility of (unknown)



recting bathymetry from overlapping, imptions of the data acquisition sys- features such as this graben will be stem is at position 1 and at point B2 direction at point 2 Knowledge of ation of the true slant range to any of possible locations, yielding the point Matching is based on edge g the look direction ambiguity illus-

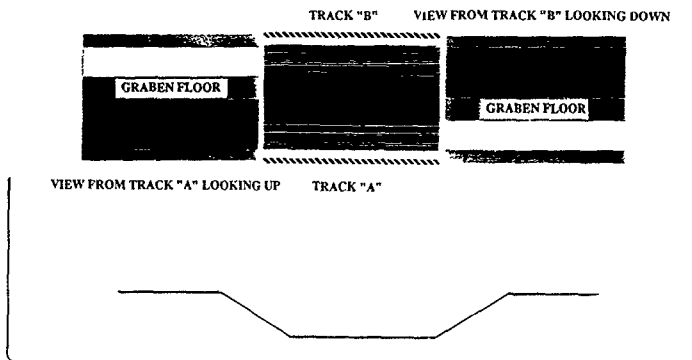


Figure 3. Test of edge-matching algorithm on synthetic data. The profile at the bottom depicts a bathymetric model of a graben, which drops from 3500 to 4100 m. There is no vertical exaggeration. The two images on the left and right are synthetic side-scan images generated from the bathymetric model and a simple reflectance rule. The bathymetric map in the middle is the result of applying the edge-matching algorithm to the two synthetic images.

cross-track topographic relief makes the position of this edge ambiguous. We alleviate this ambiguity by swinging an arc up and down about the original position along a radius of curvature equal to the known slant range. Should this arc, associated with our detected edge, intersect another arc from an opposite look direction associated with an edge of similar type, a potential match is indicated. Should the depths calculated from the two slant ranges and the coincident cross-track position X be equal within a selected margin of error, a match is signified and a depth value output.

A Test of the Algorithm: Synthetic Imagery

In this section we demonstrate the efficacy of our algorithm on synthetic imagery generated from a specified terrain model. The model we use is of a symmetric graben, which drops from 3500 to 4100 m with a slope of 1 in 3. We generate synthetic side-scan imagery from this model by specifying a towfish position and heading and defining a reflectivity model. For this test, a particularly simple model is used which specifies that a surface is black if it is sloping away from the source, gray if it is flat, and white if it is facing the source. Two overlapping images are then generated, for parallel tracks A and B south and north of the graben, respectively. Figure 3 shows at the bottom a profile across the bathymetric model of the graben and on the left and right the two synthetic images generated from this terrain model and our reflectivity function. We arbitrarily specify the directions "up" and "down" for purposes of the algorithm.

Note that the images from the two tracks are negatives and that they are both distorted due to the flat-bottom assumption made by both real systems and our model side-scan system. Facing surfaces are compressed, while shadowed surfaces are elongated. In both cases, the graben floor is compressed and displaced; however, the edge types, as defined by the image amplitude transitions at the inflection points, are invariant.

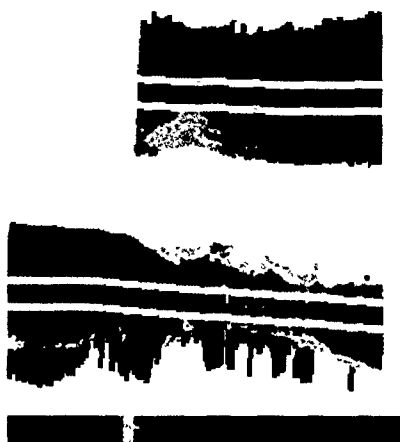


Figure 4. Mosaic of SeaMARC II bathymetry for the two tracks shown in Figure 1. Data gap is the result of the cutoff of bathymetry data at a look angle of 60° .



Figure 5. A concatenation of the bathymetry data in Figure 4 and the points produced by the application of the edge-matching algorithm to the overlapping portions of the images in Figure 1 as described in the text.



icks shown in Figure 1. Data gap is 60° .



4 and the points produced by the portions of the images in Figure 1.

under change of perspective. The down-dropping inflection points at the top of the graben (being convex upward) always produce dark-to-light transitions yielding a type 1 edge, and the bottom turning points, being concave upward, always produce light-to-dark transitions, or a type 2 edge. The sense of the intensity transition must be measured in the direction of ensonification, hence the necessity of reference to "downward"- and "upward"-looking tracks.

The image in the middle of Figure 3 is the bathymetric map resulting from application of our edge-matching algorithm to the two synthetic images. It recreates the original bathymetric model to within 20 m. The differences are due solely to round-off errors occurring in the truncations necessary to yield the integral x and y estimates required for addressing the gridded data sets. We postulate, therefore, a theoretical resolution of this technique on the order of $2N$, where N is the dimension of the square grid cell of which the imagery is constituted. Typical values for N could be in the range of 20 to 50 m for standard SeaMARC II data.

Tests on Real Data

The side-scan imagery shown in Figure 1 provides us with data for our real test of the edge-matching algorithm. Figure 4 shows the SeaMARC II bathymetry from the two tracks. Nadir water depths are in the range of 1 to 2 km. As described in the introduction, the lateral extent of the bathymetric coverage is restricted, and a data gap occurs. In the midst of this data gap, the side-scan images both show a fault. The down-thrown block appears to be to the south, so that the fault scarp resulting from the normal component of the fault motion is illuminated (dark) in the lower image (looking up) and shadowed in the upper image (looking down).

The images from both tracks were separately mosaicked into a common grid. A data structure was defined for this algorithm that allows contributions from opposite look directions to the same mosaic grid cell to be kept separate. For every cell within the image region defined by an X, Y coordinate pair, there are bins for detected edges from the "up" and "down" look directions. In this example, the edge detection threshold was set at 64. The angular range (about the angle at which the edge was detected in the "flat-bottom" image) through which the detected edges were swung was set at 15° . Finally, the depth-matching criterion was set at 20, requiring that only edges for which the calculated depths at one cell differed by less than 20 m be used. The result, concatenated with the original SeaMARC II bathymetry, is shown in Figure 5.

Although the bathymetric points generated by the edge feature-matching algorithm are admittedly sparse, they are sufficiently coherent both spatially and vertically to map the location and topography of the major fault seen in the side-scan images. Bathymetry data were not available from another source to verify the accuracy of these depth determinations, but the trend is consistent with both our visual interpretation of these side-scan data and the trend in the limited SeaMARC bathymetry that is available.

References

- Blackinton, J. G., D. M. Hussong, and J. Kosloski. 1983. First results from a combination side scan sonar and seafloor mapping system (SeaMARC II). *Proceedings of the Offshore Technology Conference*, OTC 4478, 307-311.

- Reed, T. B. IV, and D. M. Hussong. 1989. Digital image processing techniques for enhancement and classification of SeaMARC II side-scan sonar imagery. *J. Geophys. Res.* 94(B6): 7469-7490.
- Stewart, W. K. 1988. Multisensor modeling underwater with uncertain information. Ph.D. thesis, Woods Hole Oceanographic Institution/Massachusetts Institute of Technology.

Digital Image Processing Techniques for Enhancement and Classification of SeaMARC II Side Scan Sonar Imagery

THOMAS BECKETT REED IV

Hawaii Institute of Geophysics, Honolulu, Hawaii

DONALD HUSSONG

Seafloor Surveys International, Honolulu, Hawaii

The recent growth in the production rate of digital side scan sonar images, coupled with the rapid expansion of systematic seafloor exploration programs, has created a need for fast and quantitative means of processing seafloor imagery. Computer-aided analytical techniques fill this need. A number of numerical techniques used to enhance and classify imagery produced by SeaMARC II, a long-range combination side scan sonar, and bathymetric seafloor mapping system are documented. Three categories of techniques are presented: (1) preprocessing corrections (radiometric and geometric), (2) feature extraction, and (3) image segmentation and classification. An introduction to the concept of "feature vectors" is provided, along with an explanation of the method of evaluation of a texture feature vector based upon gray-level co-occurrence matrices (GLCM). An alternative to the a priori text (texture element) subdivision of images is presented in the form of region growing and texture analysis (REGATA). This routine provides a texture map of spatial resolution superior to that obtainable with arbitrarily assigned level boundaries and minimizes the possibility of mixed texture signals due to the combination of two or more textures in an arbitrarily assigned text. Computer classification of these textural features extracted via the GLCM technique results in transformation of images into maps of image texture. These maps may either be interpreted in terms of the theoretical relationships shown between texture signatures and wavelength or converted to geologic maps by correlation of texture signatures with ground truth data. These techniques are applied to SeaMARC II side scan sonar imagery from a variety of geologic environments, including lithified and nonlithified sedimentary formations, volcanic and sedimentary debris flows, and crystalline basaltic outcrops. Application of the above processing steps provided not only superior images for both subjective and quantitative analysis but also the critical ability to discriminate between outcrops with distinct lithologies but similar image intensity.

1 INTRODUCTION

Side scan sonars have disclosed the location and, to some extent, the morphology of seafloor features but have provided little of the type of quantitative information necessary for lithologic identification. This quantitative imprecision, in contrast to the successes presently being enjoyed by the terrestrial remote sensing groups, stemmed chiefly from technical hardware problems resulting in a lack of seafloor image fidelity. Now, however, the application of objective digital image processing techniques to images of superior quality and uniformity makes possible a more quantitative approach in the analysis and interpretation of synoptic seafloor imagery.

In this report a suite of digital processing techniques for the correction, enhancement, and classification of sonar images is presented. Although these techniques are described in reference to the long-range SeaMARC II (Sea Mapping and Remote Characterization) system with which the images

shown here were acquired, they are equally applicable to other digital side scan sonar data, including images from short-range systems. Finally, applications of these techniques in the enhancement and classification of a variety of seafloor images are presented.

1.1 Previous Work

Pertinent work in digital image processing is voluminous. Excellent review texts covering general theory as well as diverse applications include Pratt [1978], Andrews [1968], Rosenfeld and Kak [1982], and Ballard and Brown [1982]. Methods directly applicable to remote sensing data are presented by Schowengerdt [1983], Hord [1982], and Monk [1980]. Duda and Hart [1973] present a classic text on pattern recognition. Hartigan [1975] develops the general theory and presents many FORTRAN algorithms for cluster analysis.

Background work for sonars and underwater acoustics in general are provided by Urick [1983]. Tyce [1986] and de Mowbray [1986] provide up to date reviews of acoustic swath-mapping systems.

Sander and Clay [1968] provided an early review of side scan sonar techniques and the problems inherent in using analog recording and display. Mudie et al. [1970] produced properly scaled side scan images using transponder naviga-

Copyright 1989 by the American Geophysical Union

Paper number 89JB00109
0148-0227/89/89JB-0040\$05.00

tion and variable speed playback of images recorded on FM magnetic tape. Belderson *et al.* [1972] produced an album of sonographs corrected for along-track variations with an anamorphic camera. Flemming [1976] presented a suite of manual correction techniques for removing image distortions using nomograms and distortion ellipses.

Paluzzi [1976] and Paluzzi *et al.* [1976] provided a first account of the application of digital image processing techniques to side scan sonar images. Processing operations included analog-to-digital conversion, partial geometric rectifications, contrast enhancement, and various filtering operations. Walker [1978], Clifford [1979], and Prior *et al.* [1979] presented different methods of producing ground speed corrected and geometrically rectified sonar images, although not all are digitally based. Lewinstein *et al.* [1980] emphasized the importance of producing "mosaics" consisting of overlapping passes through an area and stressed the necessity of geometric and navigational corrections in rendering these mosaics meaningful. Teleki *et al.* [1981] also produced corrected mosaics but stressed that total geometric correction would require knowledge of bathymetric information on a pixel by pixel basis, which was not available to them. More recently, Luyendyk *et al.* [1983] described the results of subjecting digitized side scan images to the Video Image Communication and Retrieval (VICAR) image processing system at California Institute of Technology's Jet Propulsion Lab. Farre and Ryan [1985] attempted to produce stereo side scan pairs from Sea MARC I imagery, although they seem to have been caught in the tautology of geometric corrections based upon bathymetry which was derived from interpretation of un-corrected side scan data.

Finally, in the way of quantitative image analysis and pattern recognition, Pace and Dyer [1979] conducted an analysis of seafloor image texture, based on the measurement of second-order gray-level statistics of the image. By combining transformations of their own derivation with those previously utilized in the analysis of subaerial imagery [Haralick *et al.*, 1973], they were able to distinguish a number of known sedimentary bottom types with greater than 65% confidence. Reut *et al.* [1985] demonstrated an ability to distinguish imagery of six classes of homogeneous sediment type (mud, clay, sand, gravel, cobbles, and boulders) on the basis of image spectral (log of the image power spectrum) analysis.

1.2 The SeaMARC II System

SeaMARC II combines a conventional side scan sonar with a bathymetric mapping system in a single unit towed at depths of 100 m or less at speeds up to 10 knots (5 m/s). In water depths greater than 1 km, the system produces 10 km wide data swaths, permitting 100% coverage of over 3000 km of seafloor per day. A complete system description is given by Blackinton *et al.*, [1983].

Two parallel, inclined arrays are mounted on each side of the SeaMARC II towfish. The port arrays operate at 11 kHz and the starboard at 12 kHz to minimize cross-talk. By assuming a nominally flat bottom, and calculating the rate at which the outgoing pulse will have swept the bottom for cross-track distances from nadir to 5 km athwartships, the returning signal is divided into 1024 unequal intervals of time, each representing a 5-m-wide swath of the seafloor. Sampling rates are high for the near-nadir pixels and de-

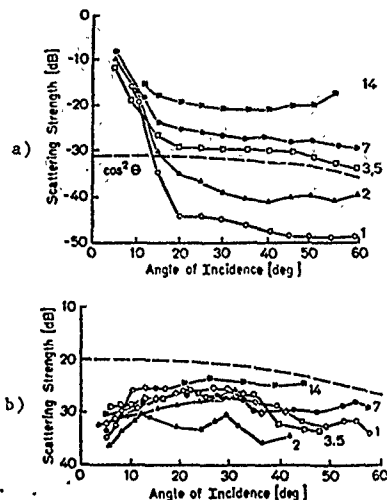


Fig. 1. Angular dependence of the strength of signal backscattered from the bottom as a function of angle of incidence at various frequencies [after Brethovitch and Lyman, 1982, Figure 134]. (a) scattering from a smooth bottom, (b) scattering from a very rough bottom.

crease in proportion to the cosine of the grazing angle. If the seafloor is in fact flat across-track, then this process will produce an image that is geometrically correct in horizontal range, but for ray bending effects. Cross-track topographic variations will however, result in image distortion. Specifics of this type of distortion, and remedies for it, are presented in section 2.

The along-track distance between sonar pulses will be a function of the ship's speed and the pulse repetition rate. At a typical rate of 1 pulse per 10 s, and a ship speed of 4 knots (4 m/s), this spacing is approximately 40 m. The bin spacing is used as the nominal along-track pixel dimension for the side scan data, yielding a digital image with theoretical ground resolution of 5 by 40 m. We stress, however, that the area of the seafloor encompassed during each pulse is generally much greater than the assumed size of the pixel, particularly in the along-track direction. The effect of this approximation is discussed below.

Three types of amplitude gains are applied to the SeaMARC II side-scan data. The first is a time varying gain (TVG) which is intended to correct for cylindrical spreading attenuation proportional to the inverse of the square of the travel time of the acoustic waves and absorption of the signal in the water ($e^{-\alpha t}$, where α is the absorption coefficient and t is time [Urick, 1983]). The second is an angle varying gain (AVG) which is intended to correct for both the nonuniformities in the transmitted beam pattern and the change in backscattered signal intensity observed at different grazing angles (Figure 1). These gains are applied automatically and are not subject to operator inter-

tion. The final gain is a scaling factor which is controlled by the operator in response to the image quality on the ship's monitor recorders.

The assumptions that the seafloor is flat, that the length of the seafloor ensounded by any portion of the beam is the product of the inter-ping period and the speed of the ship, and that the gains have all been applied correctly, are all compromises that produce a distorted image of the seafloor. Our preprocessing steps seek to correct and minimize these distortions, examples of which are presented later in this paper.

The SeaMARC II bathymetric information is acquired through the same transducers as the side scan data but is processed with different hardware and software. On transmission the transducer pairs on each side of the towfish are driven in parallel. On reception, each row in the pair is sampled independently. Therefore any signal incident upon the transducer at any angle off normal to the transducer face is detected at the two rows with a different phase lag, from which the depression angle θ of the reflector is calculated. By measuring the round trip travel time and assuming a sound speed of 1500 m/s, the slant range R to the reflector can be calculated. These values for R and θ are converted to across-track distance and depth for each reflector and contoured to produce a bathymetric map. Absolute accuracy of 2-3% of the water depth is nominal, relative accuracy is significantly better.

1.3 Objectives

In this report the original side scan sonar data have been slant range corrected to a nadir reference datum to produce images wherein the along-track and across-track scales are equal. Ship navigation has been merged with side scan pixel data to produce images free of distortions due to variable towing velocity. Examination of towfish attitude data, recorded every second, indicates that sensor pitch, roll, and yaw are of small magnitude and vary slowly for the images under consideration, and hence present only minor distortions. However, for the production of multi-image mosaics, total correction of attitude variations is applied, and the data are converted from a "line and pixel" coordinate system to a Universal Transverse Mercator projection. Given the above in combination with the SeaMARC II bathymetry as the standard SeaMARC II data set, our objectives are threefold: (1) to produce from the raw images a data set which is a geometrically and radiometrically correct representation of the seafloor, (2) to extract from these corrected images statistical features that can be recognized by a computer, and (3) to use these features to classify the images into regions of distinct acoustic and, hopefully lithologic, texture.

In order to implement these objectives, the processing steps include three classes of operations: (1) preprocessing corrections, (2) feature extraction, and (3) image classification. The desired result is a thematic classification of the images based upon a concatenation of statistical image features with ground truth data.

2 PREPROCESSING CORRECTIONS APPLIED TO SEA MARC II DATA

A side scan sonar image is a two-dimensional display of pixels, each with an associated intensity, which attempts to

model a physical realization of a four-dimensional process, namely, the interaction of sound with the seafloor. The dimensions of the process are the three Cartesian coordinates of space, which give the position and orientation of any reflector with respect to the sonar, and the fourth dimension of acoustic character (acoustic impedance and roughness). The image is an approximation of the bottom with various sources of errors. Preprocessing corrections should produce an image that is geometrically and radiometrically correct. Being geometrically correct implies that features are in their correct locations and represented by the same spatial distribution of picture elements irrespective of the slant range at which they are imaged. Being radiometrically correct implies that all contributions not indicative of actual changes in bottom acoustic character have been removed. Only when these two criteria are met can meaningful subjective or quantitative interpretations be conducted.

2.1 Radiance Transformations Background Subtraction

Three image radiometric artifacts are common to many side scan images (Figure 2). The first is the irregular band of high intensity pixels nearest to the ship's track (SeaMARC II plots strong reflectors as dark and shadows as light, so the images appears as negatives). The high intensity of these pixels is due to the contribution from near normal incidence specular and subbottom returns, which will only occur within the first few degrees from nadir. The second artifact consists of lines of high intensity pixels parallel to the ship's track which represent surface reflections of the first bottom echo. The lines nearest the ship's track are peg-leg (down to the bottom, up to the surface, and back down to the towfish again) multiples. Similar dark linear features roughly parallel to the peg-legs but at the outside edges of the image are the first bottom multiples. The presence of multiples in the image indicates a nadir bottom that is smooth of the order of the ensounding wavelength (12 cm).

The third artifact is the swath of low-intensity pixels parallel to and located approximately 3 km athwartships of the ship's track on the starboard side. This diminution of intensity is caused by an irregularity in the beam pattern, which the angle varying gain (AVG) has not been able to correct. The AVG is designed to correct for beam pattern irregularities and the variation of backscatter intensity due to change in the angle of incidence over a uniform bottom (namely, Figure 1). However, system problems or significant differences between the bottom being surveyed and the bottom from which the AVG was designed can result in severe image degradation. Chavez [1980] reported similar problems and a potential solution for side-looking airborne radar (SLAR) imagery. We have developed a different method here which results in the rectification of the shading problem as well as the multiples and specular artifacts.

In our method, a parameter set is calculated for both port and starboard sides, consisting of an average pixel intensity (Figure 3a) for strips of the images representing strips of the bottom which would be subtended by 0.25° bins of the beam athwartships. These strips parallel the track of the ship and span the range of angles from nadir to the least depression angle. These averages should be taken along a representative portion of a mosaic so that variations in IV due to local geologic variations will cancel. The transfer-

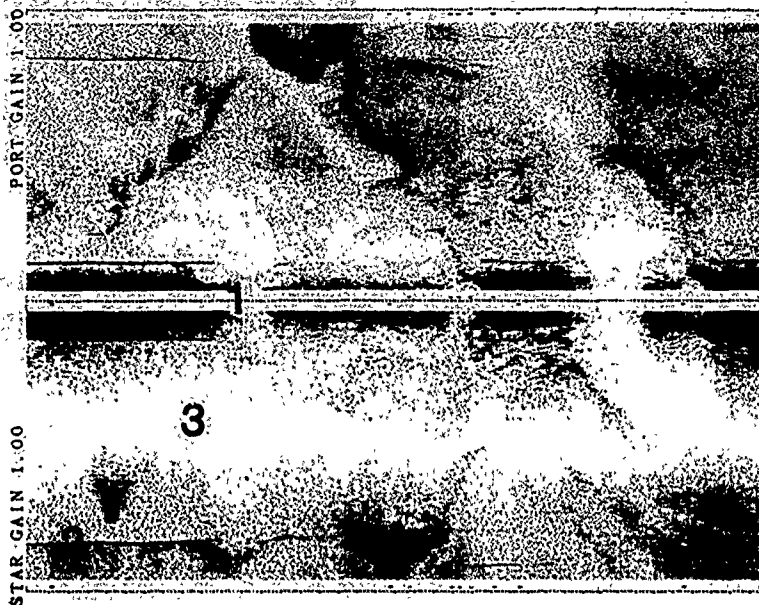


Fig. 2. SeaMARC II side scan image, containing three types of errors: (1) high amplitude near nadir specular returns; (2) peg-leg and first bottom multiples; and (3) swath of anomalously low intensity pixels on starboard side due to faulty beam pattern.

mation is accomplished by multiplying every pixel in the image located at angle increment i by a factor P_i where

$$P_i = \bar{IV} / IV_i \quad (1)$$

and \bar{IV} is the average intensity value of the entire image under consideration and IV_i is the average intensity at the angle i . Comparison of Figures 2 and 3b shows the result of this transformation. The minimization of the three artifacts is evident, while the true geologic features are minimally affected. We refer to this correction as "background subtraction" as it is largely a correction based upon removal of the average image background. In areas of relatively constant along-track geology, the processing steps involved in generation of the parameter sets may also allow a means of estimating the angle-variant backscattering function of the surface, such as seen before in Figure 1.

Chavez [1986] suggests a similar operation based upon calculation of the along-track average of each pixel column (e.g. $1 \leq i \leq 984$). Clearly, as the problems which this technique seeks to correct are angle variant, his method will only work for data from constant water depth.

Our method assumes that variations in pixel intensity due to geologic variability will be randomly distributed relative to the track of the ship and thus add destructively in the average as long as the data set is sufficiently large. As the

parameter sets are normalized by the overall average of image, the gain of the filter is independent of the geologic original gain settings. However, spurious features related to the operating system occur at fairly fixed depression angles, adding constructively in the along-track summation, yielding estimates of systematically induced cross-track errors. Hence the specular reflections (constrained to nadir positions), the peg-leg multiples (constrained to cross-track distance proportional to twice the fish depth), and the beam pattern variations (by definition a function of angle and ray path bending) will all contribute significantly to the average cross-track profile. One caveat to this method is that it does not take into account ray path bending, so that a parameter file generated from a shallow water bottom would not be appropriate for images from significantly (1000 m) deeper waters or vice versa. A simple solution to this problem which we utilize is to generate parameter files over the range of depths encountered in survey area and to index them by depth so that the required values can be used as a look-up table on the basis of the depth of the portion of the image under consideration.

2.1 Geometric Rectifications: Layover

Geometric corrections to the side scan images include along-track and across-track rectifications. The across-track

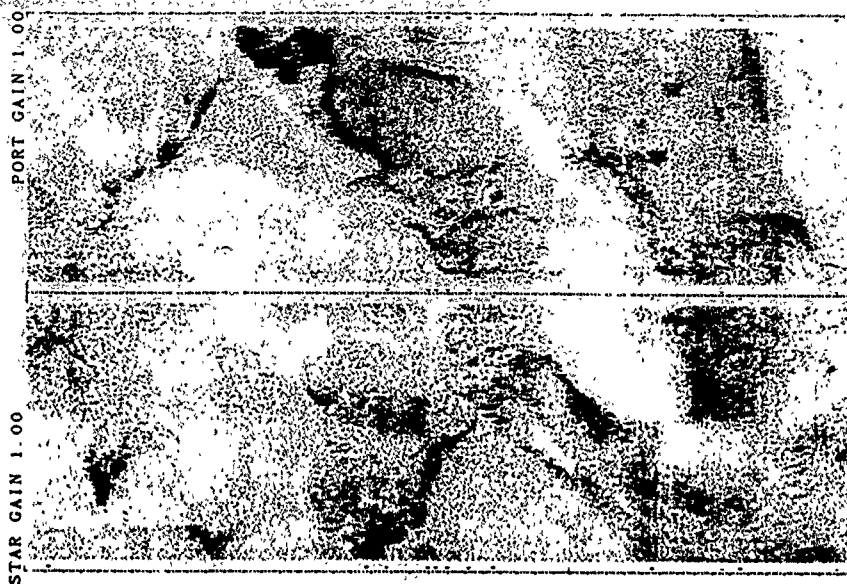


Fig. 3a. Plot of average pixel intensity versus look angle for the starboard half of the image shown in Fig. 2. Number 1 pixel is nearest the ship track. Note peaks at 1°, 12°, and 60° corresponding to the specular reflection, peg-leg, and surface multiples, respectively, and the trough about 42° corresponding to the null in the beam pattern.

correction deals with pixels which have been placed at the incorrect cross track distance, a phenomenon known as "lay over" to the airborne remote sensing community. Reflected side scan data from each "ping" (outgoing pulse) are acquired sequentially in time, i.e., linear in slant range. To convert this cross-track "slant range" image to a plan perspective without a priori knowledge of the bottom topography requires that one assume that cross-track topographic variations about some reference datum (usually the nadir

depth), are insignificant. The cross-track positions of the pixels are estimated from knowledge of the travel time, approximate sound velocity, and nadir depth. Violation of this flat bottom assumption, as often happens, will result in topographic features being incorrectly positioned, or "laid over" (Figure 1). Because of this flat bottom assumption, reflections from points A and B in Figure 1, representing off-nadir troughs and peaks, are erroneously rotated along arcs of radii equal to their slant ranges to points A and B.

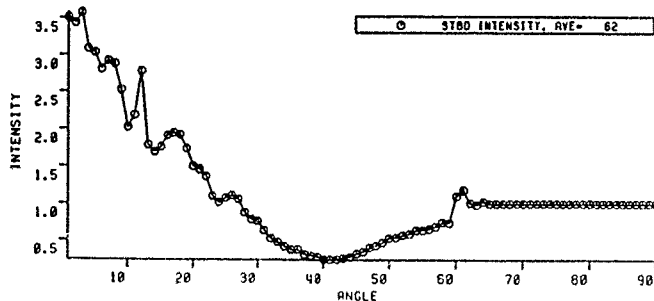


Fig. 3b. Image as shown in Fig. 3a, after background subtraction. Note removal of peaks at 12°, 60°, and 62° and the resulting profile.

age of the geology or related to ion angles, ation, and cross-track d to near-uniform to a (ish depth), on angle of ion a func-contribute One caveat nt ray path a shallow nages from 18.5. A sim to generate uted in the the routine f the nadir tion

include both cross-track

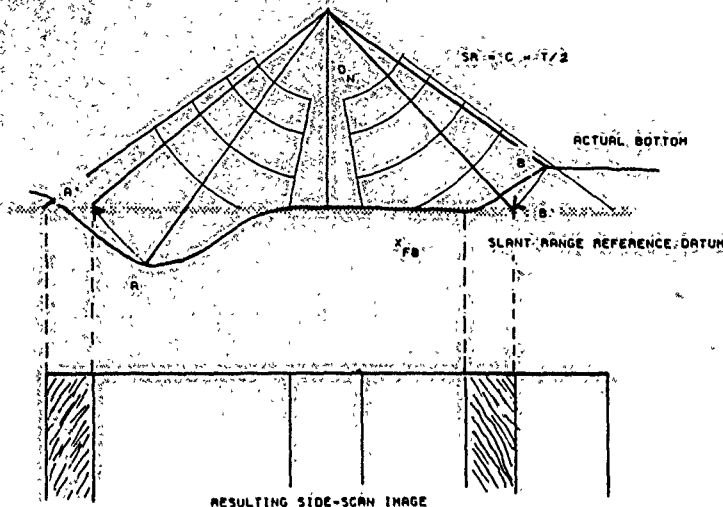


Fig. 4. Slant range correction geometry. Nominal slant range correction assumes that the bottom is flat (reference datum). Topographic deviations from this reference datum will cause features to be imaged incorrectly, as shown by the compression of the inward sloping faces of the trough and cliff. See text for details.

on the reference datum and consequently are imaged spuriously. As a result, the inward sloping faces of the trough and cliff have been foreshortened, and their boundaries have been misplaced.

This displacement is contradictory to our experience from photographic aerial imagery, wherein the taller objects appear to lean outward, away from the viewer. Furthermore, this distortion becomes more significant closer to nadir, again at odds with our experience with aerial imagery in which the distortion decreases with a decrease in parallax view angle. Finally, in mosaics containing parallel tracks with opposite look directions, similar topographic features seen in different tracks will be displaced in opposite directions, resulting in difficulties in coregistration, not to mention any quantitative analysis.

As an example of the magnitude of this effect, consider an abyssal hill rising 200 m above a reference datum of 2500 m water depth, and located 2500 m athwartships. The flat bottom assumption will cause the peak of the hill to be imaged 200 m closer to the track than it actually is. This distortion increases with water depth and depression angle, so that the same hill at a reference datum of 5000 m water depth would be misplaced by almost 430 m.

As SeaMARC II gathers explicit cross-track bathymetric information with each line of side scan data, this distortion caused by cross-track relief can be corrected on a local, pixel-by-pixel basis. Under the flat bottom assumption, side scan pixels are placed at a cross-track distance X' equal to $(SR^2 + TA^2)^{1/2}$ where SR is the slant range (sound velocity \times

arrival time/2) and TA is the towfish altitude (reference datum - fish depth). Our correction of this pixel position error is accomplished by locating the side scan pixel for which the slant range equals that of the nearest bathymetry point X, Z (Recall that SeaMARC II bathymetry coordinates are calculated from measurements of depression angle and time to a reflector and hence are independent of the side scan image based on the flat bottom assumption.) When a match is found, that pixel is placed at a cross-track position of the bathymetry point X , and all those pixels between it and the last pixel so located are stretched or compressed accordingly. The results of this transformation are shown in Figures 5, 6, and 7. Note how the scarp which strikes across the original image in Figure 5 at approximately $N45^\circ W$ is conformed to follow the contours of the bathymetry (Figure 6) after the pixel relocation (Figure 7). The most significant change in geometry is demonstrated by the secondary scarp (arrowed in the raw image and the bathymetry) which is shifted athwartships by up to 1 km and rotated clockwise by almost 20° . An obvious benefit of this rectification is that features are correctly placed on the image for interpretation and survey targeting. A more subtle benefit is the removal from the image of spurious cross-track compressions and rarefactions due to topography which might otherwise be interpreted by both man and the computer algorithms as variations in geologic character. Furthermore, bottom detect errors, caused by side swipe detection of off nadir bathymetry, and their resulting effects on the side scan image can be explicitly corrected but for small zones of

STAR GAIN: 1.00

PORT GAIN: 1.00



Fig. 5. Unprocessed side scan image corrected for slant range according to the "flat bottom" assumption.

ambiguity in the placement of side scan pixels. These zones of ambiguity occur when multiple bathymetric points yield identical slant ranges. One heuristic solution to this problem divides the amplitude of the ambiguously located side scan pixel by the number of bathymetry points with that slant range and allocates the quotient to each point.

The only assumption required by our 1-D correction method is that the side scan data be in the correct sequence athwartships, i.e., that there be no reflector at cross track distance X and elevation above the reference datum Z such that the travel time associated with it would be less than that for any reflector located at some $X > X_0$. This "correct sequence" assumption is a reasonable assumption for most

geometries and bottom types, considering the relatively high altitude (height above bottom) typically greater than 20° of the swath width at which Sea-MARC II is deployed.

2.2 Geometric Rectifications: "Point Migration"

"Point migration" refers to the spurious along-track elongation of image features due to violations of mapping assumptions. As previously mentioned, such violations are related to the integrated intensity of backscatter from a given area, which is a function of the area. The area of a point q may, therefore, be given by $q \cdot BW \cdot SL$, where BW is the swath width and SL is the slant range. The constant reflector width which Sea-MARC II uses is $2 \cdot X_0$.

reference position, pixel for bathymetry coordinates angle and the side. When a position between it is pressed shown in crosses across $45^\circ W$ is y (Figure significant primary scarp which is clockwise location is interpreted is the depressions otherwise bathym as bottom off nadir side scan zones of

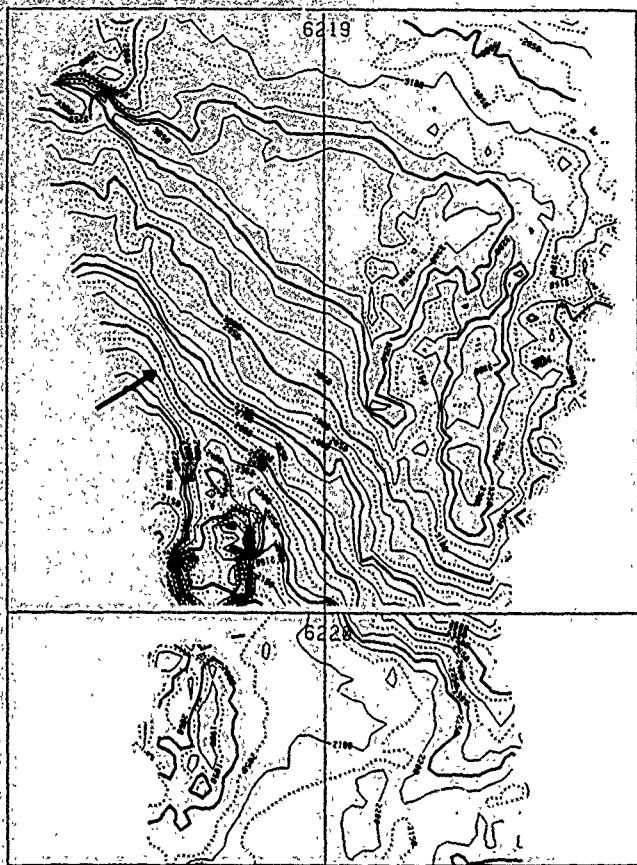


Fig. 6. SeaMARC II bathymetry for the image shown in Figure 5.

slant range increases, the along-track dimension of the area ensonified during each ping will increase from nadir to the maximum slant range. This increase in footprint size remains uncompensated when the pixels are plotted. Instead, the along-track size of each pixel is assumed to be the inter-ping spacing, typically on the order of 40 m. As the beam footprint at most slant ranges will possess an along-track dimension greater than the inter-ping spacing, any isolated strong reflector of linear dimension less than the nominal pixel length will be ensonified several times (Figure 8). The result of this phenomenon in the side scan image is demonstrated by the multitudinous "hashmarks" throughout the image (Figure 9), which are isolated point reflectors that have been repeatedly ensonified by several adjacent pings and thus plotted as linear features. It is also reasonable to

assume that strong reflectors, orders of magnitude larger in area than the beam width, will have been expanded by several additional pixels on either side in the along-track direction in a similar fashion, although this effect is not as immediately conspicuous or deleterious to image quality.

Were the azimuthal beam pattern sufficiently well known as a function of depression angle, we might solve the point spread problem in a fashion similar to that in which hyperbolic reflectors in seismic data are migrated back to their correct positions by assuming that all points at the same slant range have behaved as point hyperbolic reflectors and should all be migrated equally [Hagedoorn, 1954]. However, the extent to which point reflectors in the side scan data seem to be elongated seems to be a function of both reflector strength and strength in relation to the background, indicat-

11
12
13
14
15
16
17
18
19
20
21
22
23
24
25

STAR: GAIN: 1.00

PORT: GAIN: 1.00

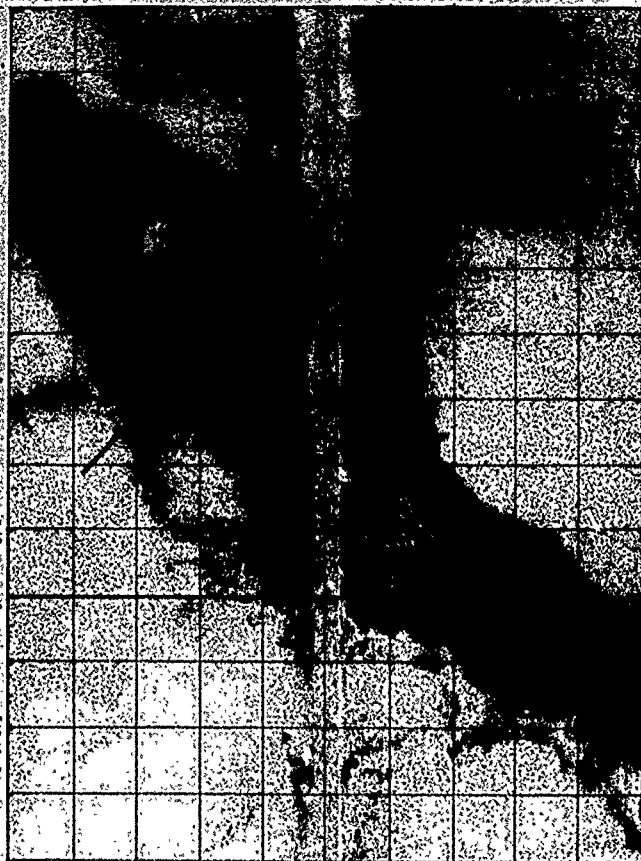


Fig. 7. SeaMARC II image after layer correction, as described in the text. A 1-km grid spacing has been superimposed upon the side scan images for the purposes of comparison. Topographic features such as the ridge (arrowed in the images) and bathymetry map) have been shifted by up to 1-km.

larger in
ended by
long-track
is not as
ality
all known
the point
ch hyper-
to their
the same
ctors and
However
scan data
h reflector
d indicate

ing that the first order approximation of the beam pattern is not sufficient (i.e., a high contrast point just outside the MB pattern may reflect enough to contribute). Furthermore, the shadows behind the point reflector are elongated along-track; these too will have to be migrated.

We correct this along-track elongation of features in the imagery via a migration routine wherein the extent of migration (i.e., the number of ping-fore and aft of the point of stacking) is a function of both the slant range to the point and the difference in intensity between the pixel at that slant range and the average intensity of a neighborhood centered about that ping-fore and aft of the point of stacking.

large slant ranges and at high contrast to their neighbors are replaced with a weighted sum of the pixel intensities from pixels fore and aft at the same slant range. From seismic migration theory, we would expect that pixels could be stacked along a hyperbola centered about the high contrast pixel, but with a half beam width of 1, the half range would have to exceed 32 km before the curvature of the hyperbola would exceed the pixel dimension of 1 km. If migrating only those objects with five bit contrast from their neighbors, we can see the aspect of the resolution, the 4400 ft resolution, is the half width of the data window, and the 1 km pixel dimension is the half width of the data window.

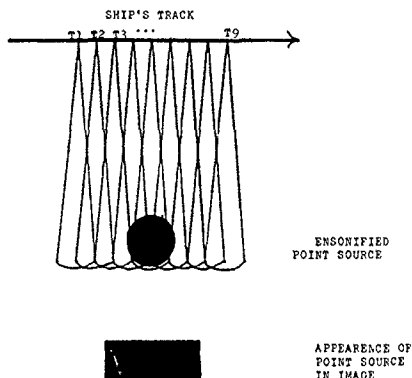


Fig. 8 Schematic diagram of the migration of a point reflector, caused by multiple ensonification

Background subtraction followed by inverse migration diminishes the along-track stretching, in favor of roughly equidimensional points that are several pixels deep. Compare in particular the lower left and upper right portions of the images (Figures 9 and 10).

After the above preprocessing rectifications, side scan images have been collected within the limits of the data, features correctly sized and located, and pixel intensity variations rendered more representative of actual changes in bottom character. Further processing steps are means of extracting quantitative information from the digital images.

3. FEATURE EXTRACTION

3.1 The Feature Vector

The chief purposes of remote sensing imagery are detection and discrimination. Synoptic imagery displays the areal distribution of terrain surface types but usually does not describe the individual terrain surfaces explicitly. Although human observers are clearly capable of interpreting such imagery, the results are subjective, not necessarily repeatable, and often more indicative of the interpreter than the object. Statistical analysis of image data provides an objective and repeatable means of identifying, distinguishing, and labeling surface types. Key to this concept of numerical analysis of imagery is the term feature vector, a numerical descriptor of N dimensions which will condense the discriminatory information contained in the image plane into a single vector for each surface type.

As an example, gray tone images might be described by intensity alone, in which case the feature vectors would be one-dimensional and areas of the image between designated thresholds would be classified as distinct ($IV < 50 = \text{class 1}$, $IV > 50 = \text{class 2}$). Feature vectors are usually multidimensional, such as from multispectral Landsat imagery, and the discriminant surfaces are hyperplanes in N -dimensional space.

For single-spectral images such as those produced by single-frequency side looking sonars and radars, classification of imagery via first-order statistics such as mean intensity is rarely viable, due to image speckle, gain changes, beam pattern variations, and variations in backscatter strength concomitant with changes in angle of incidence, all of which can result in different intensity values from a uniform reflector. Consequently, we look to second-order (point relational) statistics. For the classification of single spectral imagery such as side scan data, texture (an abstract second order feature) is more useful.

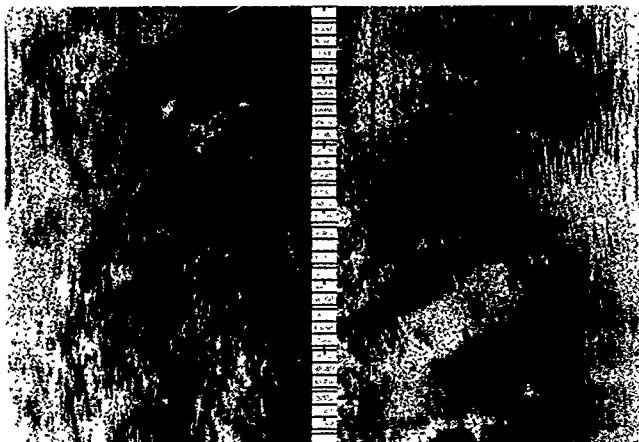


Fig. 9 Unprocessed SeaMARC II side scan image showing multiple "hashmarks" short lines parallel to the ship track caused by the phenomenon of migration.

are detected displays the usually does explicitly interpret necessarily prefer than provides an distinguish concept of e vector, a ll condense image plane

scribed by s would be designated 50 = class llly multi dngery and functional

duced by lassification intensity is beam pat length con til of which a uniform (point rel gle spectral ut second



Fig. 10. Image as in Figure 9 after background subtraction and migration. Note specifically the compression of the hashmarks in the upper right and lower left portions of the image.

3.2 Texture

Texture is an innate property of all objects, which characterizes the closely interwoven relief of the surface. Texture is strongly stationary and independent of illumination. Although it is quite easy for human observers to recognize and describe texture in empirical terms (smooth, coarse, rippled, etc.), until the past decade texture has been extremely resistant to quantification. Furthermore, measures of image texture have yet to be related to actual object dimensions, texture yields discrimination but not, as yet, definition. Several methods have been proposed over the past decade for extracting statistical texture signatures [Pratt, 1978; Laws, 1980; Haralick et al., 1973]. In this paper, we utilize the gray level co-occurrence matrix (GLCM) method of texture analysis [Haralick et al., 1973].

The GLCM method requires the creation of a secondary matrix from which second order texture statistics are estimated. Specifically let $P(x, y)$ represent the digital image over a rectangular domain $L_x=1, 2, \dots, N_x$, $L_y=1, 2, \dots, N_y$ quantized to N_g gray levels. Each GLCM is a square matrix of dimension N_g whose entries $S(i, j, \theta, d)$ express the number of times there occurs in the image a pixel of intensity i neighbored by a pixel of intensity j in the direction θ at distance $d=1$ (example of the gray level co-occurrence matrix ($\theta=0^\circ$)).

$$S(i, j, 0, d) = \# \{ (l, l') \in (m, n) \}$$

$$(L_y \times L_x) \times (L_y \times L_x)$$

$$k-m=0, |l-n|=d$$

$$P(k, j) = P(m, n) = i$$

where L_x is the horizontal and L_y is the vertical pixel dimension, and $\#$ means the number of occurrences of the pair (i, j) .

As a simple example, if the image in the text is given by

1	1	2	3	3
1	2	2	3	1
2	3	3	1	1
1	2	1	1	1
1	1	3	3	3

and the GLCM is to be evaluated in the horizontal direction ($\theta=0^\circ$) for a lag of 1, then the GLCM would be

	1	2	3	1
1	4	3	1	0
2	3	2	3	1
3	1	3	8	2
1	0	1	2	6

The element of the matrix is calculated by dividing each entry in the matrix by the total number of possible entries N_g^2 that direction and lag. The GLCM example with $\theta=0^\circ$, $R=1$ given by

$$R_{01} = 2/N_g(N_g - 1)$$

In addition, the GLCM is used to calculate the texture features, which are the first order statistics of the GLCM. The first order statistics are the mean, variance, and entropy.

To further insure rotation invariance, *Haralick et al* [1973] have suggested taking both the average and the range of the statistics that are extracted at each angle of evaluation. In general, evaluation of the matrices in the four directions given above would allow true rotation invariance for rotations of $\pi/2$ rad, and approximate rotation invariance at $\pi/4$. Our modification is to impose a normalized, inverse Euclidean distance weighting scheme upon each neighborhood of dimension $2d$ so that the square neighborhood becomes a circle of radius d and hence rotation invariant [Reed, 1987].

3.3 GLCM Features

Haralick et al [1973] suggested 14 features which can be extracted from the GLCMs. Evaluation of these 14 features over four directions and several lags makes for a rather unwieldy data set to use directly as a feature vector, to say nothing of being able to visualize the resulting class clustering. Furthermore, for a fixed number of samples, there is an optimal measurement complexity, beyond which increasing the vector dimensionality does not necessarily increase classification accuracy [Schowenegerdt, 1983]. As classification time for a feature vector of dimension N is proportional to $N^2(N-1)$ [Swain and Davis, 1978], smaller feature vectors are better.

Fortunately, some of the features in this set are strongly correlated with each other. The Karhunen-Loev transformation or principal component analysis (PCA) [Swain and Davis, 1978] provides a means for detecting this correlation and reducing the dimensionality of the data set.

Five of the original 14 features which have shown low correlation in PCA analysis are utilized here. They are

Angular second moment

$$ASM = \sum_{i=1}^{N_1} \sum_{j=1}^{N_2} \left(\frac{S(i,j)}{R} \right)^2 \quad (5)$$

Contrast

$$CON = \sum_{n=0}^{N_1-1} n^2 \left\{ \sum_{i=1}^{N_1} \sum_{j=1}^{N_2} \frac{S(i,j)}{R} \right\}_{|i-j|=n} \quad (6)$$

Entropy

$$ENT = - \sum_{i=1}^{N_1} \sum_{j=1}^{N_2} \frac{S(i,j)}{R} \log \left(\frac{S(i,j)}{R} \right) \quad (7)$$

Angular inverse difference moment

$$AIDM = \sum_{i=1}^{N_1} \sum_{j=1}^{N_2} S(i,j) / ((1+(i-j)^2) * R) \quad (8)$$

Correlation

$$COR = \frac{\sum_{i=1}^{N_1} \sum_{j=1}^{N_2} (ij) S(i,j) / R - \mu_x \mu_y}{\sigma_x \sigma_y} \quad (9)$$

where μ_x , μ_y , σ_x , and σ_y are the means and standard deviations for the row and column sums, respectively.

Four of these statistics, ASM, CON, ENT, and AIDM, have been shown to be strong estimators of wavelength variations and to be insensitive to variations in either look direction or gain settings [Reed, 1987]. ISO, a feature of our own derivation, shows similar characteristics as the above four features. It is calculated as the sum of the differences of orthogonal GLCMs, and is a measure of the isotropy of the image.

The means and ranges for these statistics may be evaluated for one or more distances of separation. The resulting set of statistics forms a feature vector of dimension N , which describes the texture of that portion of the image over which the features were evaluated and by which that section of the image will be classified.

3.4 Evaluation of Image Texture With the GLCM

To evaluate the texture of an entire image, the image is first divided into rectangular cells referred to as "texels." To optimize the potential of this texture routine, these texels should contain at least NG^2 pixels, where NG is the number of gray levels to which the image has been quantized [Pratt, 1978] in order to maximize the possibility of measuring real image texture variations.

For images quantized to 8 bits, resulting in 256 gray levels, not only would the evaluation and storage requirements of several 256 by 256 co-occurrence matrices become prohibitive, but also the texels would be so large as to be meaningless for all but the most uniform images. Aside from simple resolution considerations, this loss of significance is due to the fact that as texel size increases, the probability of creating a cell of mixed textures (a "mixel") similarly increases. To minimize the size of the texels without seriously violating the pixel volume requirements, the data are rescaled by the mean and variance of the entire image to a smaller number of intensity values, generally 16 or 32. Following this requantization, co-occurrence matrices are evaluated for each texel, and the desired feature vectors are then extracted. The remaining task is to subdivide the image into texturally distinct regions on the basis of each texel's n -dimensional feature vector.

4. CLASSIFICATION

The object of classification is to assign each pixel or texel of an image, defined by its feature vector, to a certain class, in such a way that the specified error criterion is minimized. In order to do this, the computer must be able to determine the classes that exist in an image. This list of classes must be exhaustive, separable, and of informational value. Having determined the classes present in the data, the computer must determine to which class every pixel or texel is most likely to belong. The desired result is a map in which the pixels or texels of the original image have been replaced with symbols, representing the thematic group to which the feature vector for that point belongs. There are, in general,

two approaches to achieving this end supervised and unsupervised classification.

4.1 Unsupervised Classification

Unsupervised classification is best described as clustering. The feature vectors of a subset of the image are submitted to a clustering algorithm to determine the natural groupings in the data that exist in n -dimensional feature space, where n is the number of statistical features (extracted from the co-occurrence matrices). By submitting a small, heterogeneous sample population of texels, it is hoped that representative natural groups may be determined. Although these numeric groups may or may not have discernable properties in the image or in the physical world, they may still be used as the classes into which all remaining feature vectors may be classified. Meaningful classes could then be extracted with the aid of ground truth and historical data.

The clustering algorithm utilized in this work is a modified version of the classic K -means algorithm [Hartigan, 1975]. The traditional algorithm is initialized by assuming the existence of K classes, with K to be specified by the operator, for which K approximate initial mean vectors are chosen. The initial K mean vectors may either be chosen randomly assigned by the operator, or defined by the data. In the latter approach, which we utilize, the scalar sum of each vector's components is calculated, and the vector is initially assigned to that class K for which its sum represents the k th fractional part of the range of the sums. The mean vector is the vector that defines the centroid of the K th cluster. Every texel of the training data set is then assigned to that class to which its feature vector is least distant. Distance is measured in terms of the Euclidean distance, defined as

$$ED_{xM_j} = \left[\sum_{i=1}^n (a_i - M_{i,j})^2 \right]^{1/2} \quad (10)$$

where a is the length- n feature vector, $M_{i,j}$ is the length- n centroid vector of the j th cluster, and ED is their Euclidean distance (Figure 11). After all feature vectors have been assigned to that cluster from which they are

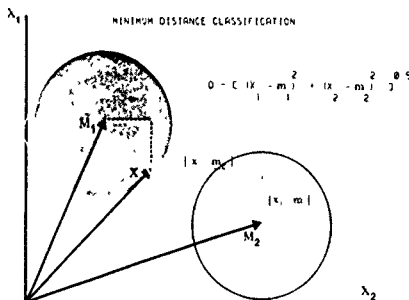


Fig. 11. Graphic example of Euclidean distance measurement. M_1 and M_2 are the centroid (mean) vectors for the two classes. X is a vector to be classified. The Euclidean distance is measured as shown by the dashed lines. Assuming equal class variances, the vector X would be assigned to the class represented by M_1 .

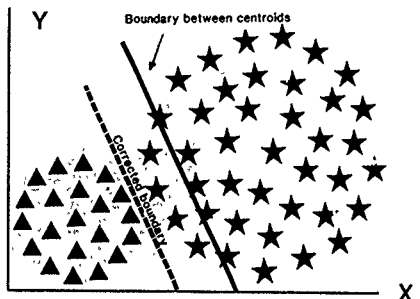


Fig. 12. A two-class (stars and triangles), two-dimensional (x and y) clustering example. A simplistic classification scheme would assume that the two classes had equal variances, and place the discriminant boundary halfway between the class centroids (the solid line). Our modification is to normalize the intercluster distances by the cluster variances, thus resulting in proper placement of the discriminant boundary (the dashed line).

minimally distant, then the cluster means are recomputed, and the process iterates until there is no significant change in the pixel assignments from one iteration to the next. In Hartigan's approach, K classes are assumed at the start. If at the end of an iteration, one class is found to have no members, the routine terminates, usually with an unsatisfactory classification. The modification developed in this paper, in the event of an empty class, is to search the remaining classes for the class with the highest variance, split it, repartition the vectors, and continue the iterations. A further modification we have added is to compute the intraclass to interclass class variance ratio (F statistic) for each of the classes at convergence. Any class whose F statistic exceeds a threshold T is split, increasing the number of classes to $K+1$, and the algorithm is reiterated.

4.2 Supervised Classification

Supervised classification can be used when one has supplementary information indicating both the existence and location of homogeneous, representative samples of every class in the image. This supplementary information usually comes in the form of historical data (maps, reports, etc.) or ground truth data (samples, photographs, etc.). It is important that all classes are represented and that the samples used to represent them contain no "mixels." Once a representative data set is obtained, the average textural vector and its standard deviation are calculated for each class, all other texels may be placed in the class to which they are most similar, according to one of several classification routines. Several, currently available routines are the minimum distance classifier [Scholz et al., 1979], the Bayes maximum-likelihood approach [Duda and Hart, 1973], and extraction and characterization of nonhomogeneous objects (ECHO) [Kittig and Landgrebe, 1976]. In their comparison of these and several other classification schemes in the classification of Landsat MSS data for agricultural areas, Scholz et al. [1979] detected a slight but consistent superiority of the minimum distance approach over the other methods. We implement a modified version of this classifier for our data (Figure 12).

STAR GAIN 1:80

PORT GAIN 1:80



Fig. 13. SeaMARC II side scan sonar image of a lava flow, located 200 km NW of Vancouver. The small feature in the top right corner is the Queen Charlotte transform fault scarp, with an associated 100-m deep of seafloor buried in. Note the 100-m vent from which the flow may have emanated and its acoustic shadow. A note on the inhomogeneity of the reflectivity of the flow in the first kilometer about the ship track.

5. APPLICATIONS

In this section we present examples of applications of the analysis and classification techniques described in previous sections to SeaMARC II sonar imagery from a variety of locations. To our methods based on the GCM method are used for segmentation of images. We also present a few semantic texture descriptors that simultaneously help to help in the process of the segmentation and classification of the

texture methods of the
first three sections.

5.1. Queen Charlotte

The first example is a side-scan sonar image of the Queen Charlotte transform fault, located 200 km NW of Vancouver. The image is shown in Figure 13. The image is a side-scan sonar image of the Queen Charlotte transform fault, located 200 km NW of Vancouver. The image is a side-scan sonar image of the Queen Charlotte transform fault, located 200 km NW of Vancouver.

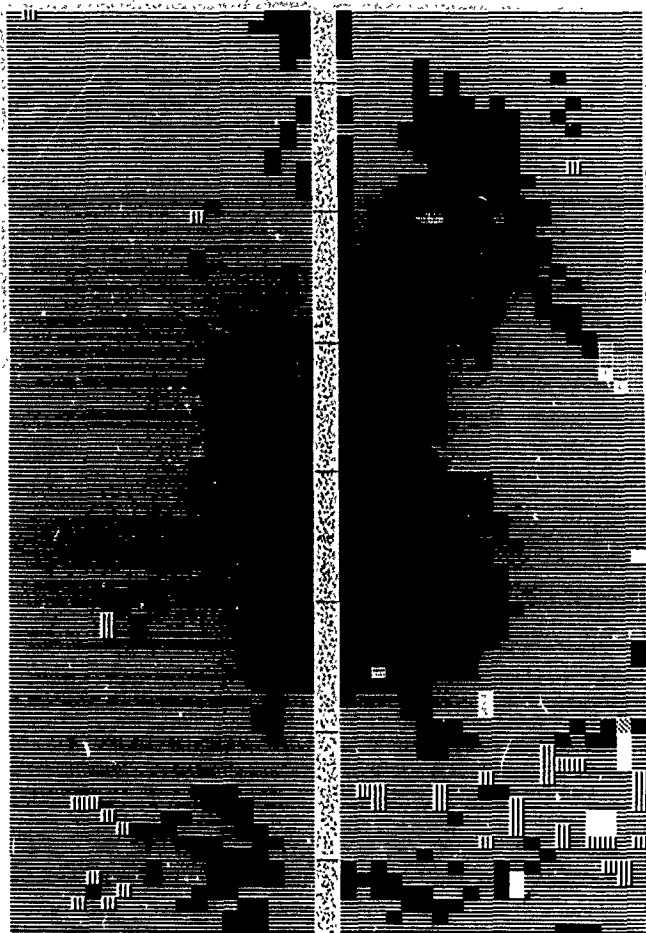


Fig. 11 Six class texture classification of the image of the lava flow as shown in Figure 10. Though the absence of ground truth image may have conclusions, the continuity of the flow (represented by the dark color) across the crack is consistent with our intuition of the flow's distribution.

knobs (Figure 13). The dark central feature is a cavity with the morphology $\rho(r) = \rho_0 \exp(-r^2/r_0^2)$ (Shen et al. 2015). We assume that the flow is continuous and homogeneous across the ship's track. The symmetric variation in water reflectivity about the ship's track is attributed to the fact that AVG did adopt the ϵ estimate technique $\epsilon(r) = 1 - \epsilon_0$ (S. MARE 2016). The flow is probably rough compared to the waves on the sea surface, so $\epsilon_0 = 0.12$ (Riley 1965). The ϵ value is $\epsilon = 1 - 0.12 \exp(-r^2/r_0^2)$ near the wave peaks, and $\epsilon = 0.12$ elsewhere.

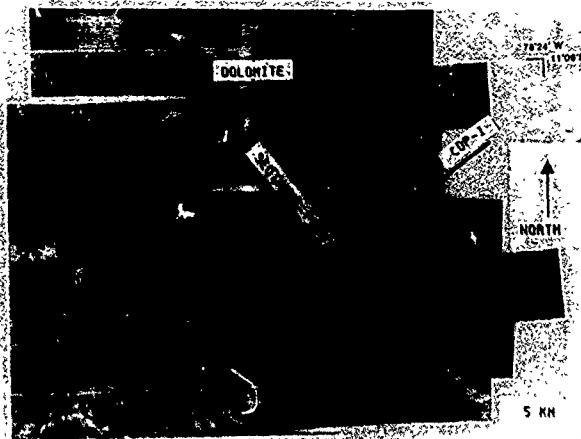


Plate 1a [Reed and Hussong]. SeaMARC II side scan mosaic of Lima Basin. Black line shows position of seismic line GDP-1 with respect to the image.

the steep back side of the volcanic mound. Many other smaller mounds occur in the lower portion of the image. The large lava flow apparently crosses the transform fault scarp, which is downdropped to the upper right portion of the image.

Application of the GLCM textural analysis to the image first requires image subdivision into texels 250 m on a side, each containing 294 pixels. Each texel spans six pings and 19 pixels, so that there are 40 texels across the 10 km width

of the image and $N/6$ texels along track, where N is the number of pings in the image. In this example the image consists of approximately 420 pings, and thus a total of 2800 texels result from the subdivision. The pixels in each texel were re-quantized to 16 intensity levels by dividing the original intensity values by 16 and rounding to the nearest integer. Statistical texture signatures consisting of the means and ranges for the features ENT, ASM, CON, ISO, and AISM evaluated at look directions of 0° , 45° , 90° , and

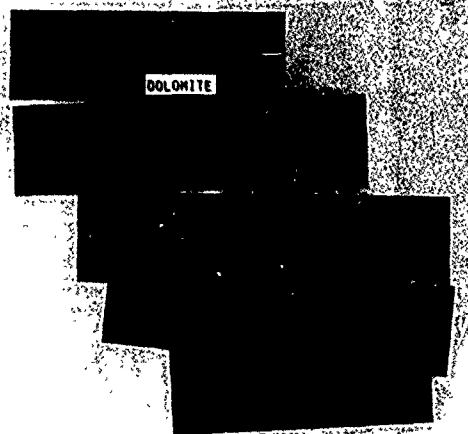


Plate 1b [Reed and Hussong]. Thematic map of mosaic shown in Plate 1a, generated by texture analysis as described in the text.

135° and lag of length 1 were calculated for each of the texels. As no bottom samples were available to us, the 2800 five-dimensional texture vectors were classified in the unsupervised mode with our modified *K*-means clustering algorithm.

Clustering of these 2800 texture vectors into the six classes resulted in the thematic map shown in Figure 14. Note how the black texels delineate the general outline of the lava flow. Specifically, note the continuity of textural mapping across the ship's track in the flow, irrespective of the near-nadir average intensity variations in the side scan image (Figure 13), demonstrating one of the chief advantages of textural analysis, i.e., its immunity to misclassification due to spurious variations in intensity.

5.2 Texture Analysis of the Lima Basin

Despite the absence of a relationship between textural signature and intrinsic surface character, texture analysis thematic maps can be produced and the thematic units assigned to lithologies. A portion of a mosaic depicting part of the continental slope offshore of Peru referred to as the Lima Basin [Hussong et al., 1985] appears in Plate 1a. The lighter portions of the image represent unlithified, hemipelagic sediments. The darker areas represent lithified Neogene sediments, mostly micrites and dolomites of varying degrees of lithification and brecciation [L. D. Kulm, personal communication, 1985]. The parallel and subparallel lineations striking N45°W are also outcrops of bedded micrites. Ground truth for the area comes from dredging [L. D. Kulm, personal communication, 1986]. Unfortunately, as the length of seafloor covered by most dredges was long in relation to the variation of outcrop type visible in the side scan image, and as the contents of most dredges were lithologically heterogeneous, most outcrops could not be correlated to specific samples. However, dredge MW85-11 sampled the dark outcrop, labeled "dolomite" in Plate 1a, and yielded only dolomites, of generally a strongly brecciated character. Due to the "mixed bag" nature of the other dredges, we were limited to two definitive sample types: hemipelagic sediments cored from the sediment pond and the dredged dolomite.

Textural analysis was conducted as described in section 5.1 for the areas of the image coincident with the bottom sample locations. Mean texture vectors consisting of the six statistics CON, ASM, ENT, ENR, COR, and ISO and their associated standard deviations were calculated from the texels in the vicinity of the samples. The entire mosaic was then subdivided into 250-m texels from which texture vectors were evaluated. The texels were classified in the supervised mode with the minimum-distance classifier (section 4.3). Those texels whose texture vectors were distinct from the mean vectors representing either dolomite or hemipelagic sediments by more than twice the standard deviation of either class were lumped in a third category: anything else. The three categories of sediments, dolomites, and anything else were assigned the colors of green, magenta, and yellow respectively, and their texels were colored accordingly. The result is shown in Plate 1b (Plate 1b is shown here in black and white). The color version can be found in the separate color section in this issue. The oval basin containing the hemipelagic sediments is clearly outlined, as is the outcrop of dolomite at its NW tip. Magenta texels

indicated several other possible outcrops of dolomite, which might not have been either detected or discriminated from other dark outcrops on a visual basis.

Although the distribution of the magenta texels about the green oval gives the impression of a synclinal or anticlinal formation, multichannel seismic data collected in this area argue against this interpretation (Figure 15 [after Hussong and Wiperman, 1981]). The inflection point on the depth section (arrowed) where the strata change from landward dipping to seaward dipping, corresponds approximately with the eastern edge of the oval sediment pond seen in the side scan mosaic in Plate 1a. Consequently, the dark outcrops west of the pond which are mapped by magenta texels are the tops of landward dipping strata, stratigraphically lower than the dark outcrops similarly mapped to the east of the pond. The fact that texture analysis has mapped stratigraphically distinct outcrops as similar does not necessarily mandate that they be the same formation, but rather that they possess similar acoustic properties, in particular, roughness or induration.

5.3 Region Growing -- REGATA

The texel, the basic unit upon which the analysis is based, is assumed to contain a subset of the image data which possesses only one homogeneous texture. The probability of spatial homogeneity of a randomly placed rectangle increases as the texel size decreases. For the GLCM to be a reasonable estimator of the image joint probability distribution, the texel should contain at least NG pixels, where NG is the number of gray levels to which the image is quantized (section 3.4). The texel therefore can neither be shrunk below a minimum size without compromising the textural analysis nor increased drastically without encountering an unacceptable number of mixels. As a compromise between spatial resolution controlled by texel size and resolution of textural features as controlled by the number of intervals to which the data are quantized, we have employed a texel measuring approximately 250 m on a side, containing 294 pixels quan-

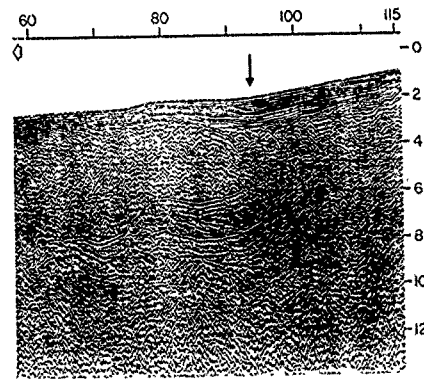


Fig. 15. Portion of CDP-1, a 24-channel common depth point seismic line gathered by Seacom Delta, Inc., as part of the Nazca Plate Project [Hussong and Wiperman, 1981].

tized to 16 gray levels. As the gray-scale recorders used for displaying the image data are capable of producing only 16 gray levels, of which human observers are rarely able to discern more than 8, texture analysis at this level is at or slightly above what is discriminable to the eye [Gregory, 1970].

In order to increase both the textural and spatial resolution, we have designed an image segmentation routine which incorporates semantics and image data. Rather than divide the image into a priori boxes which may or may not contain homogeneous patterns, we seek, via data-controlled decisions, a subdivision of the image into closed regions of limited spatial heterogeneity. One feature vector will then be used to represent each closed region. By allowing regions to grow to their natural boundaries, the probability of producing "mixels" is strongly reduced. As the regions will in general be larger than the previously used texels, classification time will be reduced concomitant with the reduction in number of feature vectors.

The following describes the implementation of Region Growing and Texture Analysis (ReGATA), a bottom-up region-growing routine. SeaMARC II data are stored in records, line-interleaved-by-pixel. Two records, containing two pings of 984 port and 984 starboard pixels, are "read in." The data for port and starboard are subdivided into cells containing two lines of 16 pixels each. The mean intensity and variance are calculated for each of these 32-pixel cells. Two tests are then conducted. The first determines if the cell is reasonably homogeneous, in order to separate the cells into the categories of "region" and "boundary." Those cells which do not pass this test of limited heterogeneity are assumed to span two regions and hence are labeled as boundary cells. An option in the program allows these cells to be either flagged as nonregion cells or quartered and annexed to the most similar adjacent region. Kettig and Landgrebe [1976] propose a test which we utilize here, consisting of the ratio of the cell standard deviation to the cell mean. If this statistic falls above some heuristic threshold, the cell is labeled as a boundary. As sonar images are inherently noisy, this threshold should be fairly high to avoid the classification of the entire image as boundaries.

The second test is the basis of annexation and region growing. For purposes of illustration, the top of the image under consideration is labeled north. Cell classification and region growing proceeds west to east, and lines are read in north to south. Each classified cell has an associated flag which indicates its status as either a boundary or region cell. If it is a boundary cell, there is no need to compare it to the cell under consideration. If it is a region cell, it has associated with it the mean and variance of the region of which it is a member. This region can consist of one or more cells. The cell under consideration is compared to the region cells immediately adjacent in the west, northwest, north, and northeast directions. Comparison in these four directions minimizes imposition of boundary direction preferences within the limitations of the cell tessellation. The logic of the comparison is that if two cells are neighbors and possess similar average value, they probably represent a uniform, connected surface in the object plane and hence should be annexed and similarly classified.

The comparison can be on the basis of either a parametric Student's t test and F statistic, or the nonparametric minimally distant means, at the operator's discretion. As

region growing requirements must be reasonably lax to prevent classifications composed entirely of boundary cells, it is imperative that the cell be annexed to the most similar region which passes the second test and not just the first region to do so.

As a region grows, its mean and variance are recomputed, and the pixels within the annexed cell augment the four GLCMs associated with the region. After the last cell from the two lines currently in memory has been classified, all regions are checked for growth in the last iteration. If they have not grown, they are considered closed, and their associated GLCMs are submitted to a subroutine which extracts the standard six-dimensional texture feature vector. The texture vector and all the pixels in the region from which it was extracted are then assigned a region number and written out to a storage file.

When the routine terminates at the end of the data file, all remaining open regions are closed by the routine and analyzed for texture. The resulting list of region-numbered, feature vectors are submitted to an unsupervised cluster analysis. The region numbers map the regions to the feature vectors in the clusters, and all pixels in all regions with similarly clustered feature vectors are mapped similarly.

The benefits of this routine are threefold: computational speed, increased spatial resolution, and increased textural fidelity. We stated above without proof that there would be fewer regions resultant from this method than texels from the arbitrary division of the image. The intuitive proof for this lies in the definition of texel as the largest tessellation unlikely to transect image region boundaries. If the regions are allowed to grow to their natural boundaries, which the texels are designed to avoid intersection of, then the grown regions will be larger and fewer in number than those resulting from an arbitrary texel subdivision of the image. Fewer regions mean fewer calls to the feature extraction subroutine and fewer vectors to classify. Furthermore, the algorithm requires but one pass through the data to produce a segmentation with texture vectors and requires only four lines of data in memory at any one time.

The cell dimension of 2 lines by 16 pixels results in a limiting resolution of approximately 80 m. This cell size was chosen because it allows quartering of the cells in the event of a boundary classification. The number of pixels, 32, also straddles the small sampling theory/large sampling theory boundary, so that parametric and nonparametric tests are approximately equally valid.

Finally, growing regions of limited heterogeneity minimizes the intercontamination of texture signatures by each other, or by boundaries, neither of which are likely to result in a representative signature. GLCMs from larger regions will contain more entries and hence will yield better estimates of image texture. By minimizing mixing and increasing estimate fidelity, the clusters formed in the unsupervised classification step should be tighter, resulting in better discriminant boundaries in the classification n space, and less confusion in the image plane.

One of the other benefits of the region growing method is that as the regions that result are in general larger than the previously used texels, the image need not be requantized to such a small number of gray levels. Specifically, regions often grow to contain hundreds to thousands of cells, each containing 32 pixels. If we analyze all closed regions for texture, but only use those with more than 100 cells for deter-

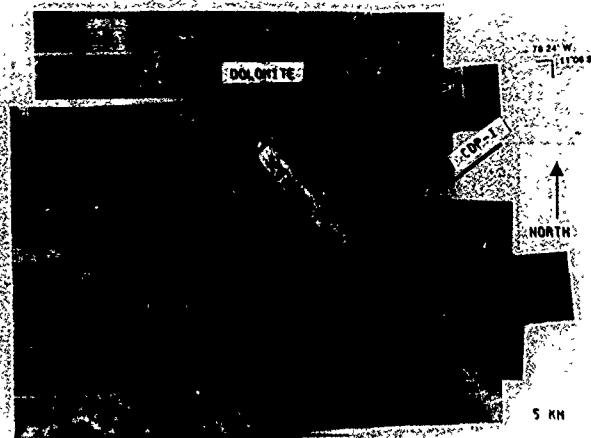


Plate 1a [Reed and Hussong], SeaMARC II side scan mosaic of Lima Basin. Black line shows position of seismic line CDP-1 with respect to the image.

the steep back side of the volcanic mound. Many other smaller mounds occur in the lower portion of the image. The large lava flow apparently crosses the transform fault scarp, which is downdropped to the upper right portion of the image.

Application of the GLCM textural analysis to the image first requires image subdivision into texels 250 in on a side, each containing 294 pixels. Each texel spans six pings and 19 pixels, so that there are 40 texels across the 10 km width

of the image and $N/6$ texels along track, where N is the number of pings in the image. In this example the image consists of approximately 420 pings, and thus a total of 2800 texels result from the subdivision. The pixels in each texel were re-quantized to 16 intensity levels by dividing the original intensity values by 16 and rounding to the nearest integer. Statistical texture signatures consisting of the means and ranges for the features ENT, ASM, CON, ISO, and AISM evaluated at look directions of 0° , 45° , 90° , and

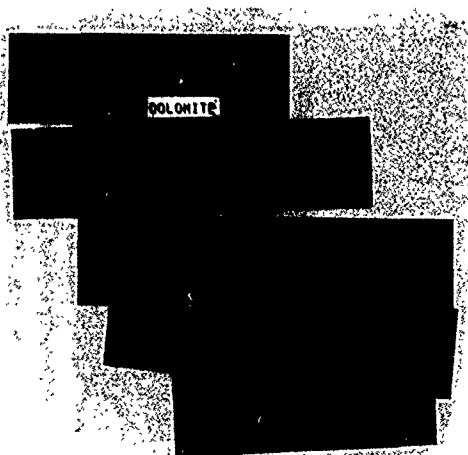


Plate 1b [Reed and Hussong] Three-class thematic map of mosaic shown in Plate 1a. A, B, C, D, E, F, G, H, I, J, K, L, M, N, O, P, Q, R, S, T, U, V, W, X, Y, Z, AA, AB, AC, AD, AE, AF, AG, AH, AI, AJ, AK, AL, AM, AN, AO, AP, AQ, AR, AS, AT, AU, AV, AW, AX, AY, AZ, BA, BB, BC, BD, BE, BF, BG, BH, BI, BJ, BK, BL, BM, BN, BO, BP, BQ, BR, BS, BT, BU, BV, BW, BX, BY, BZ, CA, CB, CC, CD, CE, CF, CG, CH, CI, CJ, CK, CL, CM, CN, CO, CP, CQ, CR, CS, CT, CU, CV, CW, CX, CY, CZ, DA, DB, DC, DD, DE, DF, DG, DH, DI, DJ, DK, DL, DM, DN, DO, DP, DQ, DR, DS, DT, DU, DV, DW, DX, DY, DZ, EA, EB, EC, ED, EE, EF, EG, EH, EI, EJ, EK, EL, EM, EN, EO, EP, EQ, ER, ES, ET, EU, EV, EW, EX, EY, EZ, FA, FB, FC, FD, FE, FF, FG, FH, FI, FJ, FK, FL, FM, FN, FO, FP, FQ, FR, FS, FT, FU, FV, FW, FX, FY, FZ, GA, GB, GC, GD, GE, GF, GG, GH, GI, GJ, GK, GL, GM, GN, GO, GP, GQ, GR, GS, GT, GU, GV, GW, GX, GY, GZ, HA, HB, HC, HD, HE, HF, HG, HH, HI, HJ, HK, HL, HM, HN, HO, HP, HQ, HR, HS, HT, HU, HV, HW, HX, HY, HZ, IA, IB, IC, ID, IE, IF, IG, IH, II, IJ, IK, IL, IM, IN, IO, IP, IQ, IR, IS, IT, IU, IV, IW, IX, IY, IZ, JA, JB, JC, JD, JE, JF, JG, JH, JI, JJ, JK, JL, JM, JN, JO, JP, JQ, JR, JS, JT, JU, JV, JW, JX, JY, JZ, KA, KB, KC, KD, KE, KF, KG, KH, KI, KJ, KK, KL, KM, KN, KO, KP, KQ, KR, KS, KT, KU, KV, KW, KX, KY, KZ, LA, LB, LC, LD, LE, LF, LG, LH, LI, LJ, LK, LL, LM, LN, LO, LP, LQ, LR, LS, LT, LU, LV, LW, LX, LY, LZ, MA, MB, MC, MD, ME, MF, MG, MH, MI, MJ, MK, ML, MM, MN, MO, MP, MQ, MR, MS, MT, MU, MV, MW, MX, MY, MZ, NA, NB, NC, ND, NE, NF, NG, NH, NI, NJ, NK, NL, NM, NN, NO, NP, NQ, NR, NS, NT, NU, NV, NW, NX, NY, NZ, OA, OB, OC, OD, OE, OF, OG, OH, OI, OJ, OK, OL, OM, ON, OO, OP, OQ, OR, OS, OT, OU, OV, OW, OX, OY, OZ, PA, PB, PC, PD, PE, PF, PG, PH, PI, PJ, PK, PL, PM, PN, PO, PP, PQ, PR, PS, PT, PU, PV, PW, PX, PY, PZ, QA, QB, QC, QD, QE, QF, QG, QH, QI, QJ, QK, QL, QM, QN, QO, QP, QQ, QR, QS, QT, QU, QV, QW, QX, QY, QZ, RA, RB, RC, RD, RE, RF, RG, RH, RI, RJ, RK, RL, RM, RN, RO, RP, RQ, RR, RS, RT, RU, RV, RW, RX, RY, RZ, SA, SB, SC, SD, SE, SF, SG, SH, SI, SJ, SK, SL, SM, SN, SO, SP, SQ, SR, SS, ST, SU, SV, SW, SX, SY, SZ, TA, TB, TC, TD, TE, TF, TG, TH, TI, TJ, TK, TL, TM, TN, TO, TP, TQ, TR, TS, TT, TU, TV, TW, TX, TY, TZ, UA, UB, UC, UD, UE, UF, UG, UH, UI, UJ, UK, UL, UM, UN, UO, UP, UQ, UR, US, UT, UU, UV, UW, UX, UY, UZ, VA, VB, VC, VD, VE, VF, VG, VH, VI, VJ, VK, VL, VM, VN, VO, VP, VQ, VR, VS, VT, VU, VV, VW, VX, VY, VZ, WA, WB, WC, WD, WE, WF, WG, WH, WI, WJ, WK, WL, WM, WN, WO, WP, WQ, WR, WS, WT, WU, WV, WW, WX, WY, WZ, XA, XB, XC, XD, XE, XF, XG, XH, XI, XJ, XK, XL, XM, XN, XO, XP, XQ, XR, XS, XT, XU, XV, XW, XX, XY, XZ, YA, YB, YC, YD, YE, YF, YG, YH, YI, YJ, YK, YL, YM, YN, YO, YP, YQ, YR, YS, YT, YU, YV, YW, YX, YY, YZ, ZA, ZB, ZC, ZD, ZE, ZF, ZG, ZH, ZI, ZJ, ZK, ZL, ZM, ZN, ZO, ZP, ZQ, ZR, ZS, ZT, ZU, ZV, ZW, ZX, ZY, ZZ.

135° and lag of length-1 were calculated for each of the texels. As no bottom samples were available to us, the 2800 five-dimensional texture vectors were classified in the unsupervised mode with our modified K-means clustering algorithm.

Clustering of these 2800 texture vectors into the six classes resulted in the thematic map shown in Figure 14. Note how the black texels delineate the general outline of the lava flow. Specifically, note the continuity of textural mapping across the ship's track in the flow, irrespective of the near-nadir average intensity variations in the side scan image (Figure 13), demonstrating one of the chief advantages of textural analysis, i.e., its immunity to misclassification due to spurious variations in intensity.

5.2. Texture Analysis of the Lima Basin

Despite the absence of a relationship between textural signature and intrinsic surface character, texture analysis thematic maps can be produced and the thematic units assigned to lithologies. A portion of a mosaic depicting part of the continental slope offshore of Peru referred to as the Lima Basin [Hussong et al., 1985] appears in Plate 1a. The lighter portions of the image represent unlithified, hemipelagic sediments. The darker areas represent lithified Neogene sediments, mostly micrites and dolomiticrites of varying degrees of lithification and brecciation [L. D. Kulm, personal communication, 1985]. The parallel and subparallel lineations striking N45°W are also outcrops of bedded micrites. Ground truth for the area comes from dredging [L. D. Kulm, personal communication, 1986]. Unfortunately, as the length of seafloor covered by most dredges was long in relation to the variation of outcrop type visible in the side scan image, and as the contents of most dredges were lithologically heterogeneous, most outcrops could not be correlated to specific samples. However, dredge MW85-11 sampled the dark outcrop, labeled "dolomite" in Plate 1a, and yielded only dolomiticrites, of generally a strongly brecciated character. Due to the "mixed bag" nature of the other dredges, we were limited to two definitive sample types: hemipelagic sediments cored from the sediment pond and the dredged dolomiticrite.

Textural analysis was conducted as described in section 5.1 for the areas of the image coincident with the bottom sample locations. Mean texture vectors consisting of the six statistics CON, ASM, ENT, ENR, COR, and ISO and their associated standard deviations were calculated from the texels in the vicinity of the samples. The entire mosaic was then subdivided into 250-m texels from which texture vectors were evaluated. The texels were classified in the supervised mode with the minimum-distance classifier (section 4.3). Those texels whose texture vectors were distinct from the mean vectors representing either dolomiticrite or hemipelagic sediments by more than twice the standard deviation of either class were lumped in a third category: anything else. The three categories of sediments, dolomiticrites, and anything else were assigned the colors of green, magenta, and yellow respectively, and their texels were colored accordingly. The result is shown in Plate 1b (Plate 1b is shown here in black and white. The color version can be found in the separate color section in this issue.) The oval basin containing the hemipelagic sediments is clearly outlined, as is the outcrop of dolomiticrite at its NW tip. Magenta texels

indicated several other possible outcrops of dolomiticrite, which might not have been either detected or discriminated from other dark outcrops on a visual basis.

Although the distribution of the magenta texels about the green oval gives the impression of a synclinal or anticlinal formation, multichannel seismic data collected in this area argue against this interpretation (Figure 15 [after Hussong and Wipperman, 1981]). The inflection point on the depth section (arrowed) where the strata change from landward dipping to seaward dipping, corresponds approximately with the eastern edge of the oval sediment pond seen in the side scan mosaic in Plate 1a. Consequently, the dark outcrops west of the pond which are mapped by magenta texels are the tops of landward dipping strata, stratigraphically lower than the dark outcrops similarly mapped to the east of the pond. The fact that texture analysis has mapped stratigraphically distinct outcrops as similar does not necessarily mandate that they be the same formation, but rather that they possess similar acoustic properties, in particular, roughness or induration.

5.3. Region Growing -- ReGATA

The texel, the basic unit upon which the analysis is based, is assumed to contain a subset of the image data which possesses only one homogeneous texture. The probability of spatial homogeneity of a randomly placed rectangle increases as the texel size decreases. For the GLCM to be a reasonable estimator of the image joint probability distribution, the texel should contain at least NG pixels, where NG is the number of gray levels to which the image is quantized (section 3.4). The texel therefore can neither be shrunk below a minimum size without compromising the textural analysis nor increased drastically without encountering an unacceptable number of mixels. As a compromise between spatial resolution controlled by texel size and resolution of textural features as controlled by the number of intervals to which the data are quantized, we have employed a texel measuring approximately 250 m on a side, containing 294 pixels quan-

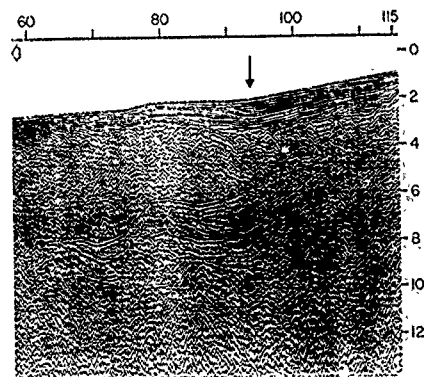


Fig. 15. Portion of CDP-1, a 24-channel common depth point seismic line gathered by Sensom Delta, Inc., as part of the Nazca Plate Project [Hussong and Wipperman, 1981].

tized to 16 gray levels. As the gray-scale recorders used for displaying the image data are capable of producing only 16 gray levels, of which human observers are rarely able to discern more than 8, texture analysis at this level is at or slightly above what is discriminable to the eye [Gregory, 1970].

In order to increase both the textural and spatial resolution, we have designed an image segmentation routine which incorporates semantics and image data. Rather than divide the image into a priori boxes which may or may not contain homogeneous patterns, we seek, via data-controlled decisions, a subdivision of the image into closed regions of limited spatial heterogeneity. One feature vector will then be used to represent each closed region. By allowing regions to grow to their natural boundaries, the probability of producing "mixels" is strongly reduced. As the regions will in general be larger than the previously used texels, classification time will be reduced concomitant with the reduction in number of feature vectors.

The following describes the implementation of Region Growing and Texture Analysis (REGATA), a bottom-up region-growing routine. SeaMARC II data are stored in records, line-interleaved-by-pixel. Two records, containing two pings of 984 port and 984 starboard pixels, are "read in." The data for port and starboard are subdivided into cells containing two lines of 16 pixels each. The mean intensity and variance are calculated for each of these 32-pixel cells. Two tests are then conducted. The first determines if the cell is reasonably homogeneous, in order to separate the cells into the categories of "region" and "boundary." Those cells which do not pass this test of limited heterogeneity are assumed to span two regions and hence are labeled as boundary cells. An option in the program allows these cells to be either flagged as nonregion cells or quartered and annexed to the most similar adjacent region. *Kelley and Landgrebe [1976]* propose a test which we utilize here, consisting of the ratio of the cell standard deviation to the cell mean. If this statistic falls above some heuristic threshold, the cell is labeled as a boundary. As sonar images are inherently noisy, this threshold should be fairly high to avoid the classification of the entire image as boundaries.

The second test is the basis of annexation and region growing. For purposes of illustration, the top of the image under consideration is labeled north. Cell classification and region growing proceeds west to east, and lines are read in north to south. Each classified cell has an associated flag which indicates its status as either a boundary or region cell. If it is a boundary cell, there is no need to compare it to the cell under consideration. If it is a region cell, it has associated with it the mean and variance of the region of which it is a member. This region can consist of one or more cells. The cell under consideration is compared to the region cells immediately adjacent in the west, northwest, north, and northeast directions. Comparison in these four directions minimizes imposition of boundary direction preferences within the limitations of the cell tessellation. The logic of the comparison is that if two cells are neighbors and possess similar average value, they probably represent a uniform, connected surface in the object plane and hence should be annexed and similarly classified.

The comparison can be on the basis of either a parametric Student's *t* test and *F* statistic, or the nonparametric minimally distant means, at the operator's discretion. As

region growing requirements must be reasonably lax to prevent classifications composed entirely of boundary cells, it is imperative that the cell be annexed to the most similar region which passes the second test and not just the first region to do so.

As a region grows, its mean and variance are recomputed, and the pixels within the annexed cell augment the four GLCMs associated with the region. After the last cell from the two lines currently in memory has been classified, all regions are checked for growth in the last iteration. If they have not grown, they are considered closed, and their associated GLCMs are submitted to a subroutine which extracts the standard six-dimensional texture feature vector. The texture vector and all the pixels in the region from which it was extracted are then assigned a region number and written out to a storage file.

When the routine terminates at the end of the data file, all remaining open regions are closed by the routine and analyzed for texture. The resulting list of region-numbered, feature vectors are submitted to an unsupervised cluster analysis. The region numbers map the regions to the feature vectors in the clusters, and all pixels in all regions with similarly clustered feature vectors are mapped similarly.

The benefits of this routine are threefold: computational speed, increased spatial resolution, and increased textural fidelity. We stated above without proof that there would be fewer regions resultant from this method than texels from the arbitrary division of the image. The intuitive proof for this lies in the definition of texel as the largest tessellation unlikely to transect image region boundaries. If the regions are allowed to grow to their natural boundaries, which the texels are designed to avoid intersection of, then the grown regions will be larger and fewer in number than those resulting from an arbitrary level subdivision of the image. Fewer regions mean fewer calls to the feature extraction subroutine and fewer vectors to classify. Furthermore, the algorithm requires but one pass through the data to produce a segmentation with texture vectors and requires only four lines of data in memory at any one time.

The cell dimension of 2 lines by 16 pixels results in a limiting resolution of approximately 80 m. This cell size was chosen because it allows quartering of the cells in the event of a boundary classification. The number of pixels, 32, also straddles the small sampling theory/large sampling theory boundary, so that parametric and nonparametric tests are approximately equally valid.

Finally, growing regions of limited heterogeneity minimizes the intercontamination of texture signatures by each other, or by boundaries, neither of which are likely to result in a representative signature. GLCMs from larger regions will contain more entries and hence will yield better estimates of image texture. By minimizing mixing and increasing estimate fidelity, the clusters formed in the unsupervised classification step should be tighter, resulting in better discriminant boundaries in the classification *n* space, and less confusion in the image plane.

One of the other benefits of the region growing method is that as the regions that result are in general larger than the previously used texels, the image need not be requantized to such a small number of gray levels. Specifically, regions often grow to contain hundreds to thousands of cells, each containing 32 pixels. If we analyze all closed regions for texture, but only use those with more than 100 cells for deter-

by lax-to-
y cells, it
y similar
the first

computed;
the four
cell from
sified, all
If they
eir associ-
h extracts
for The
n which it
nd written

data file,
outine and
numbered,
ed cluster
the feature
with simi-

computational
d textural
e would be
texels from
e proof for
tesselation
he regions
which the
the grown
hose result-
age. Fewer
subroutine
algorithm
e a segmen-
our lines of

its in a lim-
cell size was
n the event
is, 32, also
ing theory
in tests are

city minim-
res by each
ty to result
nger regions
better esti-
and increas-
unsupervised
g in better
space, and

ing method is
ger than the
quantized to
ally, regions
of cells each
ions for tex-
cells for data



Photo 2: Reed and Hussong. Three six, R-GATA map of five cells, image shown in Fig. 1, showing the "low frequency" or regions with lower than the mean frequency.

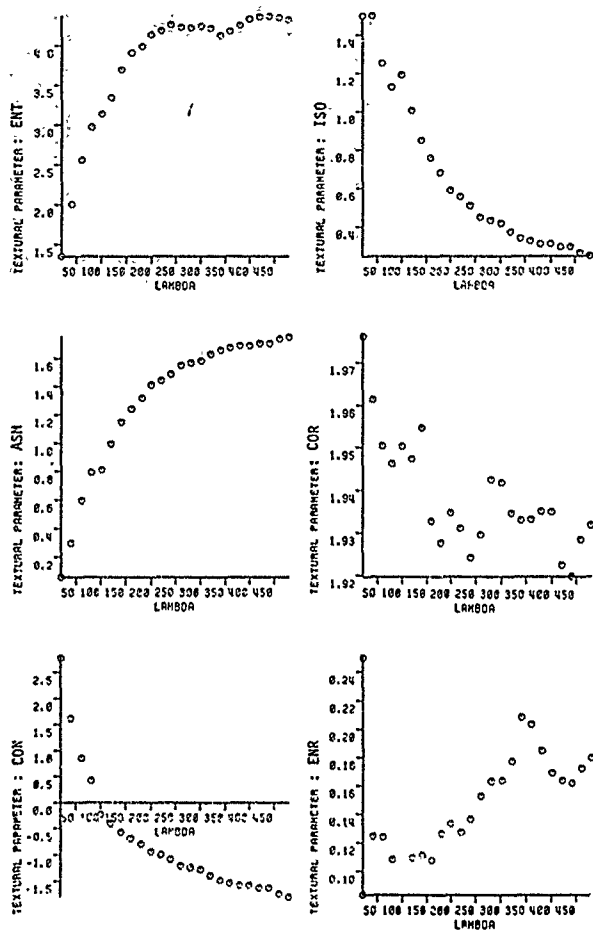


Fig. 16. Plots of the six textural parameters ASM, CON, ENT, ENR, AIDM, and ISO versus wavelength generated from analysis of synthetic side scan images [Reed, 1987]

mination of the cluster centroids, we can still classify the entire image, but with a fourfold increase in textural sensitivity

5.4 Application of ReGATA

In our application of ReGATA, the side scan image of the lava flow (Figure 13) was re-quantized to 64 gray levels and subdivided into cells containing 32 pixels, for which the average intensities and standard deviations were calculated. The nonparametric, minimally distant means rule was used for region growing, with annexation occurring if the regions differed in their means by three levels or less. All closed regions containing five or more cells were analyzed for tex-

ture and hence had associated with them the six-dimensional feature vector. In the cluster analysis which followed, only those regions containing 100 or more cells contributed to the determination of the class centroids. Those regions containing fewer than 100 cells were then placed into the class from which their feature vector was minimally distant.

Application of ReGATA to the side scan image of the lava flow and subsequent unsupervised classification yields three classes, green, purple, and blue, corresponding in the image to regions containing the lava flow and two classes of sediment, respectively (Plate 2) (Plate 2 is shown here in black and white. The color version can be found in the separate color section in this issue.) The purple appears to

correspond to the less reflective, possibly smoother sediment. The areas mapped as blue correspond to visually rougher sediments in the vicinity of the lava flow. In the original side scan image, these sediments appear darker, indicating either greater roughness or greater acoustic impedance. Possibly, the sediments near the flow are mixed with debris from the neighboring lava flow or expressing the roughness of some thinly buried previous flow. The blank areas correspond to either boundary cells or to unannexed regions containing less than five cells.

Support for the hypothesis that this texture map displays actual variations in intrinsic surface roughness is gained from comparisons of texture features with image wavelength [Reed, 1987]. Figure 16 shows plots of the six texture features discussed here (CON, ASM, ENT, ENR, COR, and ISO) against wavelength. The data were acquired from textural analysis of synthetic side scan images generated with known wavelengths. Reasonably single-valued relationships between texture and wavelength are predicted for the features CON, ASM, ENT, and ISO. The data in Table 1 show the values of these four texture features for the three classes in the thematic map (Plate 2). Comparison of the texture values in Table 1 with the plots in Figure 16 shows that each of the features CON, ASM, ENT, and ISO predict that wavelength should increase from the lava flow to the darker sediments to the lighter sediments. While no specific relationship has been proven between roughness and wavelength, Malinverno and Gilbert [1989] have shown that over the range of 1-10 km there exists an inverse linear relationship between the log of spatial frequency (wavelength) and the log of spectral density (for topographic profiles, roughness). If this relationship holds for the decimeter scales of wavelengths to which this texture analysis is sensitive, this implies roughness greater for the lava flow than either of the sediments, a conclusion consistent both with geologic intuition and our interpretation of the scattering behaviors of the lava flow and sediments.

The chief advantages of the three-class thematic map shown in Plate 2 over the six-class map in Figure 14 are the preliminary relative roughness prediction capability, increased spatial resolution of features such as the crenulations in the perimeter of the flow, and the distribution and shape of sedimented windows in the flow, plus the resolution in the three-class map of two categories of sediment. Computer time required for analysis and classification is also less for the ReGATA map. Implementation of the texture routine using the *a priori* texels required 45 minutes on a Harris model 800-2 computer. Implementation of the ReGATA routine required only eighty s. The image used for these benchmarks (Figure 13) consists of 240 pings of data, each containing 2k 8-bit pixels.

6. SUMMARY

Quantitative image processing techniques have been applied to a variety of SeaMARC II side scan sonar seafloor images. Image contrast has been enhanced via histogram manipulations. Simultaneously, undesirable operator-induced gain changes have been removed. Across-track spurious variations in image intensity due to inadequate correction of system beam pattern effects and irregular scattering properties of the bottom and overprinting due to surface reflections have been corrected by background sub-

TABLE 1. Texture Feature Vectors for the Features CON, ASM, ENT, and ISO and the Classes 1 (Sediment), 2 (Sediment), and 3 (Basalt).

	CON	ASM	ENT	ISO
Class 1	2.2994	0.0295	0.0050	1.1785
Class 2	2.0571	0.0414	0.0055	1.0540
Class 3	1.6743	0.0965	0.0125	0.8464

traction. Track-parallel linear features resulting from along-track aliasing of point reflectors have been migrated back to more appropriate dimensions. Total geometric correction based upon explicit knowledge of coregistered simultaneous bathymetric data produced images which are free of layover distortions and yield true representations of reflector position and morphology.

Application of the above techniques to a variety of imagery resulted in both superior images for subjective and computer-aided interpretations. Correlation of limited ground truth with image texture parameters has allowed first-order mapping of lithology distributions. Correlation of theoretical analysis with observed textural signatures has allowed relative prediction of surface roughnesses.

We regard these fundamental procedures for image processing and quantitative interpretation of SeaMARC II data to be the first steps in applying remote sensing techniques to seafloor swath-mapping data. Although the use of marine acoustic data, which are strongly influenced by the low speed of sound in water and susceptibility to ray path variations, is inherently more difficult than processing subaerial optical or radar images, we are confident that eventual increased quantification of seafloor data will permit widespread application of various airborne and satellite remote sensing techniques to the imaging and mapping of the seafloor.

Acknowledgments. We would like to thank Chris de Moustier and Bob Tye for thorough reviews of this manuscript. Financial assistance for this work and its publication was provided by Office of Naval Research contract N00014-87-K-181. This is Hawaii Institute of Geophysics contribution 2124.

REFERENCES

- Andrews, H. C., *Computer Techniques in Image Processing*, Academic, San Diego, Calif., 1968.
- Ballard, D. H., and C. M. Brown, *Computer Vision*, Prentice-Hall, Englewood Cliffs, N.J., 1982.
- Belderson, R. H., et al., *Sonographs of the Sea Floor*, American Elsevier, New York, 1972.
- Blackinton, J. G., D. M. Hussong, and J. Koslos, First results from a combination side scan sonar and seafloor mapping system (SeaMARC II), in *Offshore Technology Conference, OTC 4476* pp. 307-311, 1983.
- Brekhorshikh, L., and Yu. Lysanov, *Fundamentals of Ocean Acoustics*, Springer-Verlag, New York, 1982.
- Brodsky, P., *Textures: A Photographic Album for Artists and Photographers*, Dover, New York, 1966.
- Chavez, P. S., Automatic shading correction and speckle noise

- removal/mapping techniques for radar image data, in *Radar Geology, An Assessment*, JPL Pub 80-51, 251-264, 1980.
- Chavez, P. S., Processing techniques for digital sonar images from GLORIA, *Photogramm. Eng. Remote Sens.*, 52, 1133-1145, Aug. 1986.
- Chifford, P., Real-time seafloor mapping, *Sea Technol.*, 20, 22-26, 1979.
- de Moustier, C., Approaches to acoustic backscattering measurements from the deep seafloor, paper presented at *Symposium of Ocean Engineering*, Am. Soc. of Mech. Eng., New Orleans, Feb. 1986.
- Duda, R. O., and P. E. Hart, *Pattern Recognition and Scene Analysis*, Wiley-Interscience, New York, 1973.
- Faure, J. A., and W. B. F. Ryan, 3-D view of erosional scarps on U.S. continental margin, *Am. Assoc. Pet. Geol. Bull.*, 69, 722-732, 1985.
- Flemming, B. W., Side-scan sonar. A practical guide, *Int. Hydrogr. Rev.*, LIII (1), 65-88, 1976.
- Gregory, R. L., *Eye and Brain*, World University Library, London, 1970.
- Hagedoorn, J. G., A process of seismic reflection interpretation, *Geophys. Process.*, 2, 35-127, 1951.
- Haralick, R. M., K. Shanmugam, and I. Dinstein, Textural features for image classification, *IEEE Trans. Systems, Man, and Cybernetics*, SMC-3, 610-621, Nov., 1973.
- Hartigan, J. A., *Clustering Algorithms*, Wiley-Interscience, New York, 1975.
- Hord, M., *Digital Image Processing of Remotely Sensed Data*, Academic, San Diego, Calif., 1982.
- Hussong, D. M., and L. K. Wiperman, Vertical movement and tectonic erosion of the continental wall of the Peru-Chile trench near 11°30' S latitude, *Geol. Soc. Am. Mem.*, 154, 509-524, 1981.
- Hussong, D. M., T. B. Reed, W. A. Bartlett, K. L. Mansfield, B. Taylor, T. W. C. Hilde, and L. W. Kulm, SeaMARC II survey of the Peru trench and continental margin, *Eos Trans. AGU*, 66, 377, 1985.
- Kettig, R. L. and D. A. Landgrebe, Classification of multi-spectral image data by extraction and classification of homogeneous objects, *IEEE Trans. Geosci. Electron.*, GE-4, 19-20, 1976.
- Kinsler, L. E., A. P. Frey, A. B. Coppers, and J. V. Sanders, *Fundamentals of Acoustics*, John Wiley, New York, 1982.
- Laws, K. I., Textured image segmentation, Ph.D. dissertation, 176 pp. Dep. of Eng., Univ. of South Calif., Los Angeles, 1980.
- Lowenstein, C. D., K. A. Kastens, and F. N. Spiess, Display processing for side scan sonar images, in *Offshore Technology Conference*, OTC 3431, 1980.
- Luyendyk, B. P., E. J. Haje, and D. S. Simonett, Side-scan sonar mapping and computer aided interpretation in the Santa Barbara Channel, California, *Mar. Geophys. Res.*, 5, 365-388, 1983.
- Malinverno, A., and L. E. Gilbert, A stochastic model for the creation of abyssal hill topography at a slow spreading center, *J. Geophys. Res.*, 84, 1665-1675, 1989.
- Mok, J. G., Digital processing of remotely sensed images, *NASA Spec. Publ.*, SP491, 1980.
- Mudie, J., W. Normark, and E. Cray, Direct mapping of the seafloor using side scanning sonar and transponder navigation, *Geol. Soc. Am. Bull.*, 81, 1547-1554, 1970.
- Pace, N. G. and C. M. Dyer, Machine classification of sedimentary sea bottoms, *IEEE Trans. Geosci. Electron.*, GE-17, 52-56, 1979.
- Paluzzi, P., Analysis of imagery for marine resource exploration. Proceedings of Caltech/JPL Conference of Image Processing Technology, Data Sources, and Software for Commercial and Scientific Applications, JPL Spec. Publ., SP49-40, 12-1 to 12-9, 1976.
- Paluzzi, P., W. Normark, G. Hess, H. Hess, and M. Cruckshank, Computer image processing in marine resource exploration, in *Proceedings of Joint IEEE-MTS OCEANS'76 Conference*, Marine Technology Society, pp. 4D-1 to 4D-10, Washington, D.C., 1976.
- Pratt, W. K., *Digital Image Processing*, 614 pp., John Wiley, New York, 1978.
- Prior, D. B., J. M. Coleman, and L. E. Garrison, Digitally acquire undistorted side scan sonar images of submarine landslides, Mississippi River delta, *Geology*, 7, 423-425, 1979.
- Reed, T. B., IV, Digital image processing and analysis techniques for SeaMARC II side-scan sonar imagery, Ph. D. dissertation, Univ. of Hawaii, Honolulu, 1987.
- Reut, Z., N. G. Pace, and M. J. P. Heaton, Computer classification of seabeds by sonar, *Nature*, 314, 426-428, 1985.
- Rosenfeld, A., and A. C. Kak, *Digital Picture Processing*, Academic, San Diego, Calif., 1982.
- Sanders, J. E. and C. S. Clay, Investigating the ocean bottom with side-scanning sonar, in *Proceedings of 5th Symp. for Remote Sensing of the Environment*, pp. 520-517, Ann Arbor, Mich., 1968.
- Scholz, D., N. Fuhs, M. Hixson, and T. Akiyama, Evaluation of several schemes for classification of remotely sensed data: The parameters and performance, *Tech. Rep. LARS TR-041279*, La for Appl. of Remote Sens., Purdue Univ., West Lafayette Ind., 1979.
- Schowengerdt, R. A., *Techniques for Image Processing in Classification in Remote Sensing*, 249 pp., Academic, San Diego, Calif., 1983.
- Swain, P. H., and S. M. Davis (eds.), *Remote Sensing, The Quantitative Approach*, 396 pp., McGraw-Hill, New York, 1978.
- Teleki, P. G., D. G. Roberts, P. S. Chavez, M. L. Somers, and D. Twichell, Sonar survey of the U.S. Atlantic continental slope: Acoustic classification and image processing techniques, *Offshore Technology Conference*, OTC 4017, pp. 95-102, 1981.
- Tyce, R., Deep seafloor mapping systems -- A review, *Mar. Technol. Soc.*, 20, 4-16, 1986.
- Urick, R. J., *Principles of Underwater Sound*, 3rd ed., McGraw-Hill, New York, 1983.
- Walker, C. D. T., Development of a ground speed corrected side scan sonar display system, *Ultrasonics*, 16, 108-110, 1978.
- Wesza, J. S., C. S. Dyer, and A. Rosenfeld, A comparative study texture measures for terrain classification, *IEEE Trans. Systems, Man, and Cybernetics*, SMC-6, 269-285, 1976.
- T. B. Reed IV, Hawaiian Institute of Geophysics, 2525 Correa Road, Honolulu, HI 96822.
- D. M. Hussong, Seafloor Surveys International, 1221 Kapiolani Blvd., PH-40, Honolulu, HI 96814.

(Received October 21, 1987,
revised August 5, 1988,
accepted February 22, 1989)

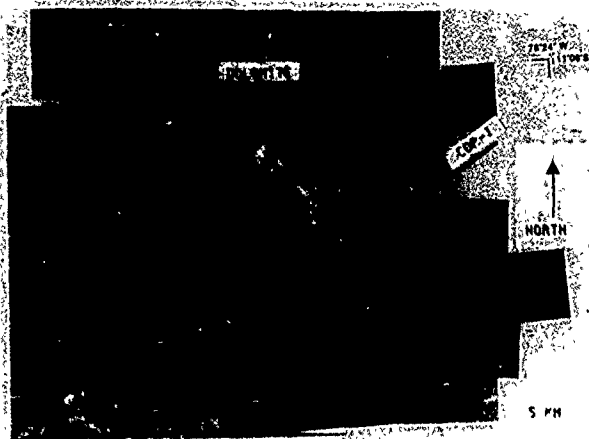


Plate 1a | *Reed and Hussong* | SeaMARC II side scan mosaic of Iana Basin. Black line shows position of seismic line CDP-1 with respect to the image

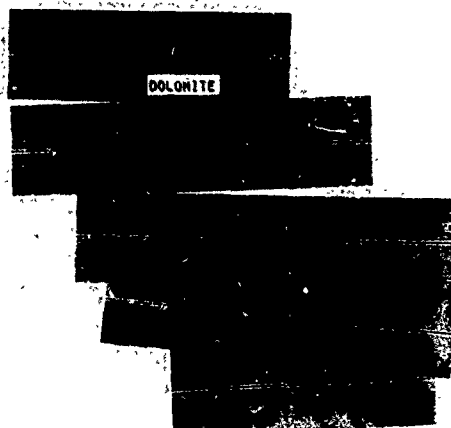


Plate 1b | *Reed and Hussong* | Three-class thematic map of mosaic shown in Plate 1a, generated as described in the text. (Color version of this figure can be found in the separate color section in this issue.)



Plate 2 | *Reed and Husong* | Three class RCGATA map of lava flow image shown in Figure 13. Pink cells correspond to either "boundary cells" or regions with fewer than five annexed cells. (Color version of this figure is available in the on-line color section of this issue.)

Contract: N00014-87-K-0181
Chemical Oceanography

Development of an In-situ Dissolved Hydrogen
Sensor for Marine Applications

Frank Sansone

GOALS

The goals of this study were to develop an in-situ sensor for measuring dissolved hydrogen in the marine environment, and to deploy the sensor in appropriate field tests. Such a sensor would be useful for detecting and mapping marine hydrothermal plumes, and could be used for studying other marine sources of hydrogen.

OBJECT

The near-term objectives of the project were to modify a commercially available fuel cell hydrogen sensor for underwater applications, and to use it to measure hydrogen in Hawaiian hydrothermal effluents. A primary field site was identified: the shoreline lava flows from Kilauea Volcano on the island of Hawaii. Sampling at this site was to combine the in-situ hydrogen measurements with analyses of other related chemical and physical parameters.

APPROACH

A Hydran 202 fuel cell hydrogen probe (Syprotec, Pt. Claire, Quebec, Canada) was modified used for use in these experiments. A 1-mil Teralon gas-permeable membrane was used for surface seawater applications. A 2-mil Teralon membrane was used for submerged applications, and was found to be suitable for depths to 2000 m. A picoammeter was used for monitoring the fuel cell's output signal. A 0-2 V analog output from the picoammeter was recorded with a battery-operated data logger. The hydrogen probe's thermistor was monitored and recorded with a second data logger. The fuel cell output current was calibrated at fixed temperatures by continuously flushing the probe with nitrogen/hydrogen mixtures of known composition and recording the output.

TASKS

The following tasks were completed during 1989: 1) the development of a prototype fuel cell sensor was completed; 2) this sensor was field tested in Pearl Harbor, Hawaii and in the waters surrounding the coastal lava flows near Kalapana, Hawaii; and 3) initial testing of an alternative sensor was completed (this sensor used a palladium-gated diode that offers greater sensitivity and faster response than the fuel cell).

RESULTS

The fuel cell sensor with a 1-mil thick gas-permeable Teralon membrane was found to have a detection limit of 10 nM dissolved hydrogen in seawater (signal/noise = 2); with a 2-mil thick membrane (used for operation at depths to 2000m) the detection limit was 15 nM. The diode sensor had a detection limit of less than 0.3 nM.

Chemical species were found to be enriched in the surface seawater plume immediately above the active underwater lava flows near Kalapana, Hawaii by the following factors: hydrogen, 15,000x ambient seawater concentrations, Mn, 75x; Cu, 6x; and Si, 5x. Water temperatures at this point reached 44°C. Lower concentrations and temperatures were observed in the surface plume with increasing distance from this point; hydrogen, Si, Mn, and Cu concentrations

were linearly related to seawater temperature. The composition of gas bubbles released during lava-seawater contact suggests that the elevated hydrogen was from the thermal dissociation of water, rather than from the release of magmatic gas. The figure shows the temperature and dissolved hydrogen distribution of the sea surface hydrothermal plume.

ACCOMP

The construction of prototype sensors successfully demonstrated the potential such instruments have for measurements of hydrogen in the marine environment. In addition, we have made the first comprehensive, integrated visual and chemical observations of direct lava-seawater interactions, which are gaining widespread recognition as major components in oceanic elemental cycles. Our Kalapana, Hawaii field site has proven to be an ideal means for examining these processes in detail.

Fuel cell hydrogen sensor for marine applications

Francis J. Sansone

*Oceanography Department, School of Ocean and Earth Science and Technology, University of Hawaii
at Manoa, 1000 Pope Road, Honolulu, HI 96822, USA*

(Received 19 February 1991; revision accepted 21 August 1991)

ABSTRACT

Sansone, F.J., 1992. Fuel cell hydrogen sensor for marine applications. *Mar. Chem.*, 37: 3-14.

A fuel cell sensor for measuring molecular hydrogen (H_2) in marine waters is described. The sensor has a detection limit of 10 nM, and has a 90% response time of 6 min when operated at 45°C, and 11 min when operated at 35°C. The sensor is particularly suitable for long-term monitoring of marine H_2 sources such as hydrothermal vents, and for real-time H_2 surveys. The utility of the instrument is demonstrated by real-time measurements of dissolved H_2 in a surface seawater hydrothermal plume resulting from coastal volcanism on the island of Hawaii.

INTRODUCTION

Seawater is close to equilibrium with atmospheric molecular hydrogen (H_2) in areas without significant local sources of H_2 ; bulk open-ocean concentrations are about 0.2-1.5 nM in the surface waters, and about 0.2-0.4 nM at depth (e.g. Herr and Barger, 1978; Herr et al., 1981; Bullister et al., 1982). However, dissolved H_2 has been shown to play an important role in a variety of biological processes in the marine environment. For example, H_2 can be produced and consumed by a number of aerobic aquatic organisms (e.g. Gray and Gest, 1965; Bullister et al., 1982), and is an important intermediate in the anaerobic oxidation of organic matter (e.g. Sansone and Martens, 1982; Scranton et al., 1984; Novelli et al., 1988).

H_2 is also known to be released to the ocean by submarine hydrothermal activity, although only a few measurements of H_2 concentrations in hydrothermal vent fluids have been reported. 'End-member' vent fluid H_2 concentrations in the range of 1-1700 μ M have been measured at the East Pacific Rise (Welhan and Craig, 1983; Lilley et al., 1983), the Galapagos Spreading Center (Lilley et al., 1983), and the Juan de Fuca Ridge (Lilley et al., 1989). In addition, H_2 concentrations up to 5.0 μ M have been reported for the surface hydrothermal plumes associated with coastal volcanism on the island of Hawaii (Sansone et al., 1990, 1991).

Bu

Go

Gre

Her

Her

Lak

Lille

fl

in

Lille

J.

Nove

19

Tc

Paus

an

50

Sanzo

me

Sanzo

sho

Sanzo

sea

173

Sato, A

Moi

Moi

Sato, M

alon

Res.

Schmid

pher

Scranto

gas II

Vielsich

501 p

Von Dar

Chem

moch

Welhan,

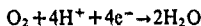
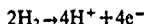
21 °N

Seafo

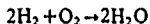
In the past, H_2 in seawater has been measured by gas chromatography in conjunction with Hg-reduction-UV-photometry detection (e.g., Sel and Seiler, 1970; Bullister et al., 1982). This method offers high sensitivity but requires the use of discrete samples and is consequently difficult for real-time analyses. In addition, its complexity limits its use for analyses. In this paper a method is described which allows the continuous measurement of H_2 in liquids and gases, and which can be used for long H_2 monitoring.

THEORY OF OPERATION

The fuel cell H_2 sensor described here is based on the platinum-catalyzed oxidation of H_2 coupled with reduction of O_2 (Vielstich, 1965)



The two half-cells involved in these reactions use a gelled 50% H_2SO_4 electrolyte, and are connected to an external circuit containing a load resistor. The overall reaction is



The resulting output current of the two half-cells, which is measured with a picoammeter, is proportional to the H_2 partial pressure within the cell. The proportionality is typically linear over six decades (see below).

A gas-permeable membrane is used to isolate the fuel cell from the sample. Because the fuel cell can consume H_2 faster than it diffuses through the membrane, the cell current is proportional to the diffusion rate through the membrane, which in turn is proportional to the H_2 partial pressure in the sample (either gas or liquid). The use of a thinner membrane, therefore, results in a larger output current than would a thicker one. The minimum practical membrane thickness is determined by the maximum hydrostatic pressure which will be subjected to.

Equation (1) indicates the need for a supply of O_2 for sensor operation. This O_2 can be supplied either by the samples being measured, or, in the case of anoxic samples, by a separate gas reservoir. The instrument used in this study contains an approximately 30 ml internal gas reservoir that can supply O_2 to the fuel cell during the analysis of O_2 -depleted seawater. After flushing with air, this reservoir is sufficient to allow sensor operation in seawater containing $1 \mu M H_2$ and no O_2 for several months.

The fuel cell's response is a function of cell temperature: higher temperatures result in faster detector response (as a result of faster membrane

larger cell output current, and greater sensitivity. For this reason, the sensor is operated at an elevated temperature (35–45°C) whenever practical. Fuel cell H_2 sensors have been used to analyze gases released from subaerial volcanic fumaroles and geological faults, thereby providing H_2 records extending for several weeks (Sato and McGee, 1982; Sato et al., 1986). Commercial fuel cell sensors are also used for monitoring H_2 in the cooling water of nuclear power reactors and in transformer cooling oil. The instrument described in this paper is a modification of this latter type of sensor.

MATERIALS AND METHODS

A Hydran 202 fuel cell H_2 sensor (Syprotec, Pointe Claire, Que., Canada) was used for these experiments (Fig. 1). The stainless steel sensor assembly is a cylinder of 6.7 cm length \times 6.5 cm diameter with a mass of 1.5 kg. The sensor was modified as follows for marine applications: the vent port to the external gas reservoir was threaded to allow the use of an Uniseal O-ring equipped sealing bolt (ABSCOA Div., AAR Hardware, Hawthorne, CA), and a Watermate underwater connector (Crouse-Hinds, Paramount, CA) was installed for the signal and thermistor outputs. The manufacturer reports the following molar response ratios for the reduced gases detected by the sensor: $CO/H_2=0.15$, $C_2H_2/H_2=0.08$, and $C_2H_4/H_2=0.01$.

A Toralox gas-permeable membrane of 25 μm thickness (Amoco Chemicals, Waltham, MA) was generally used for surface seawater applications, and a 50 μm Toralox membrane was used for submerged applications. A sensor with a 50 μm membrane was successfully tested in a hydrostatic chamber at a

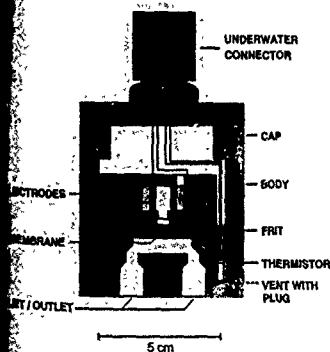


Fig. 1. Schematic diagram of the cross-section of the fuel cell hydrogen sensor.

pressure of 3000 psi (20 700 kPa) for 3 h, and at 1200 psi (8300 kPa) for 1 h; these pressures correspond to seawater depths of approximately 207 and 830 m, respectively.

The sensor was heated during non-submerged operations with a 100 V flexible silicone rubber heater (Belilove Co., San Leandro, CA) regulated by a model CN9111 digital temperature controller (Omega Engineered Stamford, CT). The heater was wrapped around the circumference of the sensor, secured with cable ties, and the assembly insulated with polyethylene (Bel-Art Products, Pequannock, NJ). The temperature controller used a K miniature thermocouple cemented to the outer surface of the sensor leading to monitor the cell temperature. This configuration allowed temperature control to $\pm 0.5^\circ\text{C}$ when analyzing gases or liquids of relatively constant temperature ($\pm 5^\circ\text{C}$). In the future we plan to use a temperature controller that can monitor the sensor's internal thermistor for better temperature regulation when surveying waters with large temperature gradients.

A 10 k Ω load resistor was used in series with the fuel cell, and a Keithley (Cleveland, OH) model 485 picoammeter was used to monitor the cell's output current. This picoammeter can operate for about 10 h on its internal batteries, which is convenient for field operations. The 0–2 V d.c. analog output of the picoammeter was recorded with a Rustak Ranger (Gulton Electronics, Greenwich, RI) battery-operated data logger equipped with a 0–2 V input module. The hydrogen sensor's internal thermistor was monitored and recorded with a second Rustak Ranger equipped with a thermistor module. The loggers have the capacity to store approximately 60 000 data points each.

Upper-ocean H_2 measurements used a deck-mounted peristaltic pump to collect samples from specific water depths and to transport the samples through the cell. The system was plumbed with polypropylene tubing of 1/4 inch diameter, and the pump was mounted upstream of the cell to prevent the possibility of a partial vacuum over the gas-permeable membrane. The water pumping rate was about 500 ml min⁻¹.

After data collection was completed, the loggers were brought ashore for data analysis and overnight recharging of the instrument batteries. Software supplied by the data logger manufacturer transfers the stored data from the loggers to an IBM-PC compatible computer for data storage, display, and analysis.

Because the sensor responds to the partial pressure of H_2 , it can be calibrated with either gas-phase or liquid-phase standards. Two pressure standards were used: 1% H_2 in air (Scott Environmental Technology, Bernardsville, NJ), and 25.1 ppm H_2 in N_2 (AIRCO, Murray Hill, NJ). Standards either were used directly or were diluted with H_2 -free N_2 in multiple-wall gas sampling bags (Calibrated Instruments, Ardsley, NY) and then transferred to the cell using a sampling pump (Accuhaler 80

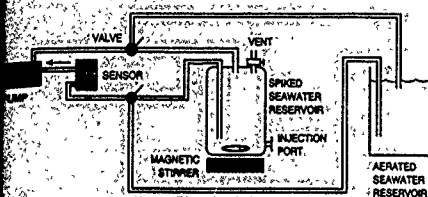


Fig. 2. Schematic diagram of the apparatus used to calibrate the sensor with aqueous solutions.

Scientific, Lincolnshire, IL). In either case, the sensor was held at a fixed temperature and flushed at a flow rate of 100 ml min^{-1} or more. The H_2 -free gas was prepared by passing 99.999% He through a CAT-01 catalytic combustion filter (Trace Analytical, Menlo Park, CA).

The above gas-phase calibration procedure was compared with liquid-phase standards prepared using the apparatus shown in Fig. 2. The latter allowed 5–100 μl volumes of H_2 gas standards to be injected via a septum into a 500 ml gas reservoir containing water recirculated through the cell. The water flow rate of about 500 ml min^{-1} was maintained by an SBE-5 centrifugal pump (Sea-Bird Electronics, Bellevue, WA), and a magnetic stirrer in the reservoir was used to keep the injected gas bubbles suspended until they were completely dissolved. Short lengths of polypropylene tubing (6.4 mm o.d., 0.8 mm wall) were used for all connections. Valves also allowed a 4 l volume of air-equilibrated seawater to be circulated. This apparatus allowed both sensor calibration and the measurement of sensor response times, the latter by producing step changes in H_2 concentrations in the seawater within the cell.

A modification of the GC method of Bullister et al. (1982) was used as an independent means of measuring H_2 in seawater. These analyses were made with a Varian (Palo Alto, CA) 3300 GC and an Hg-reduction-UV-photo-meter detector (RGD-2, Trace Analytical).

RESULTS

An example of gas-phase sensor calibration is shown in Fig. 3. It should be noted that the detector is linear over a concentration range of more than 10^3 . Operating at 35°C with a gas-permeable Torlon membrane of $50 \mu\text{m}$ thickness, the detection limit was 16 ppmv, which corresponds to a dissolved H_2 concentration in seawater of 10 nM at 23°C and 35 psu salinity (Gordon et al., 1977). The detection limit at this temperature with a membrane of $25 \mu\text{m}$ thickness was about 3 nM (data not shown).

A comparison of gas-phase vs. liquid-phase calibrations of the sensor is shown in Fig. 4. The liquid-phase calibrations were made at 23°C with 3.5%

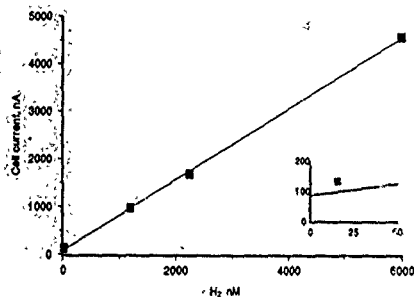


Fig. 3. Typical gas-phase calibration curve for the hydrogen sensor when operated at 35°C with a gas-permeable Teflon membrane of 50 μm thickness. Gas-phase concentrations have been converted to their equivalent equilibrium liquid-phase concentrations at 23°C and 35 psu salinity (Gordon et al., 1977). Points are data from individual analyses, line indicates the least-squares linear regression ($r^2 = 0.999$).

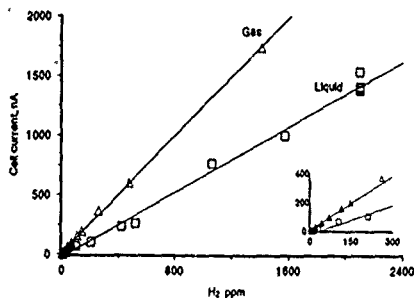


Fig. 4. Comparison of cell response using gas-phase (Δ) and liquid-phase (\square) standards. Liquid-phase concentrations have been converted to their equilibrium gas-phase concentrations at 23°C and 35 psu salinity (Gordon et al., 1977). Points are data from individual analyses, lines indicate least-squares linear regressions (gas: $\text{current} = (1.23 \times \text{concentration}) + 6.44$, $r^2 = 0.999$; liquid: $\text{current} = (0.682 \times \text{concentration}) - 26.3$, $r^2 = 0.994$).

aqueous NaCl using the apparatus shown in Fig. 2. There was a significant difference in the sensor response to gas and liquid standards with the same H_2 partial pressures, although the ratio of the two calibrations was constant over a wide range of H_2 concentrations. The latter suggests that the lower response with liquid standards was not due to simple H_2 losses from the cali-

ration apparatus, which would be expected to have proportionally larger effects at higher concentrations. It is likely that the liquid-phase calibrations reflect the effects of H_2 transfer resistance at the liquid-membrane interface as a result of the presence of an intervening liquid film layer. Such a layer would not be present during gas-phase calibrations, and should be inversely related to water velocity during liquid-phase operations (Lakshminarayanan, 1969).

Figure 5 shows cell response vs. fluid flow rate through the cell. The asymptotic increase in cell response with increased flow rate is consistent with the above-mentioned hypothesis of liquid film layer resistance. The results in Figs. 4 and 5 also demonstrate the need for accurate control of liquid flow rates during calibration and operation, and indicate that gas-phase calibrations require corrections before they can be used with liquid-phase samples. Nevertheless, the convenience of gas-phase standards makes them preferable for field calibrations.

In a separate experiment, the standard deviation for five replicate spiked seawater samples ($1.3 \mu M$) at $24^\circ C$ was 5%. The time for 90% response with a $50 \mu m$ membrane was 6 min when operating with a cell temperature of $45^\circ C$, and 11 min at $35^\circ C$; with a $25 \mu m$ membrane the 90% response time was 8 min at $40^\circ C$, 9 min at $30^\circ C$, 18 min at $20^\circ C$, and 24 min at $10^\circ C$ (data not shown).

Figure 6 illustrates the distribution of H_2 in the waters offshore of a shoreline lava flow at Kalapana, Hawaii, as measured in real time with a ship-board-operated sensor system. The H_2 isopleths in the figure were obtained with an automated contouring program (Surfer, Golden Software) using sen-

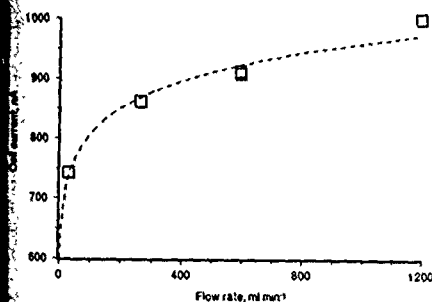


Fig. 5. Cell response vs. liquid flow rate through the cell. Data were collected using spiked tap water (about $600 \text{ nM } H_2$) with the apparatus shown in Fig. 2. Dashed line indicates power curve fit of the data (current = $573 \times \text{flow-rate}^{0.0746}$, $r^2 = 0.97$).

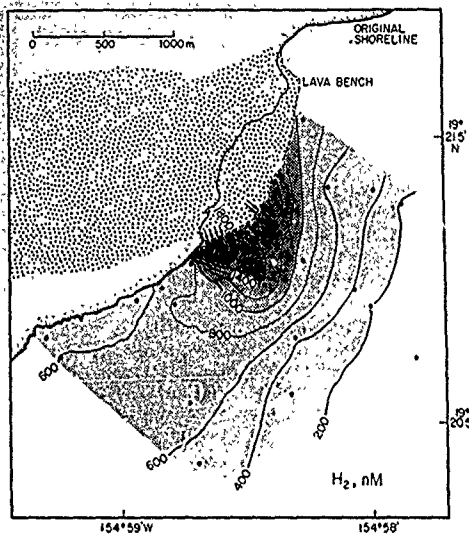


Fig. 6. Contour plot of dissolved H_2 in the surface seawater hydrothermal plume from coastal volcanism at Kalapana, Hawaii, on 23 September 1990. Concentration is computed using sensor readings at the hydrocast stations indicated by the closed circles. Contour interval is 200 nM. Arrows along the shore indicate sites of active lava entry in

the ocean. The H_2 concentrations shown in Fig. 6 are plotted vs. seawater temperature anomaly at the 29 sampling sites. The regression for these data (solid line) is similar to that obtained on previous occasions using GC analyses of surface seawater collected from hydrothermal plumes along this coastline (dashed line) (Sanson, 1990). Unfortunately, a GC detector malfunction prevented GC H_2 analyses of crete samples collected during the sensor operations for comparison with sensor results. Nevertheless, Fig. 7 demonstrates that the sensor results are comparable with those acquired by conventional methods.

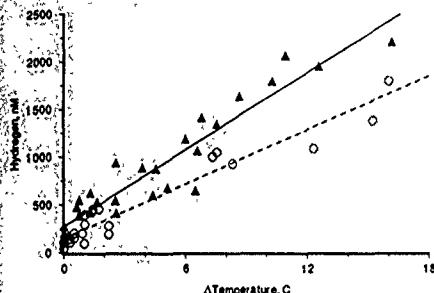


Fig. 7. ▲, Sensor-measured H_2 concentration vs. water temperature anomaly with respect to ambient offshore seawater at sites indicated in Fig. 6, solid line indicates least-squares linear regression ($H_2 = (134 \Delta T) + 276$, $r^2 = 0.90$). ○, Data from GC analyses of surface seawater collected from similar hydrothermal plumes along this coastline on three previous occasions during 1989–1990 (Sansone et al., 1992), dashed line indicates least-squares linear regression ($H_2 = (94.6 \Delta T) + 153$, $r^2 = 0.95$).

lower values obtained from GC analyses may reflect losses of H_2 during the 24–36 h storage period between sampling and analysis, a source of error that does not occur with real-time sensor analyses. This latter effect is likely to be particularly important for labile species such as H_2 .

DISCUSSION

The fuel cell H_2 sensor offers a number of advantages over the GC–mercury-reduction–UV-photometer method (Schmidt and Seiler, 1970) currently used for measuring dissolved H_2 in marine environments:

- (1) the capability for in situ analysis;
- (2) long-term stability (similar power plant monitors are recalibrated annually (C. Beauchemin, personal communication, 1989));
- (3) simple operation;
- (4) rugged construction;
- (5) moderate cost;
- (6) a lack of artifacts from sample collection, transport, storage, and manipulation.

A major advantage of this sensor over other reported H_2 sensors is its tolerance to hydrogen sulfide: it has been subjected to a H_2S -saturated aqueous solution for 30 h without loss of H_2 sensitivity (Pauss et al., 1990). Pauss et al. also reported that the sensor does respond to H_2S , albeit with a molar response ratio 2.1×10^4 times less than for H_2 . This level of interference should

be acceptable, for example, in the case of hydrothermal vents analyses. Assuming an average high-temperature hydrothermal vent end-member H_2S concentration of 7 mM (Von Damm et al., 1985), the sensor output would be elevated by the equivalent of 0.3 μM H_2 as a result of the sulfide interference. This is small compared with the 360–1700 μM H_2 concentrations measured in these vent end-members (Welhan and Craig, 1983).

Although the fuel cell sensor has a large dynamic range (about 10^6 , with an upper detection limit of about 5 mM), it cannot measure background oceanic H_2 concentrations (about 0.2–1.5 nM). Nevertheless, its detection limit of 10 nM at 35°C allows the measurement of even highly diluted hydrothermal plumes. As illustrated in Table 1, the high concentration of H_2 in end-member hydrothermal fluids relative to ambient seawater allows the fuel cell sensor to offer a usable dynamic range that is much superior to that of in situ temperature measurements and is nearly as large as those for shipboard methane, Fe and Mn measurements.

Two modes of H_2 sensor deployment are likely to utilize effectively its inherent advantages.

(1) Real-time in situ H_2 sensing on towed platforms and submersibles. This would be a direct application of the sensor described here. Such a system could prove valuable in the mapping of submarine hydrothermal vent systems (or other hydrogen sources) over large areas of the seafloor.

(2) Fixed location, real-time in situ sensor measurement of the temporal variability of hydrothermal systems. Such a system would need a means of controlling biofouling and the settling of hydrothermally produced particles

TABLE 1

A comparison of the usable dynamic ranges of hydrothermal vent sensing systems suitable for real-time or near-real time analyses

Parameter	Vent water composition	Ambient composition	Analytical precision	Usable dynamic range
Temperature (low-T vent)	30°C	4°C	0.005°C	5.2×10^3
Temperature (high-T vent)	350°C	4°C	0.005°C	6.9×10^4
Silica	16–20 μM	0.16 μM	0.002 μM	$(7.2-9.9) \times 10^3$
Methane	50–1400 μM	1 nM	0.1 nM	$(0.05-1.4) \times 10^7$
Iron	750–1660 μM	0.001 μM	0.00002 μM	$(3.7-8.3) \times 10^7$
Manganese	700–1000 μM	0.001 μM	0.00002 μM	$(3.5-5.0) \times 10^7$
Hydrogen	1–1700 μM	10 nM*	1 nM	$(0.001-1.7) \times 10^6$

Usable dynamic range = (vent water composition – ambient water composition) (or detection limit, if higher)) ÷ analytical precision. Vent water chemical composition data are for the East Pacific Rise (Welhan and Craig, 1983; Lilley et al., 1983; Von Damm et al., 1985) and the Juan de Fuca Ridge (Lilley et al., 1989).

*Detection limit of sensor

within the cell. A possible approach is the use of an ultrasonic transducer mounted within the sensor's sample cavity that would be activated at fixed intervals to dislodge attached material. This technique has been successfully used to control biofouling on in situ instruments used for estuarine pollution monitoring (R. Wollast, personal communication, 1990).

The use of a submerged sensor on towed platforms or fixed monitoring stations would require the use of signal-processing electronics mounted in a pressure case. Miniaturized electronics suitable for installation in a pressure case of 8.5 cm diameter are currently being built in the author's laboratory. This equipment uses a miniature picoammeter (Keithley model 18000-20) together with custom circuits for power supply and range control. Details will be provided in a later paper.

CONCLUSIONS

Although there is widespread interest in in situ chemical sensors for marine applications, there remain very few available for oceanographic use. The fuel cell H_2 sensor offers distinctive advantages and a few disadvantages for marine applications. On the positive side, the sensor is available at relatively moderate cost, is suitable for submersible applications, is not adversely affected by hydrogen sulfide, shows good long-term stability, and can provide near real-time measurements of H_2 concentrations. On the negative side, the sensor suffers from a relatively slow response, and an inability to measure accurately background (air-equilibrated) concentrations.

This sensor seems best suited for monitoring elevated H_2 concentrations at fixed sampling points, such as long-term in situ measurements of hydrothermal vent fluid composition. Other possible applications include deployment on research submersibles, where low-speed maneuvering is common, and operation from surface vessels under way at relatively low speeds. These applications could provide unique opportunities to advance significantly our understanding of the temporal and spatial variability of marine hydrothermal systems.

ACKNOWLEDGMENTS

Claude Beauchemin and Jean-Pierre Gibeault of Syprotec Inc. provided valuable assistance with the fabrication of the modified sensor. I also thank Thoi Nguyen, Christine Andrews, Susan Huang, Gordon Tribble, Raymond Kawamoto and Joe Resing for help with laboratory and field operations. This research was supported by the US Office of Naval Research (grants N00014-87-K-0181 and N00014-90-J-1805). This paper is SOEST Contribution 2625.

REFERENCES

- Bullister, J.L., Guinasso, N.L. and Schink, D.R., 1982. Dissolved hydrogen, carbon monoxide, and methane at the CEPEX site. *J. Geophys. Res.*, 87: 2022-2034.
- Gordon, L.I., Cohen, Y. and Standley, D.R., 1977. The solubility of molecular hydrogen in seawater. *Deep-Sea Res.*, 24: 937-941.
- Gray, C.T. and Gest, H., 1965. Biological formation of molecular hydrogen. *Science*, 148: 186-192.
- Herr, F.L. and Barger, W.R., 1978. Molecular hydrogen in the near-surface atmosphere and dissolved in waters of the tropical North Atlantic. *J. Geophys. Res.*, 83: 6199-6205.
- Herr, F.L., Scranton, M.I. and Barger, W.R., 1981. Dissolved hydrogen in the Norwegian Sea: mesoscale surface variability and deep-water distribution. *Deep-Sea Res.*, 28A: 1001-1016.
- Lakshminarayanaiah, N., 1969. *Transport Phenomena in Membranes*. Academic Press, New York, pp. 129-135.
- Lilley, M.D., Baross, J.A. and Gordon, L.I., 1983. Reduced gases and bacteria in hydrothermal fluids: the Galapagos Spreading Center and 21°N East Pacific Rise. In: P.A. Rona, K. Bostrom, L. Laubier and K.L. Smith, Jr. (Editors), *Hydrothermal Processes at Seafloor Spreading Centers*. Plenum, New York, pp. 411-449.
- Lilley, M.D., Baross, J.A., Butterfield, D.A., Olson, E.J., McDuff, R.E., Macko, S.A., Welhan, J.A. and Dahm, C.N., 1989. Volatiles in Endeavor vent fluids. *EOS*, 70: 1163.
- Novelli, P.C., Michelson, A.R., Scranton, M.I., Banta, G.T., Hobbie, J.E. and Howarth, R.W., 1988. Hydrogen and acetate cycling in two sulfate-reducing sediments: Buzzards Bay and Town Cove, Mass. *Geochim. Cosmochim. Acta*, 52: 2477-2486.
- Pauss, A., Guiot, S. and Beauchemin, C., 1990. Continuous measurement of dissolved H₂ in an anaerobic reactor using a new hydrogen/air fuel cell detector. *Biotechnol. Bioeng.*, 35: 492-501.
- Sansone, F.J. and Martens, C.S., 1982. Volatile fatty acid cycling in organic-rich marine sediments. *Geochim. Cosmochim. Acta*, 46: 1575-1589.
- Sansone, F.J., Tribble, G.W., Kelly, K.M., Resing, J.A., Sedwick, P. and Hon, K., 1990. Near-shore lava-seawater interactions at Kupapeu Point, Hawaii. *EOS*, 71: 144.
- Sansone, F.J., Resing, J.A., Tribble, G.W., Sedwick, P., Kelly, K.M. and Hon, K., 1991. Lava-seawater interactions at shallow-water submarine lava flows. *Geophys. Res. Lett.*, 18: 1731-1734.
- Sato, M. and McGee, K.A., 1982. Continuous monitoring of hydrogen on the south flank of Mount St. Helens. In: P.W. Lipman and D.R. Mullineaux (Editors), *The 1980 Eruptions of Mount St. Helens*, Washington. U.S. Geol. Surv. Prof. Paper, 1250: 209-219.
- Sato, M., Sutton, A.J., McGee, K.A. and Russell-Robinson, S., 1986. Monitoring of hydrogen along the San Andreas and Calaveras faults in central California in 1980-1984. *J. Geophys. Res.*, 91: 12 315-12 326.
- Schmidt, U. and Seiler, W., 1970. A new method for recording molecular hydrogen in atmospheric air. *J. Geophys. Res.*, 75: 1713-1716.
- Scranton, M.I., Novelli, P.C. and Loud, P.A., 1984. The distribution and cycling of hydrogen gas in the waters of two anoxic marine environments. *Limnol. Oceanogr.*, 29: 993-1003.
- Vielstich, W., 1965. *Fuel Cells* (English translation by D.J. Ives). Wiley-Interscience, London, 501 pp.
- Von Damm, K.L., Edmond, J.M., Grant, B., Measures, C.I., Walden, B. and Weiss, R.F., 1985. Chemistry of submarine hydrothermal solutions at 21°N, East Pacific Rise. *Geochim. Cosmochim. Acta*, 49: 2197-2220.
- Welhan, J.A. and Craig, H., 1983. Methane, hydrogen, and helium in hydrothermal fluids at 21°N on the East Pacific Rise. In: P.A. Rona et al. (Editors), *Hydrothermal Processes at Seafloor Spreading Centers*. Plenum, New York, pp. 391-409.

AN APPLICATION OF
THE HYDROGEN SENSITIVE PALLADIUM-INSULATOR-SEMICONDUCTOR DIODE
TO MARINE ENVIRONMENTAL STUDIES WITH CIRCUIT DESIGNS

A THESIS SUBMITTED TO THE GRADUATE DIVISION OF THE
UNIVERSITY OF HAWAII IN PARTIAL FULFILLMENT
OF THE REQUIREMENTS FOR THE DEGREE OF

MASTER OF SCIENCE
IN
ELECTRICAL ENGINEERING

MAY 1990

BY
Susan Shu-Te Huang

Thesis Committee:

Shu Lin, Chairman
Kazutoshi Najita
Francis Sansone

CHAPTER VIII

CONCLUSION

The Pd-MIS diode experiments conducted in a controlled environment have been completed; the current-to-voltage converters have been built; the underwater hydrogen sensor has been designed. Both the palladium metal insulator semiconductor diode and the fuel cell hydrogen sensor detect background concentration of hydrogen in terms of current across the sensors. The diode's currents resulting from the presence of hydrogen in the environment are in the approximate range of $10\ \mu\text{A}$ to $25\ \text{mA}$, whereas the current across the fuel cell lies approximately in the range of $10\ \text{pico amperes}$ ($1\ \text{pA} = 10^{-12}\ \text{A}$) to $100\ \text{nano amperes}$ ($1\ \text{nA} = 10^{-9}\ \text{A}$). It is much easier to measure and detect current in the μA range rather than in the pA range.

The currents in the range of mA to μA are relatively small. Before we transmit these signals through an underwater cable it is necessary to convert these weak currents to higher voltage signals (e.g. in the range of 0 to 2 volts). Generally, we prefer transmission of large signals to small signals because larger signals suffer less from the noise of the transmission medium.

By properly designing the current-to-voltage converter circuits and selecting the suitable electronic components, I was able to build these circuits in miniature.

Skill, caution and patience are required, to successfully solder these circuits on small predrilled boards. The soldered circuit together with the batteries can fit inside a steel pressure cylinder 3

in diameter and 5 inches high.

I suggest that, as future research in developing this underwater palladium hydrogen sensor, one should attempt to build the heater and the diode together; then the heater can be powered by the same batteries as the current-to-voltage converter. In addition, one should try to ease the instability and aging problems of the Pd device due to hydrogen induced drift (HID) and blister formation on the Pd surface. In order to eliminate the HID phenomenon, one can introduce a thin layer of alumina between the palladium gate and the silicon dioxide. Reducing the blister formation can be achieved by increasing the thickness of the Pd film.

TASK IV: CHEMICAL OCEANOGRAPHY

Subtask IV-A

Sub-task: Development of a In-Situ Dissolved Hydrogen Sensor for Marine Applications, Contract No. N00014-87-K-0181

Principal Investigator: Francis J. Sansone
Social Security No.: 375-46-9906
Telephone: (808) 948-8370

SUMMARY OF RESEARCH (3/1/88 - 9/20/88)

Design, Fabrication, and Testing of Improved Sensor

The fuel cell sensor has been improved in several respects (Figure 1A), the details of which are described below.

Greater sensitivity - We have increased the sensor's sensitivity by 1) using a Keithley picoammeter to measure the cell output current, rather than continuing to use a conventional shunt-type ammeter, and 2) using an optimal fuel cell from the vendor's inventory, rather than selecting it randomly. The minimum detectable limit is now 4 nM, as compared to a limit of 15 nM in our original instrument. Linear response continues to exceed five orders of magnitude.

Improved vent port sealing - We have had problems with leaks in the vent port when operating at elevated pressures. We now use a sealing screw with an integral o-ring and teflon washer (Abscoa "Uni-Seal" fastener). This modification appears to have solved the leakage problems.

Preparation of Sensor Systems for Submersible Deployment

Considerable time has been spent developing the sub-systems needed to deploy the sensor on the research submersible *PISCES V* (Figure 2A). This work is described below.

Data logger - We have determined that Rustrak Ranger handheld data loggers offer the best balance of features for our application. These instruments use rechargeable batteries, have four input channels which can handle a variety of signals, and easily transfer their data to microcomputers.

Ancillary systems - Several subsystems needed to be built for field operations. These included a power supply for the pump, underwater cables and connectors, and seawater plumbing. In addition to fabrication, these subsystems required testing and integration with the complete system.

Development of operational procedures - A variety of procedures were developed for field installation, operation, and calibration of the sensor. These procedures were tested during field operations (see below)

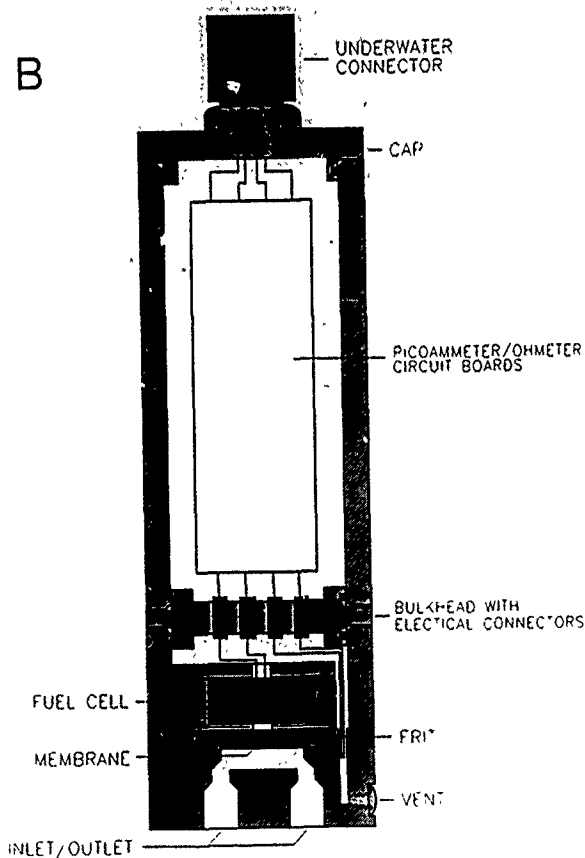
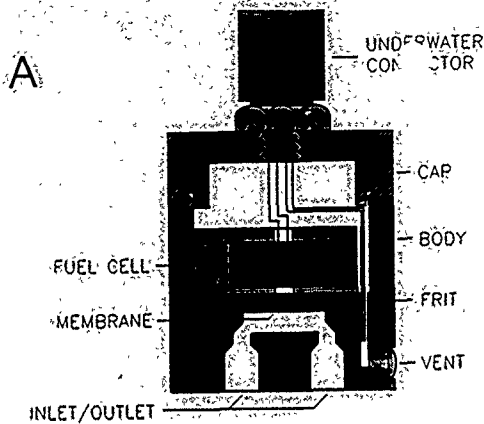


Figure 1. A) Cross-section schematic diagram of fuel cell hydrogen sensor; width of the sensor body is 2.5 inches. B) Modified sensor with integrated picoammeter/ohmmeter for use with Sea-Cat profiler/multiplexer.

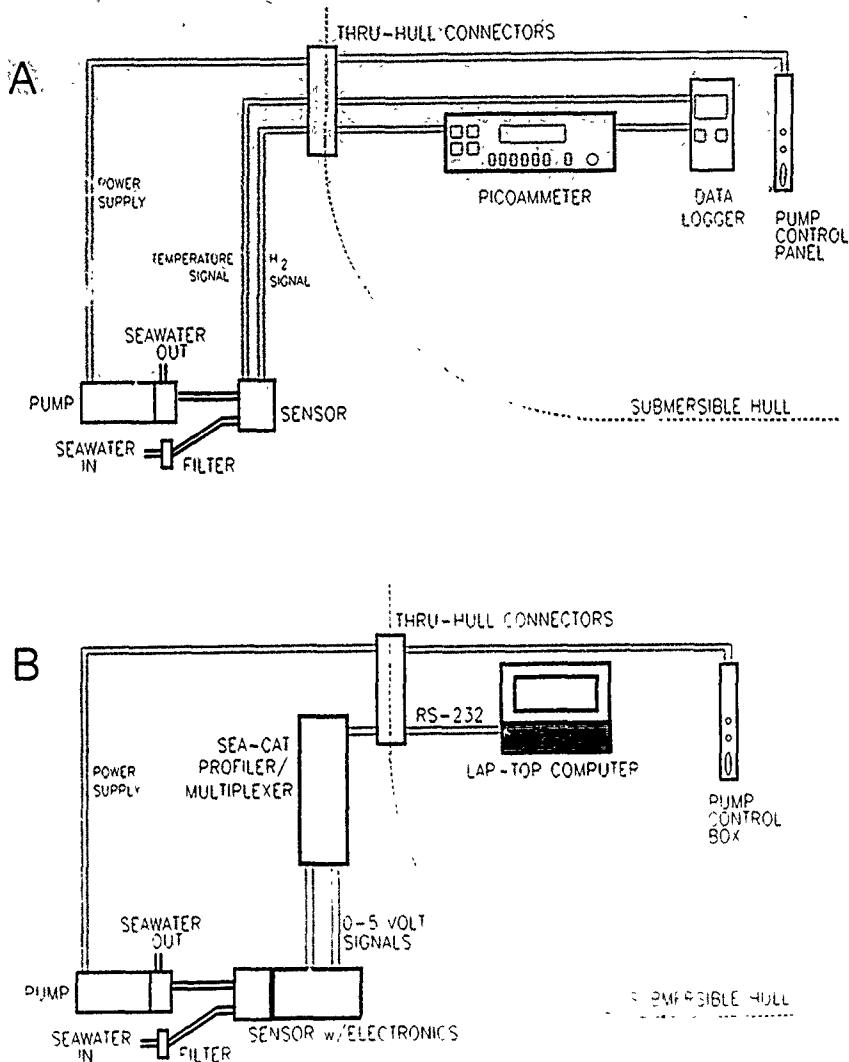


Figure 2. A) The present method of deploying the hydrogen sensor on PISCES V. B) Planned configuration of hydrogen sensor interfaced with Sea-Cat profiler/multiplexer on PISCES V.

Lab Testing

Pressure testing - Pressure tests of the sensor systems were conducted at the Engineering Support Facility, Hawaii Institute of Geophysics. These tests indicated that 2-mil thick membrane are the thinnest usable to depths of 2000 m. These tests also identified the vent port as the site most likely to leak under pressure; subsequent design changes have eliminated this problem (see above).

Calibration and linearity testing - As stated previously, these tests have indicated near-background sensitivity and a wide dynamic range for both gas mixtures and seawater. The latter experiments required the construction of a test rig for creating and circulating dilute seawater hydrogen standards. This apparatus is illustrated in Figure 3.

Response time measurement - The above-described test rig was also used to examine the response time of the system. During system optimization we have reduced the time for 90% response from 15 minutes to approximately 10 minutes.

Temperature effects - We have recently begun using a thermostated version of the apparatus shown in Figure 3 in order to determine accurately the temperature dependence of the sensor response.

Field Testing

Initial submersible deployment, Kailua-Kona, Hawaii - An initial deployment of the sensor system aboard PISCES V was conducted in July in order to determine the suitability of the system for field operations. This test was successful, and allowed planning for further field deployments.

Loihi Seamount, Hawaii - During the period of 23-30 September 1988 we plan to use the sensor system to examine the hydrogen content of hydrothermal plumes at Loihi Seamount, Hawaii. These PISCES-based deployments should result in scientifically useful data, an initial report on these dives will be given at the AGU Fall Meeting.

WHOI Workshop on Marine In-Situ Sensors

The PI was invited to participate in a workshop entitled "In-Situ Chemical Sensors for Detecting and Exploring Ocean Floor Hydrothermal Vents", which took place on June 28-29 1988 at the Woods Hole Oceanographic Institution. The workshop was sponsored by a grant from the Mellon Foundation. The activities of the hydrogen sensor project were discussed during a 15 min invited presentation by the PI.

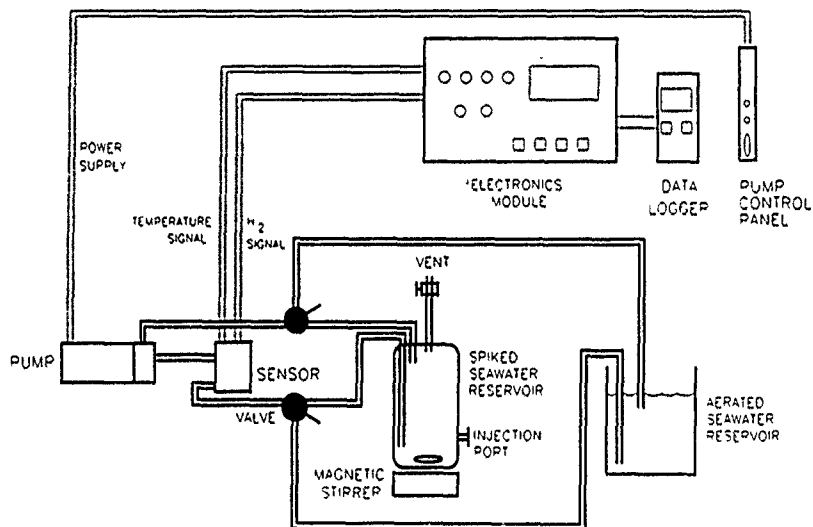


Figure 3. Apparatus used to measure the detector linearity and response rate with seawater.

Development of an In-situ Dissolved Hydrogen Sensor for Marine
Applications
1988-89

A. PROJECT SUMMARY

A commercial fuel cell sensor has been modified for use as an *in situ* monitor of dissolved hydrogen in seawater. The current project is conducting initial laboratory testing of the sensor, and will be performing preliminary field testing aboard the research submersible *PISCES V* in February 1988 during dives on the hydrothermal vents at Loihi Seamount off the Island of Hawaii. Additional funding is requested for further laboratory and field experiments to determine the potential of the fuel cell hydrogen sensor for marine applications. Laboratory experiments will include tests of sensor linearity, and the effects of temperature and hydrostatic pressure on sensor response. Submersible dives will aim to produce a three-dimensional map of hydrogen distribution around the summit of Loihi. We will also investigate the following means of improving the sensitivity of the instrument: improvements in the sensitivity and stability of the electronics, operation of the sensor at a fixed elevated temperature, and the use of a thinner gas-permeable membrane in the sensor.

B. INTRODUCTION

Although H_2 is known to be a major intermediate in aquatic and sedimentary biogeochemical cycles (e.g., Gest 1954, Gray and Gest 1965, Oremland 1983), only a very limited amount of research has been reported on biogeochemically-produced dissolved H_2 in aerobic seawater (Herr and Barger 1978, Herr et al. 1981, Bullister et al. 1982, Scranton et al. 1982), anoxic seawater (Scranton et al. 1984), and marine sediments (Novelli et al. 1987). This work has indicated that H_2 is released to seawater during bacterial and algal activity, and may serve as an indicator of these processes. In addition, relatively large amounts of H_2 are released during the corrosion of metals. Research in these areas has been significantly constrained by analytical difficulties; the analyses presently require complicated procedures using complex instrumentation (Schmidt and Seiler 1970) because of the very low concentrations involved (<1 nM in seawater, and 2-60 nM in marine sediments).

Hydrogen has also been measured in gases released from terrestrial volcanic fumaroles and geological faults (Sato and McGee 1982, Sato et al. 1986) using a fuel cell sensor similar to that proposed here, but this approach has not been used in other scientific disciplines. Measurements of H_2 in submarine hydrothermal fluids (Lilley et al. 1983; Welhan and Craig 1977, 1983) have been thus far restricted to samples collected very near the sources of hydrothermal fluids; H_2 concentrations in undiluted hydrothermal fluids are reported to be approximately 350-1700 μM .

This project aims to test and optimize a prototype instrument for the purpose of examining the utility of fuel cell sensors for real time *in situ* measurement of dissolved H_2 in the marine environment. The proposed technique will utilize a miniature fuel cell sensor that has

recently been developed for the nuclear power industry, but has heretofore not been used for environmental analysis.

The fuel cell H_2 sensor offers a number of advantages over the gas chromatograph/mercury-reduction/photometer method (Schmidt and Seiler 1970) currently used for measuring dissolved H_2 in marine environments:

- 1) capability for *in situ* analysis
- 2) very large dynamic range (upper concentration limit is 100 cc/kg)
- 3) long term stability (power plant monitors are recalibrated annually)
- 4) simple operation
- 5) lack of artifacts from sample collection, manipulation and storage.

There are two major limitations of the existing fuel cell sensor for marine applications:

- 1) the detection limit is currently approximately 15 nM
- 2) the detector currently requires approximately 3 min for a stable reading at high concentrations, although the instrument responds nearly instantaneously to changes in H_2 concentration; the response is presently 2-4 times slower at maximum sensitivity.

Despite the limitations noted above, the fuel cell sensor has the potential for considerable utility as a means of detecting the presence of hydrothermal fluids in seawater. Table 1 compares the relative usefulness of three key indicators: temperature (platinum resistance thermometry), methane (gas chromatography with flame ionization detection), and hydrogen (using existing and optimized fuel cell sensors). Even with existing fuel cells, hydrogen sensing is superior to temperature measurement of low temperature vents such as at Loihi; with an optimized fuel cell, hydrogen sensing has the potential to greatly exceed the capabilities of temperature and methane detection. The capability of *in situ* measurement makes hydrogen sensing even more advantageous.

C. RESULTS FROM CURRENT ONR SUPPORT

Instrument Description

Figure 1 shows a schematic diagram of the sensor system that was designed, built, and assembled as part of the current ONR project. The system consists of two main sub-systems: a) a submersible sensor/pump package mounted on an aluminum baseplate (Figure 2), and b) an electronics/data-logger/pump-control assembly designed for mounting in a standard electronics rack (Figure 3)

The Hydran 202 hydrogen sensor is pressure rated at 4000 psi by its manufacturer (Syprotec, Tampa, FL), which is well in excess of the 1300 psi hydrostatic pressure at the depth of the Loihi summit (approximately 1000 m). The sensor has been fitted with an underwater electrical connector, and is wired to the electronics package mounted

Table 1. A comparison of the usable dynamic range of hydrothermal vent sensing systems. Usable dynamic range = (vent water composition - ambient water composition (or detection limit, if higher)) ÷ analytical precision. Vent water methane and hydrogen composition data are for the East Pacific Rise (Whelan and Craig 1983).

Parameter	Vent water composition	Ambient composition	Analytical precision	Usable dynamic range
Temperature (low T vent)	30 C	4 C	0.005 C	5.2×10^3
Temperature (high T vent)	350 C	4 C	0.005 C	6.9×10^4
Methane	50-65 μ M	1 nM	0.1 nM	$5.1-6.5 \times 10^5$
Hydrogen (present instrument)	360-1700 μ M	15 nM (detection limit)	10 nM	$0.4-1.7 \times 10^5$
Hydrogen (optimized instrument)	360-1700 μ M	0.3 nM	0.03 nM	$1.2-5.7 \times 10^7$

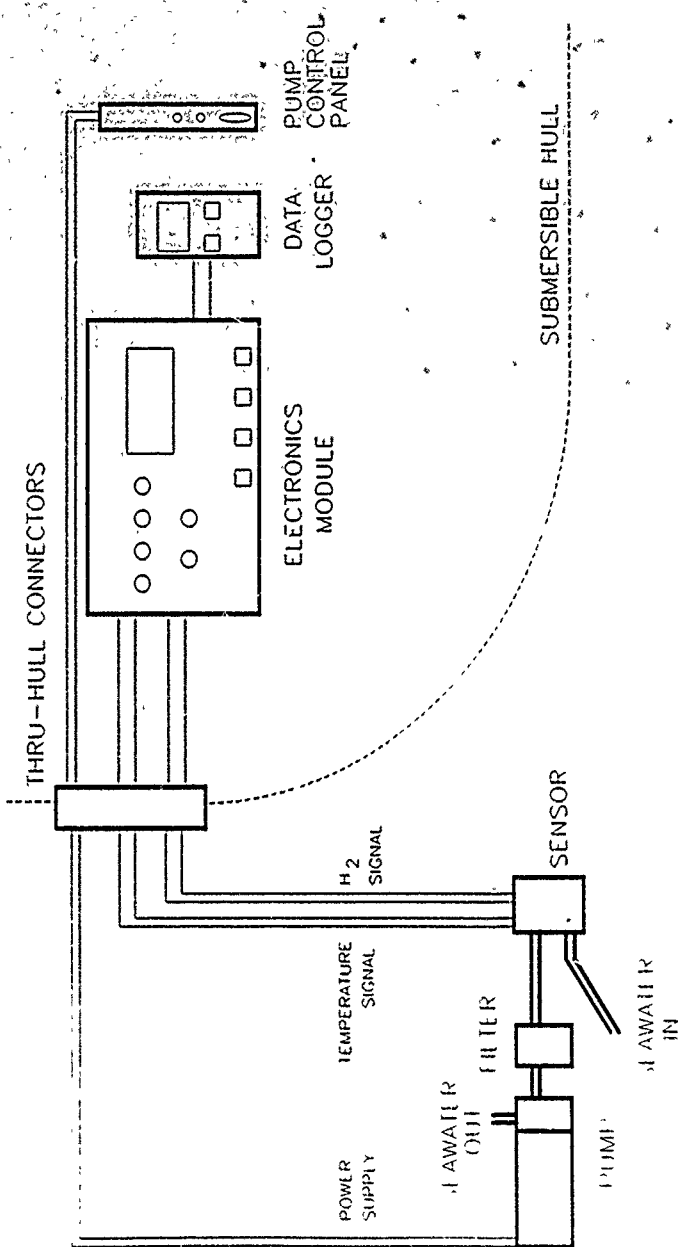
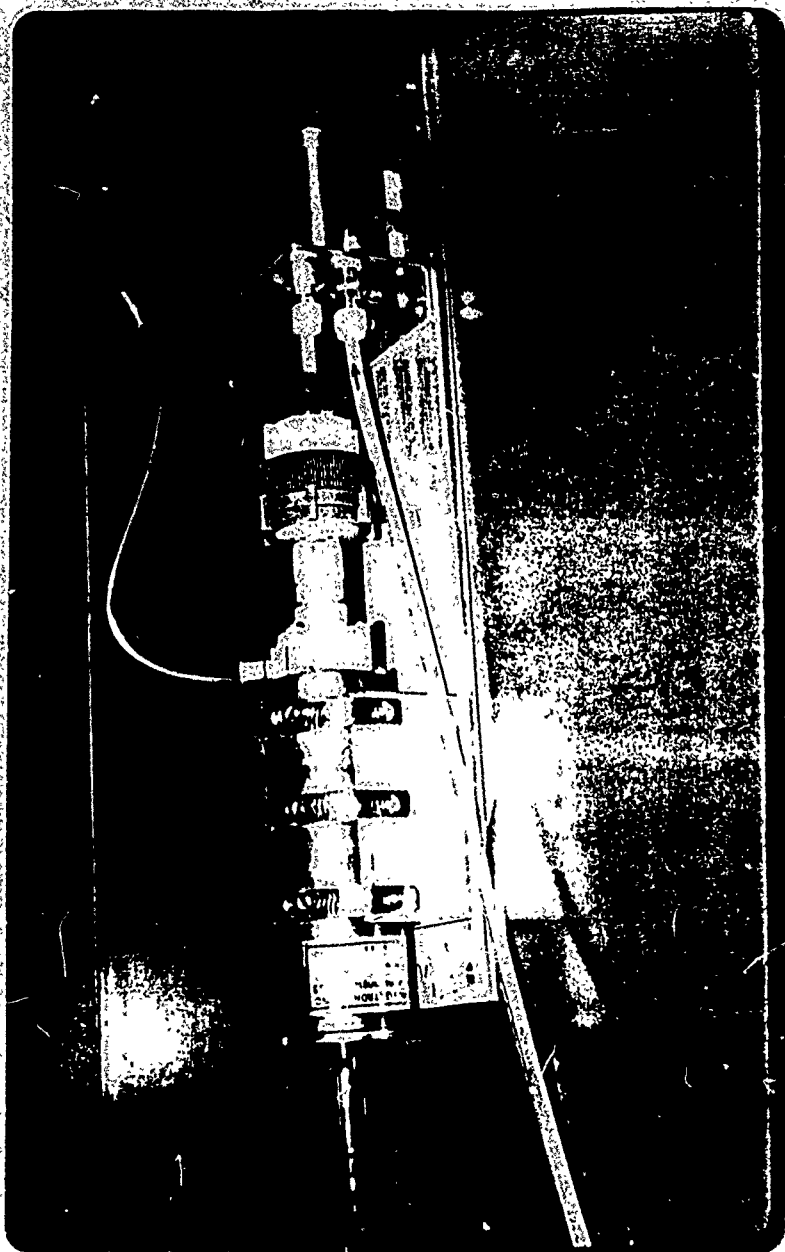
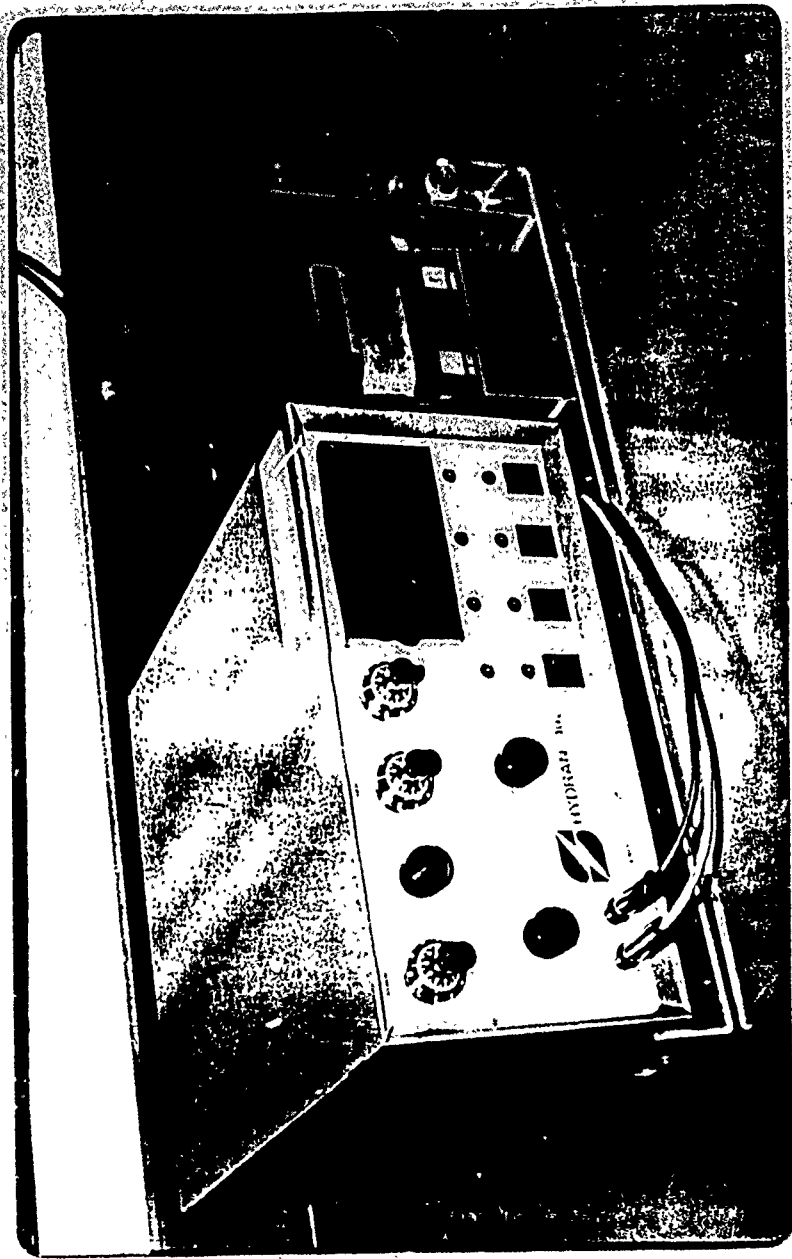


Figure 1. Schematic diagram of pump/sensor/electronics/data-logger system for PISCES V.



Hydrogen sensor and submersible pump assembly. The dimensions of the assembly are 18" D x 7" H x 4" W (46 x 10 x 10 cm).



Hydracon electronics module, data logger and pump control panel. This package is
being used for monitoring in the electronics rack aboard PISCES V.

inside PISCES V via a through-hull connector. The power supply for the submersible pump (Sea-Bird Electronics, Bellevue, WA), which is rated for 6000 m depth, is connected in a similar fashion.

The sensor/pump package will be bolted to an aluminum rail on the forward exterior of the research submersible PISCES V, and a 1/4-inch polypropylene tube will draw seawater for analysis from immediately above the pilot's viewing port. This seawater will be discharged along the port flank of the submersible after passing thru the sensor. The filter between the sensor and the pump is a coarse Teflon mesh designed to prevent the clogging of the 3 mm orifice in the pump inlet that controls the pumping rate. The sensor sends two signals to the electronics module inside the submersible: one reports the seawater temperature, and the other is the current produced by the fuel cell in response to the seawater dissolved hydrogen concentration.

The Hydran 102 electronics module provides an approximate temperature compensation of the fuel cell current signal using data from a thermistor mounted in the probe (the correction is only useful for relatively small temperature changes because it allows an approximately $0.5\%/^{\circ}\text{C}$ error after correction). The electronics module supplies a 0-2 volt signal to one channel of the four-channel portable Rustrak Ranger data logger (Gulton Industries, East Greenwich, RI). The data logger digitizes the voltage signal, and stores the data in memory for recovery after completion of the dive (the logger's storage capacity is approximately 60,000 data points). The logger can easily be disconnected from the electronics module, and brought to the support ship for data transfer and overnight recharging of the logger's batteries. Software supplied by the data logger manufacturer transfers the stored data at 9600 baud to an IBM-PC compatible computer for data storage, display, and analysis.

Laboratory Testing

In the month that has elapsed since the delivery of the sensor and electronics from the manufacturer we have used mixtures of hydrogen in air for initial testing of the system's sensitivity and linearity. These results (Figure 4) can be extrapolated to seawater samples by use of Henry's Law and the appropriate Bunsen coefficients (Gorden et al. 1977) because the sensor response is proportional to the hydrogen partial pressure in either a gas or a liquid. The detector displayed linear behavior from 20 ppm (13 nM in 35°C seawater at 24°C) to 1400 ppm (940 nM), the highest concentration tested, while operating at the second-most sensitive range. A lower detection limit should be possible with the most sensitive range, although there will be a lengthening of the response time.

Ongoing Experiments

We plan to begin shortly the laboratory testing of the system's linearity and sensitivity with recirculated seawater samples at room temperature. Upon completion of these measurements we will pressure test the sensor and pump using the seawater pressure cell at the Hawaii Institute of Geophysics Engineering Support Facility.

H2 SENSOR CALIBRATION

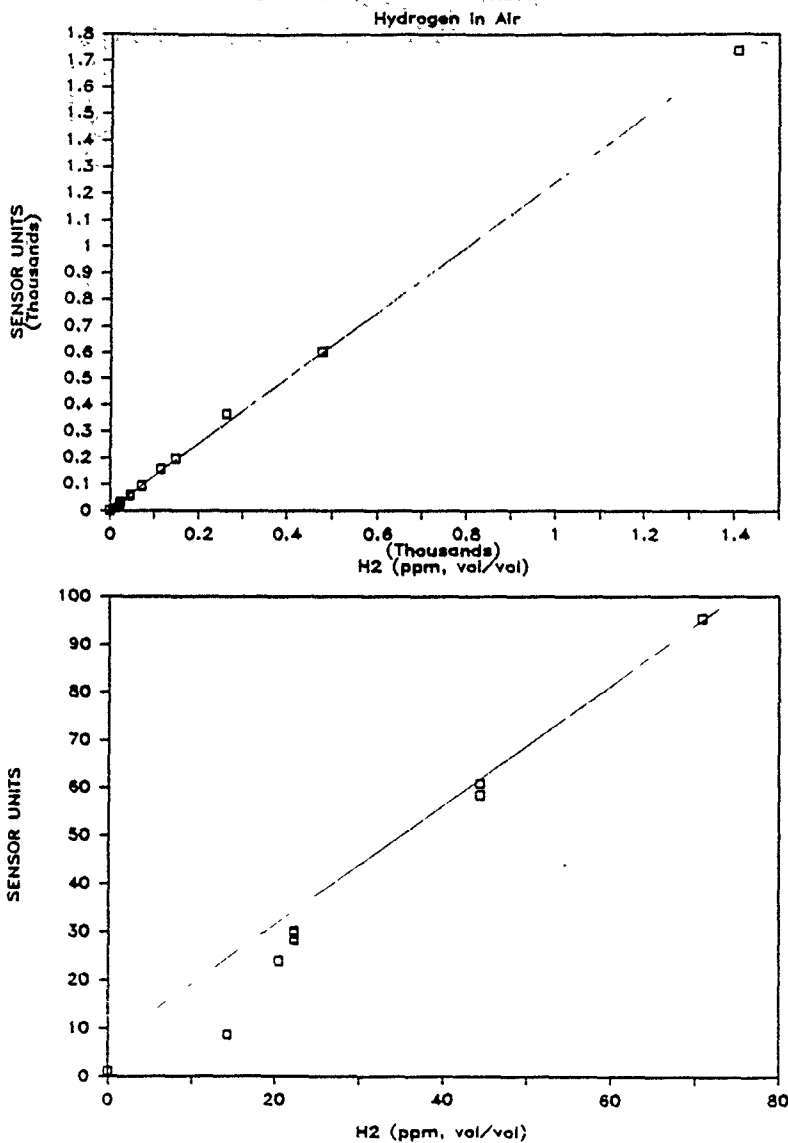
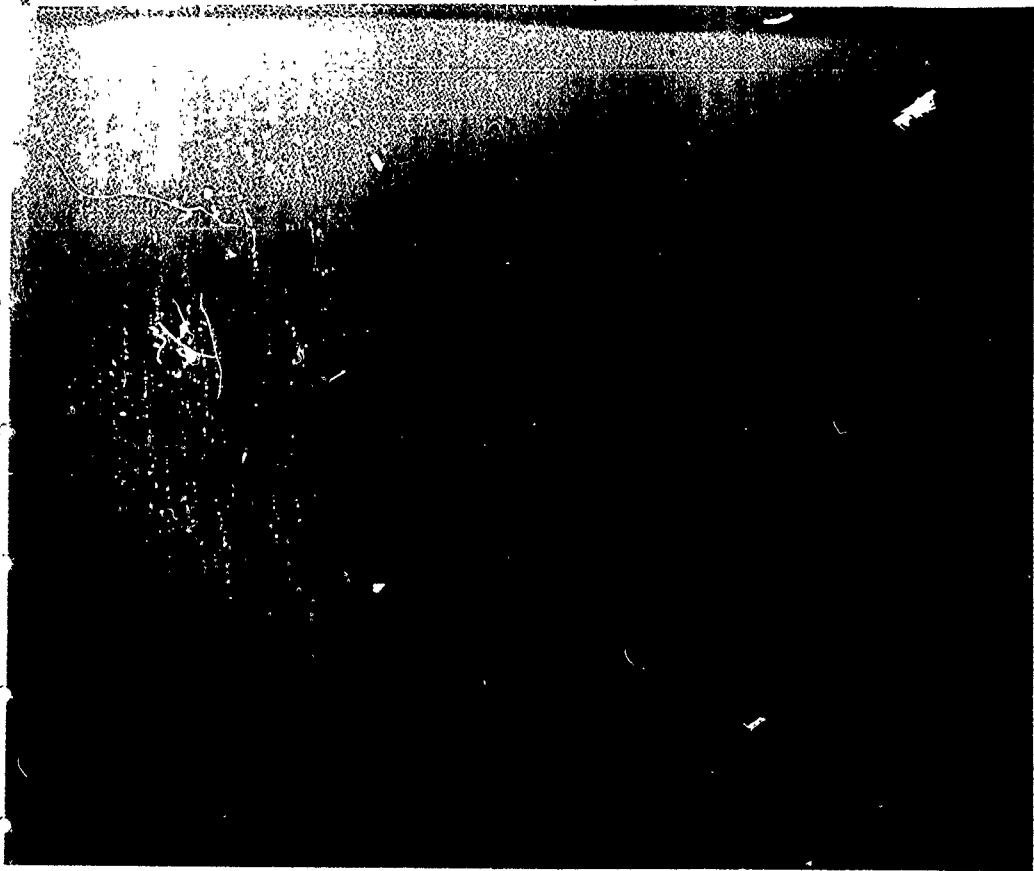


Figure 4. Calibration curve for hydrogen in air at 24°C using instrument range "E" (second-most sensitive range). The equation for the regression line is $y = 1.23x + 6.35$ ($r^2 = 0.999$). Note that, at this temperature, an air concentration of 20 ppm (vol/vol) corresponds to a seawater concentration of 13 nM (salinity = 35 ‰; Gordon et al. 1977).

The instrument will be deployed for the first time in February, 1988 during a series of PISCES V dives on Loihi Seamount. We will operate the instrument with the approximate temperature compensation currently built into the electronic module, but will also record ambient temperature data from thermistors aboard PISCES V for later correction of the raw H_2 data. This temperature correction will require data to be collected as part of the proposed research (see below).



Development of an In-situ Dissolved Hydrogen Sensor for Marine
Applications
1989-1990

RESULTS OF PRIOR RESEARCH

Sampling was conducted during May - July, 1989 at Kupapau Point, Hawaii as part of previously funded ONR research entitled "Development of an In-Situ Dissolved Hydrogen Sensor for Marine Applications", Contract No. N00014-87-K-0181, IV-A (Sansone et al. 1989). These studies were conducted in association with Dr. Ken Hon of the U.S. Geological Survey's Hawaii Volcano Observatory, which provided transportation and crews to assist with manual (shore-based theodolite) and electronic (Mini-Ranger) navigation during sampling.

Bathymetry

The nearshore bathymetry was measured with a fathometer during these cruises (Fig. 3). The incline of the seafloor in the study area is approximately 30-45°, which results in frequent slumping of the unconsolidated debris which is the dominant bottom cover. This debris is the result of the fracturing of lava upon contact with seawater.

Surface Temperature

Figure 4 shows the surface seawater temperature for the Kupapau Point region on 6/11/89. The data clearly shows the localized nature of the lava activity on this day. In contrast, sampling on 7/26/89 showed temperature anomalies at several points across the sampling area (this data has not been contoured yet, but will be available for the 11/89 ONR site visit).

Dissolved Gases

Seawater was sampled from immediately adjacent the nearshore surface and underwater lava flows from Kilauea Volcano. In summary, highly elevated levels of dissolved H_2 were measured in the surface seawater plume immediately overlying the active underwater lava flows, with lower concentrations observed as distance increased from this point. Immediately above the active flows the H_2 concentrations reached 11 μM , which is a 50,000-fold increase over the background H_2 concentration of approximately 0.2 nM; the temperature of this water as 44 °C.

Fig. 5 shows a schematic diagram of the fuel-cell sensor used to continuously monitor dissolved H_2 in seawater. The cell is 3 inches in diameter, and can be used for analyzing either gases or liquids (it responds to the H_2 partial pressure). When equipped with a 2-mil thick gas-permeable membrane the sensor can be used to depths of 2000 m, but requires approximately 12 minutes for stable readings. However, an 1-mil thick membrane can be used for surface work, which decreases the response time to approximately 8 minutes. Fig. 6 shows the setup used for sampling surface seawater H_2 concentrations at Kupapau Point. (The sensor can also be used with a submersible pump used for deepwater applications.)

Fig. 7 shows the distribution of dissolved H_2 in the surface waters offshore of Kupapau Point on 6/11/89. In this sampling the fuel-cell sensor was fitted with a 2-mil thick gas-permeable membrane, which resulted in slow detector response. Nevertheless, the hydrogen-rich surface plume is discernible from this

PROPOSAL

RADIO SHACK 01-3496
HONOLULU-KAHALA MALL
4211 WAIALAE AVE

HONOLULU, HI 96816
(808) 737-8379



Joseph. Bro
Sales Assoc

SOEST
2525 CORREA RD
ATTN LUIGI POZZI
HON, HI 96826
(808) 956-2538
956-2538

Radio Shack[®]
A Division of the Tandy Corporation

Kahala Mall
4211 Waiolae Avenue
Honolulu, HI 96816

Unit No. 01-
Tel. (808) 737-
Fax (808) 735-

Stock No.	Description	Qty.	Price	Amount
200-0145	PRO2006 SCANNER	4	439.95	1759.80
60 MONTH CONSUMER CARRY IN TSP FOR				
200-0145	PRO 2006 SCANNER	4	59.95	239.80
			SUBTOTAL	1999.60
			TAX	83.32
			TOTAL	2082.92

ISSUE DATE: 08/08/94
THIS PROPOSAL IS VALID FOR: 90 DAYS
MONTHLY RSVP PAYMENT

64.00

THIS MONTHLY PAYMENT AMOUNT MAY VARY DEFENDING ON YOUR ACCOUNT BALANCE.

COMMENTS: PRICE REFLECTS WARRANTY FOR 3 YEARS ON ALL UNITS
MAKE PURCHASE ORDER ATTN: JOE BROWN

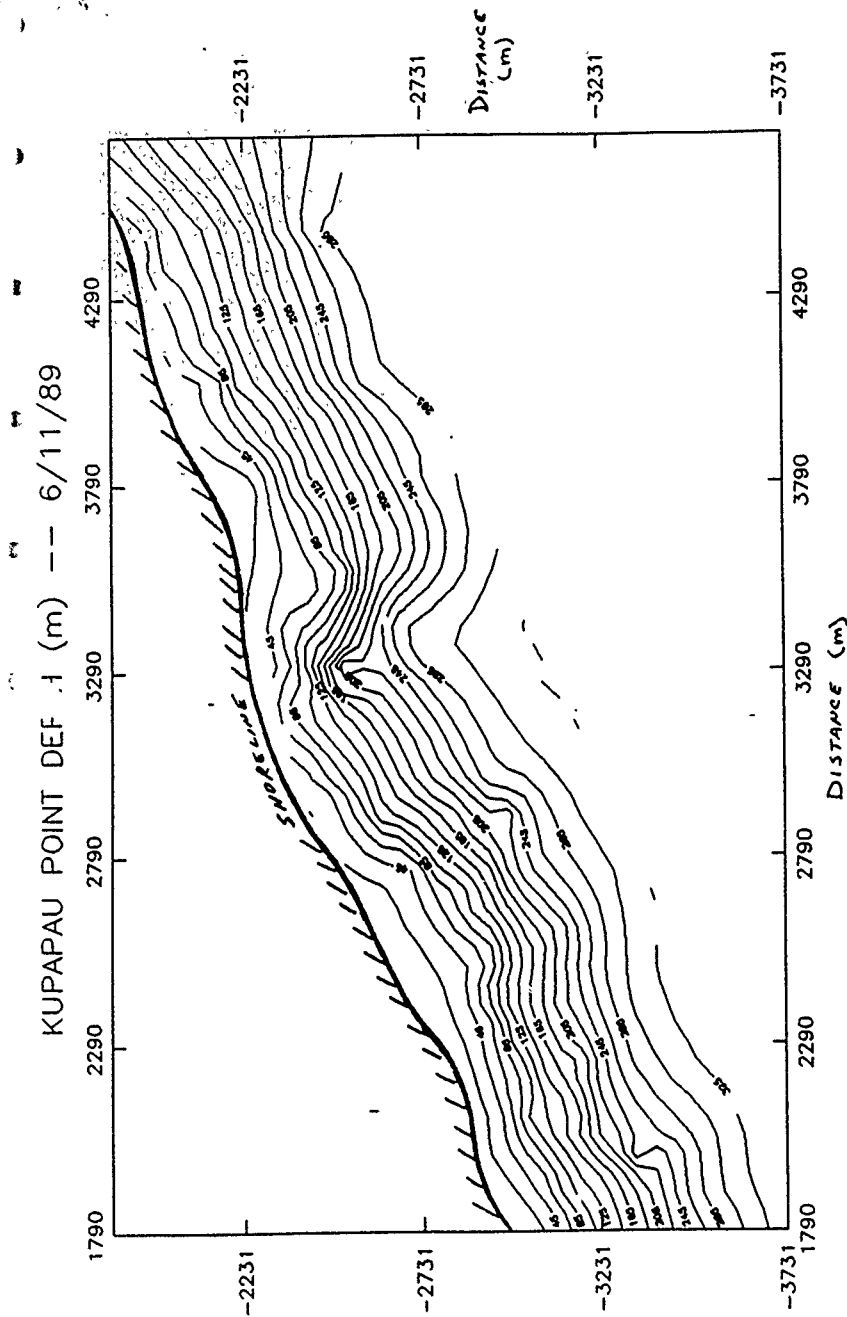


Figure 3. Nearshore bathymetry of the Kupapau Point region on 6/11/89.

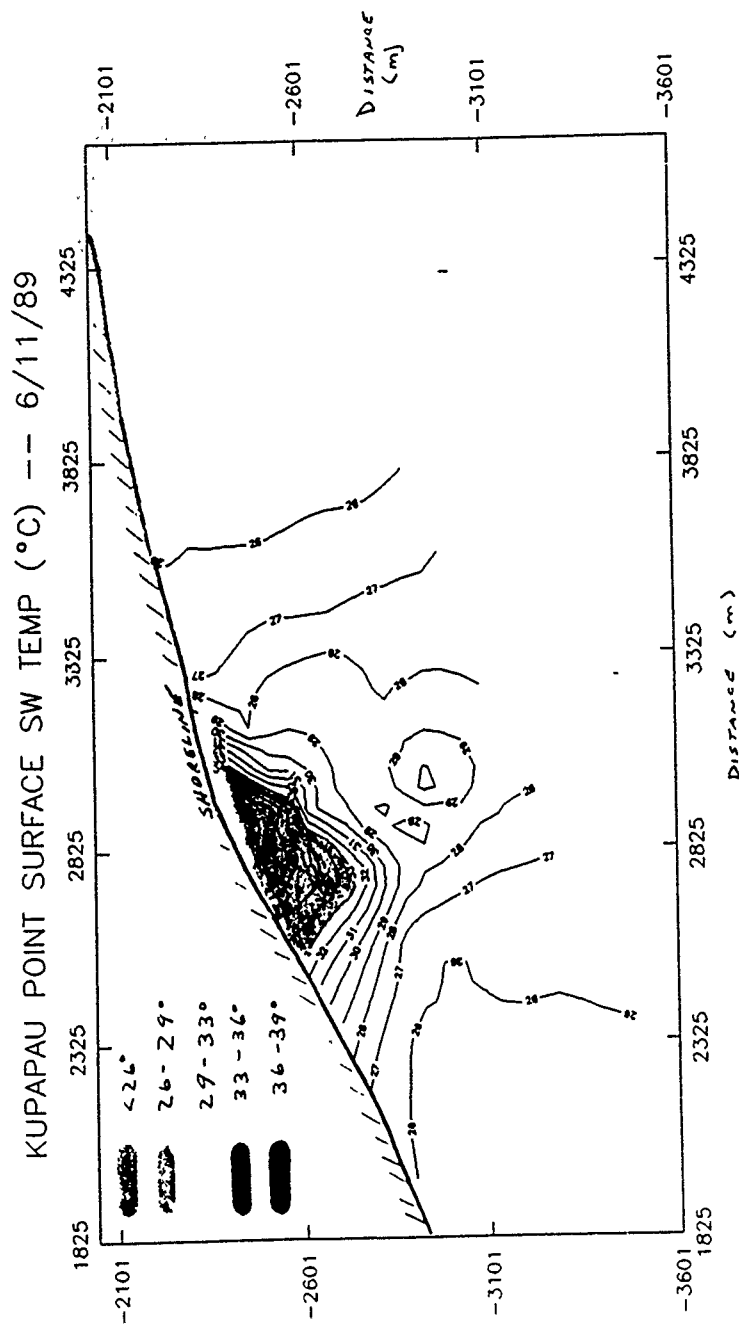


Figure 4. Surface water temperature (°C) of the Kupapau Point region on 6/11/89.

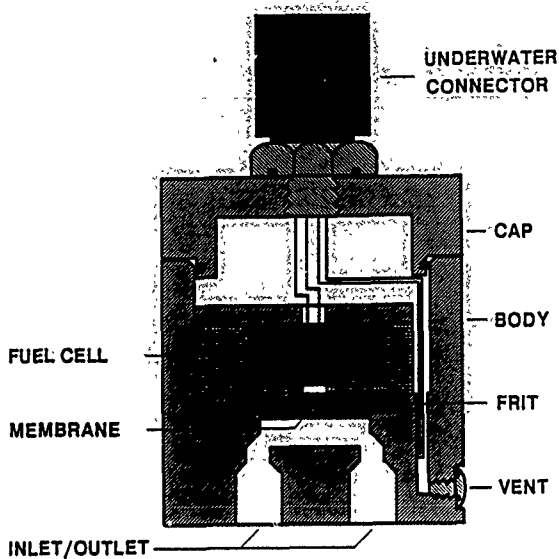


Figure 5. Schematic diagram of the fuel cell hydrogen sensor.

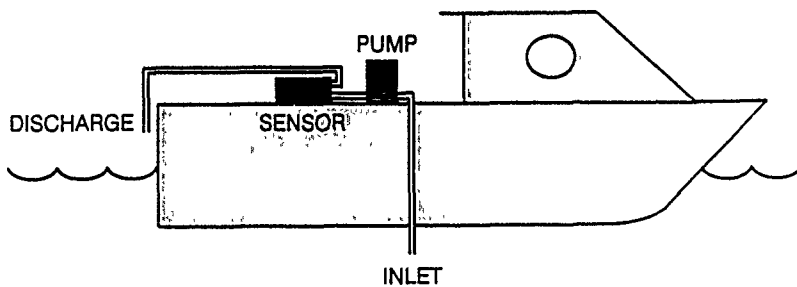


Figure 6. Schematic diagram of the sampling system used to measure dissolved hydrogen in the surface hydrothermal plume.

KUPAPAU POINT HYDROGEN (nM) -- 6/11/89

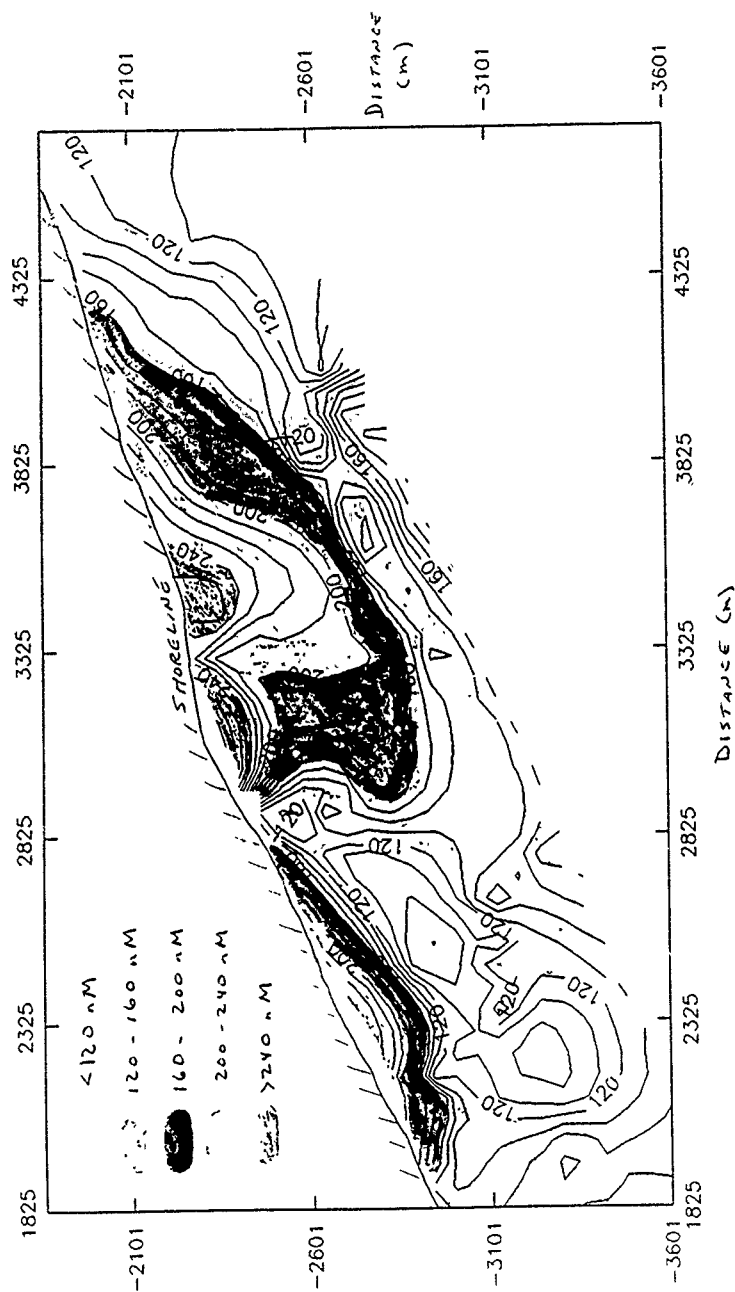
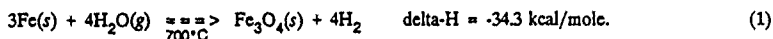


Figure 7. Surface water hydrogen concentration (nM) of the Kupapau Point region on 6/11/89.

data. Later sampling on 7/26/89 used a 1-mil thick membrane, and showed a faster response (and hence, better spatial resolution); however, the raw navigational data for that sampling has not yet been reduced, so the H_2 results cannot be contoured and compared directly with the results in this figure. Discrete surface samples collected in the thermal maximum contained $1.2 \mu M$ ($\pm 0.2 \mu M$) dissolved H_2 on 6/11/89, and $1.8 - 11 \mu M$ dissolved H_2 on 7/26/89; these samples were analyzed in Honolulu the next day using the gas-chromatography/Hg-reduction/UV-photometry method.

The dissolved hydrogen and methane concentrations of the discrete surface samples are plotted vs. water temperature in Fig. 8. The hydrogen plot shows good linearity, and an extrapolation of the trend line to $100^\circ C$ yields a H_2 concentration of $8 \mu M$. In contrast, methane concentrations in the plume were not significantly greater than the low nM levels typically found in nearshore Hawaiian waters, which is in marked contrast to the elevated CH_4 levels seen a spreading center hydrothermal plumes (e.g., Welhan and Craig 1983, Charlou et al. 1988). We believe that the H_2 in the plume is primarily due to the reaction of water with iron at elevated temperatures, which, earlier this century, was a common industrial process for H_2 production (e.g., Deming 1935):



This is consistent with the widely accepted view of local volcanologists that much of the magmatic gas is vented through the Pu'u O'o cinder cone and its associated fissures immediately after the magma reaches the surface from its source in the earth's mantle (Fig. 2) (pers. comm.: K. Hon, F. Truesdale, USGS). This interpretation is also supported by the analysis of released gas bubbles (see next section).

Gas Bubbles

Large numbers of gas bubbles are released at this site to the overlying seawater, some of which make it to the air-sea interface and are then transported to the atmosphere. The major sources of gas bubbles include the contact of red-hot sheet flows and pillow lava with seawater, the discharge of underwater hot springs (resulting from the contact of seawater with lava in buried lava tubes), and explosions occurring at the upper surface of the sheet flows (presumably due to the combustion of H_2). Bubbles collected by divers with inverted bottles were returned to our laboratory for analysis; they contained approximately 5-12% H_2 (v/v), as well as very low levels of CH_4 and CO_2 ($< 1\%$).

These results are consistent with H_2 production from the thermal dissociation of water, because the release of magmatic gas would be expected to result in higher levels of CO_2 and lower levels of H_2 being released. This is because the composition of gas released by Kilauea Volcano is typically: 0.1-30% SO_2 , 1-9% CO_2 , 0.1-1.5% H_2 , 0.1-4% H_2S , 0.005-0.2% CO , and $> 0.005\%$ CH_4 (Greenland 1987). However, He-3 measurements will be needed to determine unambiguously the relative importance of magmatic gas inputs.

Other Surface Seawater Measurements

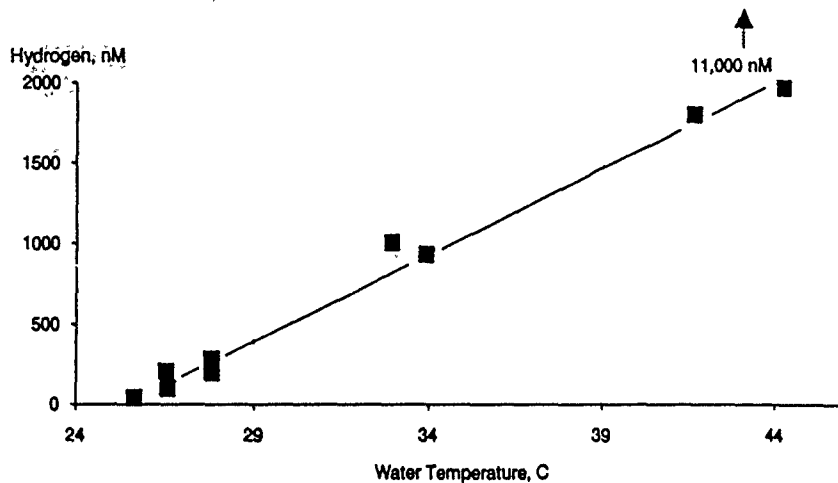
Surface seawater samples were collected for organic and inorganic nutrient, trace metal, and major ion analyses in order to determine the first-order distribution of these species throughout the plume. Except for a marked increase in silica within the plume, there was not a significant change in inorganic or organic nutrients from ambient seawater levels. Dissolved Mn was highly enriched in the plume, while Fe and Hg showed depletion. Major ion analyses have not yet been completed, but these data will be available for the November, 1989 ONR site visit.

End-Member Samples

In collaboration with P. Sedwick and G. McMurtry of the UH Oceanography Department, "end-member" samples were obtained from the orifice of an underwater hot spring at 20 m depth (temperature = $\sim 95^\circ C$, pH = ~ 6), the water feeding the spring was heated by molten lava flowing in a lava tube buried less than a few meters below the ocean bottom. The water exiting the hot spring had elevated levels of

A

KUPAPAU POINT SURFACE SEAWATER - 7/26/89



B

KUPAPAU POINT SURFACE SEAWATER - 7/26/89

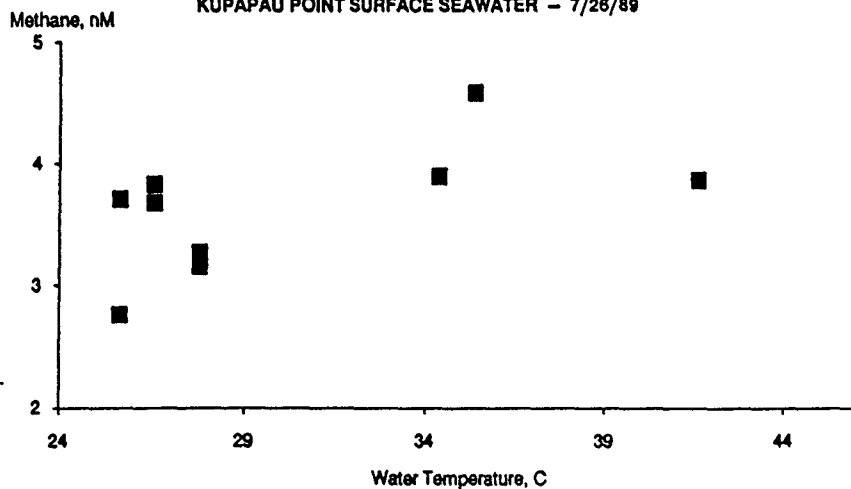


Figure 8. A) Dissolved hydrogen, and B) dissolved methane vs. water temperature for surface seawater on 7/26/89.

dissolved Mn (400x ambient seawater) and dissolved Si (40x ambient seawater); dissolved Fe was not enriched; dissolved Hg was depleted as compared to ambient seawater (Sedwick et al. 1989). These "end-member" data will be valuable in interpreting the results of the plume research proposed here (see below).

RESEARCH HYPOTHESES

The results of our initial sampling at Kupapau Point has suggested a series of research hypotheses which we wish to test during the proposed research:

1. Lava-seawater interactions will lead to observable changes in the composition of overlying seawater, and will lead to particle formation in the resultant surface plume. The effects of photochemical reactions will lead to lower rates of metal oxidation in the plume than have been measured previously in deep water hydrothermal plumes.
2. The temporal and spatial variability of the volcanic activity will result in observable variation in the composition, size, and location of the plume. The dispersal of this buoyant plume into the surrounding water will be a function of the hydrodynamic and meteorological conditions.
3. The composition of the altered seawater will help define the nature of the interactions between oligotrophic seawater and lava. The variability of the nearshore lava flows will be used to help understand the interactions with both molten and cooled lavas.
4. The surrounding bottom cover will show the effects of particle-generating lava-seawater interactions.
5. Measurements of water composition at depth on transects running offshore will indicate the real extent of submarine lava flows both downslope and alongslope.

The following section describes in detail the specific research we propose to test these hypotheses.

PROPOSED RESEARCH

In general, we will attempt to determine the dynamics of Si, Fe, Mn, Ni, Cu, Zn, As, Ca, and Mg in this system. The objectives of these studies is to determine the cycling of these elements throughout the resulting buoyant plume, and to use them in order to determine the distribution of active submarine lava downslope and alongslope.

Sampling Strategy

We propose a series of short cruises to collect water and bottom samples to test the research hypotheses outlined above. We plan to sample four times in year 1 (three times with a 26' commercial fishing boat, and once with R/V *Kila*), and three times in year 2 (two times with the fishing boat, and once with *Kila*). The boat sampling, which will be conducted over separate cruises on two consecutive days, will emphasize nearshore collection; the *Kila* cruises will emphasize deepwater sites, and will run for three days.

A CTD/transmissometer combination will be used to locate the spatial extent of the hydrothermal plume. A self-contained CTD system will be purchased partially with project funds (see "Budget Justification", below); the transmissometer will be available to us through the courtesy of Dr. Mike Mottl. Seawater samples will be collected with acid-washed Go-Flo bottles lowered on a Kevlar cable. Suspended particle samples will be collected by filtering either bottle-collected samples, or samples obtained with a ship-based peristaltic pump.

Contract: N00014-87-K-0181
Seismology & Acoustics

**Long-term ULF/VLF Ambient Noise Measurements
From Wake Island Hydrophone Array**

C. McCreery/D. Walker

Long-Term ULF/VLF Ambient Ocean Noise Measurements
from the Wake Island Hydrophone Array

Charles S. McCreery
Daniel A. Walker

Under this contract, special amplifiers were designed and fabricated for hydroacoustic monitoring. These amplifiers provided increased gain and improved anti-aliasing over earlier models and for enhancement of both short- and long-period signals. The amplifiers successful operation is indicated by the high quality of the data contained in subsequent publications, see attached final technical report and publication listing (pp. 8).

Fred K. Duennebler
Dept. of Geology and Geophysics
University of Hawaii, Honolulu, Hawaii 96822
Phone: (808) 956-4779 FAX: (808) 956-4780 EMAIL: fred@mamo.soest.hawaii.edu

SCHOOL OF OCEAN AND EARTH SCIENCES AND TECHNOLOGY



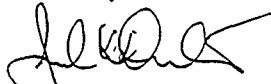
August 1, 1994

Dr. Randall Jacobson
Science Officer, Code:1125GG
Office of Naval Research
800 Quincy St.
Arlington, VA 22217-5000

Dear Randy,

Enclosed please find the final technical report for N00014-90-J-1683. As you know, the work is far from complete, but funding is no longer available to continue the work.

Sincerely,



Fred K. Duennebler

cc: Administrative Grants Officer, ONR
Director, NRL
Defense Technical Information Center
Dr. David Yount, Vice President for Research, U.H.
Dr. Barry Raleigh, Dean, SOEST
Office of Research Administration, UHM
✓ Chris, SOEST Fiscal Office

REPORT OF INVENTIONS AND SUBCONTRACTS

(Pursuant to "Patent Rights" - Contract Clause) (See instructions on Reverse Side)

Form Approved
OMB No. 0704-0187
Expires Jun 30, 1994

Public reporting burden for this collection of information is estimated to average 5 minutes per response, including the time for reviewing instructions, searching existing data sources, gathering and maintaining the data needed, and completing and reviewing the collection of information. Send comments regarding this burden estimate or any other aspect of this collection of information, including suggestions for reducing this burden, to Washington Headquarters Services, Directorate for Information Operations and Reports, 1215 Jefferson Davis Highway, Suite 1204, Arlington, VA 22202-4302, and to the Office of Management and Budget, Paperwork Reduction Project (0704-0187) Washington, DC 20503

1a NAME OF CONTRACTOR/SUBCONTRACTOR University of Hawaii		2a NAME OF GOVERNMENT PRIME CONTRACTOR	
b ADDRESS (include ZIP Code) 2540 Maile Way Honolulu HI 96822		c CONTRACT NUMBER N00014-90-J-1683	
d AWARD DATE (YYYYMMDD)		e AWARD DATE (YYYYMMDD)	
f AWARD NUMBER 900201		g AWARD DATE (YYYYMMDD)	

SECTION I - SUBJECT INVENTIONS


1 NAME(S) OF INVENTION(S) (Last, first MI)	2 TITLE OF INVENTION(S)	3 DISCLOSURE NO. PATENT APPLICATION FILED IN U.S. PATENT NO.	4 ELECTION TO FILE PATENT APPLICATIONS				5 CONFIRMATORY INSTRUMENT ON ASSIGNMENT FORWROD TO CONTRACTING OFFICE
			(1) Yes	(2) No	(3) Yes	(4) No	
None							

6 EMPLOYER OF INVENTION(S) NOT EMPLOYED BY CONTRACTOR/SUBCONTRACTOR (1) (a) Name of Employer (Last, first MI)	7 ELECTED FOREIGN COUNTRIES IN WHICH A PATENT APPLICATION WAS FILED (1) Title of Invention
(b) Name of Employer	
(c) Address of Employer (include ZIP Code)	

SECTION II - SUBCONTRACTS (Containing a "Patent Rights" clause)

8 NAME OF SUBCONTRACTOR(S)	9 ADDRESS (include ZIP Code)	10 SUBCONTRACT NO(S)	11 DEAR "PATENT RIGHTS"	12 DESCRIPTION OF WORK TO BE PERFORMED UNDER SUBCONTRACT(S)	13 SUBCONTRACT DATES (YYYYMMDD)
None			(1) Clause Number (FYMMDD)	(2) Date (FYMMDD)	(3) Award (FYMMDD)

SECTION III - CERTIFICATION

14 CERTIFICATION OF REPORT BY CONTRACTOR/SUBCONTRACTOR (Not required if Small Business)	15 NAME OF AUTHORIZED CONTRACTOR/SUBCONTRACTOR OFFICIAL (Last first MI)	16 SIGNATURE	17 DATE SIGNED
	Peter V. Garrod		7/26/94
18 Acting Director of Research			

Low Frequency Ocean Noise Analysis

N00014-90-J-1683

Final Technical Report

ANALYSIS OF LOW FREQUENCY OCEAN NOISE:

- (1) FROM A LONG-TERM EXPERIMENT ACROSS THE U.S. EAST
COAST, AND**
- (2) FROM THE WAKE ISLAND HYDROPHONE ARRAY DURING
NORTHWEST PACIFIC TYPHOONS**

Charles S. McCreery, Frederick K. Duennebie, and Daniel A. Walker
School of Ocean and Earth Sciences and Technology
University of Hawaii at Manoa, Honolulu, HI 96822

July 22, 1994

LONG RANGE OBJECTIVES

The long-range goal of this project was a better understanding of the mechanisms of generation and propagation of ambient ocean noise at frequencies between about 0.05 and 50 Hz. Although it is generally agreed that most of the ambient noise in this band is generated by ocean gravity waves, many questions remain concerning how these waves act to produce the wide variety of characteristics observed in the ocean noise spectrum. Proposed mechanisms of noise generation include open-ocean, shoreline-enhanced, and storm-enhanced non-linear gravity wave interactions, shallow water gravity wave bottom interactions, surf, and open-ocean breaking waves or whitecaps. Propagation mechanisms include acoustic waves, non-acoustic pressure fluctuations, and Rayleigh waves. We utilized two unique long-term bottom acoustic data sets to identify specific noise mechanisms and to evaluate environmental conditions under which these mechanisms are significant contributors to the ambient noise field.

PROJECT OBJECTIVES

The East Coast experiment, called the Environmentally Controlled Ocean floor NOise Monitoring Experiment (ECONOMEX), was designed to sample ambient noise in the water column and on the ocean floor across the continental shelf and slope east of Chesapeake Bay. A vertical array of hydrophones in the water column, a horizontal array of hydrophones, and three-component seismometers were deployed for several months in the spring of 1991. The experiment was designed to coincide with the Surface Wave Dynamics Experiment (SWADE) in order to take advantage of their extensive measurements of surface winds and directional ocean wave spectra in the same region. This comprehensive and long-term data set permits the identification of specific noise generation and propagation mechanisms for the continental shelf and slope, and evaluation of their contribution to the noise field under a wide variety of ocean surface conditions.

The primary goal of studying data from the Wake Island Hydrophone Array is to quantify changes in the noise field due to the extreme ocean surface conditions produced by typhoons, and to identify mechanisms by which these storms produce noise. One such storm, Typhoon Doyle, passed directly over some of the Wake hydrophones in August, 1988, and numerous other typhoons have passed near Wake since 1982, when the regular recording of digital noise samples from the array began. A secondary objective was to identify other mechanisms that contribute significantly to the noise in deep ocean basins, utilizing this unique long-

term time series. Although the Wake study lacks the comprehensive environmental data available to ECONOMEX, it is aided by regular surface wind measurements made at Wake Island by the National Weather Service, and by ocean wave estimates from U.S. Navy wave models.

SUMMARY OF RECENT RESULTS

Wake Island Hydrophone Array. Recordings of the low frequency noise field observed on the Wake hydrophones were made between 1982 and June, 1994. It is planned that recording of this valuable time series will restarted shortly and continue indefinitely. Analyses of these data up to 1988 were accomplished under this contract. Noise levels in the deep ocean near Wake show considerable structure in their variation. Winter months are especially characterized by recurring episodes of increased energy between 0.1 and 0.2 Hz that usually last several days. The episode shown in Figs. 35 and 36 of McCreery's dissertation, lasting from Oct. 29 to Nov. 3, 1988, is displayed for two of the Wake hydrophones - one at 850m depth (suspended) and the other at 5500m (bottom-mounted). These figures show the differences in noise levels from the mean at each frequency for the period shown. The shallower hydrophone (Fig. 36) detects the direct pressure signals from longer-period ocean gravity waves, seen between Oct. 30 and Nov. 3 centered at about 0.06 Hz. Narrow-band striations appear within this packet of energy, indicating dispersion with low frequencies arriving first. Making the assumption that this dispersion reflects the arrival time of a train of gravity waves at the hydrophone, the group velocity dispersion relationship yields a distance and origin time of waves that are consistent with generation by a strong extratropical cyclone that was moving to the northeast off the coast of Japan. This strongly implies that the propagation mechanism of this noise to the hydrophone is direct pressure variations at the hydrophone from waves passing overhead. However, increased noise between 0.1 and 0.2 Hz. arrives at the hydrophones more than a day earlier than the 0.06 Hz signal. If we assume that this noise was generated by the same storm, then the higher frequency energy must have traveled to the hydrophones by a much faster mechanism than ocean surface gravity waves, perhaps as Rayleigh waves generated at the storm, or at a shore line near the storm. Although we observe that the higher frequency noise is roughly twice the frequency of the lower frequency noise, it does not appear likely that the higher frequency energy is generated by the classical non-linear wave interaction microseism mechanism from waves passing directly over the hydrophone, as it arrives much earlier than the lower frequency noise.

An argument in favor of Rayleigh wave propagation for energy near the microseism peak is that the noise between 0.1-0.2 Hz measured on the deep hydrophones is 15 to 20 dB higher than levels observed on the shallow

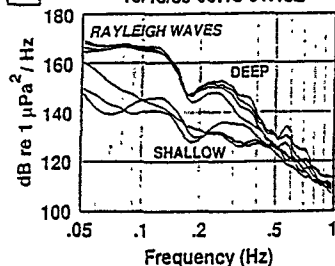
phones. This difference is similar to the relative levels for Rayleigh waves from earthquakes (FIGURE 1). To investigate this possibility further, a preliminary frequency-wavenumber analysis was made on this noise using the deep hydrophones to the north of Wake. Convincing evidence for the presence of Rayleigh waves was not found, although a more detailed analysis is warranted.

ECONOMEX. Spectral processing of long-term ambient noise data from the differential pressure gauges (DPGs) and geophones from ECONOMEX reveals a complex structure (Fig. 2). These figures show the difference from average noise level at each frequency as height above the page lit from the top of the page. While it is difficult to obtain absolute levels from this plot, the temporal structural changes in noise level are highlighted. Pressure variations at a depth of 95m on the shelf (top left figure) are dominated by distinctive modal bands of energy that are subtle or absent in the vertical geophone record (top right). Also apparent in the shallow DPG data is the direct pressure signal of ocean swell from a very distant source, increasing in frequency between 0.05 and 0.07 Hz over a period of about four days. The gravity wave group velocity dispersion formula yields a distance of about 14,000 km for the source of these waves, possibly originating at an Antarctic storm. Similar signals were observed in the ULF/VLF data off Oregon in 1991. In deeper water, both the DPG and geophone signals are characterized by packets of energy between 0.1 and 0.2 Hz that are similar to those seen in the Wake data. However, the numerous narrow features that sweep rapidly downward in frequency over a period of hours as they grow in strength have not been observed in the deep ocean near Wake. These narrow features are almost certainly related to increases in wind speed or changes in wind direction leading to the rapid building of seas from high to low frequencies. The fact that these features are not observed at the Wake hydrophones implies that the proximity of a shoreline is involved with the mechanism. Either the shoreline reflects the waves to produce wave-wave interactions over the sensors, or the noise is generated at the shoreline, and propagates to the sensors as Rayleigh waves. Work to correlate these distinctive features with particle motions and the SWADE environmental data, and possibly resolve this question, has not been accomplished.

SUMMARY OF RESULTS IN CHARLES MCCREERY'S DISSERTATION AND PUBLICATIONS

The HOLU Spectrum: The slope of the noise spectrum from roughly 0.4 to 6 Hz often saturates, reaching a particular level which is only surpassed under special circumstances. This saturation level has been

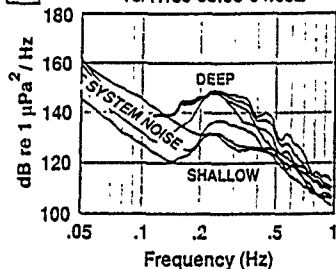
A EARTHQUAKE RAYLEIGH WAVES
10/18/89 00:15-01:15Z



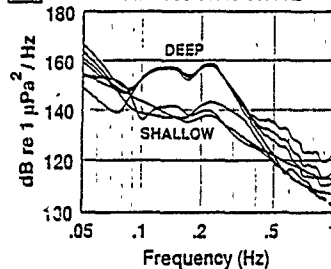
ULF OCEAN NOISE
FROM
WAKE HYDROPHONES

4 DEEP (5.5 KM)
VS
3 SHALLOW (0.8 KM)

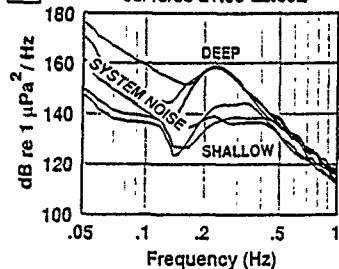
B TYPICAL AMBIENT NOISE
10/17/89 03:00-04:00Z



C HIGH AMBIENT NOISE
11/01/89 00:00-06:00Z



D BENEATH TYPHOON DOYLE
08/15/88 21:00-22:00Z



E PEAK NOISE FROM DOYLE
8/16/88 18:00-19:00Z

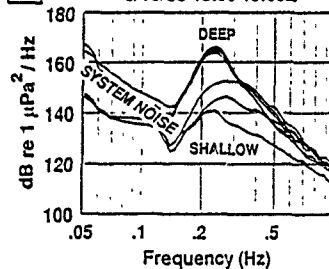


Figure 1. Wake shallow and deep hydrophone spectra showing earthquake Rayleigh waves (A), typical noise (B), high ambient noise (C), and noise at the time of typhoon Doyle (D and E).

observed many times (OSS Experiment, ULF/VLF Experiment, and others). It appears to be related to the ocean wave spectrum directly above the hydrophone, and the noise level appears to have little or no dependence on water depth. This saturation level and the slope of the noise curve are well predicted by the non-linear wave interaction mechanism for propagation to the ocean floor of pressure fluctuations from ocean wave activity (Longuet-Higgins, 1963), coupled with the predicted ocean wave spectrum (Phillips, 1980, and Hasselmann et al, 1976), with the connection between the wave spectrum and the noise spectrum made by Webb and Cox, 1986. There appears to be no dependence on wave direction in this part of the wave spectrum. The ocean wave amplitude spectrum saturates at high frequencies, as non-linear effects transfer energy to lower and lower frequencies with increasing wind speed and fetch. This saturation level is characterized by the Phillips' constant of the ocean wave spectrum. The energy in the wave spectrum is propagated downward, by one apparently lossless mechanism described by Longuet-Higgins, as pressure variations detected by hydrophones. The Phillips' constant is observed in the ocean acoustic noise spectrum as the HOLU spectrum. This is believed to be a world-wide constant, independent of ocean depth (except in very shallow water where the direct pressure mechanism begins to dominate.) At Wake, the Holu spectrum is observed to have a value of 75 dB re $1\mu\text{Pa}/\sqrt{\text{Hz}}$ at 4 Hz, and a slope of about -23 dB/oct averaged over many years of data, but with a standard deviation of less than 4 dB at 4 Hz. This observation is slightly higher than predicted by the theory, with a slightly lower slope (68 dB at 4 Hz with a slope of -25 dB/oct.) The cause of the difference is unknown, but is probably a combination of uncertainties in calibration of the WAKE hydrophones, and lack of continuous saturation at lower frequencies in the data.

Typhoon Doyle. The crossing of Typhoon Doyle over the Wake hydrophone array in 1988, provided excellent data for study of the acoustic noise spectrum under extreme conditions. Of particular interest is the depression of the HOLU spectrum at the time when winds were strongest (Figure 32, McCreery Dissertation.) When noise levels above 5 Hz reach their maximum levels when the wind speed over the hydrophone reaches its highest levels, noise levels at 2 and 3 Hz are depressed well below expected HOLU levels. One possible explanation for this phenomenon is that the high winds and breaking waves generate foam at the ocean surface that attenuates the higher frequency waves. Note that the depression of the HOLU spectrum begins and ends at about the same time as the increase in noise level above 5 Hz (thought to be generated by acoustic noise from braking waves.)

Another important observation is the change in noise level as the eye of Typhoon Doyle passed directly over hydrophone 76 (Figure 33, McCreery Dissertation.) . A slight but significant reduction in the noise level above 2 Hz. is observed, implying that an appreciable amount of the observed noise at frequencies above 2 Hz is propagated directly to the bottom without a significant horizontal path.

Correlation of estimated ocean wave spectrum with Wake hydrophone noise spectrum. The double frequency microseism mechanism of Longuet-Higgins implies that there should be a strong correlation between wave height above the hydrophone at one frequency with acoustic noise at twice that frequency. In Figure 27 (McCreery Dissertation), a correlation is made between the ocean wave spectrum at Wake predicted by the U.S. Navy Spectral Ocean Wave Model and the noise levels observed at the same time by hydrophone 74. This figure clearly shows that the expected 2:1 correlation is not observed, except possibly at frequencies below 0.2 Hz. Furthermore, the weakest correlation is seen at frequencies between 0.2 and 0.3 Hz, where the microseismic noise is highest. Above 0.3 Hz a strong correlation between 5:1 and 10:1 is observed. It is unlikely that the SOWM model could be in error enough to explain this change from the expected 2:1 correlation at frequencies above 0.2 Hz, and we have no explanation for the observed correlation. The decrease in correlation between 0.2 and 0.3 Hz suggests that much of the energy in this band (where the microseism peak is located) is generated at considerable distance from Wake.

Two documents are included as appendices to this report, the University of Hawaii PhD Dissertation of Charles McCreery, and a reprint of a paper, Correlation of deep ocean noise (0.4-30 Hz) with wind, and the Holu Spectrum - A world-wide constant. Although this is a final report, work still progresses on these results, however slowly due to lack of funds.

1993 PUBLICATIONS SUPPORTED BY ONR

- McCreery, C.S., F.K. Duennebie, and G.H. Sutton, (1993), Correlation of deep ocean noise (0.4-30 Hz) with wind, and the Holu Spectrum - a worldwide constant, J. Acoust. Soc. Am. 93 (5), 2639-2648.
- McCreery, C.S., G.H. Sutton, and T.A. Schroeder (in prep.), Long-term 0.05-1Hz deep ocean noise from Wake hydrophones: relation to north Pacific storms and waves, J. Acoust. Soc. Am.
- McCreery, C.S., F.K. Duennebie, and T.A. Schroeder, (in prep.), Ocean noise, 0.1-30 Hz, measured under a typhoon, J. Acoust. Soc. Am.

Contract: N00014-87-K-0181
Marine Geology & Geophysics

**Calibration of the Acoustic Characteristics
of the SeaMARC II System**

Haruyoshi Matsumoto

Calibration of the Acoustic Characteristics of the SeaMARC II System

Haruyoshi Matsumoto

PROGRESS DURING THE PAST YEAR (1988-89)

Under our current ONR funding, we have worked on improving the the post processing methods used on SeaMARC II data to produce more accurate maps and more faithful acoustic image representations of the seafloor surveyed with the system. The following is a short description of our new processing capabilities and results.

1. Side-scan mosaicing program

Our conventional method of mosaicing was a typical "cut-and-paste" technique based solely on the ship's navigation. This new program allows us to remove the image distortions caused by changes in the attitude of the fish. The improved corrections for the navigation, pitch, roll, and yaw of the fish result in more accurate side-scan mosaics, and better consistency between neighboring side-scan swaths (Matsumoto et al., 1986).

2. Side-scan pixel relocation program

Across the swath, our normal side-scan images are corrected only for the slant range distortion by assuming a flat bottom geometry. If the relief of the bottom is large, the error due to this assumption becomes large enough to distort the image, rendering it inadequate for quantitative analysis of the data. To correct this problem, we wrote a program which relocates the pixels across the swath based on the bathymetry data (Reed, 1987).

3. Side-scan intensity bias correction program

The intensity of our side-scan data is biased by the beam pattern and by the system's variable gains designed to compensate for a generic bottom acoustic scattering function. A new program has been written to remove all the system's gains including the beam pattern of the arrays. The resulting image intensity is unbiased, and individual pixel values represent relative backscattering coefficients at increasing angles of incidence across the swath (Matsumoto et al., 1986).

UNDERWATER TRACKING, POSITIONING & NAVIGATION TRACKPOINT II

MODEL NO.	DESCRIPTION	PRICE (USD)
4410C *	Trackpoint II Transceiver. Micro-processor based acoustic tracking system control and display unit, with most current Rev 8 software. (Telemetry option available in Rev. 5.0 and up; compass option available in Rev. 5.4 and up; 6-target tracking available in Rev. 7 and later)	\$27,450.
	Software upgrade to most current, P/N 4410FW8.020. Hardware mods may be required in older systems.	\$ 2,750.
	Rack Mount Kit (19 in) P/N 100912	\$ 125.
	Hardigg Shipping Box with insert	\$ 675. ea
4610B *	Trackpoint II combined Interrogate Transducer and Receive Hydrophone with integral VRU, calibrated to 3-D accuracy specification	\$12,375.
	Hydrophone recalibration to 3-D Standard	\$ 1,100.
	Replace Transducer end, P/N 100922-01	\$ 2,750.
	Replace Connector end, P/N 100194	775.
	Connector End Assembly Kit P/N 100194	550.
	Change of Frequency Band	\$ 4,475.
	Stainless Steel Mounting Bracket P/N 100586	\$ 350.
	Spare 3-D Cal. EPROMs (set of 2) (same for 4211A, 4212A) P/N. 101287	\$ 175
4110B-100 *	Trackpoint II to Hydrophone inter-connect cable, 100 feet complete. (Add'l lengths are \$1525 + \$7 per ft/\$23 per meter)	\$ 1,525.
4110B-250	250 ft. interconnect cable	\$ 2,400.
4110B-300	300 ft. interconnect cable	\$ 2,675.
	Underwater extension connector cable	\$ 1,975.
	Underwater junction box	\$ 950.

4. Normalization program to produce a backscatter coefficient map at uniform angles of incidence.

A backscattering coefficient map is the synthesis of all the capabilities of the SeAMARC II system. This program requires multiple side-scan images of the same area, but with different look angles. Each image is processed by the aforementioned three programs to remove the intensity bias and the geometric distortions. By coregistering these multiple images of the same bottom area, the program can derive the scattering coefficients of that bottom normalized at a desired angle of incidence. These data can then be related to the type, composition and/or roughness, of the bottom in the scattering cells whose width are between 50 to 200 m depending on the accuracy of the coregistration (i.e. navigation accuracy and attitude and bathymetric correction).

A back-scattering coefficient map of a small area near the Juan de Fuca Ridge was computed as a test of this algorithm (Matsumoto et al., 1986). The results are encouraging. The corresponding map produced for an angle of incidence of 45 degrees could be used to assess the roughness characteristics of the bottom in the area. However, for lack of knowledge of the SeAMARC II's acoustic source level, these computed backscatter coefficients are only relative. In addition, while computing another backscatter coefficient map (normalized close to the nadir angle, i.e., 15 degrees) we found that a large amount of intensity bias remains in the data. This indicates that the system's response based on the beam pattern data (originally measured in 1981 at Lake Pend Oreille, Idaho) is no longer suitable for the corrections required and a new calibration is needed.

5. Ridge following and ping stacking routine for the phase data reduction.

For each ping, the SeAMARC II phase data are regrouped into a two dimensional sample histogram of travel time vs phase angle. A new routine stacks the phase data from several pings and applies an image processing technique called ridge following. Compared to our conventional routine of modal picking, the new processing method produces a less noisy, and more consistent bathymetry map (Matsumoto et al., 1985).

FACSIMILE TRANSMITTAL



ECS COMPOSITES
ECS POLYMERIC
ECS-METALLICS

3560 Rogue River Highway / P.O. Box 188
Grants Pass, Oregon 97526 USA
Tel 503-476-8871
Fax 503-474-2479

TO: LUGIGI POZZI
COMPANY: UNIVERSITY OF HAWAII
FAX: (808) 956-2538
SUBJECT:
FROM: Tim D. Plummer, Prime Military Sales Specialist
DATE: August 10, 1994 TOTAL PAGES: MESSAGE NO.:

MESSAGE:

Dear LUGIGI

ECS Composites is pleased to provide price and delivery information in accordance with your request.

5312-3 Operating Case Qty. 1 Unit Price \$1,117.00

FOB: ORIGIN Delivery 4-6 Weeks

Best regards,

Tim D. Plummer
Prime Military Sales Specialist

Contract: N00014-87-K-0181
Chemical Oceanography

**Applications of Advanced Multichannel Laser Raman
Scattering and Laser-induced Fluorescence Spectroscopy
to Problems in Marine Chemistry**

S. Sharma/G. Taylor

E. PROGRESS TO DATE

In the past, the Raman Spectroscopy Facility at HIG has been used primarily for studies in geochemistry, petrology, and materials sciences. Since the beginning of our current funding period (March 1987), however, we have dedicated a portion of the laboratory and a large portion of our time to adapting the instruments to perform analyses on aqueous samples. We have successfully obtained spontaneous and resonance Raman spectra from 200- μ l samples placed on reflective aluminum foil using our Micro-Raman probe. We have and will continue to examine the utility of capillary tubes and hollow fiber-optic as multi-pass internally reflecting sample containers. Preliminary results and those of Schwab & McCreery (1987) suggest the usefulness of a capillary waveguide technique for analyzing dilute solutes.

Our work thus far has focused on inorganic nutrient ions. We have repeated the experiments of Baldwin & Brown (1972), Cunningham et al. (1977), and Furuya et al. (1979) to obtain spontaneous Raman spectra of NO_3 , NO_2 , and PO_4 . We have obtained detection limits (10^{-5} - 10^{-3}) for spontaneous Raman scattering comparable to those in the literature. We are able to obtain our spectra 5 to 180 times faster than previous reports and at 2.5 to 10% of reported laser powers. The intensified gated optical multichannel analyzer system (Princeton Applied Research OMA III) provides us with most of our advantage. We can run a complete spectrum with 1 sec integration times and 60 repetitive scans in 1 min, so our sample processing time is reduced and photodecomposition is much less than previously possible. We have not obtained spontaneous Raman spectra for NH_4 yet because a different set of gratings is required to measure the high frequency shifts observed with this ion, but we will examine this ion in the near future.

We have improved on sample throughput and laser power requirements, and slightly lowered detection limits obtained for nitrate, nitrite, and phosphate by spontaneous Raman scattering. To further improve detection limits, we have begun to examine possible enhancement techniques, such as Surface-Enhanced Raman Scattering (SERS), Resonance Raman Scattering (RRS), and Waveguide Internal Reflectance Raman Scattering (WIRRS). We have evaluated and continue to evaluate the SERS effect on ion spectra using silver-coated glass surfaces (frosted glass and capillary tubes) and metallic colloids (silver and gold) according to Ni & Cotton (1986) and Lee & Meisel (1982). We have repeated the experiments of Sheng et al. (1986) to evaluate the effects of sedimentation and colloidal particle size on producing SERS activity within our experimental system. We have confirmed that sedimentation of Ag-colloid produces fractions with varying SERS performance presumably due to varying particle size and degree of coagulation. With 10^{-6}M crystal violet (CV) as an analyte, we obtained SERS enhancement factors of 10^3 - 10^4 over CV without Ag-colloid. We found that SERS activity is dependent upon the colloid fraction and time elapsed after mixing analyte and colloid. For subsequent work, we have employed the most active fractions of Ag-sol.

Using a chromogenic reaction and RRS with 488 nm excitation, Furuya et al. (1980) were able to measure 28 nM NO_2 in waste and treated water and projected a detection limit of 10 nM. By combining RRS

and SERS, we are able to detect NO_2 down to 0.5nM. We repeated the experiments of Furuya et al. (1980) with the following modifications: (i) NO_2 standards were prepared in distilled water and we employed Strickland & Parsons (1972) colorimetric reaction to produce an azo dye, (ii) we used 20mW of laser power at the sample (they used 200mW), (iii) we used an OMA to obtain 120 one second scans in two minutes (their scans with a monochromator typically required 1 - 3 hours!), and (iv) we added Ag-colloid to produced the combined effects of RRS and SERS. Spectra obtained from the 488 nm excitation line for a range of NO_2 concentrations (5×10^{-10} - 5×10^{-6} M) are presented in Fig. IV-B 1. The peak at 1070 cm^{-1} seems to remain constant in intensity and seems to originate from the reagents. The peak at 1246 cm^{-1} , however, varies with NO_2 concentration and can be detectable down to 5×10^{-10} M (spectrum B; Fig. IV-B 1) which is more than an order of magnitude lower than the current standard, i.e., the chemiluminescent technique (Garside, 1982). We are currently evaluating normalization procedures for the data and examining the linearity of combined SERS and RRS responses with NO_2 concentration. Once our tunable laser is online, we will use the same approach to examine the detection limits of NH_4^+ and PO_4^{++} by RRS and SERS.

Analysis of NO_2 by our combination of Raman techniques presents several potential advantages: (i) extremely low concentrations can be detected, (ii) small sample volumes are required, e.g., 1-ml of sample was reacted with 0.02-ml of sulfanilamide and naphthylethylenediamine and 0.1-ml was analyzed, (iii) spectra can be generated in 1 - 2 min, (iv) interference from coexistent chromogenic material may not be as problematic as in colorimetric techniques, and (v) inorganic salts do not interfere with Raman scattering. We clearly have improved upon the technique reported by Furuya et al. (1980) by: (i) lowering the detection limit, (ii) minimizing photodecomposition of the sample, (iii) increasing sample throughput, and (iv) simplifying sampling procedure. The linearity of response and limitations of the technique are currently being determined. Natural fluorescent products in field samples is a potential problem that will be investigated and countermeasures such as quenching agents and near IR Fourier Transform Raman (pending outside funding) will be evaluated.

Figure IV-B 1. Combined Surface-Enhanced and Resonance Raman Scattering (SERRS) spectra of azo dye complex formed with varying concentrations of nitrite. Peak due to NO_2 concentration at 1246 cm^{-1} , normalization peak at 1070 cm^{-1} . Excitation at 488 nm and 20 mW . Spectra produced by Princeton Applied Research OMA III using 120 scans, 1-sec integration time, and 10 cm^{-1} resolution. (A) Reagent blank (1.5 x scale), (B) $5 \times 10^{-10}\text{ M NO}_2$ (1.5 x scale), (C) $1 \times 10^{-9}\text{ M NO}_2$ (1.5 x scale), (D) $2.5 \times 10^{-8}\text{ M NO}_2$ (1.5 x scale), (E) $5 \times 10^{-7}\text{ M NO}_2$ (1x scale), (F) $5 \times 10^{-6}\text{ M NO}_2$ (1x scale).

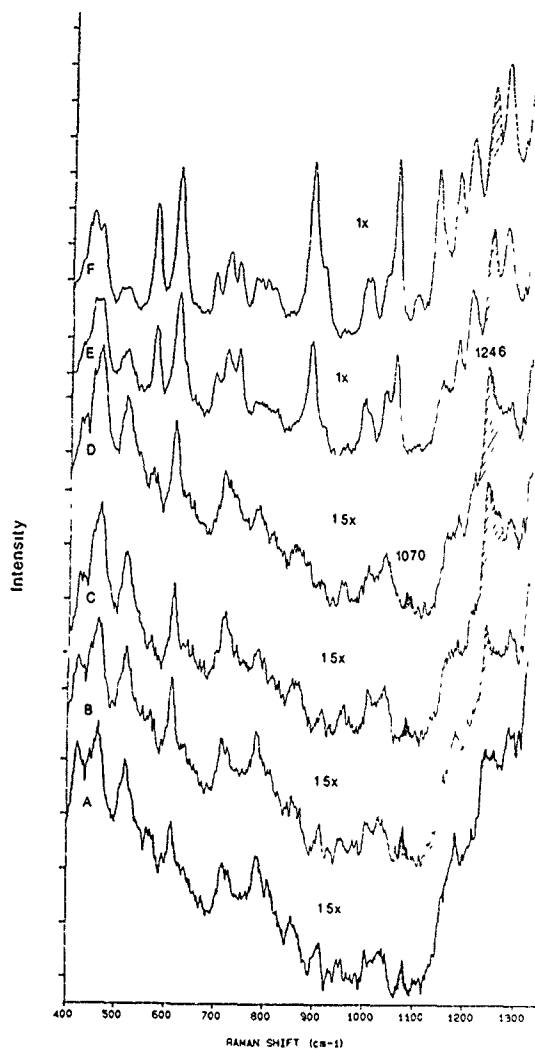


Fig. IV-B 1.

Applications of Advanced Multichannel Laser Raman
Scattering and Laser-Induced Fluorescence
Spectroscopy to Problems in Marine Chemistry

Principal Investigator: Shiv K. Sharma
Social Security No.: 213-90-7366
Telephone: 948-8476

Co-Investigator: Gordon T. Taylor
Social Security No.: 101-44-3458
Telephone: 948-8741

PROGRESS REPORT (March 1988 - December 1988)

During this grant period, our work has been focused on improving the methodology and detection limit of inorganic nutrients in seawater using a combination of resonance Raman scattering (RRS) and surface-enhanced Raman scattering (SERS) (SERRS = RRS + SERS) on silver colloids. We have found that it is possible to detect 10^{-11} M additions of NO_2^- ions in freshwater and seawater. For SERRS measurements, NO_2^- ions were derivatized as an azo dye complex (Furuya *et al.*, 1980) whose absorption spectrum overlaps with the SERS excitation profile for colloidal Ag sols. The results of this investigation were reported in a poster paper at the 1988 Spring meeting of the AGU in Baltimore, May 16-20, 1988 (Sharma *et al.*, 1988; see attached copy of poster paper for details). It was found that the 1424 cm^{-1} band corresponding to the N=N stretch of the azo dye derivative of NO_2^- varies linearly with the added concentration of nitrite (Fig. 1).

Since the AGU meeting, a flow-through SERS sampling system has been developed and its performance has been optimized (Fig. 2). Tests were conducted to determine the optimal flow rate which allowed for maximal Ag sol-analyte complex formation and minimized photodecomposition. The system was then modified based on the results of these tests. The flow-through system has a sampled volume on the order of nanoliters and requires a total sample volume of approximately 5-ml. With this system, problems associated with photodecomposition are minimized and the reproducibility of spectra from sample to sample has been substantially improved.

We have made further studies of the colloidal Ag sols with the intention of improving the enhancement of the SERRS signal. Ag and Au sols were prepared according to Lee and Meisel (1982), Sheng *et al.* (1986), Freeman *et al.* (1988), and according to our modified procedure in which concentrations of reagents (silver nitrate and sodium citrate) were increased by a factor of 13 (near solubility maximum of reagents). In accordance with other authors, we found that Ag sols reduced with citrate were the most effective SERS producers under our test conditions and were therefore used in all subsequent measurements. In tests with a 10^{-6} M standard crystal violet (C.V.) analyte, the sols made with

our modified protocol yielded the maximum SERS enhancement in the Raman spectra (Table 1). Unlike those reported in Sheng *et al.* (1986), Ag sols prepared according to Freeman *et al.* (1988) and according to our protocol show relatively small effects of sedimentation on the intensity of C.V. spectra, indicating a more uniform particle size. We therefore no longer need to sediment our sols prior to use. Ag sols prepared according to our protocol had waveumber-dependent enhancement factors of 30,300 to 62,494 relative to unenhanced C.V. spectra and were 7.0 - 7.6 times more effective than the next most effective sol (0-100 ml fraction Sheng *et al.*, 1986; Table 1).

We have repeated measurements of nitrite in seawater with these new Ag sols and our flow-through SERS system. The quality and reproducibility of the spectra has improved considerably. We are in the process of quantitative analyses of these data. We plan to present this work at the International Raman Conference in Calcutta, India, Nov. 2-6, 1988 (see attached abstract). We are also in the process of examining detection limits for phosphate, ammonium, and silicate with our improved methodology.

In the second year of the grant (Jan 1989 - Dec 1989), we propose to continue our evaluation of Raman scattering and laser-induced fluorescence multichannel spectrometric techniques for quantitative analysis of low concentrations of nutrients and selected classes of organic molecules, e.g., dissolved organic nitrogen (DON) in seawater as outlined in the original proposal. There are no changes in the second year's budget.

REFERENCES

- Freeman, R.D., R.M. Hammaker, C.E. Meloan and W.G. Fateley (1988) A detector for liquid chromatography and flow-injection analysis using surface-enhanced Raman spectroscopy. *Appl. Spectrosc.* 42, 456-460.
- Furuya, N., A. Matsuyuki, S. Higuchi and S. Tanaka (1980) Determination of nitrite ion in waste and treated waters by resonance Raman spectrometry. *Water Res.*, 14, 747-752.
- Lee, P.C. and D. Meisel (1982) Adsorption and surface-enhanced Raman of dyes on silver and gold sols. *J. Phys. Chem.*, 86, 3391-3395.
- Sharma, S.K., G.T. Taylor and K. Mohanan (1988) Detection of low concentrations of nitrite in seawater with combined surface-enhanced and resonance Raman scattering. *EOS*, 69, 373 (abstract).
- Sheng, R.-S., L. Zhu and M.D. Morris (1986) Sedimentation classification of silver colloids for surface-enhanced Raman scattering. *Anal. Chem.*, 58, 1116-1119.

Table 1. Comparison of SERS Intensities for Variety of Ag Sols
(Analyte = 10^{-6} M Crystal Violet)

Sol ^a Fraction	Abs ^b Max	Raman Intensities ^c			Enhancement Factor ^d		
		1175.6	1371.7	1620.9	1175.6	1371.7	1620.9
(mL)	(nm)	(cm ⁻¹)			(dimensionless)		
(w/o SERS)	589.9	157	184	169	1	1	1
Sheng <i>et al.</i> (1986)							
0-100	418.9	43599	41791	78138	4902	4009	8161
100-200	418.9	5983	5597	9180	340	272	485
200-300	418.9	3216	2878	4815	273	208	379
300-400	417.6	5886	5888	10093	438	374	697
400-500	420.2	9396	8955	15663	320	260	495
Freeman <i>et al.</i> (1988)							
0-500	418.9	10946	10538	19929	149	122	251
0-100	417.6	4793	4594	8435	86	70	141
100-200	417.6	7206	6733	13179	123	98	208
200-300	416.2	3684	3475	6121	62	50	96
300-400	417.6	6972	6490	12668	119	94	200
400-500	417.6	3714	3568	5942	62	51	92
13x							
0-500	445.6	42667	44073	83490	34378	30300	62494

a - Silver sol prepared according to citation and sedimented 10-d, except for 0-500 fraction. 13x = original recipe concentrated thirteen-fold.

b - Spectral absorbance maximum of analyte-sol complex.

c - Baseline-corrected peak intensities.

d - Compared to crystal violet without SERS, corrected for beam attenuation.

FIGURE CAPTIONS

Figure 1. Variation of SERS intensity at 1424 cm^{-1} (N=N stretch) for azo dye derivative as a function of added nitrite to seawater. Y-intercept represents a background concentration of $0.25\text{ }\mu\text{M}$ nitrite in the seawater. Excitation = 488.0 nm , 10 mW at sample, slit = $200\text{ }\mu\text{m}$, exposure time = 1 sec , 60 scans.

Figure 2. Schematic of flow-through SERS sampling system developed at the Hawaii Institute of Geophysics. Pumping system is a multichannel peristaltic pump with matched flows from each pump head.

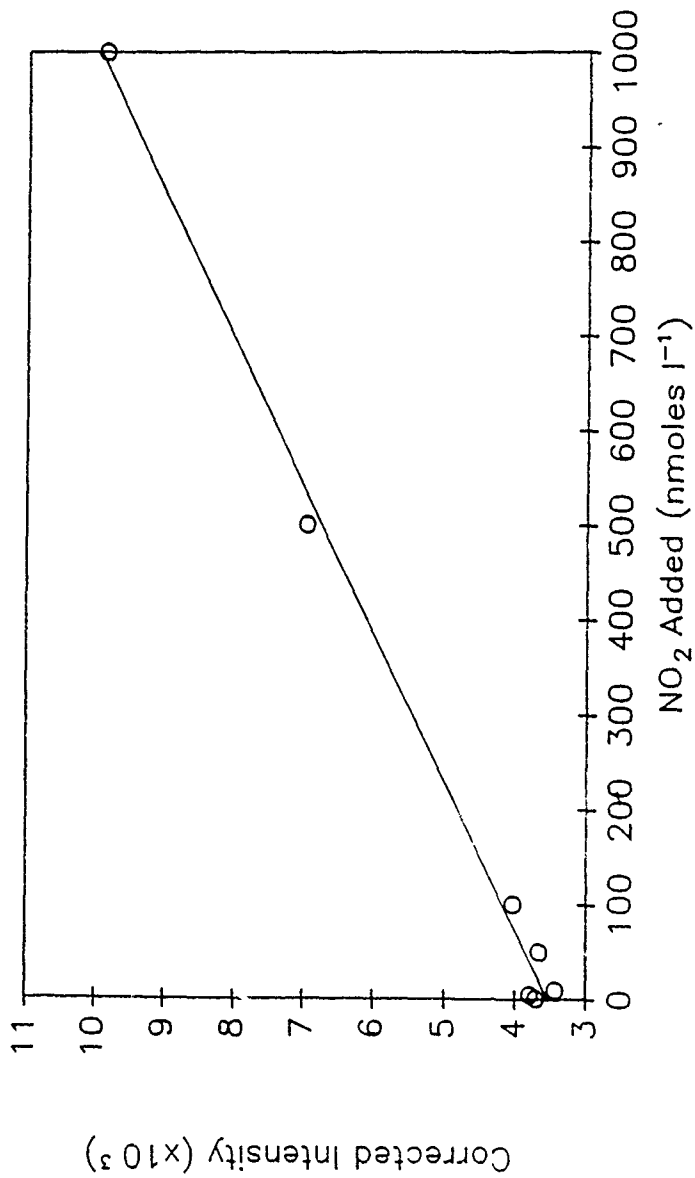


Fig. 1

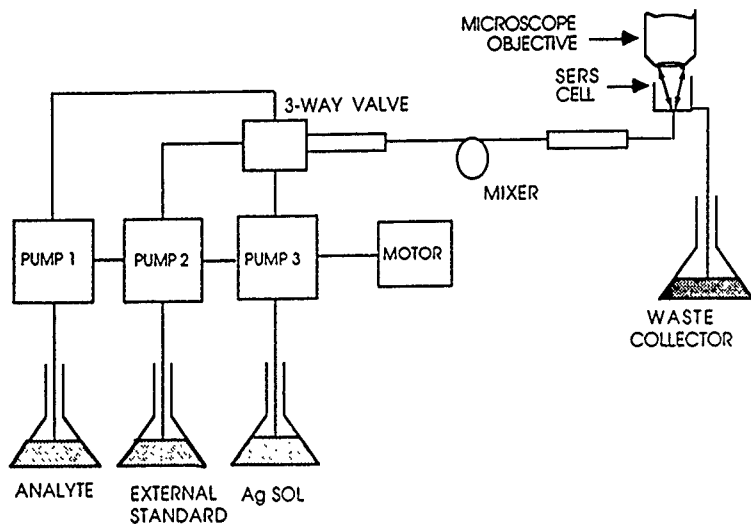


Fig. 2

AUG-15-94 MON 13:47

MICROSPACE INST

FAX NO. 2143889370

P.01

Microfilm Camera

MICROSPACE INSTRUMENTS, INC.

4751 WILBURTON DR. PO BOX 270982 DALLAS, TX 75227

TELEPHONE 214-388-0461 FAX 214-388-9370

CAGE CODE 27175

QUOTATION

QUOTATION NO. 40815-09

DATE: 08/15/94

TO: UNIVERSITY OF HAWAII

FAX: 808-956-5373

ATTN: MR. STEVE POULAS

P/N FMF-35-42C FLOW MICROFILM CAMERA

QTY 1 @ 95,166.00

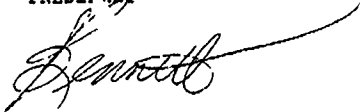
**TERMS: 15% DOWN PAYMENT WHEN ORDER IS PLACED, THEN, PROGRESS
PAYMENTS OF 15% PER MONTH.**

DELIVERY: 16 WKS ARO

**WE APPRECIATE THE OPPORTUNITY TO MAKE THIS QUOTATION AND LOOK
FORWARD TO RECEIVING YOUR ORDER.**

KIND REGARDS,

**STANLEY A. BENNETT,
PRESIDENT**



Applications of Advanced Multichannel Laser Raman
Spectroscopy to Problems in Marine Chemistry

S. Sharma and G. Taylor

1989 Progress to Date

Although measurements of all major nutrients have been performed, our work thus far has focused on nitrite in order to optimize our system and identify problems and limitations. Initially, we developed our flow injection sampling cell, silver colloid formulation, and multichannel SERRS detection using crystal violet as an analyte. Our paper, entitled "Optimization of a Flow Injection Sampling System for Quantitative Analysis of Dilute Aqueous Solutions using Combined Resonance and Surface-Enhanced Raman Spectroscopy (SERRS)", describing our technique has just been accepted for publication by Applied Spectroscopy (Taylor *et al.*, 1989). With 10^{-6} M crystal violet (CV) as an analyte, we obtained SERRS enhancement factors of $3.5 - 6.2 \times 10^4$ over CV without Ag-colloid (RRS). We found that SERRS activity is dependent upon the colloid preparation technique, time elapsed after mixing analyte with colloid, and excitation wavelength. We have been able to obtain spectra for CV as dilute as 1×10^{-12} M.

Using the azo dye derivative of nitrite (Grasshoff, 1983) and SERRS spectrometry, we obtained Raman spectra for 10^{-6} M nitrite in seawater which are much improved over Resonance Raman spectra such as presented by Furuya *et al.* (1980) (Fig. 1; note scaling factor). We have found that the quality of these spectra is pH-dependent and best results are obtained at $\text{pH} \leq 7.2$ (Fig. 2). Excellent standard curves with high correlation coefficients ($r^2 = 0.989 - 0.999$) and near zero

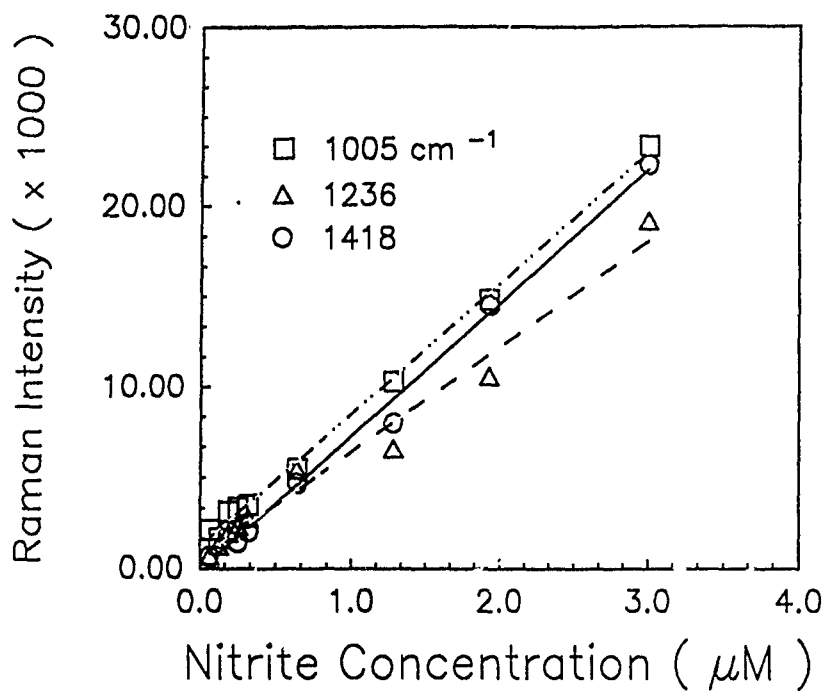


Figure 3. Standard curve for nitrite in seawater determined by baseline-corrected peak intensities of SERRS. Actual nitrite concentrations determined colorimetrically (Analytical Services). Least squares regressions for three peaks: 1005 cm^{-1} - $y = 7235x + 1252$, $r^2 = 0.999$; 1236 cm^{-1} - $y = 5819x + 587$, $r^2 = 0.989$; 1418 cm^{-1} - $y = 7371x - 109$, $r^2 = 0.996$.

intercepts were obtained for 0-3 μM additions of nitrite to seawater using baseline-corrected peak intensities for several peaks (Fig. 3). Colorimetric analysis of our seawater blank and reagents indicated a background nitrite contamination of 63 and 11 nM/assay, respectively. As a result of these relatively high contamination levels, empirical determination of our limit of detection (LOD) has not been possible thus far. We are currently taking precautions to reduce contamination problems, such as using methanol-washed and recrystallized reagents and UV-oxidized seawater to determine our LOD directly. Approximate LOD's can be calculated as three times the standard deviation of the intercept/slope (Womack *et al.* (1987) which yields values of 6 - 12 nM. Given our contamination problems and our experience with distilled water, we are confident that we can produce lower LOD's with better reagents and cleaner seawater.

We have analyzed nitrite from offshore depth profiles (20-1000 m) on two occasions and have encountered difficulty in accurately determining corrected peak intensities or areas due to variable baseline drift caused by fluorescence. To address the fluorescence problem, we analyzed untreated subsamples from the nutrient bottle casts using our SERS protocol to examine the distribution of dissolved organic matter (DOM) that may cause fluorescence. We have obtained distinctive SERS spectra for each depth indicating compositional differences in DOM with depth (Fig. 4). As an example, Figure 4 presents SERS spectra from samples from the base of the euphotic zone (130 m) and from the aphotic zone (1000 m). Spectra from both samples are obviously complex and contain a great deal of structural information. These spectra have some common features and many dissimilarities. For example, both samples share strong vibrational bands at 1362.8 and 1649.4 cm^{-1} which may be attributable to ring breathing mode of a single aromatic ring (Ar) and double ring breathing mode (Ar-Ar; e.g., naphthalene), respectively. Aromatics are notoriously fluorescent. Without detailed study by fractionation procedures and introduction of internal reference standards, we cannot confidently make assignments for other bands at present. The low frequency bands of the 1000 m spectrum appear to be more complex and have greater relative intensities than those of the 130 m spectrum suggesting some compositional differences between the DOM present at these depths.

Figure 5 presents the depth distribution of peak integrals for one minor (1004 cm^{-1} ; breathing mode of heterocyclic compound such as pyridine) and two major features. Spectra were baseline corrected to compensate for fluorescence by computer-generated polynomials. The relative abundances of all three vibrational bands (1004, 1363, and 1649 cm^{-1}) appear to vary with depth. Confidence in these data, however, are

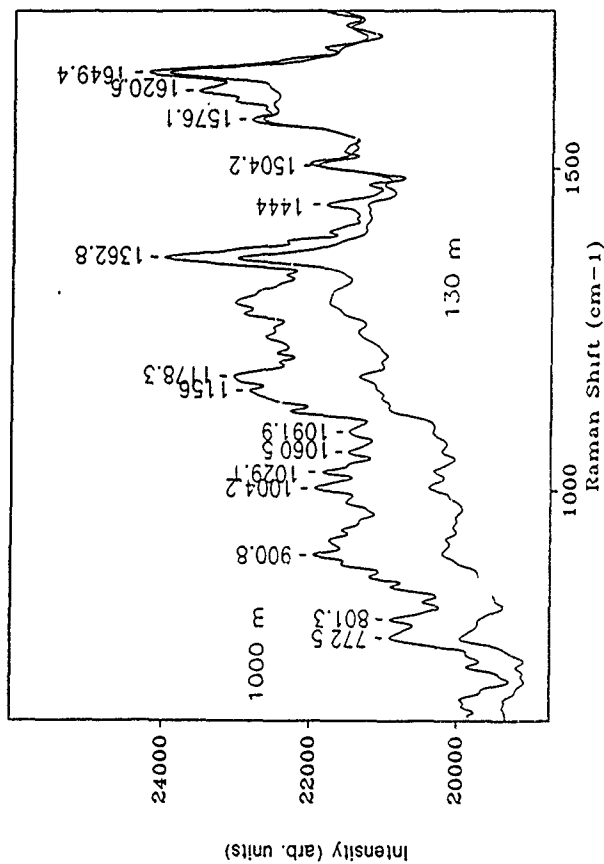


Figure 4. SERS spectra of filtered seawater collected from 130 and 1000 m at Hawaiian Ocean Time-series station (100km offshore; June 1989).

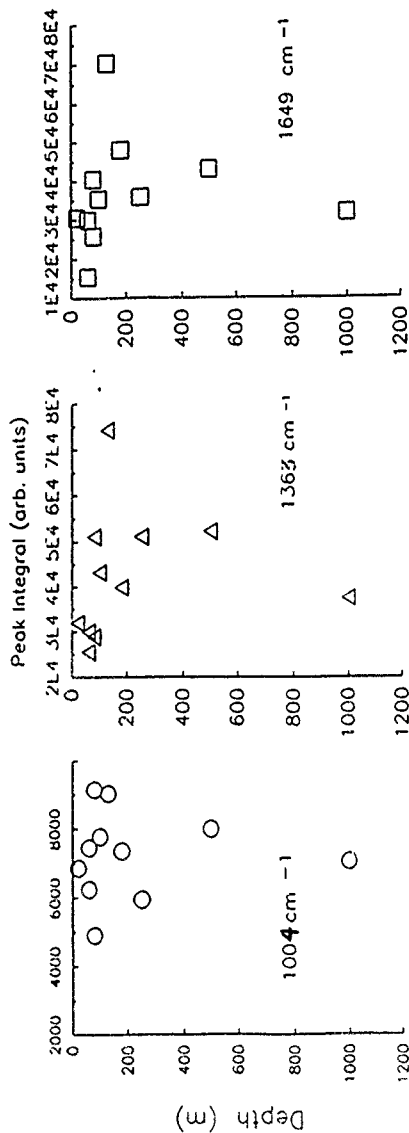


Figure 5. Vertical profiles of baseline-corrected peak integrals for three dominant spectral bands attributable to aromatic compounds.

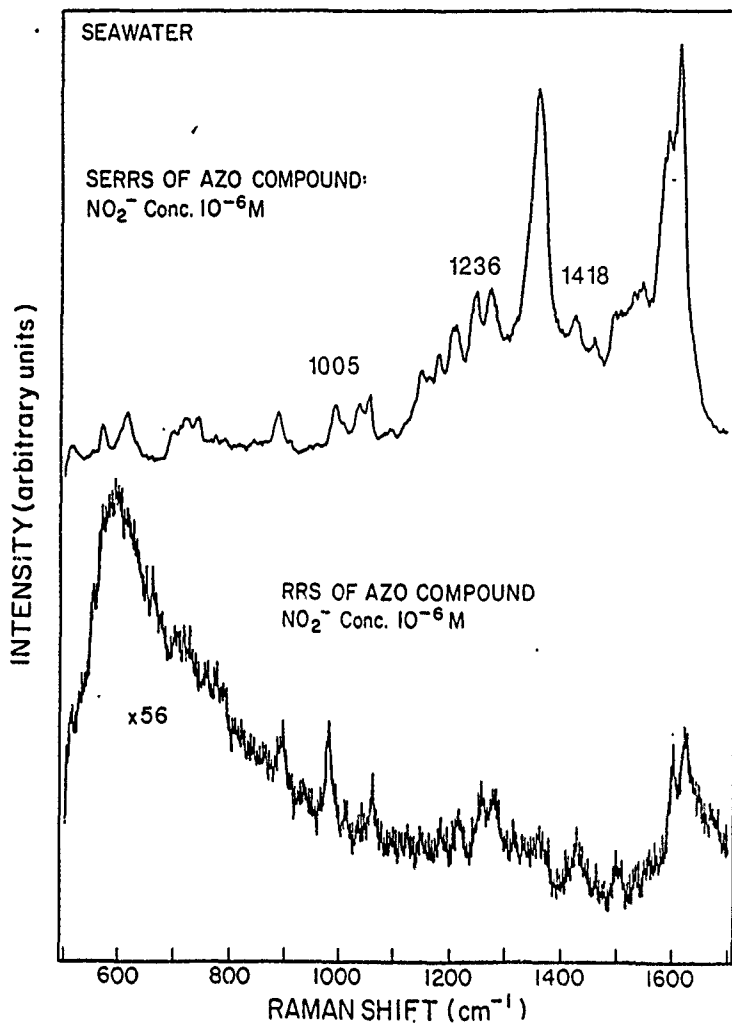


Figure 1. Combined Surface-Enhanced and Resonance Raman (SERRS) spectra of azo dye complex formed with 10^{-6}M nitrite addition to seawater (upper trace) compared to Resonance Raman scattering (lower trace).

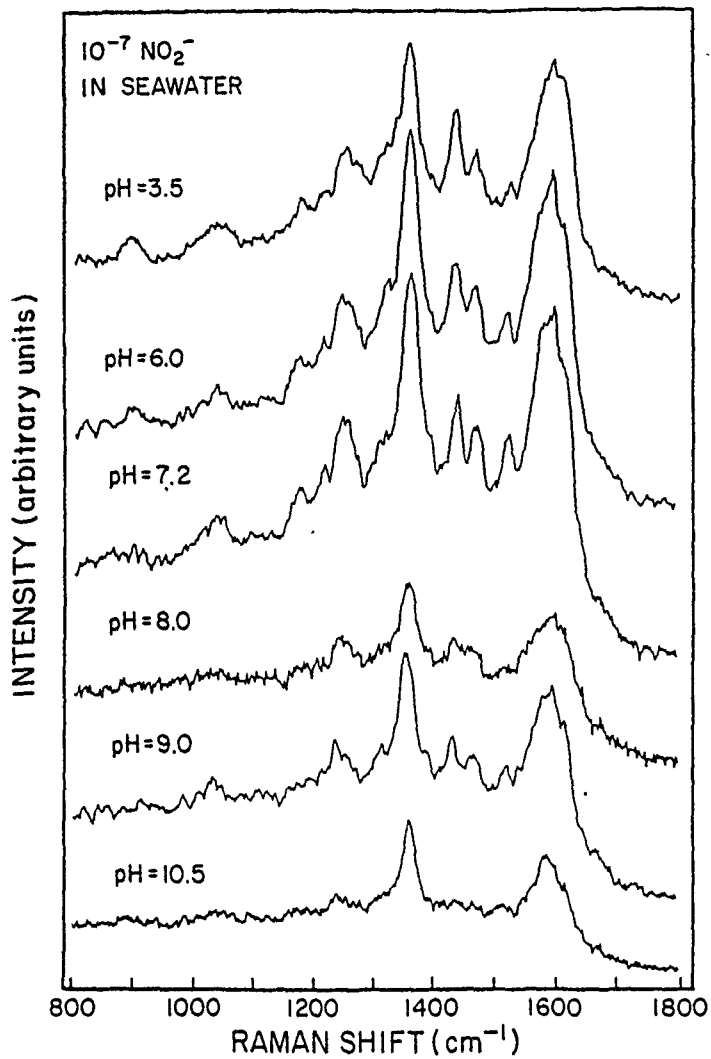


Figure 2. pH dependence of SERRS for azo dye derivative for 10⁻⁷M nitrite in seawater. pH adjusted after azo dye formed.

constrained by three correctable limitations: (i) points represent single samples, i.e., no replication due to limited sample, (ii) fluorescence varies with depth so baseline is approximated, and (iii) possible contamination of flow injection system from previous samples.

We have observed that the baselines of our nitrite spectra vary with depth presumably due to varying concentrations of fluorophores which makes quantitative analysis of seawater from different sources difficult with our current system. Since the seawater diluent for our nitrite standards is from a single source, our standard curves are by fluorescence. The observed depth-dependence in the concentrations of aromatic materials determined by direct SERS analysis supports this supposition. We are in the process of modifying our system to operate with near IR excitation so that we may produce fluorescence-free SERS spectra.

Analysis of NO_2 by our combination of Raman techniques presents several potential advantages: (i) low concentrations can be detected, (ii) small sample volumes are required, e.g., 1-ml of sample was reacted with 0.02-ml of sulfanilamide and naphthylethylenediamine and 0.1-ml was analyzed, (iii) spectra can be generated in 1 - 2 min, (iv) interference from coexistent chromogenic material may not be as problematic as in colorimetric techniques, and (v) inorganic salts do not interfere with Raman scattering. We clearly have improved upon the technique reported by Furuya *et al.* (1980) by: (i) lowering the detection limit, (ii) minimizing photodecomposition of the sample, (iii) increasing sample throughput, and (iv) simplifying sampling procedure. Natural fluorescent products in field samples is a problem that will be corrected using near IR Fourier Transform Raman spectrometry and SERS or UV-RRS.



Command/Ranging System

QUOTATION

Marine Instruments
P.O. Box 488
Cataumet, MA 02534
(508) 553-8317
FAX (508) 554-4496

Marine Instru
217 Middlesex Tur
Burlington, MA 0
(817) 270-
FAX (817) 270-

TO: UNIVERSITY OF HAWAII
DEPT. SOEST
2525 CORREA ROAD

HONOLULU, HI
USA 96822
LUIGI POZZI

PAGE 1 OF 1 PAGES

DATE OF QUOTE

03-Aug-1994

QUOTATION NUMBER

M94-234

ESTIMATED
SHIPPING DATE

45 DAYS ARO

TERMS: NET 30 DAYS

REF YOUR TELEPHONE REQUEST

IN RESPONSE TO YOUR INQUIRY REFERENCED ABOVE
EG&G IS PLEASED TO QUOTE AS FOLLOWS:

ITEM	QTY.	MODEL NO.	DESCRIPTION	UNIT PRICE	TOTAL
1	1	09055-00008	MODEL 8011A ACOUSTIC COMMAND/ RANGING SYSTEM DECK UNIT (IN PORTABLE SEALED CASE). OPERATES ON 116V OR 220 VAC.	9500.00	9500.
2	1	A1002-648010	MODEL 8012A ACOUSTIC COMMAND/ RANGING SYSTEM TRANSDUCER WITH 67 METERS CABLE. USED WITH 8011A. NOT MATCHED WITH 8011.	3600.00	3600.
3	1	09055-00085-10	8013A DIAGNOSTIC CABLES & SPEAKER FOR TESTING OF 8201/2 WITH 8011A	650.00	650.

1. THIS QUOTATION VALID FOR A PERIOD OF 60 DAYS.
ALL PRICES ARE F.O.B. ~~EX WORKS~~ MA
EXCEPT AS NOTED.

TOTAL

813750.

2. THIS QUOTATION AND ANY ACCEPTANCE THEREOF IS SUBJECT TO
(a) APPLICATION U.S. EXPORT CONTROL LAWS AND REGULATIONS AND
(b) LIMITED TO THE TERMS AND CONDITIONS ON THE FACE AND REVERSE
SIDE HEREOF.

3. DELIVERY AS QUOTED IS BASED ON CURRENT PRODUCTION AND
INVENTORY LEVELS, AND ALL UNITS ARE SUBJECT TO PRIOR SALE.

EG&G
MARINE INSTRUMENTS

J23

VICKI BARR
MARKETING ASSISTANT